NUMERICAL REPRESENTATIONS OF FLUID MIXING.

by

NIGEL HOWARD DAVIES B.Sc.(Hons).

A thesis submitted in partial fulfilment of the requirements

of the University of Glamorgan/Prifysgol Morgannwg

for the degree of Doctor of Philosophy.

The research programme was carried out

in collaboration with Brookfield Viscometers Ltd.

The Department of Mathematics and Computing,

The University of Glamorgan,

Mid Glamorgan.

CF37 1DL.

June 1993.

CERTIFICATE OF RESEARCH.

This is to certify that, except where specific reference is made, the work presented within this thesis is the result of the investigation undertaken by the candidate.

Candidate Nigel H. Davies

Director of Studies R.W. Williams.

DECLARATION.

This is to certify that neither this thesis or any part of it has been presented or is currently being submitted in candidature for any other degree other than the degree of Doctor of Philosophy of the University of Glamorgan/Prifysgol Morgannwg.

Candidate Nigel H. Davies.

CONTENTS.

ACKNOWLEDGEMENTS.

SUMMARY.

CHAPTER 9 SUMMARY, CONCLUSIONS AND RECOMMENDATIONS FOR FUTURE WORK.

Acknowledgements

Firstly, I wish to acknowledge my sincere gratitude to my director of studies, Dr. R.W. Williams, and to my supervisor Dr. D.G. Knight for their help, encouragement, guidance and constructive criticism during this research project.

Secondly, I am grateful to S.E.R.C for their financial support during the last three years.

Lastly, I would like to express my appreciation to my parents for their support and constant encouragement during the period of accomplishing this thesis.

SUMMARY

The work contained within this thesis is concerned with a theoretical investigation of both laminar and thermally driven types of cavity flow, together with an analysis of their associated mixing processes which find applications to industrial mixing and also to the environment. The mixing efficiency has been viewed from two perspectives namely the tracking of a selection of fluid particles, and also the simulation of the dispersive mixing of a coloured fluid element as carried along by the flow. This thesis also incorporates features of both Newtonian and a wide range of non-Newtonian fluids.

Chapter 1 provides the necessary background to the thesis and outlines the historical developments and the many applications of fluid flow, whilst also reviewing the main characteristics of a broad spectrum of non-Newtonian fluids.

This is followed in Chapter 2 by a comprehensive review of much of the accomplished work within the field of fluid flow and mixing, viewed from both experimental and numerical simulation perspectives. Also contained within this chapter is an overview of the relatively new science of chaos theory which finds applications in the mixing process.

Chapters 3 and 4 are concerned with the derivation and numerical solution of the complex, non-linear mathematical equations which are used to simulate the driven cavity flows, the main results of which may be seen in Chapter 5.

Chapter 6 contains the successfully completed work on simulating the Rayleigh-Benard thermally driven cavity flow problem. Consideration is given to the derivation of the governing flow equations together with an outline of their numerical solution supplied by a version of the A.D.I method. The main results and discussion of this research which incorporates a variety of fluid models of non-Newtonian fluids may be seen in Chapter 7.

Chapter 8 features a unique derivation and numerical solution of a modified version of the Lorenz equations which were developed to capture the essential features of thermal convection for a wide variety of non-constant viscosity fluids. The novel results produced are also presented, discussed and reviewed in this chapter.

Chapter 9 concludes this thesis with a summary of the successfully completed research work, and also provides a list of possible suggestions and recommendations for future work, which would further develop and enhance the present understanding of fluid flow and the corresponding mixing processes.

CHAPTER 1

INTRODUCTION

This thesis presents research work undertaken into the numerical simulation of fluid flows, obtained within the confines of a closed impermeable upright square cavity. Consideration is given to the mixing and thermal convection processes occurring within this configuration for both Newtonian and certain non-Newtonian fluids.

1.1 HISTORY AND DEVELOPMENT OF FLUID FLOW.

The flow of fluid is something with which mankind has been familiar since the earliest times, and its uses from both a domestic and an engineering viewpoint have been readily exploited. The first studies concerning fluids seem to have been carried out by the Egyptians as far back as 3000 B.C and were used in connection with ship building. Sometime later Archimedes discovered the fundamental law of buoyancy, but no real study of fluid motion itself arose until the time of Leonardo da Vinci, the famous artist and scientist. The nature and flow of fluid has subsequently been analysed by many very famous mathematicians including such notable persons as Galileo, Newton, Torricelli, Bernoulli, Laplace and others. In recent times, towards the end of the last century, many mathematical advances in the study of

fluid flow were achieved by Reynolds, Navier, Stokes, Prandtl and Von-Karman.

The equations which govern the the flow of fluid motion are complex and not many analytical solutions can be found. However, with the development of high powered digital computers, the solutions of these equations can now be approximated through numerical techniques. Due to these computing advances and improved numerical analysis techniques much interest has been re-awakened in the field of fluid flow, the study of which has many important applications to the environment in which we live.

1.2 APPLICATIONS OF FLUID FLOW.

The many applications of fluid flow analysis make it one of the most vital and fundamental of all engineering and applied scientific studies. The flows of fluids in pipes and channels make its study important from both a domestic and civil engineering viewpoint. The nature of fluid flows in machinery such as pumps, compressors, heat exchangers, jet and rocket engines and the like, make its understanding vital to all aspects of mechanical engineering. The flow of air over objects has extensive use in the design of cars, aircraft, missiles and rockets etc., where great lengths are undertaken to ensure the resulting shape is as streamlined as possible hence reducing drag.

The advances in computer technology in recent years and improvements in mathematical modelling skills, have now made it possible for the study of air flow through very complex geometries such as engine turbines. This is of great benefit to the manufacturer as the analysis of such flows can be studied in a cost effective and illuminating manner, and is a major step forward in engineering design for the future.

Fluid flow analysis also has extensive use in many geophysical and enviromental fields such as geology, meteorology, hydrology and oceanography, since the atmosphere and the vast oceans which cover approximately two thirds of the world are fluids, underlining the importance of its study. The major source of investigation within these fields pertains to the dispersion and transportation of chemical pollutants arising mainly from heavy industry, which contribute to the 'greenhouse effect' and acid rain, as well as contamination of rivers and vast oceans of the world.

Arguably one of the major applications of fluid flow analysis occurs in the industrial process of fluid mixing. The industries which use the mixing process are many and varied and range from the biotechnological, chemical, petroleum and water industries to breweries and feedstock industries. Examples from within such

industries include the mixing of paints, pharmaceuticals and the fermentation of broths.

However, apart from its almost universal industrial use, mixing is not a very well understood process, and most mixing problems are studied on a case by case basis. This is probably due to the fact that the theoretical analysis which governs the mixing of fluids is complex and difficult. The methods with which fluids are mixed in industry are diverse but many basically consist of a stirrer immersed in a tank of fluid and rotated until the desired consistency of mix is obtained.

As an example of the mixing process, we consider the flow produced by a sometimes heated multiple flight extruder screw, shown in fig(1.1*) which provides a non-homogeneous three dimensional mixing flow. This device, apart from applications to fluid mixing, is also used for fabrication of thermoplastics, the production of coated wires for electrical purposes, and plastic pipes for domestic use and in the chemical industries.

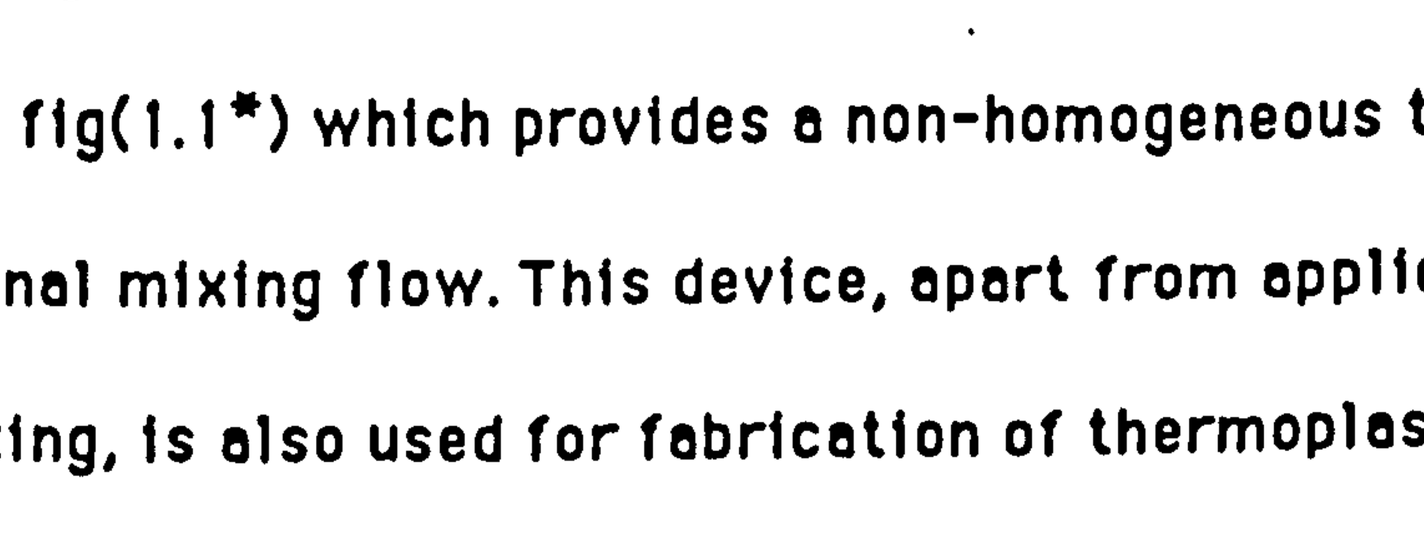

Figure (1.1*)

Diagram of a multiple flight extruder screw.

N.B.(* figures are those in the text, the remainder in appendix).

1.3 TYPES OF FLUID.

A fluid by definition is a substance which cannot withstand any tendency by applied forces to deform it, in a way which leaves its volume unchanged. It should be noted however, that the fluid may offer resistance to the deformation and this property is known as the viscosity of the fluid. In simple terms it is a measure of the thickness or 'stickiness' of the fluid. Fluids are usually classified into two groups, either liquids or gases. A liquid possesses intermolecular forces of attraction which hold it together, such that it has a definite volume but no shape. A gas on the other hand, consists of molecules in random motion which tend to disperse the gas, such that it has no definite volume or shape. A gas is highly compressible, whereas a liquid is not. In this thesis consideration will predominantly be given to fluids of the incompressible liquid variety, and the mathematical models describing the flow of such fluids will be derived from the fundamental principles of continuum mechanics. Using this theory, it is supposed that the macroscopic behaviour of the fluids considered is the same as if it were perfectly continuous in structure. Then the physical quantities such as mass and momentum associated with matter contained within a given small

volume, can be regarded as being spread uniformly over that volume instead of as in reality being concentrated within a very small part of it.

Fluids can further be sub-divided into two further categories, being either Newtonian or non-Newtonian.

Apart from common Newtonian fluids such as air and water which possess a simple chemical structure, the majority of everyday fluids encountered are of the non-Newtonian variety and consist of soaps, paints, detergents and food products, which possess a complex non-linear structure. We shall now briefly consider the relevant features of such fluids.

1.3.1 NEWTONIAN FLUIDS.

The viscosity of these fluids remain constant with time and are unchanged by any applied forces of deformation. Examples of such fluids are water, air, syrup and glycerol under normal use, at constant temperature and pressure. However, the viscosity of Newtonian fluids are known to vary with temperature, a classic example being that of motor oil.

1.3.2 NON-NEWTONIAN FLUIDS.

These are the most common type of everyday fluid (apart from air and water) and are fluids for which the viscosity generally changes with either time or applied force, at constant temperature and pressure, although counter examples exist such as the non-Newtonian constant viscosity elastic 'Boger fluid'.

Non-Newtonian fluids can be further classified as:-

(In this thesis the following terminology is adopted as generally there is no clear definition of these types of fluid.)

i) Pseudoplastic fluids, which are also known as shear-thinning fluids, and are fluids whose viscosities decrease with increasing shear forces. Pseudoplastic fluids are the most common type of non-Newtonian fluids and include various body fluids, pharmaceuticals, liquid food products, soaps and detergents.

ii) Dilatant fluids, or shear-thickening fluids, are fluids whose viscosities increase with increasing shear forces. These are fairly rare but various concentrations of starch slurries and wallpaper pastes exhibit this property.

iii) Thixotropic fluids are fluids whose viscosities decrease with time but exhibit no change with any applied shear-rate. The constant stirring of such fluids can result in a substantial lowering of their viscosity with respect to time. Gradually, however, after stirring ceases the fluid returns to its original viscosity. Examples of thixotropic fluids include various food sauces and some non-drip paints.

iv) Rheopectic fluids, also known as anti-thixotropic fluids are very rare and exhibit the property that their viscosities increase with time, at a constant deformation rate. This phenomenon is known as rheopexy, and an example of such a fluid is alkaline perbunan latex solution, Walters[112].

v) Viscoelastic fluids exhibit an elastic type of behaviour, a liquid equivalent of a rubber band, and are invariably gel like materials. Examples of viscoelastic fluids are shower gels, some doughs, egg white, polymer solutions and melts.

vi) Plastic fluids have the property of being able to suspend particles through a property known as 'apparent' yield stress. These materials behave as solids under 'small' stresses and as fluids after the critical value of the stress has been exceeded.

Examples of such fluids include common domestic liquid abrasive cleaners and thick pastes. However, we shall not consider these types of fluids within the thesis due to difficulties encountered in numerical simulation.

1.4 THE REYNOLDS' AND RAYLEIGH NUMBERS.

The two main governing parameters which affect the cavity flows considered in this thesis are the Reynolds' and Rayleigh numbers respectively, both named after the eminent pioneering persona in the field of fluid dynamics. A brief discription of each is now given.

1.4.1 THE REYNOLDS' NUMBER.

Fluid flows have become classified by use of a dimensionless parameter known as the Reynolds' number (Re) which provides the ratio of the inertial to the viscous forces in the flow. Using this parameter, there has generally emerged three distinct types of flow regimes occurring within the mixing process.

There now follows a rough guideline outlining the various types of flow based on a Newtonian fluid.

Re $\ll$ 10

Within this region primary flow is seen to occur, where the inertial forces are negligible and the viscous forces dominate the flow. When the Reynolds' number tends to zero the flow is known as creeping or Stokes flow.

10 $<$ Re $\lesssim$ 1000

This is known as the laminar or streamline region wherein the flow is said to be at medium to high speed and secondary inertial flow occurs. The inertial forces are significant and have a greater bearing on determining the nature of the flow. Due to these factors the flow tends to become more unstable as the Reynolds' number increases.

Re $>$ 1000

Here the flow generated is at very high speeds. The region is known as the transitional region, the onset of which leads to turbulent flow. When turbulence occurs the flow breaks down, becoming very random and disordered. This type of flow is ideal for the mixing of certain fluids to occur quickly and efficiently. However, for this report due to limitations in numerical simulation only flows with Re $<$1000 will be considered.

1.4.2 THE RAYLEIGH NUMBER.

This is the main governing parameter influencing the flow when free convection thermally driven cavity flows are considered. The Rayleigh number (Ra), represents the ratio of the applied temperature gradient to the viscous terms and is the product of two other dimensionless variables namely the Grashof and Prandtl numbers, which are defined later in Chapter 6. At low Rayleigh numbers, corresponding to small temperature gradients, the viscous forces dominate and the flow remains static in uniform equilibrium until a certain critical threshold value is reached, whereupon organised cellular convective motion may be evidenced, as shown in fig (1.2*). For $Ra < 10^6$ the flow is ordered and streamlined, but for higher Rayleigh numbers particularly those in the range $10^7 < Ra < 10^{10}$, the flow tends to become more disordered and eventually turbulent at the very high Rayleigh numbers near the top of this range. In this thesis however, only orderly flows will be considered.

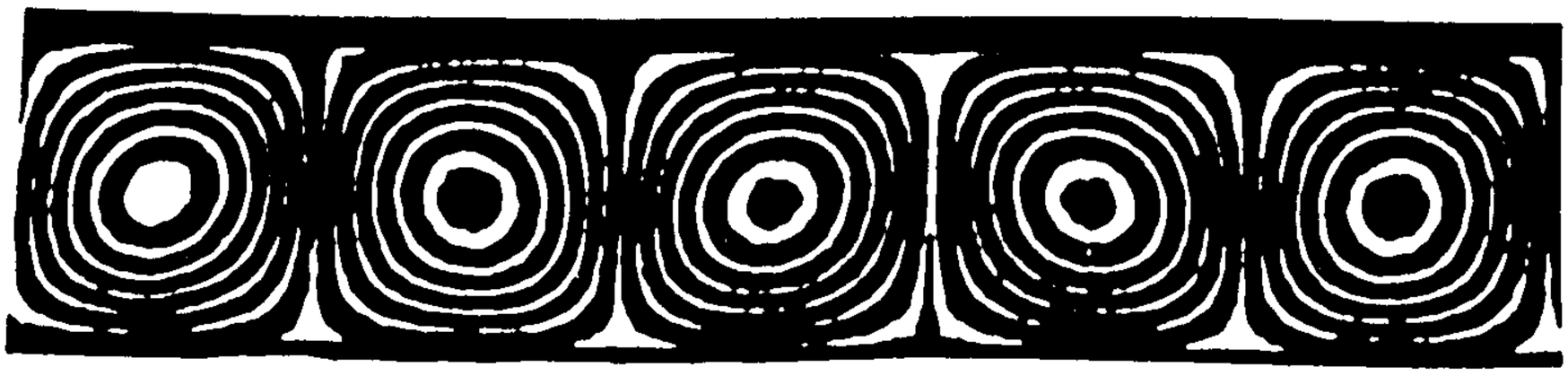

Figure (1.2*)

The Rayleigh-Benard cell configuration.

1.5 AIMS OF THE RESEARCH WORK.

In accomplishing the research work presented in this thesis we hope to gain a more thorough understanding of both laminar and thermally driven fluid flow within the cavity's geometry shown later in fig(1.3*), together with the corresponding mixing processes derived from it.

We have considered the mixing process purely from a theoretical point of view, the flow being simulated by computer modelling. The theoretical analysis of fluid flow within this geometrical configuration is complex. The simulation is obtained by numerically solving a set of coupled non-linear partial differential equations, with added complications arising when we try to simulate the flow of non-Newtonian fluids. The added complexity occurs due to the non-linearity of the fluid itself, which further increases the difficulty of the problem. Various researchers have considered flow within an enclosed cavity from an experimental standpoint, mostly for constant viscosity Newtonian fluids. Our simulated results are compared as far as possible with those obtained by physical experiment, to test whether the equations used within our proposed models accurately predict and simulate the nature of the flow generated by experiment.

Initially, to gain familiarity and understanding of the governing equations and their numerical solution, the standard test case of driven cavity flow was considered. This comprises of studying the flow patterns generated by a uniformly moving plate driven over a two dimensional square cavity, which is assumed to be of infinite length in the third dimension. This situation is a two dimensional approximation to the type of flow generated by a screw extruder fig(1.1*) discussed previously, the particular geometrical configuration shown in fig(1.3*), where for convenience the velocity component in the 'z' direction is taken to be zero.

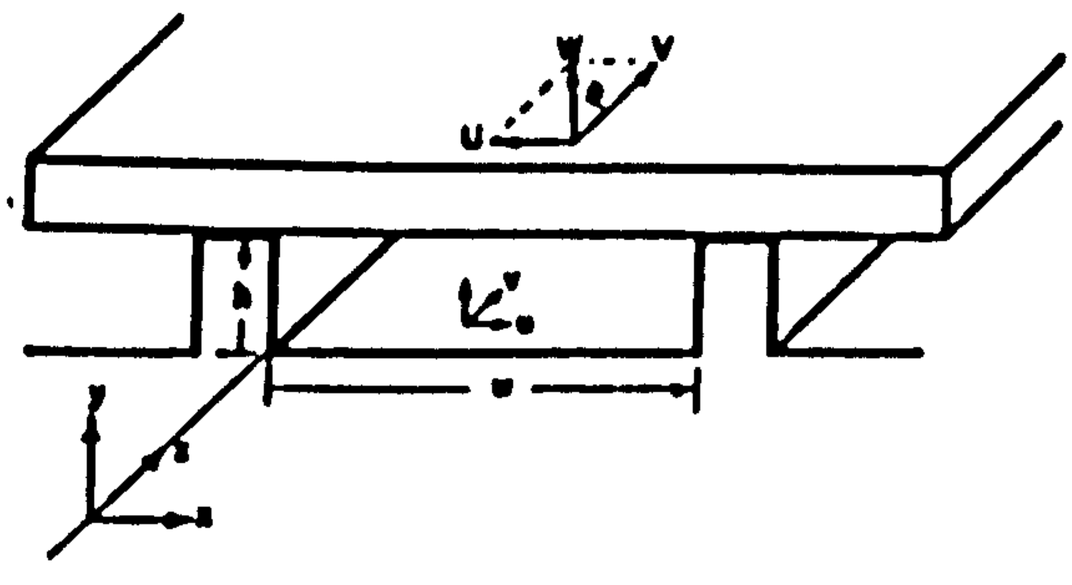

Figure (1.3*)

Diagram of the cavity geometry.

With confidence gained through our investigation and our early results showing favourable agreement with other published work for this problem, we proceeded to attempt to model various other types of cavity flow, ranging from the case whereby two walls are allowed to move simultaneously in the same or opposite directions to the novel, unique and purely theoretical case whereby all four of the cavity's walls are allowed to move in a sequential manner. This is an extension of the famous Aref[5] 'blinking vortex' system, which is a virtually unobtainable in reality, but highlights the unrestricted nature possible with computer fluid modelling.

A good indication of the efficiency of the mixing process occurring within a fluid flow can be obtained by examining the trajectories of a selection of fluid particles strategically 'placed' within the flow field. By solving the Hamiltonian structured equations governing the motion for a few particles within the cavity a numerical study of mixing can be achieved. This has been carried out for all cavity flows considered with some remarkable results indicating 'chaos' is present within certain cavity flows under relatively slow flow conditions.

Mixing can also be viewed by following the dispersive mixing of an 'injected' coloured region of fluid as it is carried along by the flow. The problem we consider is one whereby an amount of

marker dye is injected into the fluid, either Newtonian or non-Newtonian, while at rest in the cavity and then from start-up its concentration intensity is subsequently computed and plotted.

The aspect ratio of the cavity itself is also thought to play an important role in the efficiency of mixing, and has been found to provide some remarkable results, particularly for non-Newtonian fluids of the dilatant variety.

As previously mentioned one of the main interests and applications of fluid flow analysis can be found in relation to the environment we inhabit. With this in mind, a period of research was undertaken to investigate the nature of fluid flow known to exist within the atmosphere and conjectured to exist within the molten mantle of the Earth. The cause of the former fluid motion is the process of thermal convection, in which heat from the Earth's surface rises causing a stratified fluid layer to exist within the atmosphere. This layering is unstable, and gives rise to circulatory motion, the outcome of which can be seen in the formation of sand dunes in the deserts of the world. A similar method of convection is thought to occur within the mantle of the Earth, and has been put forward as an explanation of observed phenomena such as continental drift and plate tectonics[63].

The thermal convection process is in fact widespread throughout nature, evidenced not only in the Earth's atmosphere but also finds applications in the luminosity and mixing within stellar objects, insulation of buildings and nuclear reactors, and even to to growth of crystals in liquids. A simplified and much studied experimental model containing the main features of thermal convection allied to atmospheric flow already exists, and is known as the Rayleigh-Benard experiment. In this experiment a very thin layer of fluid, located between two long parallel plates is uniformly heated from below in the presence of gravity. At a critical threshold value proportional to the temperature gradient, motion is seen to occur with a regular pattern of convecting Benard cells shown earlier in fig(1.2*), simulating that occurring in the atmosphere. Most work to date seems to have been obtained using steady state governing equations with Newtonian fluids, and we aim to extend this to consider wholly time dependent flow and to incorporate some relevant features of non-Newtonian fluids. We consider the traits of viscoelasticity, thixotropy and fluids whose viscosity varies with both temperature and depth respectively, the later fluids being particularly appropriate with regards to the Earth's mantle.

The atmosphere, however, is known to behave as a turbulent fluid and the weather systems contained within it are consequently very unreliable or unpredictable, a case particularly borne out by the nature of the British weather! Lorenz[59] in 1963, motivated by the problems with the long range weather predictability, sought a way of modelling this complex phenomenon. He knew the atmosphere behaved as a turbulent fluid and the non-linear Navier-Stokes equations governing the flow were also susceptible to small disturbances, both of which would make precise weather prediction difficult. To investigate his hypothesis Lorenz used the Rayleigh-Benard system as a starting point for his research, and considered ways of drastically simplifying the system's complex equations, whilst retaining their essential features and non-linearity. Based closely on the work of Saltzman[95] but with drastic simplification, the now much celebrated and famous system of ordinary differential equations were born, which subsequently revolutionised and re-awakened much interest in the field of non-linear 'chaotic' dynamics.

Lorenz soon realised these equations were extremely sensitive to the starting conditions, such that two initially very close fluid particles could diverge from each other at an exponential rate. He also noted that in the immediate vicinity of transition from

conduction to convection, all trajectories were attracted to a finite dimensional object in space, which he termed a 'strange attractor', possessing the shape of a pair of 'butterfly wings' shown in fig (1.4*).

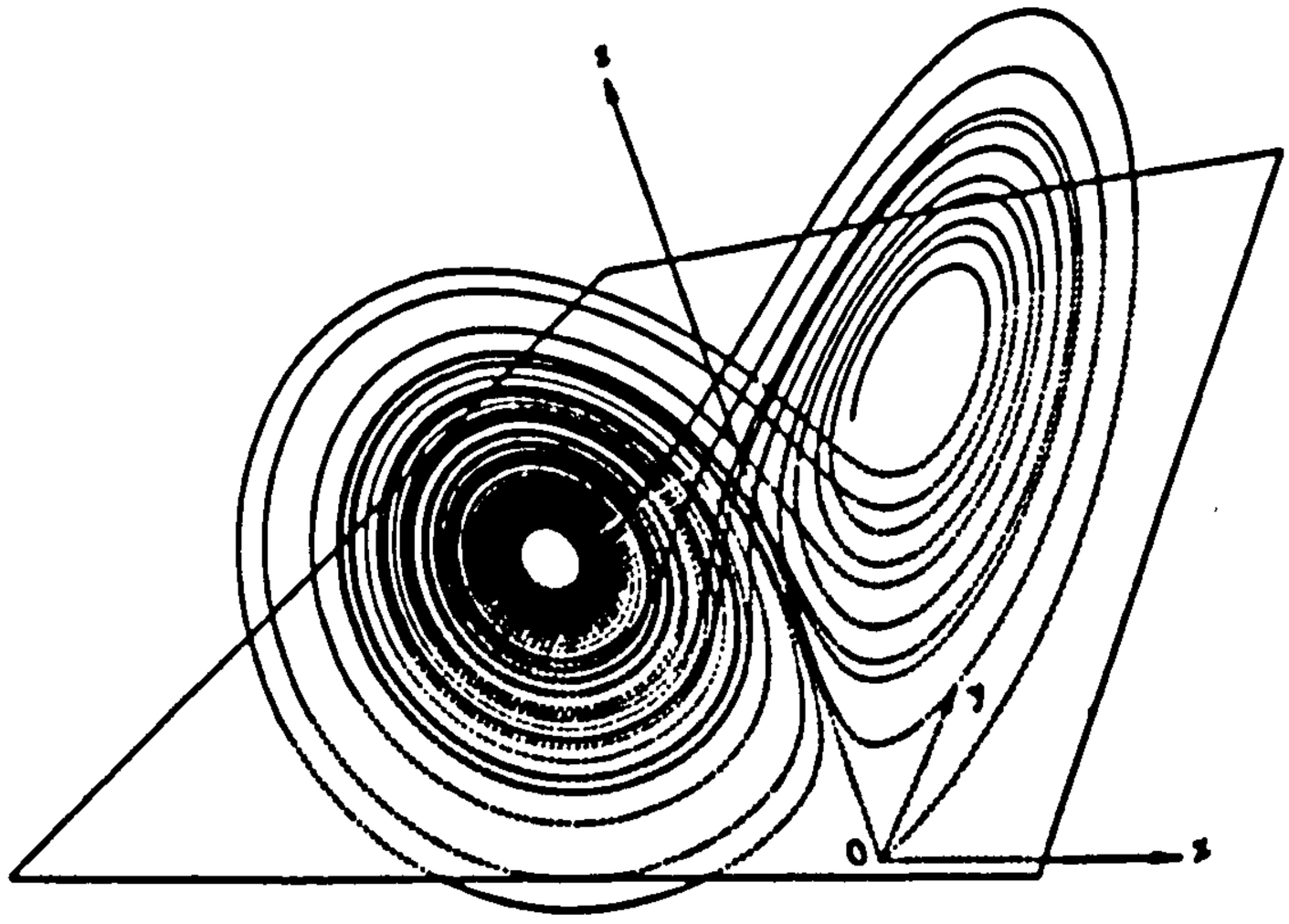

Figure (1.4*)

Diagram of the famous Lorenzian attractor.

Lorenz also noted that the trajectory motion on the attractor itself was deterministic yet totally random or chaotic, emphasising the difficulty of accurate weather prediction.

Recently, further develpoments in the field of chaos theory, consisting of the analysis of flow bifurcations, have provided an avenue for numerical simulations to play a more significant role in the simulation of fluids mixing.

In this thesis we aim to extend the pioneering work of Lorenz[59], once again to study the possibility of novel and exciting results produced by certain non-Newtonian fluids exhibiting effects ranging from pseudoplasticity to that of a weakly viscoelastic fluid. The strange attractors obtained from such approximations to the complex governing partial differential equations for the system, have been tentatively put forward as an explanation or interpretation of fluid turbulence, a still obscure and unresolved branch of science and engineering. However, the point should be made, that the motion on these strange attractors is random only in a temporal sense, unlike that of a fast flowing river for example, whose motion is random both in space and time.

The results obtained from the research outlined in this thesis are compared with those of other researchers as far as possible.

CHAPTER 2

LITERATURE SURVEY

2.1 INTRODUCTION

For this thesis a literature survey of the current information pertaining to fluid flows within an enclosed cavity of both a laminar and thermally driven variety was undertaken. In addition to this much of the current state of the art work on the relatively new theory of chaos is comprehensively reviewed. The survey's purpose is two-fold: firstly to obtain a general overview and understanding of the field in which our research interest lies, whilst gaining familiarity with the work of other researchers; and secondly to obtain experimental and theoretical results with which we may later compare and validate our own results.

The survey may be summarised as follows:-

(i) Fluid flow analysis.

(ii) Suitable numerical techniques used to obtain solutions of the governing flow equations.

(iii) Laminar driven cavity flows.

(iv) Thermally driven cavity flows.

(v) Chaos in fluid flow systems.

(vi) Experimental and theoretical investigations of fluid mixing.

2.2 FLUID FLOW ANALYSIS.

To gain familiarity with, and understanding of, fluid flow a good introductory text is Walters[111]. In this book the fundamental equations which govern fluid motion are discussed, and are found to arise as a consequence of applying Newton's second law to a moving continuum. Insight is also provided into the derivation of the rheological equations of state, which are used to model Newtonian, non-Newtonian and viscoelastic fluids. Other introductory texts providing good mathematical grounding into the field of fluid flow are Batchelor[12], Walters[112] and Bird et al[14]. Batchelor[12], in particular, provides a very comprehensive introduction into fluid dynamics, covering topics including the kinematics of flow, with applications to flows in pipes and channels, dealing with compressible, incompressible liquids and rotational flow. Bird et al[14] reviews the basic fluid dynamics outlined above, but also considers flows with non-Newtonian fluids including those exhibiting viscoelastic tendencies. Other texts we have found useful are White[115], Hughes and Brighton[47], Acheson[1], Patankhar[84], and Raudkivi and Callander[91], the latter containing a good explanation of turbulent flow.

2.3 SUITABLE NUMERICAL TECHNIQUES USED TO OBTAIN A SOLUTION OF THE GOVERNING FLOW EQUATIONS

The equations governing the flow of fluids are complex and only a limited number of analytical solutions have been obtained, and those for relatively uncomplicated fluids in simple geometries with slow flow conditions. A good review of which is available in Bodalia[16] and Havard [44]. No analytical solutions have been found for Reynolds' numbers in the range of 10 up to 1000, and so to simulate flows in this region, numerical techniques have to be employed which require the use of a substantial computer.

The two main numerical methods used to obtain a solution to fluid flow problems are the finite element method and the finite difference method, although other methods are available, but as yet have only achieved limited success when applied to non-Newtonian fluids.

The finite element method is a complicated method to understand and implement, being far more computationally involved than its rival finite difference method. However, the main advantage of the method is where the geometry is irregular. This is not the case with the present study of laminar and thermally driven cavity flow, and so the solutions are sought after using the more tractable finite difference method.

A good introduction to both methods with their applications to fluid flow is given by Crochet, Davies and Walters,(CDW)[29].

2.3.1 THE FINITE DIFFERENCE METHOD.

An excellent standard text regarding the numerical solution of mostly linear partial differential equations by the finite difference method is given by Smith[100]. The book provides a clear outline of the methods of solution, and also deals with the fundamental problems of consistency, compatibility and stability of the difference equations used to approximate the original partial differential equations (PDE's). The text also provides a good background into the direct and iterative procedures used to solve the large matrix equation systems, which arise as a consequence of using numerical techniques to provide a solution. Smith[100] does consider certain types of flow problems, but better texts regarding the application of the finite difference methods to incompressible Newtonian fluid flow problems, where the equations are more complex and non-linear are Roache[92], and Tucker[107].

The discretisation process (i.e approximating the PDE by an algebraic equation, which is then solved in its place) is well documented in latter two texts, with consideration given to the more physically intuitive control volume approach as well as the

more familiar Taylor series method of discretisation. Roache[92] in particular considers steady state and time dependent incompressible Newtonian flows in two dimensions. The two main methods of solving the flow equations by finite differences are outlined, namely, the stream function - vorticity (Ψ, ω) approach and primitive variable or (U,V,P) method.

Tucker[107] reviews work similar to Roache[92] and also includes a clear description of methods of upwinding, which are very important when considering the concentration and temperature equations, where the flow becomes very much advection dominated at higher Reynolds' and Prandtl numbers, such that the discretised equations become more unstable. The upwinding methods re-address the problem by adding the 'correct' amount of 'diffusion' into the equation, however, upwinding is far from being ideal and is very much an active area of current research, Havard[44]. Tucker[107] covers other important topics such as mesh transformation and generation, which finds a great application when the geometry is of irregular shape.

CDW[29] is an excellent text on the numerical simulation of non-Newtonian flow . This text provides insight into the governing equations of Newtonian, non-Newtonian and viscoelastic flow, as well as providing a clear outline of the solution process by finite difference and finite element methods.

Other useful texts we have found to be of great benefit when considering solution of the flow equations by various finite difference techniques are Mitchell and Griffiths[65], Young[118], Lapidus and Pinder[55], Scraton[96], Froberg[39] and Burden and Faires[19].

2.4 TWO DIMENSIONAL DRIVEN CAVITY FLOW.

The first numerical study of driven cavity flow within an enclosed rectangular geometry appears to have been conducted by Kawaguti[51] who with the aid of a small digital computer generated numerical solutions for Reynolds' numbers up to 64. Simuni, as reported by Burggraf[20], later developed this work, and considered numerical solutions of the full Navier-Stokes equations for closed cavity flows, as well as considering channel flows over forward and backward facing steps, with results being produced for Reynolds' numbers up to 1000. Mills[64], appears to have been the first to have carried out experimental work with the cavity flow set up, in an attempt to compare and validate his own numerical results. A full review of the above authors work may be found in Burggraf[20] who also published stream function, vorticity and pressure contours using steady state Newtonian fluids for Reynolds' numbers up to a maximum of 400.

A subsequent study of driven cavity flow with Newtonian fluids and steady state flow equations has been carried out by Pan and Acrivos[83], who have generated numerical solutions up to a Reynolds' number of 400, whilst further producing experimental results by rotating a wheel at different speeds over cavities of various aspect ratios generating results up to Reynolds' numbers of 2000. Later, the work of Bozemann and Dalton[17], who by using various implicit finite difference methods to yield a solution for Newtonian fluids in cavities of differing size, managed to obtain results for Reynolds' numbers of 1000. For cavities with aspect ratio of 2, the main result of both authors was the emergence of a weaker secondary, counter rotating vortex which occupies the entire lower half of the cavity.

The general results obtained by all of the afore-mentioned authors indicate that within square finite cavities at high Reynolds' numbers, the steady flow pattern obtained should consist of a single vortex with an inviscid core possessing uniform vorticity, with any viscous effects being confined td the outer 'shear' layers near the boundary. These results gave confirmation to an hypothesis originally made by Batchelor[11].

The study of driven cavity flow has ever since acquired the interest of a number of researchers, as it is the simplest example of recirculating flow with closed streamlines, and is an excellent

vehicle for the testing and validating of numerical solution algorithms. Four such workers who improved both the accuracy and acceleration to convergence of the Navier-Stokes equations within the cavity's geometry by using various implicit finite difference techniques, and also by improving the vorticity boundary approximations, are Nallasamy and Prasad[74] and Gupta and Manhoar[43] respectively, whose research we have found particularly useful. In fairly recent times two dimensional enclosed cavity flow has served as a test bed for further improvement in both finite difference and the relatively newer and more complex finte element method. A good review of numerical solutions within the cavity framework may be found in the book 'Computer Methods In Fluids [28]'. Two relevant publications contained there-in are Al-sanea et al[2] and Leonard [58], who have published steady flow results for Reynolds' numbers up to 400, together with a solution of the temperature equation for the cavity.

Chow[24] in an well written and helpful book serving as an introduction to computational fluid mechanics, considers the solution of the biharmonic stream function equation pertaining to Stokes flow within the cavity geometry, as well as producing a computer simulation of the famous Rayleigh-Benard fluid system for Rayleigh numbers up to 7000.

One of the most comprehensive studies of driven cavity flow in recent times has been produced by Cliffe et al[26] who by using the finite element method on refined grids generated solutions up to Reynolds' numbers of 1000. Olsen and Tuann[79], again using the finite element method have presented numerical solutions for recirculating flow within a square cavity for Reynolds' numbers up to 7000. The main feature of these novel results shows the break up of the main circulating vortex into two smaller secondary vorticies which occurs for Reynolds' numbers between 2000 and 3000.

A useful point of comparison with the numerical solutions obtained by the various researchers with useful analytical solutions, can be obtained by considering the nature of flow near the corners of the cavity.

Moffatt[66] and later Gupta et al[42], using dimensional arguments, have shown that near a sharp corner viscous forces tend to dominate the inertial forces such that the flow becomes virtually Stokesian. The governing equation is therefore the biharmonic stream function equation which is known to admit a separable variable form of solution in polar co-ordinates, resulting in a 4th order ordinary differential equation in terms of the polar angle, which can readily be solved subject to no-slip boundary conditions. Moffatt[66] was able to show that for angles

of incidence less than a certain critical value, the flow consisted of an infinite sequence of re-circulating eddies, while for angles of incidence larger than this value, no such recirculation of flow was obtained. Holstein and Paddon[46] have also investigated, in a theoretical sense, the flow near the sharp corner of a backward facing step. Their method assumes that in the immediate vicinity of the corner the stream function can be expanded in a power series in terms of the Reynolds' number, and incorporate their findings into a suitable finite difference scheme used to yield a numerical solution near the corner. The main features of their method are also reviewed in CDW[29]. Another useful paper concerning flows near sharp intrusive corners can be found in a paper by Fox and Sankar[40], whose major contribution involves a discussion on how to alleviate the singularities occurring at the corner points, and apply their findings to the practical case of modelling the flow in screw propellers, whose motion is governed mainly by linear P.D.E's. More recently the analysis of flow near the corner has been developed to include power law fluids, and has been investigated using a mixture of analytical and numerical techniques by Henriksen and Hassager[45].

Returning to cavity flows, some of the most recent theoretical investigational work simulating driven cavity flows has been completed by Havard[44], who using the finite element method as

Cliffe et al[26], managed to obtain steady state solutions for Newtonian fluids at various Reynolds' numbers up to 1000. In addition to this Havard[44] also considered the flow of a shear-thinning fluid within this geometry and produced steady state results for Reynolds' numbers up to 200. Havard also considered the dispersive mixing of a 'coloured' line element which involved the solution of the time dependent advection-diffusion equation. The results obtained for Reynolds' numbers up to 100 for a Newtonian fluid only are slightly artifical as the dyed line element is only allowed to be 'injected' into the cavity when the flow equations have reached steady state solutions.

Both Bodalia[16] and Havard[44] have recently considered the flow and mixing processes in more realistic three dimensional flows such as the Taylor-Couette flow, for both Newtonian and certain non-Newtonian fluids, and also contain an excellent and comprehensive review of published work on the art of mixing.

Within the last decade, much experimental work has been undertaken with the cavity flow set up, beginning with Ottino and Chella[82] who used this framework to develop in both a theoretical and experimental sense an understanding of the types of flow occurring within screw extruders and helical annular mixers. In subsequent work Chien et al[23], have carried out an experimental study of laminar mixing for several types of two

dimensional driven cavity flows but using Newtonian fluids only. The flows produced are analysed in terms of mixing efficiency by examining the deformation of various low diffusivity coloured line and and 'blob' fluid elements. Motion is generated by moving belts which are connected to motors, whose speeds are regulated by computer. Cavities of aspect ratios up to 10 have been considered for Reynolds' numbers in the range of 1 to 100. Subsequent modifications to the standard test case of driven cavity flow have also been considered, by allowing multiple wall motions, as well as a periodic discontinuous co-rotational type of flow, similar to that originally described by Aref[5], which is found to give rise to chaotic mixing. A novel experimental study of the mixing processes obtained within a trapezoidal shaped cavity is also presented along with numerical simulations of the various types of flow at low Reynolds' numbers.

Aref[5] considered the mixing process from a numerical simulation viewpoint, by analysing the deformation of a large collection of fluid particles placed near two point vorticies which were periodically 'switched' on and off, and which gave rise to the motion being termed 'the blinking vortex' flow. The geometry used was circular, the fluid assumed to be inviscid, and the system regarded as an example of an idealised stirring mechanism. Aref's system, like Chien et al[23], is time dependent

which renders the system non-integrable, which Aref[5] found to be a necessary but not sufficient condition for highly desirous chaotic mixing. A recent adaptation of this system has been considered in Moon[68] where chaotic mixing within a plastic model is considered, and provides insight into the stretching and folding mechanisms which may have taken place within the Earth's mantle over a geological time scale.

Khakhar et al [53], have also considered chaotic mixing from a theoretical viewpoint in two types of periodic flow models, namely the 'tendril-whorl' flow and a version of Aref's[5] now famous blinking vortex flow. These types of flow were also investigated by analysing the stretching and folding of material lines of 'dyed' fluid, and also by investigating the complex motions of the line elements near elliptic and hyperbolic points, as well as considering the individual flow's abilities to produce horseshoe mappings, which is a standard indication for chaos present within a system. Khakhar et al [53] have even shown that positive Lyapunov exponents exist in the Aref[5] blinking vortex flow, deducing that nearby trajectories separate at an exponential rate, indicative of a chaotic system's sensitive dependence on initial conditions.

Recently much of the work at the forefront of the analysis of chaotic mixing within enclosed cavity structures has been produced by Ottino et al[81], and Leong et al [57], while the present state of the art for chaotic mixing can be found in the well written text of Ottino[80]. These authors consider the deformation of coloured material line elements in a variety of cavity flows including those obtained from multiple sinusoidal wall motions. Ottino[80] also provides a comparison between simulation and experiment for the classic journal bearing flow, the applications of which extend to flows occurring within the Earth's mantle.

The latest literature concerning cavity flows is supplied by Jana et al[48] who consider examples of chaos enhanced transport in cellular flows. The examples and illustrations used span both time dependent boundary and jet induced turbulent flows within various sized cavities.

2.5 THERMALLY DRIVEN CAVITY FLOWS.

The convection process is ubiquitous in nature and can readily be observed in the Earth's atmosphere and oceans, as well as being partly responsible for heat and mass transference within stars like our sun, and is even the probable cause of continental plate movements, due to convective currents occurring within the Earth's mantle. Due to its practical relevance and importance with regards to flows occurring within the environment, the literature reviewed in this section falls into two main parts. Firstly a review of the so called 'double glazing problem' whose main application is to insulation of buildngs, and secondly a review of the Rayleigh-Benard problem, which can also be used to simulate flow occurring within the atmosphere and mantle of the Earth.

2.5.1 THE DOUBLE GLAZING PROBLEM.

This consists of the investigation of buoyancy induced flow within the confines of an enclosed impermeable cavity with differentially heated side walls. One of the first to consider this flow in an air/glass system was Batchelor[10], who by assuming the governing equations admit a solution in terms of a power series in terms of the Rayleigh number, produced some analytical solutions for Rayleigh numbers bordering on the turbulent regime.

Later Poots[88], by following closely Batchelor's[10] work, developed a numerical solution based on orthogonal polynomials, and produced both streamline and temperature plots for Rayleigh numbers up to 10^4 and also gave consideration to the case where there exists an angle of inclination of the hot and cold walls to the vertical. Since then the 'double glazing problem' has received much attention through both numerical simulations and laboratory controlled experiments.

Wilkes and Churchill[116] considered a time dependent finite difference computation of natural convection within this geometry with one wall uniformly heated and the other cooled, for cavities with aspect ratios up to 3:1, at Grashof numbers up to a maximum of 200,000, whereupon the difference equations became unstable. Subsequent and fairly recent studies of this problem by both Schnipke and Rice[97] using the finite element method, and De Vahl Davis[33] using finite difference techniques, have solved the double glazing problem, producing both temperature and stream function plots for Rayleigh numbers up to 10^6, the working fluid being air. Their results have become the 'bench-mark solutions' used for comparing and validating computer code used to generate numerical solutions for convection problems of this type. Even more recently the time dependent problem has been investigated for a broad range of

Rayleigh numbers with the fluid under consideration being water, and a useful reference for this work is Patterson and Armfield [85] in which a good comparison exists betweeen simulation and experiment.

One of the attractions of studying the flow patterns produced within such enclosed environments is the varied flow characteristics which emerge through a series of bifurcation phenomena as certain parameters such as the Reynolds' or Rayleigh numbers are altered. These provide a little insight into the widely observed, yet poorly understood, theory of fluid turbulence. Thomson et al [103], in their paper consider turbulent phenomena and present some predictions for buoyancy induced turbulent flow within a large cavity using a prescribed eddy viscosity model and a k-ε model. A later comparison of the theory with available data revealed that there are still many features within the models which require further modification.

However, the main thrust of our research work outlined within this thesis has focused on simulating the flow produced in the Rayleigh-Benard system. This problem is very similar to the double glazing problem outlined above, except that the buoyancy induced flow is generated by an adverse temperature gradient which exists between the top and bottom plates due to uniform of heating the lower plate. This type of flow has been studied both

experimentally, theoretically and by numerical simulation, and as previously mentioned has important applications to the environment we inhabit. Some of the major and recent works published on this system are now reviewed.

2.5.2 THE RAYLEIGH-BENARD PROBLEM.

The phenomenon of convection was re-discovered circa1900, by the famous French physicst Benard[13], although the phenomenon had been known to exist earlier, Thomson[104]. Benard carried out skillful laboratory controlled experiments with very thin layers of Newtonian fluid, confined between two parallel plates, the system being uniformly heated from below.

Benard observed at a critical value of the temperature difference (existing between the plates), the system became unstable evidenced by large scale fluid motions and the emergence of cell patterns, with warm fluid rising in some parts of the flow and colder fluid descending in others. When viewed from above this phenomenon gave rise to a symmetrical hexagonal cell structure.

The first mathematical description of this phenomena was supplied by Lord Rayleigh [90] in 1916, but contained the slightly artificial assumption of free slip boundary conditions, and Jeffreys[49] a little later developed the stability analysis to

incorporate the case of rigid boundaries. Both authors successfully predicted the critical value of the temperature difference necessary for convection to occur within their respective systems. The classic text which provides a good description of the problem and contains an excellent account of the complex linear analysis undertaken by these authors is Chandrasekhar[22], with a useful subsequent review by Brindley[18]. Since then the linear stability analysis has emerged as a powerful tool in describing the qualitative behaviour of a wide variety of complex fluid flows. Recently, for example Larson[56] has developed a linear stability analysis for viscoelastic liquids in the Taylor-Couette flow.

Ever since the pioneering works of Benard and Rayleigh were published, the Rayleigh-Benard system has been investigated by numerous researchers, using a number of tools for enlightenment. However, it has been with the development of the computer age that significant steps via numerical simulation, have contributed to a more thorough understanding of such phenomena.

Aziz and Hellums[8] present numerical solutions for natural convection in three dimenions using vector potential methods, with the fluid being heated from within. Streamline, temperature and vortcity plots are presented for a maximum Rayleigh number of 3500. Venezian[110] has, from a theoretical approach,

investigated the stabilty of a horizontal fluid layer, in which an additional horizontal sinusoidal perturbation is applied, which he found to play a significant role in delaying the onset of convection. Busse[21], a prominent researcher in this field, has also found that the two dimensional convective flow is sensitive to small three dimensional distubances when the amplitude of convection exceeds a finite critical value.

Moore and Weiss[69], have considered an application of the Rayleigh-Benard system to the problem of astrophysical convection. Using the Boussinesq approximation and the valid assumption of stress free boundary conditions, they have presented numerical solutions in the form of streamline and temperature plots for a maximum Rayleigh number of 658,000, whilst considering the effect of varying the Prandtl number in the range 0.01 to 6.8.

More recently, Daniels[36] has considered the temporal evolution of two dimensional natural convection in a shallow layer of fluid heated from below but confined laterally by rigid side walls, through both analytical and numerical simulation, and found the presence of these boundaries affects the type of solution obtained quite considerably. Arter[7], has considered three dimensional Rayleigh-Benard convection within a square plane form, producing a variety of streamline and temperature plots at

various Rayleigh and Prandtl numbers, and also derives a five modal truncation of the governing equations to produce a simplified system similar to the famous Lorenz[59] equations. Some of the most recent up-to-date work on the Rayleigh-Benard system has been carried out by Sirovich and Deane[99]. In the course of their research, a thorough investigation of the convection occurring within the Rayleigh-Benard system has been carried out, using a variety of methods ranging from, numerical simulation, time series, power spectra and probability analysis. They have also managed to calculate a positive Lyapunov exponent for the system, and like Baker and Gollub[9] have also shown the presence of a strange attractor with a dimension of $O(Ra^{0.67})$ to be present within the system. Solomon and Gollub[101], have investigated from both an experimental and theoretical approach, the chaotic transport observed between two adjacent cells in the Rayleigh-Benard system. Experimental techniques involve the use of laser doppler and shadow graph techniques with low diffusivity dyes placed between the cell boundaries, while simulation involves the computational tracking of around 10,000 fluid particles. Both methods reveal the existence of horseshoe mappings which indicate the presence of chaotic advective transport between adjacent cells of the system.

Lately Christensen and Harder[25] have begun to consider the effect, in three dimensions, of natural convection within the Rayleigh-Benard system using temperature dependent variable viscosity fluids. Numerical solutions are achieved up to Rayleigh numbers of 10^5 by utilising hybrid spectral methods. Flows obtained with variable viscosity fluids are of major importance when considering the possibility of flow within the Earth's mantle. Some of the work we have found useful when considering mantle flow is now reviewed.

2.5.3 MANTLE FLOW APPLICATIONS.

One of the important applications of studying the Rayleigh-Benard system, is the application of simulating flow probably occurring within the Earth's mantle, which is now believed to be responsible for continental plate movements, McKenzie[63].

Foster[38] seems to have been one of the first to consider a time dependent theoretical model of finite amplitude convection, using the Rayleigh-Benard system with a fluid whose viscosity is strongly dependent on depth, which he assumed to vary exponentially throughout the cavity. Numerical solutions were obtained using Fourier series to reduce the system to a set of ordinary coupled differential equations. Streamline plots were

produced for Rayleigh numbers up to 10^8 in tall thin cavities.

Subsequent numerical investigations of thermal convection within cavities were carried out by Torrance and Turcotte[106], who considered fluids whose viscosity varied at an exponential rate with both temperature and depth. Steady state streamlines and temperature contours are presented for Rayleigh numbers up to 3600. Later McKenzie, Roberts and Weiss[62] considered a time dependent simulation of mantle flow using finite difference techniques for Newtonian fluids only with stress free boundary conditions. Their paper is a comprehensive investigation which includes a discussion on transient fluid motions, and also appears to be the first to observe cell splitting instability behaviour which was found to occur at Rayleigh number 1.4×10^6 and again at 2.4×10^6.

Much work on this system has also been carried out from an experimental standpoint. One of the first to carry out experiments on the Rayleigh-Benard system using strongly temperature dependent fluids within an enclosed cavity was Turner[108], with later work on a similar problem provided by Nataf and Richter[75]. More recently White[114], has in his thesis considered the flows obtained in Rayleigh-Benard system using shadowgraph techniques for a variety of temperature dependent viscosity models, such as the exponential, super exponential and a

cosine model. Various cell structures were found to occur, the exact pattern and cell size being a direct function of the Rayleigh number. Weijermars[113], considered the evolutionary structures and possible motions pertaining to mantle flow using a simple but carefully scaled laboratory model. Two-tiered mantle convection was investigated for very large Prandtl numbers and Rayleigh numbers of order 10^4. The motion produced is analysed on the basis of snapshots showing the progressive deformation and displacement of passive flow markers, allowing reconstruction of velocity vectors, strain rates and vorticity. A numerical counter-part of Weijermars' [113] experiment is the work of Cserepes and Rabinowicz[30], who considered two-tiered mantle convection using a Newtonian fluid generating steady streamline and temperature plots for Rayleigh numbers up to $3x10^6$.

At this juncture we mention that throughout our period of research, we have aimed to investigate the convective flow for a wide variety of non-Newtonian fluids, including those which exhibit thixotropic and rheopectic tendencies. A paper which gives a tractable account of these moderately rare phenomena can be found in Kemblowski and Petera[52].

Some of the recent work on the Rayleigh-Benard system has been developed and extended to consider the convective motion occurring in binary mixtures, such as salt and water, or ethanol

and water fluid mixtures. This type of system has been studied of late by the numerical simulations and laboratory experiments of Moses and Steinberg[71], and Moore and Weiss[70] respectively. Both authors have shown that convection in a binary fluid is a convenient and easily controllable fluid feature which is extremely rich in displaying non-linear phenomena. Competitions between the Soret and Rayleigh stabilising mechanisms provide many and varied examples of bifurcations, while interactions between standing and travelling waves have been shown to contribute to observed chaotic behaviour and loss of spatial symmetry.

Within the last year attention has focused on the Rayleigh-Benard-Marargoni flows which are driven as a result of surface tension and buoyancy effects. A useful reference is Dijkstra[34] who has found the system to be capable of exhibiting a wide range on non-linear and bifurcation phenomena, and also found the cell patterns obtained depend very strongly on the free slip or no-slip type of boundary conditions imposed on the cavity's walls.

Many researchers have found the Rayleigh-Benard system and its simpler Lorenz counterpart to be rich in demonstrating chaotic behaviour. The main features of this relatively new theory are now reviewed.

2.6 CHAOS THEORY.

An excellent introductory text to the relatively new science of chaos, which is written in an extremely readable, interesting and helpful manner, is the New Scientist Guide to Chaos[76]. The articles presented within this book are written by some of the world's leading experts in the field and explain the meaning of chaos along with some of the mathematical concepts underlying it. Illustrative examples contained within the book are drawn from a wide variety of scientific disciplines ranging from astronomy to population dynamics. Two extremely relevant articles are, 'An Overview Of The Complex Bifurcation Flow Patterns Produced By The Taylor-Couette Flow', which may also be seen in a book entitled 'Fearful Symmetry[37]', and also a paper reviewing the historical origins of chaos from its humble beginnings, allied to weather forecasting, to the present day. These papers show the usefulness of fluid dynamics as a test bed for the modelling of the transition from order to turbulence. A more involved mathematical treatise on bifurcation phenomena and strange attractors occurring within the Taylor-Couette flow can be found in Mullin and Price[72], who used laser doppler techniques to measure the fluid's velocity at various points within the flow and then through time series analysis reconstruct the phase trajectories of a fluid particle's motion. They found

that the phase paths, when the Reynolds' number is about 1000, tend to be of the form of a torus which becomes 'fatter' as the Reynolds' number is increased. Chaotic particle behaviour has also recently been discovered in the eccentric Taylor-Couette flow as the Reynolds number is varied, by Nijhof et al[77].

Nowadays, many undergraduate text books on the topic of non-linear ordinary differential equations are reviewing their work to incorporate many of the relevant features and recent work in the field of chaos. Books such as Arrowsmith and Place[6] and Jordan and Smith[50], include a study of chaotic activity observed in electrical circuits, the chaos observed in the one dimensional biological iterative mappings of May[61], and a topical study of the famous Lorenz[59] system of equations, which gave birth to the theory of chaos in deterministic systems. Other useful texts which view chaos theory from a more mathematical aspect are Thomson and Stewart[105], Moon[67,68], Baker and Gollup[9], Schuster[98] and Ruelle[93]. These well written texts contain a comprehensive review of chaos theory from its origins to the modern day, and cover the basic, essential features of chaos required by both undergraduate and postgraduate students. Topics covered include analysis of the many routes to chaos which are observed in a multitude of dynamical systems, time series and power spectra analysis,

bifurcation phenomena, strange attractors as well as Lyapunov exponents and dimension.

Guckenheimer[41] reviews the main advances in the strange attractor theory of chaos allied to turbulence over the last two decades for both the Taylor-Couette and Rayleigh-Benard systems. At the end of his article useful suggestions are made which aim to direct researchers into new and unchartered territory. Another useful review paper is that of Doherty et al[35], who analyses the historical development of chaos theory, and applies the findings directly to the field of fluid mixing, in particular to those with dissipative and Hamiltonian systems. Some of the work centres around the chaotic deformation of low-diffusivity coloured-line fluid elements within the cavity flow framework, and also investigates the nature of mixing process near fixed elliptic and hyperbolic points. In this paper a simple version of the famous K.A.M theorem is also considered.

Within this thesis, some of the novel results obtained from this period of research, have been achieved by developing the pioneering works of both Saltzman[95] and Lorenz[59], to consider simple models of convective motion using a broad spectrum of non-Newtonian fluids. Saltzman, initially reduced the perturbation equations for the Rayleigh-Benard system to a infinite set of coupled ordinary differential equations, by

assuming the governing equations admitted solutions in terms of Fourier series components with time dependent coefficients. However, he subsequently reduced this system to consider five modes which satisfactory modelled convective motion.

Lorenz[59], realised that Saltzman's[95] results could be obtained if just three modes were recognised in the Fourier series expansions, and in so doing he drastically simplified the equations and produced the now famous set of three coupled non-linear ordinary dfferential equations, which can be regarded as a crude model of an idealised climate. Lorenz discovered that at a critical value of the Rayleigh number, all particle trajctories were drawn to a finite dimensional object in the phase space, on which the motion was non-periodic, highly irregular and could be described as chaotic. Lorenz called this object a 'strange attractor' and was the first of its kind to be studied; subsequently many such strange attractors have been found to exists in almost every area of science.

The Lorenz[59] system has ever since been the centre of much investigation, due to its possibility of describing some of the salient features of fluid turbulence. Later Curry[31] considered a generalised version of the Lorenz system, in which he incorporated up to 14 terms in his Fourier series expansions, and thus produced a more realistic description of convection and also

enabled larger Rayleigh numbers to be considered. The fundamental difference with this representation was that the unstable solutions in the smaller Lorenz[59] system were replaced by a toroidal structure in the Curry[31] system as the Rayleigh number enters the turbulent regime. Marcus[60], has considered the effects of truncation of series expansions used in the modal representation of the thermal convection process occurring within a sphere using a Galerkin method, and determines what physical processes are neglected when the equations are truncated too severely. The observations were that transitions from steady state to periodic and then aperiodic motion were stongly dependent not only on the Rayleigh number but also on the modal resolution used in the calculation.

Subsequent study by Curry et al[32], on the apparent transition from order to disorder within the Rayleigh-Benard problem for a Newtonian fluid layer bounded by free slip walls in two and three dimensions, have found that the chaos observed in many of the two dimensional truncated models is a direct result of an insufficient spatial resolution. They have shown that, like Curry[31], as the number of Fourier modes used in the series expansions increases, the degree of chaos observed increases at first, and then abruptly decreases, with no chaotic behaviour observed at a sufficiently high spatial resolution.

In concluding this review we note that scientists are only recently beginning to gain small insights into what is becoming known as the science of complexity. Chaos theory has sought to explain why seemingly organised systems can suddenly behave in a random and erratic manner. Recent developments within this field are applying chaos theory to such practical problems as the stock market and traffic flow and even to practical areas of traditional engineering such as ship-capsize. A recent publication providing insight into the present state of the art of chaos theory as applied to many scientific disciplines is, 'Applications of Fractals and Chaos[4].

However, in like manner a novel theory of anti-chaos has been spawned, dealing with why the reverse happens, i.e examining why some apparantly quite disorganised systems crystallise into ones which possess a high degree of underlying order, e.g an ant colony. A good intoductory text discussing these matters is Anti-chaos[3], which examines the very fine dividing line between order and disorder, chaos and anti-chaos.

2.7 EXPERIMENTAL AND THEORETICAL INVESTIGATIONS OF FLUID MIXING.

The mixing process is almost universally observed in nature, with examples readily found in the dispersion of various chemical effluents into the atmoshphere and oceans of the world as well as being seen as an everyday occurrence in the home with the making, blending and colouration of various foodstuffs.

However, despite its wide spread occurrence, usage and importance to the environment, it still remains quite a poorly understood scientific phenomenon, and has received a disproportionate lack of study. This is probably due the fact that the equations which simulate fluid flow and the associated mixing processes are very complex, the result being that even in an industrial context, mixing is treated on a case by case basis. However, within the last fifty years or so, the art of mixing has been investigated from a more scientific standpoint, using both experimental and numerical modelling.

The first comprehensive review within the field of mixing appears to have been undertaken by Quillen[89], who by utilising his practical experience, compiled a review of the principal kinds of mixers which exist together with their practical and industrial applications. Since then a host of literature has become available, some of the most relevant experimental work applicable to us has

been carried out by firstly Ulbrecht[109] and subsequently by Collias and Prud'homme[27], both authors having analysed the flow and mixing of complex non-Newtonian viscoelastic liquids. Other classic texts investigating the various aspects of art of mixing are Nagata[73] and Oldshue[78], who have considered the relative merits of numerous types of agitators available, and also provide an outline of the conditions of use.

As mentioned earlier some of the most recent work on mixing including the use of bifurcation phenomenon and chaotic mixing for various driven cavity flows, is summarised in the well written text of Ottino[80].

Lately, significant developments in the field of mixing have been made with the dawn of the computer age, enabling computer simulations to play a more active and supportive role in the understanding of fluid mixing. Spragg et al[102] appear to have been the first to undertake a theoretical analysis of a 'real life' mixing problem, consisting of modelling by numerical simulation of the streamline flow pattern and consequent dispersive mixing of a band of 'coloured' fluid produced by a disc rotating in a cylindrical vessel. A more up to date numerical simulation of the flow patterns and particle paths for this type of flow obtained from both an experimental and theoretical standpoint using Newtonain fluids, has been produced by Bodalia[16]. Even more

recently Havard[44] has investigated the coloured band and dispersive mixing for a variety of impellers in a cylindrical vessel, using the finite element method, with streamline and concentration intensity contours produced for a broad range of Reynolds' numbers up to the turbulent regime. Both Bodalia[16] and Havard[44] also contain an excellent review of the art of mixing.

CHAPTER 3

NUMERICAL SIMULATION OF VARIOUS LAMINAR DRIVEN CAVITY FLOWS.

3.1 INTRODUCTION.

In this chapter consideration is given to the flow patterns and mixing processes associated with several types of flows occurring within an enclosed cavity. Our investigation commences with the simulation of the test case of standard cavity flow. The problem itself consists of a viscous fluid contained within an enclosed cavity with impermeable walls, as shown in fig (3.1*), and the fluid is initially set into motion by an impulsively moved top plate. This system apart from being a bench-mark problem, enabling a useful check to be made on the correctness of the computer code used in the simulation, does have physical significance. The geometry and flow patterns produced are an approximation to those of a multiple flight extruder screw, shown earlier in fig (1.1*), and finds applications to industrial mixing especially in polymer processing and in the coating of thermoplastics. For this problem we have considered the simulation of both steady state and time dependent flows, using Newtonian and certain shear-dependent non-Newtonian fluid models. In this present chapter we also investigate by numerical

simulation, the variation in the concentration intensity of a dye as it disperses through the various fluid mediums, carried along by the flow. The main results of the simulations, namely the stream-function and concentration plots obtained at various Reynolds' numbers may be seen in Chapter 5.

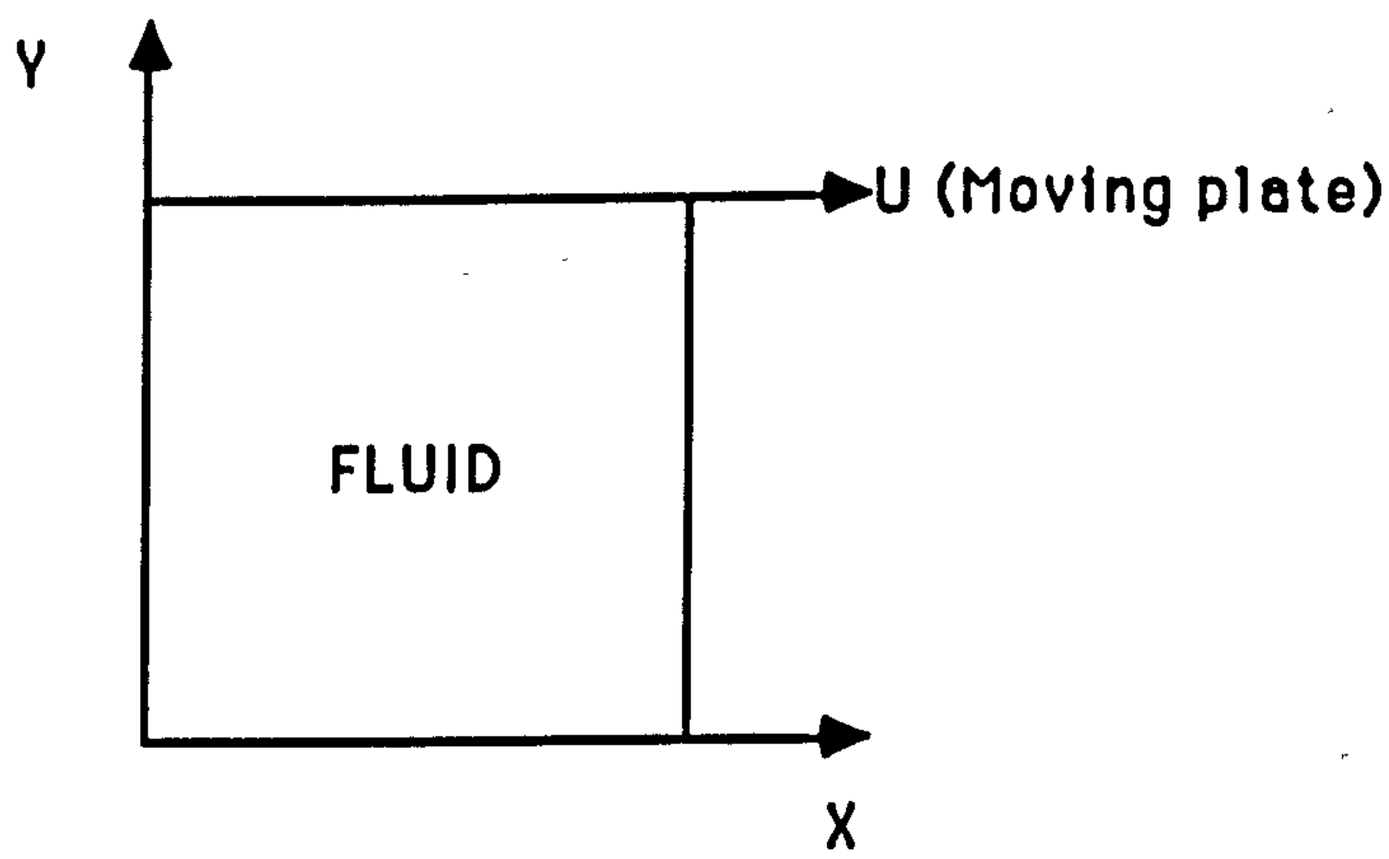

Figure (3.1*)

Diagram of cavity's geometry.

The second type of cavity flow considered is the simultaneous motion of two parallel plates or walls, which can move either in the same or opposite directions. This system's motion has been analysed experimentally by Chien et al[23] for various Reynolds' numbers ranging from 0.1 to 100. They also produced numerical solutions in terms of stream function contour plots for Reynolds' numbers of order one, for a Newtonian fluid only, which are useful for comparative purposes with our own results. The system with a few improved modifications has also subsequently been studied

by Ottino[80], using mostly laboratory controlled experiments. Chien et al[23] have also investigated experimentally, with Newtonian fluids, the flow and deformation of coloured line and 'blob' material elements, for a third type of cavity flow known as alternate periodic discontinuous co-rotational cavity flow. This type of cavity flow is very similar to the blinking vortex flow used by Aref[5] to simulate ideal mixing within a cylindrical container. Aref originally considered an inviscid fluid within the confines of a circular geometry, the agitator modelled by two point vortices, switched periodically on and off. The particle paths produced were computed numerically and are indicative of the mixing efficiency of the system. We have extended the work of Chien et al [23] and Aref[5], by considering how the system behaves at various Reynolds' numbers for certain non-Newtonian fluids, numerically computing the trajectories of the particle paths as well as simulating the stretching and folding of a material line element.

Finally we propose a novel though uniquely theoretical, and as yet unstudied form of cavity flow, whereby all four of the cavity's walls are allowed to move in a periodic discontinuous co-rotational sense, using both Newtonian and certain shear rate dependent non-Newtonian fluids throughout the simulation. The particle paths produced for this system, indicate this gives the

'optimum' mixing for a two dimensional rectangular geometry. The results of this investigation along with those produced from earlier work on standard cavity flows may be seen in Chapter 5.

3.2 THE MATHEMATICAL EQUATIONS GOVERNING DRIVEN CAVITY FLOW.

The partial differential and constitutive equations which model the flow are :-

(i) The Stress equations of motion.

(ii) The Rheological equation of state.

(iii) The Continuity equation.

(iv) The Stream-Function and Vorticity equations.

3.2.1 THE STRESS EQUATIONS OF MOTION

The stress equations of motion are also known as the Cauchy equations and describe for both Newtonian and non-Newtonian fluids alike, the relationship between the inertial forces, the pressures and the stresses due to the liquid itself, and can be derived from the application of Newton's second law to a moving continuum. Throughout the equations, which are outlined below in tensor notation, the density of the fluid is assumed constant, and for two dimensional flows using the cartesian co-ordinate system we obtain:

$$\frac{\partial P_{xx}}{\partial x} + \frac{\partial P_{xy}}{\partial y} + \rho F_x = \rho \frac{Du}{Dt} \qquad (3.1)$$

$$\frac{\partial P_{yx}}{\partial x} + \frac{\partial P_{yy}}{\partial y} + \rho F_y = \rho \frac{Dv}{Dt} \qquad (3.2).$$

In equations (3.1) and (3.2) shown above P_{xx}, P_{xy}, P_{yx}, P_{yy} are the components of the physical stess tensor, u and v are the velocity components in the x and y directions respectively, ρ is the density of the fluid, and F_x and F_y are the body forces per unit mass in the respective directions. The time derivative is defined as shown in (3.3), and is known as the material or convective derivative.

$$\frac{D}{Dt} = \frac{\partial}{\partial t} + u\frac{\partial}{\partial x} + v\frac{\partial}{\partial y} \qquad (3.3)$$

In equations (3.1) and (3.2), no body forces are assumed to act in the x direction and only gravity acts as a body force in the negative y direction. Thus the stress equations describing the flow become:-

$$\frac{\partial P_{xx}}{\partial x} + \frac{\partial P_{xy}}{\partial y} = \rho \frac{Du}{Dt} \qquad (3.4)$$

$$\frac{\partial P_{yx}}{\partial x} + \frac{\partial P_{yy}}{\partial y} - \rho g = \rho \frac{Dv}{Dt} \qquad (3.5)$$

3.2.2 THE RHEOLOGICAL EQUATION OF STATE

This is also known as the constitutive equation and gives rise to the relationship between the stresses and strains occurring within the fluid during deformation. For an incompressible general viscous fluid this takes the form :-

$$P_{ki} = -P\delta_{ki} + T_{ki} \quad \text{for } k,i = 1,2 . \tag{3.6}$$

P_{ki} is the stress tensor, P is a isotropic hydrostatic pressure, δ_{ki} is the kronecker delta tensor, and T_{ki} is known as the extra stress tensor which for a general shear rate(q) dependent purely viscous fluid is defined as:-

$$T_{ki} = 2\eta(q)\, e_{ki}^{(1)} . \tag{3.7}$$

In expression (3.7), $e_{ki}^{(1)}$ is known as the first rate of strain tensor and represents velocity gradients with distance and is defined as

$$e_{ki}^{(1)} = \frac{1}{2}\left\{\frac{\partial v_k}{\partial x_i} + \frac{\partial v_i}{\partial x_k}\right\} , \tag{3.8}$$

and $\eta(q)$ is the shear viscosity function, used to model the viscosity for non-Newtonian fluids which have a shear dominating influence. Later, in Chapter 6, when buoyancy induced thermally driven cavity flows are investigated, the viscosity is allowed to be a function of time(t), temperature(T), as well as the shear rate(q), or a suitable combination of these variables.

From the principle of balance of angular momentum it is required that $P_{kl} = P_{lk}$ and consequently in two dimensional cartesian coordinates there exists four non zero components of the rate of strain tensor namely:-

$$e_{xx} = \frac{\partial u}{\partial x}, \quad e_{xy} = e_{yx} = \frac{1}{2}\left\{\frac{\partial u}{\partial y} + \frac{\partial v}{\partial x}\right\}, \quad e_{yy} = \frac{\partial v}{\partial y}$$

The shear rate (q) is defined as the second invariant of the rate of strain tensor $e_{ki}^{(1)}$, which is given by:-

$$q^2 = 2Tr\,(e_{ki}^{(1)} : e_{ki}^{(1)})$$

where Tr denotes the trace of the tensor product, thus

$$q^2 = 2\{(e_{xx} : e_{xx}) + 2(e_{xy} : e_{xy}) + (e_{yy} : e_{yy})\}\,. \qquad (3.10)$$

Two popular choices for modelling the precise form of the viscosity function $\eta(q)$ are:-

(a) The Cross model which is given by:-

$$\eta(q) = \eta(\infty) + \frac{(\eta(0) - \eta(\infty))}{1+(\lambda q)^{1-n}} \qquad (3.11)$$

(b) The Carreau model which is given by:-

$$\eta(q) = \eta(\infty) + (\eta(0) - \eta(\infty))(1+(\lambda q)^2)^{(n-1)/2} \qquad (3.12)$$

$\eta(\infty)$ represents the infinite shear viscosity for very large deformation rates and likewise $\eta(0)$ represents the zero shear rate viscosity for very small rates of shear.

For comparative purposes we have chosen the Cross model and this will subsequently be used in the remainder of this thesis.

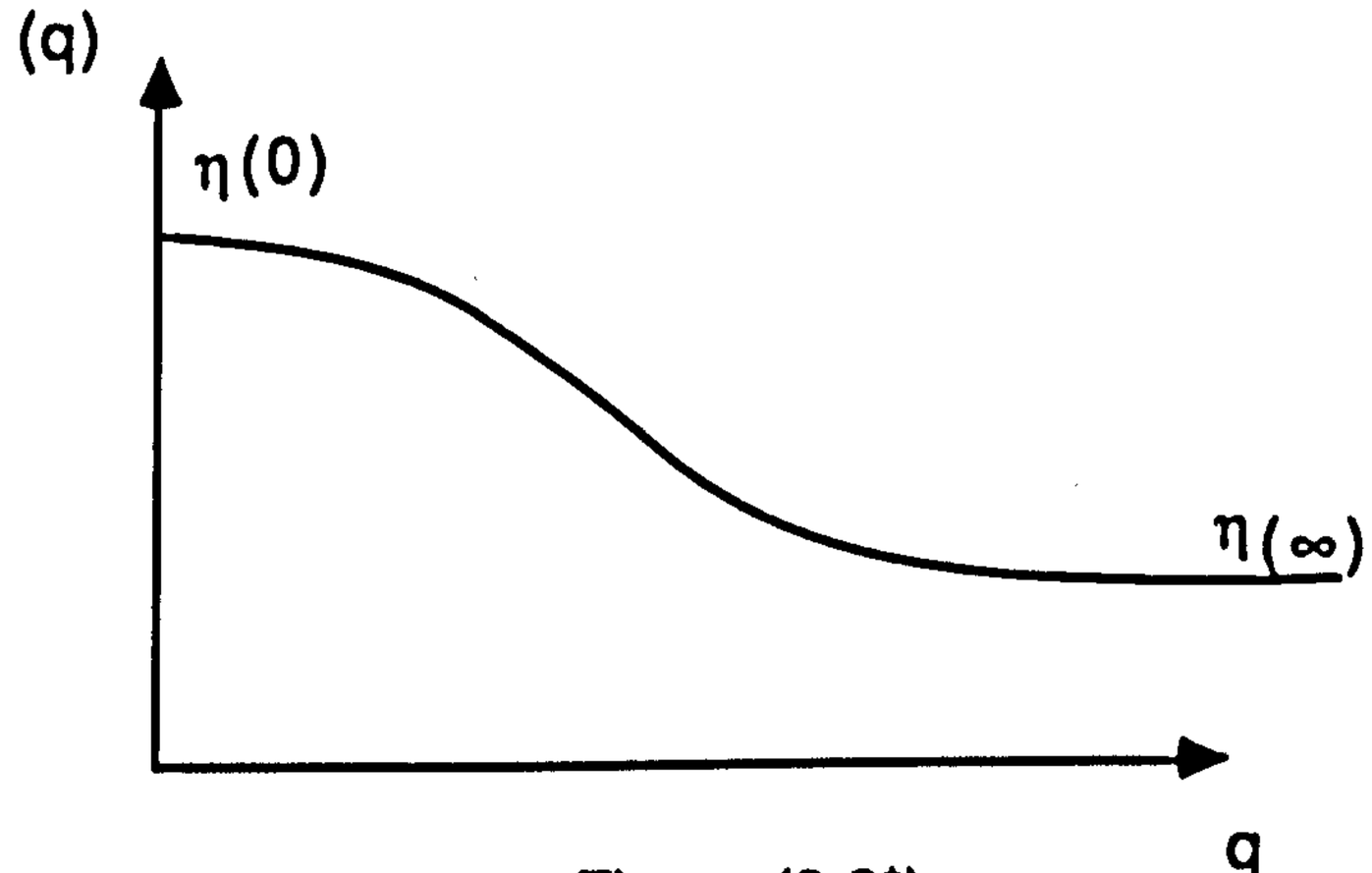

Figure (3.2*)
Graph showing shear-thinning behaviour

Using the Cross model with $n=0.5$, $\lambda=1$, $\eta(0)=1$

(non-dimensionalised value) and allowing $\eta(\infty)$ to vary between 0 and 1, i.e $0 \leq \eta(\infty) \leq 1.0$, a viscosity curve as similar to that shown above in fig (3.2*) is obtained representing shear-thinning or pseudoplastic behaviour.

However, the Cross model can also be used to model shear-thickening or dilatant behaviour, for if we let $n=0.5$, $\lambda=1$, $\eta(\infty)=1$ and vary $\eta(0)$ such that $0 \leq \eta(0) \leq 1$ then we obtain a viscosity curve of the form shown in fig (3.3*) overleaf.

In passing we mention that the values used for $\eta(0)$ and $\eta(\infty)$ throughout the simulations are non dimensionalised values.

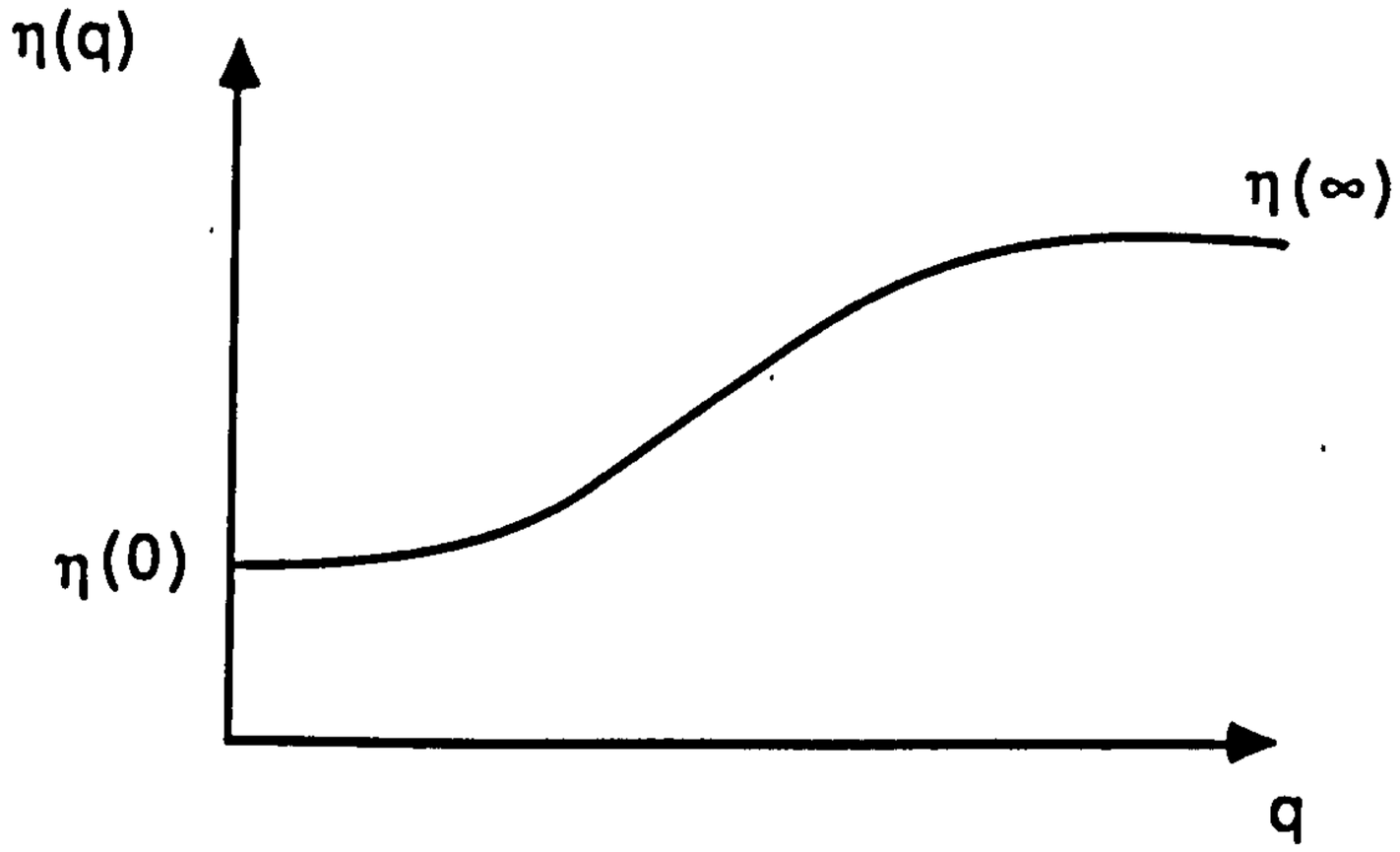

Figure (3.3*)

Graph showing shear-thickening behaviour

Upon substituting the rheological equation of state into (3.4) and (3.5) the following equations are obtained :-

$$-\frac{\partial P}{\partial x} + \frac{\partial T_{xx}}{\partial x} + \frac{\partial T_{xy}}{\partial y} = \rho \frac{Du}{Dt} \qquad (3.13)$$

$$-\frac{\partial P}{\partial y} + \frac{\partial T_{yx}}{\partial x} + \frac{\partial T_{yy}}{\partial y} - \rho g = \rho \frac{Dv}{Dt} \qquad (3.14)$$

A step towards reducing in the number of variables in the problem can be achieved by taking the curl of equations (3.13) and (3.14), which generates equation (3.15).

$$\frac{\partial^2}{\partial x \partial y}(T_{xx} - T_{yy}) + \left(\frac{\partial^2}{\partial y^2} - \frac{\partial^2}{\partial x^2}\right) T_{xy} = \rho \frac{D}{Dt}\left(\frac{\partial (u)}{\partial y} - \frac{\partial (v)}{\partial x}\right) \qquad (3.15)$$

3.2.3 THE CONTINUITY EQUATION

This equation arises from the application of the principle of conservation of mass to a moving continuum, and for an incompressible fluid with constant density in two dimensional plane flow, the equation of continuity reduces to :-

$$\text{div } \underline{v} = 0$$

or

$$\frac{\partial u}{\partial x} + \frac{\partial v}{\partial y} = 0 \qquad (3.16)$$

3.2.4 THE STREAM-FUNCTION AND VORTICITY EQUATIONS

These equations are used to reduce the number of variables further to just two, namely the stream function and the vorticity.

The stream-function $\Psi = \Psi(x,y)$ measures the flux across any streamline in the flow as a function of position, where the equation of the streamline is given by $\underline{v} \times \underline{dr} = \underline{0}$. Here $\underline{v}$ is the velocity vector, and is tangential to the streamline at every point in the flow. It is well known that the components of the velocity can be expressed in terms of derivatives of the stream function and hence must satisfy the continuity equation (3.16). Thus the velocity components may in cartesian coordinates be expressed as :-

$$u = \frac{\partial \Psi}{\partial y} \quad \text{and} \quad v = -\frac{\partial \Psi}{\partial x} \qquad (3.17)$$

The vorticity ($\underline{\Omega}$) is a measure of the swirl or rotation of the flow and is defined to be the curl of the velocity vector,

$$\text{i.e } \underline{\Omega} = \text{curl } \underline{v} = \{ 0, 0, (\frac{\partial v}{\partial x} - \frac{\partial u}{\partial y}) \},$$

hence we obtain equation (3.18) as a measure of the flow's rotation.

$$\omega = \frac{\partial v}{\partial x} - \frac{\partial u}{\partial y} \qquad (3.18).$$

The vorticity may also be expressed in terms of the stream function for by using (3.17) we obtain

$$\frac{\partial^2 \Psi}{\partial x^2} + \frac{\partial^2 \Psi}{\partial y^2} = - \omega \qquad (3.19)$$

Thus referring once again to equation (3.15), and taking into account equations (3.7), (3.8), together with the continuity equation (3.16) we arrive after a little manipulation at the general equation of non-Newtonian flow, with just two unknowns Ψ and ω. This is shown overleaf in (3.20) and is expressed in the computationally convenient self adjoint form, which is used for the remainder of this thesis.

3.2.5 THE GENERAL NON-NEWTONIAN FLOW EQUATION.

$$\eta(q)\frac{\partial\omega}{\partial t} = \frac{\partial(\eta(q)^2\frac{\partial\omega}{\partial x})}{\partial x} + \frac{\partial(\eta(q)^2\frac{\partial\omega}{\partial y})}{\partial y} - \eta(q)\left\{\frac{\partial\Psi}{\partial y}\frac{\partial\omega}{\partial x} - \frac{\partial\Psi}{\partial x}\frac{\partial\omega}{\partial y}\right\}$$

$$- \eta(q)\left\{ 4\frac{\partial^2\eta(q)}{\partial y\partial x}\frac{\partial^2\Psi}{\partial x\partial y} + \left(\frac{\partial^2\Psi}{\partial y^2} - \frac{\partial^2\Psi}{\partial x^2}\right).\left(\frac{\partial^2\eta(q)}{\partial y^2} - \frac{\partial^2\eta(q)}{\partial x^2}\right)\right\} \qquad (3.20)$$

Equation (3.20) needs to be solved in conjunction with (3.19).

Note here that if $\eta(q)$ is given a constant value in (3.20) the usual time dependent Newtonian flow equation is obtained, and also if we make $\partial/\partial t = 0$, then the general steady state non-Newtonian equation is produced.

3.2.6 THE CONCENTRATION EQUATION.

The other partial differential equation we numerically solve for the driven cavity flow problem is the time dependent concentration equation. This is derived from the application of the law of conservation of a substance to a moving continuum and an outline of its derivation may be found in standard texts such as Bird, Stewart and Lightfoot[15]. It is assumed that no generation or loss of concentration due to chemical reactions occurring within the cavity takes place, and neglects any buoyancy effects by assuming the 'dye' is of the same chemical composition and density as the rest of the fluid.

The concentration equation we use is shown in (3.21) overleaf.

$$\frac{\partial C}{\partial t} + u\frac{\partial C}{\partial x} + v\frac{\partial C}{\partial y} = K_c\left(\frac{\partial^2 C}{\partial x^2} + \frac{\partial^2 C}{\partial y^2}\right) \qquad (3.21)$$

Here, K_c is the diffusion coefficient and u and v the velocities in the x and y directions respectively, which may also be conveniently expressed in terms of the stream-function by using equation (3.17).

Using this equation consideration is given to the theoretical investigation of colour band dispersive mixing produced within the cavity due to fluid motion.

3.3 MOTION OF A FLUID PARTICLE.

The trajectory of a fluid particle may be obtained for all types of cavity flow considered by numerically solving the Hamiltonian system of equations (3.22) shown below, subject to the initial condition $x(0)=x_0$ and $y(0)=y_0$ for each fluid particle under consideration. Throughout our simulation up to a maximum of nine particles, strategically placed within the cavity are simultaneously traced, which have been found under certain conditions (discussed in Chapter 5) to behave in a chaotic manner.

$$\frac{dx}{dt} = u = \frac{\partial \Psi}{\partial y} \qquad (3.22)$$

$$\frac{dy}{dt} = v = -\frac{\partial \Psi}{\partial x}$$

The necessary numerical solution of the equations governing the flow, and of particle the path trajectories within this section are discussed in Chapter 4.

CHAPTER 4

THE NUMERICAL SOLUTION OF THE EQUATIONS GOVERNING VARIOUS LAMINAR DRIVEN CAVITY FLOW.

4.1 INTRODUCTON.

In this chapter we will discuss the numerical solution of the partial differential equations outlined in Chapter 3, governing the flow produced by various laminar driven cavity flows. The vorticity (3.20), stream-function (3.19), and the concentration (3.21) equations, because of their non-linearity, do not generally lend themselves easily to analytic solutions subject to prescribed boundary conditions (which will be discussed later), and so numerical techniques have to be employed to yield a solution.

The numerical solution of differential equations is not a new concept, having its origins back in the seventeenth century with the pioneering work of Leonard Euler, but has been aided significantly by the recent development of high speed and powerful computers. The numerical solution of our PDEs consists of a set of numbers obtained at specific points within the flow domain, from which the distribution of the dependent variable of the desired PDE can be constructed. In one sense the numerical method is similar to a laboratory controlled experiment, in which a set of instrument readings enables the distribution of a

measurable quantity to be constructed within the domain of investigation.

At present there are four basic popular numerical methods available to obtain numerical solutions of the PDE's outlined above. These are, the finite element method, the finite difference method, boundary element and spectral methods. The most tried and tested of these methods when applied to non-Newtonian flow problems are the finite element and finite difference techniques, both of which yield comparatively good results.

All numerical techniques approximate the original partial differential equation by an algebraic equation which is then solved in place of the original differential equation. The solutions obtained, although being approximate, are not approximate in the sense of being crude, but rather are as accurate as the data warrants, or as accurate as is necessary for the technical purposes for which the solutions are required(Smith[100]). Throughout this thesis we have chosen to numerically solve the governing partial differential equations by the finite difference method. This is due to the fact it is well documented, much tried and tested, easy to follow and implement into computer code, as well as being less computationally involved than its rival finite element method for our rectangular cavity geometry.

The computational stage of all numerical methods for solving problems of any complexity involves a great deal of arithmetic, thus in general it is usual to arrange whenever possible for one solution to suffice a variety of different problems. This is achieved by expressing all the equations in terms of non-dimensional variables, consequently all problems with the same non-dimensional formulation can be dealt with by means of one solution.

4.2 NON-DIMENSONALISATION OF THE FLOW EQUATIONS.

The equations (3.19), (3.20) and (3.21) can be non-dimensionalised by writing:

$$x' = x/L,\ y' = y/L,\ u' = u/U,\ v' = v/U,\ \omega' = L\omega/U,\ t' = Ut/L,$$

$$\Psi' = \Psi/UL,\ q' = q/U,\ \eta' = \eta/\eta(0),$$

where the dashed notation represents the non dimensionalised variables, U is a reference velocity, L is a length of the cavity, u and v are the components of the velocity vector in x and y directions respectively, t represents the time, η the viscosity, ω the vorticity, Ψ the stream-function and q the shear-rate. Using the new variables the non-dimensionalised form of equations (3.19) and (3.20) become on dropping the dashed notation :

$$\eta Re \frac{\partial \omega}{\partial t} = \frac{\partial}{\partial x}\left(\eta^2 \frac{\partial \omega}{\partial x}\right) + \frac{\partial}{\partial y}\left(\eta^2 \frac{\partial \omega}{\partial y}\right) - \eta\left(\frac{\partial \Psi}{\partial y}.\frac{\partial \omega}{\partial x} - \frac{\partial \Psi}{\partial x}.\frac{\partial \omega}{\partial y}\right)$$

$$- \eta Re\left(4\frac{\partial^2 \eta}{\partial y \partial x}\frac{\partial^2 \Psi}{\partial x \partial y} + \left(\frac{\partial^2 \Psi}{\partial y^2} - \frac{\partial^2 \Psi}{\partial x^2}\right).\left(\frac{\partial^2 \eta}{\partial y^2} - \frac{\partial^2 \eta}{\partial x^2}\right)\right) \quad (4.1).$$

$$\frac{\partial^2 \Psi}{\partial x^2} + \frac{\partial^2 \Psi}{\partial y^2} = -\omega \quad (4.2)$$

where $Re = \rho UL/\eta(0)$, η is the variable viscosity function, which we presently assume varies predominantly with shear-rate, but may also in later work vary with both temperature and time. The main effect of non-dimensionalising is to introduce a parameter (Re) known as the Reynolds' number, which emerges as the sole dimensionless parameter needed for the specification of the dynamical state of the flow fields with geometrically similar boundary and initial conditions.

The Reynolds' number as well as being characteristic of the flow does have physical significance, for it is a measure of the ratio of the inertial to viscous forces. When $Re \ll 1$, the viscous forces tend to dominate the flow and similarly when $Re \gg 1$ the inertia forces predominate. (Batchelor[12]).

The Reynolds' number utilised in this thesis is used for comparitive purposes, as the viscosity value for shear dependent fluids can vary greatly from place to place throughout the flow domain.

4.3 BOUNDARY CONDITIONS FOR THE STREAM-FUNCTION AND VORTICITY EQUATIONS.

Equations (4.1) and (4.2) need to be solved subject to certain initial and boundary conditions. The boundary conditions are the conditions that the dependent variable of the partial differential equation is required to satisfy at each point around the boundary curve of the solution domain, this in our case being the walls of the cavity. On the walls themselves we impose a no-slip condition, for when solving viscous flow problems it is customary for fluid velocity at the walls of the cavity to be the same as the speed of the boundary, that is the fluid adheres to the boundary walls.

Because of the no-slip condition, there exists on the surface of the walls a 'boundary' layer through which vorticity is generated, diffused and convected. Although this is known to occur the actual values of vorticity on the walls are not known analytically and consequently have to be approximated. We chose as our approximation the well known Woods formulae CDW[29], which have to be applied with a knowledge of the previously calculated interior vorticity values. The advantage in using these formulae is that the error involved in our use of the approximation is consistent with the overall error in the numerical method we use to solve the vorticity and stream-function equations.

The use of the no-slip condition also implies that the stream function has a constant value at each point along the boundary, which for simplicity is taken to be zero. Both sets of boundary conditions for equations (4.1) and (4.2) are of the Dirichlet type as shown in fig (4.1*) and fig (4.2*) for standard cavity flow.

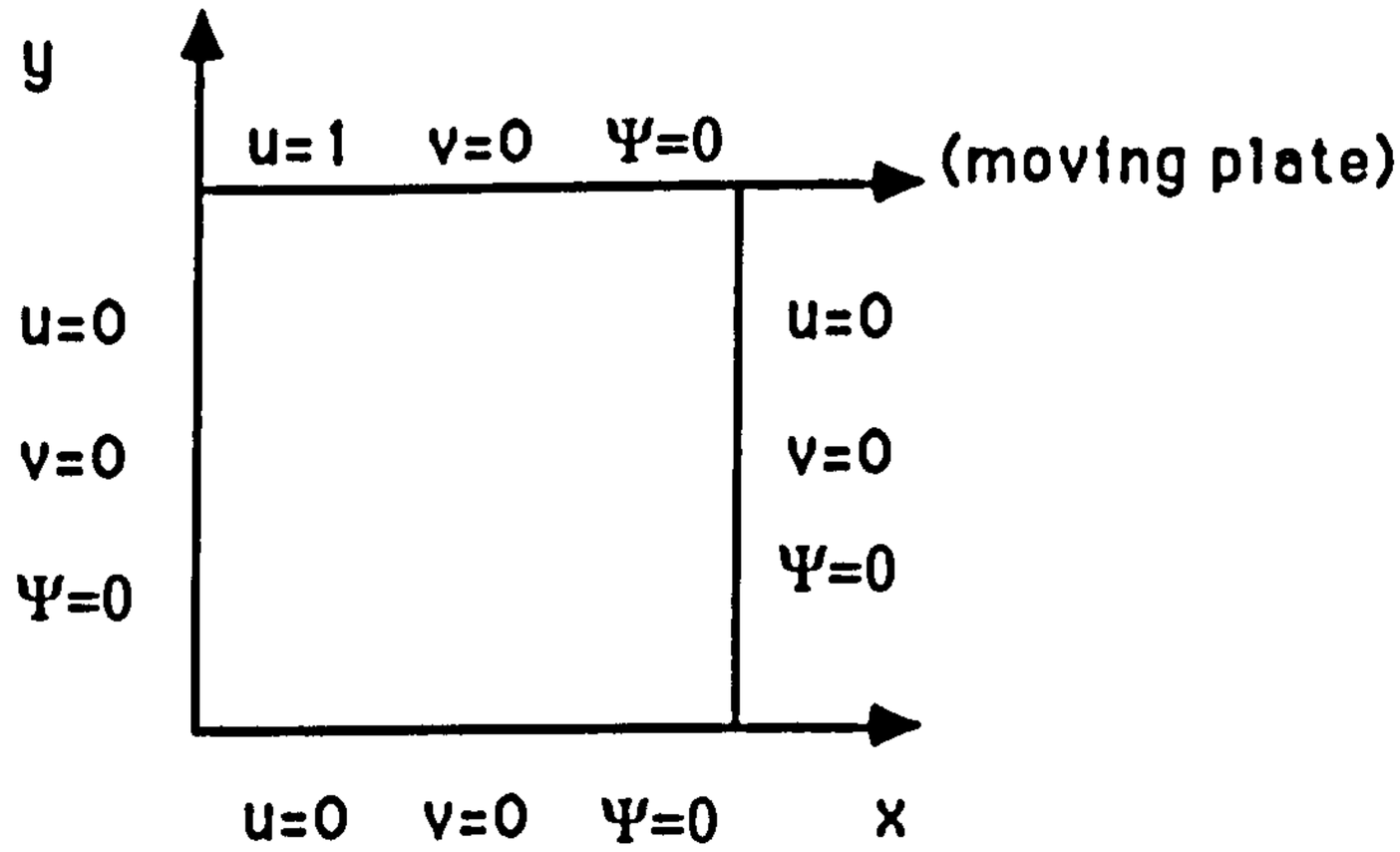

Figure (4.1*)

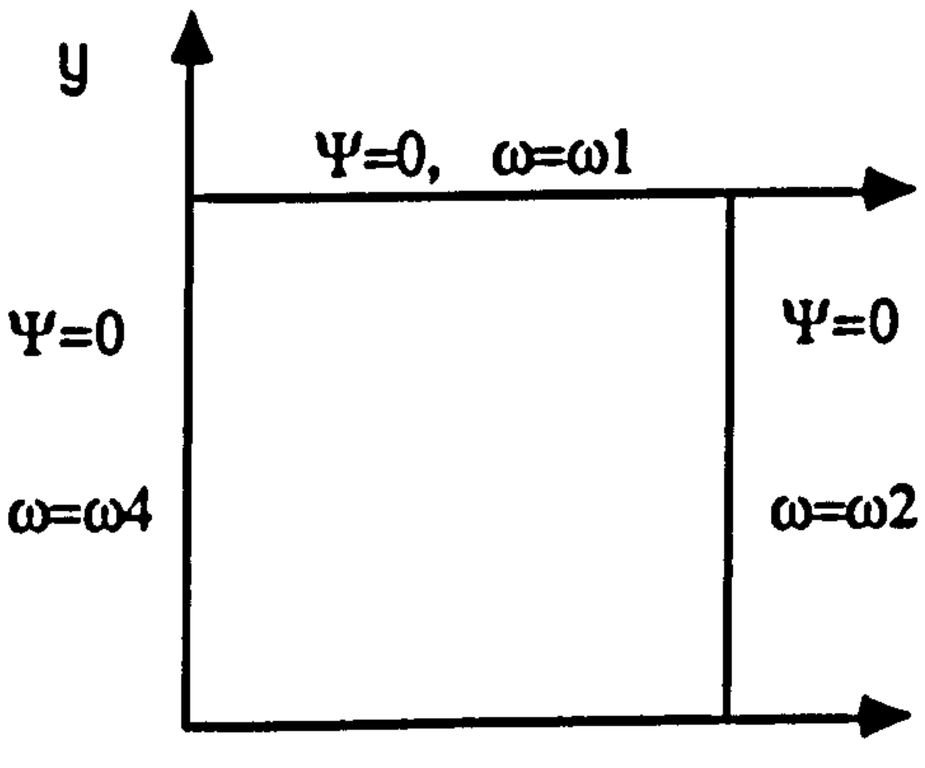

Figure (4.2*)

Boundary conditions used in the simulation of driven cavity flow.

4.3.1 THE VISCOSITY BOUNDARY VALUES.

The viscosity for shear-dependent fluids is determined from using the Cross model (3.11), and thus to implement the viscosity boundary values the shear-rate needs to be evaluated on each of the cavity's walls.

The non-dimensionalised deformation rate q is given by :

$$q = U\{(\partial^2\Psi/\partial y^2 - \partial^2\Psi/\partial x^2) + 4(\partial^2\Psi/\partial x\partial y)\}^{1/2} \qquad (4.3)$$

which is obtained from the second invariant rate of strain tensor outlined in Chapter 3. On the boundaries, the top plate for example, this bears much simplification for by using the velocity conditions it can be seen that $q = |\omega|$, where $|\,.\,|$ represents the modulus. A similar expression exists for the other three remaining walls, thus the value for q can be substituted into the Cross model enabling the viscosity values on the boundary to be determined. For temperature dependent fluids (Chapter 6) a similar procedure is followed, with the boundary viscosity being given in terms of a Reynolds or Arrhenius type formula.

4.4 THE CONCENTRATION EQUATION.

The concentration equation defined in Chapter 3, (3.21), is non-dimensionalised in the usual way, the main result being the introduction of two dimensionless parameters, the Reynolds' number and the Schmidt number. Like the Reynolds' number the Schmidt number does have physical significance as it describes the relationship between the viscosity and the molecular diffusivity (K_c), and is defined as:

$$Sc = \eta(0)/\rho k_c.$$

The non-dimensionalised concentration equation is:

$$\frac{\partial C}{\partial t} + \left(\frac{\partial \Psi}{\partial y}\frac{\partial C}{\partial x} - \frac{\partial \Psi}{\partial x}\frac{\partial C}{\partial y} \right) = D\left(\frac{\partial^2 C}{\partial x^2} + \frac{\partial^2 C}{\partial y^2} \right) \qquad (4.4)$$

The first term of the equation represents time dependence, the second convection and the third diffusion, with D=1/ReSc. The Schmidt number is generally taken to be 50 for comparative purposes with Havard[44]. It can also be seen from equation (4.4) that as Re increases the concentration equation becomes very much advection dominated.

4.4.1 BOUNDARY CONDITIONS OF THE CONCENTRATION EQUATION.

These are of the homogeneous Neumann type, that is instead of specifying the dependent variable at every point on the boundary such as in the Dirichlet conditions, the gradient or flux condition that of $\partial C/\partial n$ is specified at every point along the boundary, where n is the outward normal. The cavity's walls are assumed to be impermeable and consequently no flux can be transported through them, the result being that $\partial C/\partial n = 0$, on each of the boundary walls, as shown below in fig (4.3*).

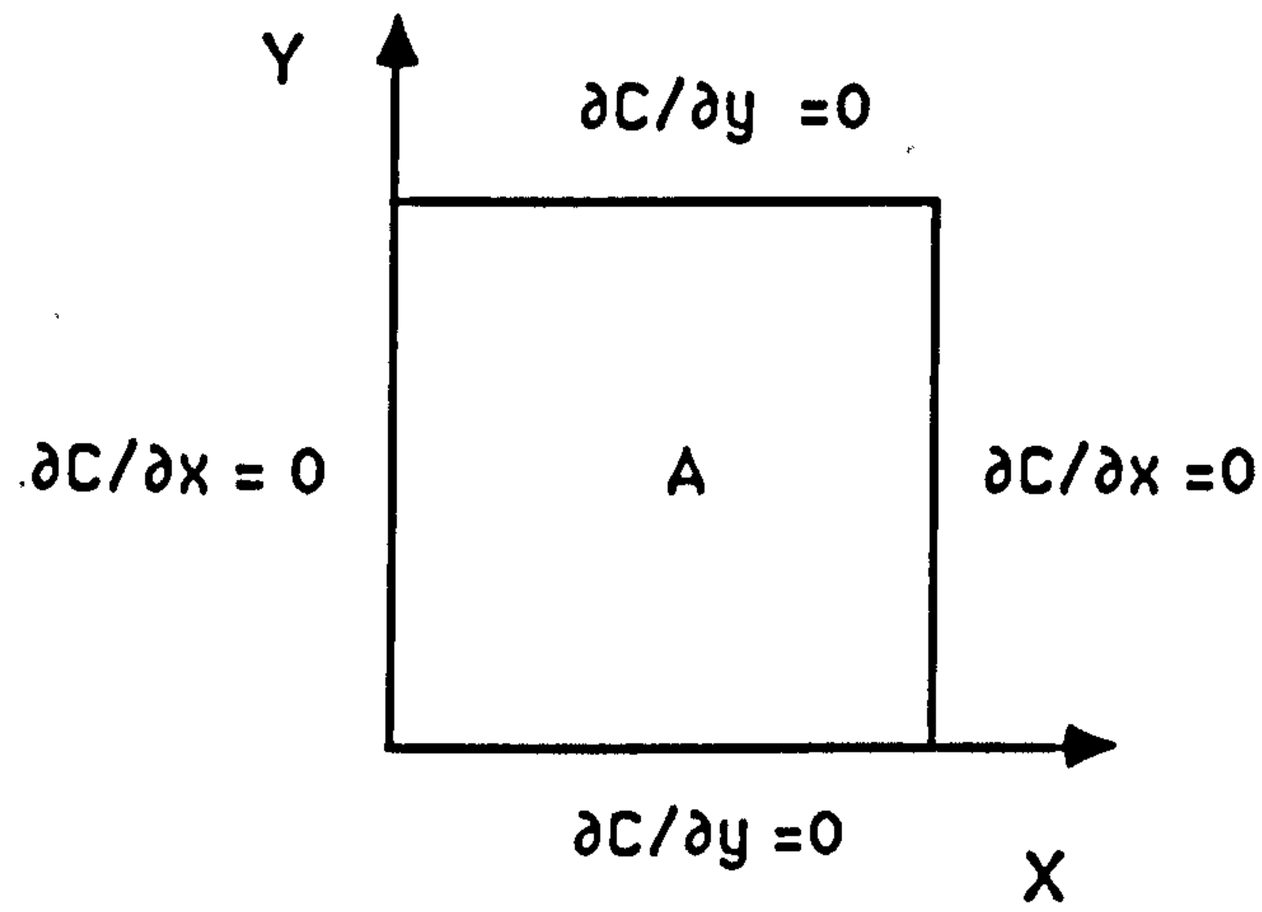

Figure (4.3*)

Boundary conditions for the concentration equation.

4.4.2 INITIAL CONDITIONS.

As described previously in Chapter 3, the problem is one of 'injecting' a quantity of dye into the top half of the cavity while at rest, and observing how the concentration intensity varies with time. The amount of dye within the cavity remains a constant due to conservation, and this can be a useful check on how the solution is proceeding. For this reason the total concentration per unit area (A) is chosen to be unity, i.e

$$\iint_A C(x,y,t)\, dA = 1 \qquad (4.5).$$

The integration is performed numerically using the trapezium rule, the error in which is consistent with the overall discretisation error. The initial concentration distribution generally used is as shown in fig (4.4*).

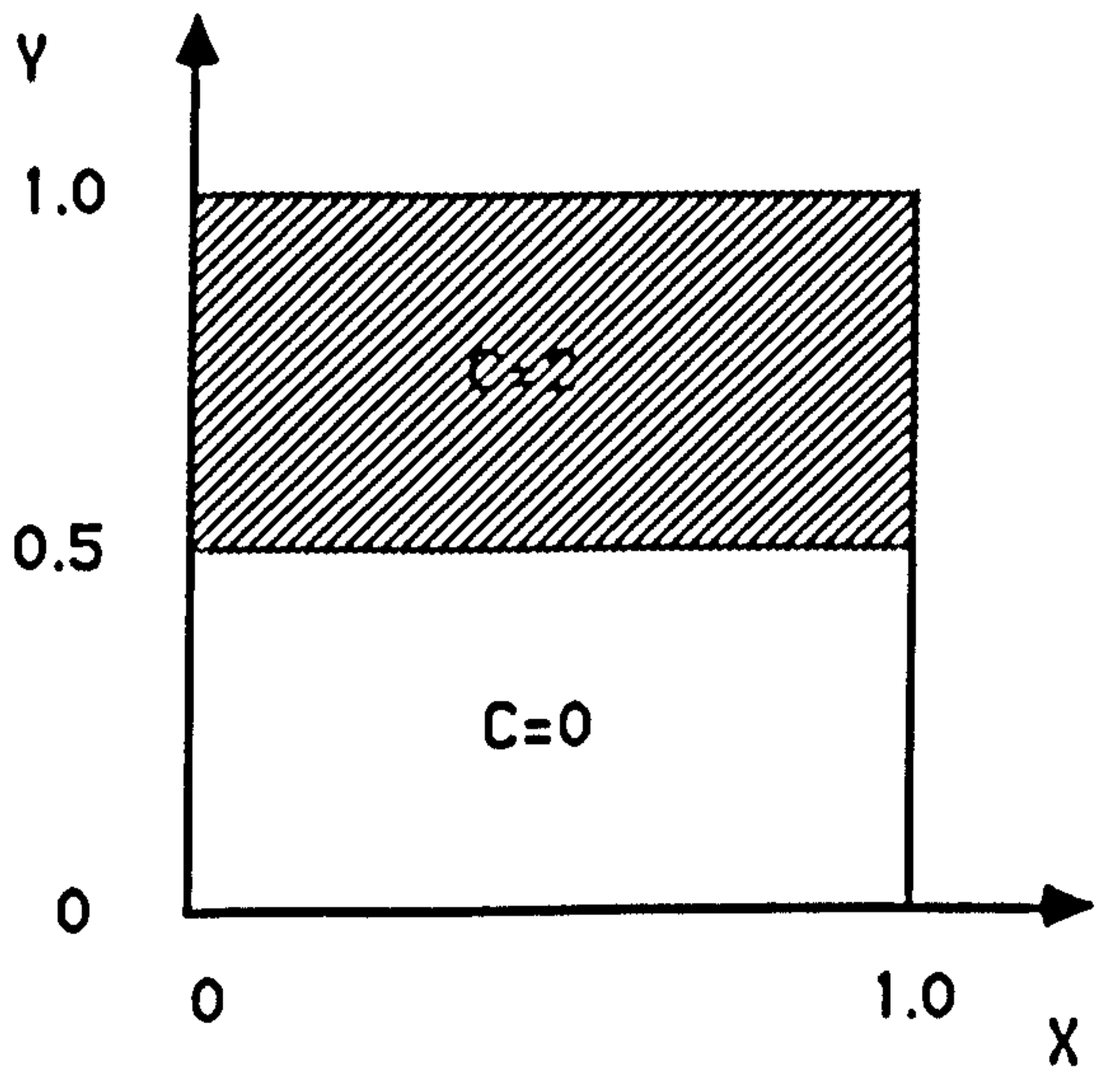

Figure (4.4*)

The initial concentration distribution of the cavity.

4.5.1 THE FINITE DIFFERENCE METHOD

Using the finite difference method the domain of solution of the partial differential equation (PDE) bounded by a closed curve is overlaid with a regular grid or mesh as shown overleaf in fig(4.5*).

The mesh consists of equally spaced lines drawn parallel to the x and y directions respectively, defined in space by:

$x_i = ih$ for i=0 to N, $y_j = jk$ for j=0 to M and in time by $t=n\delta t$, where N,M are the number of grid points in the x and y directions respectively and δt is the time increment, n being the number of these increments required to reach a desired time. The grid spacing in the x and y directions is defined by $h=x_N/N$, $k=y_M/M$ such that Nh=1, Mk=1.

Let $\phi(x, y, u, u_x, u_y, u_{xx}, u_{yy}, u_{xy}, u_t) = 0$ (4.6)

represent a typical second order PDE which we desire to solve, possessing an analytical solution u = u(x,y,t). We define the numerical solution of equation (4.6) to be a set of numbers {u(i,j,n)} arising from the solution of a system of difference equations approximating the PDE, where u(i,j,n) is an approximation to $u(x_i,y_j,t_n)$ the value of the exact analytical solution at a grid point. We assume the value of u at a non-integer grid point may be found by interpolation. It is usually expected

that as the mesh becomes more refined that u(i,j,n) becomes closer to the analytic solution at that grid point, however this is never actually obtained in practice due to computational rounding error in evaluating the arithmetic, but this is usually very small.

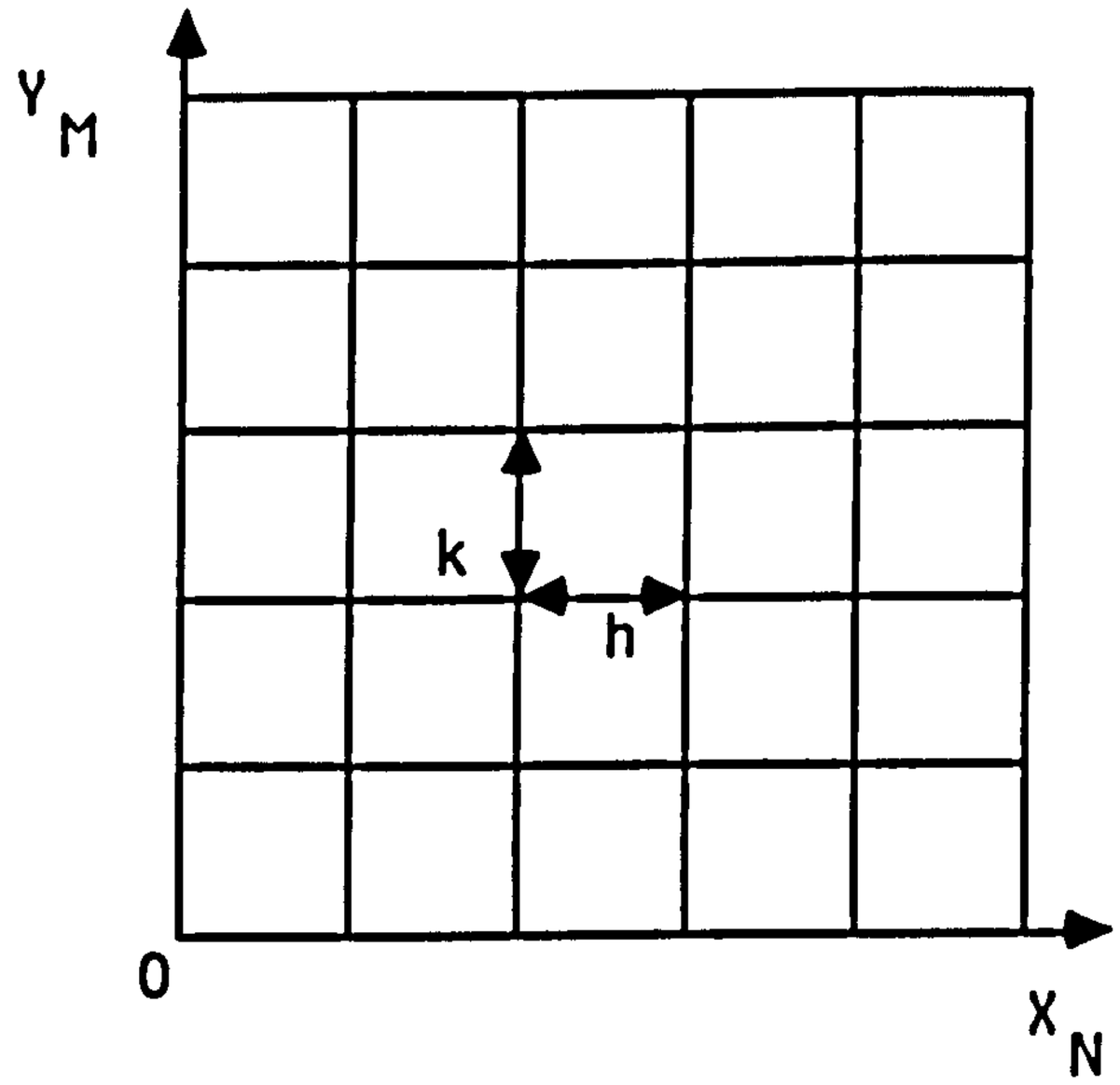

Figure (4.5*)

Diagram of the mesh structure overlaying the cavity.

4.5.2 FINITE DIFFERENCE APPROXIMATIONS TO THE DERIVATIVES.

The most usual and best known method of deriving finite difference approximations for the derivatives is by means of Taylor series. It is assumed that u(x,y,t), the analytic solution of equation(4.6), is continous and its fourth order derivatives exist within the domain of solution. Then by considering (4.7) and (4.8) overleaf, where subscripts denote differentiation with respect to that variable, we obtain:

$$u(x_{i+1},y_j,t_n)= u(x_i,y_j,t_n) + hu_x(x_i,y_j,t_n) + \frac{h^2}{2}u_{xx}(x_i,y_j,t_n) + \frac{h^3}{3!}u_{xxx}(x_i,y_j,t_n) + \frac{h^4}{4!}u_{xxxx}(\xi^+_i,y_j,t_n) \quad (4.7)$$

$$u(x_{i-1},y_j,t_n)= u(x_i,y_j,t_n) - hu_x(x_i,y_j,t_n) + \frac{h^2}{2}u_{xx}(x_i,y_j,t_n) - \frac{h^3}{3!}u_{xxx}(x_i,y_j,t_n) + \frac{h^4}{4!}u_{xxxx}(\xi^-_i,y_j,t_n) \quad (4.8)$$

upon adding (4.7) and (4.8) and using fact that

$$u_{xxxx}(\xi^+_i,y_j,t_n) + u_{xxxx}(\xi^-_i,y_j,t_n) \leq 2u_{xxxx}(\xi_i,y_j,t_n)$$

where $x_{i-1} < \xi_i < x_{i+1}$ produces

$$\frac{u(xi+1,yj,tn)-2u(xi,yj,tn)+u(xi-1,yj,tn)}{h^2} = u_{xx}(x_i,y_j,t_n)+ E_1 \quad (4.9)$$

where $E_1 = \frac{h^2}{12}u_{xxxx}(\xi_i,y_j,t_n)$.

Similarly subtracting (4.8) from (4.7) gives

$$\frac{u(xi+1,yj,tn)-u(xi-1,yj,tn)}{2h} = u_x(x_i,y_j,t_n) + E2 \quad (4.10)$$

where $E_2 = \frac{h^2}{6}u_{xxx}(\xi_i,y_j,t_n)$.

we have ignored the $O(h^2)$ truncation terms in both (4.9) and (4.10) and writing $u(x_i,y_j,t_n) = u_{ij}^n$, the derivatives may be written as:

$$\frac{\partial^2 u(x_i,y_j,t_n)}{\partial x^2} = \frac{u_{i+1j}^n - 2u_{ij}^n + u_{i-1j}^n}{h^2} \qquad (4.11)$$

$$\frac{\partial u(x_i,y_j,t_n)}{\partial x} = \frac{u_{i+1j}^n - u_{i-1j}^n}{2h} \qquad (4.12)$$

and similarly

$$\frac{\partial^2 u(x_i,y_j,t_n)}{\partial y^2} = \frac{u_{ij+1}^n - 2u_{ij}^n + u_{ij-1}^n}{k^2} \qquad (4.13)$$

$$\frac{\partial u(x_i,y_j,t_n)}{\partial y} = \frac{u_{ij+1}^n - u_{ij-1}^n}{2k} \qquad (4.14)$$

for i=1 to N-1 and j=1 to M-1.

4.5.3 THE TIME DERIVATIVE

Employing a Taylor series approximation once again produces:

$$u(x_i,y_j,t_{n+1}) = u(x_i,y_j,t_n) + \delta t \frac{\partial u(x_i,y_j,t_n)}{\partial t} + \frac{\delta t^2}{2}\frac{\partial^2 u(x_i,y_j,t_n)}{\partial t^2} + \ldots\ldots \qquad (4.15)$$

Truncating after the fourth term and re-arranging gives:

$$\frac{u(xi,yj,tn+1)-u(xi,yj,tn)}{\delta t} = \frac{\partial u(x_i,y_j,t_n)}{\partial t} + \frac{\delta t}{2}\frac{\partial^2 u(x_i,y_j,t_n)}{\partial t^2} + \ldots\ldots \qquad (4.16).$$

Ignoring the local truncation error of $O(\delta t)$, and writing in standard notation the time derivative may be expressed as:

$$\frac{\partial u(x_i,y_j,t_n)}{\partial t} = \frac{uij^{n+1} - uij^n}{\delta t} \qquad (4.17).$$

This method of discretisation renders the equations simply explicit, but does have the disadvantage that time increments, especially for large Reynolds' numbers, need to be quite small to

ensure that the difference equations are stable. This will be discussed in more detail later in this chapter.

4.6 DISCRETISATION OF THE FLOW EQUATIONS.

By focusing our attention on the numerical values obtained at the grid points of the mesh used to cover the flow domain, we have in essence replaced the continuous information contained within the exact analytical solution of the PDE, with a set of discrete values. The algebraic equations involving unknown values of the dependent variable u in (4.6) at a chosen grid point are termed discretised equations, and are derived directly from the PDE itself by using difference approximations for the derivatives. It is these algebraic discretised equations which we aim to solve to provide an approximation to the analytical solution of the PDE.

By replacing the derivatives of Ψ and C in the governing flow equations (4.2), (4.4) with respect to x,y,t by the difference approximations shown above, and upon simplifying produces the following set of discretised equations.

4.6.1 THE DISCRETISED STREAM-FUNCTION EQUATION.

$$k^2(\hat{\Psi}_{i+1\,j}+\hat{\Psi}_{i-1,j}) - 2(h^2+k^2)\hat{\Psi}_{ij} + h^2(\hat{\Psi}_{ij+1}+\hat{\Psi}_{ij-1}) = -(hk)^2\hat{\omega}_{ij} \qquad (4.18).$$

4.6.2 THE DISCRETISED CONCENTRATION EQUATION.

$$C_{ij}^{n+1}=(A_2+A_4)C_{ij-1}^{n} + (A_1+A_3)C_{i-1j}^{n} + (1-2(A_1+A_2))C_{ij}^{n}$$

$$+ (A_1-A_3)C_{i+1j}^{n} + (A_2-A_4)C_{ij-1}^{n} \qquad (4.19).$$

$$A_1 = \frac{\delta t D}{h^2},\ A_2 = \frac{\delta t D}{k^2},\ A_3 = \frac{\delta t b_1}{2h},\ A_4 = \frac{\delta t b_2}{2k},\ b_1 = \frac{\partial \Psi}{\partial y},\ b_2 = -\frac{\partial \Psi}{\partial x} \qquad (4.20).$$

4.6.3 THE DISCRETISED VORTICITY EQUATION.

This is discretised in a slightly different way to the others due to the presence of $\partial/\partial x(\eta^2\ \partial\omega/\partial x)$ and $\partial/\partial y(\eta^2\partial\omega/\partial y)$ terms. We have used a method which is similar to that used in the control volume approach. The control volume method applies various conservation laws to a macroscopic control volume and is an alternative way to produce the discretised equations governing the flow. It offers a more intuitive derivation with more physical significance, but eventually reduces to the same finite difference equations. A full account of this method can be found in Tucker[107], Roache[92] and Pantankar[84].

Equation (4.1) may be discretised as before with central differences being used whenever possible, the only exception occurs when treating the expression $\partial/\partial x(\eta^2\partial\omega/\partial x)$, where η^2 is presently taken to mean $(\eta(q))^2$. However, this presents no real problem and may be discretised by treating the expression as the

first derivative of a first derivative. With reference to fig (4.6*) we write:

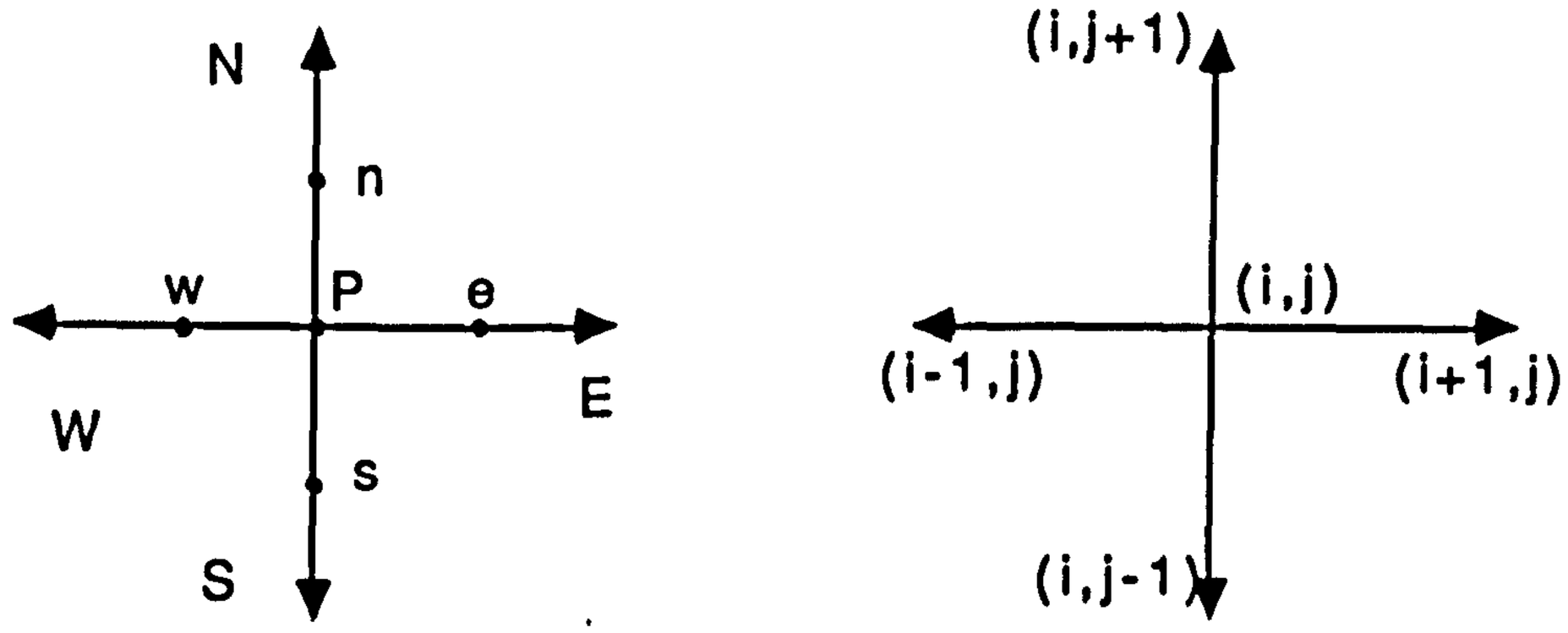

Figure (4.6*)

$$\frac{\partial}{\partial x}(\eta^2 \frac{\partial \omega}{\partial x}) = \frac{\{(\eta^2 \omega_x)^e - (\eta^2 \omega_x)^W\}}{h}$$

$$= \frac{\{(\eta^2)^e \frac{(\omega^E - \omega^P)}{h} - (\eta^2)^W \frac{(\omega^P - \omega^W)}{h}\}}{h}$$

$$= \frac{\{(\eta^2)^e(\omega^E - \omega^P) - (\eta^2)^W(\omega^P - \omega^W)\}}{h^2} \qquad (4.21)$$

and in a similar manner we obtain

$$\frac{\partial}{\partial y}(\eta^2 \frac{\partial \omega}{\partial y}) = \frac{\{(\eta^2)^n(\omega^N - \omega^P) - (\eta^2)^s(\omega^P - \omega^S)\}}{k^2} \qquad (4.22)$$

The remainder of the terms in equation (4.1) may be approximated in the usual manner using the central differencing techniques described earlier. The final result is equation (4.23).

$$w_{ij}^{n+1} = (1-(c1+c2+c3+c4))w_{ij}^{n}+(c1-c5)w_{i+1j}^{n}+(c2+c5)w_{i-1j}^{n}$$

$$(c3+c6)w_{ij+1}^{n} + (c4-c6)w_{ij-1}^{n} - c7F_{ij}^{n} \qquad (4.23)$$

Where

$$c1=\frac{\delta t(\eta^2)^e}{\eta^p Reh^2}\ ,\ c2=\frac{\delta t(h^2)^w}{\eta^p Reh^2},\ c3=\frac{\delta t(h^2)^n}{\eta^p Rek^2},\ c4=\frac{\delta t(h^2)^s}{\eta^p Rek^2},$$

$$c5=\frac{\beta 1}{2h}\ ,\ c6=\frac{\beta 2}{2k}\ ,\ c7=\frac{\delta t}{\eta pRe}\ ,\ b1=\frac{\partial \Psi}{\partial y}\ \ b2=\frac{\partial \Psi}{\partial x},\ \text{and}$$

$$F_{ij}^{n}=\eta^p Re\left(4\frac{\partial^2\eta^p}{\partial y\partial x}\frac{\partial^2\Psi}{\partial x\partial y}+\left(\frac{\partial^2\Psi}{\partial y^2}-\frac{\partial^2\Psi}{\partial x^2}\right).\left(\frac{\partial^2\eta^p}{\partial y^2}-\frac{\partial^2\eta^p}{\partial x^2}\right)\right)$$

In the above expressions N is the grid point(i,j+1), S=(i,j-1),

W=(i-1,j), E=(i+1,j) and P=(i,j). The lower case letters n,s,w,e signify the mid-points between the uppercase letters representing the grid points of the mesh shown in fig (4.6*).

At this juncture attention is drawn to the fact that near the top two corner points, in case of standard cavity flow, singularities exist due to the velocity gradients becoming increasingly large, resulting in the shear rate and the vorticity becoming infinite at these points. This does introduce an immediate problem into our proposed method of solution as these points are used in evaluating the cross derivative for both the viscosity and the stream-function. However, methods are available which help alleviate the problem caused by the corner singularities, and

some of these may be found in CDW[29] and Gupta et al[42]. The flow near the corner singularities is discussed later in this chapter.

A problem which naturally arises from the way in which the above derivatives are represented, is how to model the viscosity at intermediate grid points(n,s,w,e). Initially we defined the viscosity to be the average value of the respective adjacent grid points. For example, with reference to fig(4.6*),

$$(\eta^e)^2 = 0.25\ (\eta^E + \eta^P)^2 \qquad (4.24)$$

and likewise by symmetry similar expressions exist for the other three points. However, an approximation incorporating more information, and of the same accuracy is given by the less obvious formula given by Williams[117],

$$(\eta^e)^2 = (6(\eta^P)^2 + 3(\eta^E)^2 - (\eta^W)^2)/8 \qquad (4.25)$$

which has the advantage of 'packing' more information into the model, and once again by symmetry, similar expressions exist for the other three points.

Lastly, we discuss how to deal with the cross derivative of the form $\partial^2\Psi/\partial x\partial y$ which, due to the cavity's geometry, especially near the sharp corners where singularites exist, creates a few problems. For the present it seems reasonable to discretise the cross derivative $\partial^2\Psi/\partial x\partial y$ as $\partial/\partial x(\partial\Psi/\partial y)$, i.e the derivative of a derivative. Then following the usual procedure, we produce:-

$$\frac{\partial^2\Psi}{\partial x\partial y} = \frac{\{(\Psi_{i+1,j+1} - \Psi_{i-1,j+1}) - (\Psi_{i+1,j-1} - \Psi_{i-1,j-1})\}}{4hk}$$

which is $O(h^2,k^2)$ accurate and thus consistent with the other approximations. However, alternative discretisation formulae exist for the cross derivatives which by-pass the corner singularities, and these may be seen in CDW[29].

4.7 THE NUMERICAL TREATMENT OF BOUNDARY CONDITIONS.

For the vorticity and stream function equations, whether time dependent or not, the boundary conditions are of the Dirichlet type, the dependent variable being specified at each grid point around the boundary. The vorticity on the boundaries of the cavity is specified by the Woods formulae (CDW[29]) based on a knowledge of the interior stream-function and vorticity values, and are preferred due to the fact that they preserve the second order accuracy of the difference equations.

As an example for standard cavity flow the vorticity on the top moving wall is given by

$$\omega_{iM} = -\frac{3}{k^2}(\Psi_{iM-1} + kv_t) - \frac{1}{2}\omega_{iM-1} \qquad (4.27),$$

for j=M, and i=1 to N-1,and similar expressions exist for all cavity's walls, where 'v_t' represents the speed top plate.

The stream-function has a constant value on each of the cavities walls as a consequence of the no-slip conditions imposed, and for simplicity we take this value of stream-function to be zero on all four of cavities walls.

$\Psi_{i0}=0$, $\Psi_{iM}=0$ for i=0 to N and $\Psi_{0j}=0$, $\Psi_{Nj}=0$ for j=0 to M. (4.28)

The boundary conditions for the concentration equation are of the homogeneous Neumann type, i.e the gradient or flux condition $\partial C/\partial n$ being specified as zero on all of cavity's walls, where n represents the outward normal to the surface. As the walls are assumed to be impermeable, $\partial C/\partial n=0$ on each boundary.

The derivative boundary conditions are approximated in the usual way using central differencing, again to preserve the $O(h^2,k^2)$ accuracy. The method however gives rise to what are known as 'ghost points', which are points which lie outside the solution domain. However, by assuming that the original discretised equation and the boundary derivative difference equations hold true simultaneously, these ghost points may be eliminated and an expression for C_{ij}^{n+1} is obtained in terms of previously calculated values.

For the concentration equation, at the corner points two expressions for the derivatives exist simultaneously, and again by assuming that both hold true concurrently with the discretised concentration equation, then an expression for c_{ij}^{n+1} at the four

corner points can be produced. A good discussion on derivative boundary conditions can be found in CDW[29] and Smith[100].

4.8 CONSISTENCY AND STABILITY.

The questions which naturally arise from the discretised finite difference approximations to the original PDE are, how good are the approximations in representing the differential equation, and how stable are the numerical solutions which they produce?

During the discretisation process, by using truncated Taylor series approximations for the derivatives contained within the original PDE, we have introduced into the approximating difference equations a discretisation error. However if the grid becomes more refined then the discretisation error can usually be seen to approach zero, so that the difference equations may be seen to be compatible or consistent with the original PDE. In theory this is always achieved by choosing ever more refined grids, yet as the grid becomes more refined the number of equations needed to be solved increases so that the time taken to solve these equations also increases and the effect of rounding errors becomes more pronounced, which is not always acceptable.

The stability of finite difference approximations is concerned with the unstable growth or the stable decay of arithmetic errors

associated with the computer operations needed to solve the finite difference equations. Theoretically an analytic solution to any one of the difference equations exists, yet due to rounding errors in the computer arithmetic which are committed as the explicit calculation is carried out, then an analysis of whether these errors amplify or decay, characterises the stability of the numerical scheme used to solve the difference equations.

If the difference approximation is stable then any computational errors which arise can be made arbitrarily small. For linear PDE's we know due to a celebrated theorem of Lax[54] that if the difference scheme used is compatible and stable then we are assured of convergence. However, as most of the PDE's we require to solve are non-linear then even if the stability and compatability conditions of the difference operator are satisfied, no suitable theorem currently exists to guarantee convergence.

There are many methods which have been developed to investigate the stability of the difference equations depending on whether the equations are time dependent or not. Two of the most widely used are the matrix method and the Von-Neumann method, the latter being used primarily for time dependent parabolic equations. Using this method for our time dependent discretised equations we define the difference equations to be stable if small

pertubations δ_{jl}^{n} in the exact solution of the difference equation remained bounded as time becomes infinite ($n\to\infty$).

The Von-Neumann method is essentially a Fourier method, and is extremely useful for the study of non-linear parabolic PDE's, CDW[29]. The perturbation at a grid point(j,l) at a given time level(n) is expressed sinusoidally as:

$\delta_{jl}^{n} \sim \xi^{n} e^{i\sigma_1 jh}\, e^{i\sigma_2 lk}$, where $i=\sqrt{-1}$, and ξ is known as the amplification factor. For stability we require that $|\xi|<1$. The errors which are propagated during computation are known to satisfy the difference equations themselves and so substituting for δ_{jl}^{n} in each difference equation approximating the PDE produces the necessary conditions for the difference scheme to be stable. A full account of the method may be found in texts such as CDW[29], Smith[100] and Lapidus and Pinder[55].

We now give the stability and compatibility results for both time dependent and steady flows which we have considered.

For the time dependent PDE's , namely the vorticity (4.1), and concentration (4.4), equations, the error due to discretisation is found to be $O(\delta t, h^2, k^2)$, so it can be seen that as the mesh becomes more refined, (i.e h,k->0), and if δt is sufficiently small, then the discretisation error tends to zero, and the difference equations are compatible with the PDE's themselves.

From applying Von-Neumann analysis to these same equations we have found the vorticity equation to be stable provided that $\delta t \leqslant Reh^2/4$, and likewise the concentration equation is stable provided $\delta t \leqslant h^2/4D$. These limitations were also found to be borne out in practice.

The stream-function equation (4.2) contains no time dependent terms, and is therefore a steady state equation. The stability of the difference equations approximating all steady state type problems may be found directly from analysing the computational molecule or stencil, which for the stream-function equation is of the form shown in fig(4.7*).

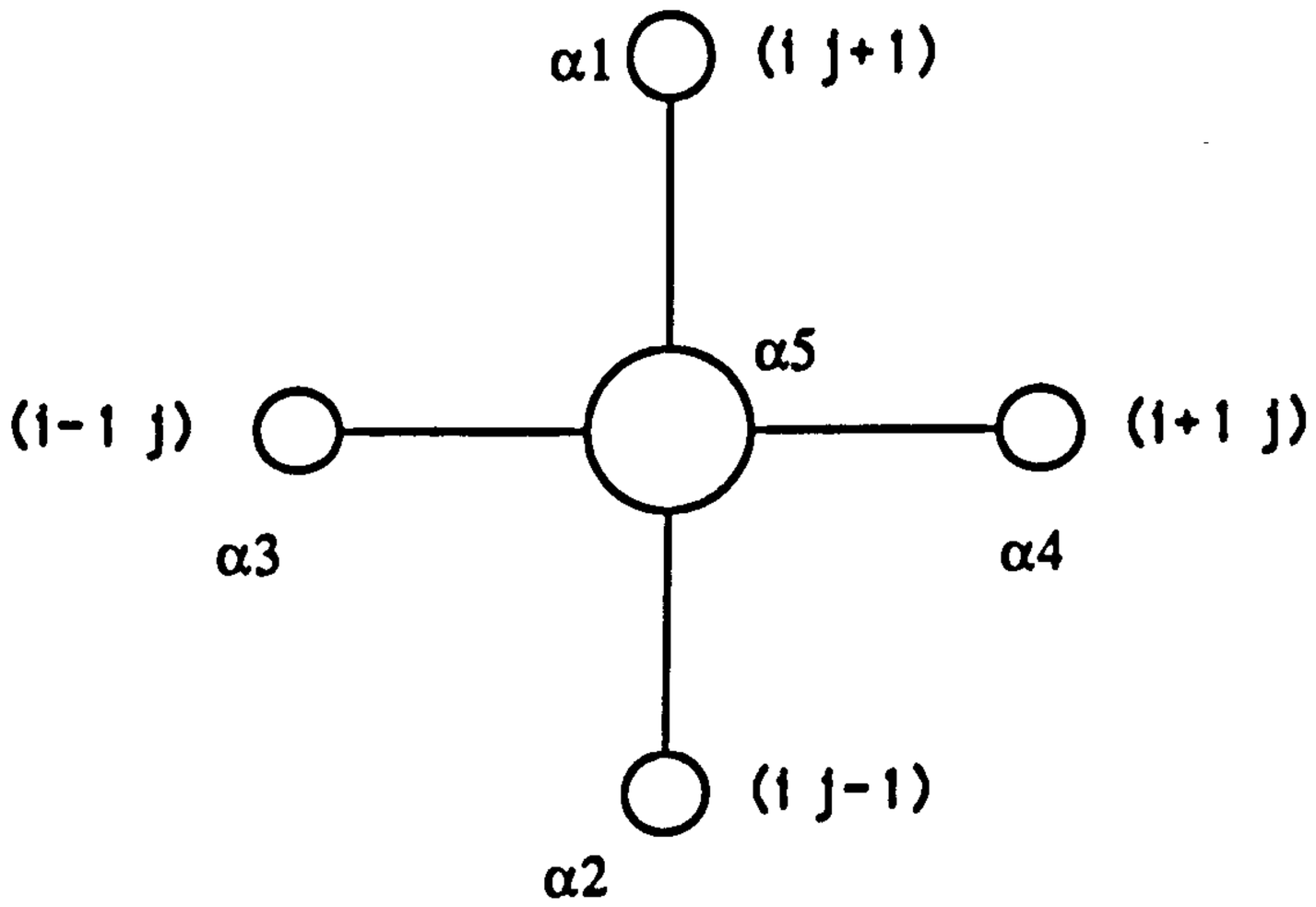

Figure (4.7*)

The computational molecule for the stream function equation.

Where with reference to fig(4.7*) we have:

$$\alpha 5 = -2(h^2+k^2),\ \alpha 1 = \alpha 2 = h^2,\ \alpha 3 = \alpha 4 = k^2 \qquad (4.29)$$

For stability it is required that the molecule possesses diagonal dominance, such that $\alpha 5 \geqslant \alpha 1 + \alpha 2 + \alpha 3 + \alpha 4$ with at least one strict moduli inequality for some (i,j). Using the values given above in (4.29) the computational molecule may clearly be seen to be diagonally dominant. The second constraint we impose on the stencil is that all four of the satellites of $\alpha 5$ must be positive. For the stream-function equation all satellites are positive definite, hence both criteria are satisfied and the molecule or stencil is said to be stable. The error due to the discretisation process is of the order $O(h^2,k^2)$ from which it can be seen as the mesh is refined, the error diminishes to zero, showing the stencil of the approximating difference equation to be compatible with the Poisson type stream-function PDE. The stream-function equation is an example of a linear PDE which is part of a strongly non-linear system, but for small changes in the Reynolds' number the linear stability analysis provided Lax's theorem, is indicative of convergence.

By convergence we mean $\Psi(i,j) \rightarrow \Psi(x_i,y_j)$ as $h,k \rightarrow 0$.

A further example occurs by considering the steady state vorticity equation which we have also employed when simulating steady cavity flow. The PDE itself may be obtained directly from (4.1) by taking $\partial/\partial t=0$. The corresponding difference equation is:

$$K1\omega_{ij} = K2\omega_{ij-1} + K3\omega_{i-1j} + K4\omega_{i+1j} + K5\omega_{ij+1} - \eta_{ij}F \qquad (4.30)$$

where F is specified after (4.23) and

$$K1 = -\{\frac{(\eta^2)^e + (\eta^2)^w}{h^2} + \frac{(\eta^2)^n + (\eta 2)^s}{k^2}\}$$

$$K2 = \{\frac{(\eta^2)^s}{k^2} - \frac{\eta Re\beta 2}{2k}\}$$

$$K3 = \{\frac{(\eta^2)^w}{h^2} + \frac{\eta Re\beta 1}{2h}\}$$

$$K4 = \{\frac{(\eta^2)^e}{h^2} - \frac{\eta Re\beta 1}{2h}\} \qquad (4.31)$$

$$K5 = \{\frac{(\eta^2)^n}{k^2} + \frac{\eta Re\beta 2}{2k}\}$$

$$\beta 1 = \frac{\partial \Psi}{\partial y}, \quad \beta 2 = -\frac{\partial \Psi}{\partial x}$$

For stability we require $K1 \geq K2+K3+K4+K5$ which is satisfied,

and also $K2,K3,K4,K5 \geq 0$ which occurs if

$$\frac{-2(\eta^2)^n}{\eta^p \beta 2 k} \leqslant Re \leqslant \frac{2(\eta^2)^s}{\eta^p \beta 2 k} \quad \text{and} \quad \frac{-2(\eta^2)^w}{\eta^p \beta 1 h} \leqslant Re \leqslant \frac{2(\eta^2)^e}{\eta^p \beta 1 h} \qquad (4.32)$$

hold true simultaneously.

4.9 NUMERICAL METHODS USED TO SOLVE THE FINITE DIFFERENCE EQUATIONS

The finite difference methods employed to solve the non-linear system of partial differential equations with prescribed boundary conditions gives rise to a system of non-linear algebraic simultaneous equations of form $A\underline{x}=\underline{b}$ where A is a $(N-1) \times (N-1)$ square matrix and $\underline{b}$ a $((N-1) \times 1)$ column

vector. The number of equations produced is generally large and hence the solution generates a problem in itself, and the task of solving the system has to be undertaken with the aid of a powerful computer. The two main methods used to tackle the problem numerically are :

(i) Direct methods

(ii) Iterative methods.

Direct methods solve the algebraic system of equations in a pre-determined number of steps using algorithms such as Gaussian elimination or triangular decomposition, at the end of which the solution is obtained. However for explicit difference equations these are generally more computationally costly than iterative methods which are easier to code and use less computer memory.

4.9.1 ITERATIVE METHODS.

Iterative methods are used for solving systems of algebraic equations when A is large, diagonally dominant, and when the matrix coefficients are sparse but with A well conditioned. An iterative method of solution also becomes attractive when direct methods require more computer storage than is convenient. The iterative method used for solving the system of algebraic equations is one in which a first approximation or initial guess is

used to calculate a second approximation to the solution which is hoped to be better than the first. This second approximation is then used to generate a third approximation and so on until convergence is hopefully obtained.

However, the equations which govern the flow of a moving plate or wall over the cavity are non-linear, and the resulting algebraic system of equations produced is also non-linear, and it is these non-linear systems of equations which must be solved iteratively.

At each iteration the system is linearised using previously calculated values and the resulting linear system is solved to provide an updated approximation to the solution. Whatever iterative method is used to overcome the non-linearity of the system, there is rarely a mathematical theory which will guarantee convergence, however if convergence is attained for the system stated above, the solution is usually unique.

The iterative method used is said to be convergent when the differences between the successive iterates tend to zero as the number of iterations increase. In practice this is never the case, but what is important is that successive iterates converge fairly rapidly to values that agree within some small pre-specified accuracy or tolerance limit.

When dealing with steady state problems the convergence criteria used is:

$| \omega_{ij}^{P+1} - \omega_{ij}^{P} | < \varepsilon 1$ and $|\Psi_{ij}^{P+1} - \Psi_{ij}^{P}| < \varepsilon 2$ where P represents the iteration number.

This convergence criterion was used during implementations of the well known Jacobi and Gauss-Seidel algorithms which will be discussed later. To try to accelerate convergence an adapted S.O.R method was attempted. The convergence criteria for this scheme is a little different to the previous Jacobi and Gauss-Seidel methods, and is defined in section (4.9.4) of this chapter.

In the computer programs used to numerically solve the steady state problems, we choose based on experience and the findings of other research workers e.g Havard[44], $\varepsilon 1$ and $\varepsilon 2$ to be 0.005. When time dependence enters the equations no tolerance limits are imposed for the vorticity and concentration equations, and the program terminates after a prespecified time.

Using iterative techniques to solve the algebraic system of equations does have the disadvantage in that every time it is used it introduces a global rounding error into the calculations. However, with modern day computers the global rounding error is recognised as being very small, consequently most of the errors involved in solving PDE's by the finite difference method arise

from the local truncation error in approximating the derivatives themselves.

The simplest and easiest iterative methods to set up on a computer are those of Jacobi, Gauss-Siedel and various S.O.R methods, which are outlined below, and are known as classical iterative methods.

Other more involved iterative methods such as the pre-conditioned conjugate gradient method (CDW[29]) and Stone's strongly implicit method (Smith[100]) are available, but these are more complicated and use more computer memory although they can be significantly faster. Thus on balance of ease of computing and computer time not being critical, the former methods were implemented.

4.9.2 THE JACOBI ITERATIVE METHOD.

Jacobi's method for solving a linearised system of form $A\underline{x}=b$, expresses the (n+1)th iterative approximation exclusively in terms of the n'th iterative values, that is the new values at any instant are calculated explicitly from the old or previous iterative values. (At the end of each iteration in our computer program the new values are set equal to the old values and the process continues until convergence is obtained). Jacobi's method can be expressed in matrix notation by decomposing A into three

simpler matrices D, L and U with D consisting of all the diagonal entries of matrix A, L the lower triangular matrix and U the upper triangular matrix. Consequently the system of algebraic equations may be written as $(D-L-U)\,\underline{x} = \underline{b}$ and the Jacobi iteration written as :-

$$D\,\underline{x}^{(n+1)} = (L+U)\underline{x}^{(n)} + \underline{b} \quad \text{or} \quad \underline{x}^{(n+1)} = D^{-1}(L+U)\,\underline{x}^{(n)} + D^{-1}\underline{b} \qquad (4.33).$$

The iteration may generally be expressed in the form $\underline{x}^{(n+1)} = G\,\underline{x}^{(n)} + \underline{c}$ and this is true for all the iterative methods which will be considered.

Using an initial guess $\underline{x}^{(0)}$ the iterative method uses the matrix G and $\underline{c}$ to generate a new approximation $\underline{x}^{(1)}$, which is then used to generate a 'better' approximation $\underline{x}^{(2)}$ and so on.

With the Jacobi iteration $G = D^{-1}(L+U)$ is known as the point Jacobi iteration matrix. It is well known (see for example CDW[29] , Smith [100], Froberg[39]) that the particular iterative method used will converge if $\rho(G) < 1$ where $\rho(G)$ denotes the eigenvalue of largest modulus of G, i.e the spectral radius of the matrix. Thus for Jacobi iteration we require $\rho(D^{-1}(L+U)) < 1$

4.9.3 THE GAUSS-SEIDEL METHOD

This method is very similar to the Jacobi iterative method except it speeds up convergence considerably by using the newest calculated values as soon as they are available. In matrix notation the Gauss-Seidel iteration is defined as :-

$(D - L)\underline{x}^{(n+1)} = U\,\underline{x}^{(n)} + \underline{b}$ hence it can be seen that;

$$\underline{x}^{(n+1)} = (D - L)^{-1}U\,\underline{x}^{(n)} + (D - L)^{-1}\underline{b} \qquad (4.34)$$

where $\underline{c}=(D-L)^{-1}\underline{b}$ and $G = (D - L)^{-1}U$ is the point Gauss-Seidel iteration matrix for the general iteration scheme and following the Jacobi method for convergence it is required that :

$\rho(G) = \rho((D - L)^{-1}U) < 1$.

4.9.4 THE S.O.R METHOD.

This is a modified form of the Gauss-Seidel iteration known as successive over relaxation. The method itself involves the use of a variable parameter ξ which hopefully accelerates the convergence to solution. The method of solving the large algebraic system of simultaneous equations using the S.O.R method is given below.

The S.O.R iteration is defined as $\underline{d} = \xi\underline{d}_1$ (4.35)

where $\underline{d}$ and $\underline{d}_1$ are the correction or displacement vectors obtained after each iteration, for the S.O.R and Gauss-Seidel methods respectively. If the relaxation parameter ξ takes a value

in the range $1 < \xi < 2$ the system is said to be over relaxed, and likewise if in range $0 < \xi < 1$, the system is under relaxed. When $\xi = 1$ the Gauss-Seidel iteration scheme is obtained.

From the Gauss Seidel iteration (4.34),

$\underline{x}^{(n+1)} = D^{-1}L\underline{x}^{(n+1)} + D^{-1}U\underline{x}^{(n)} + D^{-1}\underline{b}$ then

$\underline{d}_1 = \underline{x}^{(n+1)} - \underline{x}^{(n)} = D^{-1}L\underline{x}^{(n+1)} + D^{-1}U\underline{x}^{(n)} + D^{-1}\underline{b} - \underline{x}^{(n)}$.

Then using (4. 35) we obtain

$\underline{x}^{(n+1)} - \underline{x}^{(n)} = \xi(D^{-1}L\underline{x}^{(n+1)} + D^{-1}U\underline{x}^{(n)} + D^{-1}\underline{b} - \underline{x}^{(n)})$

and after gathering like terms and simplifying, the S.O.R point iteration scheme is:

$$\underline{x}^{(n+1)} = (1-\xi D^{-1}L)^{-1}((1-\xi)I + \xi D^{-1}U))\underline{x}^{(n)} + (1-\xi D^{-1}L)^{-1}\xi D^{-1}\underline{b}, \quad (4.36)$$

where $G = (1-\xi D^{-1}L)^{-1}((1-\xi)I + \xi D^{-1}U))$, $\underline{c} = (1-\xi D^{-1}L)^{-1}\xi D^{-1}\underline{b}$,

and as usual for convergence we require $\rho(G) < 1$.

For the Gauss-Seidel iteration convergence is obtained if $|\omega^{(P+1)}(G.S) - \omega^{(P)}| <= \mu$, with μ being a pre-specified tolerance limit. For the S.O.R iteration, the difference between the P'th and (P+1)'th iterates becomes :

$$\delta\omega = |\omega^{(P+1)} - \omega^{(P)}| = |\omega^{(P+1)}_{S.O.R} - \omega^{(P)}|$$

$$= |(1-\xi)\omega^{(P)} + \xi\,\omega^{(P+1)}(G.S) - \omega^{(P)}|$$

$$= |\xi||\omega^{(P+1)}(G.S) - \omega^{(P)}|$$

$$= |\xi||\mu|$$

and convergence is obtained when $|\delta\omega| < \varepsilon 1|\omega max|$, where $\delta\omega$ is the

difference in ω values at each nodal point after each iteration, and ωmax is the biggest difference between successive iterates over the whole grid.

4.10 THE VORTICITY CONSTRAINT.

Once a convergent solution for the linearised system of equations is obtained, it is desirable to know how well behaved the solution is. A useful check on the numerical computation is given by the vorticity constraint, whereby the total vorticity generated by the flow is calculated. The total value of the vorticity within the cavity is given by the expression

$$\iint_A \omega \, dA = \iint_A \text{curl } \underline{v} \, dA \qquad (4.37)$$

where the double integral is taken over the area (A) of the cavity. Applying Stokes' theorem to this expression yields :-

$$\iint_A \text{curl } \underline{v} \, dA = \int_C \underline{v} . d\underline{r} = \int_C u dx + v dy \qquad (4.38)$$

where $\underline{v}$ represents the velocity vector having components u and v in the x and y directions respectively and 'c' is the simple closed curve representing the boundary of the cavity. The integration is carried out taking the anticlockwise direction as positive, by convention as in fig (4.8*).

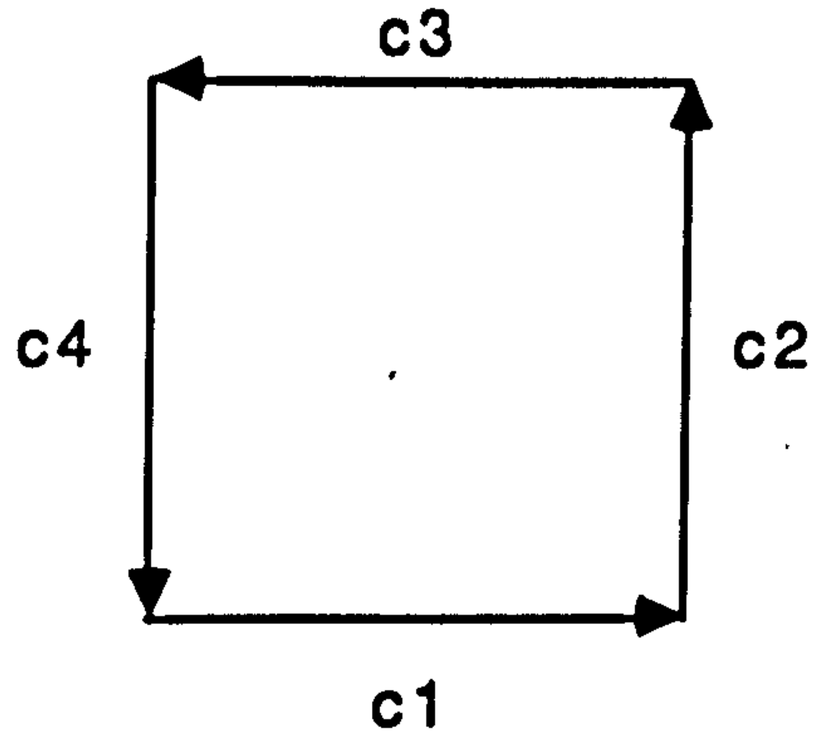

Figure (4.8*)

For standard cavity flow, where only the top wall moves with a constant speed U=1, we obtain:

$$\iint_A \text{curl } v \, dA = \int_{c3} U dx = -U = -1 \qquad (4.39).$$

This expression is subsequently altered for various other types of cavity flow considered, having a value of -2 for example for the case of continuous co-rotational flow. Expression (4.39) was evaluated numerically by applying the trapezium integration rule to the double integral, the error in the approximation being of $O(h^2)$. Since the total sum of the vorticity over the cavity is constant, regardless of the solution method chosen to solve the algebraic system of equations, this expression is useful for comparative purposes. It was found that on a very coarse grid such as (10 X 10) the vorticity integral was typically in error by about 15%. However as the mesh becomes more refined (40 X 40) the error reduces to about 5%.

4.11 IMPLEMENTATION OF THE JACOBI/GAUSS-SEIDEL/S.O.R METHODS.

For familiarisation with and to gain understanding of the iterative methods discussed previously, the computer programs used to solve the flow equations were written in the Pascal programming language, as this was the language with which I was most familiar.

Schematics of the solution processes for solving the governing equations are now presented for both steady state and time dependent flows, and may be seen in figures (4.9*) and (4.10*) shown overleaf.

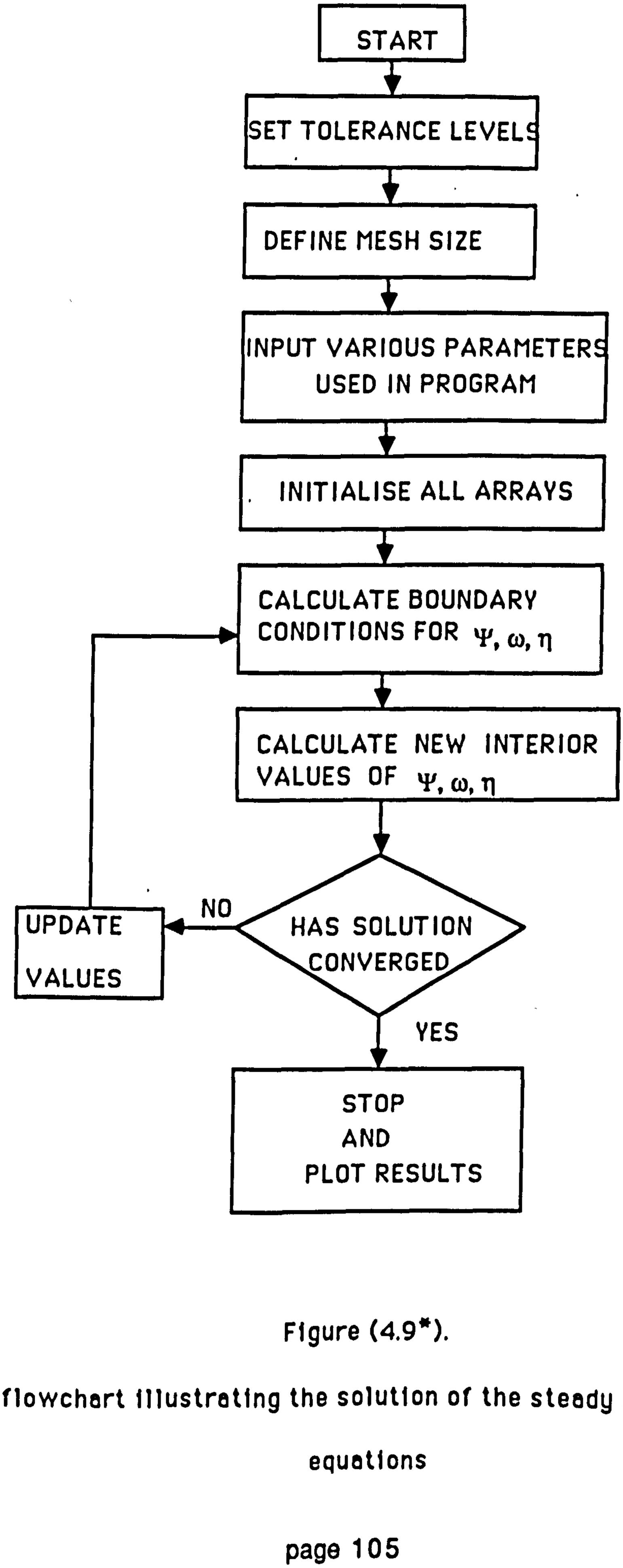

Figure (4.9*).

A flowchart illustrating the solution of the steady state flow equations

The implementation of both the Jacobi and Gauss-Seidel methods were both found to produce excellent results which are comparable with published work of other researchers for the test case of standard cavity flow. The Gauss-Seidel iterative method, using the newest calculated values as soon as they become available, was found to aid the convergence rate for the afore-mentioned steady state problems significantly, approximately solving the matrix system of equations roughly twice as quickly as the corresponding Jacobi method.

With confidence gained from the results of these two methods, the S.O.R method was attempted so as to improve convergence to solution even further. At first this method was found not to give very good results, which was a little disappointing and surprising, as the other applications of linear methods had worked well. Yet, we subsequently attempted to modify the existing S.O.R method to obtain satisfactory results while improving the convergence rate in the solution process.

All iterative methods considered so far , may be expressed in the form $\underline{x}^{(n+1)} = G\underline{x}^{(n)} + \underline{c}$, from which it can be seen that the initial guess or approximation to the final solution is important regarding the speed of convergence. If this can be improved then it seems likely that the rate of convergence will be accelerated.

The solution procedure for the S.O.R method is similar to that outlined in fig (4.9*) but with a few exceptions.

At the initialisation phase we use a solution already obtained for a Newtonian fluid at Re=0.01, as a initial approximation to the final solution. The relaxation parameter ξ can be obtained in various ways. For linear systems it may be set at the optimum value (Smith[100]), but as our system is non-linear, we preferred to update the value of the parameter by inspection after ten or so iterations. This provides greater flexibility, as well as acting as a smoothing device when moving to higher Reynolds' numbers, without initiating divergence. The modified version of the S.O.R iterative procedure, has generated results comparable with Jacobi and Gauss-Seidel methods, and has been found to significantly accelerate convergence.

In a further attempt to accelerate convergence, the Newton-Raphson method for non-linear systems was examined. However, the method was seen to be difficult to implement and the resuting matrix system of equations produced would need to be solved by one of the afore-mentioned iterative methods discussed above. Ideally the Newton-Rhapson method should produce a quadratic rate of convergence which is highly desirable, however the necessity of linear method to solve the resulting

matrix equations would render the procedure a linear one with no overall significant advantage gained.

(Modifications for the time dependent solution process are shown overleaf in fig(4.10*)).

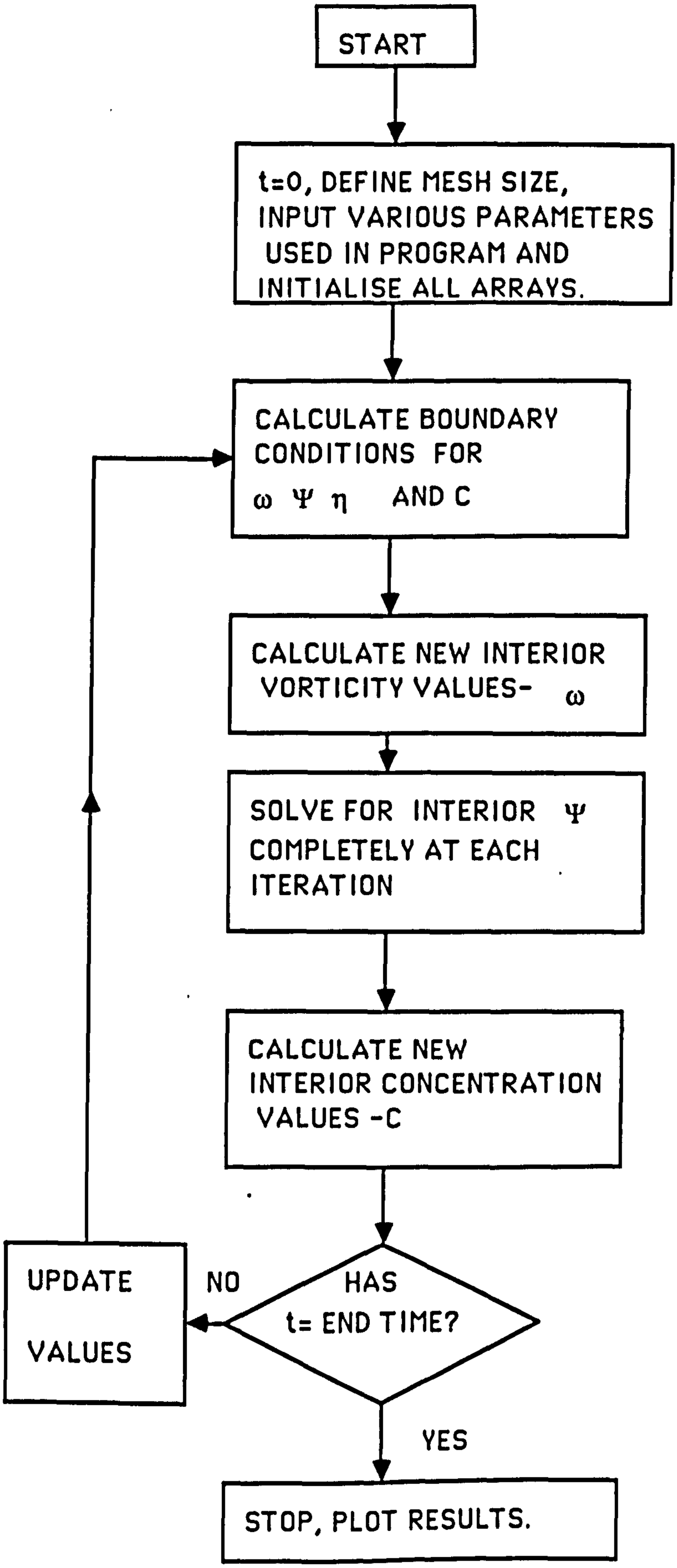
START
t=0, DEFINE MESH SIZE, INPUT VARIOUS PARAMETERS USED IN PROGRAM AND INITIALISE ALL ARRAYS.
CALCULATE BOUNDARY CONDITIONS FOR ω Ψ η AND C
CALCULATE NEW INTERIOR VORTICITY VALUES- ω
SOLVE FOR INTERIOR Ψ COMPLETELY AT EACH ITERATION
CALCULATE NEW INTERIOR CONCENTRATION VALUES -C
HAS t= END TIME?
NO
UPDATE VALUES
YES
STOP, PLOT RESULTS.

Figure (4.10*)

4.12 NATURE OF THE FLOW NEAR CORNER POINTS.

The flow of the fluid contained within the cavity is set in motion by one or more driving walls. These moving walls meet the stationary walls at right angles at the corner point. It is the motion of the fluid near these corner points which we now investigate, for both Newtonian and certain non-Newtonian fluids.

Consider the motion of fluid near the top right hand corner shown in fig(4.11*) the case under consideration being that of standard cavity flow, caused by the motion of the top wall alone. We assume the usual no-slip boundary conditions apply and that the top wall moves at constant speed U.

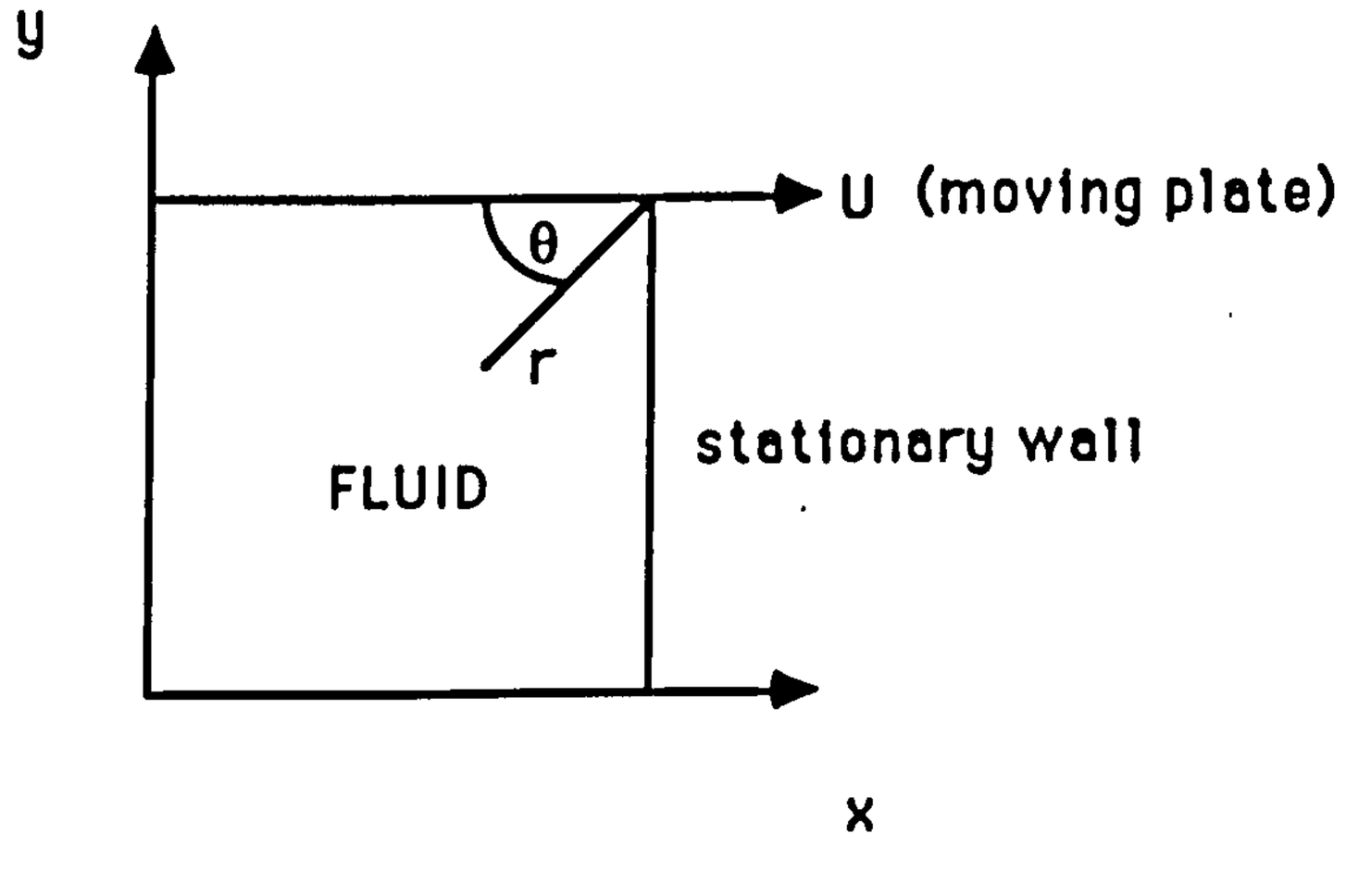

Figure (4.11*)

Diagram of the corner.

The flow of a Newtonian fluid within the cavity is governed by the Navier-Stokes equations, expressed in stream-function and vorticity notation as:

$$\Delta^2\omega = Re\left(\frac{\partial\omega}{\partial t} + \underline{v}.\,\Delta\omega\right) \qquad (4.40)$$

$$\Delta^2\Psi = -\omega \qquad (4.41)$$

where Δ represents the gradient operator, Δ^2 the Laplacian operator.

Near the corner itself Moffatt[66] has shown that the viscous forces tend to dominate the inertial forces such that the Reynolds' number tends to zero. Thus equation (4.40) reduces to

$$\Delta^2\omega=0 \qquad (4.42)$$

and this together with (4.41), produces

$$\Delta^4\Psi = 0 \qquad (4.43)$$

which is known as the Stokesian flow equation, and is known to have a variable separable form of solution. Gupta et al[42] have also considered the flow of a steady Newtonian fluid near the corner using a semi-analytic technique. From dimensional arguments they have shown that when (4.43) is expressed in polar co-ordinates then the solution is of the form

$$\Psi(r,\theta) = r^{k+1}f_k(\theta) \qquad (4.44)$$

where for Stokesian flow k=0. Consequently utilising equation (4.41) we find the vorticity near corner is given by

$$\omega= r^{-1}g(\theta) \qquad (4.45),$$

from which we see that as r->0 the vorticity becomes infinite, and hence singularities exist at all corner points similar to fig(4.11*) above for all types of laminar flow considered. The shear-rate q, near the corner using(4.3) and (4.44), is also found to be of form

$$q=r^{-1}\,h(\theta) \qquad (4.46),$$

which like the vorticity becomes infinite at the corner itself.

By expressing $\Delta^4\Psi=0$ in terms of polar co-ordinates and substituting (4.44) with k=0, yields a fourth order ordinary differential equation in terms of $f_0(\theta)$ given by:

$$f^4_0(\theta) + 2f^2_0(\theta) + f_0(q) = 0. \qquad (4.47).$$

Equation (4.47) possesses a general solution of the form

$$f_0(q)= (A\theta+B)\cos\theta + (C\theta+D)\sin\theta \qquad (4.48)$$

and is subject to the following boundary conditions obtained from Ψ:

$$f_0(0)=0,\ f_0(\pi/2) = 0,\ f_0^{1}(0) = U,\ f_0^{1}(\pi/2) = 0, \qquad (4.49)$$

where the superscript '1' denotes d/dθ, and from which we obtain:-

$$A= \frac{4U}{(4-\pi^2)},\ B=0,\ C= \frac{2\pi U}{(4-\pi^2)}\quad D= \frac{\pi^2 U}{(\pi^2-4)} \qquad (4.50)$$

Thus the solution of the Stokesian flow equation 'near' the corner is:

$$\Psi(r,\theta) = \frac{rU}{(\pi^2-4)}(-\pi^2\sin\theta + 4\theta\cos\theta + 2\pi\theta\sin\theta) \qquad (4.51)$$

$$\omega(r,\theta) = \frac{-4U}{r(\pi^2-4)}(\pi\cos\theta - 2\sin\theta) \qquad (4.52)$$

The streamlines for a similar problem near the lower left hand corner of a cavity, where the lower wall moves with a speed with -U is shown in fig(4.12*) from Batchelor[12].

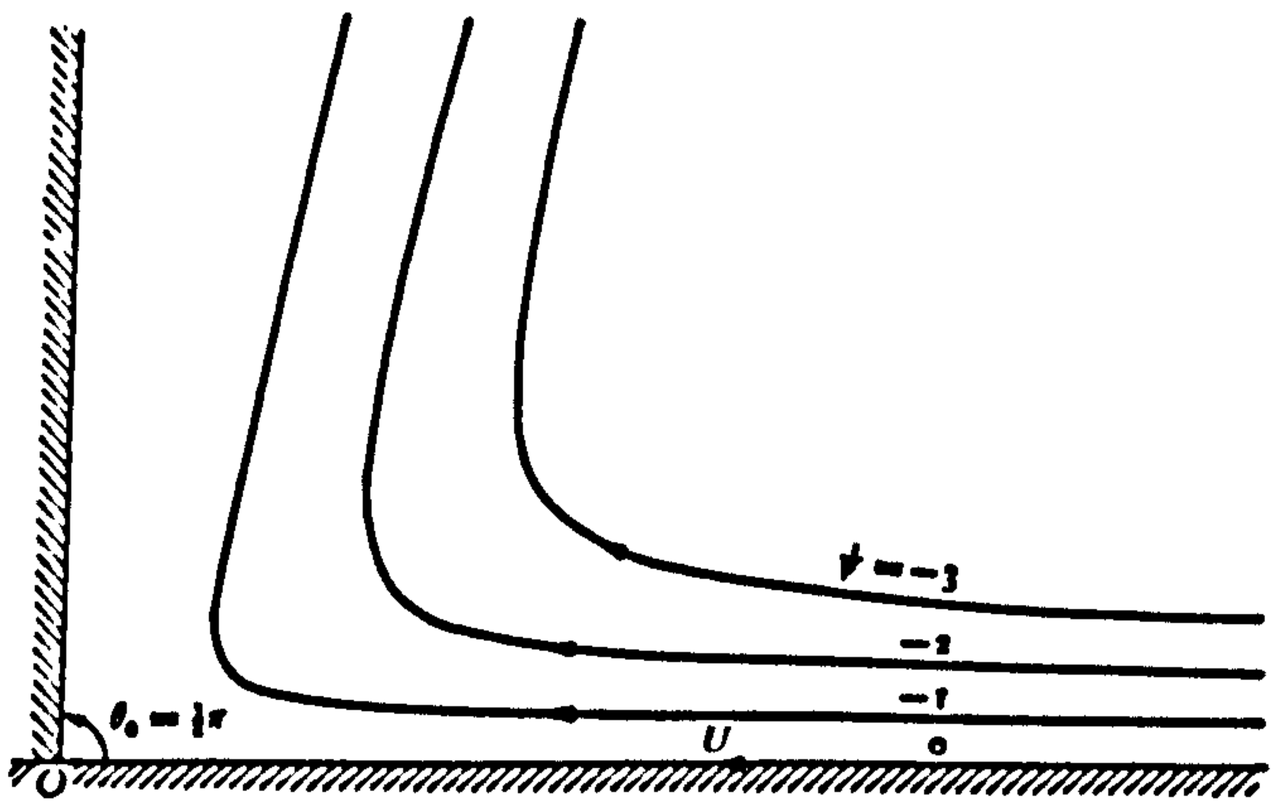

Two-dimensional flow in a corner due to one rigid plane sliding on another (arbitrary units for ψ).

Figure (4.12*)

Streamline flow near a corner for a Newtonian fluid.

4.12.1 NATURE OF FLOW NEAR CORNERS FOR NON-NEWTONIAN FLUIDS.

Here, like its Newtonian counterpart, employing no-slip boundary conditions we assume that near the corner the viscous forces dominate proceedings such that Re->0. Using this assumption the non-Newtonian flow equation(4.1) near the corner simplifies to (4.53), where the subscripts denote differentiation with respect to those variables.

$$\eta\Delta^2\omega + 2(\eta_x\omega_x + \eta_y\omega_y) - 4\eta_{yx}\Psi_{yx} - (\Psi_{yy}-\Psi_{xx})(\eta_{yy}-\eta_{xx})=0 \quad (4.53)$$

This as usual is solved in conjunction with equation(4.41). The fluid's variable viscosity is represented by η, which we assume can be a function of shear-rate q, temperature T, and time t, i.e

$$\eta=\eta(q,T,t) \quad (4.54).$$

Following closely the work of Gupta et al[42] we also assume that (4.53) admits a separable form of solution given by(4.44) where we take $k < 1$, thus making $\Psi=0$ at the corner itself. The vorticity and shear-rate expressions at the corner are again defined by (4.45) and (4.46). We firstly consider the flow near the corner for a shear-dependent fluid, whose apparent viscosity may be simulated by the Cross model(3.11).

Using our expression for shear-rate(4.46) the Cross model has the form:

$$\eta(q) = \alpha + r^{m(1-k)}\, B(\theta) \qquad (4.55)$$

where $m=n-1$ and $0< m <1$, and $\alpha = \eta(\infty)$.

Likewise substituting the relevant expressions for Ψ,ω,η into (4.53) and simplifying produces:

$$(\alpha + r^{m(1-k)}\, B(\theta))\, \Delta^2\omega + C(\theta) r^{(m-1)(1-k)-2} = 0 \qquad (4.56)$$

and from equation (4.45) we may further deduce that

$$\Delta^2\omega = r^{k-3} Z(\theta) \qquad (4.57),$$

therefore writing (4.53) as:

$$\Delta^2\omega\left(1 + \frac{C(\theta)\, r^{(m-1)(1-k)-2}}{(\alpha + r^{m(1-k)}\, B(\theta))\, r^{k-3} Z(\theta))} \right) = 0 \qquad (4.58)$$

we finally obtain

$$\Delta^2\omega\left(1 + \frac{C(\theta)\, r^{m(1-k)}}{Z(\theta)(\alpha + K(\theta)\, r^{m(1-k)})} \right) = 0 \qquad (4.59).$$

Noting here that $0< m(1-k) <2$, it may be seen that as $r\to 0$, $\Delta^2\omega \to 0$ or $\Delta^4\Psi \to 0$ showing once again that the flow near the corner for shear-dependent non-Newtonian fluids is approximately Stokesian.

A similar analysis has also been undertaken for time dependent fluids, exhibiting thixotropic and dilatant tendencies. To achieve this, based closely on the work of Kemblowski and Petera[52], we propose the following model for the apparent variable viscosity,

$$\eta(q,t) = \eta_c(q) + (\eta(0) - \eta_c(q))e^{-at} \qquad (4.60)$$

where $\eta_c(q)$ is the Cross model representing either shear-thinning or thickening behaviour, 'a' is a constant of the paricular fluid and is approximately $5x10^{-3}$. This model yields a similar result to (4.59) above, the exception being the introduction of a time dependent terms into the expression shown in (4.61), where

$$\chi(t) = \alpha(1-e^{-at})+e^{-at}.$$

$$\Delta^2\omega\left(1 + \frac{C(\theta)\, r^{m(1-k)(1+e^{-at})}}{Z(\theta)(\chi(t) + K(\theta)\, r^{m(1-k)(1+e^{-at})})} \right) = 0 , \qquad (4.61).$$

showing once again that the flow becomes Stokesian near the corner.

4.13 THE NUMERICAL SOLUTION OF EQUATIONS GOVERNING THE EVOLUTION OF THE PATH OF A FLUID PARTICLE.

The trajectory of a fluid particle may be found by solving the following system of ordinary differential equations(ODE'S) given below in (4.62),

$$\frac{dx}{dt}(t) = u(x(t),y(t))$$

$$\frac{dy}{dt}(t) = v(x(t),y(t)) \qquad (4.62)$$

subject to the initial conditions $x(0)= x_0$, $y(0)= y_0$, where u,v are the velocity components in the x and y directions respectively.

In our work the trajectories of up to nine particles within the framework of the cavity's geometry, can be traced for the various types of laminar driven flows considered.

However, the velocity field is not known analytically, but has been obtained numerically at a set of discrete points (x_i,y_j) covering the flow domain, by firstly solving the stream-function equation(4.2), and then using $u=\partial\Psi/\partial y$ and $v=-\partial\Psi/\partial x$, so that the respective speeds in x and y directions are known at each grid point.

Initially the vorticity(4.1), stream function(4.2) equations were solved by simple explicit methods which yielded very good results when compared with model solutions published by other researchers, but has the drawback of being only $O(\delta t,h^2,k^2)$ accurate.

To improve this situation the A.D.I method of Peacemann and Rachford[96] was later implemented, which gave equally good results while being $O(\delta t^2,h^2,k^2)$ accurate, and this solution method is fully discussed in Chapter 6. So in solving system (4.62), to be consistent we sought a method which was also $O(\delta t^2)$ accurate and easy to implement. Both criteria can be satisfied by adopting a second order Runge-Kutta method known as the modified-Euler method(Burden-Faires[19]). Writing (4.62) more neatly as:

$$\frac{d\underline{r}(t)}{dt} = \underline{V}(\underline{r}(t)) \qquad (4.63),$$

where $\underline{r}(t) = (x(t)\ \ y(t))$ and $V = (u,v)$

we obtain

$$\underline{r}(t+\delta t) = \underline{r}(t) + \frac{\delta t}{2}\{\underline{V}(\underline{r}(t)) + \underline{V}(\underline{r}')\} \qquad (4.64),$$

where $r' = \underline{r}(t) + \delta t\{\underline{V}(\underline{r}(t))\}.$ (4.65)

This is an initial approximation resulting from an application of Euler's method applied to system (4.62), thus enabling the new position of the particle to be located after each time increment δt. At $t=0$, each fluid particle is located at a fixed grid point and for $t > 0$ its position is calculated directly from equation(4.64). However after just one time increment, the particle will probably occupy the existing space between adjacent grid points, where the velocity field is not known, even in terms of discretised quantities. In order to overcome this we assume the velocity components at non integral grid points may be approximated by the following bi-linear Taylor series interpolation formula.

$$V_k(x',y') = a_k + b_k x' + c_k y' + d_k x' y' \qquad (4.66),$$

for $k=1,2$ and where $v_1=u, v_2=v$, and where x' and y' represent the local co-ordinates within a single grid square or cell as shown in fig(4.13*).

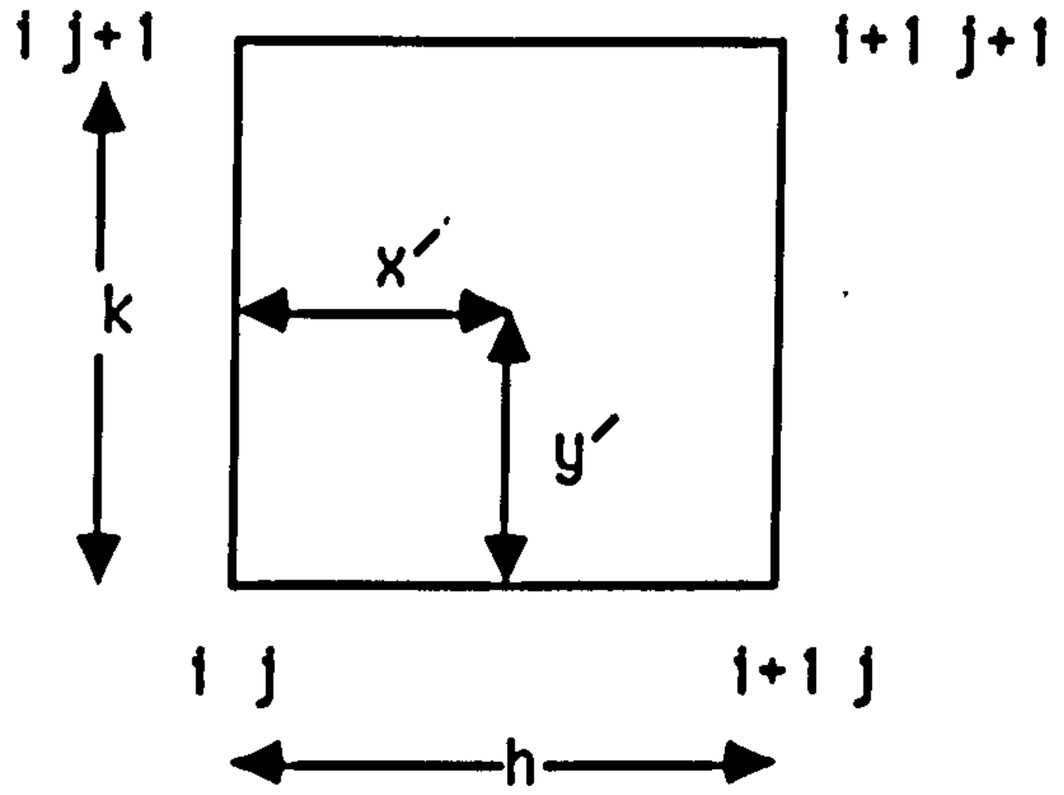

Figure (4.13*)

Diagram showing the local co-ordinate system within each cell.

The coefficients a_k, b_k, c_k, d_k are expressions involving the actual velocities at the neighbouring grid points of the cell, and are defined as:

$$a_k = V_k(i,j),\quad b_k = \frac{V(i+1,j) - V(i,j)}{h},\quad c_k = \frac{V(i,j+1) - V(i,j)}{k} \qquad (4.67)$$

$$d_k = \frac{V(i+1,j+1) - V(i+1,j) - V(i,j+1) + V(i,j)}{hk}$$

A check is also incorporated as to whether the particles' new position is at a grid point, or whether it is at some part of the cell wall. If this is the case then the respective speed can be represented by:

$$V_k(x',y') = d_2d_3V_k(i+1,j) + d_3d_1V_k(i,j) + d_1d_4V_k(i,j+1) + d_2d_4V_k(i+1,j+1) \qquad (4.68)$$

Where the d_l values for $l=1,2,3,4$, represent the distances from

the respective walls of the cell as shown in fig(4.14*).

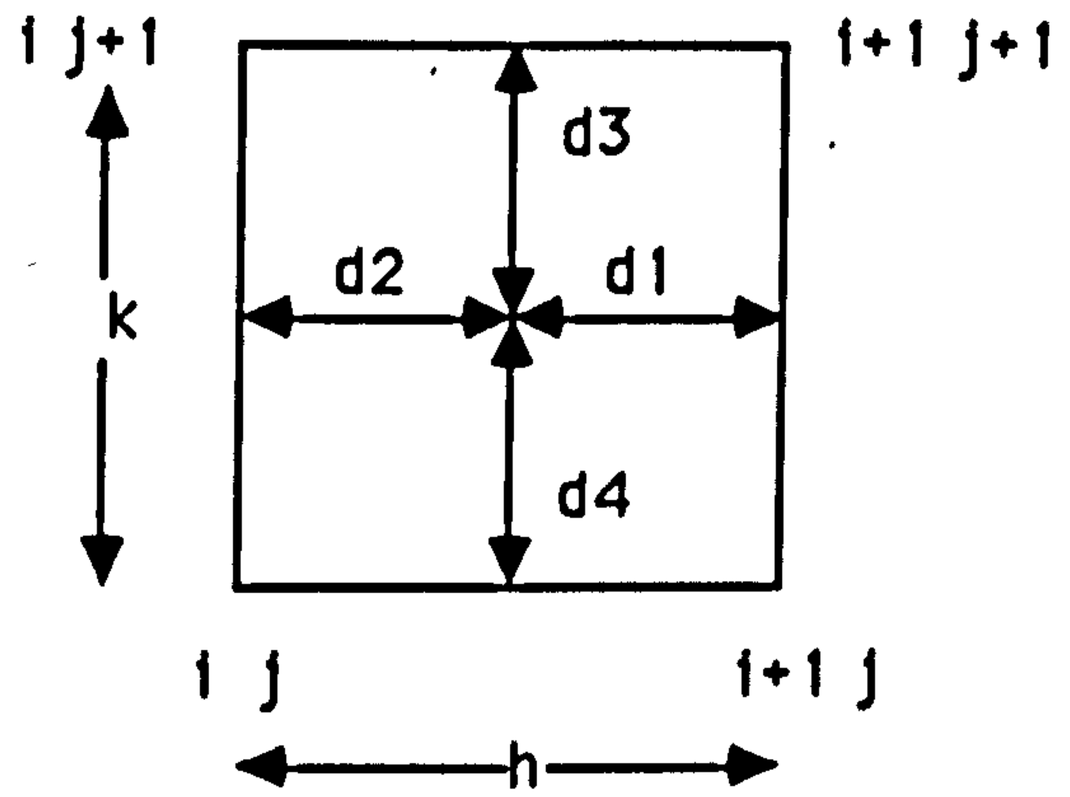

Figure (4.14*).

Diagram showing inter cell interpolation.

THE SOLUTION PROCESS.

A diagramatic description of the solution process for solving the time dependent system (4.62) is shown in fig(4.15*) below, and the results of which may be seen in Chapter 5.

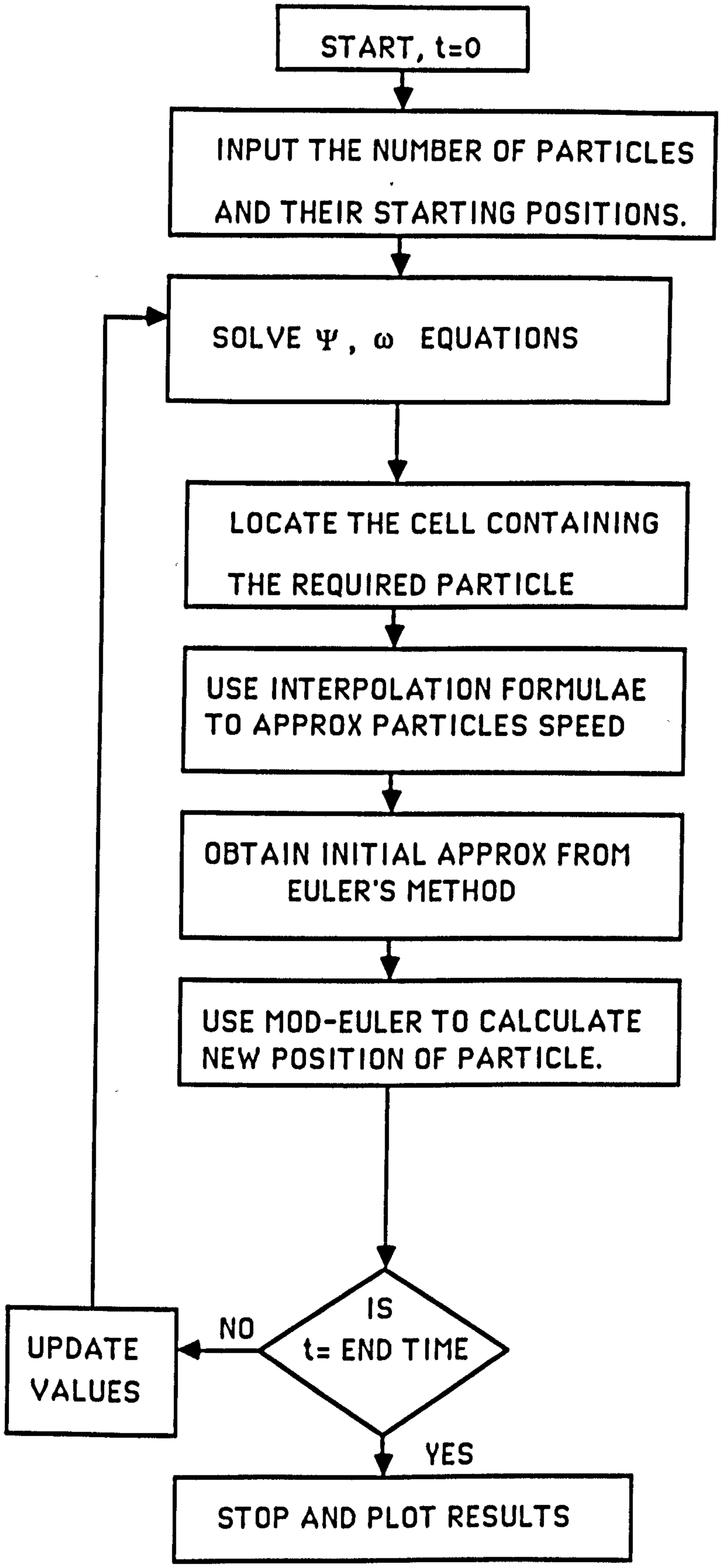

Figure (4.15*)

Flowchart indicating the tracking of a system of particles.

4.14 SUMMARY.

This chapter has been concerned with the techniques used to successfully generate a numerical solution of either, the steady state or time dependent, complex non-linear flow equations. A description of the discretisation process is included, along with the relative merits of the scheme chosen, together with an outline of the iterative computer algorithms used to provide a solution of the large matrix system of equations, which result from the discretisation process.

Also contained within this chapter is an investigation of the flow of a variety of non-Newtonian fluids near the corners of the cavity where the vorticity is singular in value. By utilising analytical techniques, the nature of the flow in the immediate vicinity of the corner, for all fluid considered, was found to be approximately Stokesian.

Finally, a numerical solution to the Hamiltonian equations representing the motion of a fluid particle are discussed, together with an outline of a suitable computer algorithm used to obtain a solution.

CHAPTER 5

RESULTS FROM DRIVEN CAVITY FLOW SIMULATIONS.

5.1 INTRODUCTION

In this chapter results are presented for the various types of driven cavity flow discussed earlier in Chapters 3 and 4, ranging from the standard test case with one wall moving, to the unique purely theoretical case whereby all four walls are allowed to move in a periodic discontinuous co-rotational sense.

Both steady state and time dependent flows are considered, for both Newtonian and certain shear dependent non-Newtonian fluids; namely those exhibiting pseudoplastic and dilatant tendencies. Results are also obtained from the solution of the concentration equation, which provides insight into the colour band and dispersive mixing of a dye within the cavity due to the fluid motion. In addition, particle path trajectories are presented for the various cavity flows which also provide a further understanding of the efficiency and the mechanics of the mixing process involved.

The steady state flow equations are 'solved' using the classical iterative methods outlined in Chapter 4. Initially, in like manner the time dependent flow and concentration equations were also 'solved' numerically by utilising the simple explicit methods outlined in Chapter 4. However the accuracy of solution was

subsequetly improved and the time step increased by using a version of the A.D.I method developed by Peacemann and Rachford[96], a tractable account of which is given in Chapter 6.

We consider firstly the results obtained from the standard test case, in which the top wall alone moves, for Newtonian and the non-Newtonian fluids mentioned above.

N.B (* figures in text, others in appendix).

5.2.1 NEWTONIAN FLUID.

The steady state solutions for a Newtonian fluid in the case of standard cavity flow were obtained on a 40 x 40 noded mesh, for Reynolds' numbers in the range of 1 to 400, the latter being found to be the largest practically attainable on such a mesh. The time dependent case was also considered and was found to settle down to give the steady state solution, after less than 5 seconds of simulation time.

For low Reynolds' numbers, Re=1 for example, one main vortex is produced the centre of which is located half way along and three quarters of the way up the cavity at (0.5,0.75), and the resulting streamlines produced shown in fig(5.1) can be seen to be symmetric about the vertical line through the middle of the cavity. As the Reynolds' number increases, the central vortex is found to move in the direction of the moving plate, symmetry is

lost and the vortex centre is positioned lower in the cavity. At Re=400 for example, shown in fig(5.2), the vortex centre is found at (0.55,0.65) and follows the pattern predicted by the Batchelor model[11]. We also note that as the Reynolds' number increases to a maximum of 400, a weaker secondary counter-rotating vortex is also produced near the bottom right hand corner of the cavity, the size of which is found to be proportional to the Reynolds' number.

Similar Results have been obtained by Cliffe et al[26], who used the (U,V,P) finite element method to solve the problem for a Newtonian fluid, using a 57 X 57 noded mesh. This mesh is considerably more refined than ours, but the results published for Re=1 and 400 fig(5.3) and Fig(5.4) show close agreement with our own, despite a slightly less refined mesh, and thus provide a validation for our computer code used to generate the solutions.

Recent experimental results at low Reynolds' numbers concerning the standard test case of driven cavity flow for Newtonian fluids have been produced by Chien et al[23], Leong et al [57] and Ottino[80]. The cavity used throughout their experiments is rectangular, with dimensions of width 10.3cm and height 6.2cm, the top plate's velocity is 2.69cm/s and the Reynolds' number for the system is calculated to be 1.7. The resulting streamline picture is shown in fig(5.5) and is similar to

our numerical simulation for a similar geometry with Re=1 fig(5.1), the primary vortex having the same shape and position in the flow domain.

Bozemann and Dalton[17] have also published results for the standard cavity flow problem for a Newtonian fluid, and have also considered flow patterns produced in cavities of varying aspect ratio (i.e ratio of the cavity's height to its width). For an aspect ratio of 1 (square cavity), at low Reynolds' numbers, one primary vortex is seen to occur, the centre of which has coordinates (0.5,0.75) which is in agreement with our results for Re=1.

Bozemann and Dalton also considered the position of the vortex centre as a function of the Reynolds' number. They discovered that the vortex centre moves in a path similar to that of a question mark, returning to the centre of the cavity at high enough Reynolds' numbers, which again confirmed Batchelors' prediction [11]. Contour plots were also published by Bozemann and Dalton for cavities of aspect ratio 2, at Reynolds' number 100, for Newtonian fluids fig(5.6), the main feature being the emergence of two main counter-rotating vortices, the weaker of the two occupying the lower part of the cavity. Comparing this with our own plot fig(5.7) for the same Reynolds' number and geometry, it can be seen that the two plots are in reasonably close agreement, taking into account that our plate moves in the opposite direction

to that of Bozemann and Dalton. The slight 'wiggles' produced on our plots are caused by a weak secondary vortex, a lack of mesh refinement, and due to the contouring package chosen. We have also considered the case of aspect ratio equal to 0.5 with Re=100, the streamlines shown in fig(5.8) show weak circulation near vortex centre(1.4,1.7).

5.2.2 PSEUDOPLASTIC FLUID.

To simulate the flow of a Pseudoplastic (shear-thinning) fluid in the cavity, the Cross model for fluid viscosity was used, taking the infinite shear viscosity and the zero shear viscosity to be 0.1 and 1 respectively. The steady state results shown in fig(5.9) and fig(5.10) are for Reynolds' numbers 1 and 130, the latter being the largest Reynolds' number for which convergence could be obtained using a 40 x 40 noded mesh. Comparing streamline plots for a Newtonian fig(5.1) and pseudoplastic fluids at Re=1, we observe that the vortex centre of the pseudoplastic fluid is higher than in the corresponding Newtonian case, the streamlines are symmetrical, and the circulation is weaker as can be seen from the increased distances between the streamlines, and this effect becomes more pronounced at higher Reynolds' numbers.

The reason for this is due to the shear-thinning nature of the fluid itself, allowing the fluid to move more swiftly near the top plate where the viscosity is thinnest. This fact is also borne out by considering streamline plots for both Newtonian and pseudoplastic fluids at Re=130 fig(5.11) and fig(5.10) respectively. The vortex centre for the pseudoplastic fluid is more central in the cavity, and the circulation of flow is weaker as can be seen from the larger spacing between the contour lines. We also note the emergence once again of a weak counter-rotating vortex near bottom right hand corner. The flow pattern produced for a pseudoplastic fluid, is similar to that of a Newtonian fluid at much higher Reynolds' numbers. Havard[44] has also numerically simulated the driven cavity flow problem for a pseudoplastic fluid using a finite element approach, the result shown in fig(5.12). Comparing our result fig(5.9) at Re=1 with Havard's, it can be seen that both are in very close agreement.

5.2.3 DILATANT FLUID.

To simulate a dilatant (or shear-thickening) fluid in the cavity the Cross viscosity model was again used, except this time the infinite shear viscosity was set to be 1 and the zero shear viscosity to be 0.1. Steady state streamline plots are presented in figs (5.13), (5.14) and (5.16) respectively for Reynolds'

numbers 1,130 and 300, the latter again being the maximum Reynolds' number obtainable for convegence using a 40 x 40 grid.

On comparing the dilatant fig(5.13) with the Newtonian fluid fig(5.1) at Re=1, very little difference is seen between the two. Both have the primary vortex centre at (0.5,0.75), the only difference appears to be that the contour lines for the dilatant fluid are slightly more compact around the vortex centre than in the Newtonian case, indicating that circulation is more vigorous. The stronger circulation is highlighted further by comparing the Newtonian flow pattern fig (5.15) with that of a shear-thickening fluid at Re=300, fig(5.16). Analysing the two plots we observe that the vortex centre for the dilatant fluid is lower than the Newtonian case, and the circulation is very much stronger which can be seen from the quite densely packed streamlines. This is due to the shear-thickening nature of the fluid making flow more difficult near the top plate, and it can also be seen that the corner eddy is larger for the dilatant fluid than for the Newtonian case at the same Reynolds' number.

5.3.1 <u>OTHER CAVITY FLOWS.</u>

A second type of cavity flow we have considered is the case whereby two plates move simultaneously in the same or opposite directions as shown below in fig(5.17*).

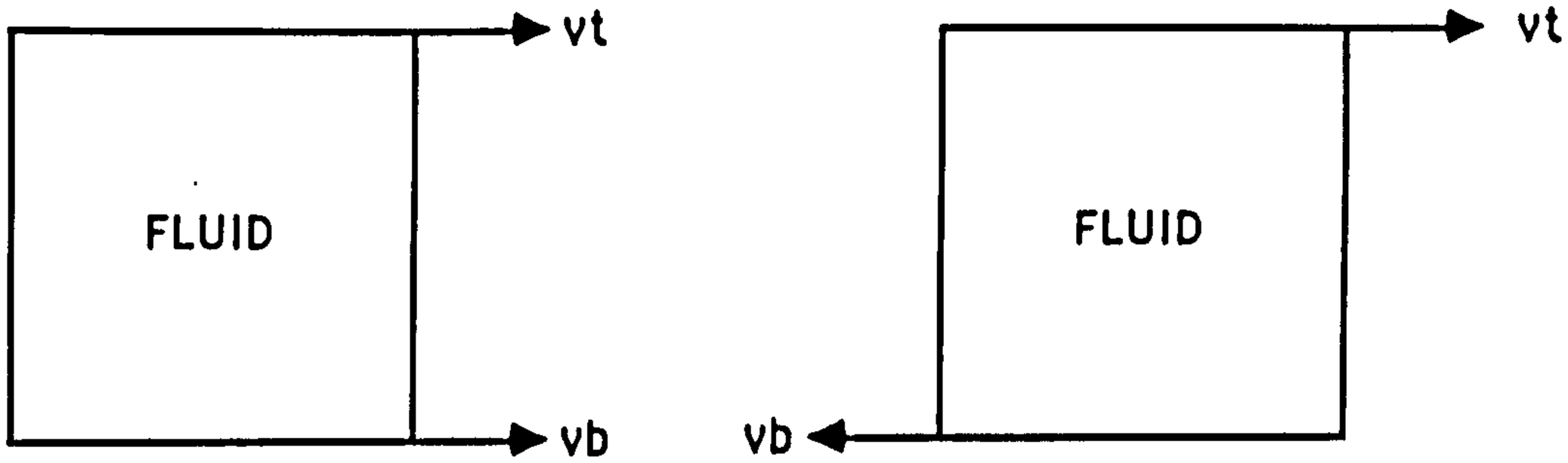

Figure (5.17*)

Diagram illustrating simultaneous plate motions.

This cavity flow has been studied mostly on an experimental basis by Chien et al[23], Leong et al[57] and Ottino[80], by visual means of deformation of coloured material line and 'blob' elements, for Reynolds' numbers in the range 0.1 to 100, yet all results published are for low Reynolds' numbers of order 1. In addition to this Chien et al[23] have produced numerical streamlines for this type of cavity flow at Reynolds' number one, which may be seen in figures (5.18) and (5.19).

In the course of our numerical simulations for this system, we have produced streamline contours at various Reynolds' numbers up to and larger than 100, and have also considered the flow

patterns produced for fluids showing characteristics of pseudoplasticity and dilatancy .

A selection of these results may be seen in figures (5.20) to (5.35). We shall now consider each type of cavity flow on a separate basis.

5.3.2 TWO PLATES SIMULTANEOUSLY MOVING IN THE SAME DIRECTION.

This type of flow is also known as counter rotational flow, and for the case of a Newtonian fluid at Reynolds' number one fig(5.20), our streamline plots can be seen to agree well with those of Chien et al[23], shown in fig(5.18). Two main vortices are produced being symmetrical mirror images of each other. The streamlines are closed loops, being symmetrical about the cavity's vertical and horizontal mid-lines, the vortex centres being found at approximately (0.5,0.2) and (0.5,0.8), that is a fifth of the way in from the top and bottom walls along the vertical centre line of the cavity. Streamline plots produced for both pseudoplastic and dilatant fluids at Re=1 were found to be practically indistinguishable from the Newtonian case, hence only one contour plot is shown, fig(5.20). As the Reynolds' number increases the vortex centres both move in the direction of the moving plates gradually becoming angled into the corners of the

cavity, and at higher Reynolds' numbers the difference in the type of fluid used in the simulation becomes more apparent. We have noticed that with increased Reynolds' number symmetry is broken along the vertical centre line, but is always maintained about the horizontal centre line of the cavity, the line of zero flow, and gap size between the streamlines increases indicating the circulation becomes weaker.

This trend is observed for all fluids considered and we find that the pseudoplastic fluid generates results comparable with a Newtonian fluid but at much higher Reynolds' numbers and likewise the reverse effect has been noted for dilatant fluids. A selection of results is now presented for various Reynolds' numbers for all fluids considered in figures (5.20) to (5.26), showing the usual trends, the latter three being the largest attainable Reynolds' number for which sensible results were obtained on a 30x30 grid.

5.3.3 TWO PLATES IN SIMULTANEOUS MOTION IN AN OPPOSITE SENSE.

This type of flow is also known as continuous co-rotational flow, and again has been studied experimentally for a Newtonian fluid by the previously stated authors. At low Reynolds' numbers

(Re=1) our streamline plots fig(5.27) compare well with those of Chien et al[23] previously shown in fig(5.19).

The resulting streamlines again are closed loops, which are almost square in appearance near the cavity's walls and becoming more rectangular near the central portion of the cavity. The experimental streamlines supplied by Leong et al[57] and Ottino[80] fig (5.28) also show similar behavior, becoming more circular as the centre of the cavity is approached. As is the case with the previous flow, the difference in the resulting streamlines produced for all three fluids considered at low Reynolds' numbers is negligible, and consequently only one streamline plot is shown, that of a Newtonian fluid, fig (5.27). However, as usual as the Reynolds' number is increased the differences in the test fluids used becomes more apparent. The general trends observed are, with increased Reynolds' number the outer streamlines become sheared similar to a parallelogram in shape, while the inner streamlines become more oval in character, and giving the appearance of stretching along the positive diagonal (y=x) of the cavity which is more pronounced for pseudoplastic fluids than the others.

It is further noticed with increased Reynolds' number symmetry is preserved and the gaps between the streamlines increase indicating circulation is weaker. Similar results were produced

for all the fluids considered in this section and were found to manifest the usual expected traits as discussed earlier. A selection of results for various Reynolds' numbers may be seen in fig(5.29) to fig(5.35), again the latter streamline plots are obtained at the highest attainable Reynolds' numbers for the respective fluids.

5.3.4 THE ASPECT RATIO OF THE CAVITY.

In this section we consider the effect of the cavity's aspect ratio (namely the ratio of the cavity's height to width) on the flow pattern produced. The problem considered is one in which the fluid under test is placed within a cavity of aspect ratio either bigger or less than one, whereby we allow the possibility of two simultaneous wall motions, either in the same or opposite sense. For this problem both time dependent and steady state solutions have been produced, for creeping or slow flow conditions, i.e Re=1.

In the situation when one wall alone moves at aspect ratio 2, the results produced at Re=1 for all three fluids considered were akin to those previously studied for a square cavity, manifesting the usual expected trends. However, at aspect ratio of 2, for a dilatant fluid, where two walls are allowed to move in the same or opposite direction some remarkable and novel results are

produced, which are a direct result of the cavity's geometrical configuration.

If the two plates move in the same direction the final steady or unchanging solution of the time dependent flow equations consists of two counter-rotating vorticies, of almost equal strength, each occupying approximately half of the cavity about the vertical centre line, with one vortex located higher in the cavity as shown in fig(5.36). We have also discovered that the solution is not unique, for by disturbing the system at the start by altering the initial guess slightly, and giving the stream function a small rogue value at a particular grid point, a second solution emerges which is a mirror image of the first, shown in fig(5.37). We have also found that as the Reynolds' number increases, streamlines synonymous with usual cavity flows of a Newtonian or pseudoplastic fluid are produced, which indicates that the increase in Reynolds' number acts as stabilising influence for the system. These two results are in contrast to that obtained from the steady state equations which produce the expected streamlines, shown in fig(5.38). The time dependent results however we believe to be perfectly viable, caused by the non-linearity of the problem and due to the shear-thickening nature of the fluid itself, inhibiting motion near the plates, forcing flow to occur in the thinner middle portion of the cavity.

The bifurcation of solutions although unproven experimentally as far as the author is aware are intuitively, perfectly legitimate solutions. It is worth noting here that no such solutions were found to occur for Newtonian or pseudoplastic fluids which generated streamlines in agreement with other published experimental and theoretical work Jana et al[48], as shown in fig(5.39) and (5.40) for a Newtonian fluid. We have found similar results to occur using dilatant fluids for aspect ratios of up to 4, and consequently are not shown.

In like manner some unusual results can be obtained again for a dilatant fluid in cavity of aspect ratio 2 if two plates are moved simultaneously in opposite directions. Here two counter-rotating vortices are seen to occur again occupying half of the cavity about the vertical centre line, but this time one vortex is considerably stronger than the other, as shown in fig(5.41). Again the solution generated is in contrast to that obtained for a similar geometry using the steady state equations of motion, and as with the case above the solution is not unique under the initial perturbation, which produces a mirror image solution, shown in fig (5.42).

At aspect ratios less than one, different flow patterns are seen to emerge, again solely for a dilatant fluid in contrast to Newtonian or pseudoplastic fluids. Surprisingly at aspect ratio

0.5, no 'peculiar' solutions are seen to occur when both plates are moved in same or opposite directions simultaneously, but are found to emerge for a shear-thickening fluid at an aspect ratio of 0.33, where the wall motions are in opposite directions. In this case three vortices are produced, the two weaker ones near the top and bottom walls, with a stonger circulating one in the middle portion of the cavity where viscosity is thinnest, shown in fig(5.43). This solution is unique under perturbation, but yet again contrasts with that produced by steady state flow equations, shown in fig(5.44). Similar solutions are obtained as the aspect ratio decreases and consequently are not shown. It is worth noting here that all solutions for aspect ratios less than a half for all fluids we have considered, when both plates moved in same directions, were well behaved and yielded the usual expected results. Two counter rotating vortices are produced each occupying half of the cavity about the horizontal centre line, which are symmetrical mirror images of each other, becoming flatter with weaker circulation as aspect ratio decreases.

A diagrammatic representation of the unusual bifurcation (or possibly 'trifurcation' [37]) of theoretically possible results for a dilatant fluid in a cavity of aspect ratio 2 is shown in fig(5.45*).

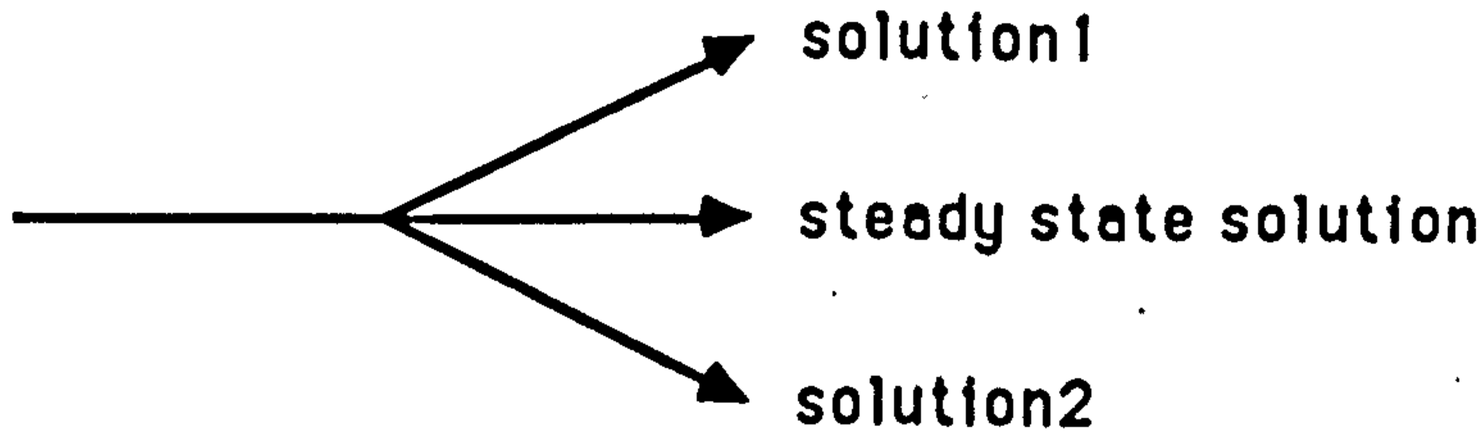

Figure (5.45*)

Diagram showing the bifurcation of possible results.

5.4 CONCENTRATION FIELD RESULTS.

In this section results are presented for the colour band and dispersive mixing generated by the flow patterns of the various cavity flows previously considered. The problem is one in which a quantity of dye, consisting of the same viscosity and make-up as the test fluid, is 'injected' into the cavity while the fluid is at rest, such that it occupies the entire top half of the cavity, the initial configuration shown earlier in fig(4.4*) of Chapter4. The assumption that the dye is consistent with the test fluid in every way is important since it enables us to neglect any generation of the substance due to chemical reaction and also to disregard any buoyancy forces which would otherwise exist due to concentration gradients. The concentration fields are set up as a direct consequence of the flow, the simulations being obtained at various time intervals, a selection of which may be seen in figures (5.46) to (5.60).

Throughout our numerical simulations the Schmidt number(Sc) was given a constant value of 50 for comparative purposes with Havard[44], while the Reynolds' number is taken to be either 1 or 100. All simulations were run on various sized grids, ranging from 10x10 to 40x40 and produced quantitatively similar results, the concentration calculation error check diminishing to less than 5% for more refined grids.

We shall now consider the concentration field results for each cavity flow in turn.

5.4.1 STANDARD CAVITY FLOW.

This problem has recently been considered by Havard[44] for a Newtonian fluid only at Reynolds' numbers 1 and 100 for time intervals up to six seconds using a finite element method with upwinding techniques used for higher Reynolds' numbers. However, Havard[44] only 'injects' the same quantity of dye as ourselves into the cavity, when the steady state solution of the governing flow equations has been obtained. Ours is a more realistic wholly time dependent problem, the dye being injected into the cavity at the start while the fluid is at rest. The computer simulations were undertaken for Newtonian, pseudoplastic and dilatant fluids, the computer program being run for a simulated time of 5.2 seconds at Re=1 at which time it is

taken that 50% mix has occurred, Havard[44]. The resulting concentration fields may be seen in figures (5.46), (5.47) and (5.48) for the above mentioned fluids respectively.

Comparing our results for a Newtonian fluid fig (5.46) with those of Havard[44] fig (5.49), who presumably chose not to plot field lines greater than unity, both figures show similar trends in being the same shape and position in the flow domain and thus showing favorable agreement. Comparing the concentration field obtained for pseudoplastic and dilatant fluids fig (5.48) and fig(5.47) respectively, with that obtained for a Newtonian fluid fig(5.46), it can be seen that all results show a degree of similarity, whilst reflecting the distinctive properties of the respective fluids themselves. For a pseudoplastic fluid fig(5.48) we observe that the contour lines are located at slightly higher positions in the cavity and more dispersed than the corresponding Newtonian pattern. This is a direct result of the shear-thinning nature of the pseudoplastic fluid allowing more rapid motion near the top plate where the fluid is thinnest. Conversely the reverse effect may be seen when comparing the dilatant and Newtonian concentration fields, figures (5.47) and (5.46) respectively. Here the field lines are lower and more compact than for a Newtonian fluid, this again a result of the shear-thickening nature of the

fluid inhibiting motion near the top plate, consequently the main flow region being located lower in the cavity.

The concentration of a substance in two dimensions is usually defined as the amount of that substance per unit area. Consequently by examining the area near the lower left quiescent corner under the '9' contour (being approximately triangular), it can be seen that the pseudoplastic fluid covers a larger area than the Newtonian fluid which in turn covers a wider area than a dilatant fluid.

This indicates that a greater spread of concentration will occur more quickly within a shear-thinning fluid at low Reynolds' numbers, which is in-line with intuition.

As previously mentioned in Chapter 3, as the Reynolds' number increases the concentration equation becomes very much advection dominated. Results are now presented for the case where Re=100 for a simulated time of five seconds, using a non-upwinded approach. The results are shown in figures (5.50), (5.51) and (5.52) respectively. For a Newtonian fluid fig(5.50) our results compare quite well with those of Havard[44], fig(5.53) who used an upwinding strategy to introduce artificial diffusion into the problem. Comparing the pseudoplastic results fig(5.51) with the Newtonian fig(5.50), it can be seen that the location of the coloured band is once again higher in the cavity and less

spread out, particularly near the top plate, than for a Newtonian fluid. The results for a dilatant fluid fig(5.52) are similar to those obtained for a Newtonian fluid, except the coloured band is a little higher in cavity and less spread out near the top plate. As can be seen from all contour plots at this Reynolds' number, the lack of diffusion present results in poor mixing, and this is true for all the various cavity flow considered.

5.4.2 TWO PLATES SIMULTANEOUSLY MOVING IN SAME DIRECTION.

At low Reynolds' numbers (Re=1) within square cavities the concentration field plots shown for all three fluids considered at a simulated time of five seconds, showed very little difference and are comparable with that produced by a Newtonian fluid as shown in fig (5.54). The contours almost possess a symmetrical structure about the horizontal centre line of the cavity, the lines of concentration intensity being approximately mirror images of each other. However, the concentration values are approximately twice as high in the top half of the cavity than those found in the lower half, and this is found to be true for all simulation times up to about 11 seconds whereby a homogeneous concentration is found to exist within the cavity. The reason for this is due to the nature of the flow. The streamlines for this type of cavity flow shown previously in fig (5.20) can be seen to consist of two

vortices being mirror images of each other, each occupying the top and lower halves of the cavity. Between the streamlines however, there exists a region of no flow, which is destructive to quick and efficient mixing. This results in the mixing process being relatively slow, and at a place where diffusion plays an important part in the overall mixing process. This effect is magnified at higher Reynolds' numbers with the coloured band being permanently compressed between the streamlines in the zero flow region, the concentration being slightly more spread out near the left hand wall where the circulation is weaker, and diffusion effects are greatest. All three fluids considered produced very similar results comparable with a Newtonian fluid shown in fig (5.55). In cavities of aspect ratio 2 at low Reynolds' numbers, both Newtonian and pseudoplastic fluids under steady state and time dependent flow conditions generate similar concentration field results as those for a square cavity. The exception again is that of a dilatant fluid in time dependent flow, which produces unusually good mixing results results due to the generation of two perpendicular circulatory vortices which effectively distribute the dye throughout the cavity. The concentration field for this flow after 2 seconds may be seen in fig(5.56), which also possesses a mirror image as the flow patterns are not unique as discussed earlier.

5.4.3 TWO PLATES SIMULTANEOUSLY MOVING IN OPPOSITE DIRECTIONS

The flow is induced by the top and bottom plates moving simultaneously in opposite directions, and the resulting streamlines may be seen in fig(5.27) referred to earlier for a Newtonian fluid at Re=1. At low Reynolds' numbers it was found once again that the concentration plots obtained for all three fluids showed little difference, all being in close comparison with that of a Newtonian fluid shown in fig (5.57). The non-upwinded concentration contours produced are, however, decidedly different from the two types of cavity flow discussed previously. The lines indicative of the concentration intensity are more wave like in appearance, perhaps an indication that this flow is more convection oriented, and almost symmetrical about the positive diagonal (y=x) of the cavity. At higher Reynolds' numbers (Re=100) the flow once again is very convection dominated, the coloured band of fluid forming an reverse 'S' type structure being asymmetrical about the cavity's vertical centre line.

Results for all fluids considered show similarities and differences characteristic of the individual fluids themselves. The dilatant fluid fig(5.59) is found to be very similar to the Newtonian case(5.58), whilst for the pseudoplastic fluid

fig(5.60), the band of concentration is positioned higher in the cavity, less spread out, with more of a definite wave appearance.

The results were obtained on 30x30 and 40x40 grids to reduce errors, the simulations being run for 3 seconds, after this at approximately 5 second the results tended to become unstable and are consequently are not shown.

5.5 DISCONTINUOUS PERIODIC CAVITY FLOW AND PARTICLE PATHS.

In this section we seek ways to improve the mixing process produced by the various cavity flows, and we also view the mixing efficiency of the flow from a different perspective by considering the trajectories of some fluid particles. The larger the area covered by the particle paths the better the mixing.

It is well known that when the stream-function has one degree of freedom then the Hamiltonian structured equations describing the trajectory of a particle within the fluid, outlined in Chapter 3, are integrable. This being the case the particle paths tend to follow the main streamlines of the flow, which results in poor mixing. In recent times it has come to light that one possible way to improve mixing is to make the stream function time dependent and periodic, by doing so the stream function possesses an additional degree of freedom and the Hamiltonian particle path equations become non-integrable, resulting possibly in

deterministic chaotic particle motion, and consequently improving mixing efficiency.

One possible way to achieve this is to consider discontinuous periodic co-rotational cavity flow, an illustration of which may been seen fig(5.61*), for up to three periods(T) of motion.

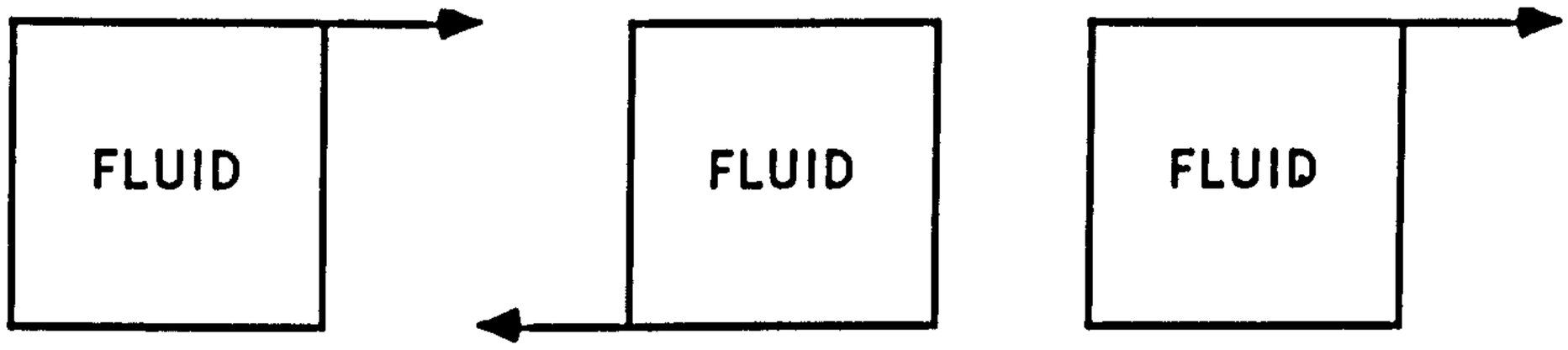

Figure (5.61*)

Diagram illustrating an example of discontinuous periodic co-rotational driven cavity flow.

This type of flow was investigated originally by Aref[5] within the confines of a cylindrical container for an incompressible inviscid fluid, as an approximation to an ideal stirring environment. Aref's system consisted of two point vortices separated by a fixed distance switched periodically on and off, hence the name 'blinking vortex'. Aref computed numerical solutions to the Hamiltonian equations describing particle motion and found them to be chaotic.

More recently this type of flow has been analysed by Chien et al [23], Leong et all[57] and Ottino[80], within the confines of a cavity, for a Newtonian fluid at low Reynolds number, utilising visual aspects of the deformation of coloured line and circular fluid elements. These authors have found that this type of flow has the ability to produce horseshoe mappings, and a previous study by Khakhar et al [53] has also shown that the flow is capable of producing positive Lyapunov exponents, both being strong indications that the system is chaotic. We have developed the work of these authors by considering the particle trajectories for this type of flow, for certain non-Newtonian fluids of the pseudoplastic and dilatant variety, and for higher Reynolds' numbers.

The basic parameters which govern the flow apart from the type of fluid used are the period of motion (T), and the Reynolds' number (Re). From our numerical simulations we have found that the more important of these two parameters is the period T. Throughout our simulations it is assumed that the top plate , moves initially for period T, in a uniform manner from start up, which creates a vortex half way along and approximately three quarters of the way up the cavity. Then after the time period has been reached, the top plate stops and the lower plate begins to move, in an opposite direction to the top plate but for the same

time period, eventually creating an identical mirror image counter-rotating vortex in the lower half of the cavity. This process is then repeated until the desired simulated time consisting of a fixed number of time periods is reached.

We have found that for small value time periods T, typically of order 0.1,0.2 seconds produces poor mixing as the particle paths produced tend to adhere to the streamlines of the flow, similar in appearance to those of shown in fig(5.27) except being slightly more 'wobbly'. At higher values of T equal to one second the mixing efficiency of the system improves fig(5.62), producing path lines similar to Aref's system fig(5.63). The mixing however is zonal or regional and almost periodic, being very good near the centre of the cavity with much intermingling of particles, yet not so productive near the outer regions of the cavity. If a particle is located in centre of the cavity at the start it will remain in this region for all subsequent time and likewise for a particle found near the cavity's wall, it makes a tour of the cavity but always on its outskirts near the walls. No intermingling of particles placed near the centre and those near the walls is seen to occur. Upon increasing T further, the mixing efficiency of the system becomes greatly improved being most fruitful in our case when T has value of two seconds. Here the particle paths are deterministic yet 'chaotic', and cover a very wide area of the

cavity almost filling it. A particle which starts at the cavity's centre is soon found to appear in circulatory motion near the cavity's walls, and equally, a particle located initially near the extremities of the cavity frequently in the course of its motion will occupy space in the centre of the cavity. Much intermingling of particle paths is found to occur at this value of the period, and an initial line of vertical or horizontal particles is seen to spread throughout the cavity, showing the mixing to be good. A selection of results for Newtonian, pseudoplastic and dilatant fluids for Re=1, T=2s, and time of 60s, may be seen in figures (5.64) to (5.67). In addition to this the concentration field after 5 seconds is presented at Re=1 for this type of flow, shown in fig(5.68).

All particle path trajectories for the three types of fluid considered are all very similar in appearance. It can be seen however, that the particle paths for a pseudoplastic fluid fig(5.66) appear to be less spread out, and more tightly bound together, particularly in the centre of the cavity where the viscosity is thickest. By contrast the reverse effect may be seen for a dilatant fluid fig(5.65), where more motion is observed to occur in the central region where the viscosity is thinnest. A particle which is 'placed' near a vortex centre at the start, is soon seen to leave that region and make a tour of the central portion of the cavity, encompassing a region around the second

vortex centre in the other half of the cavity. It has also been noted that the particle paths traced out for a dilatant fluid are almost periodic in nature often returning very close to their initial starting point, which is especially true of those near the cavity's walls. This effect is not as well defined for either Newtonian or pseudoplastic fluids.

We have also considered the motion of the particle for various time periods at higher Reynolds' numbers. It has been found that for all values of T considered that as the Reynolds' number increases the particles tend to become trapped once again between the streamlines of the flow, as typified by fig(5.69) for a pseudoplastic fluid at Re=100, where the flow is advection dominated and consequently the mixing is less effective. This result is consistent with the concentration field results also showing that mixing is less effective at higher Reynolds' numbers due to a lack of diffusion present.

In trying to further improve the mixing efficiency for two dimensional cavity flows, we have considered the artificial case whereby we allow all four of the cavities walls to move in a discontinuous co-rotational sense, similar to a Aref blinking vortex system with four time dependent vortex centres. Results are presented in figures (5.70) to (5.75) for particle path trajectories at Reynolds' numbers 1 and 100, for Newtonian,

pseudoplastic and dilatant fluids. In addition to this the resulting concentration field lines are presented for this unique flow, for Re=1 for a time of 5s, and may be seen in fig(5.76).

At low Reynolds' numbers the particle trajectories for all fluids considered appear quite similar. The particles tend to cover a large area of the cavity which shows that the mixing is good. The motion of the various particles is similar to that of a hypo-cycloidal path, the particles travelling in curved arcs which periodically loop in on themselves, thus thrusting a particle on the outskirts of the cavity into the central portion where the intermingling of the particles occurs most frequently and back out again.

Comparing the trajectories of the particles within the various fluids it can be seen once again, as with the blinking vortex case of Aref[5], that the best mixing occurs in regions where the fluid's viscosity is thinnest. This manifests itself with a dilatant fluid fig(5.74), whereby most of the efficient mixing occurs in the central portion of the cavity, and for a pseuodoplastic fluid fig(5.72) in the fact that lots of intermingling of particle occurs slightly nearer the walls of the cavity. For a Newtonian fluid fig(5.70) it can be seen that particles are fairly evenly spread throughout the cavity.

It was also noted that as the Reynolds' number increased the mixing becomes worse, due to the fact there is less diffusion present, borne out in the observation that there is less intermingling of the various fluid particles, which tend to be confined into regions of flow near their initial locations. Some plots for Newtonian, pseudoplastic and dilatant fluids at Re=100 are shown in figs(5.71), (5.73) and (5.75) respectively.

5.6 NUMERICAL SIMULATION OF LINE DEFORMATION.

In this section we discuss the numerical simulation of the folding and rotation of a line marker dye, initially injected into the cavity as a vertical strip along the vertical centre line of the cavity. This again has been studied experimentally by Chien et al [23], Leong et al[57] and Ottino[80], for a Newtonian fluid within a closed cavity, using a marker dye of low diffusivity but with the same viscosity as the test fluid.

Initially, we tried to model this phenomenon by solving the concentration equation (4.4) with zero diffusion using the well known 'leapfrog' method. However, due to numerical instabilities with the solution scheme used, the results were of poor quality and the method abandoned. Partial success however can be obtained if we assume that the line element whose deformation we are interested in consists of a number of particles. Then after

a desired time interval the position of the respective particles are noted, and a suitable spline function used to link them together in order. The results produced are for a Newtonian fluid in the case of standard cavity flow, and are shown in fig(5.77), along with the case of continuous co-rotational flow in fig(5.79), which can be seen to be in favourable comparison with the experimental results of Ottino[80], figures (5.78) and (5.80) respectively.

These figures capture the essential features of the line element deformation within the flow.

5.7 SUMMARY.

Within this chapter consideration has been devoted to the flow patterns and associated mixing processes accompanying a variety of simulated driven cavity flows. Both steady state and time dependent flows have been investigated, for simulations ranging from the standard test case, where one wall alone moves, to the unique theoretical case whereby all four of the cavity's walls are allowed to move in a discontinuous periodic co-rotational manner. Three types of fluid were used throughout the simulations namely, Newtonian, and fluids which are strongly dependent on shear-rate, and exhibit pseudoplastic and dilatant tendencies. The mixing efficiency of each flow was investigated

from two view points, firstly by analysing the dispersive mixing of a 'coloured' portion of fluid, 'injected' into the cavity at rest as it is carried along with the flow, and secondly by the tracing of a selected number of fluid particles strategically 'placed' within the flow field.

The main features emerging from this work were, the poorest mixing is obtained in cavity flows where either one wall or simultaneous opposing wall motions exist. For this type of flow the particle paths for all fluids considered, were found to adhere to the streamlines of the flow, which therefore results in poor mixing. It was also noted that for these types of flow, as the Reynolds' number increases the flow becomes more advection dominated, which for Reynolds' numbers in the range we have considered (up to 100), was found to be of insufficient strength to provide efficient mixing. The most rapid mixing within this framework was found to occur at low Reynolds' numbers, which indicates the dominant role that diffusion plays within the mixing process.

The cavity's aspect ratio was also found to be a significant factor with regards to the time dependent flow patterns and mixing ability of a dilatant fluid. At low Reynolds' numbers within cavities of aspect ratio 2, some unusual results were produced by the dilatant fluid, which under perturbation were

found not to be unique but possess a mirror image solution. Both of these results were in direct contrast to those obtained by the steady state flow equations, using the same fluid and geometry. The novel results we believe are legitimate, and show that a bifurcation of possible results simultaneously exist for a dilatant fluid at this Reynolds' number within such cavities. Similar results were also obtained in cavities of both larger and smaller aspect ratios. However, it was also noted this effect is prevalent only for creeping flow conditions and as the Reynolds' number increases the flow returns to the usual flow pattens expected. No such peculiar results were noted for any of the other fluids considered. It also became apparent during the course of our investigation that the mixing efficiency of all flows considered could be drastically improved by making the stream function both time dependent and periodic. This was implemented by considering a version of the famous Aref[5] 'blinking vortex' flow, obtained by allowing a periodic discontinuous co-rotational motion of both top and bottom plates. Like Aref[5], we discovered the flow has the ability to produce chaotic particle motion which is highly desirous for good mixing. Subsequent study by Ottino[80] has also shown this flow is capable of generating horseshoe mappings which are also indicative of a chaotic system. However, the most efficient

cavity flow with regards to mixing was achieved by developing the work of Aref[5] to consider a uniquely theoretical case whereby all four of the cavity's walls are allowed to rotate in a discontinuous periodic manner. This was also found to produce chaotic particle trajectories covering a wider area than the blinking vortex flow, showing an increased mixing efficiency. Again at higher Reynolds' numbers the flow is advection dominated which consequently resulted in poorer mixing being obtained.

CHAPTER 6

THERMALLY DRIVEN CAVITY FLOW

6.1 INTRODUCTION

The problem which will be considered in this chapter is that of thermally driven cavity flow. The problem consists of modelling the convective motion produced due to the thermal heating of a fluid, which is placed within the confines of a closed rectangular or square cavity with fixed immovable and impermeable walls, as shown in fig (6.1*).

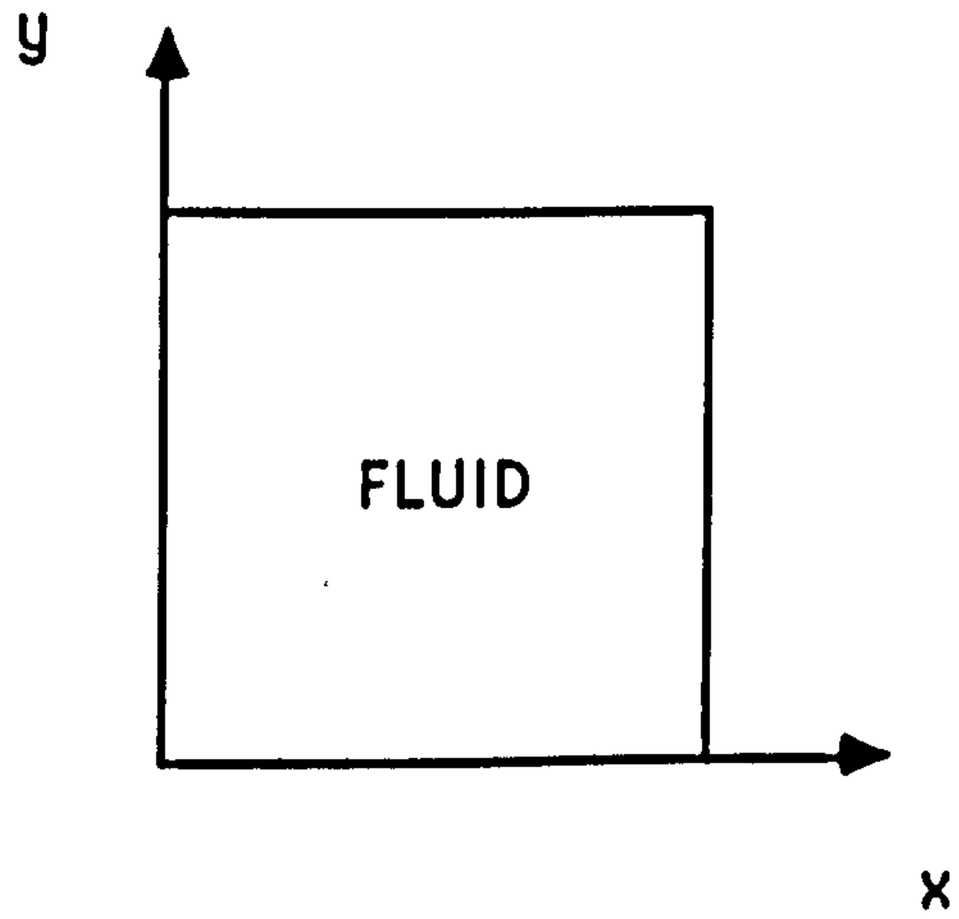

Figure (6.1*)

Diagram of the cavity's geometry.

Thermal convection is the basis of several important and spectacular phenomena observable on our planet and throughout the entire universe. Examples can readily be found in the circulation of the atmosphere and oceans, which to a large extent

determine, short and medium term weather changes. It has also become widely accepted that convection plays an important part in the motion of continental plates, which is probably due to convective movements in the Earth's upper mantle.

The convection process itself is also the basis for the transfer of heat and matter within stellar structures such as our sun, and this phenomenon in turn affects the sun's solar activity considerably.

The fluid within the cavity shown in fig(6.1*) is uniformly heated from below in the presence of a gravitational field. The density of the fluid is no longer treated as a constant but allowed to vary with temperature, consequently the fluid nearer the hotter bottom wall is less dense, due to thermal expansion, than the fluid above it, and this configuration is known to be potentially unstable. If we consider an arbitrary parcel of fluid near the hotter lower wall, then if this is displaced slightly upward it will experience an Archimedes buoyancy force which will assist its motion even further. Likewise if we consider a parcel of fluid near the cooler top wall, if this is displaced it will enter a region of less dense fluid and will be assisted on its descent further by gravity.

Benard[13] circa 1900, was the first person to study this phenomenon in a laboratory controlled experiment.

Benard's experiment was slightly different to the actual problem which we consider, although it does contain essentially the same features. Benard carried out skillful experiments on slender layers of fluid which were confined between two very long parallel plates whose dimensions were significantly larger than the width of the fluid. Benard observed that the system's stability was dependent upon two factors, the temperature gradient which exists between lower and upper walls and the fluid's viscosity which tends to oppose the motion. It is these two effects which are constantly in competition with each other, and which contribute to the instability of the system.

Benard observed that if only very small changes in temperature existed between the two plates, the system remained in a state of equilibrium, and that no visible motion was produced. In this phase the viscous forces tend to dominate the flow and heat is simply conducted through the fluid like a solid, and evacuated through the top wall into the surrounding environment. However as the temperature gradient between the two plates is gradually increased, at a certain critical value ΔT_c , the whole system becomes unstable and the fluid begins to perform bulk motion which is evidenced in the emergence of organised convective cells, with hot fluid rising in some parts of the flow and descending in others.

However, it was sometime after Benard discovered this phenomenon that any mathematical description of the instability arose. Lord Rayleigh[90] in 1916 appears to be the first to have produced a mathematical analysis of the Benard system, and since his pioneering paper there has emerged a host of literature on the subject, the standard text of which was published by Chandrasekhar[22] in 1961. However, inspite of this wealth of literature on the subject, the Benard convection system is still an active area of current research.

Most experimental and theoretical work to date has been carried out for Newtonian fluids, and we will extend this to incorporate features of some non-Newtonian fluids including in particular phenomena such as thixotropy, rheopexy, and fluids with strong viscosity dependence on temperature and depth. In addition to this, the flow and deformation of a weakly viscoelastic liquid will be considered together with the usual models for pseudoplastic and dilatant fluids.

6.2 THE EQUATIONS GOVERNING THERMALLY DRIVEN FLOW.

The equations used to model the convective flow induced by heating both Newtonian and certain types of non-Newtonian fluids in the presence of a gravitational field, are derived from basic laws of conservation of mass, linear momentum and energy. The resulting non-linear coupled partial differential equations are similar to those comprehensively derived in Chapter 3. The major difference is that the density of the fluid is no longer constant but is a variable dependent on the temperature. This renders the problem more complex than previously studied, but, by utilising a further assumption known as the Boussinesq approximation we can obtain a system of partial differential equations which retain the essential features of those discussed in full in Chapter 3. This states that, provided the temperature gradients which exist between top and bottom walls are not 'too large', the density may be regarded as a constant in all terms used in the equations, the exception is the buoyancy force term, which in our case is manifest in terms of $\partial T/\partial x$ in the vorticity equation (6.4) below, expressed in divergence form.

As outlined in Chapter4, it is customary to arrange whenever possible for one solution to suffice a variety of different parameter values. This can be achieved by expressing the governing equations in terms of non-dimensionalised variables.

We choose to non-dimensionalise in the following standard way, where the prime denotes the non-dimensionalised variables.

$$x'=x/L,\ y'=y/L,\ t'=t\eta_0/\rho_0 L^2,\ u'=uL\rho_0/\eta_0,\ v'=vL\rho_0/\eta_0$$

$$\Psi'=\rho_0\Psi/\eta_0,\ \omega'=\omega\rho_0 L^2/\eta_0,\ T'=(T-T_0)/(T_1-T_0)\ .$$

L is a characteristic length of the cavity,

ρ_0 is the initial density of the fluid,

$\eta_0=\eta(0)$, the Newtonian viscosity,

α the coefficient of thermal expansion for the fluid,

T_0, T_1 the constant temperature of the cooler and warmer walls of cavity.

When expressed in dimensionless form the governing equations become upon dropping the prime notation:

$$\rho(T)=\rho_0(1-\alpha(T-T_0)) \qquad (6.1)$$

$$\frac{\partial u}{\partial x}+\frac{\partial v}{\partial y}=0 \qquad (6.2)$$

$$\frac{\partial T}{\partial t}+\frac{\partial\Psi}{\partial y}\frac{\partial T}{\partial x}-\frac{\partial\Psi}{\partial x}\frac{\partial T}{\partial y}=\frac{1}{Pr}\left(\frac{\partial^2 T}{\partial x^2}+\frac{\partial^2 T}{\partial y^2}\right) \qquad (6.3)$$

$$\eta\frac{\partial\omega}{\partial t}=\frac{\partial}{\partial x}(\eta^2\frac{\partial\omega}{\partial x})+\frac{\partial}{\partial y}(\eta^2\frac{\partial\omega}{\partial y})-\eta\left(\frac{\partial\Psi}{\partial y}\frac{\partial\omega}{\partial x}-\frac{\partial\Psi}{\partial x}\frac{\partial\omega}{\partial y}+4\,\frac{\partial^2\eta}{\partial y\partial x}\,\frac{\partial^2\Psi}{\partial x\partial y}\right)$$

$$-\eta\left(\frac{\partial^2\Psi}{\partial y^2}-\frac{\partial^2\Psi}{\partial x^2}\right).\left(\frac{\partial^2\eta}{\partial y^2}-\frac{\partial^2\eta}{\partial x^2}\right)+Gr\frac{\partial T}{\partial x} \qquad (6.4)$$

$$\frac{\partial^2\Psi}{\partial x^2} + \frac{\partial^2\Psi}{\partial y^2} = -\omega \qquad (6.5)$$

The main effect of the non-dimensionalising process is the introduction of two new parameters, namely the Grashof number (Gr), and the Prandtl number (Pr). The Prandtl number expresses the ratio of the fluid's kinematic viscosity to the thermal diffusivity constant k; Pr=v/k, whilst the Grashof number is defined as $Gr= \alpha g L^3(T_1-T_0)/v^2$, and is meaure of the ratio of buoyancy to viscous effects occurring within the flow. The product of both the Prandtl number and Grashof number is called the Rayleigh number (Ra) which has emerged as the characteristic driving force of the flow.

6.2.1 VISCOSITY MODELS.

Contained within equation (6.4) above, is the variable viscosity term 'η' sometimes known as the apparent viscosity. In our simulations we will consider several models for the apparent viscosity function which represent fluids exhibiting Newtonian, pseudoplastic, dilatant, thixotropic and rheopectic properties, as well as those whose viscosity shows a strong dependence on both temperature and depth.

For a Newtonian fluid 'η' is a constant in equation (6.4), and given the non-dimensional value of one. For fluids whose viscosity is dependent upon shear-rate alone, namely those of the pseudoplastic (shear-thinning) and dilatant (shear-thickening) variety, the apparent viscosity may be approximated by using the Cross model defined in Chapter 3.

In modelling the viscosity function of a thixotropic or rheopectic fluid (such as paint or gum), we have followed closely the work of Kemblowski and Petera[52], and in so doing we have adopted the following model for the apparent viscosity shown in equation (6.6).

$$\eta(q,t) = \eta_c(q) + (\eta(0) - \eta_c(q))e^{-at} \qquad (6.6).$$

The apparent viscosity of these fluids is dependent both on shear-rate and time, $\eta_c(q)$ represents the Cross viscosity model, and 'a' is a constant of the fluid considered and is typically of the order 5×10^{-3}. The prescribed model has the following properties: At zero time and shear-rate, the fluid has the Newtonian viscosity value, however, as time and shear-rate become very large the fluid obtains an equilibrium value of the infinite shear viscosity. Also, as time progresses to a large value, with the shear-rate remaining finite the fluid's viscosity is given by the Cross model. The rare phenomenon of rheopexy (or negative thixotropy) can also be simulated by using (6.6) by reversing the

parametric values of $\eta(0)$ and $\eta(\infty)$ used in the equation to model thixotropy. In addition to investigating the above fluids, we also consider 'η' to be a function of temperature (T), which has a tendency to alter the fluids viscosity, and this can be modelled by using either the Reynolds' formula $\eta(T)= \eta(0)e^{-kT}$, or the Arrhenius reaction type equation, $\eta(T)= \eta(0)e^{-k/T}$, where k is a constant depending on the fluid considered in the simulation. However, Torrance and Turcotte[106] in considering the convective flow of a fluid with strong viscosity dependence on temperature, which is of use in many geophysical flows especially those pertaining to the Earth's mantle, have proposed the following model shown in

equation (6.7).

$$\eta(T)= \eta(0)e^{\,k(0.5-T)} \qquad (6.7).$$

Torrance and Turcotte[106] also proposed a model in which the viscosity of fluid is dependent on the depth. It is known that within the Earth's mantle the pressure increases strongly with depth due to the hydrostatic head, it is therefore expected that this increase in pressure will also lead to a significant increase in viscosity. The pressure variations within the mantle are assumed to be negligible and so it seems sensible to replace the viscosity's pressure dependence with that of depth dependence

according to the following formula (6.8) shown below, where y repesents the depth of fluid.

$$\eta(y)= \eta(0)e^{k(0.5-y)} \qquad (6.8)$$

6.2.2 <u>BOUNDARY CONDITIONS.</u>

Equations (6.3), (6.4) and (6.5) need to be solved subject to certain prescribed initial and boundary conditions. The stream function is a constant on each cavity's boundaries, which for simplicity is taken to be zero. The vorticity on the boundaries can be specified in two ways, which depends on the type of problem considered. The first using the well known Woods solid wall formula, based on a prior knowledge of interior stream function and vorticity values, as discussed previously in Chapter 3 for an enclosed cavity. The second employs a shear-free boundary condition, whereby the vorticity is zero at all points along the boundary, which is representative of analysing the motion of a cell with liquid boundaries within the Rayleigh-Benard system. In the course of our investigation, we have implemented both sets of boundary conditions and have found them to have an important effect on the final steady solution produced.

For the temperature equation (6.3) we impose a constant adverse non-dimensional temperature difference between the top and bottom cell boundaries of one degree, and to preserve the

symmetry of the problem the cavity's side walls are insulated, hence $\partial T/\partial x = 0$ on each of these boundaries.

A summary of the boundary conditions used for this problem can be seen in fig(6.2*) below.

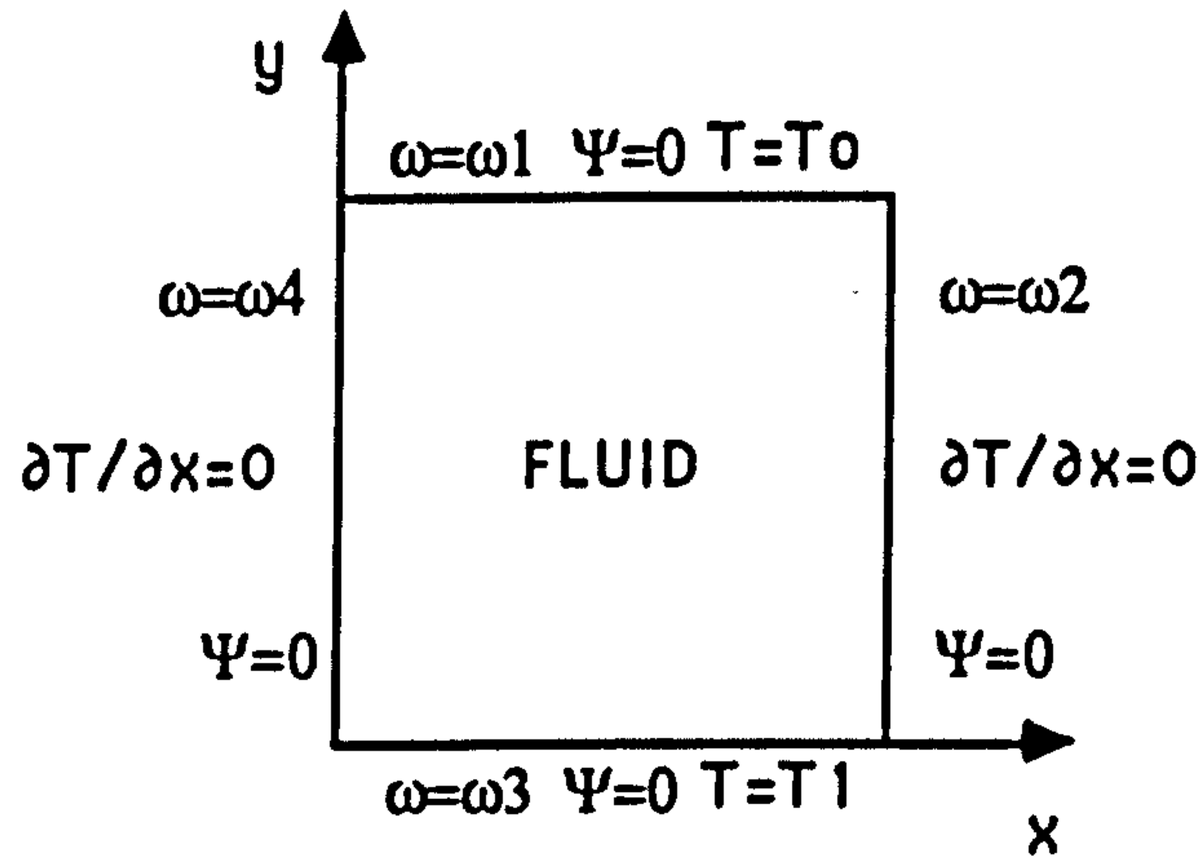

Figure (6.2*)

Diagram showing the boundary conditions used for the thermally driven cavity flow problem.

6.2.3 NON-NEWTONIAN VISCOELASTIC LIQUID.

In this present chapter consideration is also given to the simple modelling of fluid elasticity through the incorporation of a second order equivalent non-Newtonian viscoelastic term. This type of fluid is currently thought to approximate in a simple way that which exists within the mantle of the Earth [63]. The equations we use to simulate this phenomenon are essentially the same as those of (6.3),(6.4) and (6.5) discussed above, the major difference being an additional elastic stress term contribution

(expresssed in tensor notation) σ_{1k}, for 1, k=1,2 to the vorticity equation (6.4), shown below in equation (6.9).

$$\eta\frac{\partial\omega}{\partial t} = \frac{\partial(\eta^2\frac{\partial\omega}{\partial x})}{\partial x} + \frac{\partial(\eta^2\frac{\partial\omega}{\partial y})}{\partial y} - \eta\{\frac{\partial\Psi}{\partial y}\frac{\partial\omega}{\partial x} - \frac{\partial\Psi}{\partial x}\frac{\partial\omega}{\partial y} + 4\frac{\partial^2\eta}{\partial y\partial x}\frac{\partial^2\Psi}{\partial x\partial y}\}$$

$$- \eta\,(\frac{\partial^2\Psi}{\partial y^2} - \frac{\partial^2\Psi}{\partial x^2}).(\frac{\partial^2\eta}{\partial y^2} - \frac{\partial^2\eta}{\partial x^2}) + Gr\frac{\partial T}{\partial x}$$

$$-\eta\{\frac{\partial}{\partial y}(\frac{\partial}{\partial x}\sigma_{xx} + \frac{\partial}{\partial y}\sigma_{yx}) - \frac{\partial}{\partial x}(\frac{\partial}{\partial x}\sigma_{xy} + \frac{\partial}{\partial y}\sigma_{yy})\} \quad (6.9)$$

The elastic stress term is defined in terms of the first rate of strain tensor according to

$$\sigma_{1k} = -2W\overset{\nabla}{e}_{1k}(1) \quad (6.10).$$

Here W is a non-dimensionalised parameter known as the Weissenberg number which has emerged as the main flow characteristic for viscoelastic liquids, and $\overset{\nabla}{e}ik^{(1)}$, is known as the upper convected derivative and is defined as,

$$\overset{\nabla}{e}_{1k}(1) = \frac{D}{Dt}eik^{(1)} - L\,eik^{(1)} - eik^{(1)}\,L^T \quad (6.11)$$

where $$L = \frac{\partial(u,v)}{\partial(x,y)} \quad (6.12)$$

and L^T is the transpose of L,

with $\frac{D}{Dt}$ the material derivative defined earlier in Chapter 3.

The boundary conditions for this problem once again are essentially those shown in fig(6.2*), with the exception being additional boundary conditions for the elastic stress terms.

On the boundaries themselves $\nabla e_{1k}^{(1)}$ can be simplified depending on the flow considered, and together with equation (6.10), the additional elastic stress boundary conditions reduce to,

$$\sigma_{xx} = 0, \quad \sigma_{yy} = -2W\omega^2, \quad \sigma_{xy} = -W\,\partial\omega/\partial t \qquad (6.13)$$

for the left and right hand vertical walls of the cavity, ω being the specified value of the vorticity on a particular wall. Similarly for the top and bottom horizontal walls of the cavity,

$$\sigma_{yy} = 0, \quad \sigma_{xx} = -2W\omega^2, \quad \sigma_{xy} = W\partial\omega/\partial t. \qquad (6.14)$$

6.3 THE NUMERICAL SOLUTION OF THE EQUATIONS GOVERNING THERMALLY DRIVEN CAVITY FLOW.

We now discuss the numerical solution of the governing flow equations, (6.3), (6.4) and (6.5). As seen from the earlier work undertaken on standard cavity flow discussed in Chapters 3 and 4, to obtain analytical solutions of non-linear coupled partial differential equations (P.D.E's) of the type mentioned above, is extremely difficult and probably impossible. Therefore, to solve the equations numerical methods have to be employed which require the extensive use of a fairly large computer. There is no unique way to numerically solve a P.D.E, and each case needs to be treated on its own merits.

The work carried out to date has concentrated on the numerical solution of the equations which simulate flow for Newtonian and certain non-Newtonian fluids for the case of driven cavity flow described in detail in Chapter 4.

Finite difference methods were used to approximate the governing P.D.E's and both steady state and time dependent flows were considered. Central differencing was used wherever possible for the space derivatives, but for the time derivatives a forward difference operator had to be used. This makes the solution produced less accurate, but has the advantage that the discretised equations solved are explicit. The overall accuracy of the solution generated is $O(\delta t, h^2, k^2)$ where a typical value for δt used in the computer simulation was 0.001.

This situation in many respects was considered to be unacceptable, as the restriction on upon the time step δt meant that a very large number of iterations were needed to cover very small time intervals. So the main priority was to find a fairly easy to implement numerical algorithm to solve the equations which would firstly, improve the accuracy of the solution to $O(\delta t^2, h^2, k^2)$, and secondly, to increase the time step without affecting the quality of the results produced, and thereby enabling longer time intervals to be considered. Both criteria can be satisfied by using a modified version of the

Peacemann-Rachford alternating direction implicit method[96], or A.D.I for short. The price paid for the desired improvement is that, the discretised equations are now rendered implicit and not explicit as before, which makes the solution process some what more difficult. However, after implementation the algorithm was tested on standard cavity flow and was found to give equally good results. A short discussion of the A.D.I method now follows.

6.3.1 THE A.D.I METHOD.

The alternating direction implicit method developed by Peacemann-Rachford[96] is an ingenious mixture of explicit and implicit methods and is used to solve parabolic P.D.E's such as (6.3) and (6.4) above. As an illustration of the solution process we now consider solving the temperature equation (6.3) by this method.

As usual the solution domain, (i.e. the rectangular or square cavity) is covered by a uniform grid consisting of N x M nodal points as shown in fig(4.5*). The P.D.E is then approximated at each nodal or grid point by an algebraic discretised equation. The temperature equation (6.3) is discretised in the following manner,

$$\frac{(T_{ij}^{t+\delta t/2} - T_{ij}^{t})}{\delta t} + \frac{u}{2h}(T_{i+1j} - T_{i-1j})^{t+\delta t/2} + \frac{v}{2k}(T_{ij+1} - T_{ij-1})^{t}$$

$$= \frac{1}{Pr}\left(\frac{(T_{i+1j} - 2T_{ij} + T_{i-1j})^{t+\delta t/2}}{h^2} + \frac{(T_{ij+1} - 2T_{ij} + T_{ij-1})^{t}}{k^2} \right) \qquad (6.15)$$

for i= 1 to N-1 and j=1 to M-1, and where $u = \frac{\partial \Psi}{\partial y}$, and $v = -\frac{\partial \Psi}{\partial x}$.

The terms with superscript $t+\delta t/2$, imply the expressions are evaluated at a 'fictitious' time step, and $t+\delta t/2$ itself is taken to be some intermediate value approximation between the old time t and the new time $t+\delta t$. Further by letting

$q1 = 0.25\ \delta t\ u\ h^{-1}$, $q2 = 0.25\ \delta t\ v\ k^{-1}$, $q3 = 0.5\ \delta t/(Pr\ h^2)$,

$q4 = 0.5\ \delta t/(Pr\ k^2)$,

and upon carrying out a little algebraic manipulation the discretised equation (6.16) is produced.

$$-(q1 + q3)\,T_{i-1j}^{t+\delta t/2} + (1 + 2q3)\,T_{ij}^{t+\delta t/2} - (q3 - q1)\,T_{i+1j}^{t+\delta t/2}$$

$$= (q4 + q2)\,T_{ij-1}^{t} + (1 - 2q4)\,T_{ij}^{t} + (q4 - q2)\,T_{ij+1}^{t} \qquad (6.16)$$

It is worthwhile noting, that all the unknown intermediate values contain the same suffix 'j', that is they correspond to the same y value yj while i varies. For a given value of 'j' we can write down equation (6.16) for each value of 'i' ranging from 1 to N-1. This set of (N-1) equations in (N-1) unknowns can then be solved by

standard direct methods such as Gaussian elimination, followed by back-substitution.

This process is then repeated for each value of 'j' ranging from 1 to (M-1). In other words, at each time step we require the solution of (M-1) sets of (N-1) simultaneous equations, and it is well known that this solution process requires substantially less computation than solving an entire set of (N-1)(M-1) set of equations in (N-1)(M-1) unknowns at each iteration. Moreover, we are in fact dealing with tridiagonal sets of equations, which are fairly easy to solve numerically. Some standard algorithms are available for such sets of equations and can be found in many numerical analysis texts, such as Smith[100].

The procedure outlined so far, is in fact implicit in the 'x' direction and explicit in the 'y' direction. So as to avoid any bias in one direction or the other we proceed from fictitious time $t+\delta t/2$ to $t+\delta t$ using a similarly discretised equation which is now implicit in y and explicit in the x direction. The resulting equation is

$$-(q2 + q4)\, T_{ij-1}^{t+\delta t} + (1 + 2q4)T_{ij}^{t+\delta t} - (q4 - q2)T_{ij+1}^{t+\delta t}$$

$$= (q3 - q1)T_{i+1j}^{t+\delta t/2} + (1 - 2q3)T_{ij}^{t+\delta t/2} + (q3 + q1)T_{i-1j}^{t+\delta t/2}$$

(6.17)

This involves the solution of (M-1) sets of simultaneous equations each involving (M-1) unknowns, and is used to calculate the new temperature values at every internal nodal point at time t+δt. So by using equations (6.16) and (6.17) in order, we perform a complete time step from t to t+δt. The values of T_{ij} at time t+δt/2 are merely recognised as an intermediate solution and are not regarded as serious approximations to T_{ij} at any particular time. The A.D.I method works particularly well when the boundary conditions are of the fixed Dirichlet type, but can easily be modified to accomodate the Neumann type, or a mixture of both, further examples of which may be found in Mitchell and Griffiths[65].

The chief modification arises where the boundary conditions are of the Neumann variety as shown in fig(6.2*), where, by assuming that the normal boundary condition holds true simultaneously with the respective discretised equation, any ghost points which arise can be eliminated, and a separate discretised boundary equation can be produced. This is then incorporated into the solution process at the intermediate stage by solving a tridigonal set of N x (M-1) simultaneous equations, providing intermediate values of the temperature on both vertical walls as well as the interior points. Likewise similar stencils exist for the insulated

walls at the t+δt time step which enable the new temperature values to be calculated, apart from the new interior values.

Similar discretised equations are obtainable for the vorticity equation(6.4) or (6.9) in which the boundary conditions consist of the easier to manage Dirichlet type, being either of the shear-free variety or specified by the Woods formula. The solution process however is identical to that of the temperature equation discussed above.

The steady state Poisson stream-function equation (6.5), uses the newly calculated vorticity values, and is solved completely at each iteration by the Jacobi or Gauss-Seidel methods discussed earlier in Chapter 4, pertaining to driven cavity flow.

An outline of the overall numerical solution procedure is shown later in fig(6.4*).

6.3.2 CONSISTENCY AND STABILITY.

By solving the parabolic temperature and vorticity equations (6.3) and (6.4) respectively by the A.D.I method, the discretisation error is found to be of order $O(\delta t^2, h^2, k^2)$, which is an improvement on that obtained by the explicit method of solution, described in detail in Chapter 4. It can also be seen that as h, k, δt ->0 the discretisation error also tends to zero, showing

that the discretised equations are compatible with the governing partial differential equations.

The stability of the discretised equations can be obtained directly from observing their computational molecule or stencil. For example, consider the tempertature equation at the intermediate time step t+δt/2 shown in (6.16), which possesses the computational molecule shown in fig(6.3*).

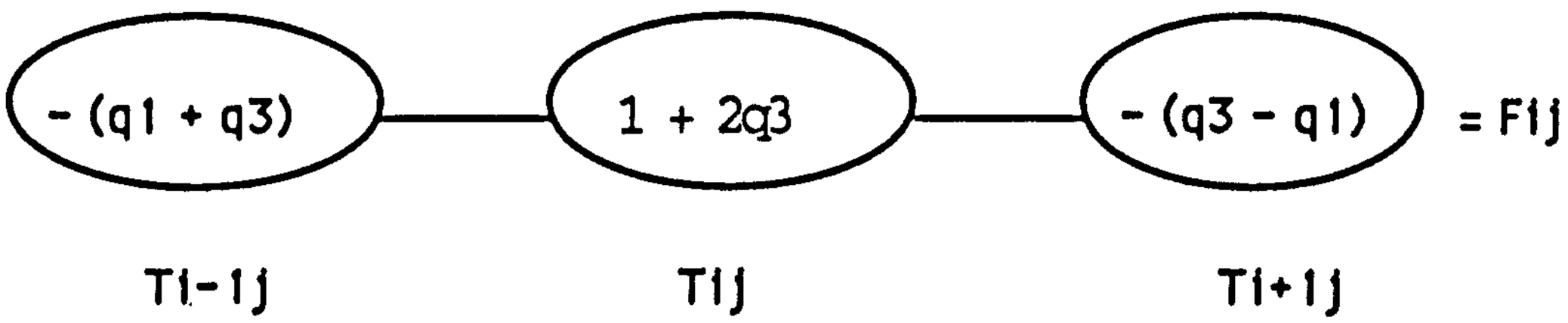

Figure (6.3*)

where $q1 = \frac{\delta t u}{4h}$ $q2 = \frac{\delta t v}{4k}$ $q3 = \frac{\delta t}{2Prh^2}$, $q4 = \frac{\delta t}{2Prk^2}$,

F_{ij} is a composition of discretised values at time t, and u,v are the respective velocities in x and y directions.

For the computational stencil or molecule to remain stable it is required that two constraints imposed upon it hold true simultaneously. The first constraint is that the stencil exhibits diagonal dominance, and the second is that the off-diagonal elements are positive or equal to zero. From fig(6.3*) above it can clearly be seen that the molecule possesses diagonal dominance, and that the off diagonal elements are positive or zero if

$q3 \geqslant q1$, which leads to a criterion that $uhPr \leqslant 2$. A similar molecule can be obtained from the second step of the solution process at time level $t+\delta t$, which again is found to be diagonally dominant, and off diagonal element positive if $vkPr \leqslant 2$.

In like manner, stencils can be obtained for the non-Newtonian vorticity equation(6.4) or (6.9), which are diagonally dominant with the off diagonal elements being positive if both

$$-\frac{(\eta^2)^w}{h\eta^p} \leqslant \frac{u}{2} \leqslant \frac{(\eta^2)^e}{h\eta^p} \quad \text{and} \quad \frac{(\eta^2)^s}{k\eta^p} \leqslant \frac{v}{2} \leqslant \frac{(\eta^2)^n}{k\eta^p}$$

hold true simultaneously.

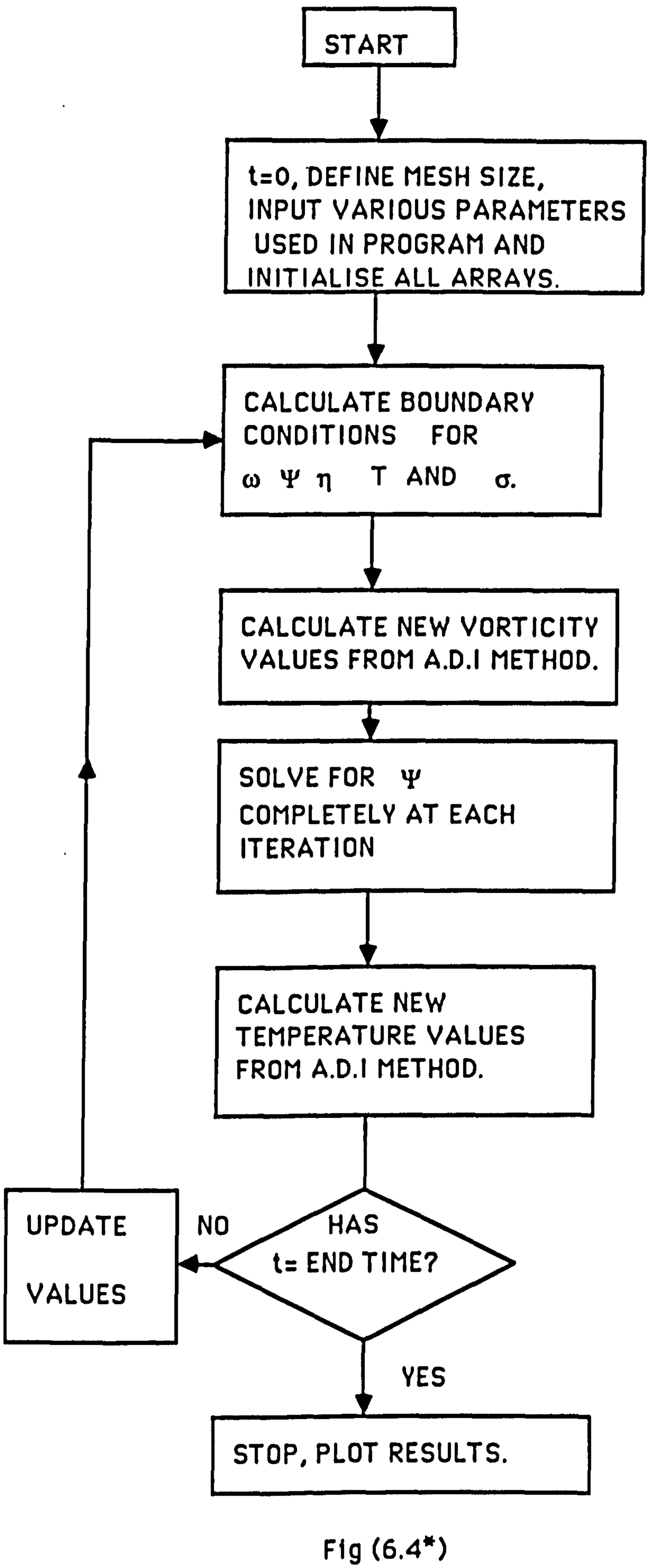
START
t=0, DEFINE MESH SIZE, INPUT VARIOUS PARAMETERS USED IN PROGRAM AND INITIALISE ALL ARRAYS.
CALCULATE BOUNDARY CONDITIONS FOR ω Ψ η T AND σ.
CALCULATE NEW VORTICITY VALUES FROM A.D.I METHOD.
SOLVE FOR Ψ COMPLETELY AT EACH ITERATION
CALCULATE NEW TEMPERATURE VALUES FROM A.D.I METHOD.
HAS t= END TIME?
NO
UPDATE VALUES
YES
STOP, PLOT RESULTS.

Fig (6.4*)

6.4 OTHER CONVECTION PROBLEMS.

After solving the above mentioned equations the major problem we faced was how to validate our results. Fortunately a number of other researchers have undertaken similar problems in modelling thermal convection and for similar geometries as our own. Although almost all the literature available is concerned with Newtonian fluids, this still serves as a useful comparison.

The most comprehensive numerical study of thermal convection within an enclosed cavity has been applied to a problem which has become known as 'the double glazing problem'. This problem has a wide varity of applications, ranging from nuclear reactor insulation, ventilation of rooms to crystalline growth in liquids, and is widely used for validating computer codes. Numerous results have been published, both numerical and analytical. The most notable of these are by De vahl Davis[33], Schnipke and Rice [97], Batchelor[10] and Poots[88].

The problem consists of simulating the two dimensional flow of a Newtonian Boussinesq fluid within an upright square cavity. Both velocity components are zero on all the cavity walls, therefore making the stream function constant. No-slip conditions are also employed on all walls, the vorticity along the boundaries being specified by some given formula. The main difference however occurs in the temperature boundary conditions. For in

this instance it is the horizontal walls which are insulated, and the two vertical walls which are differentially heated causing a temperature gradient to exist between them. The ensuing motion of the system is caused as a direct result of temperature gradient being perpendicular to the buoyancy force. A schematic of the problems boundary conditions is shown in fig (6.5*) below.

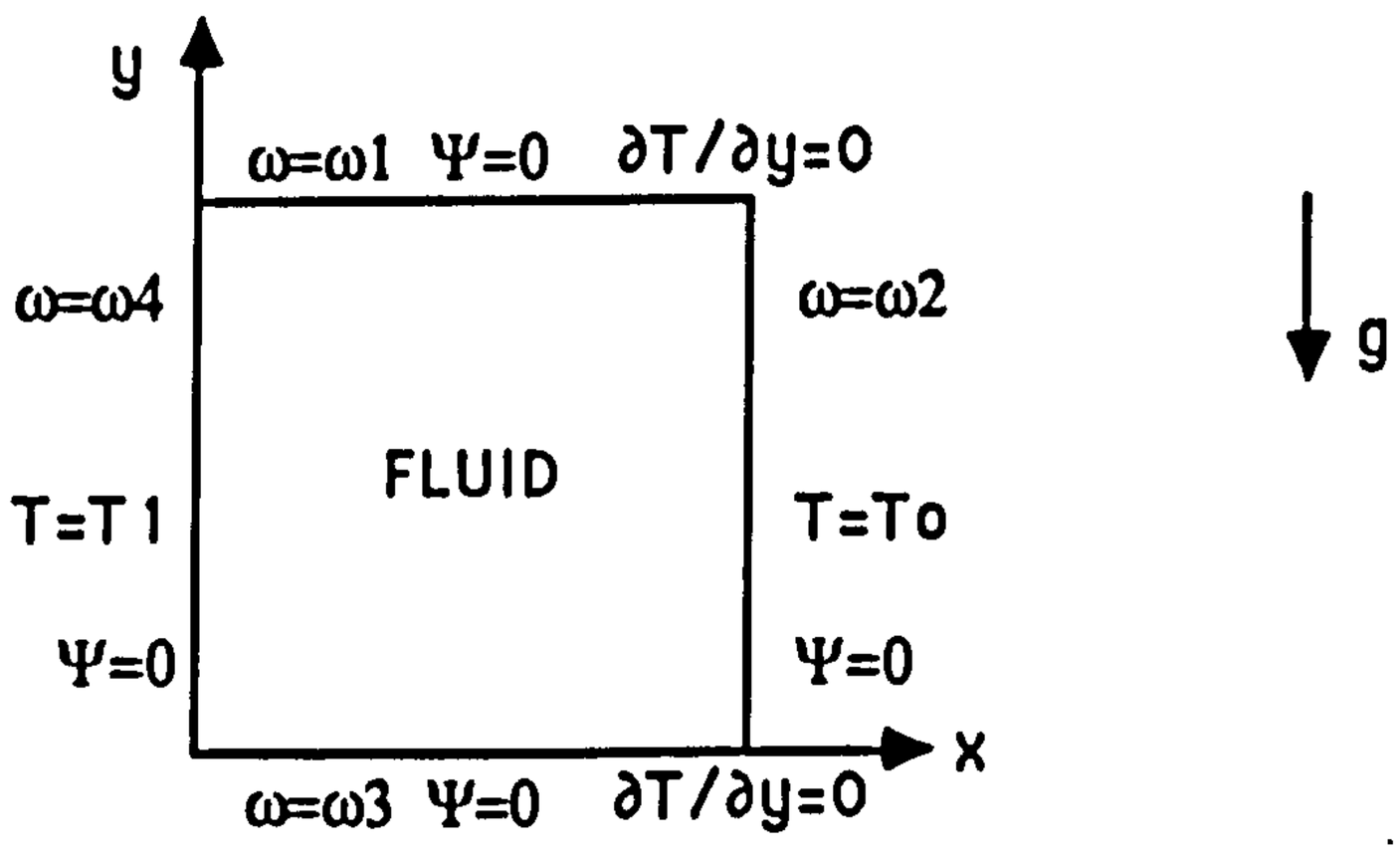

Figure (6.5*)

Boundary conditions of the 'double glazing' problem.

Results for this system have been generally produced for Rayleigh numbers ranging from 10^3 to 10^6 with Pr=0.71, using both finite difference and finite element formulations. A direct comparison between our results for Rayleigh numbers up to 10^5 and the standard benchmark solutions can be seen in Chapter 7.

Moore and Weiss[69], and Mckenzie, Roberts and Weiss[62] have considered the modelling of thermally driven convection for two specific instances occurring in nature. Moore and Weiss[69]

investigated convection within a stellar medium, while Mckenzie et al[62] numerically simulated convection for a Newtonian fluid within the Earth's mantle. By both author's own admission the models of these natural phenomena contain some idealised assumptions, but stress that the models are only aimed towards an understanding of this widely observable complex process of convection. Both authors solve essentially the same equations by finite difference methods with essentially the same boundary conditions as ourselves, which assume the stream function is constant on all walls, and by the stress-free assumption the vorticity is zero on all walls, as shown in fig(6.6*) overleaf. Typical values of Rayleigh number used in both formulations extend to a maximum of about 10^6, as in fact is the case with most authors we have found, and it is the final steady state solution which is sought after and any initial transient flows which may be of interest are not usually produced.

Simulations concerning thermal convection of a steady state non-Newtonian fluid have been provided by Torrance and Turcotte[106], who in relation to their numerical simulation of flow within the Earth's mantle considered the variable viscosity to be a function of temperature, and depth, given by the formulae (6.7) and (6.8) above. Results have been produced for Rayleigh

numbers up to 3600, and a comparison with our own work may be seen in Chapter 7.

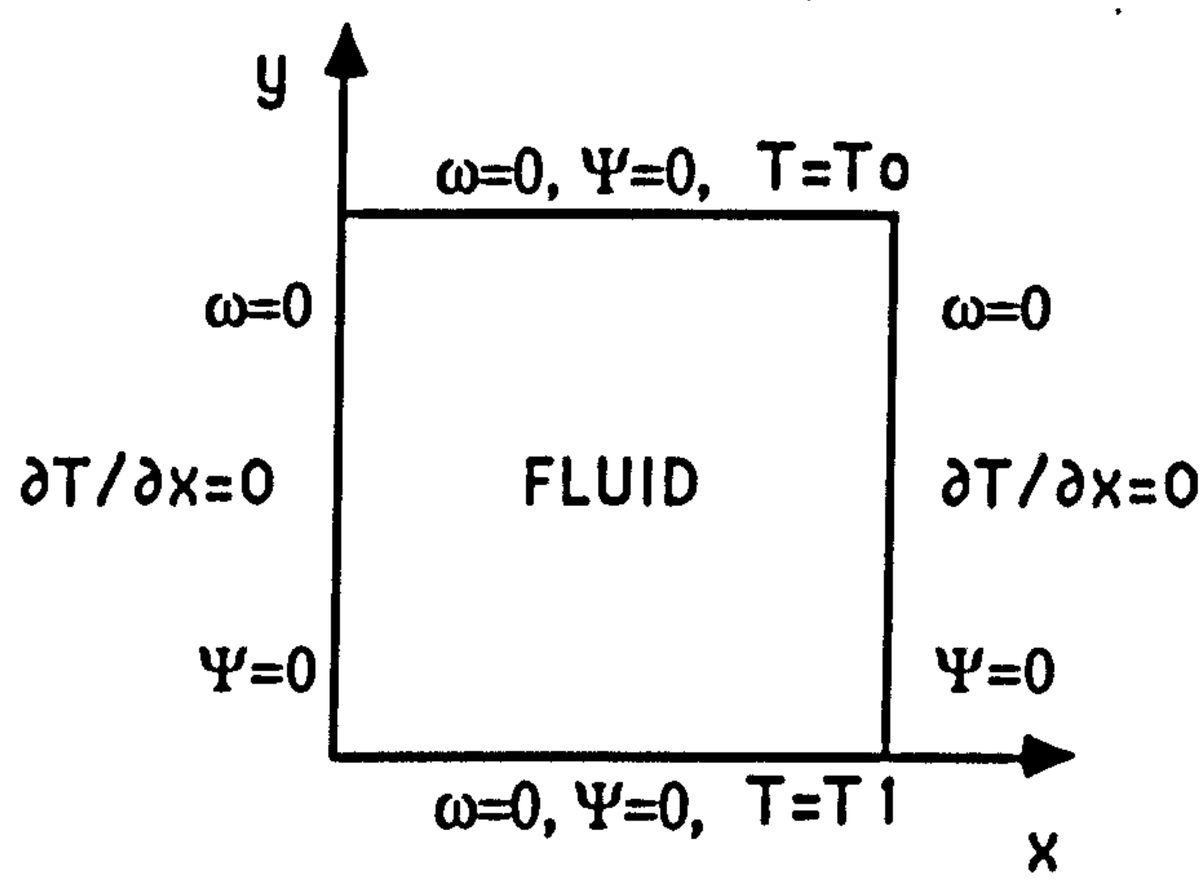

Figure (6.6*)

Diagram showing the boundary conditions (shear free) used in the Rayleigh-Benard simulation.

CHAPTER 7

RESULTS AND DISCUSSION OF THERMALLY DRIVEN CAVITY FLOW.

7.1 INTRODUCTION

In this chapter results are presented and discussed for the time dependent thermally driven cavity flow problem described in detail in Chapter 6. During the course of our investigation various fluid models have been considered which aim to incorporate features of Newtonian and certain non-Newtonian flow, and a comparison is made of their respective behaviours. Fluids which exhibit pseudoplastic, dilatant, thixotropic and rheopectic properties have been considered together with fluids whose viscosity is strongly dependent on temperature and depth. In addition to this we have also investigated the flow of a weakly viscoelastic fluid which is thought to have particular relevance to motion within the Earth's mantle.

Throughout our investigation we have considered the effect of imposing two distinct types of boundary conditions for the vorticity, firstly specifying the boundary vorticity by the Woods formula, used earlier for the case of standard cavity flow with solid walls, and secondly employing the shear-free symmetry boundary conditions which forces the vorticity like the stream function to have a constant value of zero on each of the cavity's

boundaries, which in this case are assumed to be fluid . These two separate boundary conditions for the vorticity have been found to play a significant role in determining the outcome and stability of the solutions produced.

In presenting the results of this chapter we have sought to exhibit the steady solutions, and in using this terminology we refer to an evolutionary solution which does not subsequently significantly alter with respect to time. It is worth noting that although this is the case the results are not the steady state answers, in which no time dependence would be considered in the governing flow equations. For all the problems we have investigated most solutions become steady between five to ten seconds of simulation time.

Before moving specifically to consider each of the afore-mentioned fluids in turn, we will discuss some of the common features of the Rayleigh-Benard thermally driven cavity flow problem which pertain to all the fluids we will consider.

7.2 GENERAL FEATURES OF THE THERMALLY DRIVEN CAVITY FLOW PROBLEM.

In all cases considered, if no adverse temperature difference is applied between top and bottom plates irrespective of the type of boundary conditions used, the fluid will remain at rest in uniform equilibrium in which all parts of the fluid are identical and possess symmetry throughout the entire plane. If heat is momentarily supplied to the lower plate and then removed the initial disturbance to the system will die away, the system returning to its equilibrium state. However, if a constant supply of heat is uniformly applied to the lower wall the system can gradually be induced away from equilibrium. If the temperature difference stated in terms of the Rayleigh number (Ra) defined in Chapter 6 is small, the system adopts a simple but unique state whereby the heat energy supplied is transported through the fluid by conduction. During this phase although no visible motion is observed, significant changes are occurring within the fluid, namely the emergence of stratified fluid layers of differing densities, the lighter fluid being found at the bottom and the denser material near the top of the cavity, and this top heavy configuration is potentially unstable. Upon increasing the Rayleigh number the system is moved further away from equilibrium and at a certain critical value of the Rayleigh number,

(shown for the various fluids considered in fig(7.70*) near the end of this chapter), instability enters, being evidenced in the emergence of convective cells near the bottom corners of the cavity. The motion of these cells however, is gradually damped out due to retarding viscous forces which is consistent with the prediction derived from the linear theory, first published by Rolyeigh[90]. If the Rayleigh number is further increased the two cells grow with time, but not at the exponential rate predicted by the linear theory. The reason is that the non-linear terms in the governing equations are no longer negligible and also due to the viscous forces which inhibit the motion. The overall result is that two finite counter rotating cells are produced each of which fill half of the cavity. Frequently however, this is not the final state of the system, for at this Rayleigh number the initial two cell configuration can become unstable and both cells merge to form one large rotating cell which fills the cavity. The reason for this occurrence is still uncertain. Upon increasing the Rayleigh number further the reverse process is often seen to occur, the one cell itself becoming unstable and gives birth to two symmetric counter rotating cells. We have noticed this effect to be periodic and occurs from low Rayleigh numbers to those up to 1.4×10^6, this being the largest value obtainable throughout our investigations.

The system can be seen to have moved from exhibiting no motion to the case where quite complex convective motion occurs, with cold dense fluid falling in some parts of the flow and warmer lighter fluid rising in others. The phenomena observed in the Rayleigh-Benard system are reminiscent of the symmetry breaking patterns observed for the famous Taylor-Couette flow system which exhibits similar complex behaviour, with the emergence of stacked cells which develop into wavy and turbulent vortices as the Reynolds' number is gradually increased.

Based on experimental evidence for Newtonian fluids, it has been observed that at very high Rayleigh numbers the system becomes 'fuzzy', entering a regime whereby chaotic motion is observed. This is a pre-cursor of turbulence, a much studied and yet still very obscure area of fluid dynamics. However this is currently well outside our range of solutions and consequently is not investigated.

The actual physical laboratory experiment of Benard is still perfectly reproducible so that all the above mentioned phenomena can be readily observed, yet it still throws up a further surprise. The exact determination of the convection cells has been justified by the linear theory analysis of Rayleigh[90]. However, the directional rotation of the cells is still apparently left to

chance, and so a unique situation arises between determinism and chance.

A similar situation has been found to occur within our simulations, and we have found that the cell rotation and configuration depend very stongly upon the initial temperature guess used whilst iteratively solving the complex equations governing the system. In all cases considered using the initial distributions $T(x,y)=0$ and $T(x,y)=1-y$ at $t=0$, for the initial temperature of the system finally yields two identical 'mirror image' solutions, showing that a bifurcation has taken place within the system, illustrated in fig (7.1*) below.

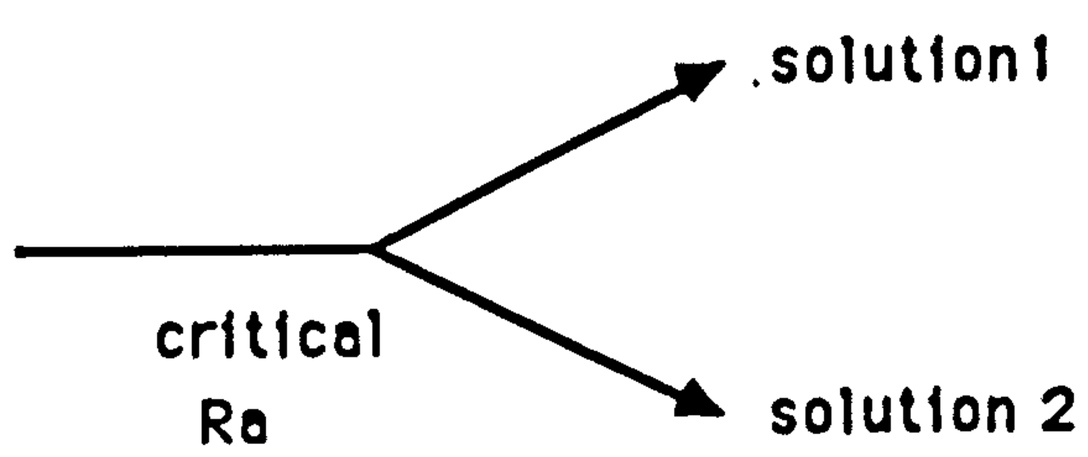

Figure (7.1*)

Bifurcation phenomena in the Rayleigh-Benard problem.

Consequently, all results presented are for the initial guess of $T(x,y)=0$, but it is worth bearing in mind that a second legitimate set of mirror image solutions also exist.

7.3 COMPARISON WITH OTHER PUBLISHED WORK.

To validate the computer code used in the solution of the Rayleigh-Benard problem outlined above, we have applied our solution algorithm to the standard test case of buoyancy induced thermally driven cavity flow, with differentially heated side walls. This is the 'bench-mark' solution for all convection problems of this variety, and has become widely known as 'the double glazing problem', but has many other practical consequences for a wide variety of circumstances ranging from nuclear reactor insulation to the growth of crystals in liquids[97].

Many authors have considered the double glazing problem using both analytical (Batchelor[10], Poots[88]), and numerical (Schnipke and Rice[97]), techniques. However, we have selected the bench-mark solutions published by De Vahl Davis[33], since the author has solved the problem for Rayleigh numbers within our range of 10^3 to 10^5 using the stream function vorticity formulation together with a modified A.D.I solution process, which is akin to our approach. Most authors however, are interested in the steady state formulation and therefore their governing equations take no account of time dependence, and also the techniques of non-dimensionalisation of the governing equations vary from author to author, and so a direct comparison

is not always possible. Despite this fact a comparison of our 'steady' solutions figs (7.2) to (7.7), with the bench mark streamline and temperature solutions of De- Vahl Davis[33] fig (7.8) show favourable agreement. It can be seen that as the Rayleigh number is increased from 10^3 to 10^5 one large clockwise rotating cell is always produced, which becomes flatter and more unstable near the cavity's centre. This is also reflected in the corresponding temperature profiles which indicate the strength of convection increases with higher Rayleigh numbers, being almost vertical near the side walls and horizontal near the central portion of the cavity at Rayleigh number 10^5, the highest we found to be obtainable.

7.4 NEWTONIAN FLUID.

With confidence gained through successful comparison of our results with bench mark solutions, we proceeded to consider the solutions obtained for a Newtonian fluid undergoing thermal convection for the Rayleigh-Bernard problem with the boundary vorticity specified by the Woods solid walls formula. Throughout all our simulations the Prandtl number (Pr) is fixed at a value of 7, near that of water, and the Grashof number (Gr) allowed to vary.

The system was found to become unstable and produce continuous circulatory convective motion at a critical Rayleigh number of 3300. For moderately low Rayleigh numbers up to and including that of 10^4 the inital solution consists of two symmetric mirror image counter rotating cells. However, as time progresses this motion is either sustained or as frequently happens, one cell may grow at the expense of the other and a steady solution comprised of one anti-clockwise rotating cell is produced which almost fills the entire cavity, as shown in fig(7.9). The resulting streamlines are closed loops which give the appearance of being sheared near the cavity's walls, and becoming more circular near the vortex centre, located in the cavity's middle. The streamlines are symmetric about both of the cavity's main diagonals and the gaps between neighbouring streamlines are fairly constant indicating circulation is uniform throughout the cell.

The corrseponding asymmetric temperature profile is shown in fig(7.10) and indicates that warm fluid rises near the right hand wall with the colder denser fluid falling near the opposite wall, the convective current evidenced by the 'S' shaped curves, and the temperature at the centre of the cavity being approximately the average of the top and bottom walls. A good illustration of the instability of the two initially symmetric cells can be witnessed

by examining the particle paths of five equally spaced particles, initially placed in a horizontal line half way up the cavity, and shown in fig(7.11).

Upon increasing the Rayleigh number to a maximum of 10^5 for this particular configuration the reverse process of that which occurred at $Ra=10^4$ is produced. The steady solution is comprised of two symmetric mirror image counter rotating cells which possess a distinctive 'bean' shape appearance, as shown in fig(7.12). The resulting streamlines are more densely packed near the extremities of the cell, the gaps between which gradually increase as the two vortex centres, located in the middle of each cell and approximately half way up the cavity are approached, indicating circulation is weakest there. The corresponding symmetric temperature profile shown in fig(7.13) reveals the convective motion consists of cold fluid falling down the cavity's middle and warmer fluid rising near the cavity's walls.

We now consider the results obtained for a Newtonian fluid when the vorticity is specified as zero on each of the 'cavity's' walls, employing the shear free boundary conditions, which are representative of fluid boundaries.

The system with this configuration was found to be unstable and produce sustained convective motion at a critical Rayleigh number of 1700, which is in line with the linear theory

prediction, Acheson[1]. The system behaves in a similar fashion to that described above using the non-zero vorticity boundary conditions, with either sustained motion occurring of two cells or the annihilation of one of the cells to leave one large cell. Upon increasing the Rayleigh number to 10^4, the steady solution shown in fig (7.14), consists of two symmetric mirror image counter rotating cells, each occupying half of the cavity. The streamlines are closed loops being rectangular in shape near the walls of the cavity, the gaps of which increase as the more oval vortex centres are approached, showing weaker circulation occurs there. The corresponding temperature profile fig (7.15) is symmetric although not as spread out as with non-zero vorticity case, and shows the motion is comprised of cold fluid descending near the cavity's centre and warmer fluid rising near the respective vertical walls. Upon further increasing the Rayleigh number to 10^5 a similar result is obtained except one cell has grown slightly at the others expense and occupies about two thirds of the cavity, symmetry is lost and this is also highlighted in the temperature profile, so the indications are that the two cell structure is becoming unstable at this Rayleigh number. This is confirmed by analysing the result obtained at Rayleigh number 10^6 shown in fig(7.16), in which the steady solution consists of one large almost symmetric clockwise rotating cell which fills

the entire cavity. The streamlines are closed loops, square in appearance near walls of cavity and becoming more circular near the vortex centre located in the middle of cavity. As usual the increase in separation between neighbouring streamlines as the centre is approached indicates weaker circulation is found there.

The temperature profile fig(7.17) shows the temperature throughout most of the cavity is uniform obtaining a value which is the average of the top and bottom plates. This result agrees with the published findings of both Moore and Weiss[70] using a initial linear temperature distribution throughout the cavity, and McKenzie, Roberts and Weiss[62], shown in figs(7.18) and(7.19) respectively, who considered a similar geometry and boundary conditions, their results pertaining to stellar convection and mantle flow respectively. McKenzie et al[62] have also found that when $Ra=1.4x10^6$ the one cell becomes unstable and gives birth to two almost identical touching mirror image counter rotating cells. This result we confirm to be true, shown in figs(7.20) and (7.21) respectively, and find that the streamlines are very densely packed near the cavity's centre and near the walls, the effect becoming less noticeable as the vortex centres are approached, which are located a little lower in the cavity. McKenzie et al[62] have also found this pattern to be repeated at $Ra=2.4 \times 10^6$, and suggest this instability is caused by a 'blob' of

cold fluid forming near the cooler top plate which falls vertically in the cavity's centre destroying the one cell and creating two in its wake.

On comparison the results obtained using both sets of boundary conditions for vorticity are quite similar, both showing evidence of periodic bifurcation of one cell into two and the reverse phenomenon. However, the major noticeable differences are the critical value of the Rayleigh number for the shear-free case is approximately half that where the vorticity boundary conditions are specified by the Woods solid wall formula, showing that the non-zero vorticity boundary values act as a stabilising influence on the system. The difference in boundary conditions is also highlighted by the shape of the cells produced. When vorticity is non-zero on the cavity's walls, if two cells are produced they have a unique 'bean' shape structure due to shearing stresses present on the cavity's walls which are not present in the shear free case and which gives rise to more rectangular cells. A similar effect can be observed if only one cell is produced.

7.5 PSEUDOPLASTIC FLUIDS.

In this section steady flow results will be presented for a pseudoplastic fluid, whose apparent viscosity is simulated by the Cross model defined in Chapter 3. The system for a pseudoplastic (or shear-thinning) fluid was found to become unstable and produce sustained circulatory motion at a critical Rayleigh number of 3200 for the non-zero boundary vorticity case, and found to reduce to a value of 1400 when conditions are relaxed to those of the shear-free formulation, which is in line with intuition using lower viscosity fluids. We will now consider results obtained firstly for the case of non-zero vorticity on each of the cavity's walls.

At Rayleigh number 10^4, the steady solution consists of two mirror image counter rotating 'bean' shaped cells, very similar in fact to that produced for a Newtonian fluid with the same configuration but at higher Rayleigh number, shown previously in fig(7.12), the exception being the vortex centres are located slightly lower in the cavity which is a direct result of the shear-thinning nature of the fluid, allowing swifter motion near the warmer lower plate where fluid is thinnest. The temperature profile is also symmetric about the vertical mid plane of the cavity (x=0.5) indicating the colder fluid falling near the centre

and warmer fluid rising near the walls. However, upon increasing the Rayleigh number to its maximum of 10^5 for our 30x30 grid, a markedly different steady solution shown in fig (7.22) is obtained. The solution consists of two approximately mirror image counter rotating cells of equal strength, which possess symmetry about the horizontal centre line of the cavity (y=0.5). The respective vortex centres being located approximately two fifths of the way along the cavity and one quarter, and three quarters up the cavity respectively. Similar peculiar results were obtained on various grid sizes which gave credence to the novel solution being of a legitimate nature. The corresponding temperature profile, fig(7.23) also reflects this strange occurrence, with symmetry being obtained about (y=0.5). The motion revolves separately within each half of the cavity, in the top portion clockwise motion occurs, caused by warmer fluid ascending near the left hand wall and the colder fluid descending near the right hand wall, while the exact reverse is observed to occur in the lower section of cavity, thus causing the counter rotating flow. The temperature profile along with the cells themselves show a degree of similarity with the usual solutions generated except being rotated through ninety degrees. The unusual though legitimate result is similar to that obtained by a dilatant fluid whilst involved in co-rotational cavity driven flow

shown in fig(5.36) in Chapter 5, the peculiarity being a direct result of the fluid used and the non-linear terms present in the governing equations.

When the boundary vorticity is specified by the shear-free conditions, the steady solution obtained at $Ra=10^4$, shown in fig(7.24) consists of one large clockwise rotating cell, plus two weakly counter rotating vortices near the top left and bottom right hand corners. The circulation of the main cell is fairly fast as can be seen from the very densely packed streamlines, the gaps between which gradually increase as the central vortex is approached. The solution possesses symmetry about the main diagonals of the cavity, also giving the impression of stretching and compression along these diagonals giving rise to its skew shape. The corresponding asymmetric temperature profile fig(7.25) indicates that the strongest circulation takes place near the walls of the cavity, evidenced by a strong 's' shaped kink in the middle of the cavity, where the temperature as usual is approximately the average of the adverse temperature gradient.

At Rayleigh number 10^5 the steady solution fig(7.26), comprises of one large anticlockwise rotating cell almost filling the cavity, together with two very weak corner vortices located along the negative diagonal ($y=-x$) of the cavity, which are not shown. The solution is similar to the that of a Newtonian fluid at $Ra=10^6$

with the cell rotation in opposite direction. The corresponding temperature profile shown in fig(7.27) shows most of the anticlockwise motion is confined to a centrally heated core of uniform temperature. Upon increasing the Rayleigh number further to 5×10^5, we observe the one cell has become unstable and bifurcated to give two almost symmetric counter rotating cells. The major difference here is that the temperature profile consists of an upward rising plume in the cavity's centre, with the colder denser fluid falling near the cavity's walls. This is in contrast to the usual sequence of events, the results shown in fig(7.28) and (7.29) respectively, the slight wobbles in the plots are due to lack of mesh refinement.

7.6 DILATANT FLUIDS.

To simulate the flow of a dilatant or shear thickening fluid the Cross model is again used, the viscosity parameter values being the exact opposite of those for a pseudoplastic fluid. The main feature is that the fluid is initially thin and then as a consequence of shearing due to convective motion the fluid's viscosity gradually increases. This feature is also borne out in the fact that the critical Rayleigh number for which sustained circulatory motion is obtained is 1000 with non-zero vorticity boundary values, and 400 if the boundary conditions are of the

of the shear-free kind. These are significantly lower than those of Newtonian and pseudoplastic fluids but are easily explained in terms of the fluid's initial viscosity being very low, significantly less than 1 in value and therefore offering less opposition to motion.

The steady solution obtained on a 30x30 grid at $Ra=10^4$ for the case of non-zero vorticity specified on the walls shown in figures (7.30) and (7.31) respectively, are mirror image solutions of that obtained by a Newtonian fluid show in fig(7.9). Upon increasing the Rayleigh number to a maximum of 10^5, the steady solution consists of two counter rotating cells which initially were symmetric but gradually one grows at the other's expense occupying two thirds of the cavity, similar again to a Newtonian fluid at the same Rayleigh number but with the opposite mirror image configuration. Thus the main result for a dilatant fluid when non-zero vorticity boundary conditions are applied is that the solutions are always opposite to those obtained for the Newtonian case.

At $Ra=10^4$ for a dilatant fluid when shear-free vorticity boundary conditions are used the resulting solution is identical to that of a Newtonian fluid shown in fig(7.14), two symmetric rectangular cells being obtained. As the Rayleigh number increases to 10^5 the steady solution shown in fig(7.32), consists

of one large clockwise rotating cell which gives the appearance of being stretched along the diagonal (y=-x) of the cavity. The streamlines are closed loops, square-like in appearance near the cavity's walls and becoming more circular near the vortex centre located in the middle of the cavity. The gaps between the neighbouring streamlines also increase as the centre is approached, indicative of weaker circulation present there. The corresponding temperature profile shown in fig(7.33) also complements the streamline plot showing the various ascending and descending motions of the hot and cold fluid involved in clockwise convective motion. Upon increasing the Rayleigh number further to a maximum of $5x10^5$ shown in fig(7.34), it once again becomes evident that the large cell structure has become unstable producing two counter rotating mirror image rectangular cells in its wake. The significant difference is that the vortex centres are now located considerably higher up in the cavity, being approximately central to each cell and three fifths of the way up the cavity, this being a direct consequence of the shear thickening nature of the fluid inhibiting motion in the lower portion of the cavity. The corresponding temperature profile may be seen in fig(7.35), showing colder fluid descending in cavity's centre, spreading out near the warmer lower plate and with warmer fluid rising near the walls, and the temperature within

each half showing a tendency to become uniform with a value equal to half of the temperature gradient.

7.7 TEMPERATURE DEPENDENT VISCOUS FLUIDS.

In this section we consider the effect on the thermal convective motion produced in the Rayleigh-Benard system when the fluid's viscosity exhibits a strong dependence on temperature. This type of situation arises in many geophysical flows and is particularly relevant to flow thought to exist within the Earth's mantle. For comparative purposes, throughout this period of investigation, the Prandtl number defined in Chapter 6 is taken to be a constant equal to 7. However, in contrast the mantle consists of very viscous liquid rock and consequently this forces the Prandtl number to become so large it can be considered to be infinite, and thus the temperature equation (6.3) becomes wholly advection dominated. In spite of this fact, the essential features of flow within the Earth's mantle are present within our system and some progress in understanding the flow mechanics can be made.

The temperature dependent viscosity function may be modelled in various ways, the most common are those of the Reynolds' and Arrhenius types given in Chapter 6. However, for particular relevance to flow within the mantle of the Earth we follow

closely the work of Torrance and Turcotte[106], using their modified Reynolds' type formula shown in equation (6.7), where the constant 'k' in the exponential term governs the rate at which the viscosity changes with temperature.

Torrance and Turcotte[106] with this formula considered a steady state version of our governing equations discussed in Chapter 6, and have published results for Rayleigh numbers up to 3600 for various viscosity values, using the shear-free boundary conditions.

We develop their work by incorporating more realistic time dependence, extention to higher Rayleigh numbers and also by considering the effect of imposing non-zero vorticity values on the cavity's walls.

When k=0 in formula (6.7) the fluid obtains a constant Newtonian viscosity value and for comparative purposes our results, figs(7.36) and (7.37), are shown alongside those published by Torrance and Turcotte[106], fig(7.38), these results at Ra=3600, Pr=1, using shear free vorticity boundary values and with a 1.4 x1 rectangular cavity, and can be seen to be in favourable agreement.

If we now revert to the more familiar square cavity configuration increasing both the k value to 1 and Ra to 10^4 with zero vorticity on the boundaries, the steady solution shown in fig(7.39) comprises of two mirror image counter rotating

rectangular cells, similar in fact to that of a Newtonian fluid but with opposite rotation. The temperature profile is also the reverse of the corresponding Newtonian result and shown in fig(7.40), the warmer fluid rising in cavity's centre and colder fluid descending near the vertical walls. If the k value used in formula (6.7) is subsequently increased to 10 the viscosity difference between top and bottom walls is equals $2\eta(0)\sinh(0.5k)$, varying by a factor of 143 from case where k=1, the fluid is then very thin near the hot lower wall and much thicker near the colder top wall, inhibiting motion. The resulting solution fig(7.41) has two counter rotating mirror image cells but are significantly reduced in size as motion is confined to lower half of cavity where the viscosity is lowest and fluid thinnest. The corresponding temperature profile fig(7.42) also confirms this, showing convection occurring in the lower portion of the cavity while near the top of cavity heat is transported via conduction alone.

If the Rayleigh number is now further increased to a maximum obtainable value of 10^5, when k=1, again using shear-free vorticity boundary conditions, the steady solution simply consists of two counter rotating almost symmetric cells each filling half of the cavity, a result witnessed by us on numerous occasions. However, as k is increased to a value of 5 a quite

different solution emerges. The steady solution obtained, shown in fig(7.43), displays one large non-symmetric clockwise rotating cell occupying the lower three quarters of the cavity. The main cell is flatter than usual in appearance, the vortex centre being lower in cavity and to the right where fluid is thinnest and askew from centre, with a weaker sister counter rotating cell found near top left hand corner. The corresponding temperature profile is shown in fig(7.44). .

We have also investigated the effect on the solutions obtained when vorticity is allowed to have a non-zero value specified by the Woods formula along its boundaries. At low Rayleigh numbers of order 3600 when Pr=1 and k=0, i.e a Newtonian fluid, the steady solution produced is similar in appreearance to that shown in fig(7.36) being uniformly symmetric but counter rotating with weaker circulation strength. This again is an indication that non-zero vorticity boundary conditions act as a stabilising influence, a fact also highlighted by the differing value for the critical Rayleigh number for which sustained circulatory motion is obtained, shown in fig(7.70*) at the end of this chapter.

Upon increasing Ra to 10^4 with k=1 the highest obtainable with this particular configuration, the steady solution consists of one large clockwise rotaing cell, very similar in fact to that produced by a dilatant fluid shown in fig(7.30), both of which are mirror

images of the result for a Newtonian fluid shown in fig(7.9).

If the Rayleigh number is further increased to a maximum of 10^5 along with k=1, the steady solution fig(7.45), consists of two symmetric inverted bean-shaped counter rotating cells similar to that obtained by a Newtonian fluid at this Rayleigh number shown in fig(7.12) but turned on its head. The corresponding temperature profile also shown in fig(7.46) is symmetric about the cavity's middle and indicates the warm fluid rising sharply in centre of cavity while colder fluid falls near the walls.

In passing we mention that the other formulae have been investigated with regards to the modelling of fluids exhibiting viscosity dependence on temperature and the results noted, however as the viscosity variation throughout the cavity is reasonably low, no new results were found to occur. The general solutions consist of two fairly symmetric cells at $Ra=10^4$ which become unstable and merge to form a large central cell at $Ra=10^5$, for both non zero and shear-free vorticity boundary conditions.

7.8 VISCOSITY DEPENDENCE ON DEPTH.

In this section results are presented for the case where the fluid viscosity under consideration varies exponentially with depth, for a range of Rayleigh numbers which may be appropriate to flow within the Earth's mantle. Our work is based closely on the work of Foster[38], who considered time dependent solutions of a fluid whose viscosity increased exponentially with depth, whilst being internally heated. Fourier series techniques were used to yield a solution and results published for Rayleigh numbers of order 10^8. Torrance and Turcotte[106] have also considered a similar problem for steady state convection of a depth dependent viscosity fluid heated from below, publishing results for modest Rayleigh numbers up to 3500, using shear-free vorticity boundary conditions.

We will primarily extend the work of Torrance and Turcotte[106] to incorporate the features of a wholly time dependent problem with more realistic Rayleigh numbers pertaining to flow within the mantle, as well as investigating the effect of non-zero wall vorticity on the solutions produced. The apparent viscosity formula is similar to that of the temperature dependent case and shown in Chapter 6 in equation (6.8).

We firstly consider the results using the shear free boundary conditions for k values in the range 1 to 5.

When k=1 at Ra=10^4 the steady solution obtained shown in fig(7.47) consists of one large square cell possessing an anticlockwise circulation pattern. The cell however is not symmetrical, the vortex centre being slightly to the left of centre. The streamlines are closed loops which become circular near the vortex centre where it is also noticeable that the gaps between the streamlines have increased, indicating weaker circulation is found there. The corresponding complementary temperature profile is shown in fig(7.48), and indicates cold fluid falling near the left hand wall with the warmer lighter fluid ascending near the opposite wall. Upon increasing the k value at this Rayleigh number, the one cell structure is seen to become unstable producing a two cell structure in its place, the cell motion is also found to be translated further up the cavity where the fluid is thinnest. A typical solution occurs when the k value is increased to a maximum 'value' of 10. The steady solution shown in fig(7.49) comprises of two symmetric mirror image counter rotating cells which are confined to the upper half of the cavity where the fluid's viscosity obtains its lowest value. This fact is also perceived by analysing the corresponding temperature profile shown in fig(7.50), where the only convective motion occurs within the top half of the cavity, and heat is transported through the main bulk of now very thick fluid by conduction. The highest

Rayleigh number obtainable for this configuration was at $Ra=10^5$ with k=1. This solution consists of two symmetric counter rotating mirror image cells similar to the corresponding Newtonian case at $Ra=10^4$ shown in fig(7.14), except rotation is in opposite direction, and consequently is not shown.

When the boundary conditions for the vorticity are allowed to be non-zero, the largest Rayleigh number for which a steady solution is obtainable was for $Ra=10^4$, with k=1 shown in fig(7.51). The resulting solution may be seen to consist of two weak counter rotating cells one slightly bigger than the other. It is noticeable that the vortex centres are where circulation is weakest, and located higher in the cavity than for most similar cases due once again to the viscosity being lower there. The corresponding temperature profile fig(7.52), reflects the cell configuration and shows colder fluid descending near the cavity's centre while warmer fluid rises in convective motion near the walls.

7.9 WEAKLY VISCOELASTIC FLUIDS.

In this present section consideration is given to the transient convective motion produced by a weakly viscoelastic liquid, as a result numerically solving the equations outlined in section (6.2.3) of the previous chapter. The relevance of the solutions are again appropriate to the type of flow thought to exist within the Earth's mantle which consists of molten rock exhibiting both solid and liquid properties.

The main characteristics influencing the flow are the Rayleigh number, the vorticity boundary conditions being non-zero or shear-free, together with the Weissenberg number which provides a relative measure of the importance of the normal and tangential stresses, occurring within the fluid whilst in motion.

During the course of our research we have found the highest Weissenberg number obtainable was 10^{-4} for Rayleigh numbers greater or equal to 10^{4}, however, these could only be obtained on relatively less refined 10x10 grids. The corresponding results usually consisted of two symmetric counter rotating cells and consequently are not shown. However, if the Rayleigh number is increased, the mesh needs to become more refined and it was found necessary to obtain a solution that the Weissenberg number must be lowered, to a value of 10^{-6} on 30x30 sized grid. This

significantly reduces the elasticity input to the problem, in most instances being almost negligible.

However, the most significant effect if viscoelasticity is present within the framework of the Rayleigh-Benard problem has been found to occur with a weakly viscoelastic pseudoplastic fluid, at a Weissenberg number of 10^{-5}, the result being obtainable only on a 20x20 grid. In the course of simulation it also readily became apparant that a steady solution for this configuration did not exist, the solution itself tending to show periodic and cyclic nature.

At 5 seconds of simulation time, the solution shown in fig(7.53) comprises of one large central clockwise rotating cell, together with 2 smaller counter rotating vortices, located near the corners on the cavity diagonal (y=-x). The symmetry of the solution is also preserved about the main diagonals of the cavity with the streamlines being noticeably more compact near the extremities of the cell, spreading out more as the central vortex centre is approached and indicative of the weaker circulation found there. The corresponding and complementary temperature profile is shown in fig(7.54) and reveals most of the colder fluid circulates in a clockwise direction near the right hand wall with the reverse effect observed near the opposite wall.

At a time of 10 seconds a similar solution is obtained and shown in fig(7.55), except this time being rotated in a clockwise direction through ninety degrees. The noticeable difference is the corner vortices now lying on the cavity's main diagonal (y=x) have grown in size and also rotate in the opposite direction to that which occurred at the time of 5 seconds, this consequently is also true for the central cell which has become more elongated due to the increased size of corner vortices. The temperature profile indicating the various complex thermal motions is shown in fig(7.56).

At 15 seconds the solution, fig(7.57), consists of one large central cell rotating in a counter clockwise direction, which almost fills the cavity and gives the appearance of stretching along the diagonal (y=-x) and compressed due to weaker counter rotating corner vortices located on the cavity's main diagonal. The stream function values have increased in size implying greater vigour of circulation, and the complementary temperature profile fig(7.58), shows a large 's' shaped structure in the centre of the cavity showing the direction of the rising and falling plumes of hot and cold fluid.

Finally at a simulated time of 20 seconds the solution almost reverts back to the original configuration obtained after 5 seconds, with one large central clockwise rotating cell aligned on

the main diagonal of the cavity, coupled with two smaller counter rotating corner vortices located near the corners as shown in fig (7.59). The corresponding asymmetric temperature profile for this case is shown in fig(7.60), indicating the substantially weaker motion of the respective warm and cold fluid sections.

At higher Rayleigh numbers the solution mesh needs to be further refined, and this forces the Weissenberg number to be lower and thus decreasing the elasticity contribution to the problem and the results obtained show very little difference to those previously obtained for inelastic fluids.

When we allow the vorticity on the cavity's walls to take on non-zero values all results obtainable irrespective of grid size or Rayleigh number could only be obtained for Weissenberg number 10^{-6}. At $Ra=10^4$ the solution obtained for both a viscoelastic Newtonian fluid and a viscoelastic dilatant fluid are exact mirror image solutions of each other, the latter being very similar to that of the corresponding case of a Newtonian fluid shown previously in fig(7.9). This result also highlights the fact that the elastic contribution when applied to a Newtonian fluid tends to reverse the structure, configuration and rotation of the result produced for the corresponding Newtonian case, this being well a known trait of viscoelastic liquids, e.g Walters[111]. The corresponding temperature profiles are asymmetric showing the

various ascending and descending convection currents transporting the heat around the cavity, the latter case again identical to that shown in fig(7.10). The solution obtained for a weakly elastic pseudoplastic fluid at this Rayleigh number is also similar to those mentioned above, with one large clockwise rotating cell being produced as the steady solution, slightly flatter than produced for those shown earlier.

Upon increasing the Rayleigh number to a maximum obtainable of 10^5 for this particular configuration, the results obtained for the viscoelastic Newtonian case are not significantly different from those of the corresponding Newtonian case shown in fig(7.12) This is also true for the viscoelastic pseudoplastic case, the result being similar to that of a pseudoplastic fluid shown in fig(7.22), but possessing a larger slightly faster top counter rotating horizontal cell. The major difference in solution at this Rayleigh number can be found in that of the viscoelastic dilatant fluid. The steady solution for this case consists of one large non-symmetric clockwise rotating cell shown in fig(7.61) the vortex centre of which is found to be slightly above the cavity's centre and to the right. The streamlines produced are approximately square near walls and become more circular as the slightly weaker circulating vortex centre is approached.

The complex complementary temperature profile is shown in fig (7.62) and is indicative of the fluid's motion.

7.10 THIXOTROPIC/RHEOPECTIC FLUIDS.

In this section we review the results obtained by numerically solving the equations outlined in section (6.2) where the apparant viscosity is modelled using equation (6.6) which aims to simulate fluids whose viscosities alter with time as well as shear-rate. The value of the constant 'a' in the exponential term of equation (6.6) controls the rate at which the viscosity alters with time. Known, measured values of this constant are usually very small, a thixotropic drilling mud may for example have a value of $a = 5 \times 10^{-3}$. This means at low simulation times the fluid maintains an approximately constant viscosity value, the resulting solutions being almost identical to those of a Newtonian fluid, whereas as time becomes infinite the solution alters to that obtained for either a pseudoplastic or dilatant fluid according to the parameters chosen in the Cross model. We are unable, however, due to limited computer facilities to obtain very high simulation times, and so to witness this effect on a shorter time scale the constant 'a' was given an arifical value of 5. This, however, was found to damp out any time dependence on the viscosity function very quickly and therefore is

also unsuitable. Thus, a compromise was reached by using a value of 'a'= 1. We now consider the results obtained for a thixotropic fluid using this 'a' value for the case of non zero and shear-free vorticity boundary conditions.

When non-zero vorticity values are specified on the walls of the cavity, the resulting steady solution at Re= 10^4 consists of two symmetric 'bean' shaped mirror image counter rotating cells, with a corresponding temperature profile revealing cold fluid descending in the cavity's middle while warmer fluid rises near the walls. The result is almost identical to that of a Newtonian fluid shown in fig (7.14) for the same configuration. At a higher Rayleigh number of 10^5, the largest obtainable by us, the corresponding solution, shown in figs(7.63) and (7.64) respectively, can be seen to be a mirror image solution of the unusual result generated by a pseudoplastic fluid shown earlier in fig(7.22). The result possesses the same features but the flow patterns are reversed.

When the vorticity boundary conditions are relaxed to those of the shear-free variety, the initial solution consists of two rectangular symmetric and counter rotating cells each of which fill half of the cavity identical to that of a Newtonian fluid with this configuration shown in fig(7.14). However, at 5 seconds of simulation time these cells are seen to possess a more bean

shaped structure, which finally at time of 10 seconds degenerates to a final steady solution comprising of three vortices as shown in fig(7.65), similar to that produced by an viscoelastic pseudoplastic fluid discussed earlier. The central clockwise rotating vortex is elongated and lies on the main leading diagonal of the cavity. The two counter rotating vortices are located near the top and bottom corners of the cavity lying on the opposite negative diagonal (y=-x). The corresponding complex temperature profile shown in fig(7.66) also reflects the three cell structure indicating the movement of the various hot and cold sections of the fluid carried around the cavity by the convection current. Upon increasing the Rayleigh number once again to 10^5, no significant change was observed from that of pseudoplastic fluid with this configuration shown in fig(7.26).

By using the exact opposite viscosity values for a thixotropic fluid in equation(6.6) the relatively rare phenomenon of rheopexy can be simulated in the Rayleigh-Benard problem. With non-zero vorticity specified on the walls at $Ra=10^4$, the steady solution for a rheopectic fluid consists of two quite weakly counter rotating rounded cells each filling half of the cavity, shown in fig(7.67). The corresponding temperature profile fig(7.68), complements this result showing colder fluid gently cascading down the cavitiy's middle with the reverse occurrence near the

walls. Upon increasing Ra to a maximum of 10^5, the steady solution obtained showed a high degree of similarity with the result generated by a thixotropic fluid at $Ra=10^4$ with shear-free boundary conditions shown in fig(7.65).

When the vorticity is given a value of zero on each of the cavity's wall the results obtained at both $Ra=10^4$ and 10^5 show no new features to those obtained by a dilatant fluid used in the simulation for this particular geometrical configuration shown in fig(7.30) to (7.32), and consequently are not shown.

7.11 PARTICLE PATHS AND MIXING.

In concluding this section a few brief remarks are given concerning the particle path trajectories and mixing efficiency of the Rayleigh-Benard problem.

In most of the cases considered, the motion of a selected initial horizontal line of particles placed in the central portion of the cavity was found to adhere very closely to those of the streamlines of the flow generated for all Rayleigh numbers in the ranges considered. The particles sometimes spiralling into the vortex centres of the two cell configuration for Rayleigh numbers up to $Ra=10^4$, showing the flow to be consistently weaker there.

The mixing efficiency of the Rayleigh-Benard system compared with the other driven standard cavity flows was also

investigated, by numerically solving the concentration equation (4.4), using the same initial conditions for the line of marker dye filling the top half of the cavity as shown in fig(4.4*). The system was found to provide a homogeneous mix for all Rayleigh numbers up to 10^4 (for which Re=1) after, less than 3 seconds of simulation time compared with approximately 11 seconds for the corresponding driven cavity flows discussed in earlier in Chapter 5. A typical concentation plot is shown in fig(7.69) for a Newtonian fluid at a time of 2 seconds for $Re=10^4$ with zero vorticity specified along the boundaries. It shows the marker dye following the convection current, falling in the cavities centre and rising near the cavity's walls, the two counter rotating vortices creating a flow which is perpendicular to the initial configuration of the dye, thus providing an effective mixing process. The type of flow produced is evocative of that produced by a rotating impeller in a cylindrical container of liquid. The two cells initially formed are found to stir the fluid to overall consistency even before as previously mentioned, the two cells may merge into one.

Following closely the initial line of investigation undertaken with standard cavity flow case, it was again thought the aspect ratio of the cavity would play an important part in the mixing process for the Rayleigh-Benard problem. However, upon

subsequent investigation with cavities of aspect ratios between 0.25 and 4, for all fluids considered, it was found to have very little effect, the flow patterns produced being very similar to those obtained for the square cavity.

7.12 SUMMARY.

Within this chapter attention has focused on the novel results obtained by solving the time dependent equations simulating the flow of a broad spectrum of non-Newtonian fluids within the Rayleigh-Benard system. The majority of fluids considered were found to produce steady or unchanging solutions after about 5s of simulation time, the exception being that of a weakly viscoelastic fluid, which exhibits considerable transitory motion.

The two kinds of vorticity boundary conditions used within the simulations, were found to have an important bearing on the stability and outcome of the cell configuration obtained. Firstly, it was noted that the use of the Woods solid wall formula generated cell structures which were more curved in appearance, in fact being almost bean-shaped. This is due to the shear stresses present on the cavity's walls which pull, stretch and twist the fluid giving rise to the curved appearance. The use of the shear-free symmetry boundary condition specifying the

vorticity to be zero on the cavity's walls, consequently produced cells which were more square or rectangular in appearance, due to the absence of wall shear stresses. Higher Rayleigh numbers could be obtained in the case where the vorticity is zero on the cavity's boundaries as opposed to the Woods solid wall formula case, which indicates that non-zero vall vorticity acts as a stabilising influence on the system.

A periodic behavioural occurrence of cell splitting and subsequent re-unification, has been observed for most of the fluids considered as the Rayleigh number is allowed to increase to a maximum of 10^5 or 10^6 in the course of our simulations.

The type of solution obtained was also found to be strongly dependent and sensitive to the initial temperature value used in the numerical solution process, for by letting T(x,y)=0 or T(x,y)= 1-y at the start, it has been found that two sets of mirror image solutions can be obtained. Finally it has been observed that for the majority of non-Newtonian fluids the cell structure gravitates to regions where the fluid is thinnest, which is in line with physical intuition.

The main results of this period of research are summarised in fig (7.71*), for the case of vorticity specified by the shear-free case and fig(7.72*), for the vorticity specified by the Woods formulae.

FLUID	Ra critical $\omega \neq 0$	Ra critical $\omega = 0$
Newtonian	3300	1700
Thixotropic	3300	1700
Rheopectic	1050	450
Pseudoplastic	3200	1400
Dilatant	1000	400
Visco-elastic	3200	1600
Temperature Dependent (k=1)	1900	1050
Depth Dependent (k=1)	3500	1700

Figure (7.70*)

A table of critical Rayleigh numbers, obtained for various fluids using both non zero ($\omega \neq 0$), and shear free ($\omega = 0$) boundary conditions.

NUMBER OF CELLS OBTAINED AT A GIVEN RAYLEIGH NUMBER

FLUID	10E4	10E5	5X10E5	10E6	1.4X10E6
NEWTONIAN	2	2		1	2
PSEUDO-PLASTIC	1	1	2		
DILATANT	2	1	2		
THIXOTROPIC (a=1)	1	1			
RHEOPECTIC (a=1)	1	1			
DEPTH DEPT. K=1	1	2			
K=10	2				
TEMP DEPT. K=1	2	2			
K=5	2	2			
K=10	2				

Figure (7.71*)

NUMBER OF CELLS OBTAINED

AT A GIVEN RAYLEGH NUMBER

FLUID	10E4	10E5
NEWTONIAN	1	2
PSEUDO-PLASTIC	2	2
DILATANT	1	2
THIXOTROPIC (a=1)	2	2
RHEOPECTIC (a=1)	2	2
DEPTH DEPT. K=1	1	2
TEMP DEPT. K=1	1	2

Figure (7.72*)

CHAPTER 8

THE 'LORENZ' EQUATIONS FOR NON-NEWTONIAN FLUIDS.

8.1 INTRODUCTION.

In this chapter we consider a modified version of the much studied and celebrated system of ordinary differential equations(O.D.E's) known as the Lorenz equations. These equations originally arose out of a desire to investigate convective motion known to exist within the atmosphere and allied with this, a desire to investigate the feasibility of long-term weather prediction.

Lorenz[59] however, was very much aware that the atmosphere behaved as a turbulent fluid and its motion governed by a set of coupled partial differential equations, which were non-linear and showed extreme sensitivity to small changes. Lorenz, recognising the fact that the equations showed modes of instability, had the intuitive feeling that these two facts would make weather forecasting over long periods very difficult.

To test this hypothesis, Lorenz sought a way of modelling atmospheric conditions while simplifying the governing mathematical equations without losing their essential non-linearity and instability. He approximated atmospheric conditions by considering a thermally conducting fluid contained within a two dimensional rectangular region, shown later in

fig(8.2*), uniformly heated from below. Based closely on the work of Saltzman[95], Lorenz represented the solution of the stream function, and temperature equations in terms of double Fourier series expansions in space, which only had time dependent coefficients. Upon substituting these expressions into the governing equations and through simplification by retaining the lowest order terms used in the Fourier coefficients, the now famous Lorenz equations were born.

The Lorenz equations are:

$$\dot{X} = -\sigma X + \sigma Y$$

$$\dot{Y} = -XZ + rX - Y \qquad (8.1)$$

$$\dot{Z} = XY - bZ$$

Where the superscripted • denotes differentiation with respect to time, σ is the Prandtl number, b describes the geometry of the rectangular space under consideration and 'r' is proportional to the Rayleigh number. In the system (8.1), X(t) is related to the strength of convection, Y(t) is proportional to the temperature gradient and Z(t) represents the deviation from the linear temperature dependence along the vertical direction. These ordinary differential equations in X,Y,Z describe the dynamics of flow and temperature within the considered rectangle, the result of which can be thought of as an 'ideal' climate.

Lorenz obtained solutions to the system (8.1) by means of numerical integration, and found quite dramatic results. For a certain critical value of 'r', Lorenz discovered that the system generated a peculiarly shaped object which he termed an 'attractor', to which all nearby trajectories were drawn, and yet whilst belonging to this bounded region of space, the trajectories moved in a highly irregular, or chaotic manner.

The attactor has no volume in three dimensional space, and is neither a simple one dimensional line, nor a smooth two dimensional surface, in fact it has a calculated dimension of 2.06 and is therefore known as a 'strange attractor'. The attractor itself shown fig (8.1*) has two separate branches or 'wings' and was the first chaotic attractor of its kind to be studied.

Since then many other chaotic attractors have been discovered in areas of science ranging from biology, ecology and chemistry, to astronomy, electronics and lasers. The most notable of which are Rossler's band and the one-dimensional quadratic maps of May[61].

We now discuss what is generally meant by chaotic motion.

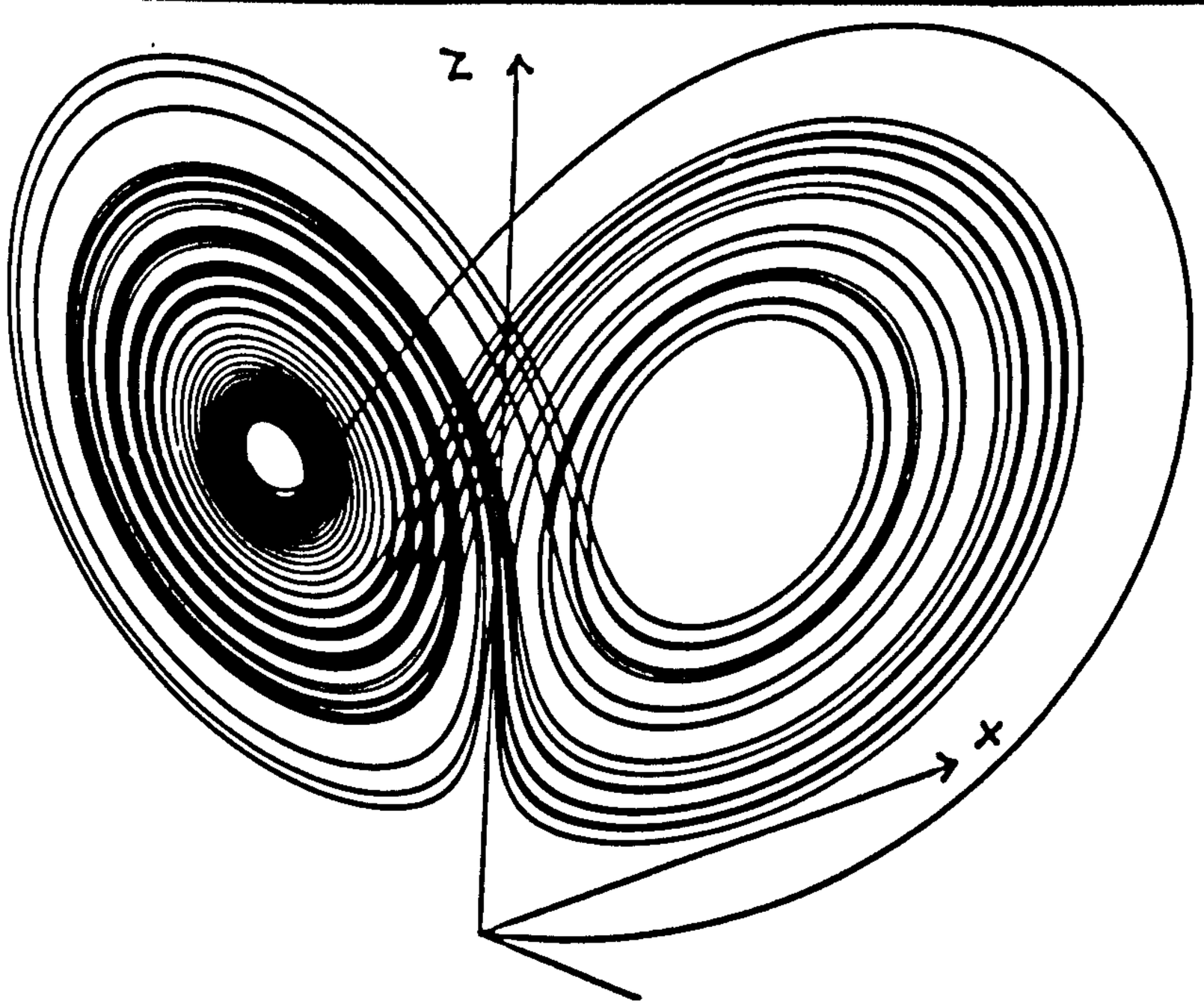

Figure (8.1*)

The Lorenzian chaotic attractor.

8.2 CHAOTIC MOTION.

Since this is a relatively recent area of study, an opportunity arises to summarise the main features of chaotic dynamics.

Consider an autonomous set of ordinary differential equations such as the Lorenz equations (8.1) which model some scientific phenomenon such as convection, then the system can be represented more compactly as:

$$\dot{X}(t) = F_r(X(t)) \qquad (8.2).$$

Here r is an external parameter, proportional to the Rayleigh number in the Lorenz equations, and $X(t)$ the solution of a system represented by (8.2), subject to an initial condition $X(0)=X_0$.

If the position of the initial point is now altered slightly to $\underline{X}(0)+\underline{\delta X}(0)$, then the value of $\underline{X}(t)$ will also change. For most systems of type (8.2) we usually expect a small change in the initial conditions to result in a small change in the solution $\underline{X}(t)$. However, where a system is known to have sensitive dependence on initial conditions this is not the case, in fact for such systems as time increases, the small initial displacement grows exponentially fast according to $\underline{\delta X}(t) = \underline{\delta X}(0)\exp(\lambda t)$, where λ measures the rate of divergence of the respective trajectories. It is this discovery of systems having sensitive dependence on initial conditions which has given rise to the recent emergence of chaos theory, and this can lead to 'unstable' systems, where predictability is not available when the initial conditions are not known exactly.

Sensitive dependence on initial conditions is not a new concept, but was noted near the turn of the century by Poincare and later by Hadamard. However, the phenomenon has only recently been re-discovered and investigated with the help of modern day computers, which enable a step by step solution of the differential equations to be calculated and subsequently plotted.

In this chapter we extend the work of Lorenz, by considering some non-Newtonian fluids, the results of which are shown

in figs(8.6) to (8.12), and find applications to geophysical flow in the Earth's mantle and to mixing.

8.3 A MODIFIED LORENZ SYSTEM OF EQUATIONS FOR NON-NEWTONIAN FLUIDS.

Consider a Rayleigh-Benard experiment as shown in fig(8.2*), where it is assumed that a constant temperature gradient is maintained between top and bottom walls, the side walls are insulated, and gravity acts in the negative y direction.

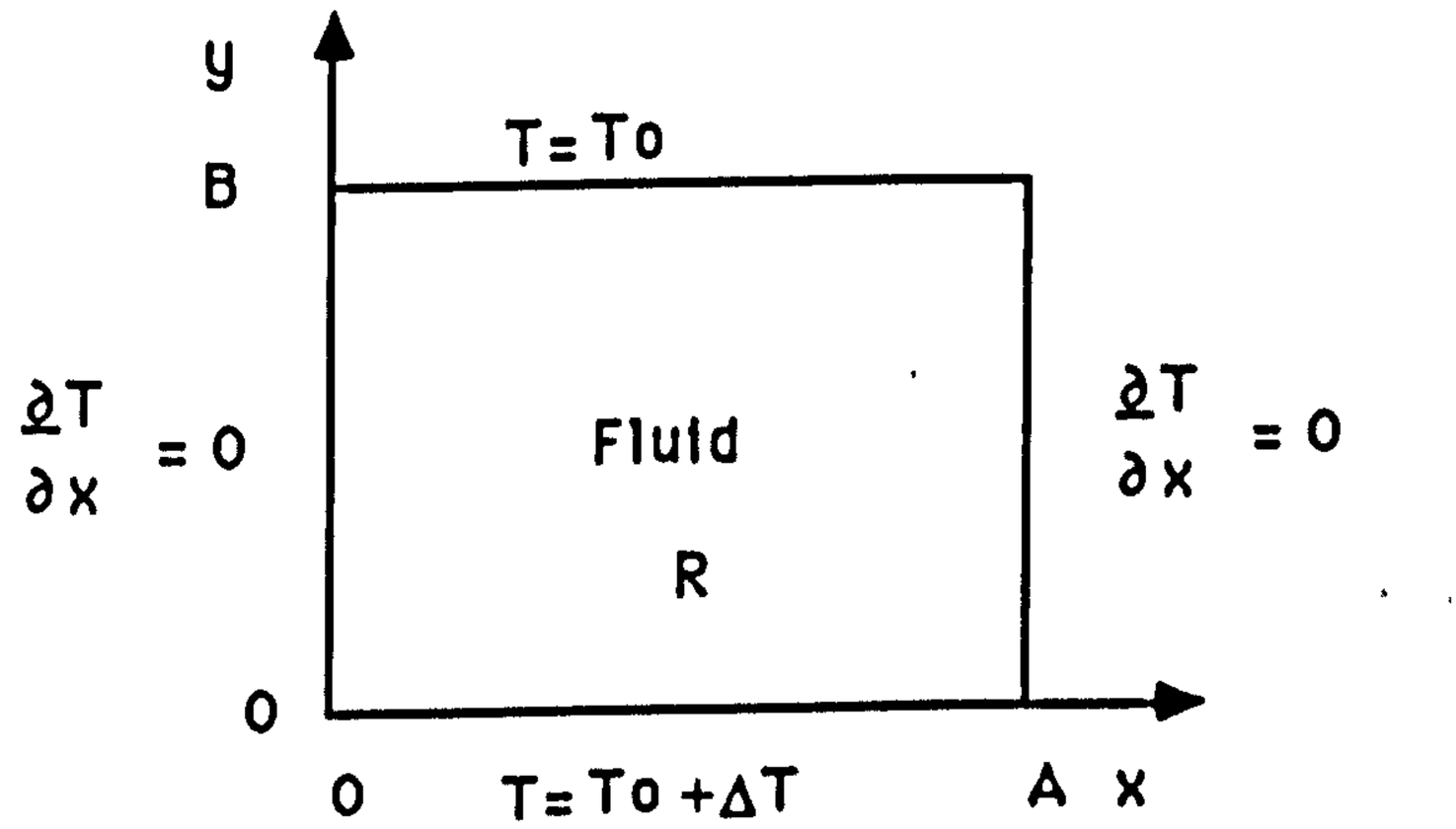

Figure (8.2*)

Diagram showing the prescribed boundary conditions for the simulation.

To simplify things further, it is also assumed the system is translationary invariant in the z direction (into the paper), such that the convection rolls produced extend to infinity.

We also make use of the Boussinesq approximation such that the only significant term having dependence on temperature is the density of the fluid. The ensuing two dimensional motion is described in terms of the velocity $\underline{V}(x,y,t)$ and the temperature field $T(x,y,t)$. The basic mathematical equations used to describe the motion are the temperature equation (6.3) and the Cauchy stress equations(3.1,2) together with the rheological equation of state (3.6) and continuity (3.16) as defined in Chapter 3.

When the temperature gradient is insufficently large to produce convection, heat is conducted through the fluid, and the temperature profile is a linear function of height namely $T_0(y)$.

As a next step we introduce a deviation $\theta(x,y,t)$ away from the linear profile by writing:

$$T(x,y,t) = T_0(y) + \theta(x,y,t) \qquad (8.3),$$

then on substituting this expression into the temperature equation (6.3), we obtain:

$$\frac{\partial\theta}{\partial t} - \frac{\partial\Psi}{\partial y}\frac{\partial\theta}{\partial x} + \frac{\partial\Psi}{\partial x}\frac{\partial\theta}{\partial y} - \frac{\Delta T}{B}\frac{\partial\Psi}{\partial X} = \frac{1}{Pr}\left(\frac{\partial^2\theta}{\partial x^2} + \frac{\partial^2\theta}{\partial y^2}\right) \qquad (8.4).$$

Where $u= -\partial\Psi/\partial x$ and $v= \partial\Psi/\partial y$ and for simplicity we make the symmetry boundary conditions for θ to be:

$$\theta(x,0,t) = \theta(x,B,t)=0 \qquad (8.5)$$

$$\frac{\partial\theta(0,y,t)}{\partial x} = \frac{\partial\theta(A,y,t)}{\partial x}=0 \qquad (8.6)$$

with A and B are shown in fig (8.2*).

The equations describing the fluids motion within the rectangle are:

$$\eta\frac{\partial\omega}{\partial t} = \frac{\partial}{\partial x}(\eta^2\frac{\partial\omega}{\partial x}) + \frac{\partial}{\partial y}(\eta^2\frac{\partial\omega}{\partial y}) - \eta(\frac{\partial\Psi}{\partial y}\frac{\partial\omega}{\partial x} - \frac{\partial\Psi}{\partial x}\frac{\partial\omega}{\partial y}) + 4\eta\frac{\partial^2\eta}{\partial y\partial x}\frac{\partial^2\Psi}{\partial y\partial x}$$

$$+ \eta(\frac{\partial^2\Psi}{\partial y^2} - \frac{\partial^2\Psi}{\partial x^2}).(\frac{\partial^2\eta}{\partial y^2} - \frac{\partial^2\eta}{\partial x^2}) + \gamma g\frac{\partial\theta}{\partial x} \qquad (8.7)$$

$$\omega = \frac{\partial^2\Psi}{\partial x^2} + \frac{\partial^2\Psi}{\partial y^2} \qquad (8.8)$$

$$\rho(T) = \rho_0(1 - \gamma(\theta)). \qquad (8.9)$$

For simplicity like Lorenz[59], we choose shear-free vorticity boundary conditions making $\omega=0$ on all four of the cavity's walls. Following Lorenz we now assume that the linear perturbations of the stable solutions of equations (8.4), (8.7) and (8.8) admit solutions in terms of a double Fourier series expansions, the first relevant terms of which are given by:

$$\Psi(x,y,t) = hX(t)\sin(\alpha x)\sin(\beta y) \qquad (8.10)$$

$$\theta(x,y,t) = \sqrt{2}fY(t)\cos(\alpha x)\sin(\beta y) - fZ(t)\sin(2\beta y) \qquad (8.11)$$

where h and f are non-dimensional constants, and $\alpha A = \beta B = \pi$.

Substituting these expressions into the equations (8.4), (8.7) and (8.8), neglecting the viscosity derivatives and any X^2, Y^2 or Z^2 terms, which are taken to be of secondary importance when compared with the size of the disturbances, the peturbed modified system of Lorenz equations for a non-Newtonian fluid are produced.

The modified system of equations is:

$$\begin{aligned} \dot{X} &= -\sigma\eta(q,T,t)X + \sigma Y \\ \dot{Y} &= -XZ + rX - Y \qquad (8.12). \\ \dot{Z} &= XY - bZ \end{aligned}$$

The major difference between (8.1) and (8.12) the introduction of a non-constant viscosity term in the X equation describing the fluids circulatory motion, which increases the non-linearity of the equations. We will now investigate the effect this has on the system by considering some simple models describing the influence of the non-constant viscosity term.

8.3.1 SHEAR-THINNING FLUID.

In order to simulate this phenomenon we make use of the Cross model discussed earlier in Chapter 3 and re-stated here for convenience.

$$\eta(q)= \eta(\infty) +(\eta(0) - \eta(\infty))/(1+\sqrt{q}) \qquad (8.13)$$

where $\eta(0)$ and $\eta(\infty)$ are the zero and infinite shear rates respectively, and the shear-rate q is given by the expression

$$q^2=(\Psi_{yy} - \Psi_{xx})^2 + 4(\Psi_{xy})^2 \qquad (8.14).$$

The subscripts denote second order partial derivatives with respect to x and y. Substituting (8.10) into (8.13) and taking the modulus for greatest shear effect yields

$$|q|=|\alpha^2+\beta^2|\,|h|\,|X(t)| \qquad (8.15).$$

Expression (8.15) is then substituted for q in (8.13) and if we assume $\eta(\infty) \approx 0$ and $\eta(0) = 1$, then the shear-thinning behaviour may be approximated by

$$\eta_c(q)=1/(1+p\sqrt{|X|}) \qquad (8.16)$$

where 'p' is a constant, typically of order 0.1 in this work.

The modified $\dot{X}$ component equation of (8.12) then becomes

$$\dot{X}(t) = -(\sigma X/(1+p\sqrt{|X|})) + \sigma Y \qquad (8.17).$$

The $\dot{Y}(t)$ and $\dot{Z}(t)$ equations are the same as those in the original Lorenz system shown in (8.1) and remain unaltered for all cases considered.

8.3.2 SHEAR-THICKENING FLUID.

To describe this type of fluid behaviour, we again make use of the Cross model, taking $\eta(0) = 1$ and $\eta(\infty) = 2$ for best effect. This together with our approximation for the shear-rate produces:

$$\eta_c(q) = (1 + 2p\sqrt{|X|}) / (1 + p\sqrt{|X|}) \qquad (8.18)$$

and therefore the $\dot{X}$ component equation of (8.12) becomes:

$$\dot{X}(t) = -(\sigma X\,(1 + 2p\sqrt{|X|}) / (1 + p\sqrt{|X|})) + \sigma Y \qquad (8.19)$$

8.3.3 THIXOTROPY.

In seeking to describe the phenomenon of a fluid decreasing its viscosity with time at a constant (equilibrium) shear-rate, we consider a model based closely on the work of Kemblowski and Petera[52]. The idealised model we use is:

$$\eta(q,t) = \eta_c(q) + (\eta(0) - \eta_c(q))e^{-at} \qquad (8.20)$$

where 'a' is a constant of the fluid considered, typically of order 5×10^{-3} in value. This model has the property that initially, at zero time and shear-rate, the fluids viscosity is that of a

Newtonian fluid, and then as both time and deformation rate become very large, the fluid due to structural breakdown, obtains the infinite shear viscosity specified by the Cross model, and so realistically models the behaviour of a thixotropic fluid for simulation purposes. Using our approximation for shear-thinning behaviour gives:

$$\eta(q,t) = ((1- e^{-at})/(1+p\sqrt{|X|})) + e^{-at} \qquad (8.21),$$

and finally substituting (8.21) into the $\dot{X}$ component of (8.12) produces:

$$\dot{X} = -(\sigma X(1- e^{-at})/(1+p\sqrt{|X|})) - \sigma X\, e^{-at} + \sigma Y \qquad (8.22).$$

8.3.4 RHEOPEXY (NEGATIVE-THIXOTROPY).

To mimic this behaviour we use expression (8.20) together with our viscosity model for shear-thickening fluid (8.18). This model possesses features which are the exact reverse of the previously discussed thixotropic model. Initially at zero time and shear rate, we assume the fluid is Newtonian and then as both time and deformation rate become large the fluid becomes thicker, almost obtaining a viscosity value twice that of a Newtonian fluid. Using this model we derive the $\dot{X}$ component of system (8.12) to be:

$$\dot{X}(t)= -\sigma X\,((1+2p\sqrt{|X|})(1-e^{-at})\,/(1+p\sqrt{|X|})) - \sigma X e^{-at} + \sigma Y \qquad (8.23).$$

8.3.5 TEMPERATURE DEPENDENCE ON VISCOSITY.

There are many models available which seek to describe the change in a fluid's viscosity due to an increase or decrease in temperature (T), for simplicity we choose to use the Reynolds' formula which is defined as :

$$\eta(T) = \eta_0 e^{-CT} \qquad (8.24).$$

Where T is represented by expression (8.3) and C is constant of the fluid known as the thermal conductivity which for air has a typical value of 10^{-2}. From (8.3) we see θ is variable over the region (R) considered in fig (8.2*), consequently so is $\eta(T)$. It therefore seems appropriate to take the mean value of $\eta(T)$ over the rectangle, in so doing we obtain,

$$\overline{\eta} = \eta_0 A^{-1} B^{-1} \iint_R \exp(-CTo(y)).\exp(-C\theta)\, dR. \qquad (8.25)$$

We assume $|C\theta|<1$ so that $\exp(-C\theta)\approx 1-C\theta$, $To(y)=(1-y/B)\Delta T$ and completing the necessary integration we obtain:

$$\overline{\eta} = \eta_0(1-e^{-C\Delta T})(C\,\Delta T)^{-1}(1-\xi Z(t)) \qquad (8.26),$$

and after some manipulation, the $\dot{X}$ component equation of the system (8.12) becomes:

$$\dot{X}(t) = -\sigma_1 X(1-\xi Z) + \sigma Y \qquad (8.27)$$

Where ξ is constant, typically of order 10^{-5}, and $\sigma_1 \approx \sigma$.

8.3.6 WEAKLY ELASTIC FLUID.

To obtain the modified Lorenz system for a weakly elastic liquid we need to use the Cauchy stress equation of motion as defined in Chapter 3, which written in tensor notation is :

$$\frac{\partial P_{kl}}{\partial x_k} + \rho F_l = \rho \frac{Dv_l}{Dt} \qquad (8.28)$$

where

$$P_{kl} = -P\delta_{kl} + T_{kl} \qquad (8.29)$$

and where we take the extra stress component (T_{kl}) for a weakly elastic fluid to be:

$$T_{kl} = 2\eta_o \left(\eta(q,T,t)\, e_{kl} - \lambda \overset{\nabla}{e}_{kl} \right) \qquad (8.30)$$

and following Bodalia[16] we take $\lambda \approx 10^{-4}$.

Retaining only first order linear terms, we approximate $\overset{\nabla}{e}_{kl}$ by:

$$\overset{\bullet}{e}_{kl} \approx \frac{\partial e_{kl}}{\partial t} \qquad (8.31)$$

Finally upon substituting these expressions into (8.28), using the Fourier series representations for Ψ and θ, and non-dimensionalising time by writing $t'=jt$ we obtain the $\dot{X}$ component of the system to be:

$$\dot{X}(t) = - (\sigma X \eta(q,T,t)/(1-\sigma j\lambda)) + \sigma Y/(1-\sigma j\lambda) \qquad (8.32).$$

The product $\sigma j\lambda$ is very small such that $1-\sigma j\lambda \approx 1$, so equation (8.32) is basically the Newtonian equivalent when η is constant.

8.3.7 NUMERICAL SOLUTION OF THE NON-NEWTONIAN LORENZ EQUATIONS.

The coupled non-Newtonian Lorenz equations are highly non-linear and consequently do not possess any analytic solution, and so to obtain a solution numerical techniques are employed. Fortunately a number of computer aided packages are available which provide a numerical solution using a variety of Runge-Kutta methods. One such package we have used in order to provide the graphical solutions shown in figures (8.6) to (8.12), is Phaser [86]. These results were obtained by using a variety of time steps, all of which produced similar results which gave credence to the final solutions obtained.

8.4 STABILITY ANALYSIS OF THE NON-NEWTONIAN LORENZ SYSTEM.

The modified Lorenz system for non-Newtonian fluids is shown in (8.33), where η represents the variable viscosity function.

$$\begin{aligned} \dot{X} &= -\sigma\eta X + \sigma Y \\ \dot{Y} &= -XZ + rX - Y \\ \dot{Z} &= XY - bZ \end{aligned} \tag{8.33}$$

The stability of this system is dependent upon the external control parameter r, which is proportional to the Rayleigh number. For low values of r, which represent low thermal driving, high viscous damping and therefore high thermal conductivity, we would expect the rest state solution (0,0,0) to be a stable equilibrium point. To see if our system correctly models this behaviour we investigate the stability matrix of system (8.33) at the origin. Writing system (8.33) more compactly as $\dot{\underline{X}}(t)=E_r(\underline{X}(t))$ we define the stability matrix S as the Jacobian:

$$S = \frac{\partial E_r^{\,i}(\underline{X})}{\partial X^j} \quad \text{for } i,j=1,2,3.$$

The system's stability being given by the nature and sign of the eigenvalues S produces. For (8.33) upon neglecting terms involving the viscosity derivatives which can be shown to be quite small, the stability matrix S becomes:

$$S = \begin{bmatrix} -\sigma\eta & \sigma & 0 \\ r-Z & -1 & -X \\ Y & X & -b \end{bmatrix} \qquad (8.34)$$

At the origin the eigenvalues λ_i i=1,2,3, generated by S are:-

$$\lambda_1 = -b, \quad \lambda_{2,3} = 0.5\,(-(\sigma\eta+1) \pm \sqrt{((\sigma\eta+1)^2 - 4(\sigma\eta-r\sigma))}) \qquad (8.35).$$

From this it can be seen that all the eigenvalues are negative, and the origin is a stable equilibrium point, provided $r < \eta$, i.e the thermal driving is insufficient to overcome the viscous damping. As r increases the equilibrium point at the origin should lose stability as the influx of heat produces a convective roll, which occurs as the buoyancy of the rising warm fluid overcomes the inertia forces.

When $r = \eta$ at the origin, the eigenvalues of S become:

$$\lambda_1 = -b, \lambda_2 = 0, \lambda_3 = -(\sigma\eta+1) \qquad (8.36)$$

from which it can be seen that not all the eigenvalues are negative, hence the origin is now marginally stable. In fact at $r = \eta$ a bifurcation occurs, the origin changing in nature from a stable attracting point to a unstable saddle point. Some feeling for this may be obtained by reducing system (8.33) to a two dimensional equivalent, by assuming $Z=\dot{Z}=0$, and constructing a corresponding phase diagram.

For values of $r > \eta$, two other equilibrium points occur which have non-zero real solutions. These may be found by equating $\dot{X}=\dot{Y}=\dot{Z}=0$ in system (8.33). The resulting equilibrium points are:-

$$X = \pm\sqrt{(b(r-\eta)/\eta)} = \pm\gamma$$

$$Y = \pm\sqrt{(b\eta\,(r-\eta))} = \pm\delta \qquad (8.37)$$

$$Z = r - \eta = \varepsilon$$

These new equilibrium points emerge from (0,0,0) as r passes through the critical value $r=\eta$. They are equidistant from origin and mirror images of each other as shown in fig (8.3*).

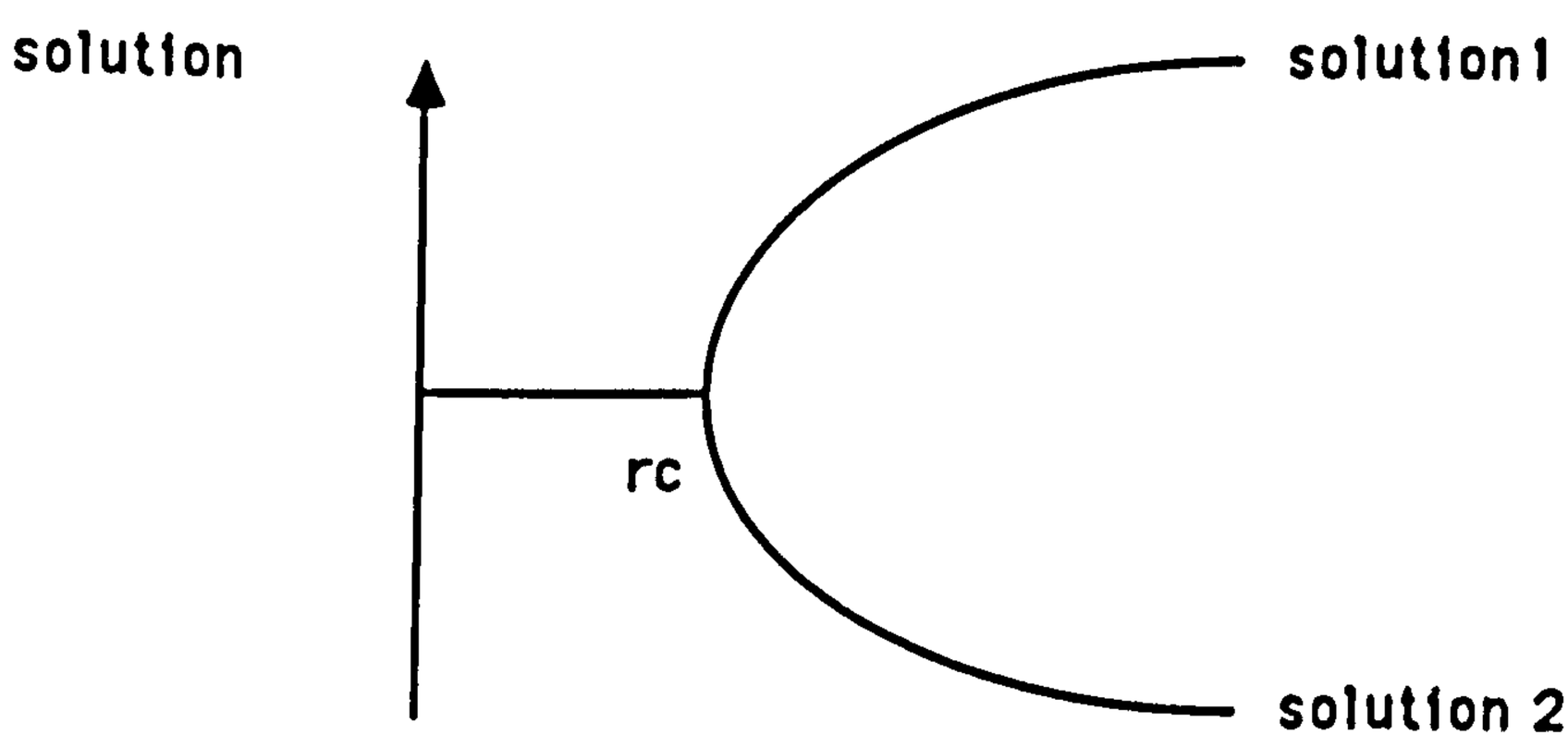

Figure (8.3*)

Diagram illustrating the bifurcation phenomenon.

As the rest state is now no longer stable, the system's dynamics tend to eventually settle down to one or the other of these new fixed points. The stability matrix of the system at $(+\gamma,+\delta,\varepsilon)$ is:

$$S = \begin{bmatrix} -\sigma\eta & \sigma & 0 \\ r-\varepsilon & -1 & -\gamma \\ \delta & \gamma & -b \end{bmatrix} \qquad (8.38)$$

The eigenvalues of S can be found from the characteristic equation:

$$\lambda^3 + (\sigma\eta + b + 1)\lambda^2 + b(\sigma\eta + \sigma)\lambda + 2b\sigma(r-\eta) = 0 \qquad (8.39).$$

We note that when $\eta=1$ we obtain the characteristic equation for a Newtonian fluid.

From experimental evidence the system is known to have a critical value for r (r_c), at which it becomes unstable. Following Lorenz[59], we assume that at the critical value of r the system undergoes a Hopf bifurcation and at this value the eigenvalues of (8.39) become purely complex. Then an approximation for r_c is

$$r_c = \frac{\sigma\eta^2(\sigma\eta+b+3)}{(\sigma\eta-1-b)} \qquad (8.40)$$

and in evaluating r_c an upper bound is imposed on the viscosity function η.

It was found by Lorenz for a Newtonian fluid only, and subsequently by us that at this value of r the trajectories become chaotic.

From our numerical simulations carried out using the Z-X plane, we have found that there exists a range of 'r' values between r=η and r_c, such that a particle initially located near the origin will be attracted to one of the new equilibrium points P_1 or P_2, shown later in fig(8.4*), in the form of a stable spiral. As r's value is gradually increased, a limit cycle is seen to emerge around the same point, and eventually at higher increments of r, the trajectory's motion around that particular equilibrium point is seen to resemble that of an unstable spiral, which takes the particle to the other mirror image equilibrium point, where a similar sequence of events is observed to occur. The chaotic motion however is only seen to occur at $r=r_c$, due to the increased thermal driving causing a greater degree of instability. The system now possesses three unstable equilibrium points, a saddle at the origin and following a trajectory near the other two points shows the presence of unstable spiral structures.

Since none of the equilibrium points are attracting, the system's final behaviour cannot be steady motion. The trajectories themselves tend to occupy a finite region of the state space enclosing all three fixed equilibrium points, and is such that no

trajectory leaves the region and all nearby trajectories are attracted to it. While within the bounds of the attractor the trajectories motion is highly erratic and unpredictable, due to initially close trajectories diverging at an exponentially rate.

Our modified version of the Lorenz equations (8.33) like its parent system is dissipative, that is, non-volume preserving, for

$$\frac{\partial \dot{X}}{\partial x} + \frac{\partial \dot{Y}}{\partial y} + \frac{\partial \dot{Z}}{\partial z} = -(\sigma\eta + b + 1) \tag{8.41}$$

and from Liouville's theorem:

$$\frac{dV(t)}{dt} = -(\sigma\eta + 1 + b)V(t) \tag{8.42}$$

$$V(t) = V_0 \exp(-\sigma\eta - 1 - b)t \tag{8.43}$$

$$\lim_{t \longrightarrow \infty} V(t) = 0 \tag{8.44}$$

where V(t) represents a fluid volume element at time t and V_0 being the initial volume at time zero.

As the system is dissipative, all ensembles will constantly decrease in volume with time, and as Lorenz[59] himself originally discovered this need not imply that the ensembles shrink to a point, but they may approach a surface or a set having zero volume, e.g a line. In passing we mention that a stability analysis accounting for time dependent thixotropic/rheopectic fluids has also been undertaken using a 4 X 4 Jacobian matrix and

was found to give similar results to the above but with the inclusion of an extra eigenvalue which has a value of zero.

8.5 MOTION ON THE ATTRACTOR.

In this section we investigate how the localised motions around each equilibrium point fit together to form the strange attractor.

Consider a point near the origin in the Z-X plane. When $r > r_c$ the trajectory will move away from the origin (P_o) as it is an unstable saddle and will initially move in the form of an arc around point P_1 shown in fig(8.4*).

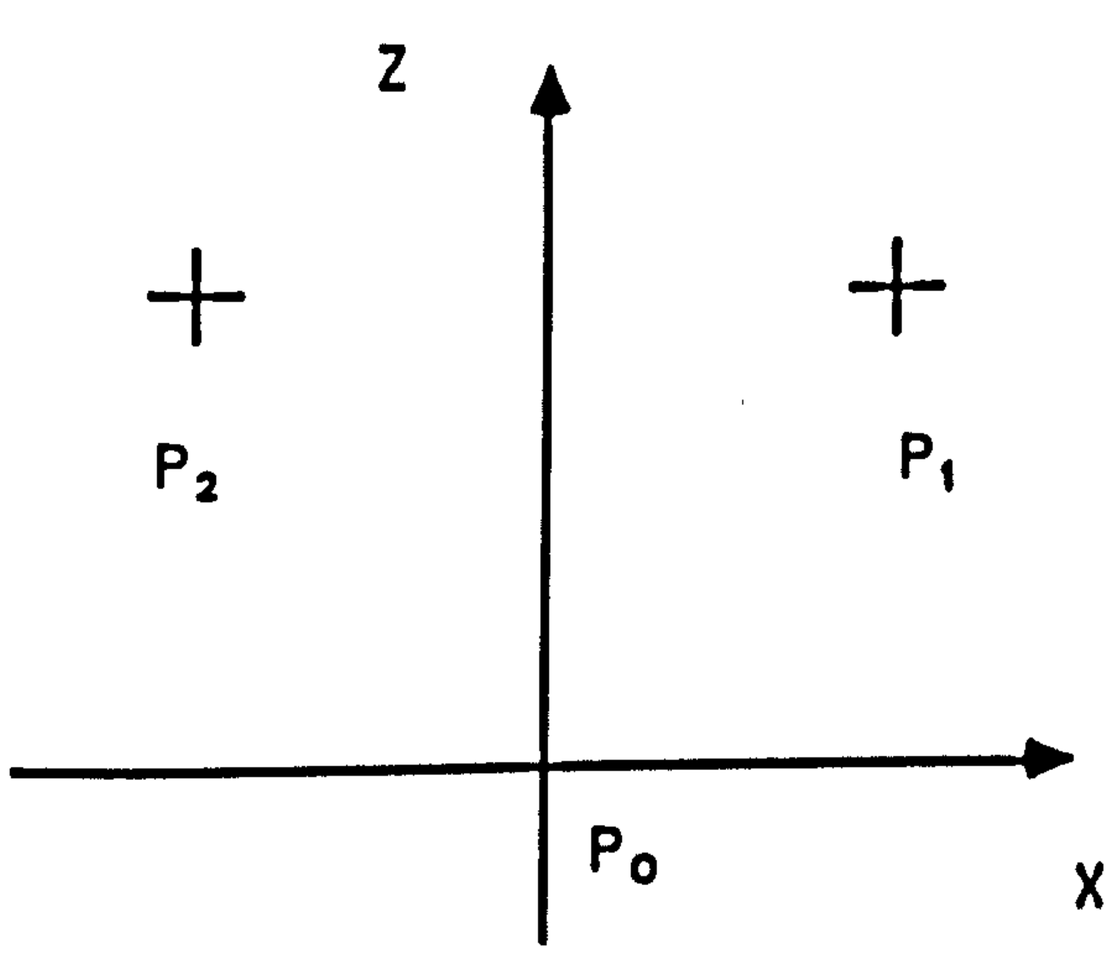

Figure (8.4*)

The motion continues around P_1 until it reaches the Z axis which is half way between points P_1 and P_2. Once it has crossed the Z axis the trajectories motion comes under the influence of P_2. The trajectory is seen to wind itself around P_2 in the form of a gradually increasing or unstable spiral, until its value is large enough to cross the Z axis where the resulting motion is determined by P_1. The trajectory now begins to wind itself around P_1 as an unstable spiral, yet at this point the motion becomes very difficult to predict. The number of turns around each equilibrium point is not fixed, nor does it settle down into any pattern, the motion is deterministic and yet chaotic. The final result is a stange attractor of the type shown previously in fig (8.1*). This basic motion has also been found to underlie all the non-Newtonian fluids which we have attempted to model. Further detailed discussion of the motion on the similar Lorenzian attractor may be found in Thomson and Stewart[105].

8.5.1 TABLE OF r_c VALUES.

Shown in fig (8.5*) is a table of the critical r values, at which point the various non-Newtonian fluid systems begin to exhibit chaotic motion. The values shown are partly derived from theory, and partly due to observation from the numerical simulations.

FLUID	rc VALUE	PARAMETER VALUES
Newtonian	24.76	
Shear-thinning	18.12	
Shear-thickening	35.67	
Thixotropic	18.12	a=0.05
Rheopectic	35.67	a=0.01 or a=0.05
Weakly-elastic	24.76	σj= 0.0367, λ= 0.0001
Temperature	25.0	ξ = 0.000025 C=0.01

Figure (8.5*)

The critical Rayleigh numbers used in the simulations.

8.6 RESULTS AND CONCLUSIONS.

The Rayleigh-Benard experiment is a system which exhibits particularly rich chaotic behaviour. The original Lorenz[59] equations and our own modifications to the Lorenz system to incorporate features of certain non-Newtonian fluids, only realistically describe the motion in the immediate vicinity of the transition from heat conduction to convection. This is due to the fact that we only recognise three spatial Fourier coefficients which only model simple rolls, to describe the motion fully and at

higher Rayligh numbers, more Fourier coefficients need to be considered, but the equations obtained would still require numerical solution.

Many routes to chaos have been discovered by various researchers for the Rayleigh-Benard experiment, Pommeau and Mannerville[87] having found an intermittency route, while others support a Feigenbaum period doubling route. However, in our analysis we restrict ourselves to the Ruelle, Takens and Newhouse[94] route to chaos, that of bifurcations leading to a strange attractor.

All modifications to the Lorenzian system which we have considered have been found to exhibit a critical value of r (r_c)for which chaotic motion is seen to occur. The result being a curious object known as a strange attractor, occupying a finite bounded region of state space, to which all trajectories are drawn and remain within for all subsequent time, and yet while on the attractor all 'nearby' trajectories separate at an exponential rate.

The highly irregular and unpredictable motion of a trajectory contained within the attractor is not primarily due to any external sources, such as noise or the system having infinite degrees of freedom, for we recognise only three. The main reason why the system behaves in an erratic manner at the critical value of r is due to the equations themselves.

The deterministic equations describing the motion are highly non-linear and are very sensitive to small changes in the initial conditions.

The system does show a bifurcation route to chaotic behaviour, gradually changing from a stable to an unstable system, for various values of r the governing external parameter of the system. All the strange attractors produced for the various non-Newtonian fluids discussed earlier are shown in figs (8.6) to (8.12), and possess a form which is similar in shape to the Lorenz attractor fig(8.7), having two branches resembling a pair of 'butterfly wings'. The 'size' of the attractor produced for each type of fluid considered is also found to be directly proportional to the 'size' of the Rayleigh number. For thinner fluids the critical Rayleigh number is less than that for a Newtonian fluid, due to less viscous opposition and consequently the attractor produced shown in fig(8.6) is smaller in 'size' than its Newtonian counterpart, fig(8.7). Likewise the reverse effect can be evidenced when considering the simulation of a shear-thickening fluid fig(8.8) with a larger attractor being produced. The variation in the inclination of each attractors 'wings' was also found to be dependent on the type of fluid used, which in turn is affected by the critical Rayleigh number.

For thicker fluids the angle of inclination is found to be quite acute, which is found to gradually increase as thinner fluids are considered.

The results obtained for both thixotropic and rheopectic fluids were found to be heavily reliant on the exponential (e^{-at}) term in equations (8.22) and (8.23) respectively. Realistically 'a' has a measured value of 5×10^{-3} for a thixotropic drilling mud, however in a manner similar to the results discussed in Chapter 7, employing this value means running the computer program used to solve the equations, for a substantial amount of time before any effects of thixotropy or rheopexy are produced. Likewise by increasing a's value to 1 very little effect is observed on the system due to the time dependent nature of the fluid. Thus a compromise is reached by using a value of a=0.01 or 0.05.

For a thixotropic fluid, at r=18.12 (the critical value for a pseudoplastic fluid) the trajectory of a particle placed near the origin is initially damped out, forming a stable spiral structure around eqilibrium point P_2 in fig (8.4*). This is due to the fact that initially the fluid adopts the viscosity of a Newtonian fluid, thus by choosing an r value less than the critical value for a constant viscosity fluid (r_c=25), there is insufficient thermal driving to produce convective rolls and the viscous forces dominate, hence the damping effect.

However, as time progresses the exponential term in the governing $\dot{X}$ equation (8.22), diminishes and the fluid becomes more shear-thinning in nature. At this point the trajectories motion around P_2, takes the form of an unstable spiral which eventually becomes chaotic, producing an attractor similar to that of a pseudoplastic fluid and can be seen in fig(8.9). At higher values of r, r=25 for example, the particle trajectories were initially found to resemble those obtained by a Newtonian fluid. However, as time evolves the attractor diminishes in size with a gradual increase in wing separation similar to that obtained by a pseudoplastic fluid, the resulting attractor shown in fig(8.10).

For a rheopectic fluid the results were found to depend more strongly on the chosen value for 'a' in the exponential terms of of equation (8.23). As with the afore mentioned thixotropic case to realistically observe the time dependent effects on a relatively short time scale we chose to use a compromised value of a=0.01 or 0.05, both of which produced similar results shown in fig(8.11) and fig(8.12) respectively.

Taking $r > r_c$ of a dilatant fluid (r=36), we initially found that the trajectory's motion tended to damp out to a point as the fluid gradually increases in viscosity from that of a Newtonian fluid at t=0. For the case where a=0.01, the initial damping motion takes the particle away from the eventual chaotic attractor,

temporarily residing at a fixed point, then gradually as time progresses the trajectory may be seen to back-track on itself in the form of a straight line until it arrives at one of the fixed equilibrium points, P_1 in fig(8.4*). As time evolves further the motion around this fixed equilibrium point takes the form of an unstable spiral which eventually becomes chaotic producing an attractor similar to that of a dilatant fluid, with the wing separation being more acute. As "a's" value is increased to 0.05, a similar sequence of events is observed to occur with the exception that the inital damping motion takes the fluid particle almost immediately to the fixed equilibrium point P_1, which gradually becomes unstable exhibiting chaotic motion as time progresses.

The strange attractors produced for both temperature dependent and weakly viscoelastic fluids, showed very little difference to that of a Newtonian fluid fig(8.7), which from analysing the equations used to model the phenomena, was as expected.

Lorenz's original results showed the difficulty and unpredictability of long term weather prediction, our results for certain non-Newtonian fluids tend to show similar trends, and find applications in the field of mixing as well as to the turbulent convective motion of thermally conducting fluids thought to exist

within the Earth's mantle and stellar objects, the luminocity of which is also determined by convective mixing.

8.7 SUMMARY.

Within this chapter we have developed the work of Lorenz[59], and have derived a simplified system of three non-linear coupled ODE's, which model thermal convection and the associated mixing processes for a wide variety of non-Newtonian fluids. The fluids used in the simulation exhibit properties ranging from pseudoplasticity to those whose viscosity is strongly temperature dependent. In addition to this we have also investigated the convective motion of a weakly viscoelastic fluid, which has direct relevance to simulating the flow probably occurring within the Earth's mantle.

The main difference in the derivation of our equations from those of Lorenz[59], is the inclusion of a variable viscosity term, which we have allowed to be a function of shear-rate, temperature and time, and appears in the first term of the $\dot{X}(t)$ component equation, which significantly increases the non-linearity of the equations. Consequently these equations do not possess an analytic solution, and were therefore solved by numerical techniques.

The results obtained for all the fluids considered showed no really new variations in the route to chaos, but show bifurcation phenomena evolving to a strange attractor of the Lorenzian variety. However, significant alterations in the size of the attractor and the inclination of its 'wings' were seen to be produced as different fluids were used in the simulations, which also depend on the particular critical Rayleigh number of that fluid.

CHAPTER 9

SUMMARY, CONCLUSIONS AND RECOMMENDATIONS FOR FUTURE WORK.

9.1 INTRODUCTION.

The theoretical research work presented within this thesis has focused upon the numerical simulation of two particular types of fluid flow produced within the confines of a two dimensional impermeable, rectangular or square cavity.

These are:-

(i) Cavity flows generated by uniformly 'driven' wall motions.

(ii) Cavity flows induced from buoyancy effects due to the constant uniform heating of the underside of the cavity.

In addition to this, and allied closely with the flows generated in (ii), we have developed the pioneering work of Lorenz[59] to investigate the chaotic convective motion for a broad spectrum of non-Newtonian fluids.

Novel results have been produced for a wide variety of fluids which incorporate features of both Newtonian and non-Newtonian flow, the distinctive characteristics of each have been noted, together with the efficiency of the mixing process derived from it for a selected range of parameter values.

9.2 WALL DRIVEN CAVITY FLOW.

As a useful starting point for the commencement of our research program, the standard test case of driven cavity flow was considered, whereby the flow generated as a result of a plate uniformly driven over a two dimensional cavity is analysed. The idealised flow patterns obtained are similar to those produced by fluid flowing over a deep hole, and can also be used as an approximation to the mixing patterns produced by a multiple flight extruder screw, a widely used industrial mixer.

This initial problem provided the necessary familiarity in deriving the governing flow equations, and also enabled the computer algorithms developed to produce an approximate numerical solution to these equations, using finite difference methods, to be rigorously tested. At first, only steady state solutions were obtained, with results generated using a Newtonian fluid only, for Reynolds' numbers in the range of 1 to 400. These results on comparison with other workers such as Pan and Acrivos[83], Bozemann and Dalton[17] and Cliffe et al[26], were found to be in very favourable accord. Recently, Havard[44] has analysed the flow obtained for a variable viscosity shear-thinning fluid within this framework, using the finite element method. We too have considered this case and our results for Reynolds' numbers up to 130 were found to be in good

agreement with those produced by Havard[44]. This work was subsequently extended to analyse the flow produced by a dilatant or shear-thickening fluid, with novel results being obtained for Reynolds' numbers up to 300, (as in all cases) the latter number being the largest obtainable on a 40x40 noded mesh.

With confidence gained from the validation of our results with those of other research workers, the standard test case was developed to include more realistic features of time dependence. The time dependent flow equations were initially 'solved' using simple explicit calculations and found to settle to give the steady state solutions within 5 seconds of simulation time. However, due to the time derivative being approximated by a forward difference operator the overall accuracy of the solution obtained decreased. This situation was remedied by utilising a version of the A.D.I method developed by Peacemann and Rachford [96]. This method although being considerably more difficult to program, had the advantage not only of increasing the overall accuracy of the solution obtained, but also at moderately low Reynolds' numbers enabled the time step to be significantly raised, thus enabling longer simulation times to be considered.

Using these equations the mixing efficiency of the standard test case could be investigated. This was achieved in two ways, firstly by simulating the dispersive mixing of a band of 'coloured'

fluid 'injected' into the cavity while at rest, and then by solving the time dependent advection/diffusion concentration equation from start up, so that its motion can be analysed. Havard[44] has recently considered a similar yet more unrealistic problem for Newtonian fluid only, by 'injecting' the dye into the cavity only when the steady state flow solution has been obtained, results having been produced for Reynolds' numbers in the range of 1 to 100. Both sets of results show a high degree of similarity within this range.

The work was subsequently further developed to investigate the mixing processes obtained (within this same geometry) for shear-dependent non-Newtonian fluids of the pseudoplastic and dilatant variety, new results again produced for Reynolds' numbers up to 100.

The efficiency of the mixing process has also been viewed from a different perspective by tracking the motion of a selected number of fluid particles strategically 'placed' within the cavity, which was achieved by numerically solving the Hamiltonian structured equations of motion.

During the course of our simulations it became apparent that the nature of the flow near the cavity's corners, where both the shear-rate and vorticity become singular in value, needed to be investigated.

This was made possible by following closely the work of both Moffatt[66] and Gupta et al[42], which was carried out for Newtonian fluids, and it can be seen from the analysis undertaken within this thesis that in the immediate vicinity of the corners even the flow of shear-dependent non-Newtonian fluids can be regarded as Stokesian, the flow being dominated by viscous forces.

Due to a relatively good measure of success with the results obtained for the standard test case, it was decided to try and improve the mixing process for the cavity flow problem by allowing multiple wall motions, either simultaneously or in a discontinuous co-rotational periodic fashion.

These types of flow have been considered mostly on an experimental basis for the cavity geometry by Ottino et al[81] using Newtonian test fluids, with numerical simulations being obtained for low Reynolds' numbers in the case where two parallel wall motions occur simultaneously in the same or opposite directions. We have extended their work to consider flows obtained at much higher Reynolds' numbers in the range 1 to 100 for Newtonian, pseudoplastic and dilatant fluids.

The cavity's aspect ratio was also found to have a significant effect on the solution and mixing process, with novel results being obtained especially for a dilatant fluid at low Reynolds'

numbers. Aref[5] originally considered a periodic discontinuous flow which became known as the 'blinking vortex flow', within the confines of a cylindrical vessel for an inviscid fluid, and used it as an example of an idealised stirring mechanism. Ottino[80] subsequently generated a similar type of flow using the cavity geometry, by allowing periodic discontinuous co-rotational plate motion, and produced experimental results concerned with the deformation of material line elements, again for Newtonian fluids only at low Reynolds' numbers. Both Ottino[80] and a previous study by Khakhar[53] showed this type of flow is capable of generating chaotic mixing. In this thesis we have once again extended their work to consider the mixing obtained at higher Reynolds' numbers for Newtonian and shear-rate based non-Newtonian fluids. The mixing process was viewed, as usual, by analysing particle path trajectories as well as following the dispersive mixing of a band of 'coloured' fluid as it is carried along with the flow. This work was further developed to consider a unique theoretical case whereby all four of the cavity's walls are allowed to move in a discontinuous co-rotational periodic fashion. Novel results have been generated for a variety of fluids for Reynolds' numbers up to 100.

9.3 RESULTS AND CONCLUSIONS.

1. For all of the cavity flows considered, the best mixing is seen to occur at low Reynolds' numbers, typically those near creeping flow. At low Reynolds' numbers the diffusion coefficient in the advection/diffusion concentration equation is quite large, and diminishes as the Reynolds' number is increased where the flow becomes very much advection dominated. This is also evidenced by analysis of the particle path trajectories, which become more regional or zonal in their mixing at higher Reynolds' numbers. The poorest mixing was found to occur within standard cavity and two plate simultaneous motion cavity flows, where the particle paths simply adhere to the streamlines of the flow resulting in poor mixing.

2. The mixing efficiency of cavity flows can be improved by making the stream function both time dependent and periodic. This results in the Hamiltonian equations governing the particle trajectories becoming non-integrable, which is found to give rise to a chaotic particle motion that is highly desirous for quick and efficient mixing. The two governing parameters for these types of periodic discontinous flow have emerged to be the Reynolds' number, and the period plate motion (T). At low T values the particles simply adhere to the streamlines which is destructive

to good mixing, but as T is increased to a value of two seconds at low Reynolds' numbers the best 'chaotic' mixing is seen to occur.

3. The cavity's aspect ratio is also found to play a significant part in the type of mixing obtained. Novel results have been produced for a time dependent dilatant fluid within cavities of aspect ratios of 2 and 1/3, at low Reynolds' numbers. These peculiar results are in contrast to the steady state solutions and are a direct result of the non-linearity of the equations and the fluid used.

The solutions obtained for a dilatant fluid are not unique for by disturbing the system slightly from the start, its exact mirror image solution can be obtained, showing that the system can undergo a bifurcation of possible solutions. It has also been noted that increasing the Reynolds' number acts as a stabilising influence on this system.

9.4 THERMALLY DRIVEN CAVITY FLOWS.

In this section the main investigative theoretical research work undertaken for the numerical simulation of thermally driven cavity flows is summarised. The problem considered is similar to that of the famous Rayleigh-Benard experiment in which the buoyancy induced flow is generated by uniformly heating from

below a layer of fluid confined between two long, ideally infinite parallel plates. The main characteristic of the flow is the Rayleigh number which is proportional to the adverse temperature gradient existing between the two parallel plates, or in our case the cavity's walls. At a critical value of the Rayleigh number the system is found to become unstable, symmetry is broken and uniform cellular convective motion sets in. This phenomenon is similar to that which is known to exist within the Earth's atmosphere, and is partly responsible for its turbulent nature, as well as being an efficient mixing mechanism for the dispersion of chemical effluent arising from the industrial environment around us. The convection process itself is widely evidenced in nature, being responsible for such events as mass transference, mixing and luminocity of stars and the loss of heat in buildings. Recently, the convection thought to occur within the Earth's mantle has been put forward as a logical explanation of continental drift and plate tectonics[63], which affords a further opportunity for numerical simulation of fluid flows to play a more significant role in many geophysical sciences.

In carrying out a literature survey, it came to light that most of the research work available to date, both experimental and theoretical, seems to have concentrated on the steady state flow equations of a Newtonian fluid within the confines of the cavity

geometry, with surprisingly little theoretical or experimental work produced for non-Newtonian fluids. However, much work has been undertaken for fluids whose viscosity varies with temperature, where a considerable amount of results both experimental and theoretical have been published, for example Turner[108] and Torrance and Turcotte[106]. It has also been noticed that most workers also consider the problem using shear-free boundary conditions which forces the vorticity to be zero on each of the cavity's boundaries.

Throughout the course of this research, the main thrust has been to develop the work of previous researchers, and to incorporate time dependence into the governing flow equations, making use of the Boussinesq approximation, which enables the density to be treated as a constant except for the buoyancy force term. We have also considered the convective flow produced for a broad spectrum of non-Newtonian fluids, using both shear-free and non-zero vorticity boundary conditions and these were found to play an important part in the type of solutions produced. The fluid models used capture the essential properties of pseudoplasticity, dilatancy, thixotropy, and rheopexy as well as fluids whose viscosity is strongly dependent on both temperature and depth respectively. In addition to this, new results have been produced for a weakly viscoelastic fluid, and this, together with the fluids

mentioned above, is thought to be particularly relevant to flow within the Earth's mantle.

The complex non-linear time dependent partial differential equations, were once again numerically 'solved' using a modified version of the A.D.I method developed for the driven cavity flow problem. To enable the approximate solutions generated to be validated, our attention was drawn to the standard ' bench-mark solutions' for thermally driven cavity flow with differentially heated side walls. This problem finds extensive use in the insulation of buildings and has become widely known as the . 'double glazing problem'. Our results for Rayleigh numbers in the range of 10^3 to 10^5 were compared with the bench-mark solutions and found to be in very favourable agreement, the vortices produced being the same size, strength, shape and located at similar positions within the cavity.

9.5 RESULTS AND CONCLUSIONS.

1. For all fluids considered, irrespective of the type of vorticity boundary conditions employed, a periodic pattern of behaviour was found to occur. Initially, at a certain critical value of the Rayleigh number, two mirror image counter rotating cells are produced, which as time progresses can either sustain their own motion or merge to form one large cell.

Upon subsequent increments of the Rayleigh number the one cell configuration was also found to become unstable, collapsing to leave two approximately equal cells with increased rotation in its wake. This pattern of behaviour has been found to occur from moderately low Rayleigh numbers, to those of order 10^6.

2. The vorticity boundary values used are found to have a significant role in determining the outcome of the final solution produced. If non-zero wall vorticity is specified using a Woods formula approximation, the cell configuration produced is more curved in appearance, and almost 'bean' shaped for the case of two cells. This can be explained in terms of the shear stresses present on each of the cavity's walls, which tend to 'pull, stretch and twist' the fluid. These results are in contrast to those obtained when zero vorticity boundary values are used, the cells being more rectangular and symmetrical, as no wall stresses are present.

3. The non-zero vorticity boundary values have also been found to act as a stabilising influence on the system. The critical Rayleigh numbers for the onset of sustained circulatory motion were found to be approximately twice as high for all fluids considered using these boundary conditions, than those obtained

using the shear-free variety. This is also reflected in the fact that the maximum Rayleigh number obtainable on a 40x40 grid for Newtonian fluid using non-zero vorticity boundary conditions was of order 10^5 and increases by a factor of 10 when the shear-free case is considered.

4. Novel results have been produced for a variety of non-Newtonian fluids for Rayleigh numbers up to 10^5, the maximum attainable in the course of our research. Attention is drawn in particular to the transient nature of viscoelastic liquids and to the peculiar results obtained by a pseudoplastic fluid at $Ra=10^5$, using non-zero vorticity boundary conditions. The results are due entirely to the inherent non-linearity of both the equations and fluid used.

5. The Rayleigh-Benard system, for all fluids considered, has been found to be sensitive to initial disturbances, which result in bifurcation phenomena. The crucial factor in determining the cell configuration and rotation was found to depend strongly on the initial temperature guess used in the numerical solution process for the system. By choosing the temperature at all points either to be zero at the start, or to vary linearly with height, two sets of mirror image solutions can be obtained.

6. The mixing efficiency of the Rayleigh-Benard flow was investigated by means of analysing the dispersive mixing of a 'coloured' band of fluid initially 'injected' into the cavity while at rest, such that it fills the entire top half of the cavity. Then by 'solving' the time dependent concentration equation, its subsequent motion is traced. The mixing was found to be rapid even at fairly low Rayleigh numbers, less than 3 seconds of simulation time needed for homogeneous mix to be obtained. The system is ideal for swift mixing, as the flow generated is perpendicular to the inital configuration of the dye.

7. No chaotic motion was observed for a selected number of fluid particles strategically 'placed' within the cavity, for all fluids considered, up to a maximum Rayleigh number of 10^6.

9.6 NON-NEWTONIAN LORENZ EQUATIONS.

In this section we review the main features of the successfully completed novel research work concerned with extending the pioneering work of Lorenz[59], for Newtonian flow only, so as to incorporate some characteristics of more complex non-Newtonian fluids.

In deriving the now famous set of three non-linear coupled ordinary differential equations(O.D.E's), Lorenz was primarily

interested in the feasibility of 'long term' weather prediction. He knew the equations governing the motion of fluid within the atmosphere were complex non-linear (P.D.E's) which were sensitive to the initial conditions. In seeking to model atmospheric flow Lorenz based much of his work on the Rayleigh-Benard experiment, which is a similar to flow within the atmosphere, but stripped to its bare essentials. By following closely the work of his predecessor Saltzman[95], Lorenz assumed the governing (P.D.E's) would admit solutions in terms of double Fourier series with time dependent coefficients. Saltzman had previously used this approach, and obtained an infinite set of (O.D.E's) to describe the systems convective motion, but had observed that as time progressed only a few of the Fourier modes contributed significantly to the final motion produced. Lorenz[59] subsequently took advantage of this fact, recognising only three modes which had time dependent coefficients, X(t),Y(t) and Z(t). X(t) is proportional to the circulation strength of a large convective roll assumed to occur within the confines of an enclosed cavity with shear free vorticity boundary conditions, and Y(t), Z(t) represent temperature fluctuations throughout the cavity. By doing this Lorenz drastically simplified the governing equations without losing their non-linearity, and obtained a very

simple model of atmospheric conditions, which can be thought of as an ideal climate.

These equations however, still needed to be 'solved' by numerical methods, and in so doing Lorenz obtained some very peculiar results, what we today call chaotic motion. Lorenz observed that the equations were very sensitive to the initial conditions set for the problem, and at the critical value of the Rayleigh number at which convection occurred, all particle trajectories were attracted to a fixed, finite region of the phase space which was neither a fixed point or limit cycle, but a peculiar figure whose structure resembled a pair of butterfly wings. Lorenz noticed that while all particles were drawn to this 'strange attractor', on the attractor itself two nearby trajectories would diverge from each other at an exponential rate. This contributed to the particle trajectories becoming highly unpredictable, random erratic or 'chaotic'. From these results Lorenz concluded there is a fundamental difficulty in obtaining accurate long term weather predictions, unless the initial conditions are known exactly.

In the course of our research we have duly extended the work of Lorenz[59] for Newtonian fluids, to consider the motion obtained by a variety of non-Newtonian fluids showing tendencies ranging from pseudoplasticity and thixotropy, to weak viscoelasticity.

The main difference in the equations derived for describing the convective motion for non-Newtonian fluids is the emergence of a variable viscosity term in the first term of the $\dot{X}(t)$ equation representing the circulatory motion, which further increases the non-linearity of the equations.

9.7 RESULTS AND CONCLUSIONS.

1. For all types of non-Newtonian fluids which we have sought to model, no essentially new routes to chaos have been observed, but all support the Ruelle, Takens and Newhouse[94] scenario, of bifurcations leading to a strange attractor, resembling a pair of butterfly wings.

2. The size of the attractor produced is found to be directly proportional to the critical Rayleigh number of the particular fluid considered. For thinner fluids the critical Rayleigh number is smaller, due to less viscous opposition, and consequently the attractor is more diminished in size than that of a Newtonian fluid. The reverse is also true for thicker fluids simulated.

3. The inclination of the attractors 'wings' is also found to be dependent on the non-Newtonian fluid used, which in turn is proportional to the critical Rayleigh number. For thick fluids of the dilatant variety, the angle of inclination of the wings is quite acute, and gradually increases in size when thinner fluids are considered.

4. The results obtained for thixotropic and rheopectic fluids, were found to be strongly time dependent as expected, with the essential governing parameter being the exponential term (e^{-at}) in the equations used to model these types of flow. For a thixotropic fluid by choosing a value of r greater than or equal to that obtained for a Newtonian fluid, the attractor produced initially resembles that of the classical Lorezian format. However, as time progresses the attractor decreases in size with increased separation between the wings, producing an attractor similar that of a pseudoplastic fluid. For a critical value of r near that of a pseudoplastic fluid, quite a different form of particle motion is observed. The initial motion is damped out with the particle residing at one of the two mirror image equilibruim points away from the origin. This is due to initially insufficient thermal driving causing the viscous forces to dominate. However, as time progresses the particles trajectory

around the equilibrium point can be seen to be that of an unstable spiral which eventually becomes chaotic as the fluid becomes more shear-thinning in nature, again producing an attractor similar to that of a pseudoplastic fluid.

For rheopectic fluids, choosing r values larger than or equal to the critical value obtained for a dilatant fluid, the initial particle motion is once again damped out. Depending on the value for 'a' chosen in the equations the particle either temporarily resides at a point away from the two mirror image quilibrium points and gradually backtracks on itself until it reaches one or the other of the equilibrium points, or in fact almost immediately moves toward them. However, in both cases as time progresses the motion around these equilibrium points becomes unstable and produces an attractor similar to that obtained by dilatant fluid which is in line with intuition.

5. The attractors produced, for either a temperature dependent or a weakly elastic fluid, showed very little difference to the results obtained for a Newtonian fluid. This is primarily due to the mode that the variable viscosity function is expressed in, without further Fourier series approximation.

6. The non-Newtonian Lorenz system of equations exhibits features of chaotic motion, as a direct result of insufficient spatial resolution being accounted for in the Fourier series expansions. However, as Lorenz himself pointed out, the equations derived are only valid in the immediate vicinity of conduction to convective motion.

7. The novel research work completed within this section finds applications in the fields of convective mixing, being particularly relevant to mixing processes occurring within the Earth's mantle. Also the shape and size of the attractors produced, together with their erratic and unpredictable motion, can be put forward as a a contribution to the explanation of fluid turbulence (in a temporal sense), a still very obscure and poorly understood area of fluid dynamics.

9.8 RECOMMENDATIONS FOR FUTURE WORK.

The successfully completed research work within this thesis has we believe provided a basis for future work, which would enhance, develop and contribute further, to a better understanding of fluid flows and their associated mixing processes.

Using the main results of this research work we aim to publish three scientific papers; firstly, on the effect of dilatant fluids in driven cavity flows with varying aspect ratios, in the second place the results of employing a wide variety of non-Newtonian fluids in the Rayleigh-Benard system, and thirdly the findings obtained from examining the Lorenz system of equations again using a broad spectrum of non-Newtonian fluids.

A list of possible extensions to this research work is now given.

1. The work on driven cavity flows can be developed to simulate flows using a broader selection of fluid models, with particular consideration given to those of a more complex non-Newtonian nature such as the implicit Oldroyd/Maxwell type viscoelastic liquids .

2. A further analysis of the mixing efficiency for a variety of non-Newtonian fluids can be achieved from tracing the deformation of a line element of 'dyed' fluid, which is assumed to consist of a vast array of fluid particles. By tracking its motion, the location of regions and islands of mixing can be found, together with periodic or hyperbolic points and bifurcation phenomena. This work however, will need the extensive use of a powerful computer and a suitable algorithm.

3. The work completed for the two dimensional driven cavity flow system finds a natural extension in considering the flows and mixing processes obtained within a more realistic three dimensional framework. This can be investigated either in a three dimensional rectangular volume, or by considering the flow between two concentric cylinders, the famous Taylor-Couette flow, but for a wide range of non-Newtonian fluids.

4. An interesting prospect would be to consider the chaotic mixing and the motion of various fluid particles for a variety of non-Newtonian fluids, obtained by a periodic discontinuous motion of the concentric cylinder system used in Taylor-Couette flow.

5. Further investigation also needs to be undertaken to locate the precise reason for the cell structure instability found to occur within the thermally driven cavity flow simulations.

6. Flows generated at higher Rayleigh numbers on more refined grids would be advantageous, providing a possible avenue for the development and understanding if at all possible, of fluid turbulence.

7. The non-Newtonian Lorenz equations need to be derived incorporating more terms in the Fourier series expansions to give a more realistic description of thermally induced convective motion. Also consideration should be given to deriving these equations where non-zero vorticity boundary conditions are employed on each of the cavity's walls.

8. An interesting extension to our work would be to derive non-Newtonian Lorenz equations for thermally generated flow between two concentric cylinders or spheres, which will provide a more realistic model of atmospheric and mantle flow conditions.

9. A further development of current topical research activity, would be to consider the flow patterns a bifurcation phenomena associated with a binary fluid mixture using at least one non-Newtonian fluid.

REFERENCES

[1] ACHESON D.J.

Elementary Fluid Dynamics,

Oxford Applied Mathematics and Computing Science Series,

Oxford University Press, 1990.

[2] AL-SANEA, S.A et al

Computation Of Two-Dimensional Elliptic Flows, Including Heat Transfer.

Computer Methods in Fluids,

Pentech Press Limited.,1980.

[3] ANTICHAOS.

Channel 4 publications 1992.

[4] Proceedings of the International State of the Art Seminar on:

"THE APPLICATIONS OF FRACTALS AND CHAOS"

Sponsored by The British Computer Society. 1992.

[5] AREF. H.

J. Fluid Mech. 1984, 143, 1-21.

[6] ARROWSMITH D.K and PLACE C.M.

Dynamical Systems,

Chapman and Hall Mathematics, 1992.

[7] ARTER W.

J. Fluid Mech. 1985, 152, 391-418.

[8] AZIZ K. and HELLUMS J.D.

The Phys. of Fluids 1967, 10, no.21, 314-324.

[9] BAKER G.L and GOLLUB J.P.

Chaotic Dynamics (An Introduction),

Cambridge University Press, 1990.

[10] BATCHELOR G.K.

Quart. App. Math. 1954, 12 ,209-233.

[11] BATCHELOR G.K.

J. Fluid Mech. 1956, 1(2), 177-190.

[12] BATCHELOR G.K.

Introduction to Fluid Dynamics,

Cambridge University Press, 1967.

[13] BENARD H.

Annls. Chim Phys. 1901, 23, 62.

[14] BIRD R.B., ARMSTRONG R.C. and HASSAGER O.

Dynamics of Polymeric Liquids, Vol.1, Fluid dynamics.

John Wiley and Sons, 1977.

[15] BIRD, STEWART and LIGHTFOOT.

Transport Phenomena, John Wiley and sons, 1960.

[16] BODALIA V.

Ph.D Thesis 1986,

Depts. of Chem. Eng, Maths and Computer Science,

The Polytechnic of Wales.

[17] BOZEMANN J.D and DALTON C.

J. of Comp. Phys. 1973, 12. 348-363.

[18] BRINDLY J.

J. Inst. Math. Applics. 1967, 3, 313-343.

[19] BURDEN R.L AND FAIRES J.D.

Numerical Analysis, Fourth edition.

Boston, Mass. Pws-Kent Pub. co. 1989.

[20] BURGGRAF O.B.

J. Fluid Mech. ,1966, 24, 113-151.

[21] BUSSE F.H.

J. Fluid Mech. 1972, 52(1) 97-112.

[22] CHANDRASEKHAR S.

Hydrodynamic and Hydromagnetic Stability.

Oxford University Press, 1961.

[23] CHIEN W.L et al

J. Fluid Mech. 1986, 170, 355- 377.

[24] CHOW, CHUEN-YEN.

An Introduction to Computer Fluid Mechanics.

John Wiley and Sons,1979.

[25] CHRISTENSEN U and HARDER H.

Int. J. Geophys. 1991, 104, 213-226.

[26] CLIFFE K.A et al.

Theoretical Physics Division,

U.K. AERE, Harwell Rep.R.9202, 1978.

[27] COLLIAS D.J and PRUD'HOMME R.K.

Chem. Eng. Sci. 1985, 40, 1495.

[28] COMPUTER METHODS IN FLUIDS, (ed. K.Morgan et al)

Pentech Press, London: Plymouth, 1980.

[29] CROCHET M.J, DAVIES A.R and WALTERS K.

Numerical Simulation of Non-Newtonian Flow.

Rheology Series1, Elsevier 1984.

[30] CSEREPES L. and RABINOWICZ M.

Planetary Science Letters, (1985/86), 76, 193-207.

[31] CURRY J.H.

Commun. Math. Phys. 1978, 60, 193-204.

[32] CURRY J.H et al

J. Fluid Mech. 1984, 147, 1-38.

[33] De VAHL DAVIS G.

Int. J. for Num. Meth. in Fluids, 1983, 3, 249-264.

[34] DIJKSTRA H.A.

J. Fluid Mech. 1992, 243, 73-102.

[35] DOHERTY M.F. et al.

(Review Article no.27)

Chem. Eng. Sci. 1988, 43, no.2, 139-183.

[36] DANIELS P.G.

J. Fluid Mech. 1984, 143, 125-152.

[37] FEARFUL SYMMETRY.

STEWART I. and GOLUBITSKY M.

Blackwell, 1992.

[38] FOSTER T.D.

J. of Geophysical Research 1969, 74, 685-693.

[39] FROBERG C.E.

Numerical Mathematics,

Benjamin/Cummings, 1985.

[40] FOX L. and SANKAR R.

J. Inst. Maths. Applics. 1969, 5, 340-350.

[41] GUCKENHEIMER J.

Ann. Rev Fluid Mech. 1986, 18, 15-31.

[42] GUPTA M.M et al

J. of Comp. and Fluids, 1981, 9, 379-388.

[43] GUPTA MURLI M. and MANOHAR RAM P.

J. Comp Physics, 31, 265-268,1979.

[44] HAVARD S.P.

Ph.D. Thesis, 1989.

Dept. of Maths and Computing,

The Polytechnic of Wales.

[45] HENRIKSEN P. and HASSAGER O.

J. Rheology 1989, 33(6), 865-879.

[46] HOLSTEIN H. and PADDON D.J.

J. non-Newt. Fluid Mech 1981, 8, 81-93.

[47] HUGHES W.F and BRIGHTON J.A.

Theory And Problems Of Fluid Dynamics.

Schaum's Outline Series, McGraw-Hill Book Company, 1967.

[48] JANA S.C. et al

Phil. Trans. R. Soc. Lond A (1992) 338, 519-531.

[49] JEFFREYS J.

Phil. Mag. Series 7, 2 ,833,1926.

[50] JORDAN D.W. and SMITH P.

Non-linear Ordinary Differential Equations (second edition)

Oxford Applied mathematics and Computing Science Series,

Clarendon Press, Oxford. 1988.

[51] KAWAGUTI M.

J. Phys. Soc. Japan, 1961, 16, 2307.

[52] KEMBLOWSKI Z. and PETERA J.

Rheol. Acta 1979, 18, 702-710.

[53] KHAKHAR et al

J. Fluid Mech. 1986, 172, 419-451.

[54] LAX, P.D.

Numerical Solution of Partial Differential Equations:

Finite Difference Methods, (third edition),

Oxford Applied Mathematics and Computing Series, 1985, p.72

[55] LAPIDUS L. and PINDER G.F.

Numerical Solution of Partial Differential Equations

in Science and Engineering.

John Wiley and sons Inc.1982.

[56] LARSON. R.G.

Rheol. Acta,1992, 31, 213-263.

[57] LEONG C.W. et al

J. Fluid Mech.1989, 209, 463-499.

[58] LEONARD, B.P

The Quick Algorithm: A Uniformly Third-Order

Finite-Difference Method for Highly Convective Flows.

Computer Methods in Fluids,

Pentech Press,1980.

[59] LORENZ E.N.

J. Atmos. Sci. 1963, 20,130-141.

[60] MARCUS P.S.

J. Fluid Mech. 1981, 103, 241-255.

[61] MAY R.M.

Nature, 1976, 261,459-467.

[62] McKENSIE D.P, ROBERTS J.M. and WEISS N.O.

Convection in the Earth's Mantle:

Towards a Numerical Simulation.

J. Fluid Mech., 1974, 62, 465-538.

[63] McKENSIE D.P.

Scientific American,1983, 249, no.3, 50-68.

[64] MILLS R.D.

J. Roy. Aeron. Soc,1965, 69, 714-718.

[65] MITCHELL A.R. and GRIFFITHS D.F.

The Finite Difference Method in Partial Differential Equations.

Wiley, 1980.

[66] MOFFATT H.K.

J. Fluid Mech. 1964, 18, 1-18.

[67] MOON F.C.

Chaotic Vibrations

(An Introduction For Applied Scientists And Engineers)

John Wiley and Sons Inc.1987.

[68] MOON F.C.

Chaotic and Fractal Dynamics.

(An Introduction For Applied Scientists And Engineers)

Wiley-Interscience Publications,

John Wiley and Sons Inc. 1992.

[69] MOORE D.R and WEISS N.O.

J. Fluid Mech. 1973, 58(2), 289-312.

[70] MOORE D.R and WEISS N.O.

Phil. Trans. R.Soc. Lond A(1990) 332, 121-134.

[71] MOSES E. and STEINBERG V.

Physical Reviews A 43 (no.2), 1991.

[72] MULLIN T. and PRICE T.J.

An Experimental Observation of Chaos Arising

from the Interaction of Steady and Time Dependent Flows.

Letters to Nature, vol.340, 27 July 1989.

[73] NAGATA. S.

Mixing: Principles and Applications

John wiley and Sons London 1975.

[74] NALLASAMY M. and KRISHNA PRASAD K.

J. of Comp. Phys. 15 429-448, 1974.

[75] NATAF H.C and RICHTER F.M.

Physics of the Earth and Planetary Interiors,

1982, 29, 320-329.

[76] NEW SCIENTIST GUIDE TO CHAOS.

Ed. Nina Hall, Penguin,1991.

[77] NIJHOF et al

Proceedings of the IMA/EROFTAC Conference on New Techniques

in Mathematical and Computational Modelling of Turbulent

Diffusion and Mixing in Industrial and Environmental

Problems, 1991.

[78] OLDSHUE J.Y.

Fluid Mixing Technology.

Mcgraw-Hill, New York, 1983.

[79] OLDSEN M.D. and TUANN SHIH-YU.

Proceedings of the Third International Conference on Finite Elements in Flow problems, 1980, 143-152.

[80] OTTINO J.M.

The Kinematics of Mixing: Stretching, Chaos And Transport.

Cambridge University Press, 1989.

[81] OTTINO et al

Nature, 1988, 333, 419-425.

[82] OTTINO J.M. and CHELLA. R.

Polymer Engineering and Science, 1983, 23, 364-379.

[83] PAN F. and ACRIVOS A.

J. of Fluid Mech. 28, 43-655, 1967.

[84] PATANKAR S.V.

Numerical Heat Transfer and Fluid Flow,

Mcgraw-Hill, 1980.

[85] PATTERSON J.C. and ARMFIELD S.W.

J. Fluid Mech. 1990, 219,469-497.

[86]PHASER.

HUSEYIN KOCAK

Differential and Difference Equations Through

Computer Experiments, Second Edition.

Springer-Verlag, New York Inc.,1989.

[87] POMMEAU Y. AND MANNEVILLE Y.

Phys. Lett. 1979, 75A,1,1979.

[88] POOTS G.

Quart. Journ. Mech. and Applied Math. 1958, 11, 258-273.

[89] QUILLEN C.S.

Chem. Eng. 1954, 61, 6.

[90] LORD RAYLEIGH

Phil. Mag. S. 6. 1916, Vol.32, No.192.

[91] RAUDKIVI A.J and CALLANDER R.A.

Advanced Fluid Mechanics. Edward Arnold (publishers) Ltd. 1975.

[92] ROACHE P.J.

Computational Fluid Dynamics.

Alberquerque, Hermosa Publishers, 1976.

[93] RUELLE D.

Chaotic Evolution and Strange Attractors.

Cambridge University Press, 1989.

[94] RUELLE, TAKENS AND NEWHOUSE.

Deterministic Chaos (An Introduction), pp114

Schuster, H.G.

Weinheim: Physik-Verlag, 1984.

(VCH Publishers).

[95] SALTZMAN B.

J. of the Atmos.Sci. 1962, 19, 329-341.

[96] SCRATON R.E.

Further Numerical Methods in Basic

Edward Arnold, 1987.

[97] SCHNIPKE R.J. and RICE J.G.

Int. J. for Num. Meth. in Eng. 1987, 24, 117-128.

[98] SCHUSTER H.G.

Deterministic Chaos: An Introduction

Weinheim: Pysik-Verlag. 1984.

(VCH- Publishers).

[99] SIROVICH L and DEANE A.E.

J. Fluid Mech. 1991, 222, 251-265.

[100] SMITH G.D.

Numerical Solution of Partial Differential Equations:

Finite Difference Methods, Second Edition, Clarendon Press,

Oxford, 1978.

[101] SOLOMON T.H. and GOLLUB J.P.

Physical Review A. 1988, 38, no.12, 6280-6286.

[102] SPRAGG et al.

Proceedings of the Fourth International Conference on

Numerical Methods in Laminar and Turbulent Flows vol.1, 1985.

C. Taylor(editor), Pineridge Press, Swansea, pp 39-50.

[103] THOMSON C.P et al

Int. J. For Num. Meth. In Eng. 1987, 24, 89-99.

[104] THOMSON J.J.

Phil. Mag (4), 1885, 10, 330.

[105] THOMSON J.M.T and STEWART H.B.

Non-linear Dynamics and Chaos

John Wiley, 1988.

[106] TORRANCE K.G. and TURCOTTE D.L.

J. Fluid Mech. 1971, 47(1), 113-125.

[107] TUCKER C.L.(III).

Fundamentals of Computer Modelling for Polymer Processing.

Hanser Publishers, Munich, Vienna, New York, 1990.

[108] TURNER J.S.

Earth and Planetary Letters, 1973, 17, 369-374.

[109] ULBRECHT J.

Chem. Eng. 1974, 347.

[110] VENEZIAN G.

J. Fluid Mech. 1969, 35 (2), 243-254.

[111] WALTERS K.

Rheometry, Chapman and Hall, London, 1975.

[112] WALTERS K.

Rheometry: Industrial Applications

John Wiley and Sons, 1980.

[113] WEIJERMARS R.

Tectonophysics, 1988, 154, 97-123.

[114] WHITE D.B.

Ph.D. Thesis.

University of Cambridge, 1982.

[115] WHITE F.M.

Viscous Fluid Flows, McGraw-Hill, 1974.

[116] WILKES J.O. and CHURCHILL S.W.

J. A.I.ch.E, 1966, 12, no.1, 161.

[117] WILLIAMS R.W.

Private Communication.

[118] YOUNG D.

Iterative Solution of Large Linear Systems.

Academic Press, New York, 1971.

NUMERICAL REPRESENTATIONS OF FLUID MIXING.

by

NIGEL HOWARD DAVIES B.Sc.(Hons).

APPENDIX OF FIGURES

A thesis submitted in partial fulfilment of the requirements

of the University of Glamorgan/Prifysgol Morgannwg

for the degree of Doctor of Philosophy.

The research programme was carried out

in collaboration with Brookfield Viscometers Ltd.

The Department of Mathematics and Computing,

The University of Glamorgan,

Mid Glamorgan.

CF37 1DL.

June 1993.

APPENDIX OF FIGURES

CONTENTS

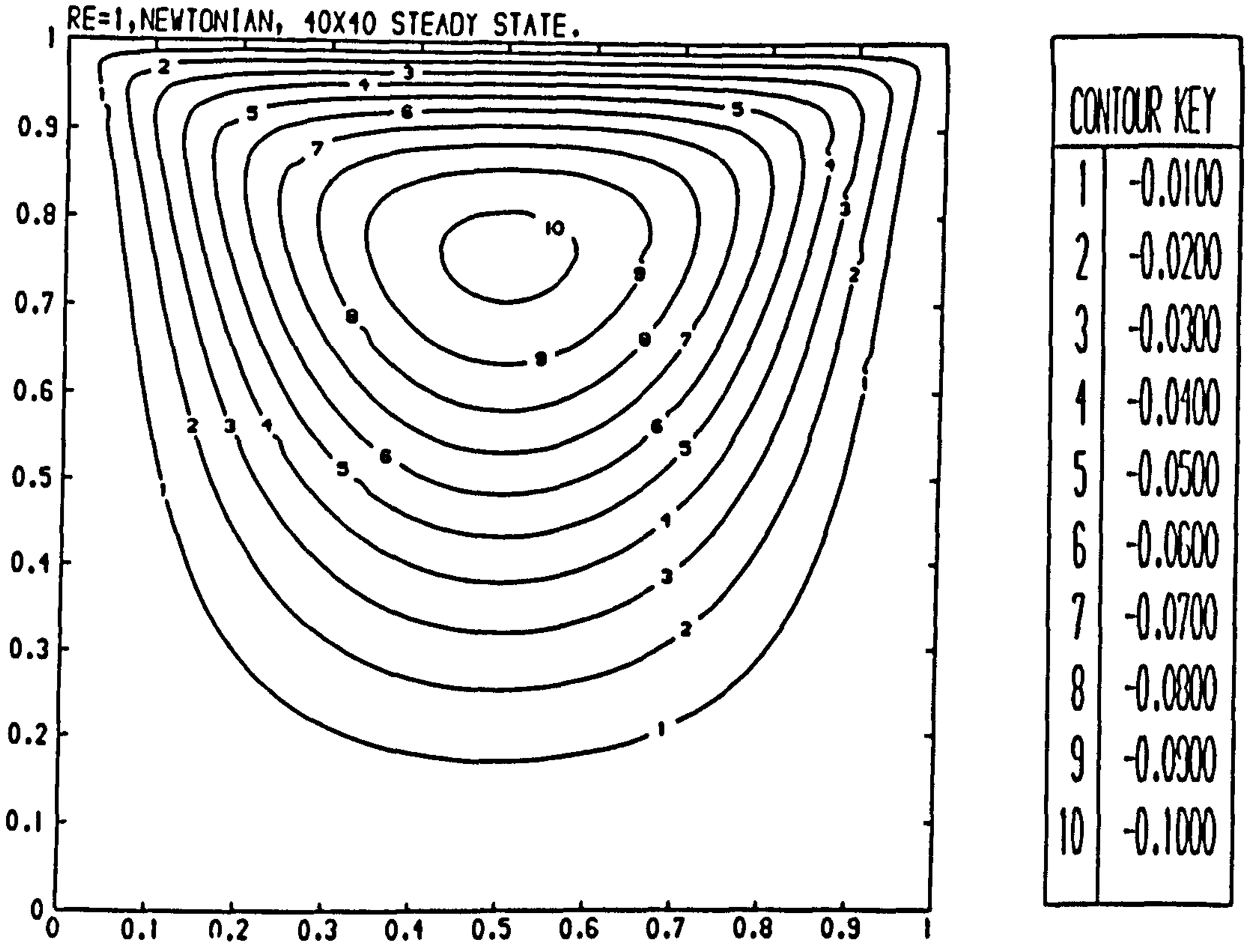

Figure (5.1) Streamlines of a Newtonian fluid at Re=1.

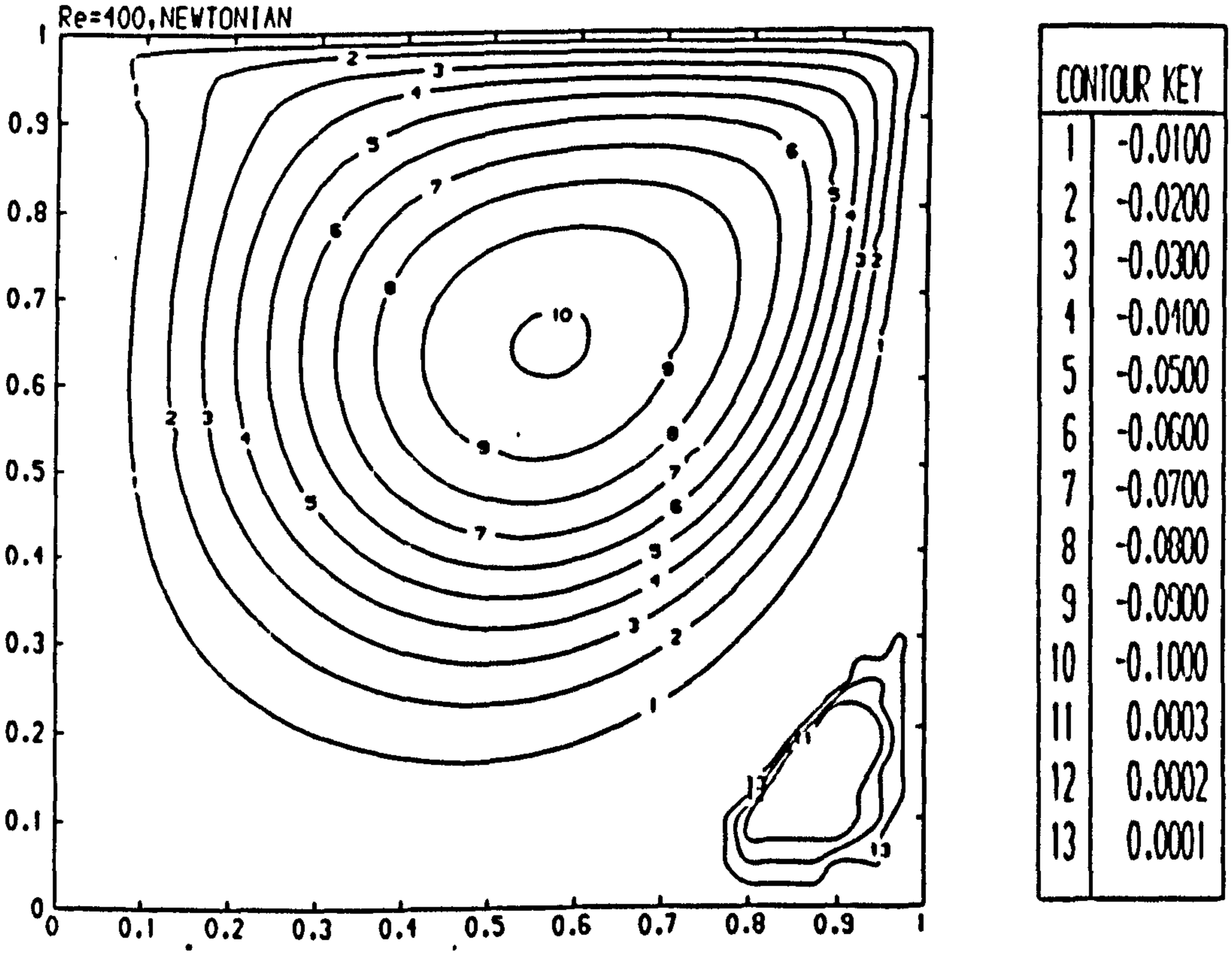

Figure (5.2) Streamlines of a Newtonian fluid at Re=400.

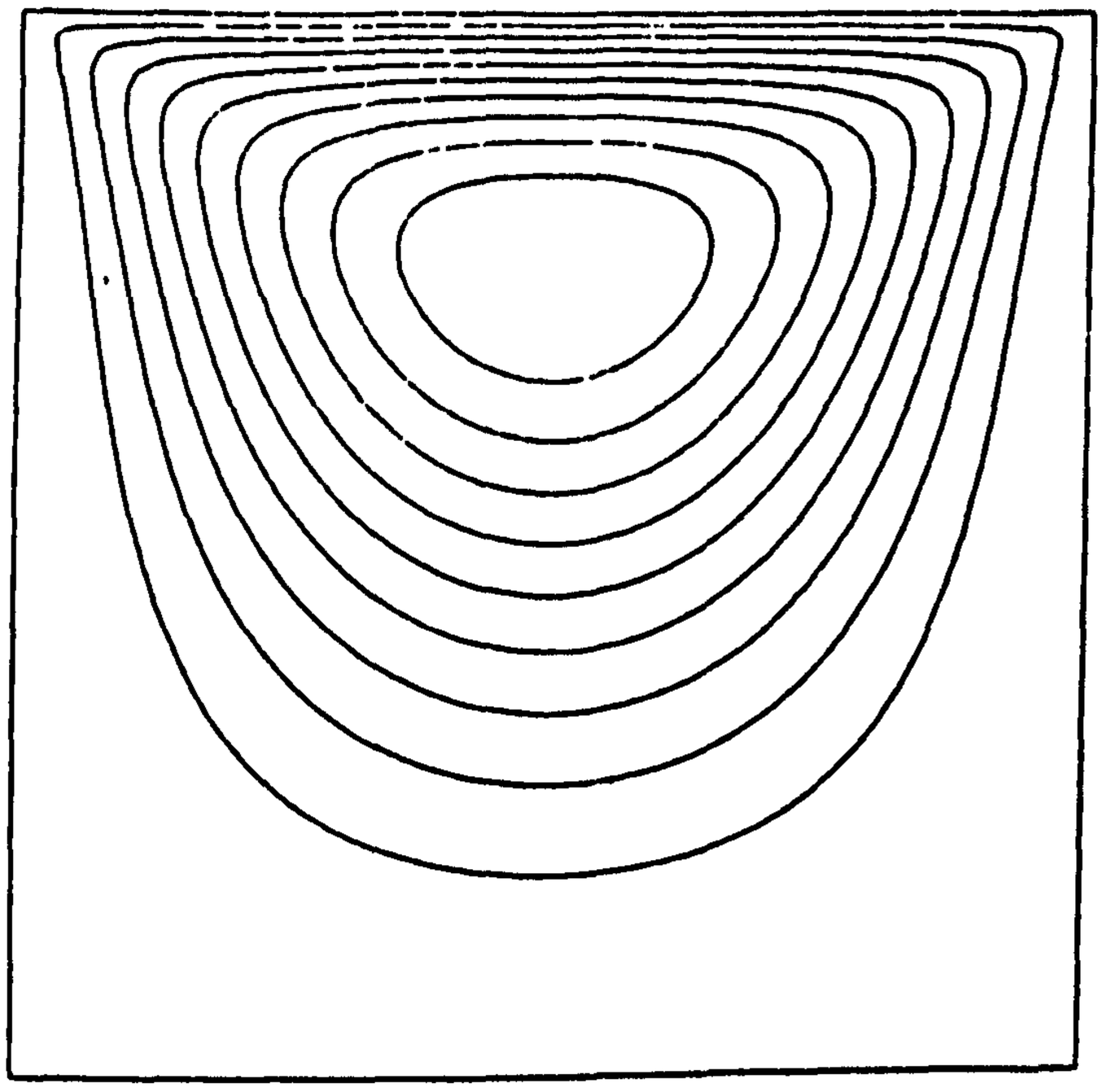

Figure (5.3) Streamline contours of Cliffe et al[26] at Re=1.

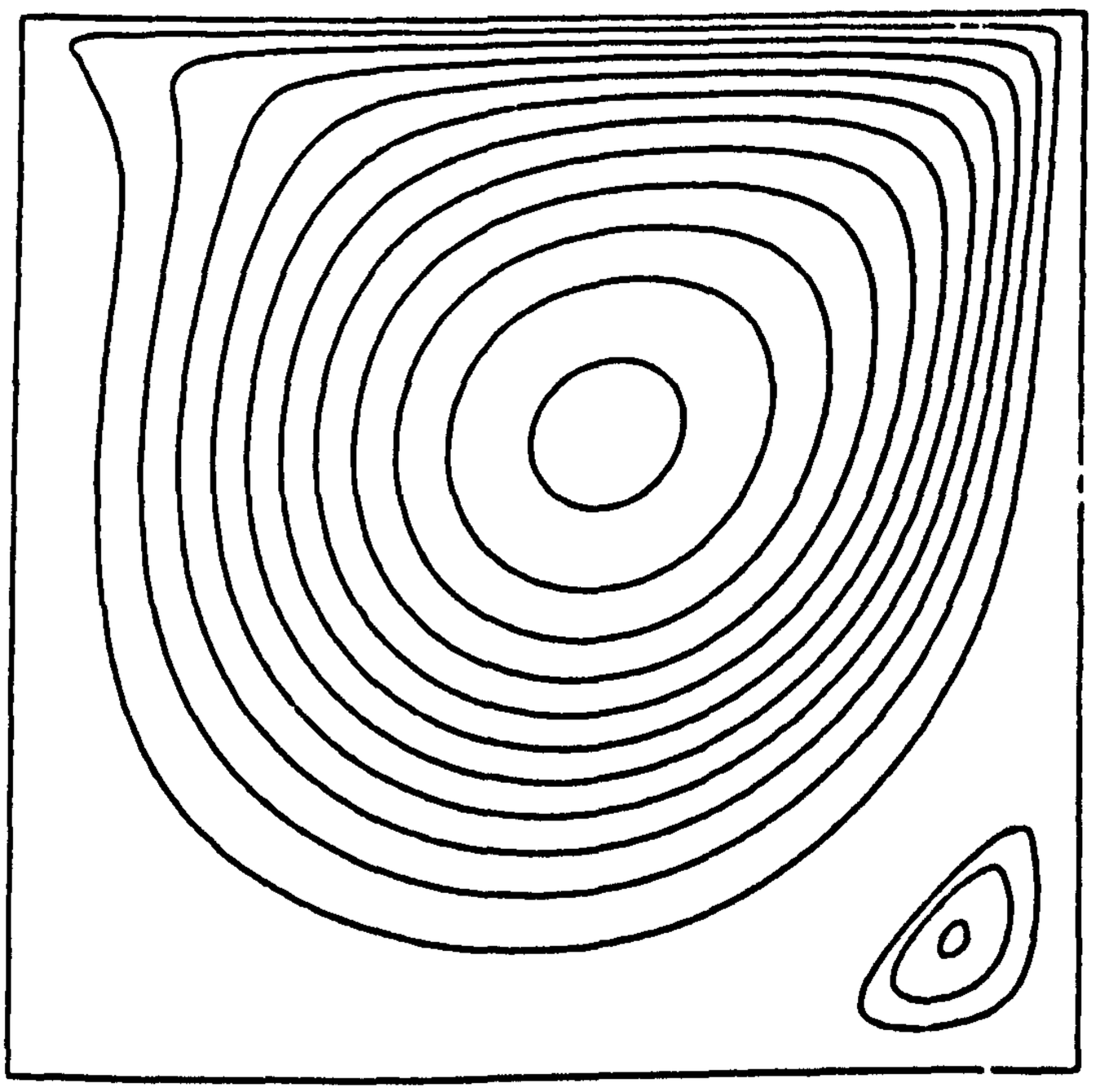

Figure (5.4) Streamline contours of Cliffe et al[26] at Re=400.

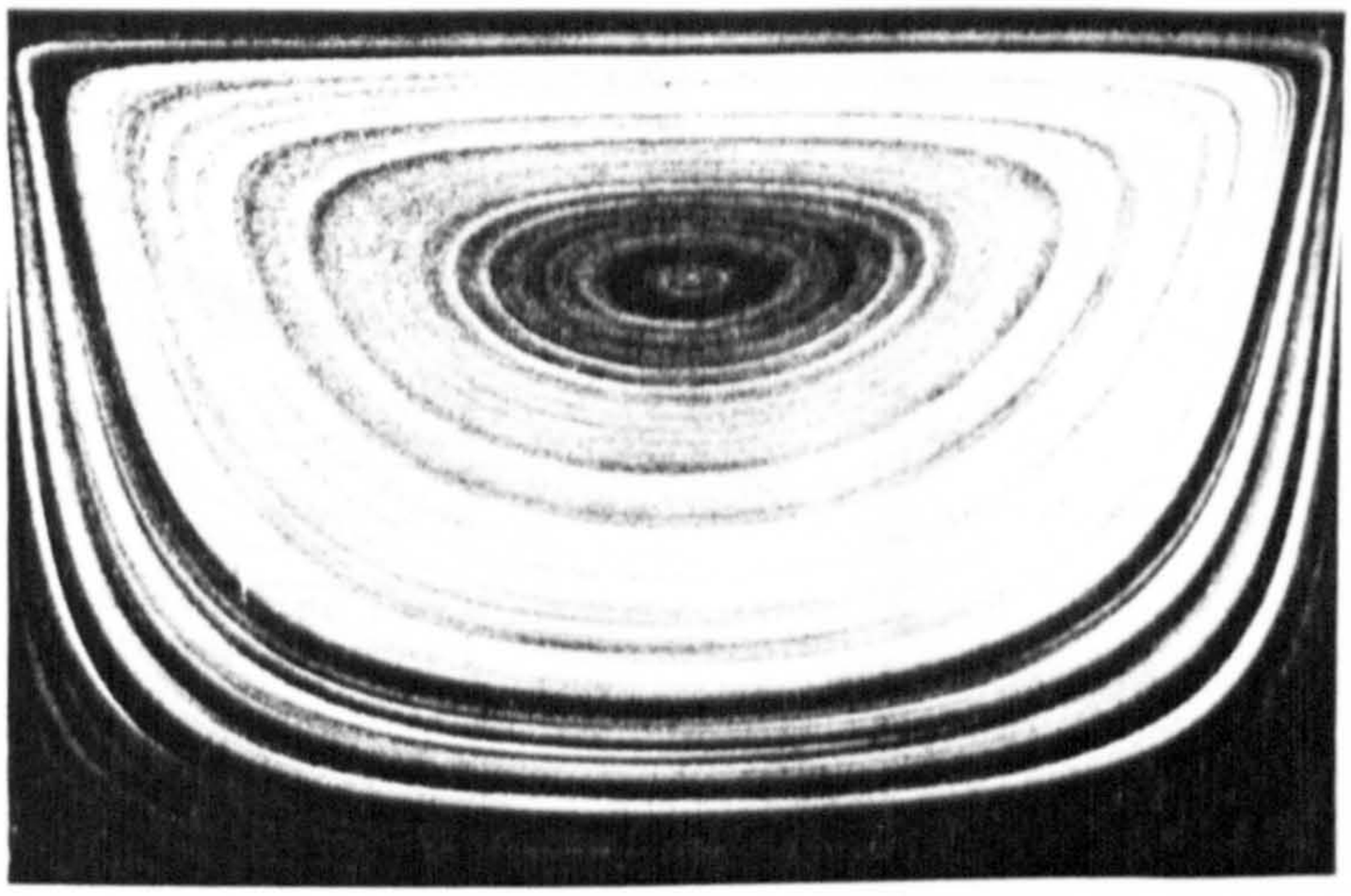

Figure (5.5) Experimental streamlines at Re=1.7 by Ottino[80].

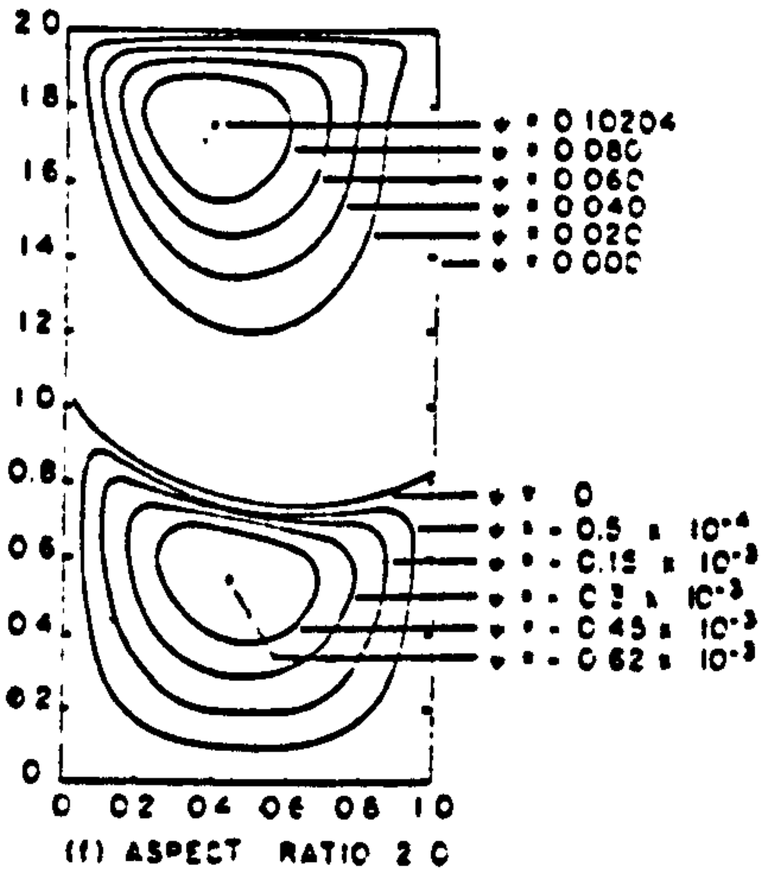

Figure (5.6)

(Bozemann and Dalton)

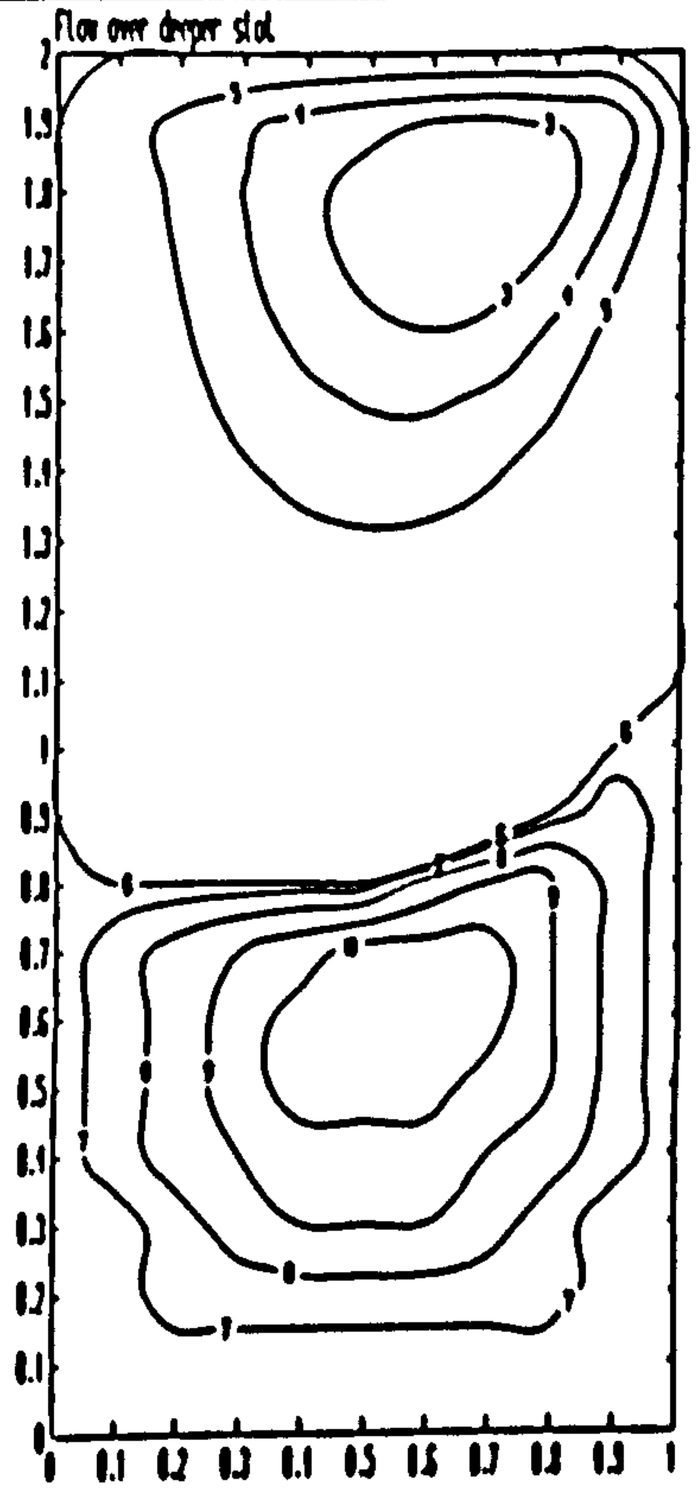

CONTOUR KEY	
1	-0.1020
2	-0.0800
3	-0.0600
4	-0.0400
5	-0.0200
6	0.0000
7	0.0001
8	0.0002
9	0.0003
10	0.0005
11	0.0006

Figure (5.7)

A comparison of streamline contours for a Newtonian fluid at Re=100, in a cavity of aspect ratio 2, between Bozemann and Dalton[17] and ourselves.

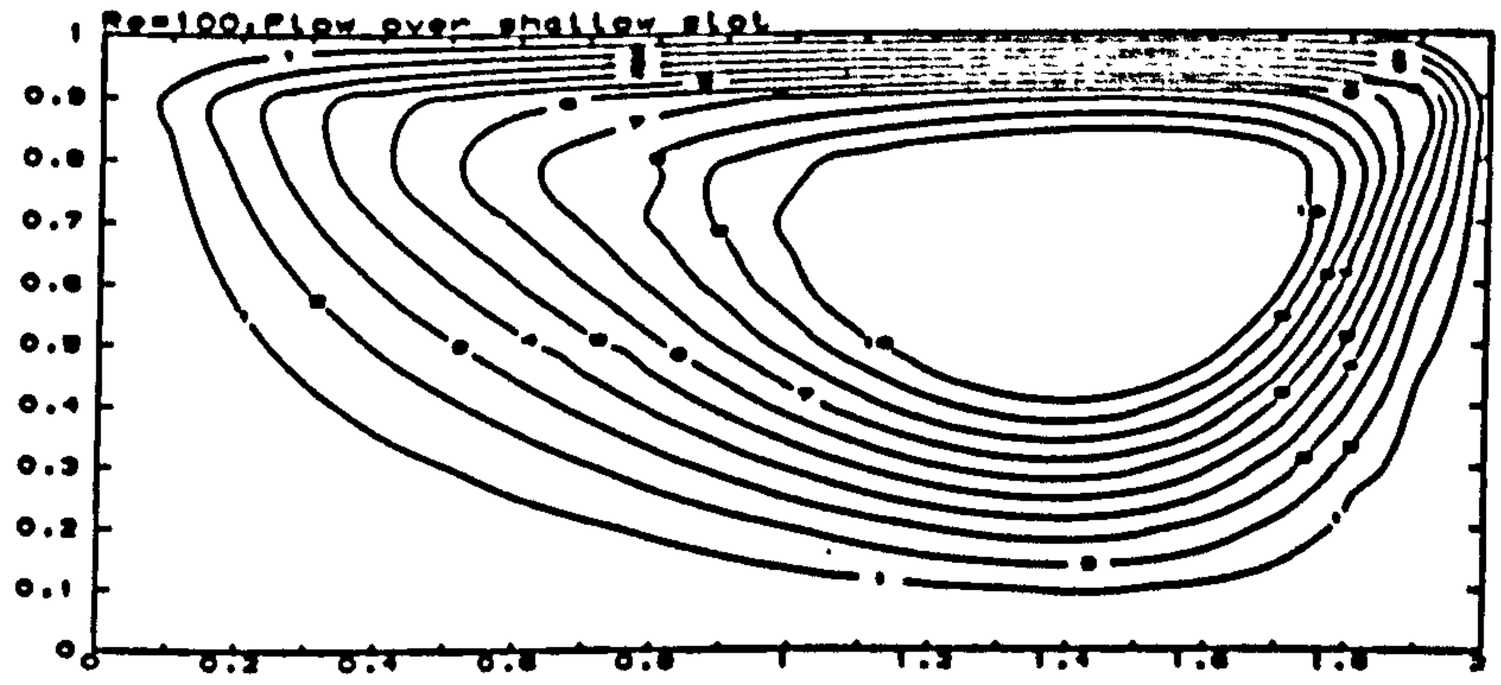

CONTOUR KEY	
1	-0.0100
2	-0.0200
3	-0.0300
4	-0.0400
5	-0.0500
6	-0.0600
7	-0.0700
8	-0.0800
9	-0.0900
10	-0.1000

Figure (5.8)

Streamlines of a Newtonian fluid at Re=100 in a cavity of aspect ratio 0.5.

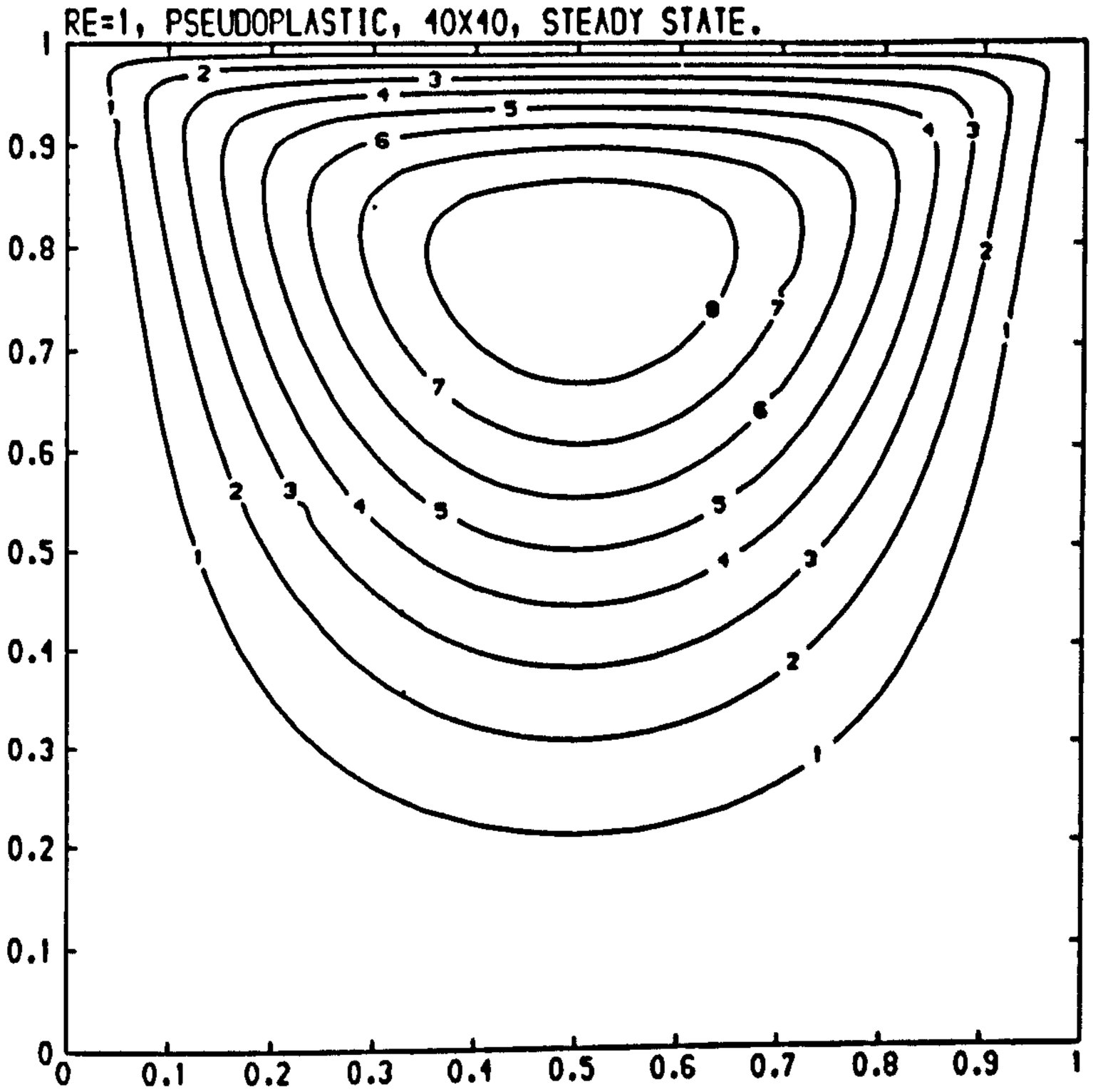

CONTOUR KEY	
1	-0.0100
2	-0.0200
3	-0.0300
4	-0.0400
5	-0.0500
6	-0.0600
7	-0.0700
8	-0.0800
9	-0.0900
10	-0.1000

Figure (5.9) Streamlines of a pseudoplastic fluid at Re=1.

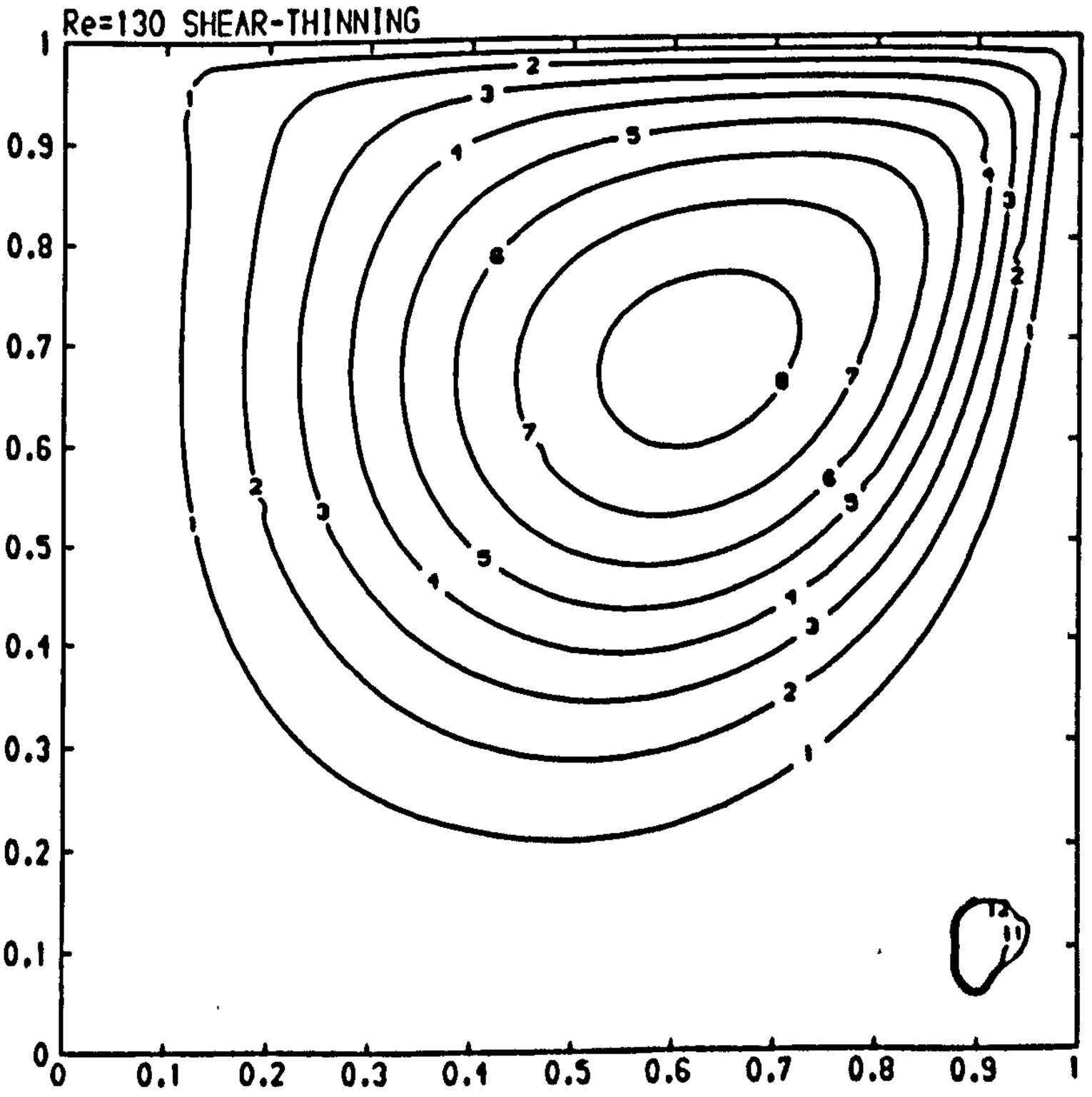

CONTOUR KEY	
1	-0.0100
2	-0.0200
3	-0.0300
4	-0.0400
5	-0.0500
6	-0.0600
7	-0.0700
8	-0.0800
9	-0.0900
10	-0.1000
11	0.0000
12	0.0000

Figure (5.10) Streamlines of a pseudoplastic fluid at Re=130.

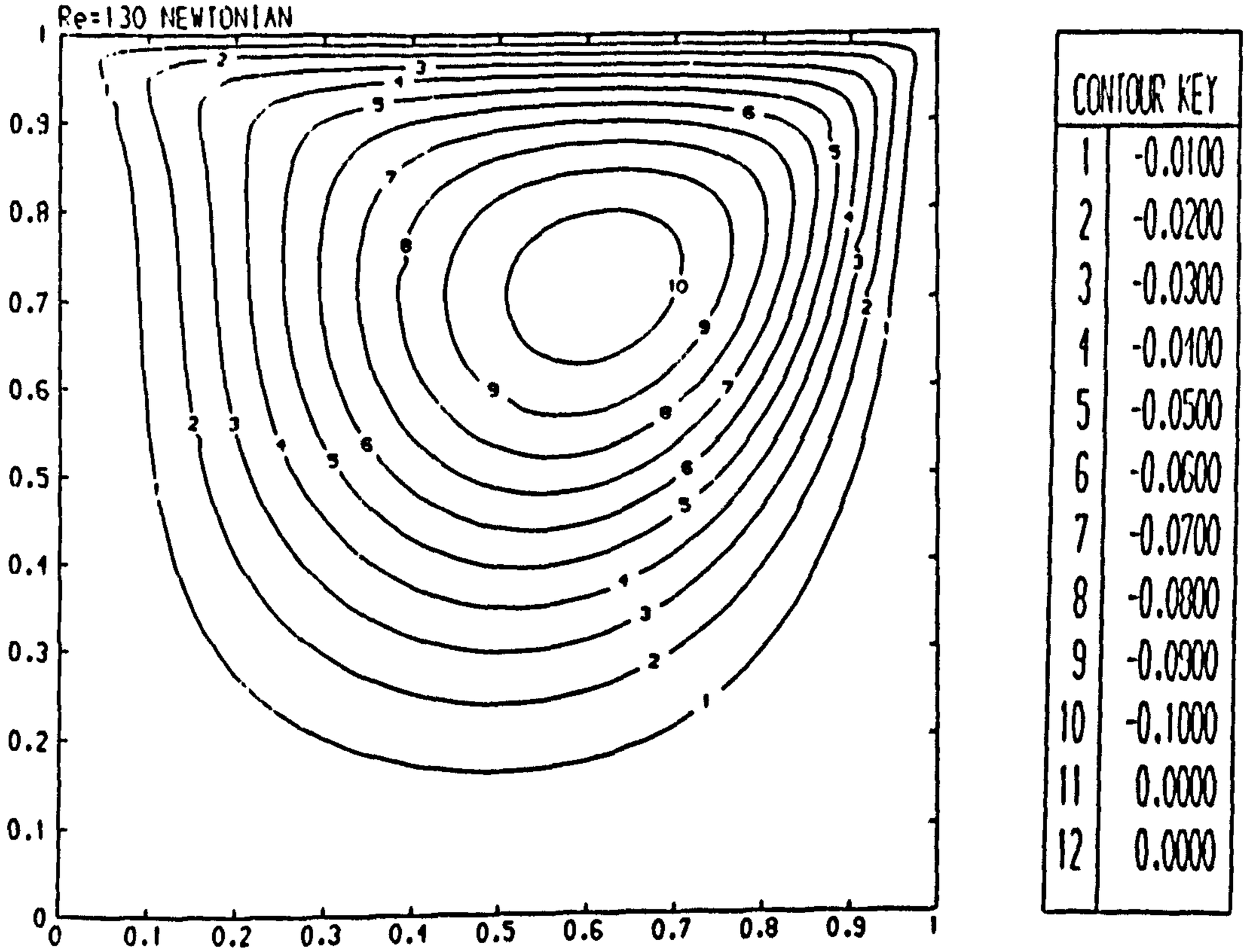

Figure (5.11) Streamlines of a Newtonian fluid at Re=130.

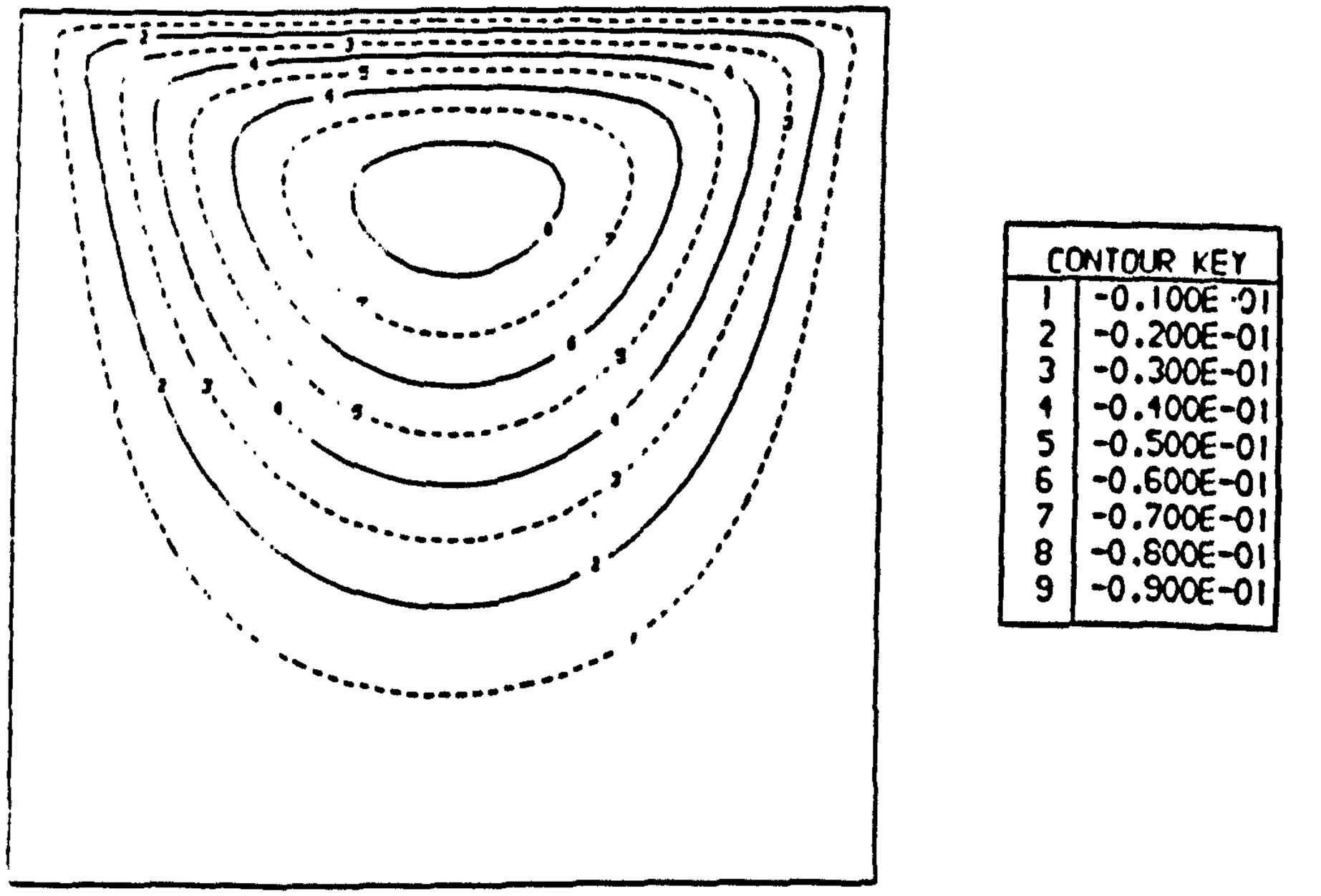

Figure (5.12) Streamlines of a Pseudoplastic fluid at Re=1 by Havard[44].

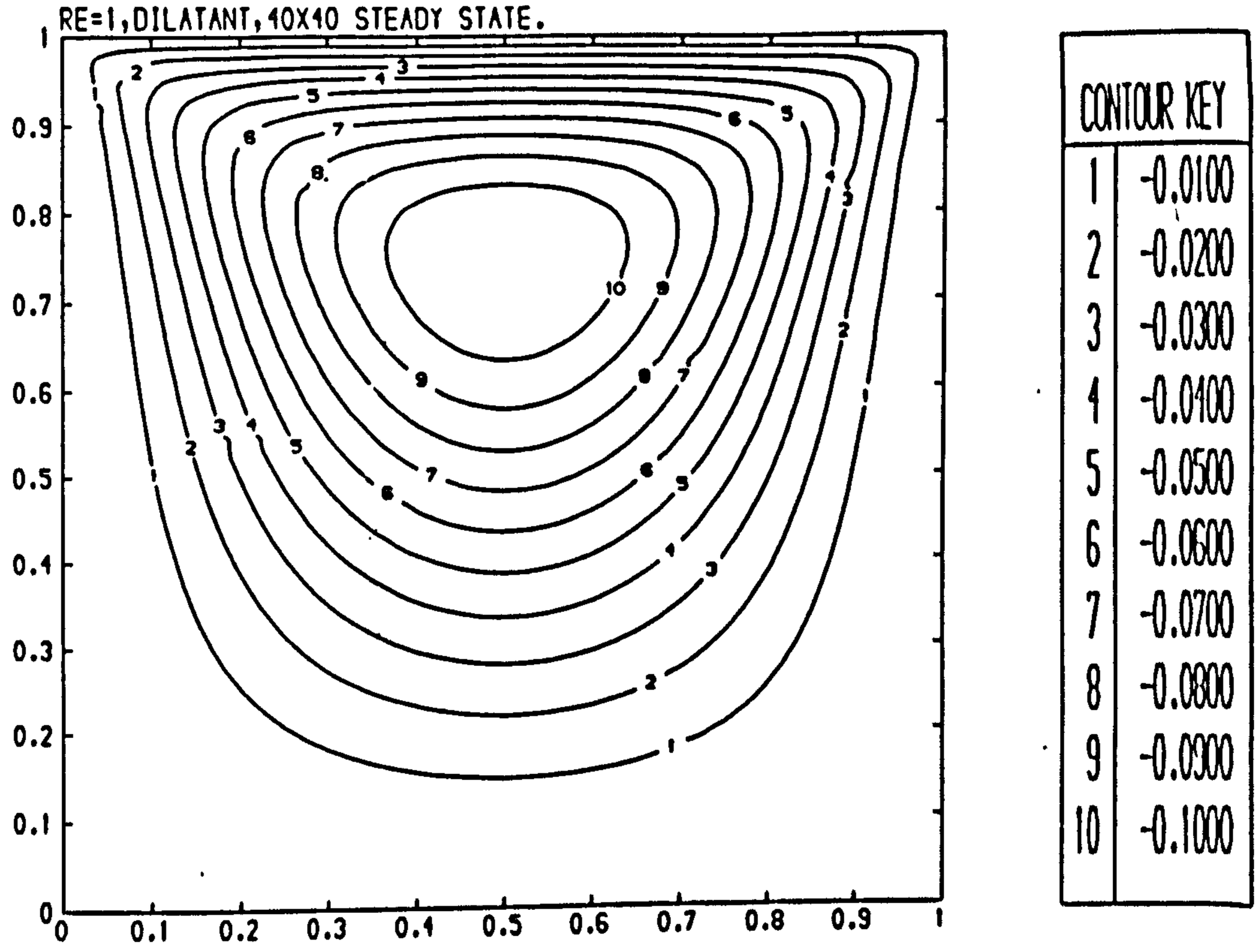

Figure (5.13) Streamlines of a dilatant fluid at Re=1.

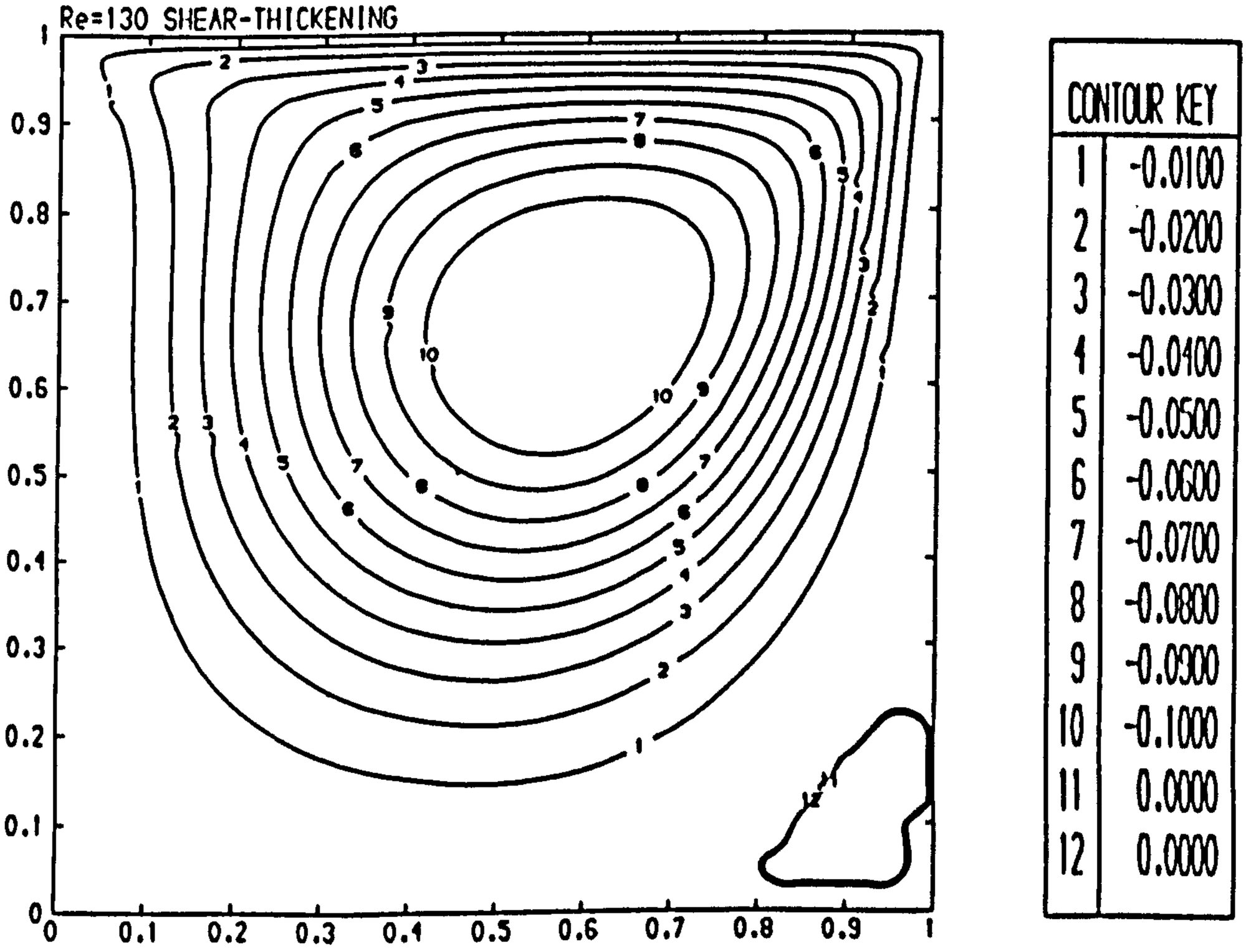

Figure (5.14) Streamlines of a dilatant fluid at Re=130.

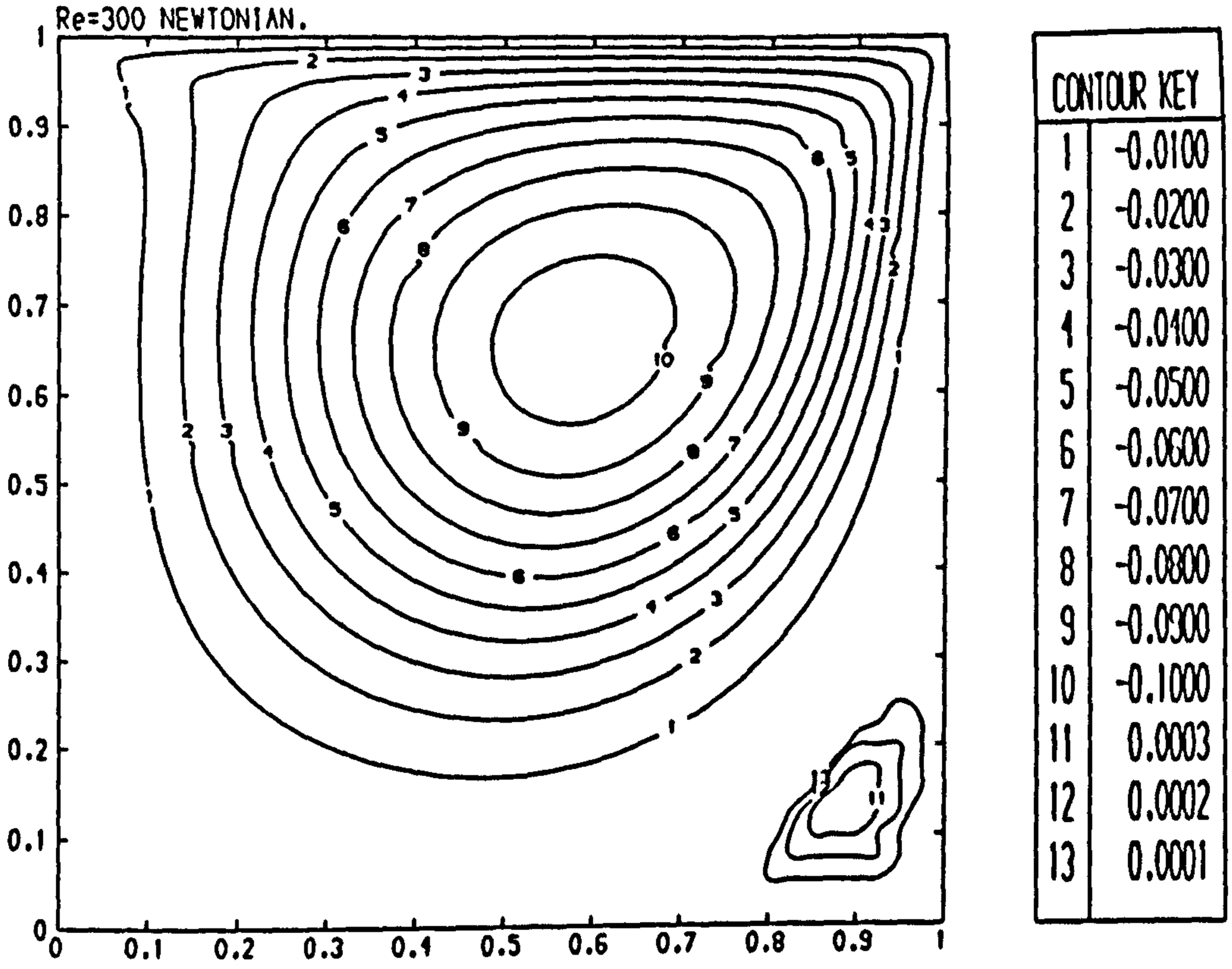

Figure (5.15) Streamlines of a Newtonian fluid at Re=300.

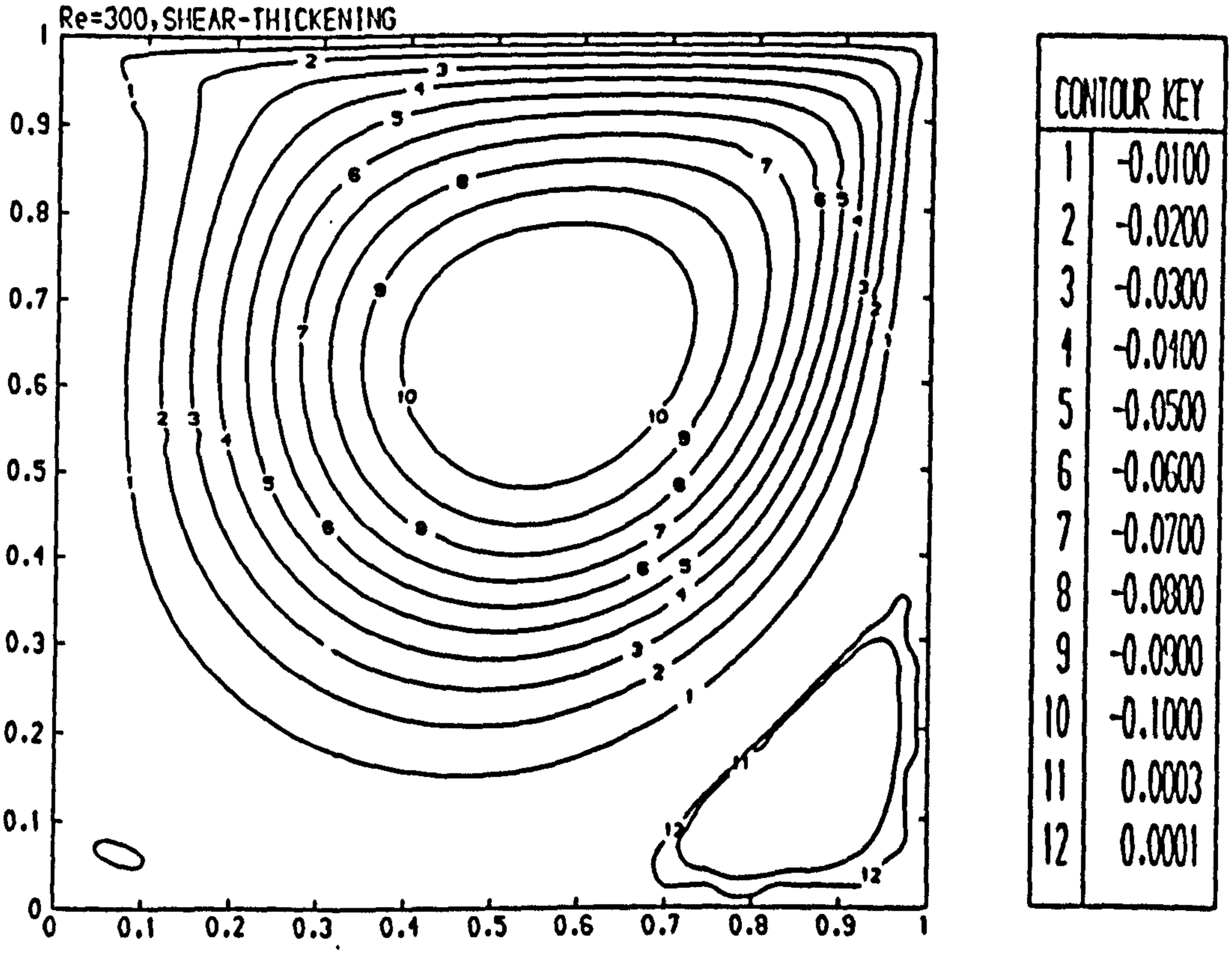

Figure (5.16) Streamlines of a dilatant fluid at Re=300.

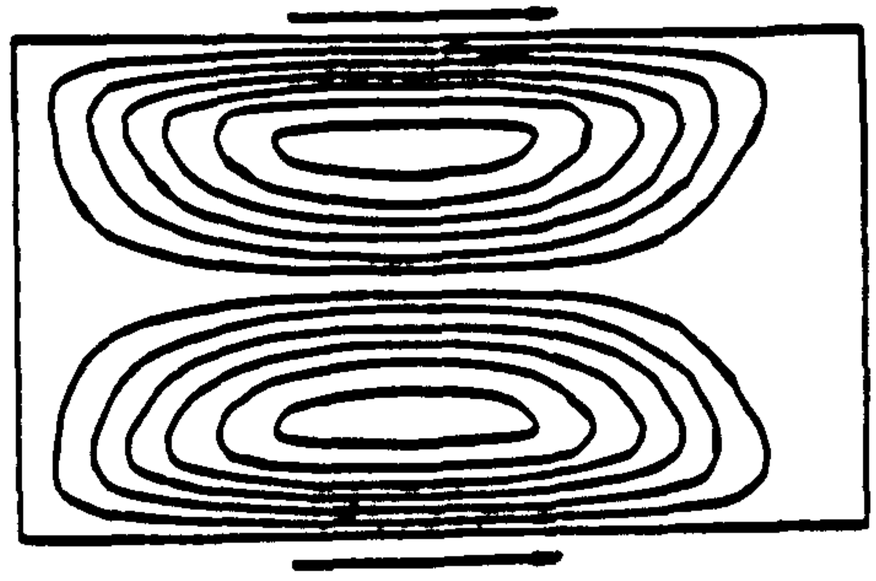

Figure (5.18) Streamlines of a Newtonian fluid at Re=1, by Chien et al[23], with both walls at same speed and in same direction. (vb=vt)

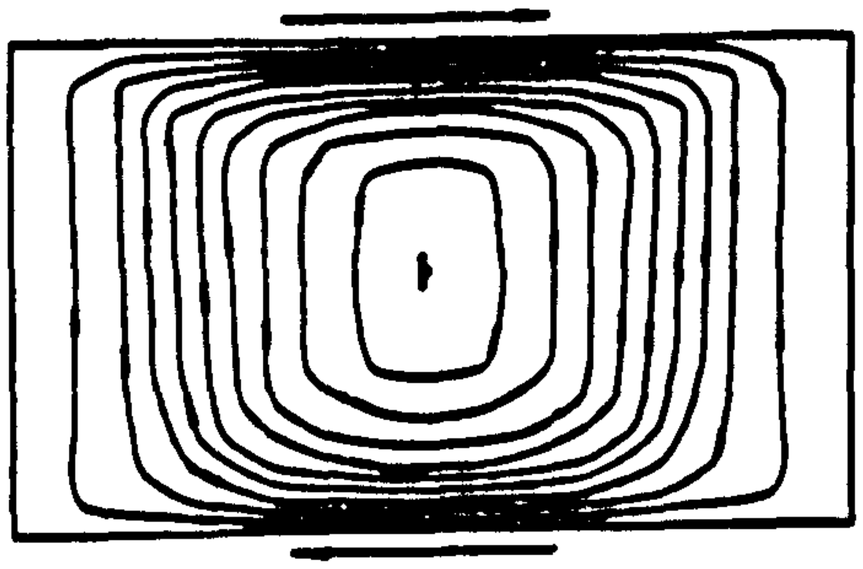

Figure (5.19) Streamlines of a Newtonian fluid at Re=1, by Chien et al[23], with both walls at same speed and in opposite directions. (Vb=-vt)

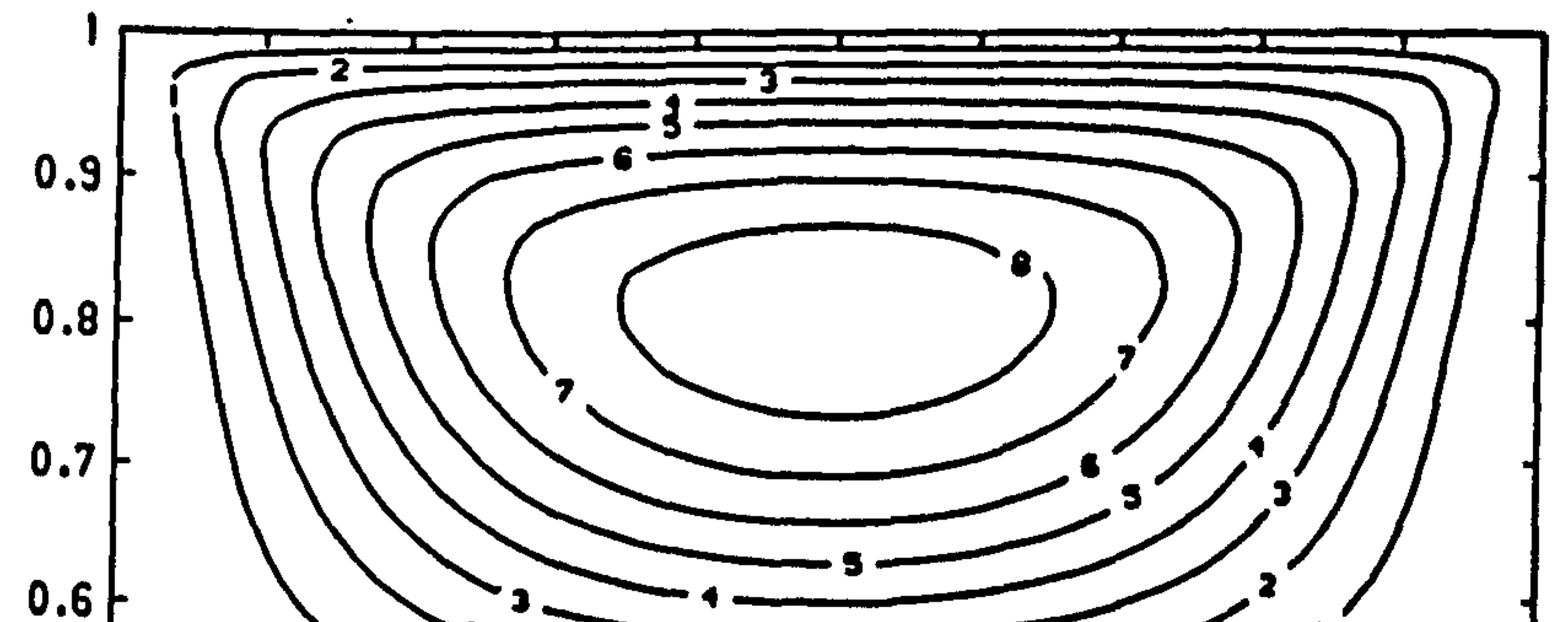

CONTOUR KEY	
1	-0.0100
2	-0.0200
3	-0.0300
4	-0.0400
5	-0.0500
6	-0.0600
7	-0.0700
8	-0.0800
9	-0.0900
10	-0.1000
11	0.0100
12	0.0200
13	0.0300
14	0.0400
15	0.0500
16	0.0600
17	0.0700
18	0.0800
19	0.0900
20	0.1000

Figure (5.20) Streamlines of a Newtonian fluid at Re=1, vb=vt=1.

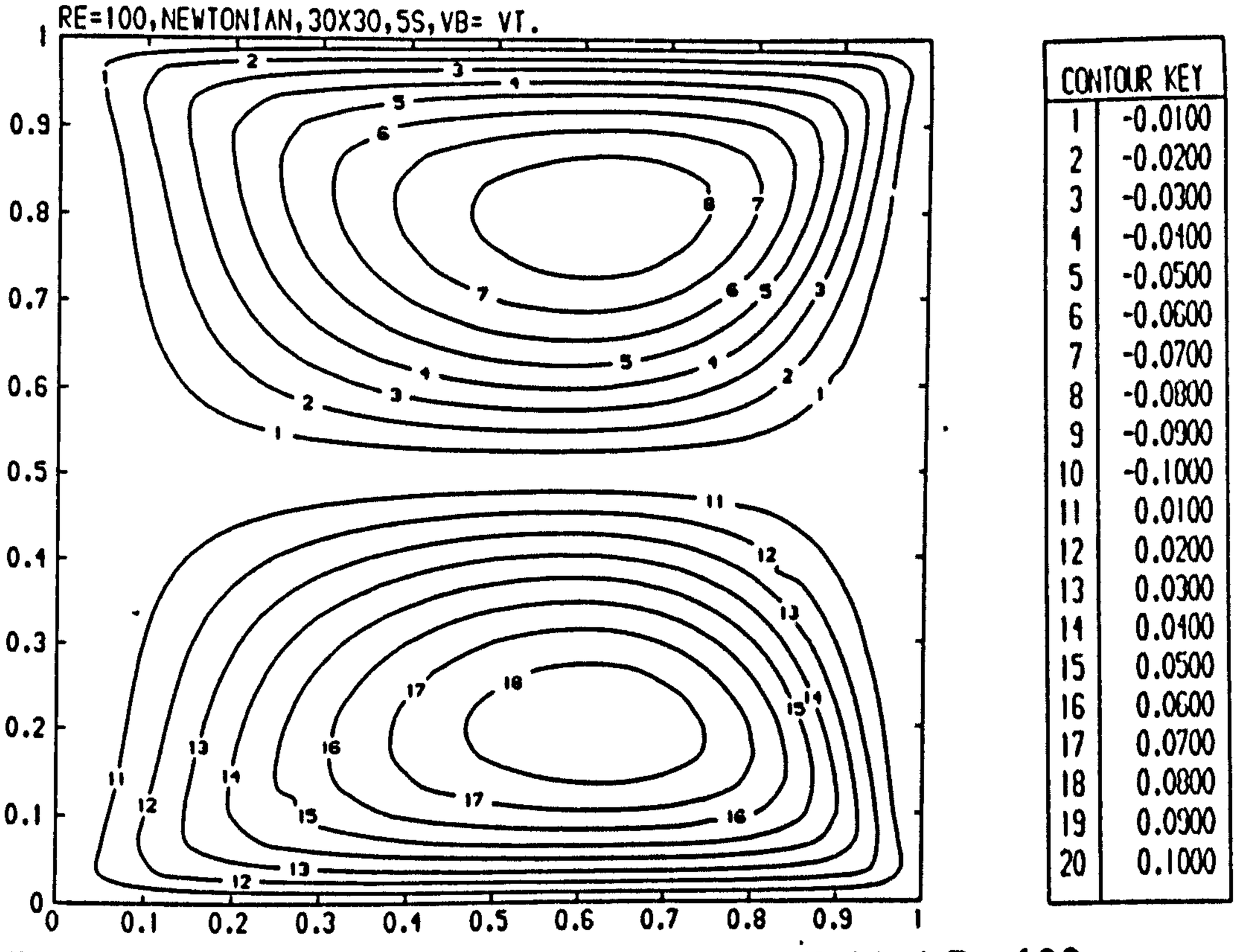

Figure (5.21) Streamlines of a Newtonian fluid at Re=100, Vb=Vt=1.

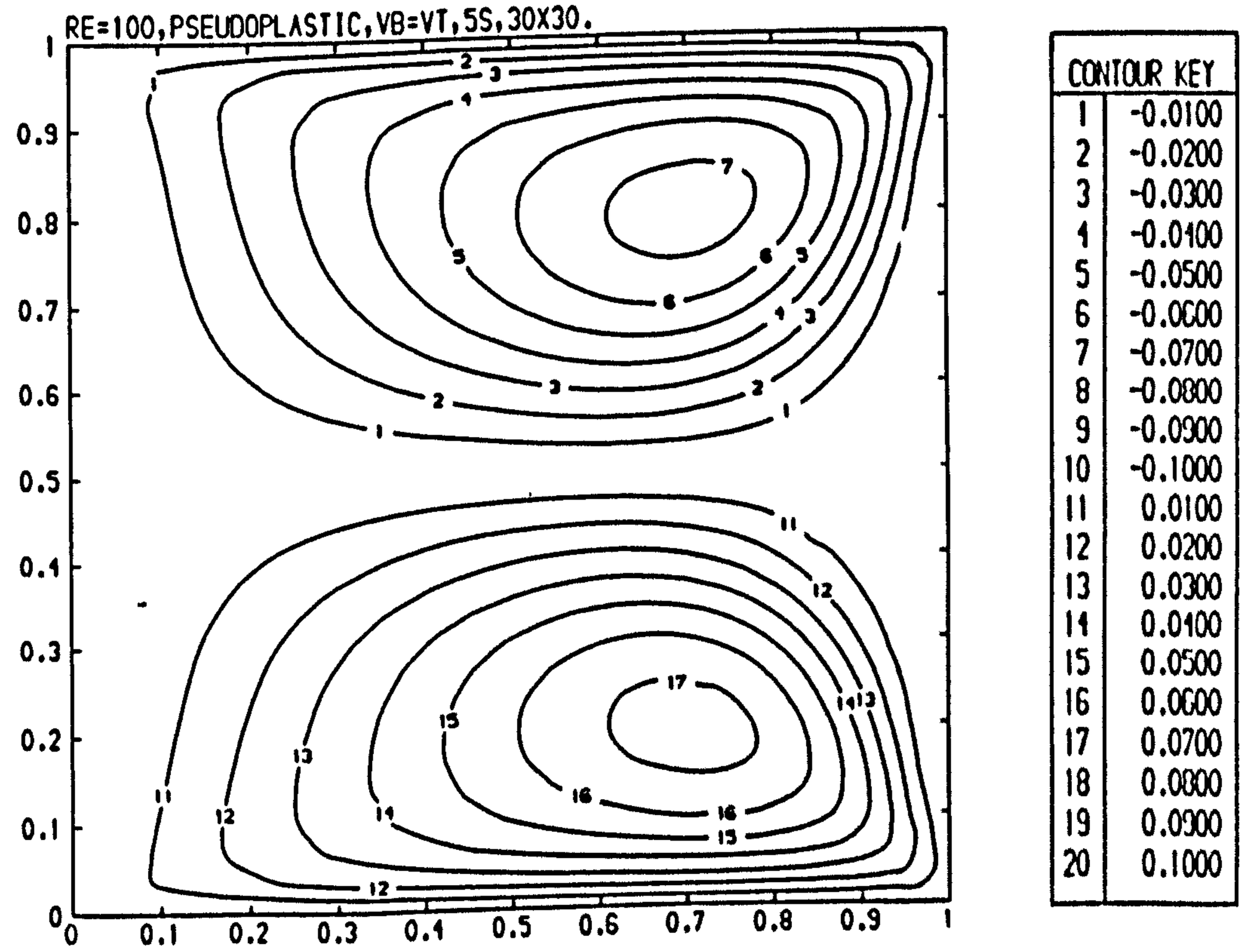

Figure (5.22) Streamlines of a pseudoplastic fluid at Re=100, Vb=Vt=1.

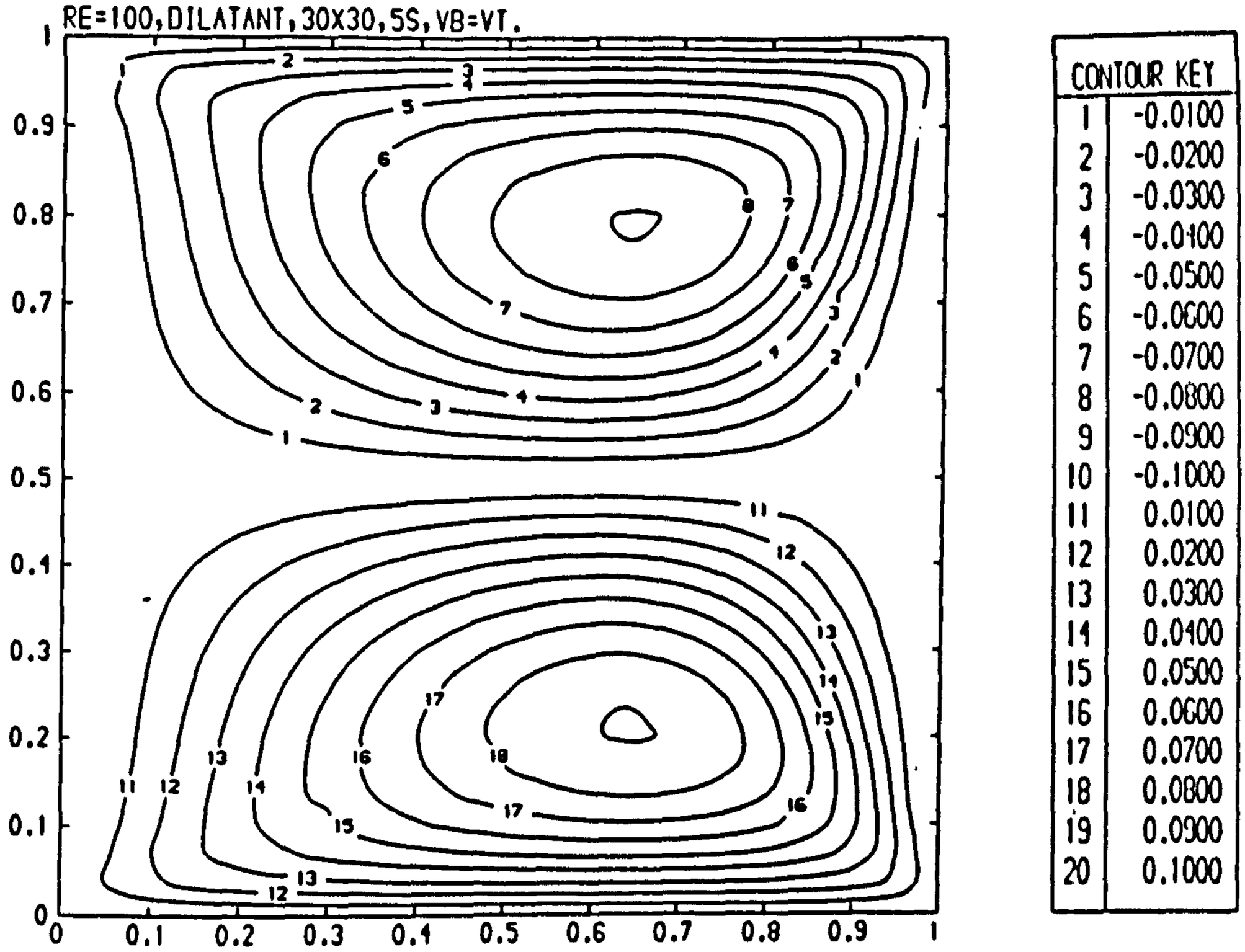

Figure (5.23) Streamlines of a dilatant fluid at Re=100, vb=vt=1.

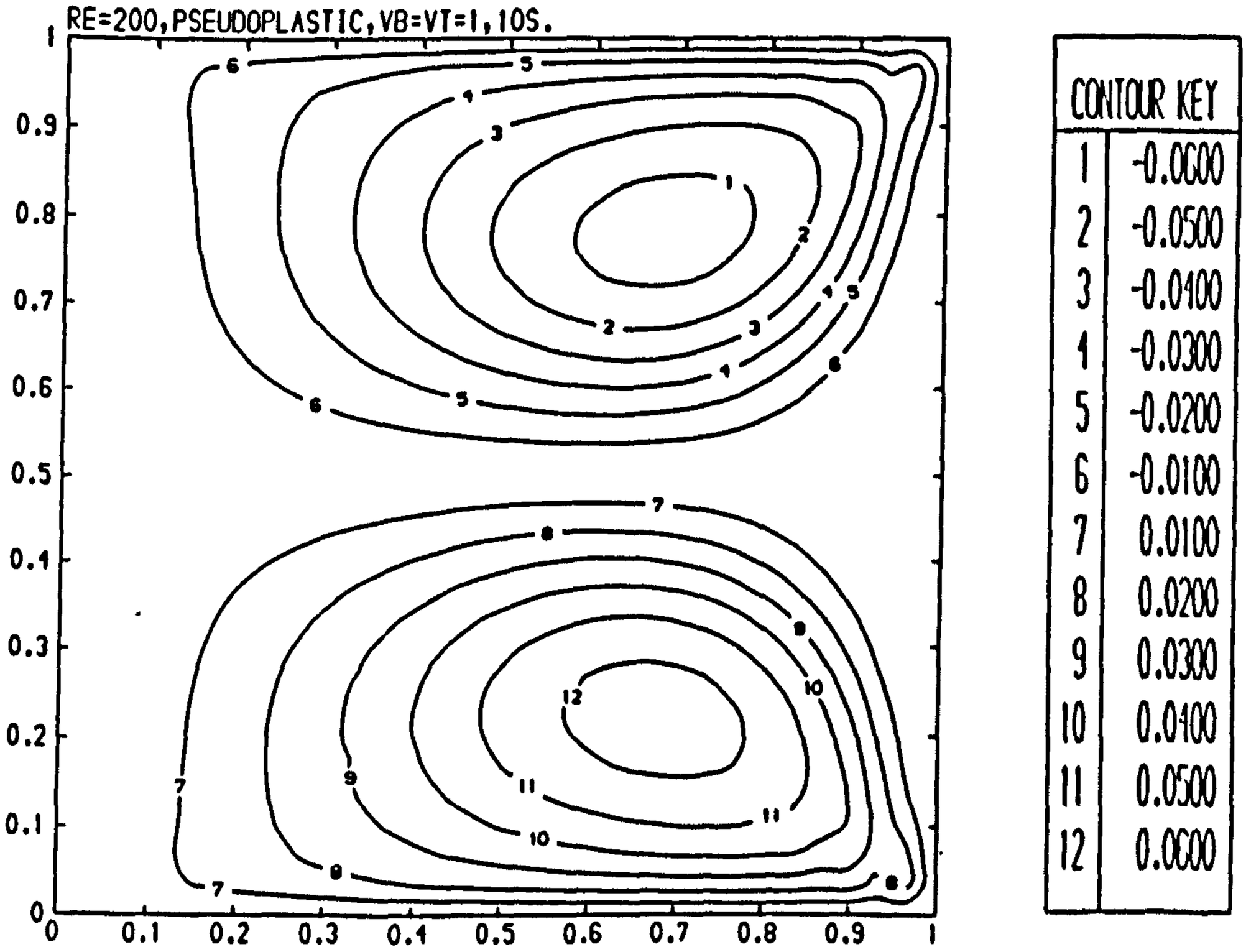

Figure (5.24) Streamlines of a Newtonian fluid at Re=200, vb=vt=1.

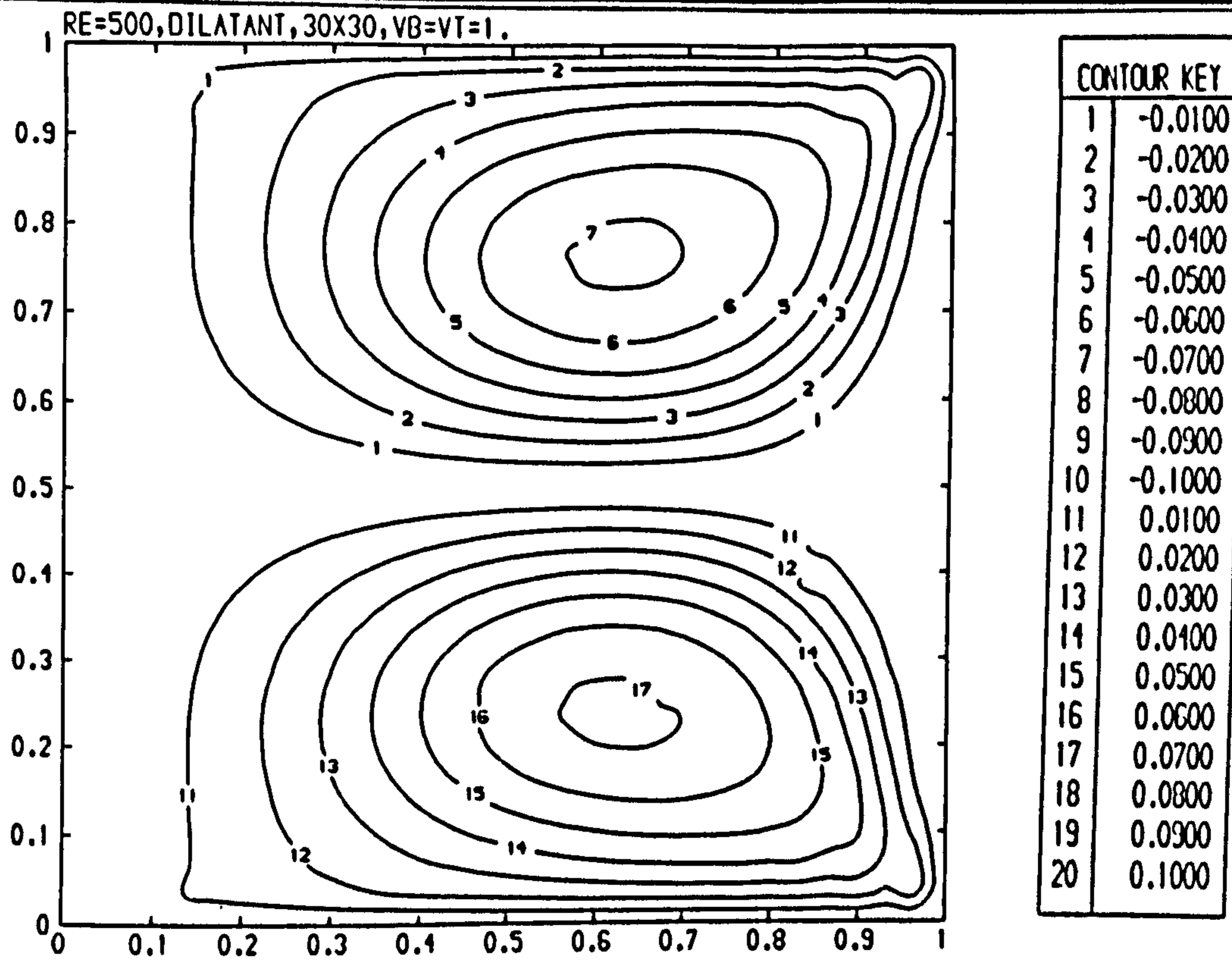

Figure (5.25) Streamlines of a dilatant fluid at Re=500, vb = vt= 1.

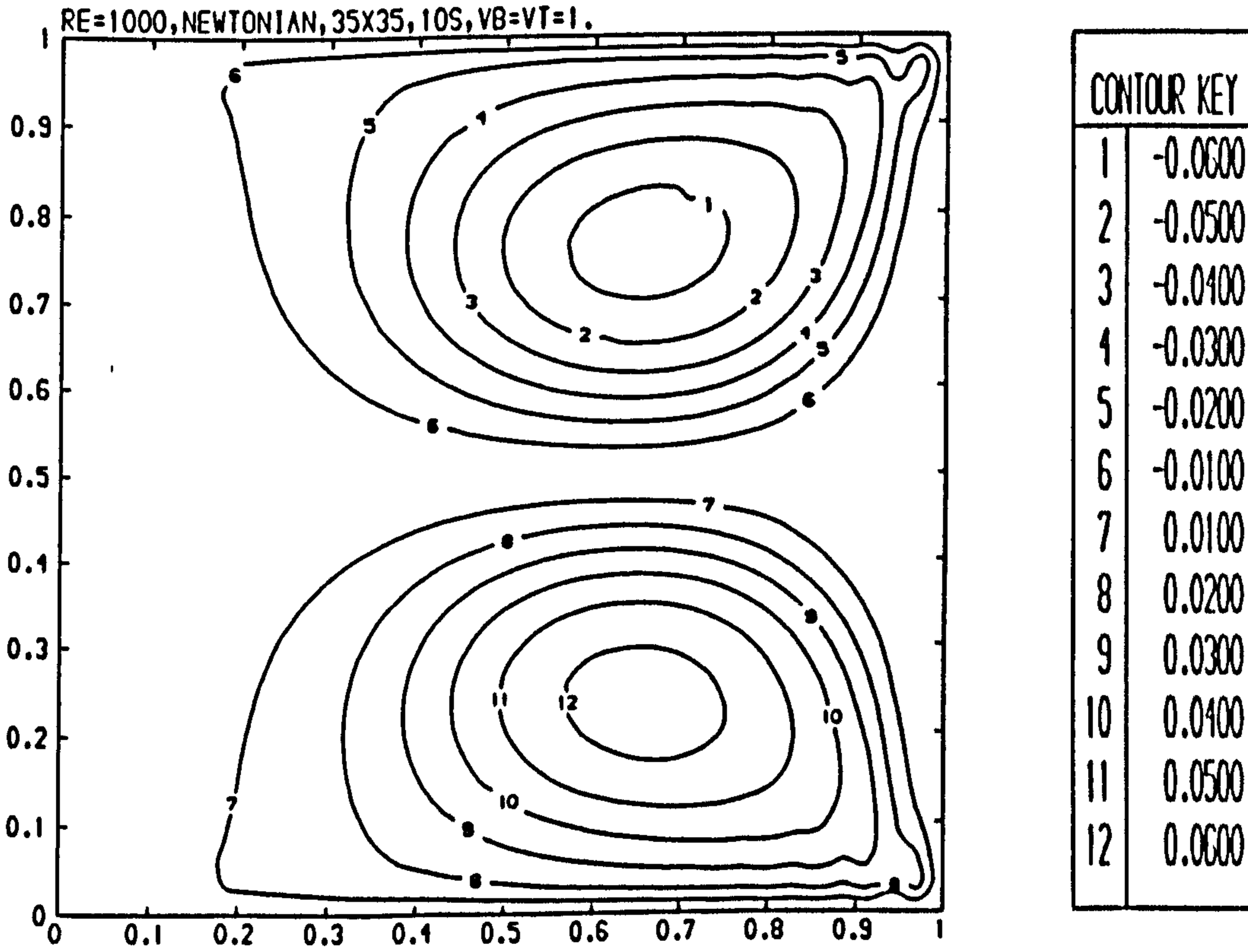

Figure (5.26) Streamlines of a Newtonian fluid at Re=1000, vb=vt.

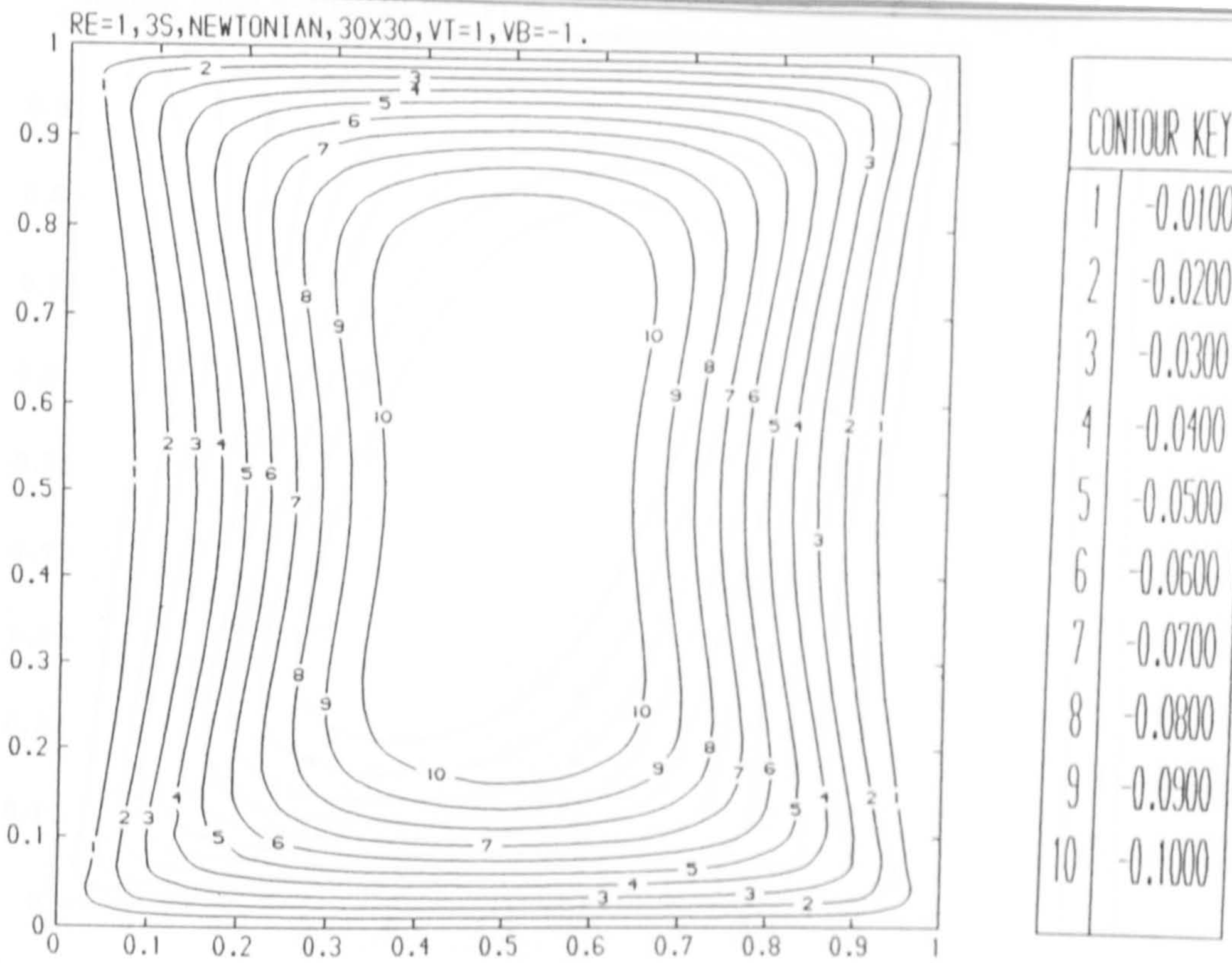

Figure (5.27) Streamlines of a Newtonian fluid at Re=1, vb= -vt= -1.

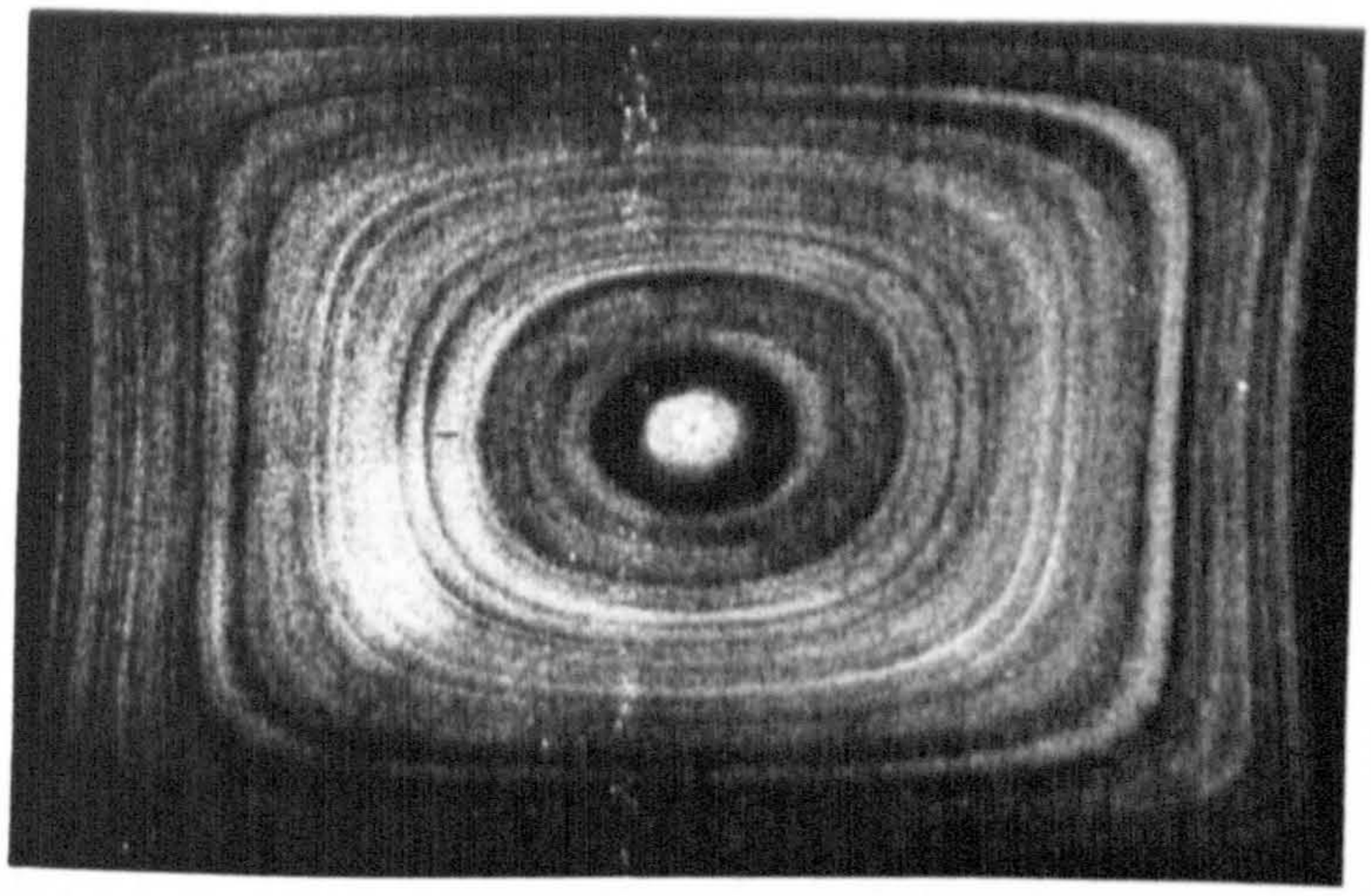

Figure (5.28) Experimental streamlines at Re=1.7 by Ottino[80], vb= -vt= -1.

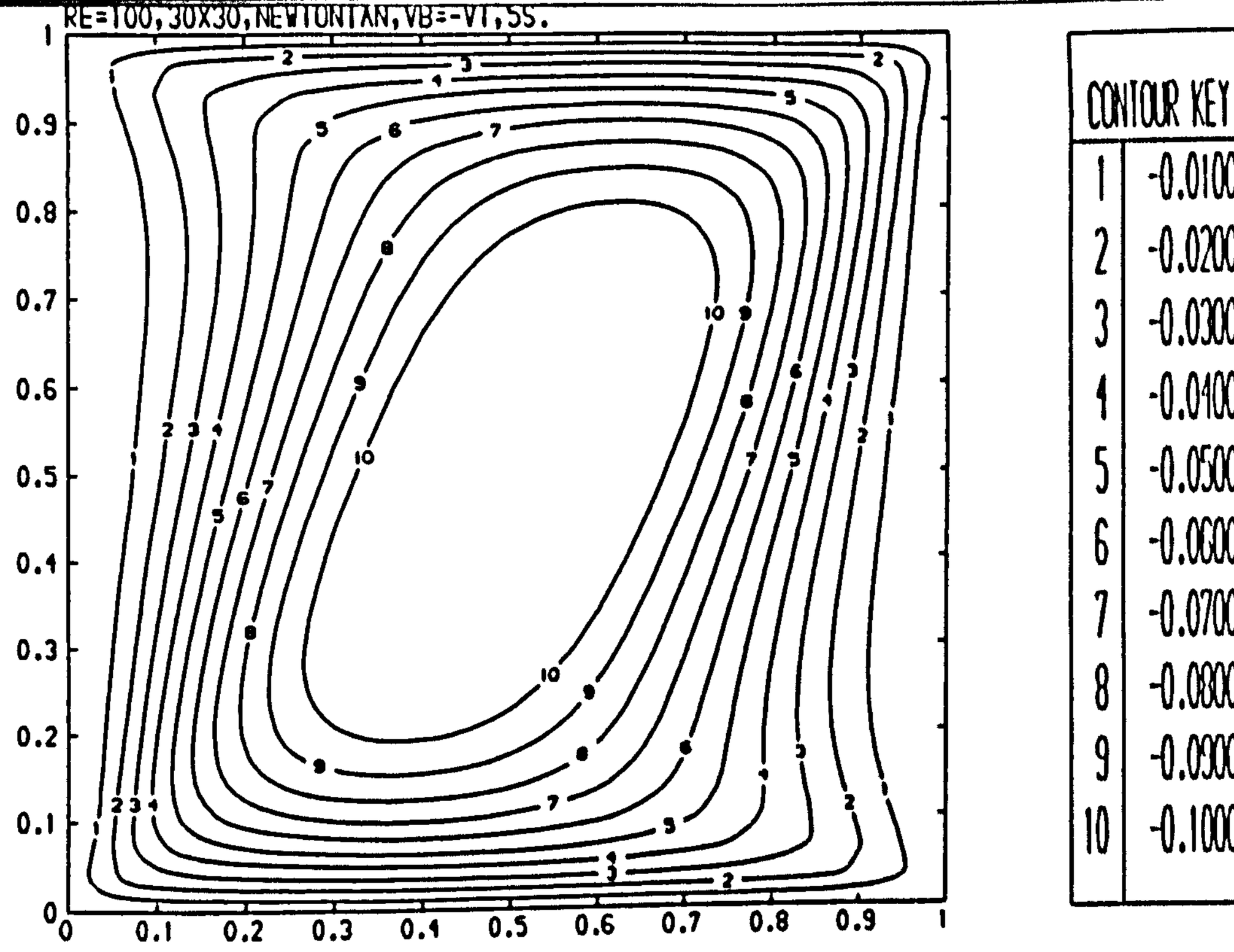

Figure (5.29) Streamlines of a Newtonian fluid at Re=100, Vb= -vt= -1

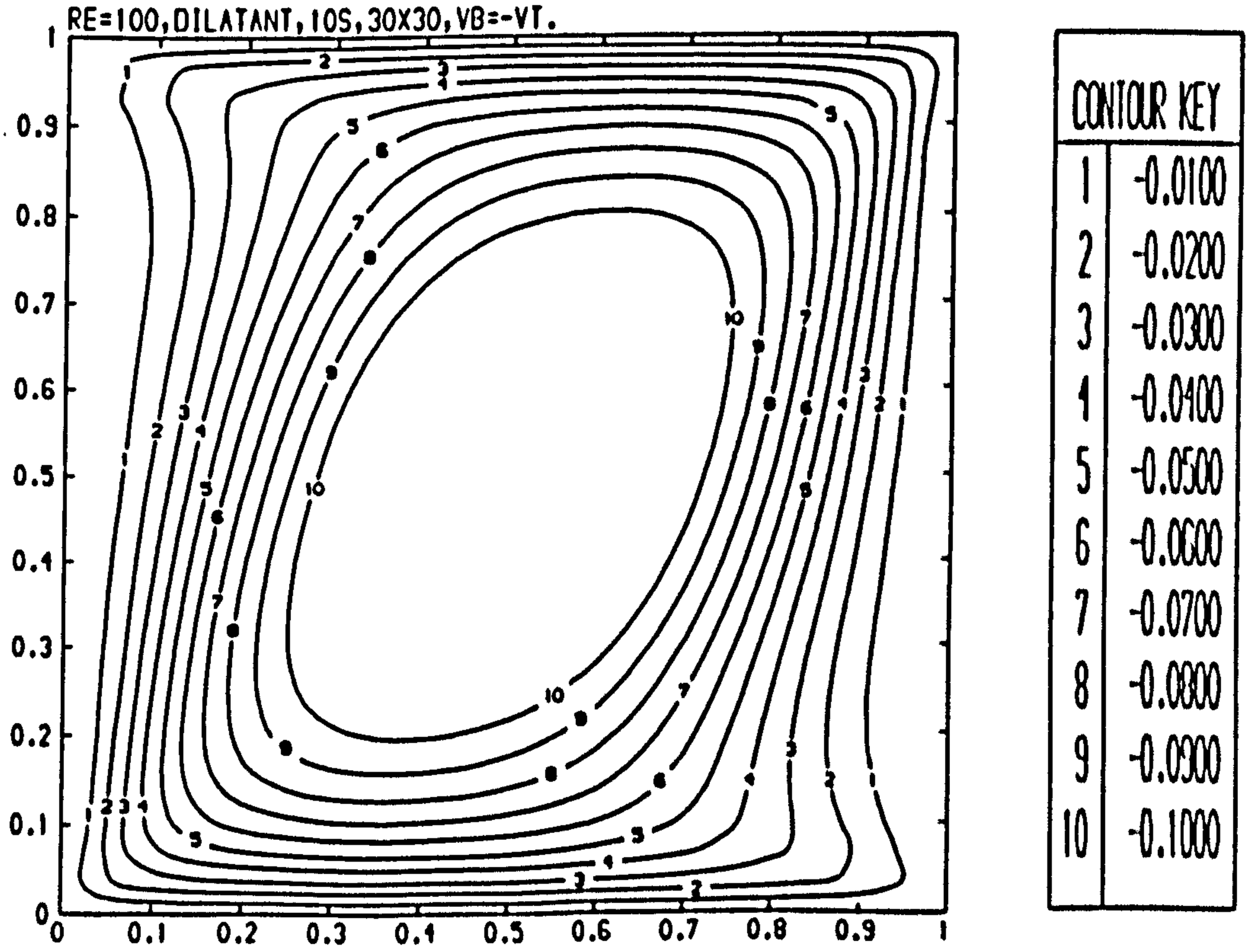

Figure (5.30) Streamlines of a dilatant fluid at Re=100, Vb= -vt= -1.

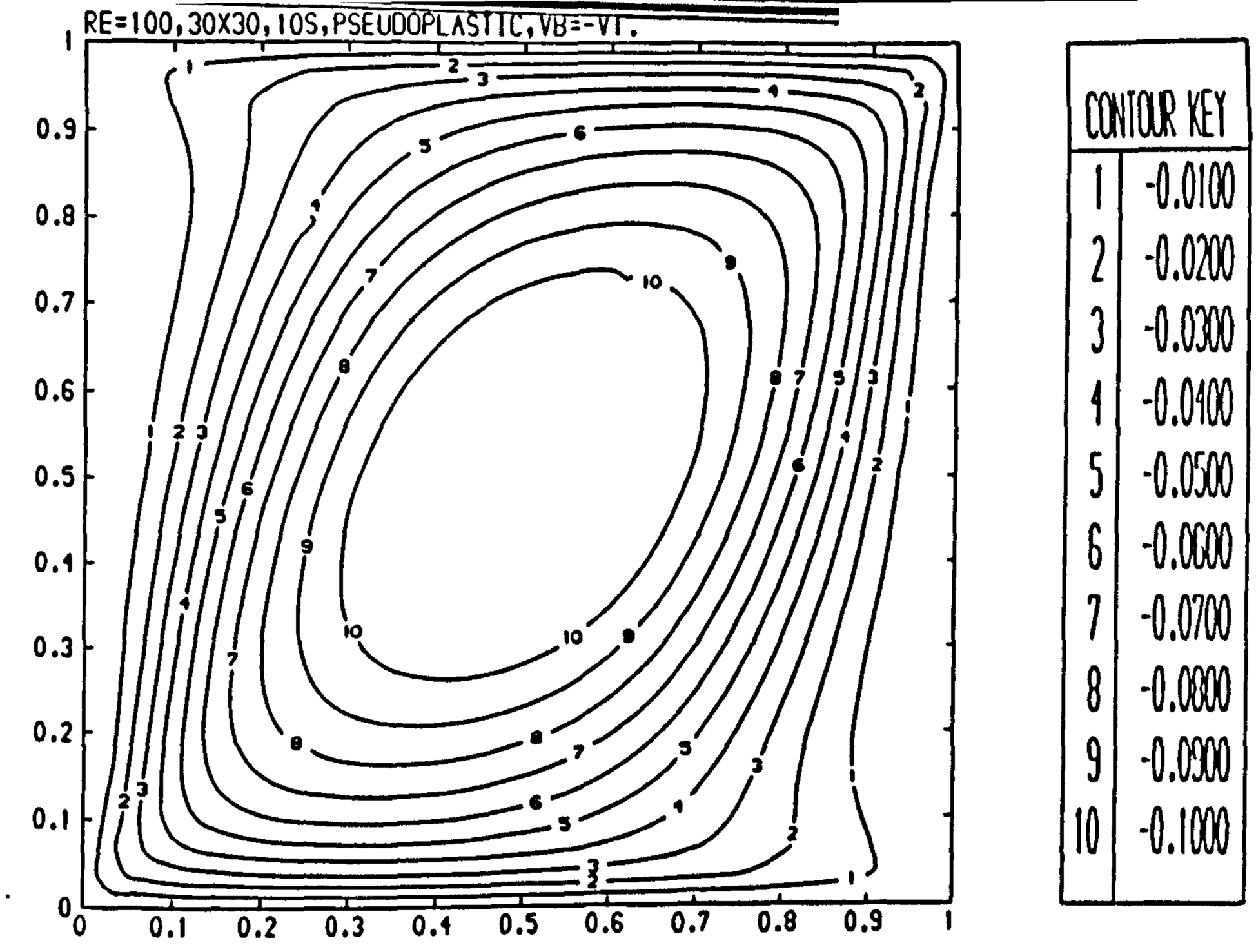

Figure (5.31) Streamlines of a pseudoplastic fluid at Re=100, Vb= -vt= -1.

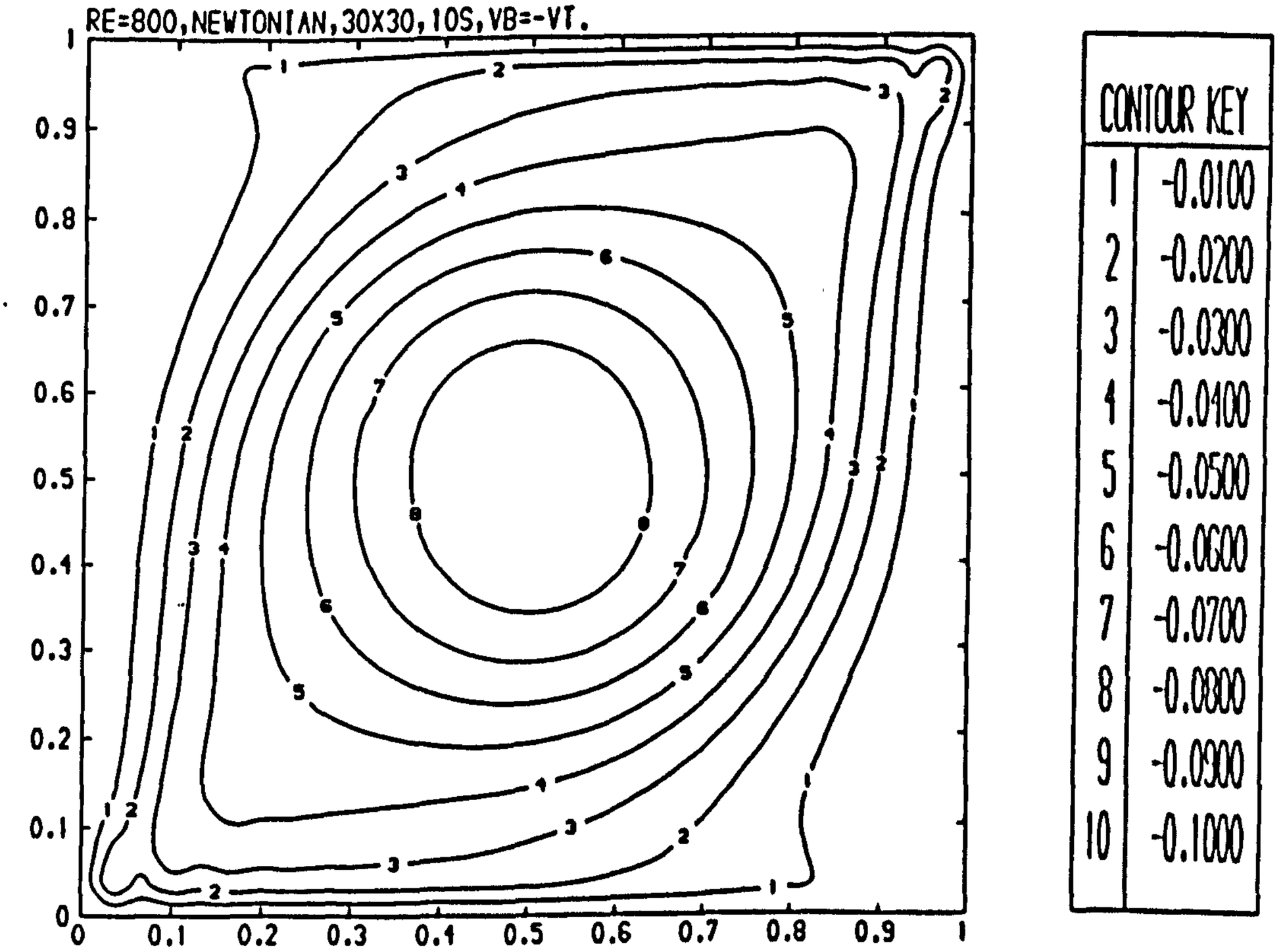

Figure (5.32) Streamlines of a Newtonian fluid at Re=800, Vb= -vt= -1.

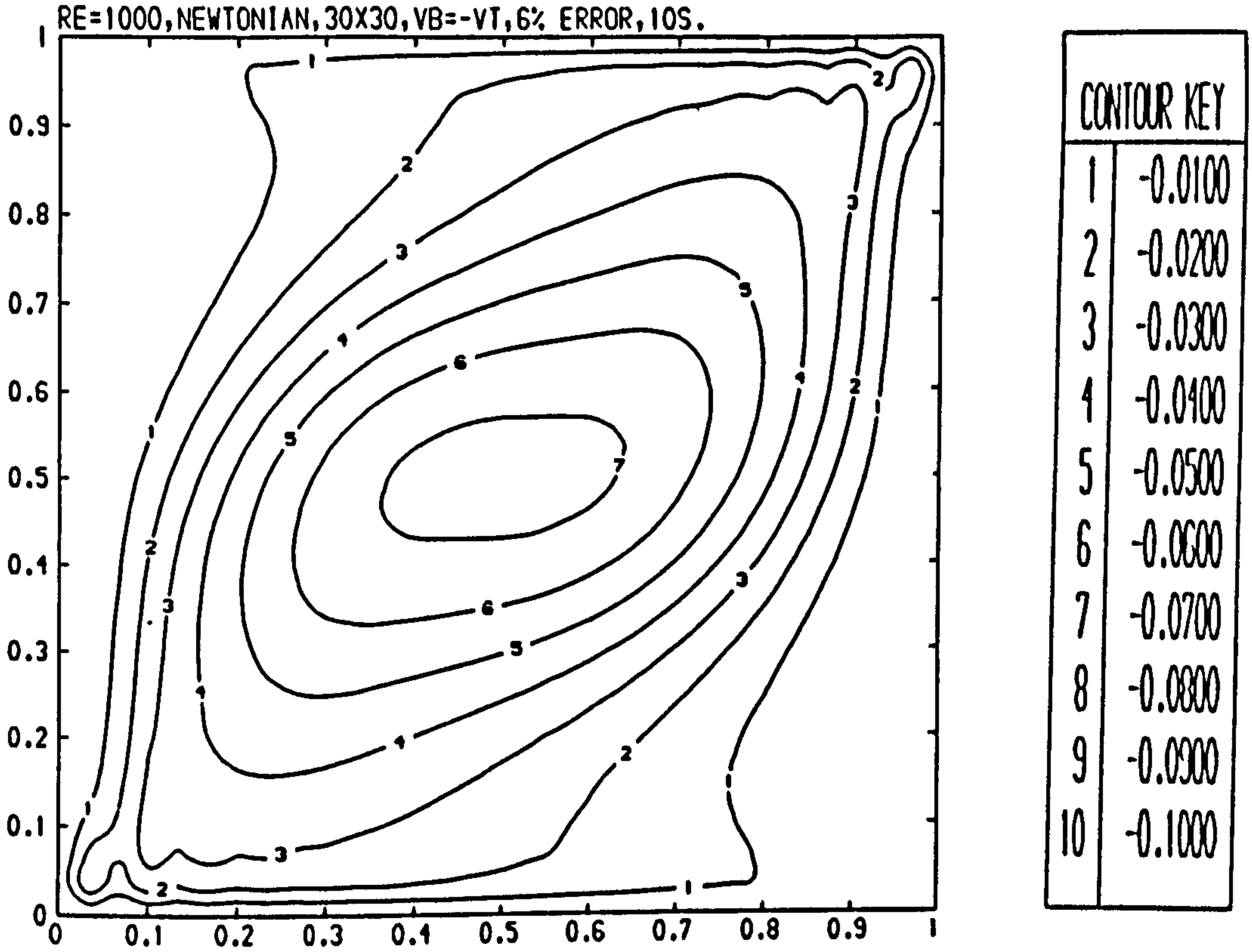

Figure (5.33) Streamlines of a Newtonian fluid at Re=1000, Vb= -vt= -1.

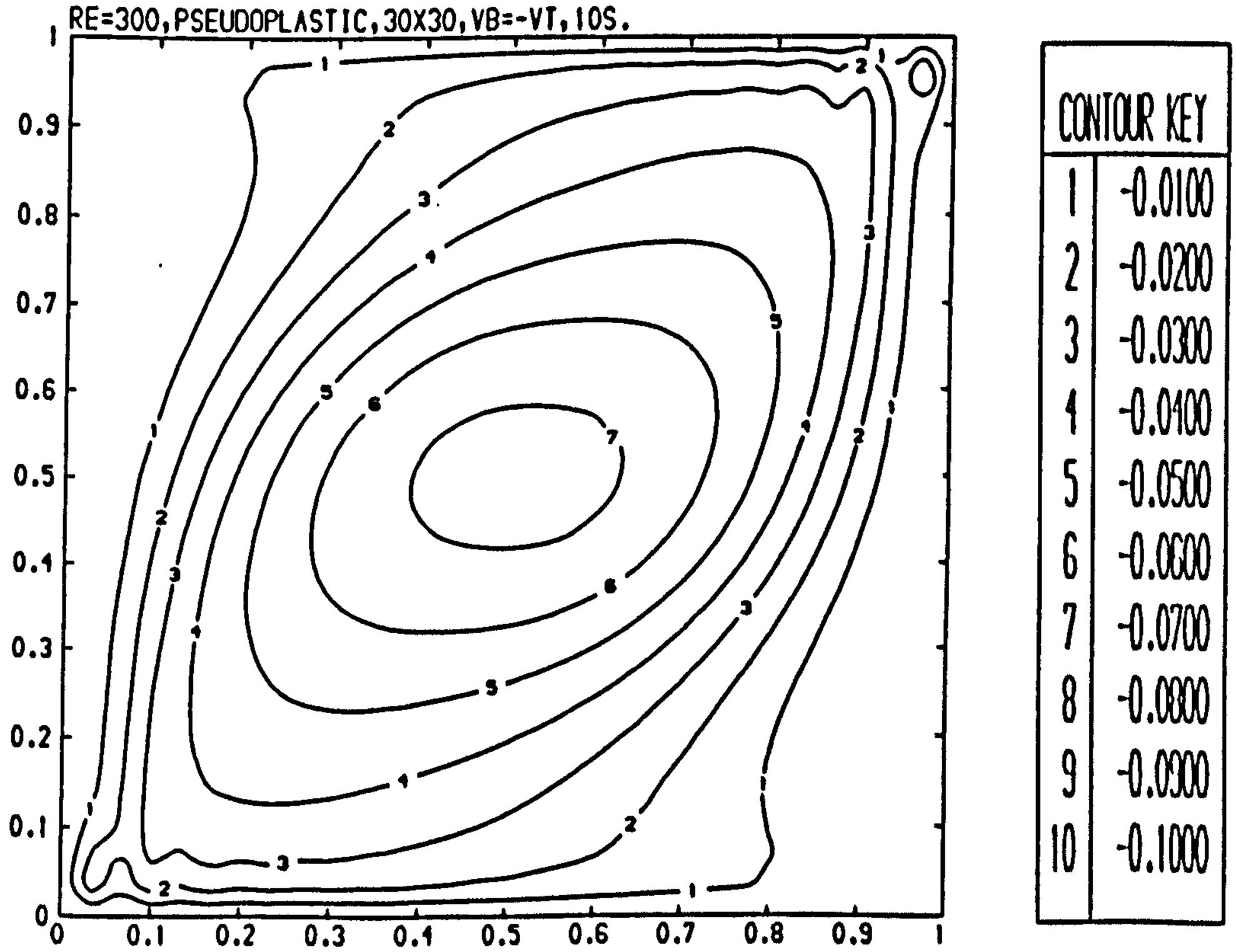

Figure (5.34) Streamlines of a pseudoplastic fluid at Re=300, Vb= -vt= -1.

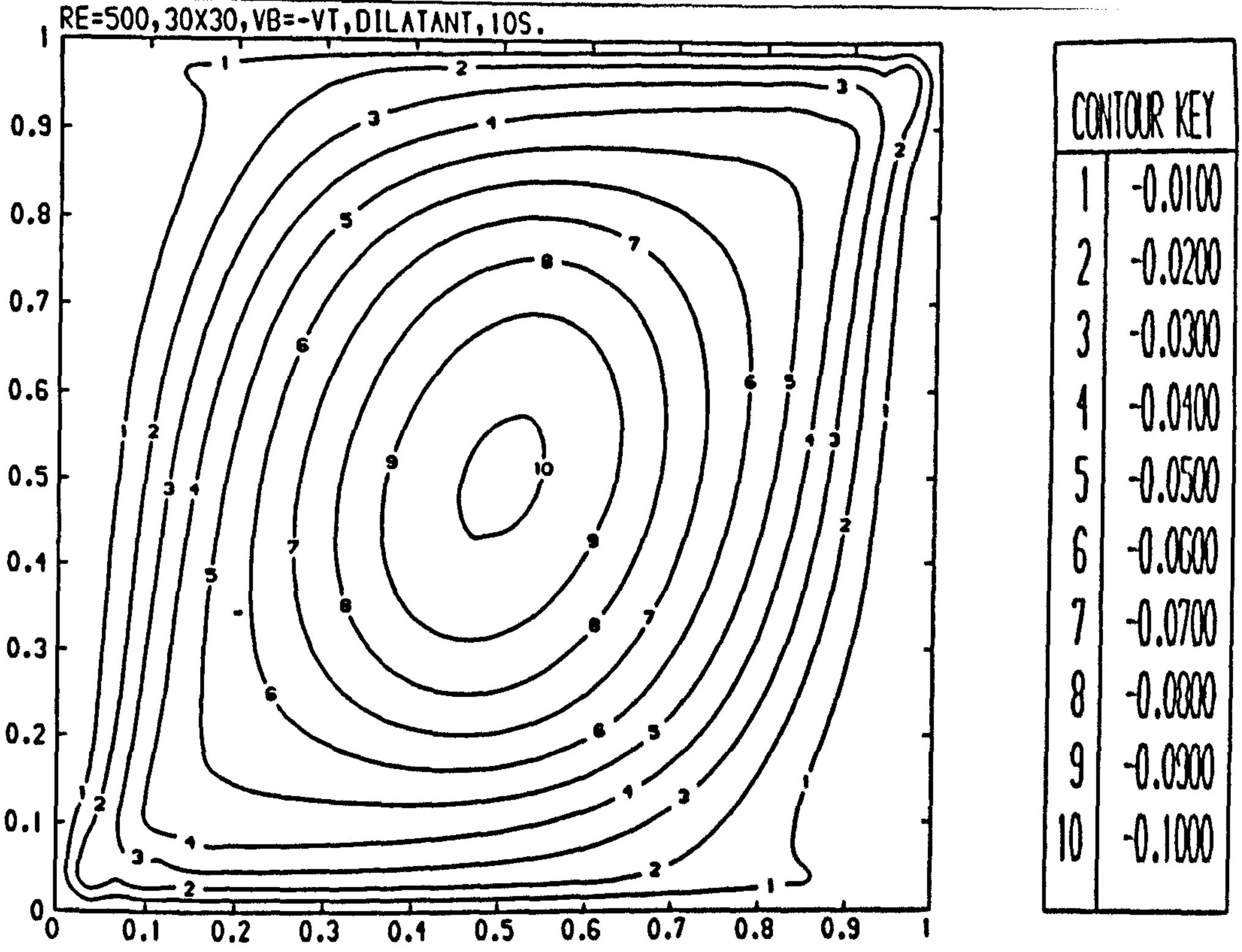

Figure (5.35) Streamlines of a dilatant fluid at Re=500, Vb= -vt= -1.

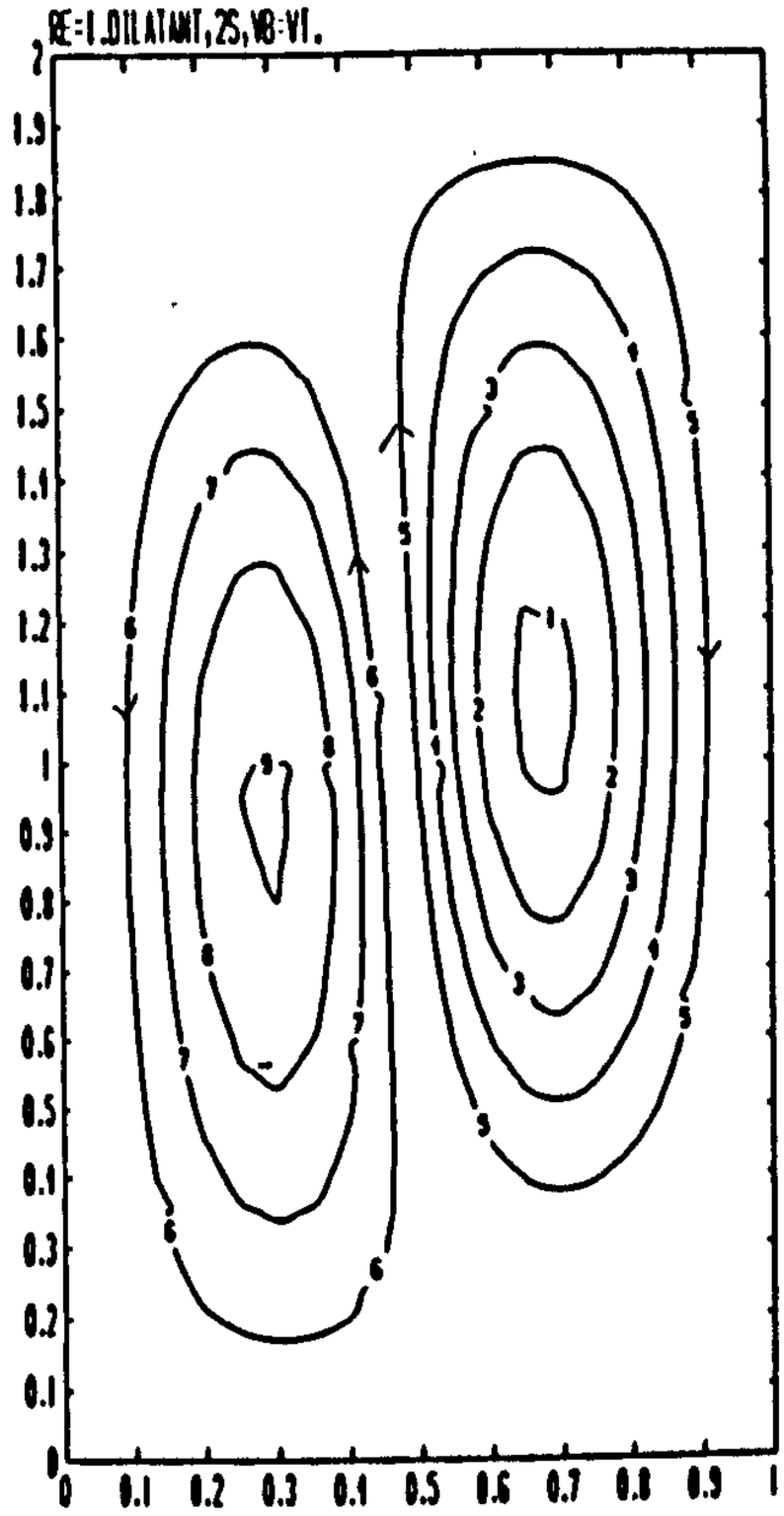

CONTOUR KEY	
1	-0.5000
2	-0.4000
3	-0.3000
4	-0.2000
5	-0.1000
6	0.1000
7	0.2000
8	0.3000
9	0.4000

Figure (5.36)

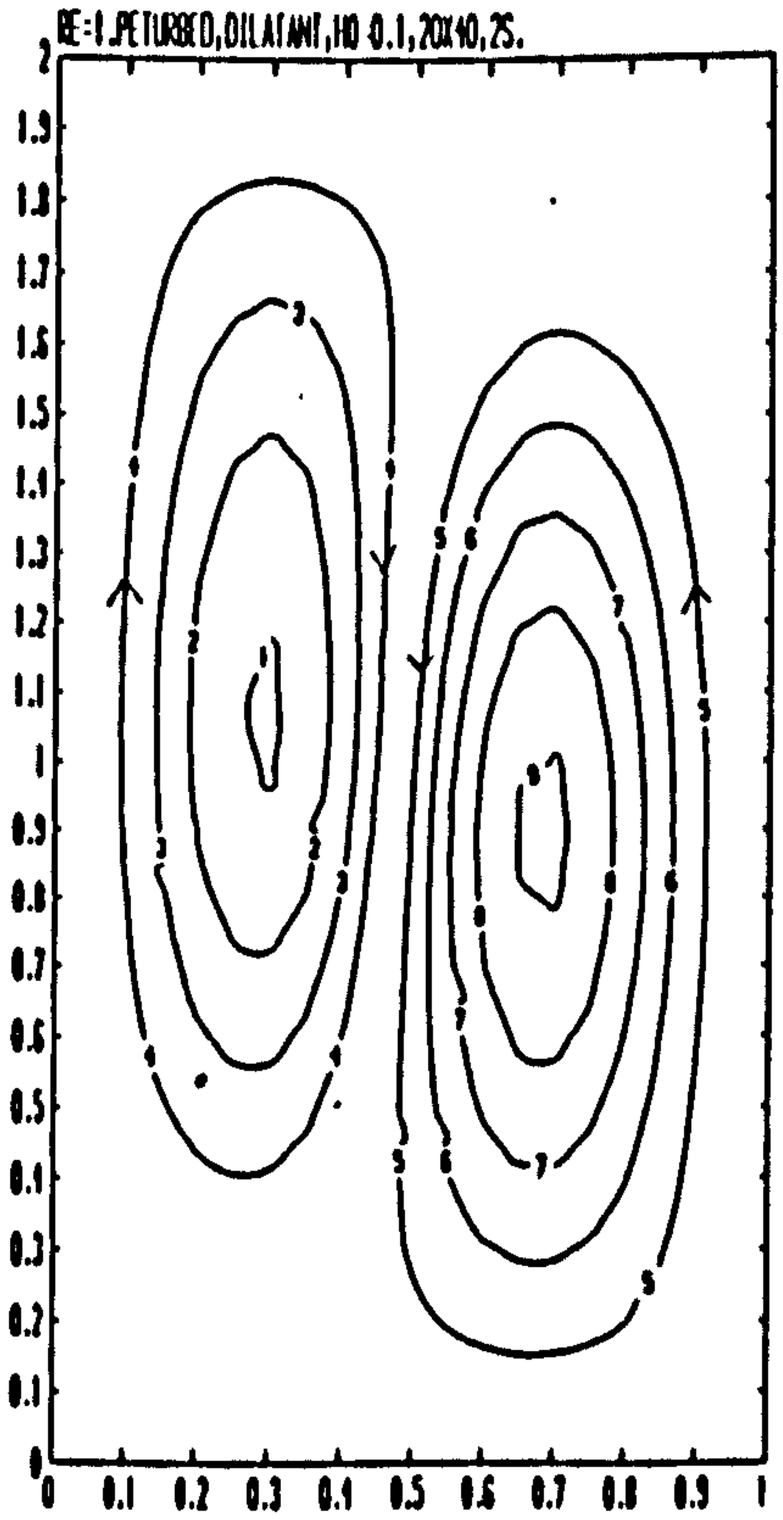

CONTOUR KEY	
1	-0.4000
2	-0.3000
3	-0.2000
4	-0.1000
5	0.1000
6	0.2000
7	0.3000
8	0.4000
9	0.5000

Figure (5.37)

Steady streamlines of a time dependent dilatant fluid at Re=1 in cavities of aspect ratio 2 with vb=vt=1.

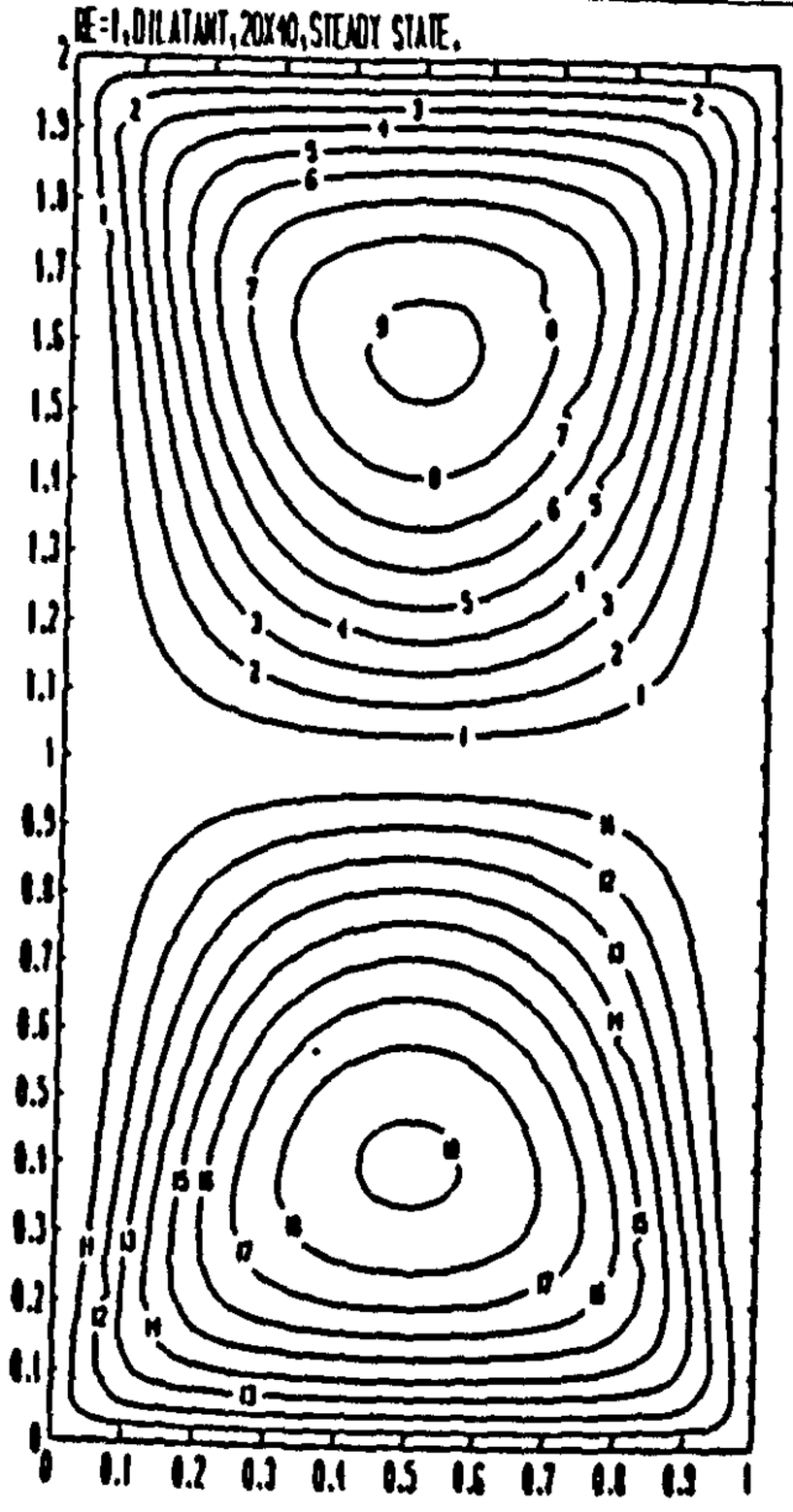

CONTOUR KEY	
1	-0.0100
2	-0.0200
3	-0.0300
4	-0.0400
5	-0.0500
6	-0.0600
7	-0.0700
8	-0.0800
9	-0.0900
10	-0.1000
11	0.0100
12	0.0200
13	0.0300
14	0.0400
15	0.0500
16	0.0600
17	0.0700
18	0.0800
19	0.0900
20	0.1000

Figure (5.38) Steady state streamlines of a dilatant fluid at Re=1 in a cavity of aspect ratio 2 with vb=vt=1.

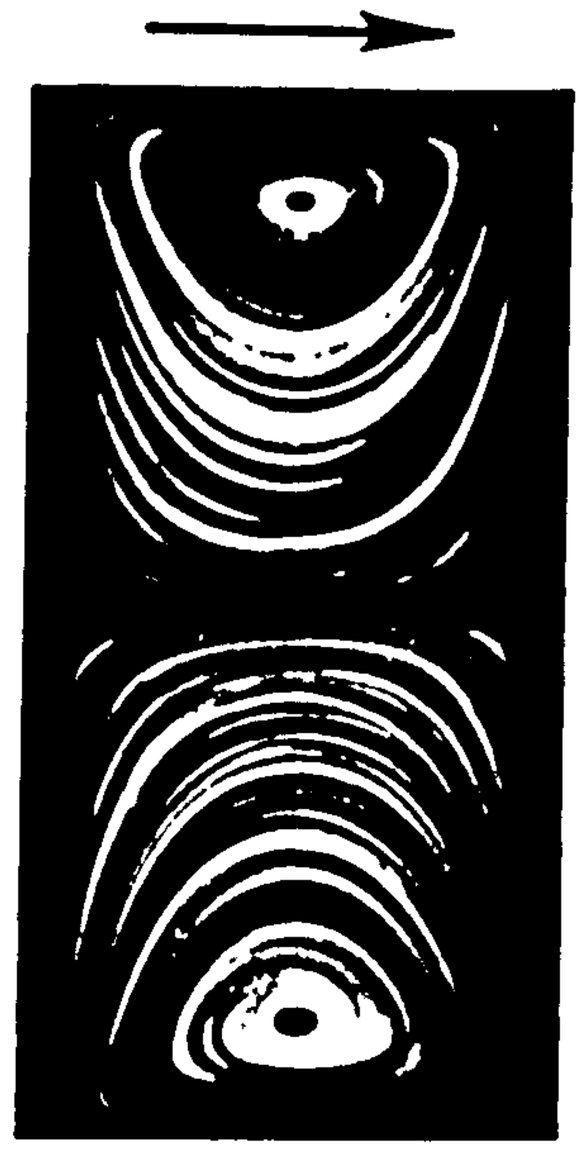

Figure (5.39) Experimental streamlines produced by Jana et al [48], at Re=1,vb=vt=1, cavity's aspect ratio =2.

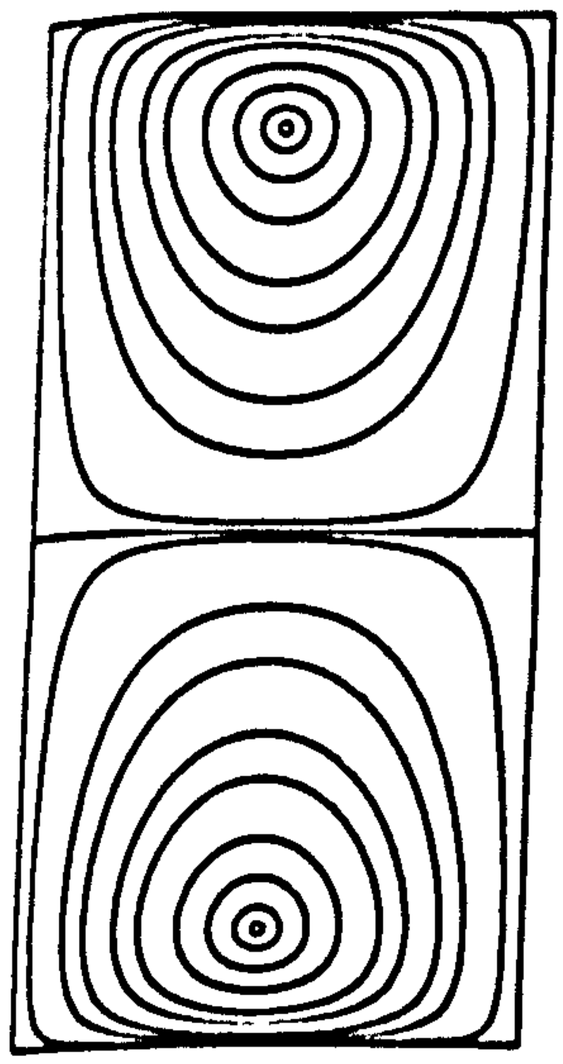

Figure (5.40) Theoretical streamlines produced by Jana et al [48], at Re=1,vb=vt=1, cavity's aspect ratio =2.

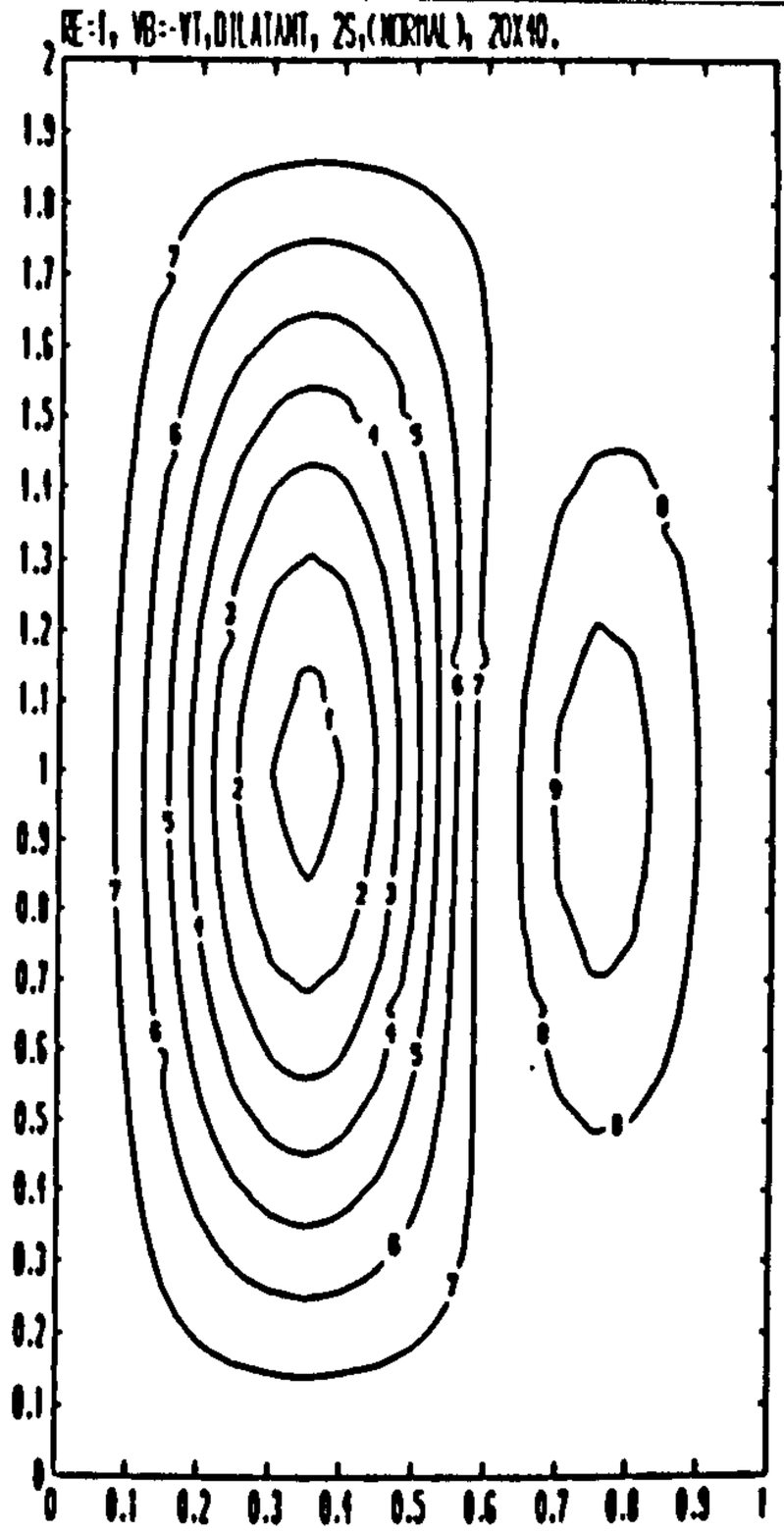

CONTOUR KEY	
1	-0.7000
2	-0.6000
3	-0.5000
4	-0.4000
5	-0.3000
6	-0.2000
7	-0.1000
8	0.1000
9	0.2000
10	0.3000

Figure (5.41)

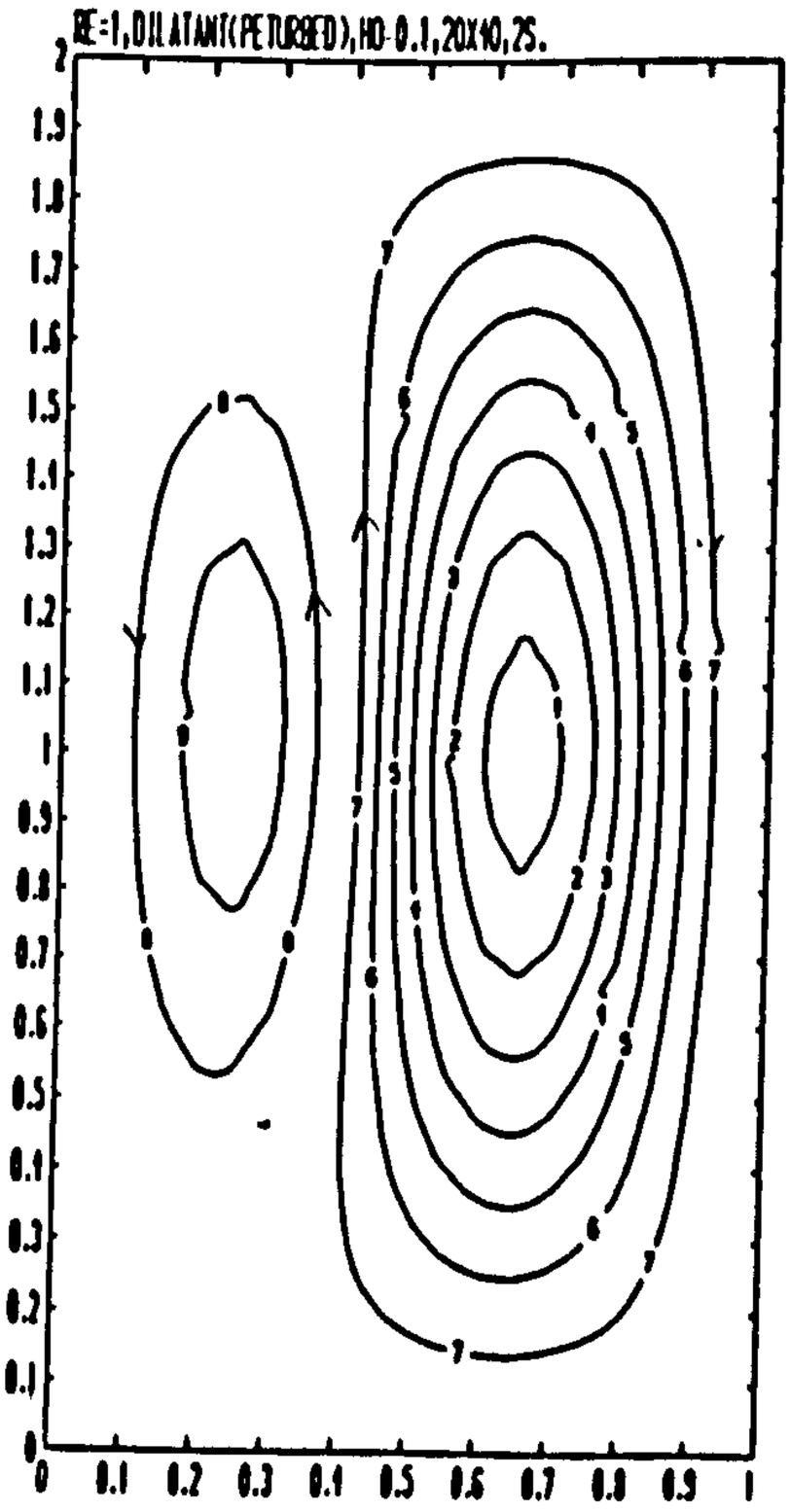

CONTOUR KEY	
1	-0.7000
2	-0.6000
3	-0.5000
4	-0.1000
5	-0.3000
6	-0.2000
7	-0.1000
8	0.1000
9	0.2000
10	0.3000

Figure (5.42)

Steady streamlines for a time dependent dilatant fluid at Re=1 vb=-vt=-1, cavity's aspect ratio =2.

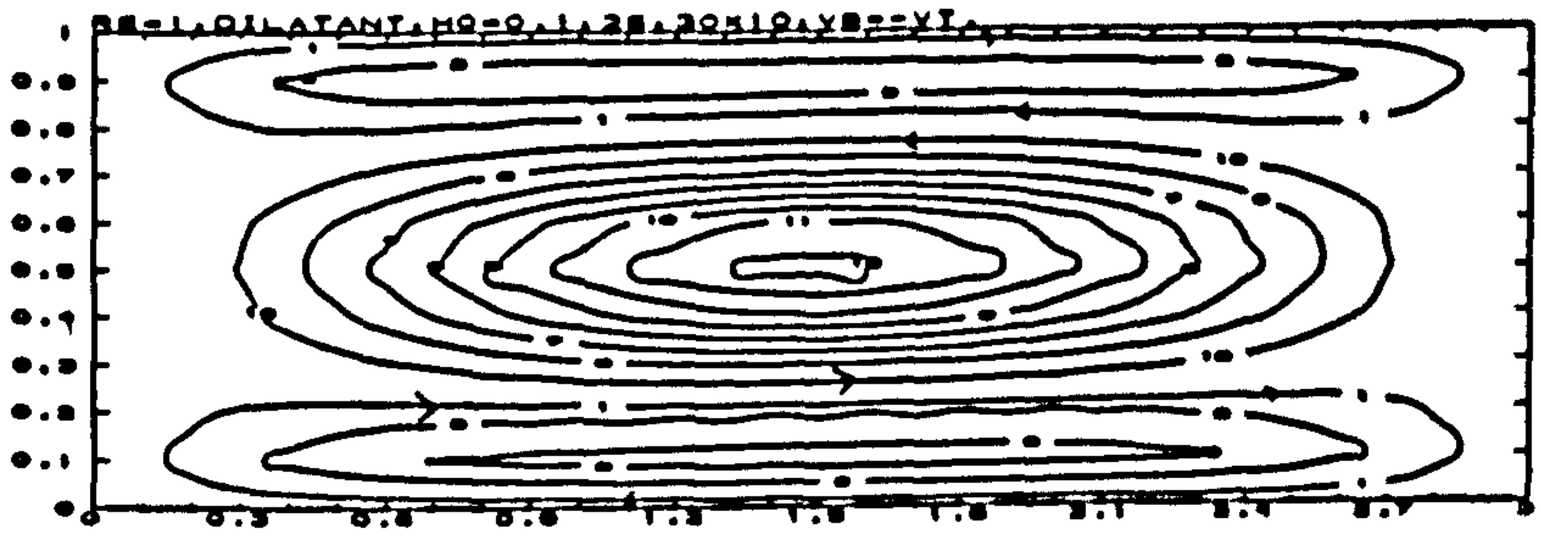

CONTOUR KEY	
1	-0.0100
2	-0.0300
3	-0.0500
4	-0.0700
5	-0.0900
6	0.1000
7	0.1500
8	0.2000
9	0.2500
10	0.3000
11	0.3500
12	0.4000
13	0.0500

Figure (5.43) Steady streamlines for a time dependent dilatant fluid at Re=1, vb= -vt=-1, cavity's aspect ratio=0.33.

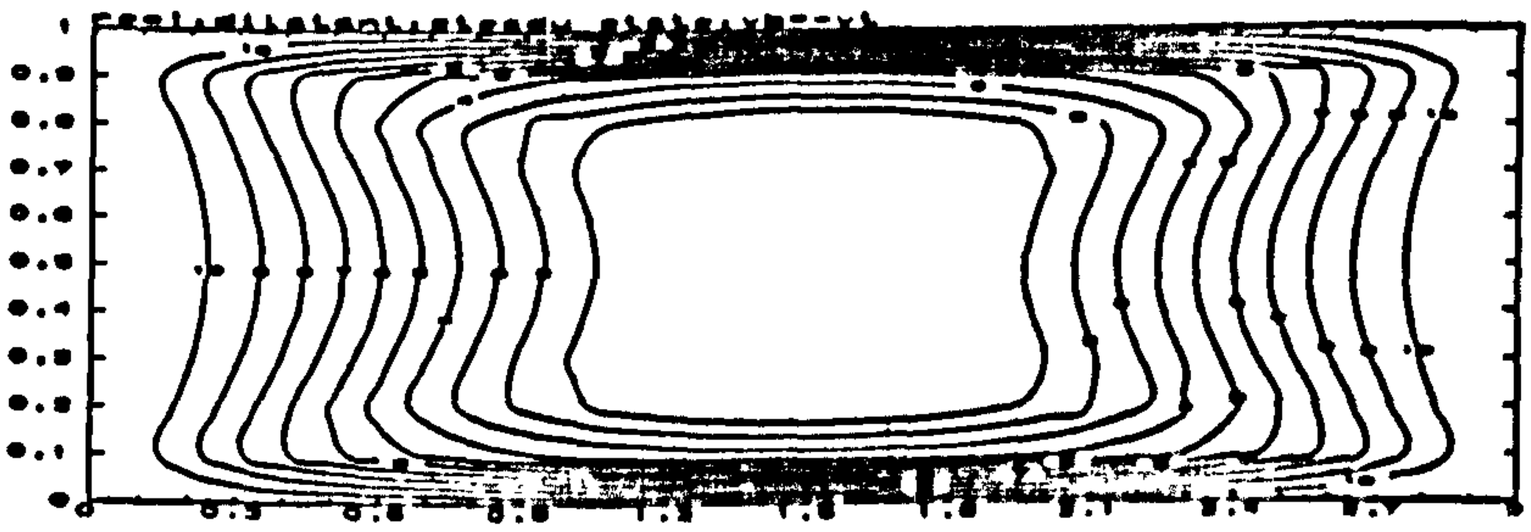

CONTOUR KEY	
1	-0.1000
2	-0.0900
3	-0.0800
4	-0.0700
5	-0.0600
6	-0.0500
7	-0.0400
8	-0.0300
9	-0.0200
10	-0.0100

Figure (5.44)

Steady state streamlines for a dilatant fluid at Re=1, vb= -vt=-1, cavity's aspect ratio=0.33.

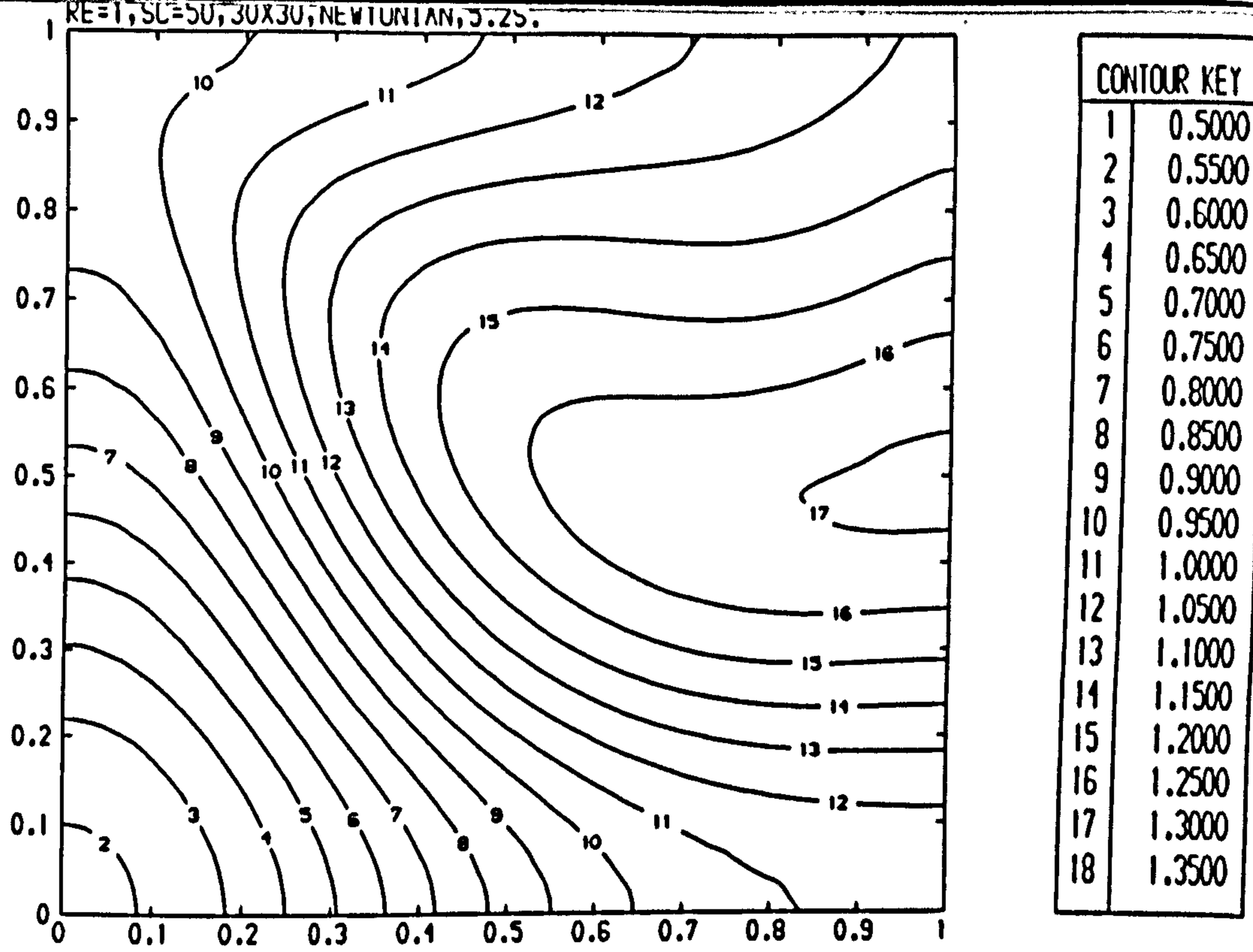

Figure (5.46) Concentration contours for a Newtonian fluid at Re=1, Sc=50, 5.2 seconds.

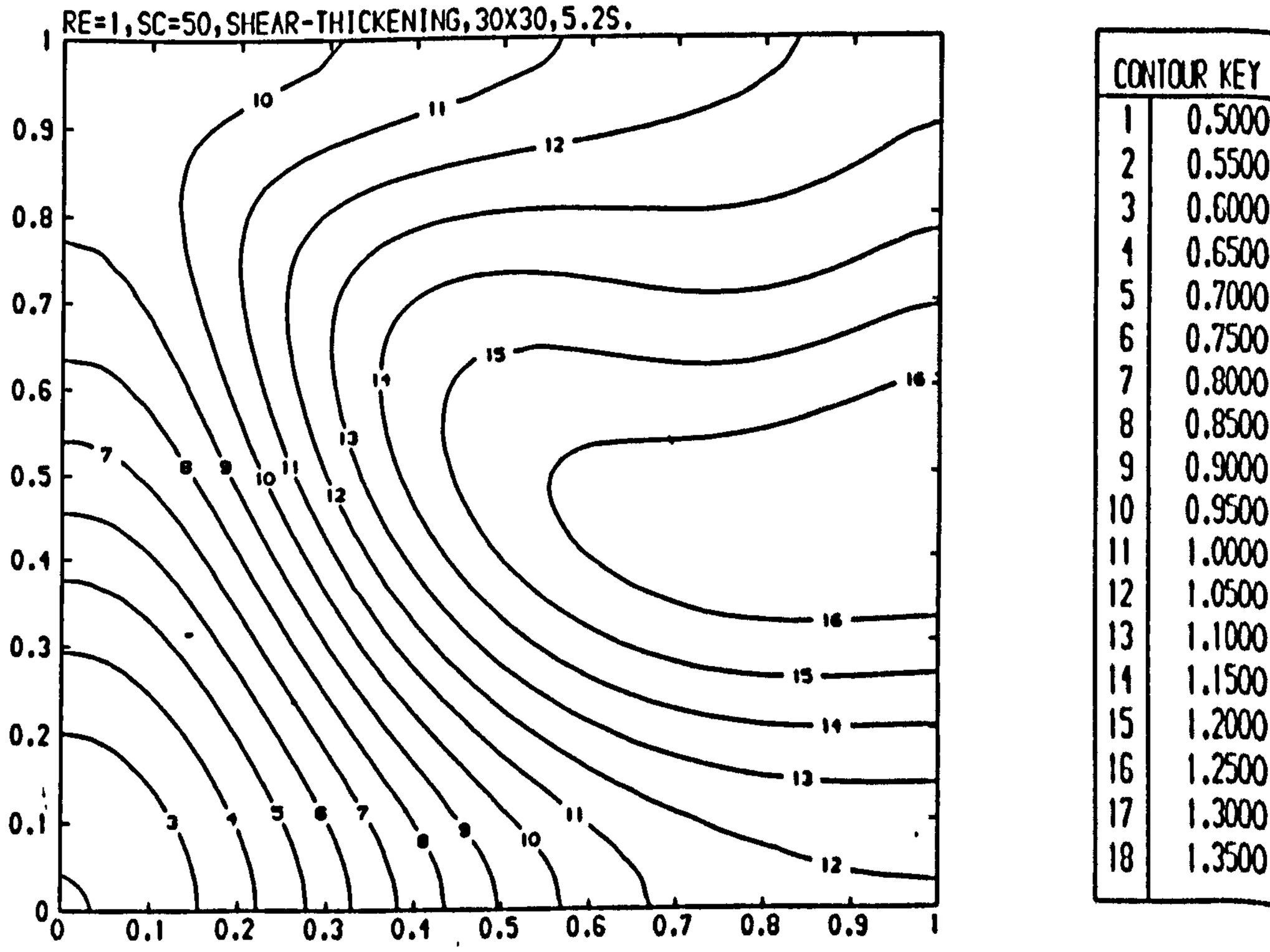

Figure (5.47) Concentration contours for a dilatant fluid at Re=1, Sc=50, 5.2 seconds.

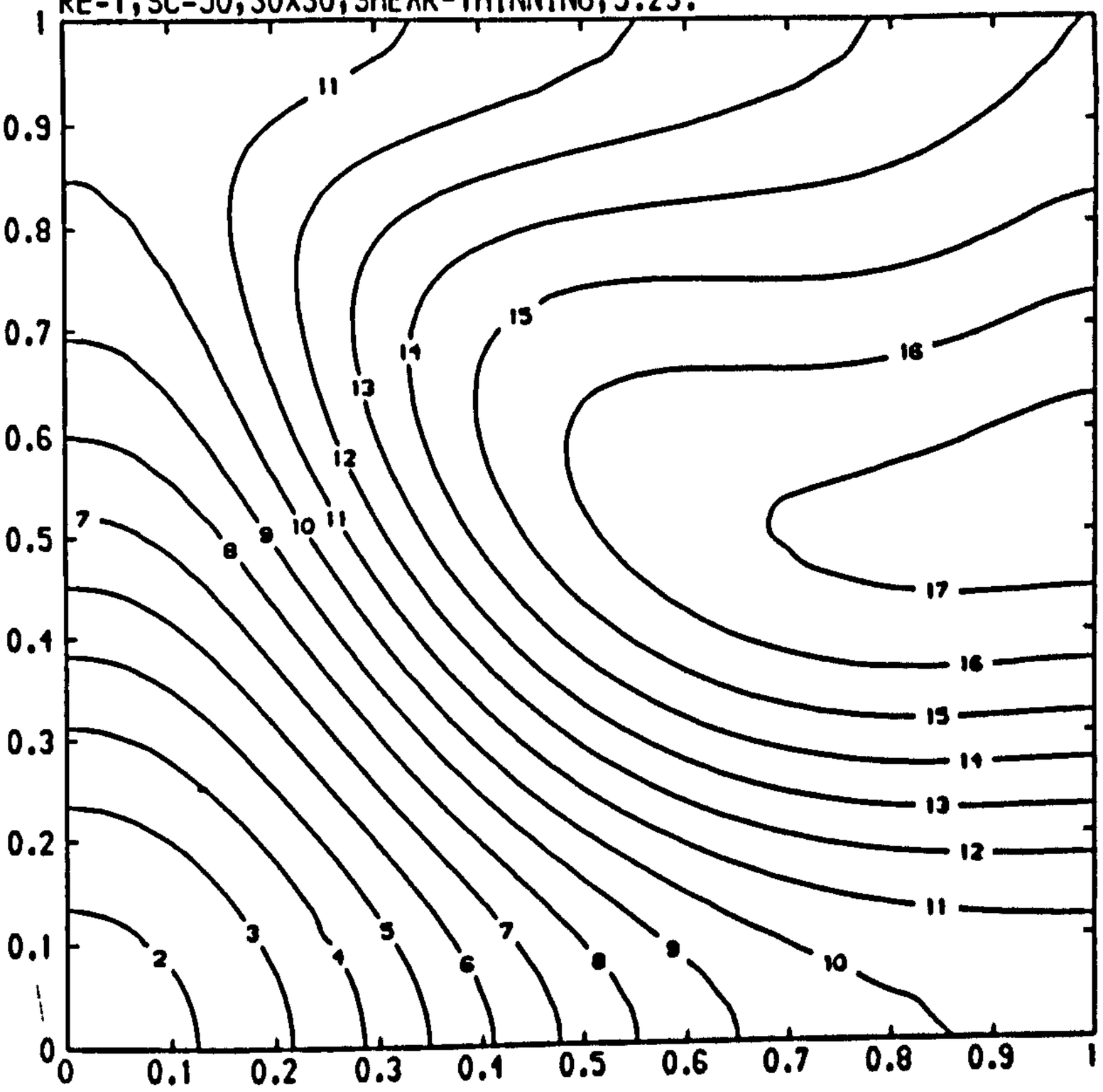

CONTOUR KEY	
1	0.5000
2	0.5500
3	0.6000
4	0.6500
5	0.7000
6	0.7500
7	0.8000
8	0.8500
9	0.9000
10	0.9500
11	1.0000
12	1.0500
13	1.1000
14	1.1500
15	1.2000
16	1.2500
17	1.3000
18	1.3500

Figure (5.48) Concentration contours for a pseudoplastic fluid at Re=1, Sc=50, 5.2 seconds.

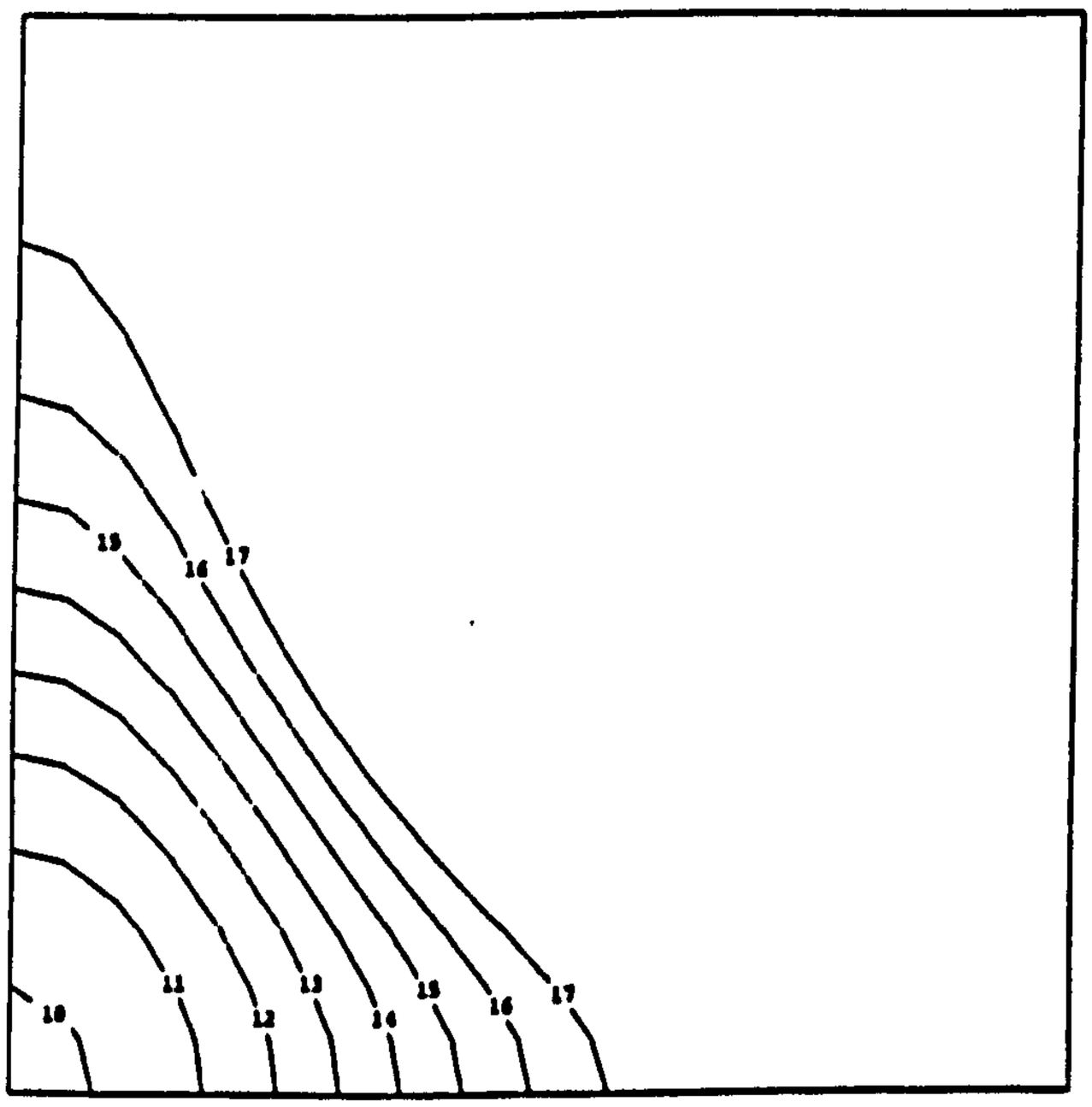

CONTOUR KEY	
1	0.100E+00
2	0.150E+00
3	0.200E+00
4	0.250E+00
5	0.300E+00
6	0.350E+00
7	0.400E+00
8	0.450E+00
9	0.500E+00
10	0.550E+00
11	0.600E+00
12	0.650E+00
13	0.700E+00
14	0.750E+00
15	0.800E+00
16	0.850E+00
17	0.900E+00

Figure (5.49) Concentration contours for a Newtonian fluid at Re=1, Sc=50, 5.2 seconds by Havard[44].

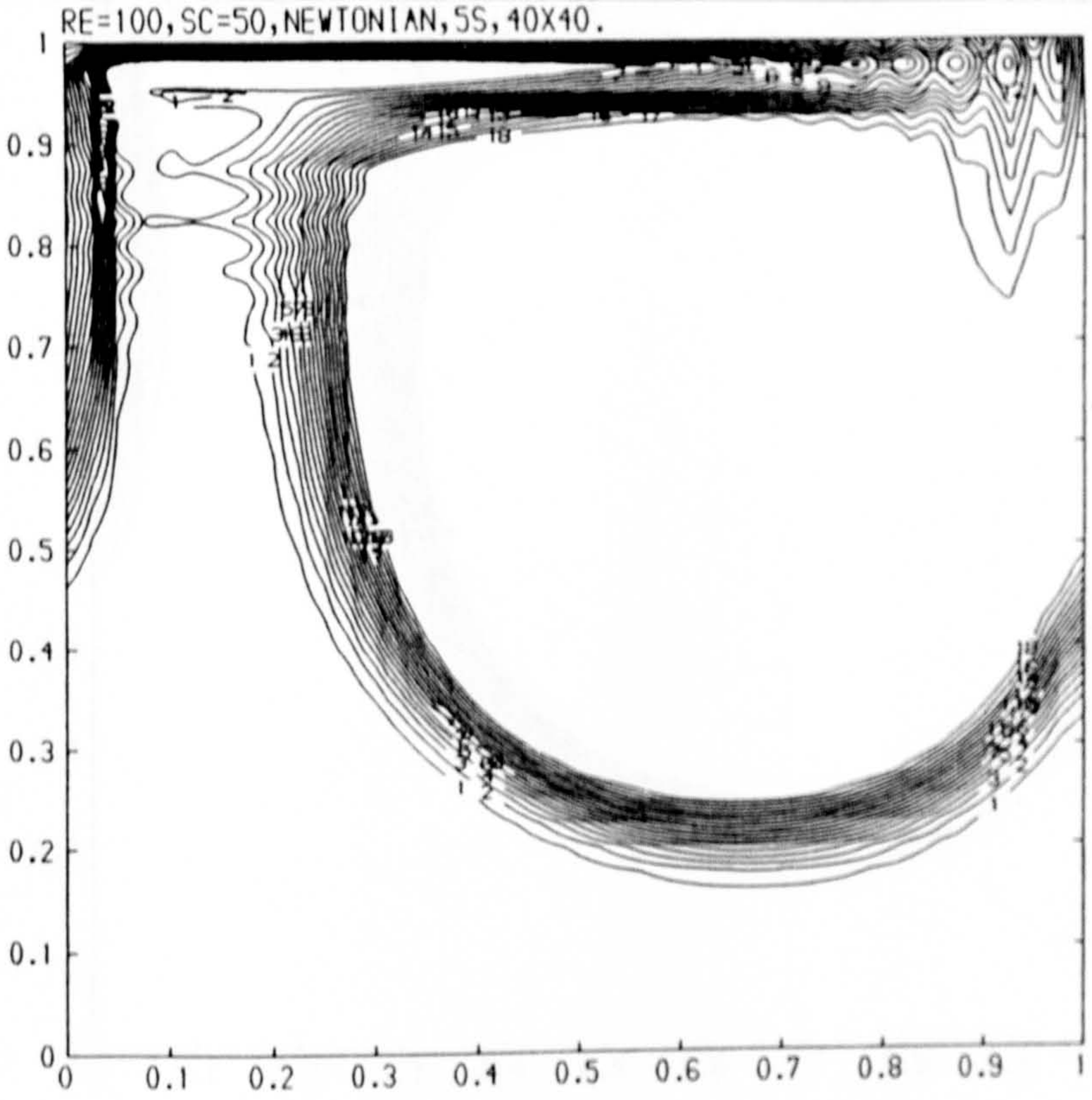

CONTOUR KEY	
1	0.1000
2	0.2000
3	0.3000
4	0.4000
5	0.5000
6	0.6000
7	0.7000
8	0.8000
9	0.9000
10	1.0000
11	1.1000
12	1.2000
13	1.3000
14	1.4000
15	1.5000
16	1.6000
17	1.7000
18	1.8000

Figure (5.50) Concentration contours for a Newtonian fluid at Re=100, Sc=50, 5 seconds.

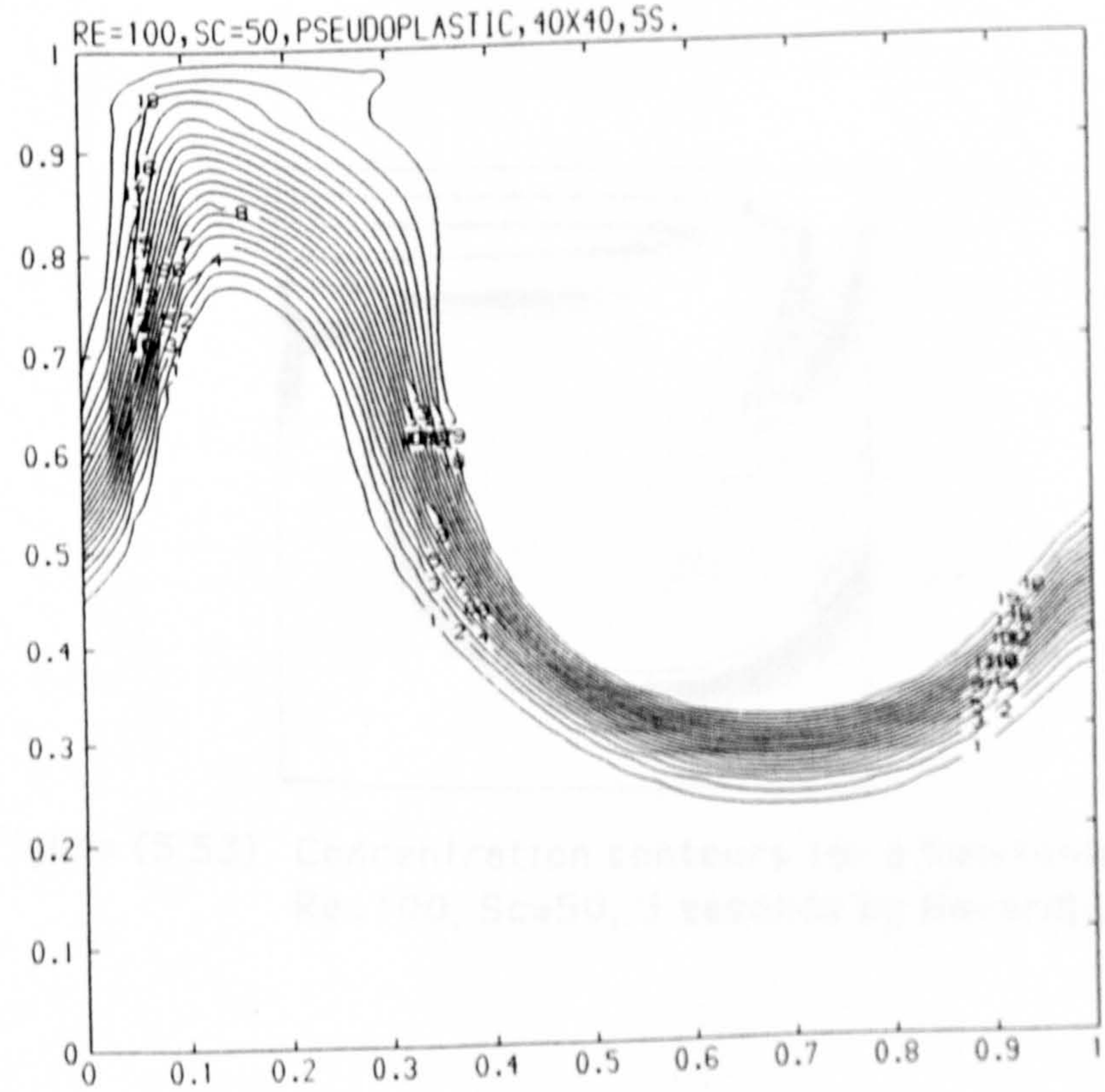

CONTOUR KEY	
1	0.1000
2	0.2000
3	0.3000
4	0.4000
5	0.5000
6	0.6000
7	0.7000
8	0.8000
9	0.9000
10	1.0000
11	1.1000
12	1.2000
13	1.3000
14	1.4000
15	1.5000
16	1.6000
17	1.7000
18	1.8000
19	1.9000

Figure (5.51) Concentration contours for a pseudoplastic fluid at Re=100, Sc=50, 5 seconds.

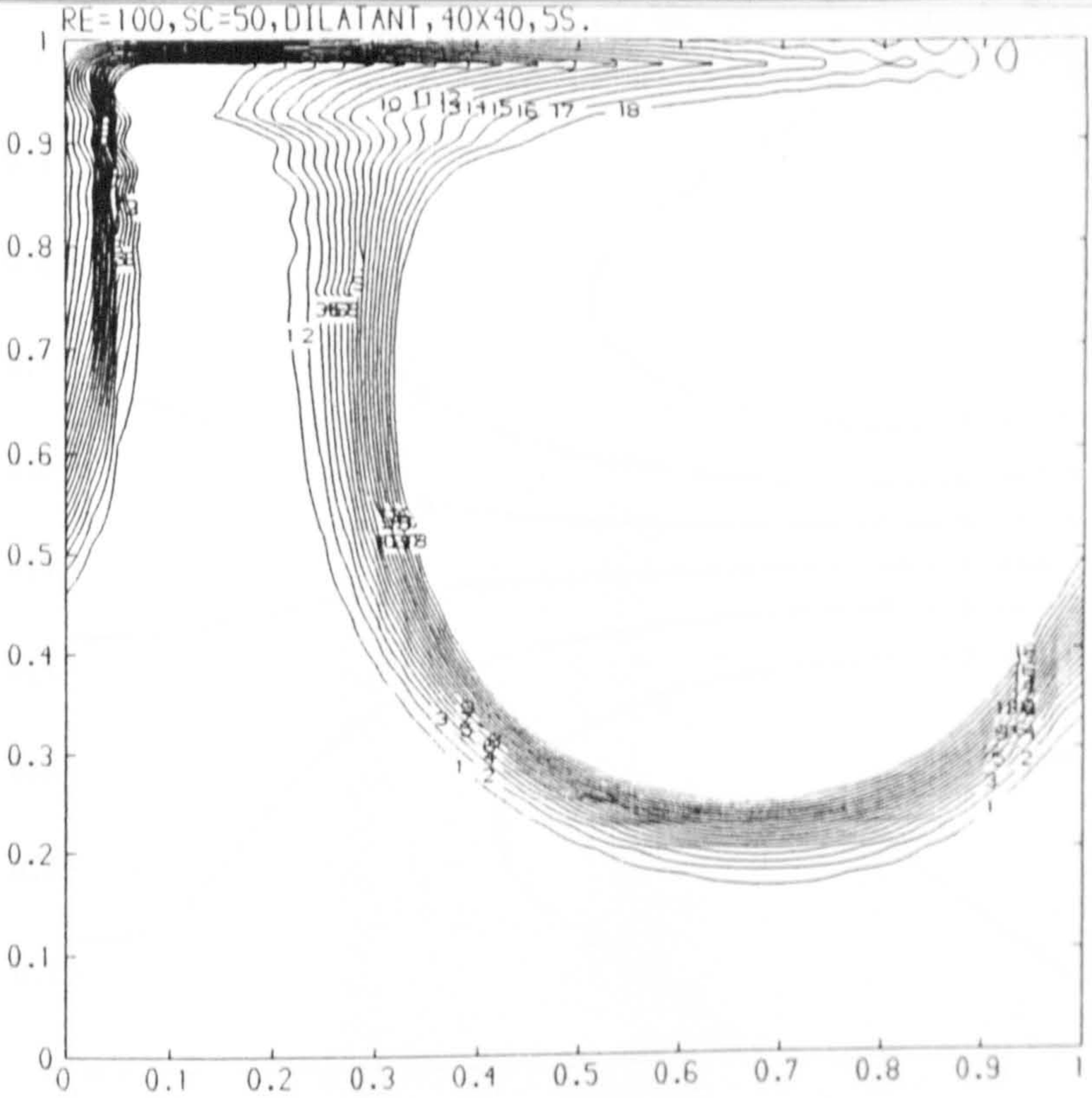

CONTOUR KEY	
1	0.1000
2	0.2000
3	0.3000
4	0.4000
5	0.5000
6	0.6000
7	0.7000
8	0.8000
9	0.9000
10	1.0000
11	1.1000
12	1.2000
13	1.3000
14	1.4000
15	1.5000
16	1.6000
17	1.7000
18	1.8000

Figure (5.52) Concentration contours for a dilatant fluid at Re=100, Sc=50, 5 seconds.

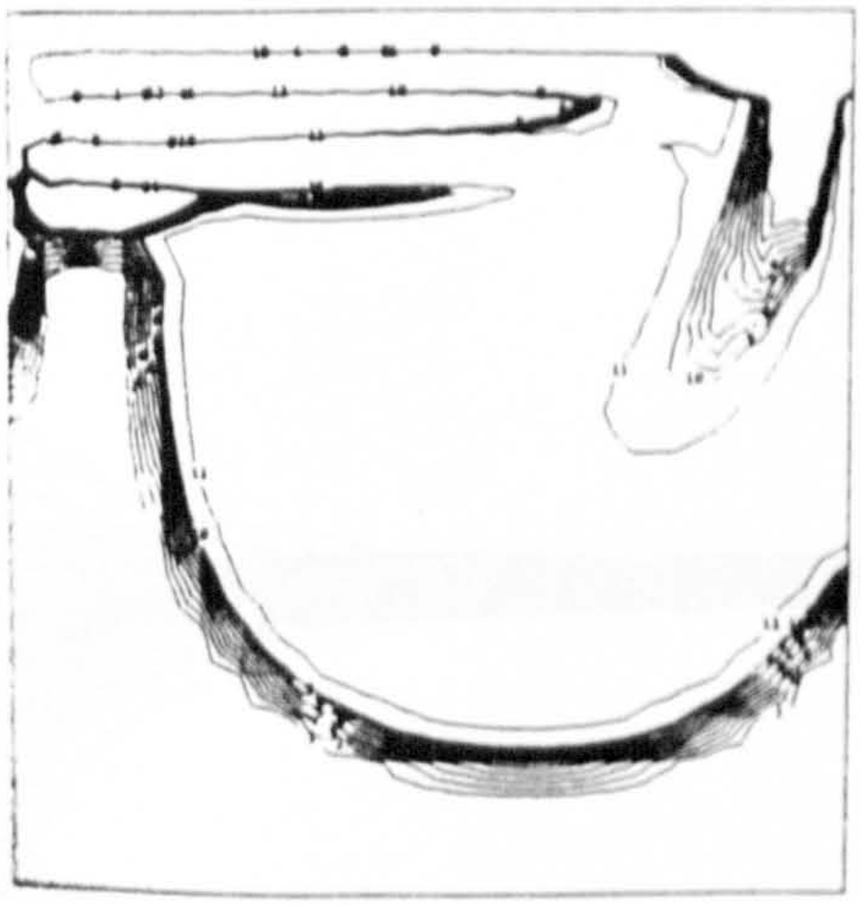

CONTOUR KEY	
1	0.100E+00
2	0.200E+00
3	0.300E+00
4	0.400E+00
5	0.500E+00
6	0.600E+00
7	0.700E+00
8	0.800E+00
9	0.900E+00
10	0.100E+01
11	0.150E+01

Figure (5.53) Concentration contours for a Newtonian fluid at Re=100, Sc=50, 5 seconds by Havard[44].

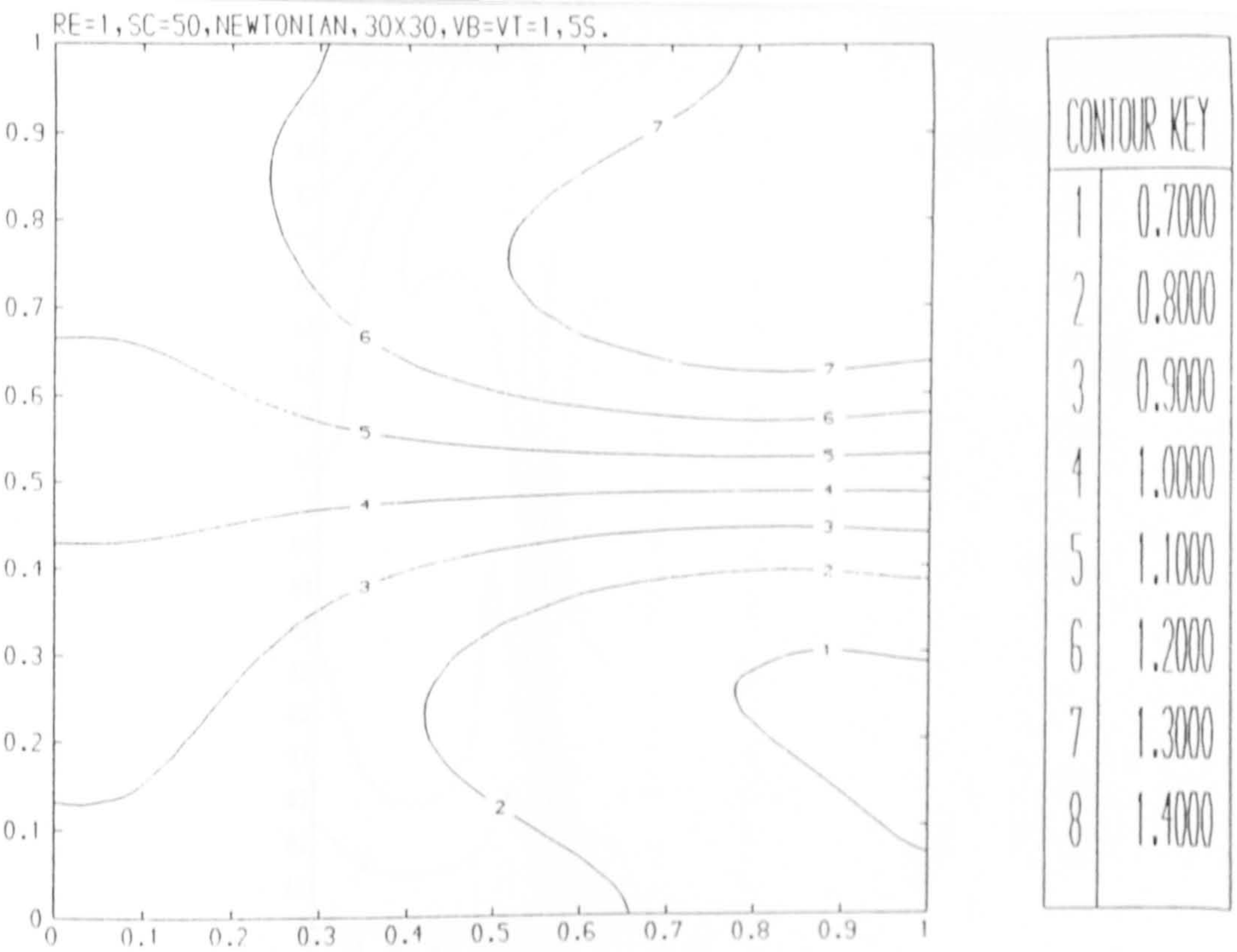

Figure (5.54) Concentration countours for a Newtonian fluid at Re=1, Sc=50, vb=vt=1, 5 seconds.

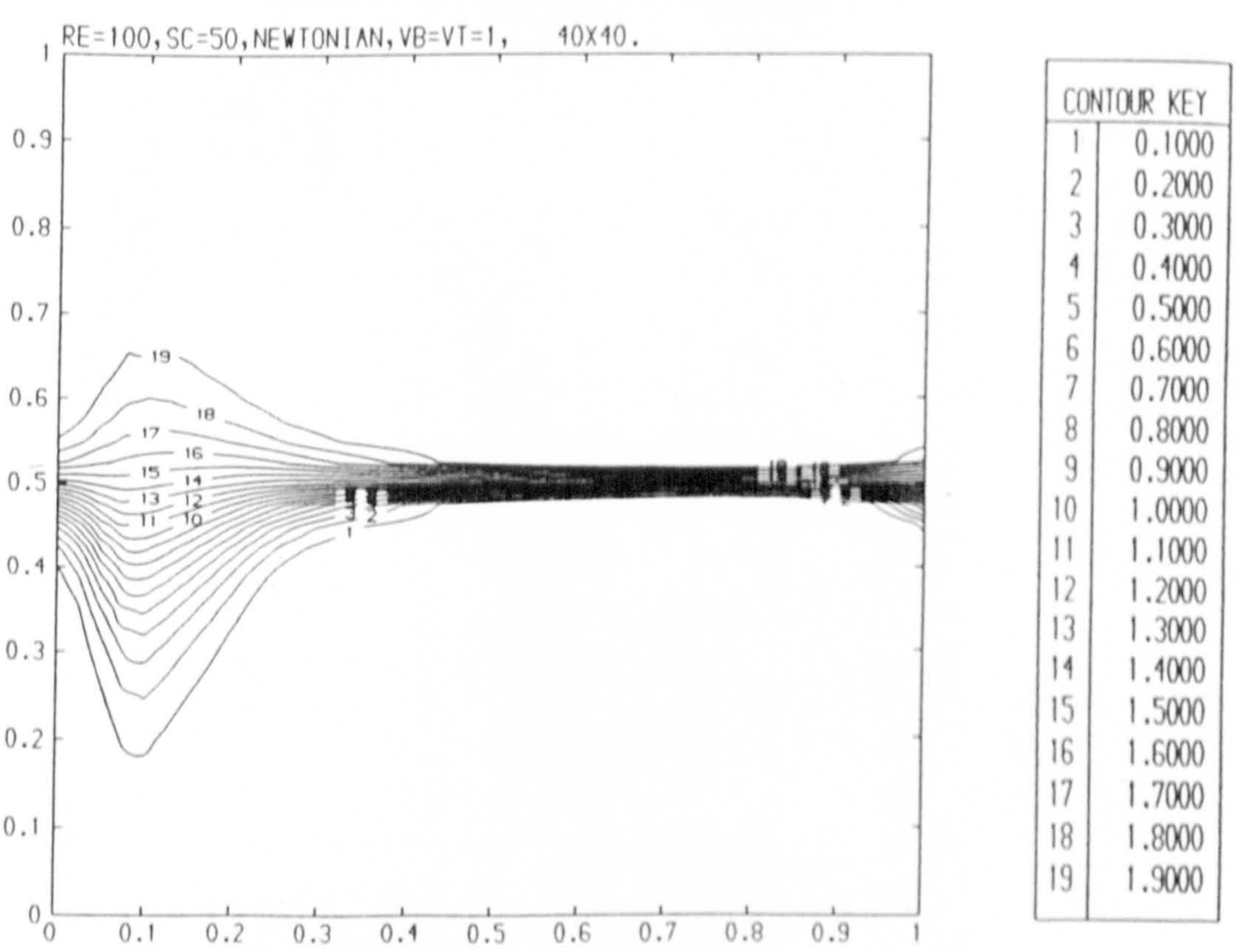

Figure (5.55) Concentration contours for a Newtonian fluid at Re=100, Sc=50, vb=vt=1, 5 seconds.

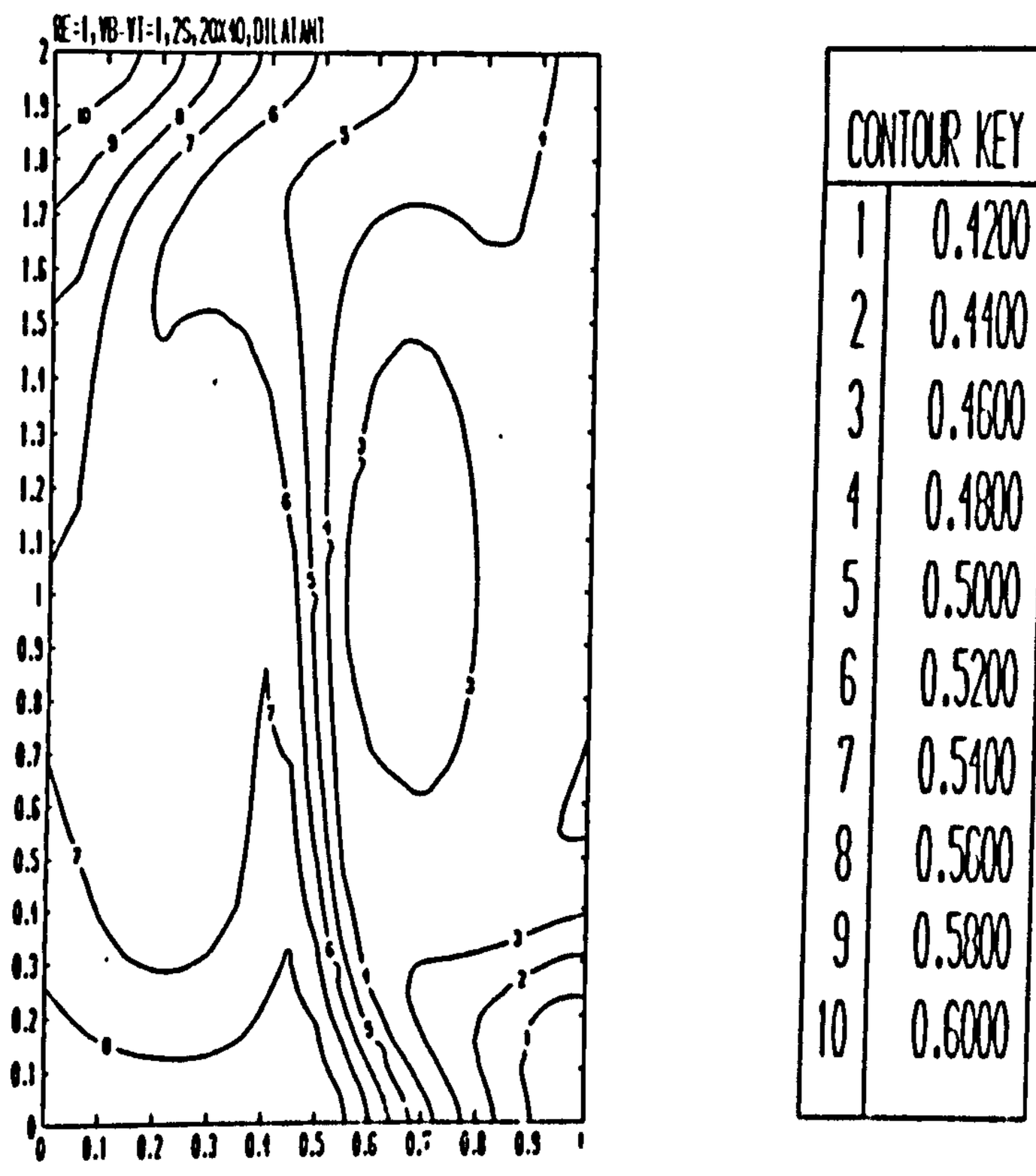

CONTOUR KEY	
1	0.4200
2	0.4400
3	0.4600
4	0.4800
5	0.5000
6	0.5200
7	0.5400
8	0.5600
9	0.5800
10	0.6000

Figure (5.56) Concentration contours for a time dependent dilatant fluid at Re=1, Sc=50, vb=vt=1, cavity's aspect ratio =2, time 2 seconds.

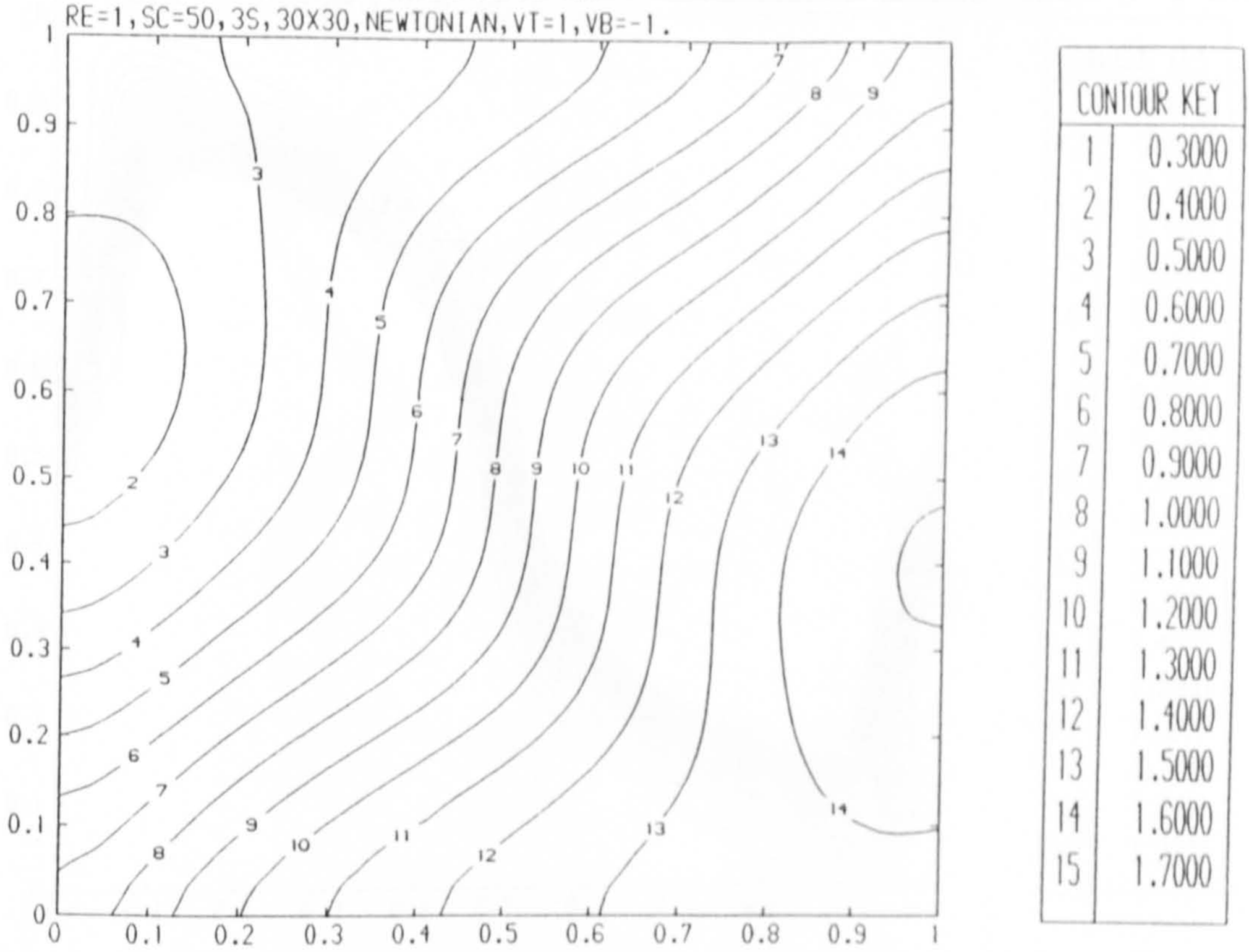

Figure (5.57) Concentration contours for a Newtonian fluid at Re=1, Sc=50, vb=-vt=-1, 3 seconds.

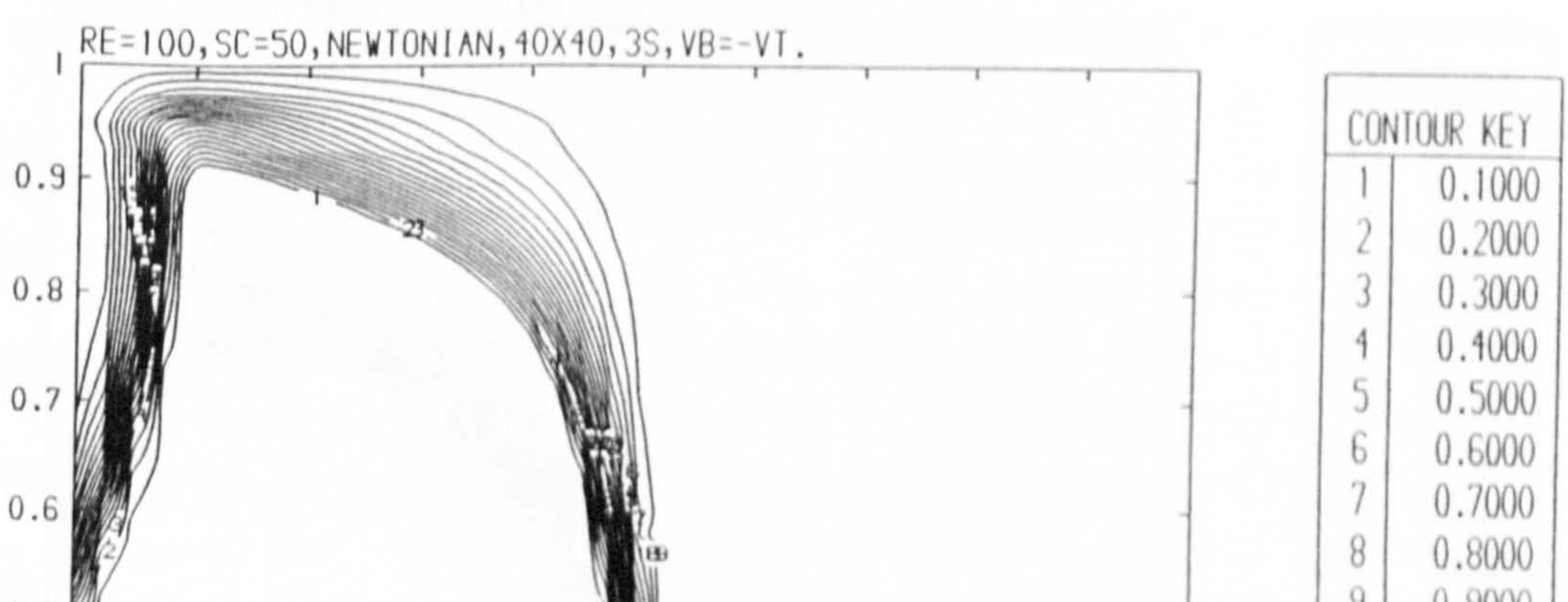

Figure (5.58) Concentration contours for a Newtonian fluid at Re=100, Sc=50, vb=-vt=-1, 3 seconds.

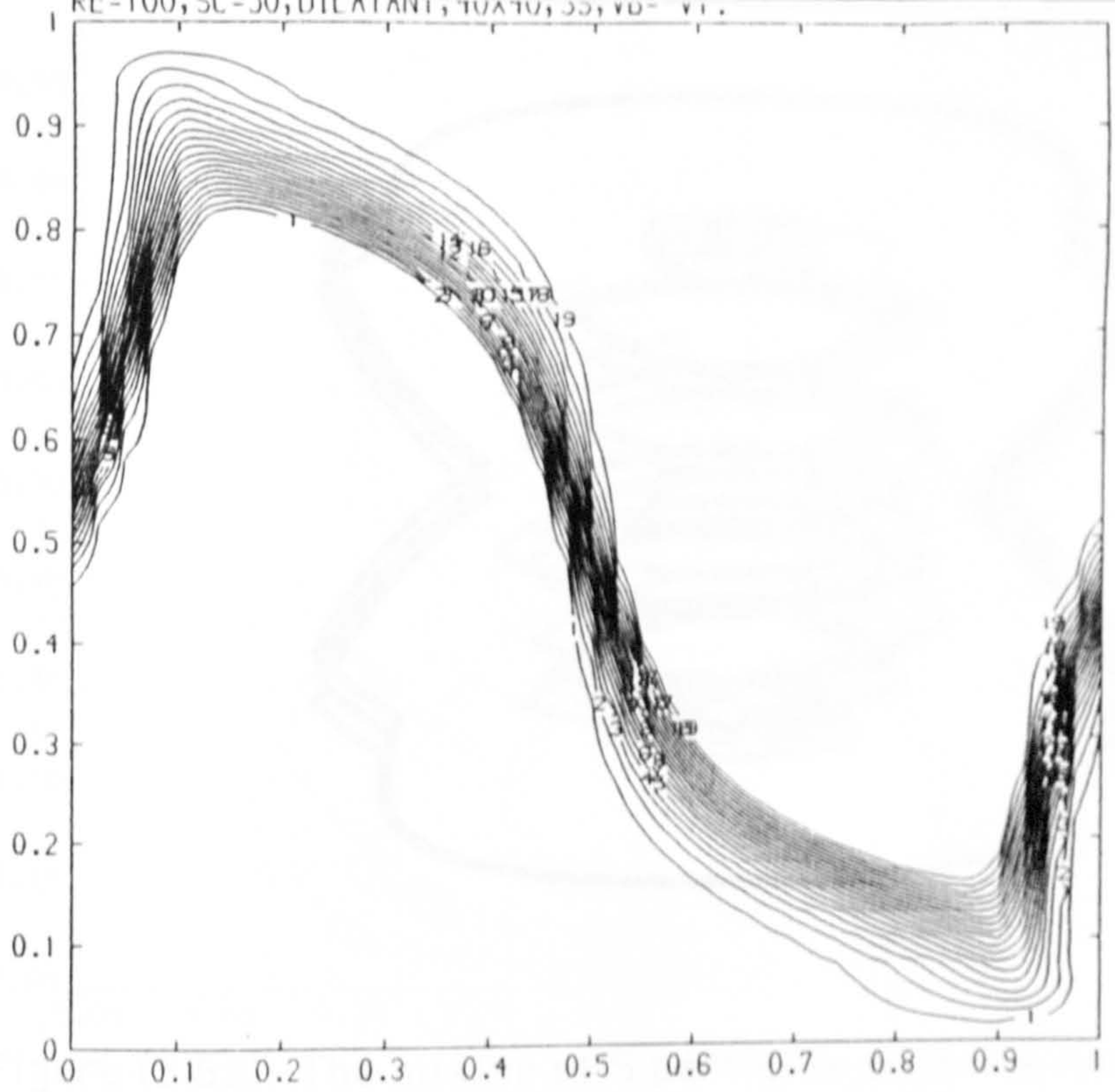

CONTOUR KEY	
1	0.1000
2	0.2000
3	0.3000
4	0.4000
5	0.5000
6	0.6000
7	0.7000
8	0.8000
9	0.9000
10	1.0000
11	1.1000
12	1.2000
13	1.3000
14	1.4000
15	1.5000
16	1.6000
17	1.7000
18	1.8000
19	1.9000

Figure (5.59) Concentration contours for a dilatant fluid at Re=100, Sc=50, vb=-vt=-1, 3 seconds.

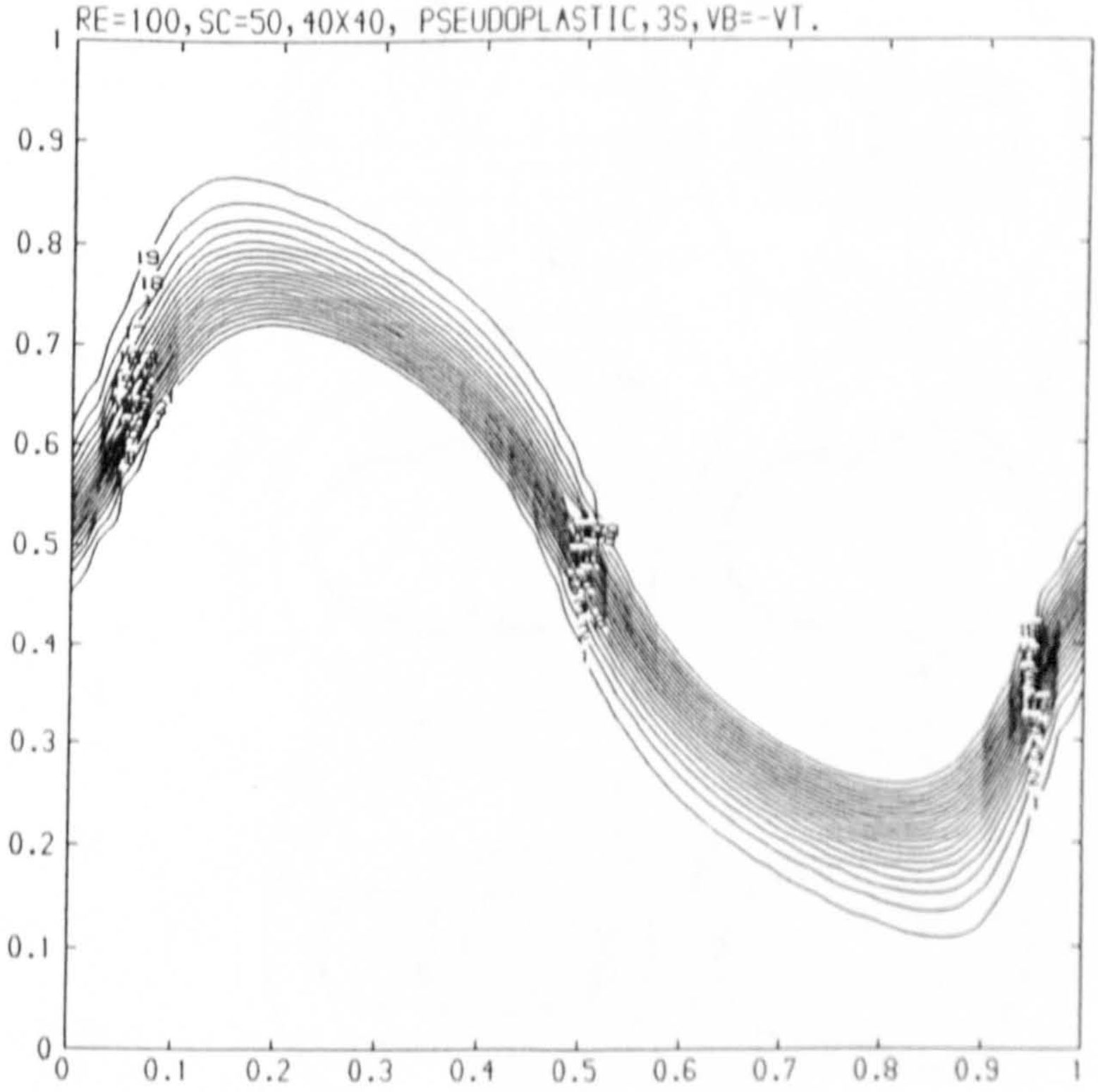

CONTOUR KEY	
1	0.1000
2	0.2000
3	0.3000
4	0.4000
5	0.5000
6	0.6000
7	0.7000
8	0.8000
9	0.9000
10	1.0000
11	1.1000
12	1.2000
13	1.3000
14	1.4000
15	1.5000
16	1.6000
17	1.7000
18	1.8000
19	1.9000

Figure (5.60) Concentration contours for a pseudoplastic fluid at Re=100, Sc=50, vb=-vt=-1, 3 seconds.

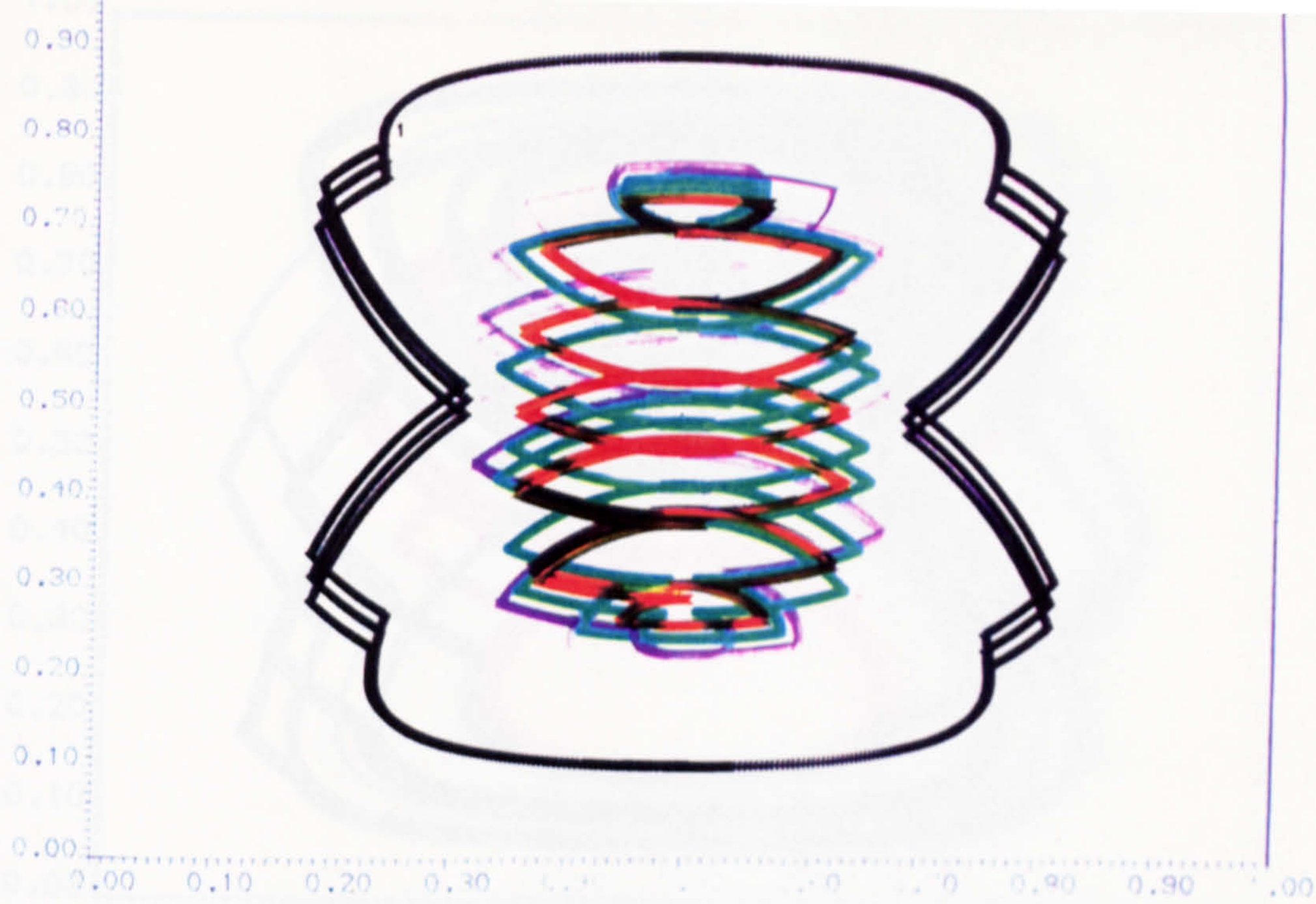

Figure (5.62) *The mixing of 5 particles within a Newtonian fluid at Re=1, after 60s, T=1s, initially placed in the vertical line in the cavity's centre.*

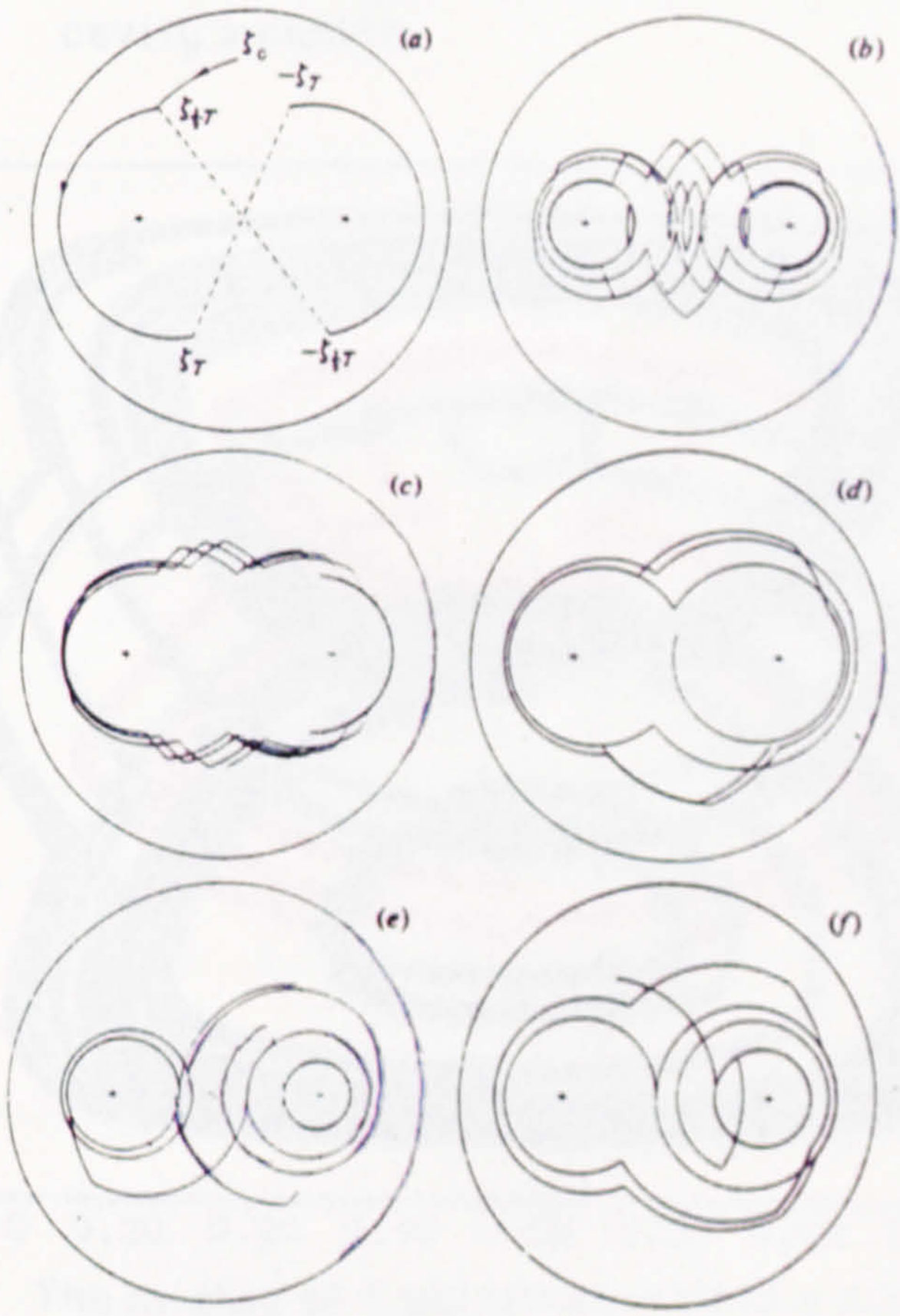

Figure (5.63) *The chaotic particle mixing evidenced by Aref using an inviscid fluid in 'blinking vortex flow'.*

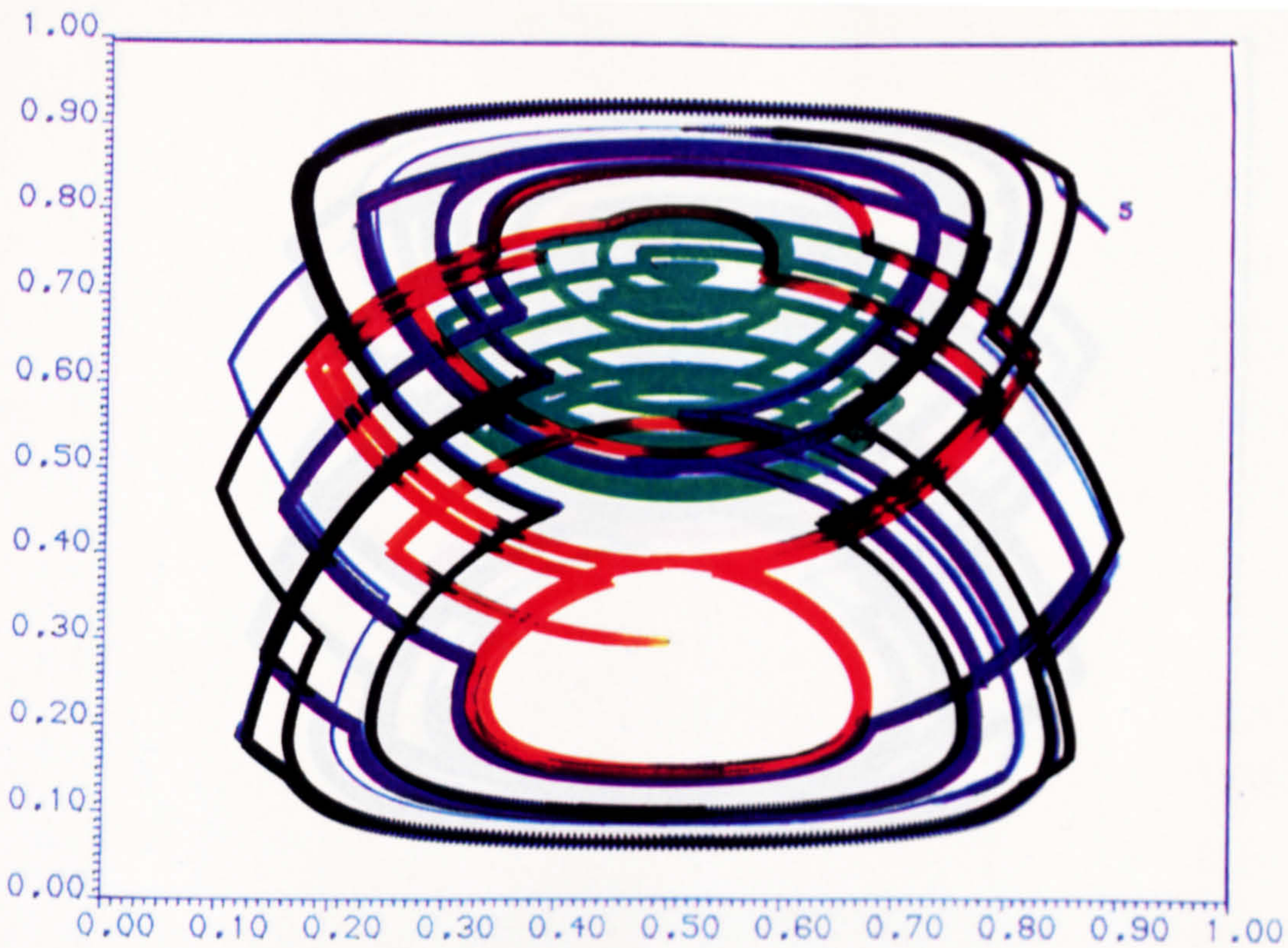

Figure (5.64) The mixing of 5 particles within a Newtonian fluid in blinking vortex flow at Re=1, after 60s, T=2s, initially placed in the vertical line in the cavity's centre.

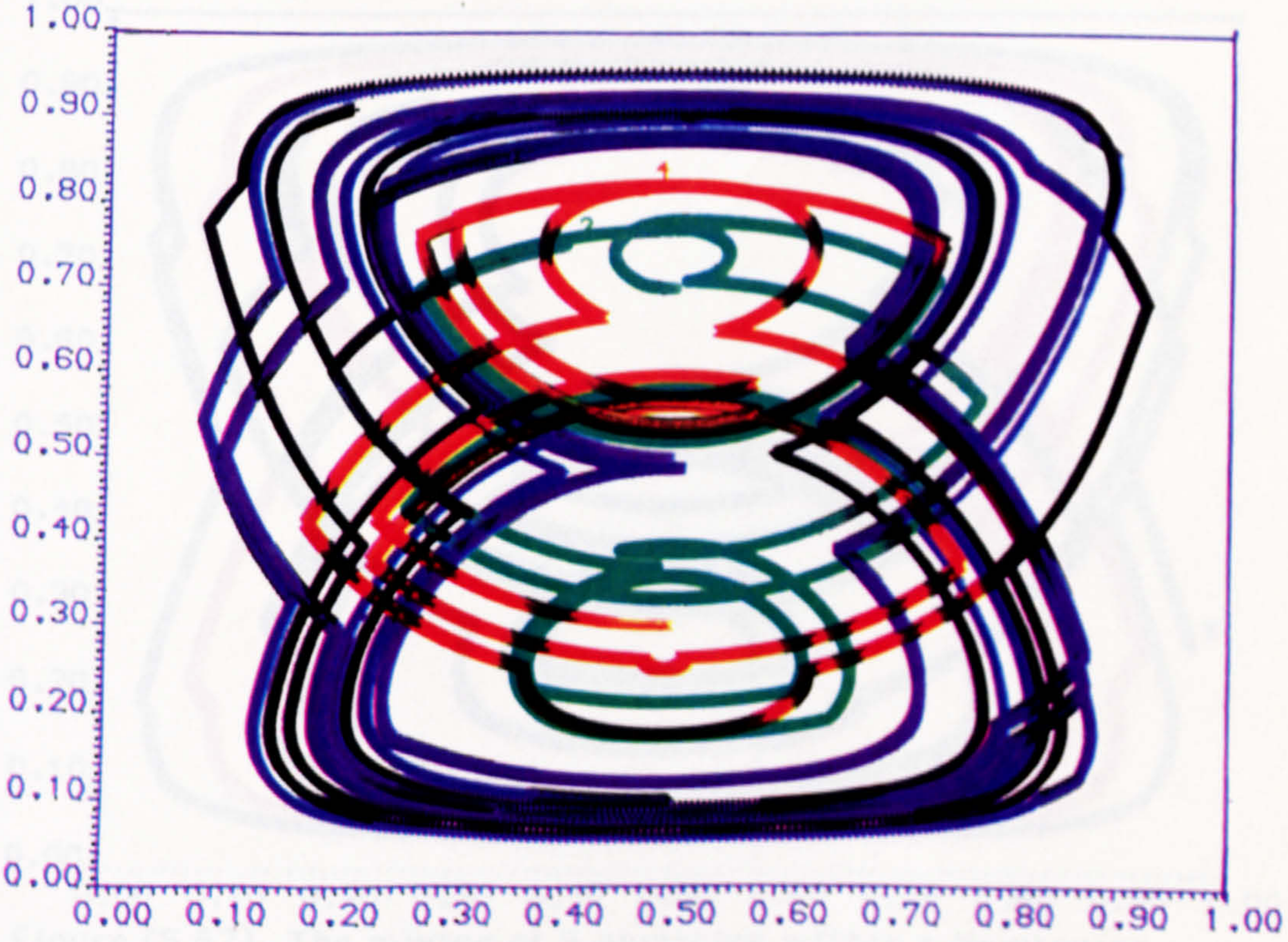

Figure (5.65) The mixing of 5 particles within a dilatant fluid in blinking vortex flow at Re=1, after 60s, T=2s, initially placed in the vertical line in the cavity's centre.

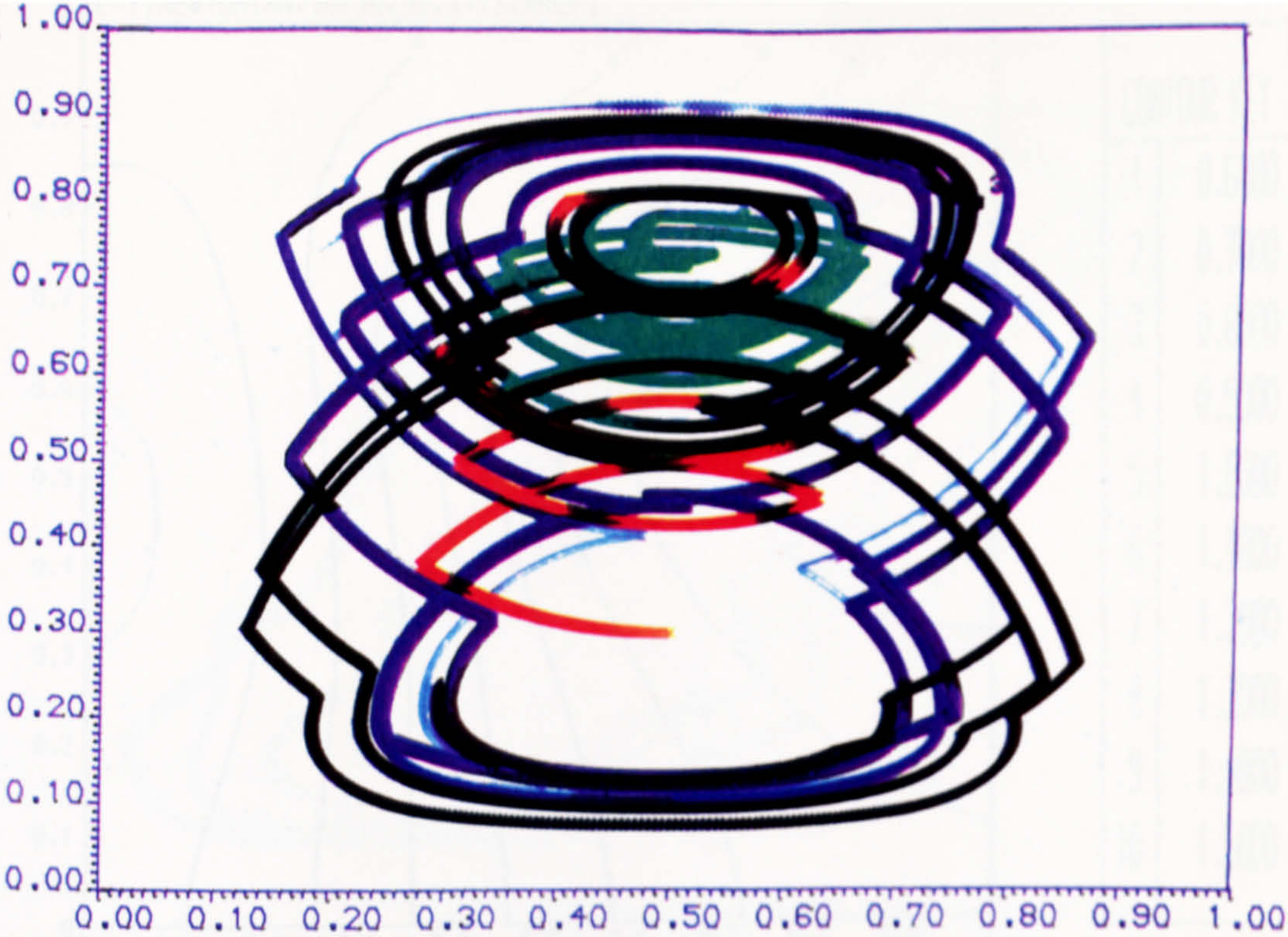

Figure (5.66) The mixing of 5 particles within a pseudoplastic fluid in blinking vortex flow at Re=1, after 60s, T=2s, initially placed in the vertical line in the cavity's centre.

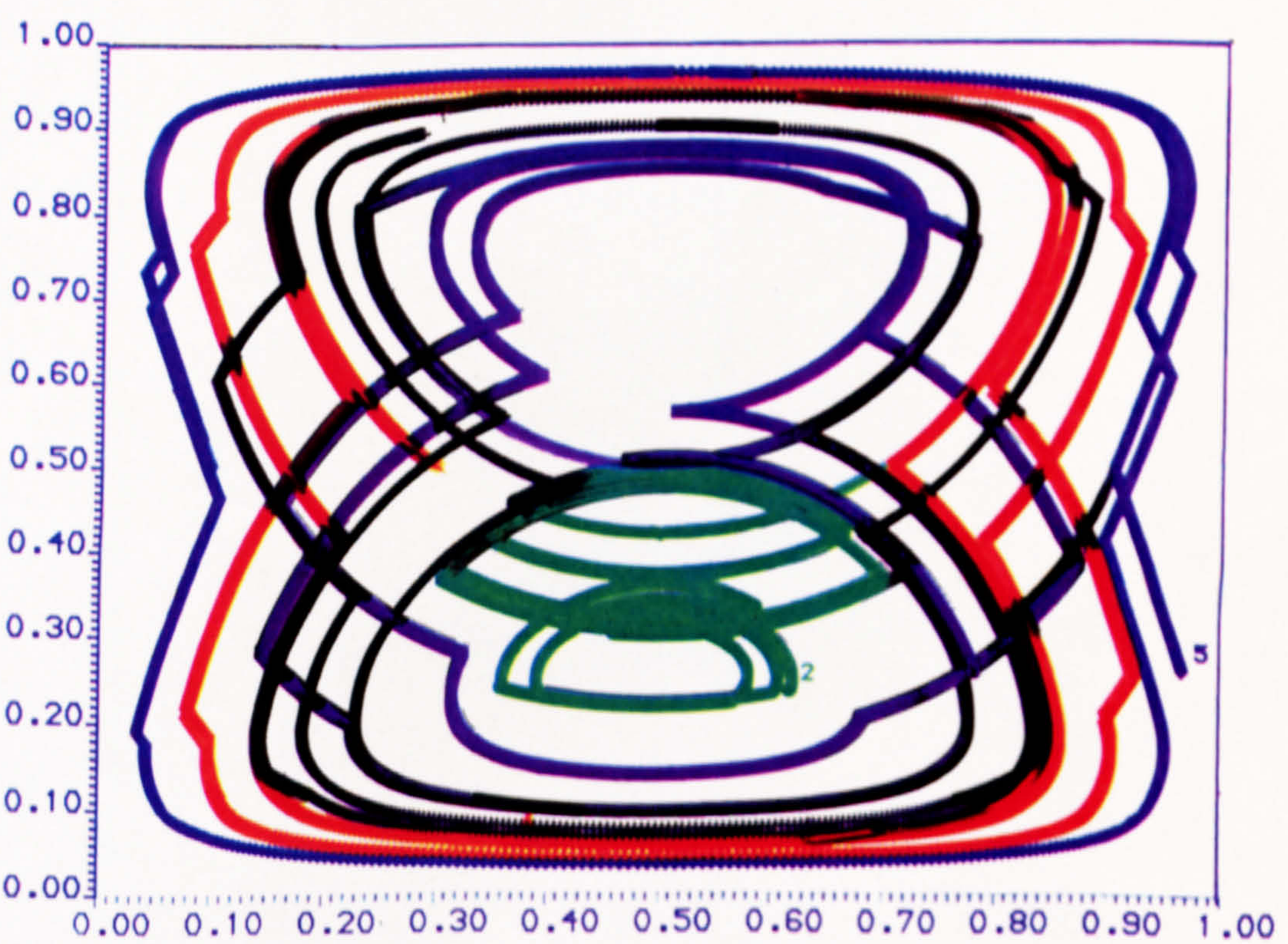

Figure (5.67) The mixing of 5 particles within a Newtonian fluid in blinking vortex flow at Re=1, after 60s, T=2s, initially placed in the horizontal line in the cavity's centre.

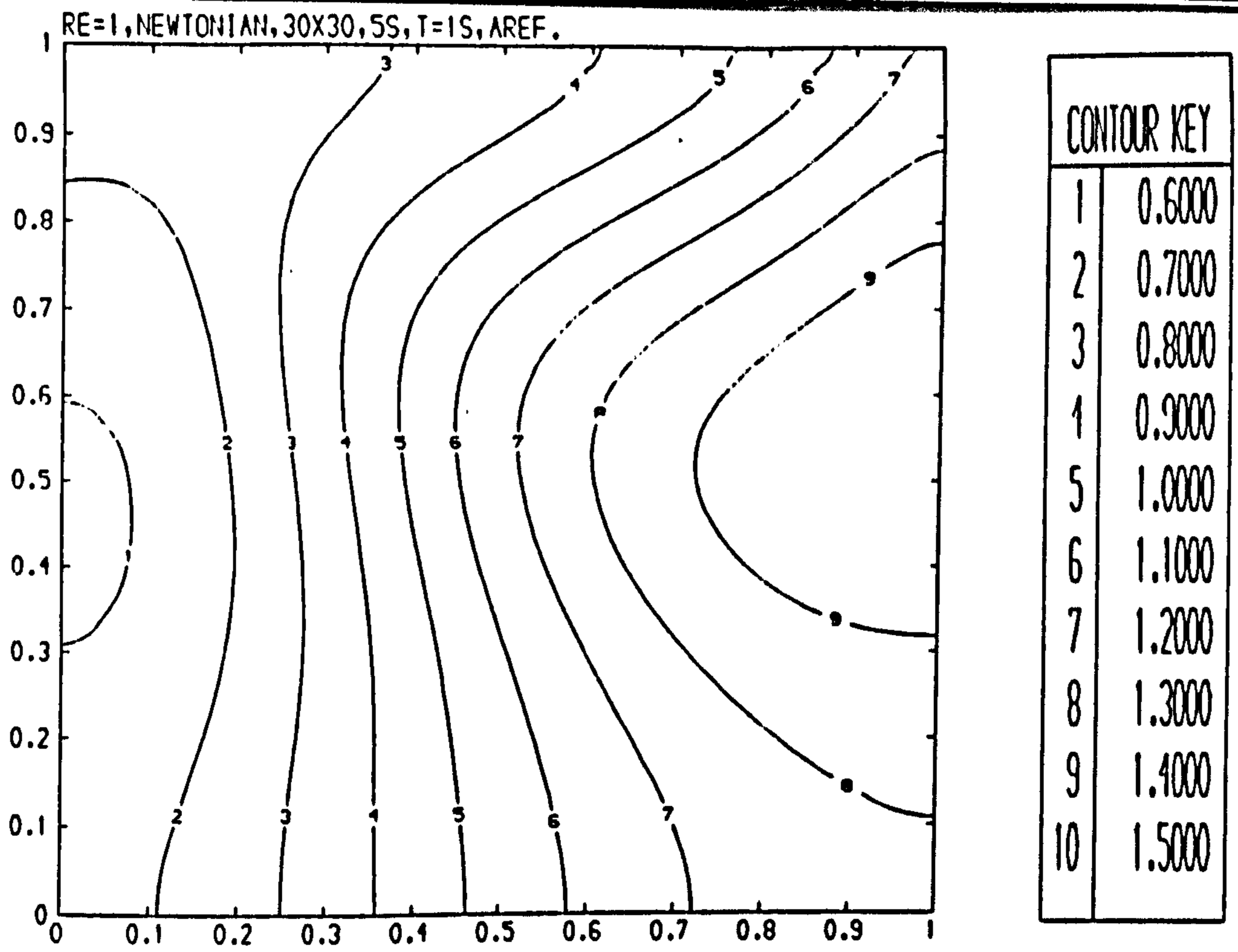

Figure (5.68) The concentration contours of a Newtonian fluid at Re=1 Sc=50, T=1s, time 5s, undergoing Aref type 'blinking vortex flow'.

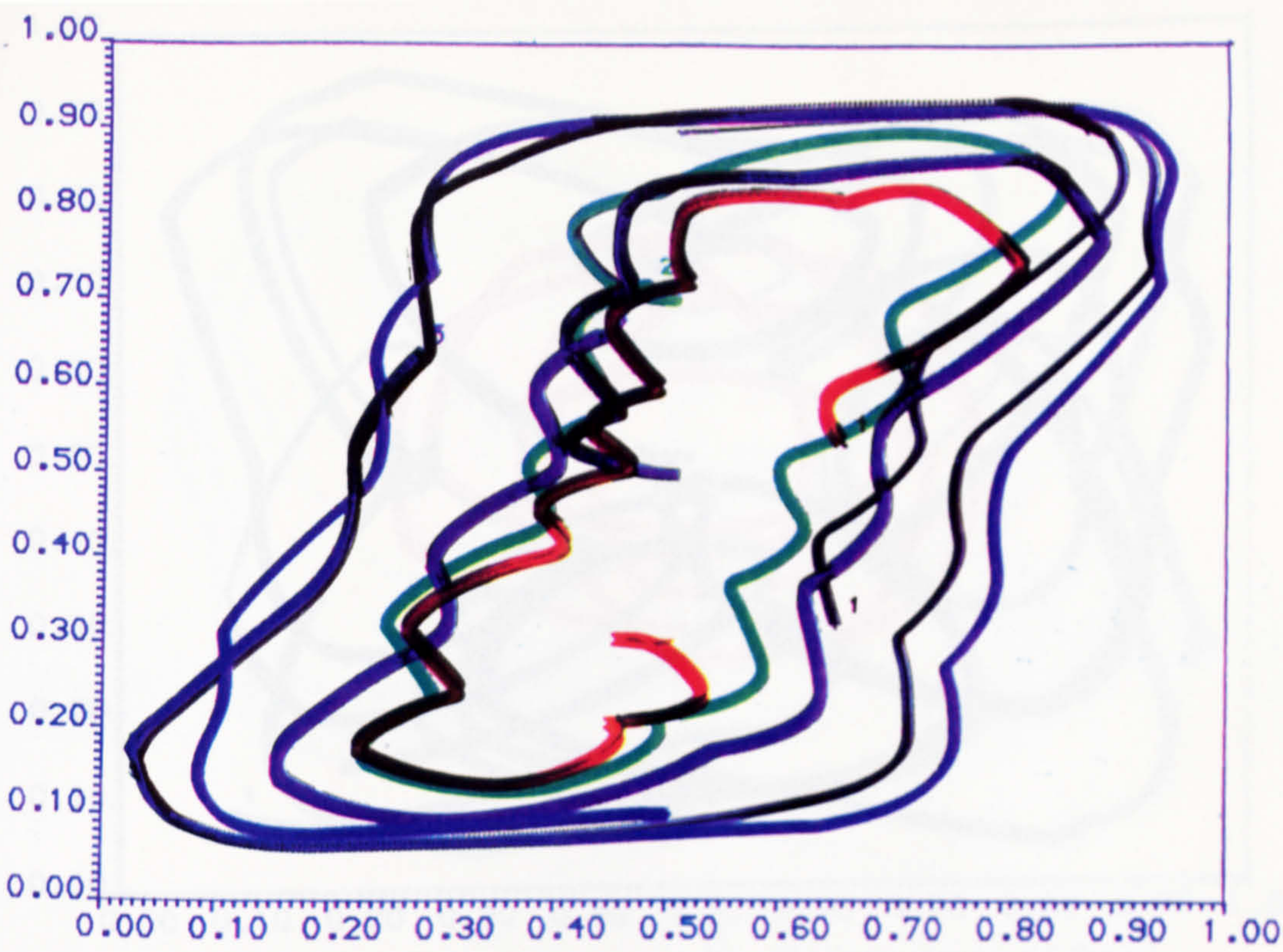

Figure (5.69) Particle mixing for a pseudoplastic fluid in blinking vortex flow at Re=100, T=2s, time 60s.

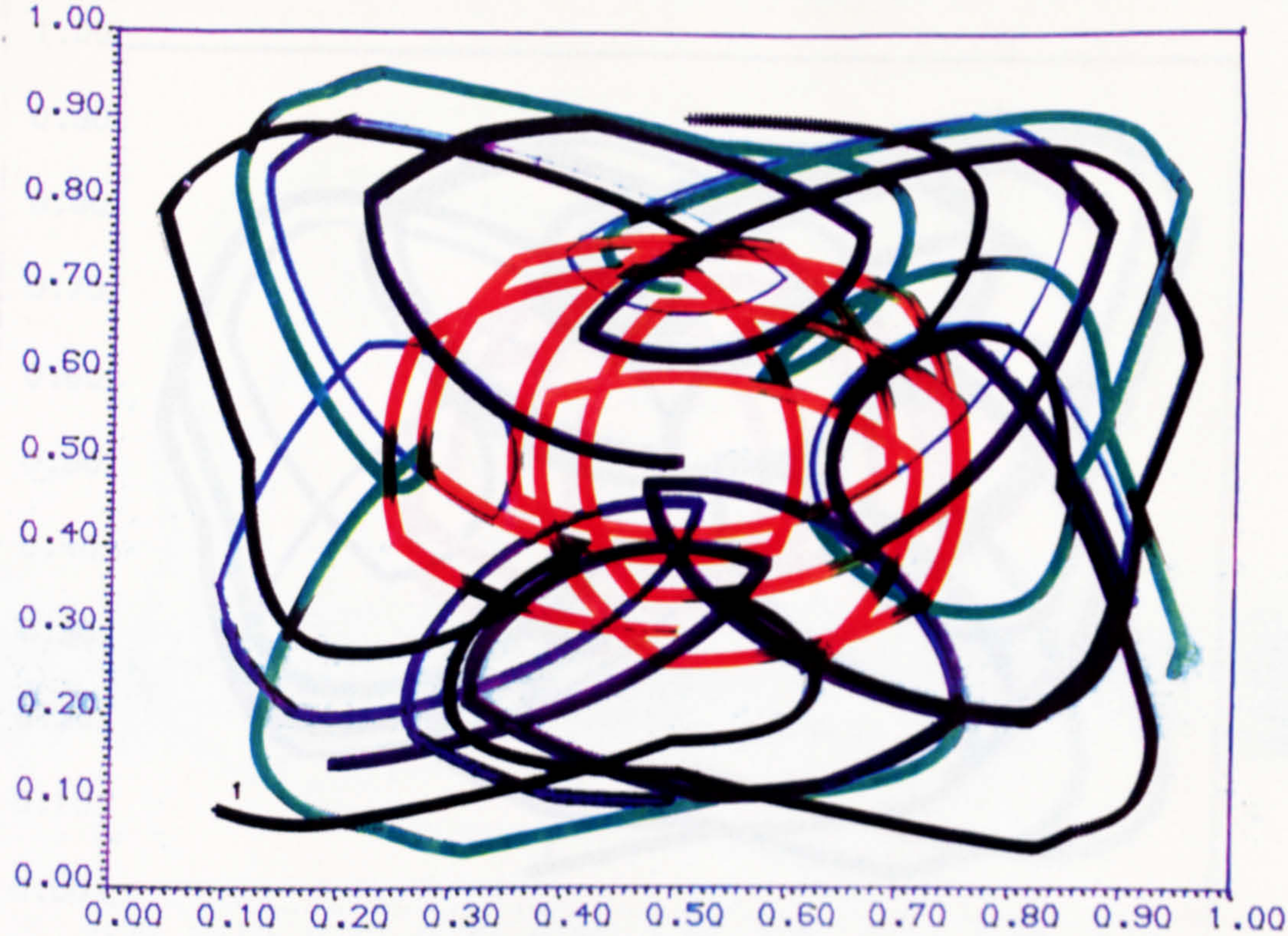

Figure (5.70) Particle mixing for a Newtonian fluid at Re=1, T=2s, time 60s, 4 walls in discontinuous co-rotational motion.

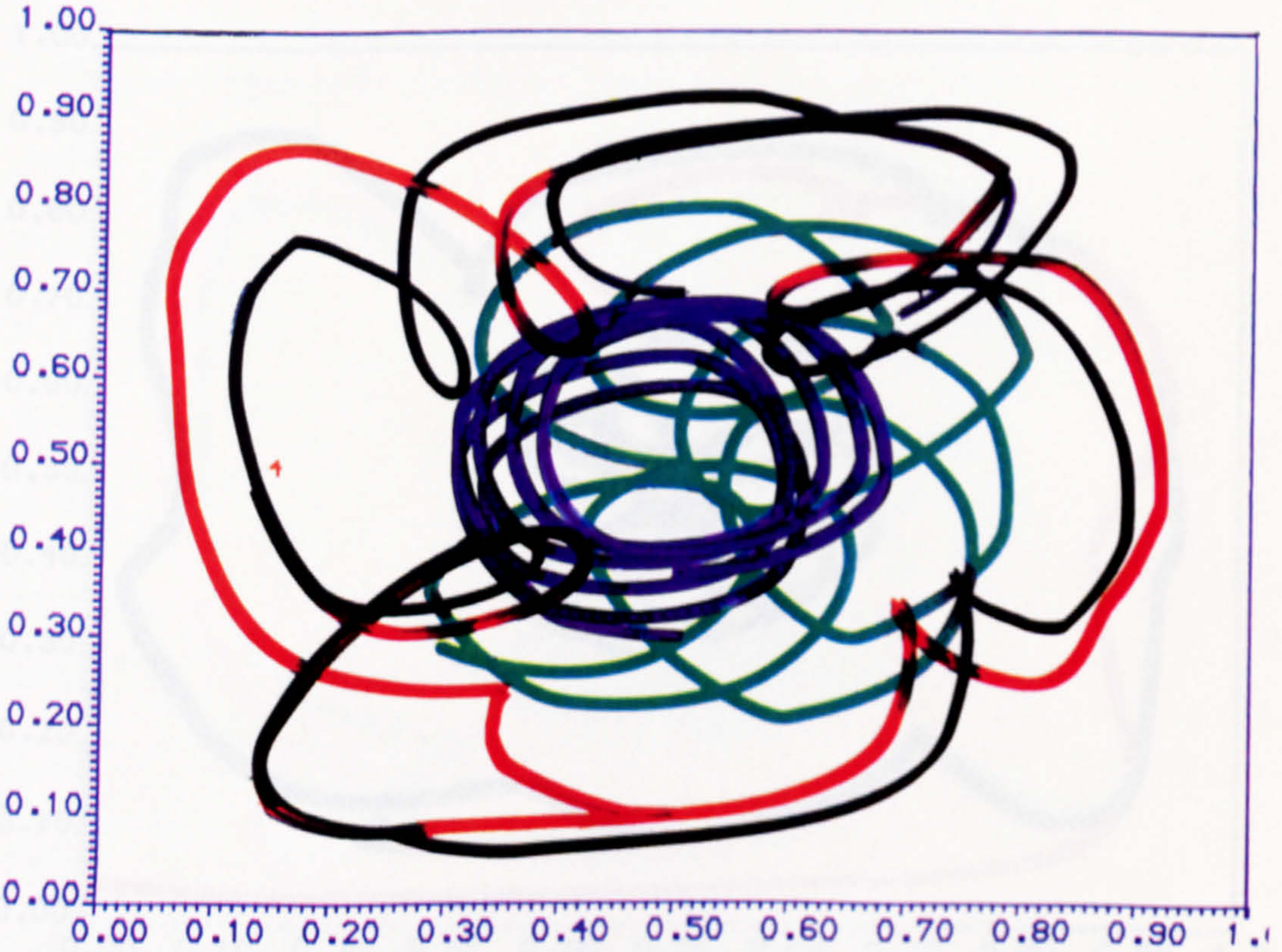

Figure (5.71) Particle mixing for a Newtonian fluid at Re=100, T=2s, time 60s, 4 walls in discontinuous co-rotational motion.

Figure (5.72) Particle mixing for a pseudoplastic fluid at Re=1, T=2s, time 60s, 4 walls in discontinuous co-rotational motion.

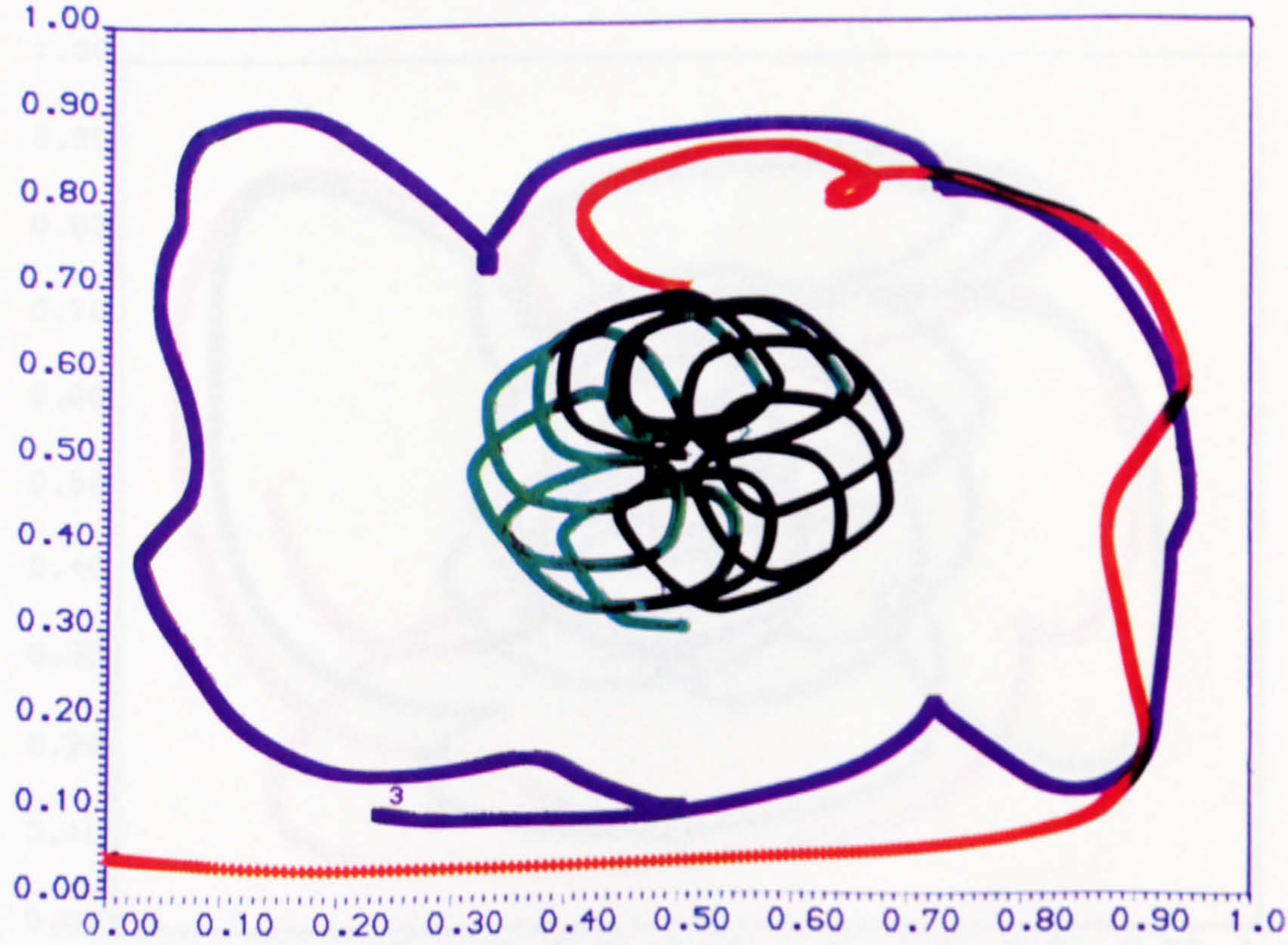

Figure (5.73) Particle mixing for a pseudoplastic fluid at Re=100, T=2s, time 60s, 4 walls in discontinuous co-rotational motion.

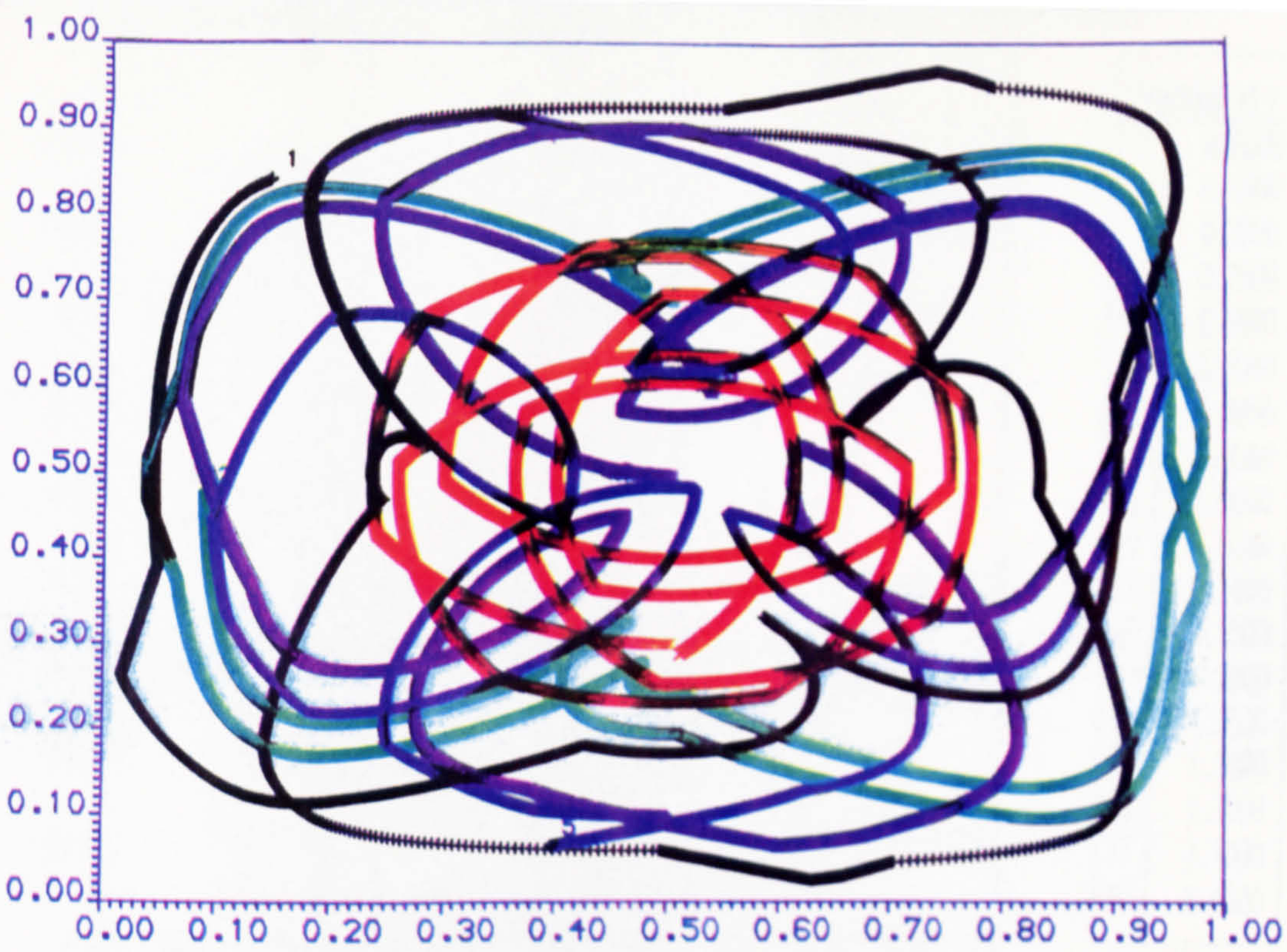

Figure (5.74) Particle mixing for a dilatant fluid at Re=1, T=2s, time 60s, 4 walls in discontinuous co-rotational motion.

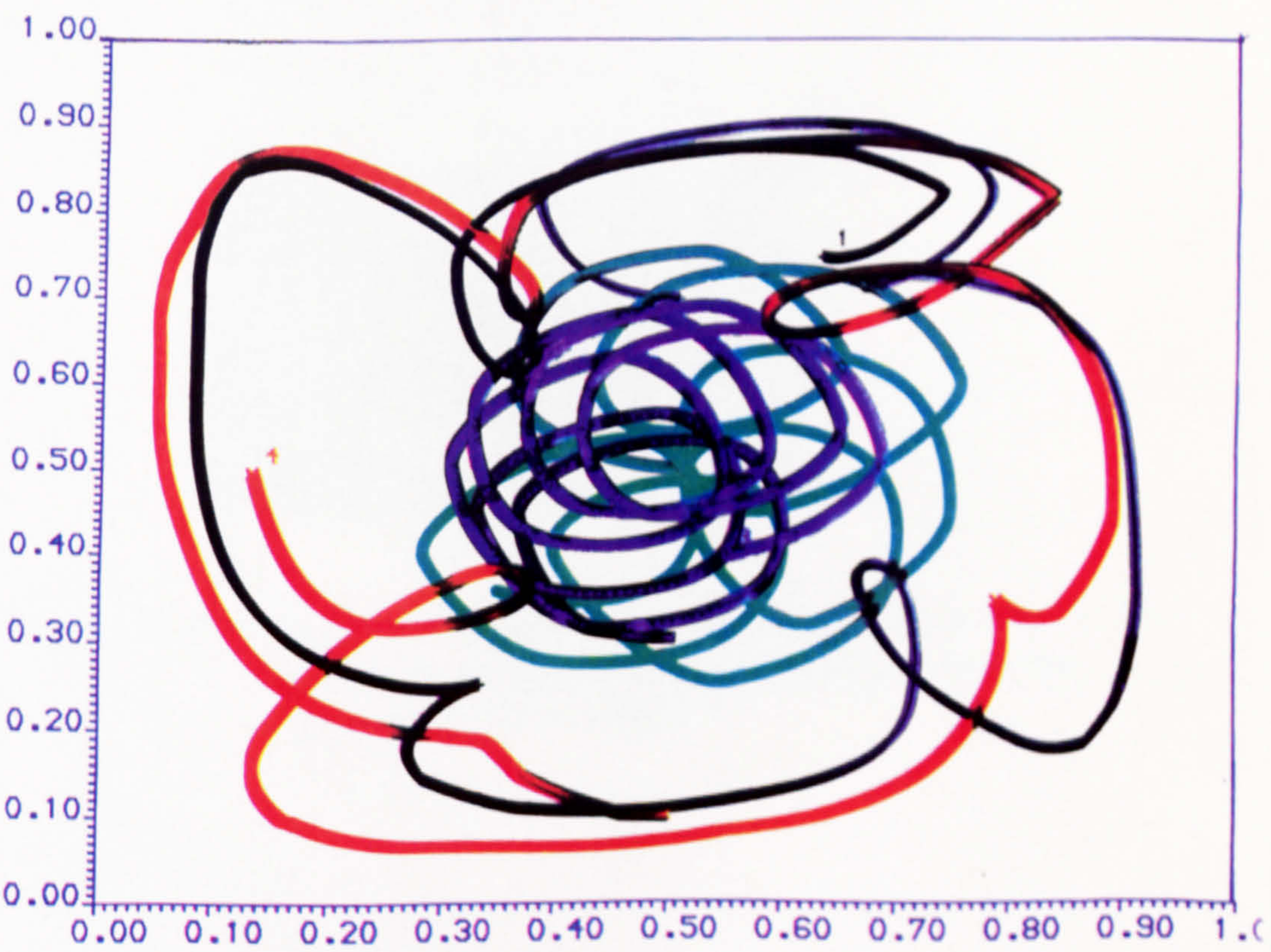

Figure (5.75) Particle mixing for a dilatant fluid at Re=100, T=2s, time 60s, 4 walls in discontinuous co-rotational motion.

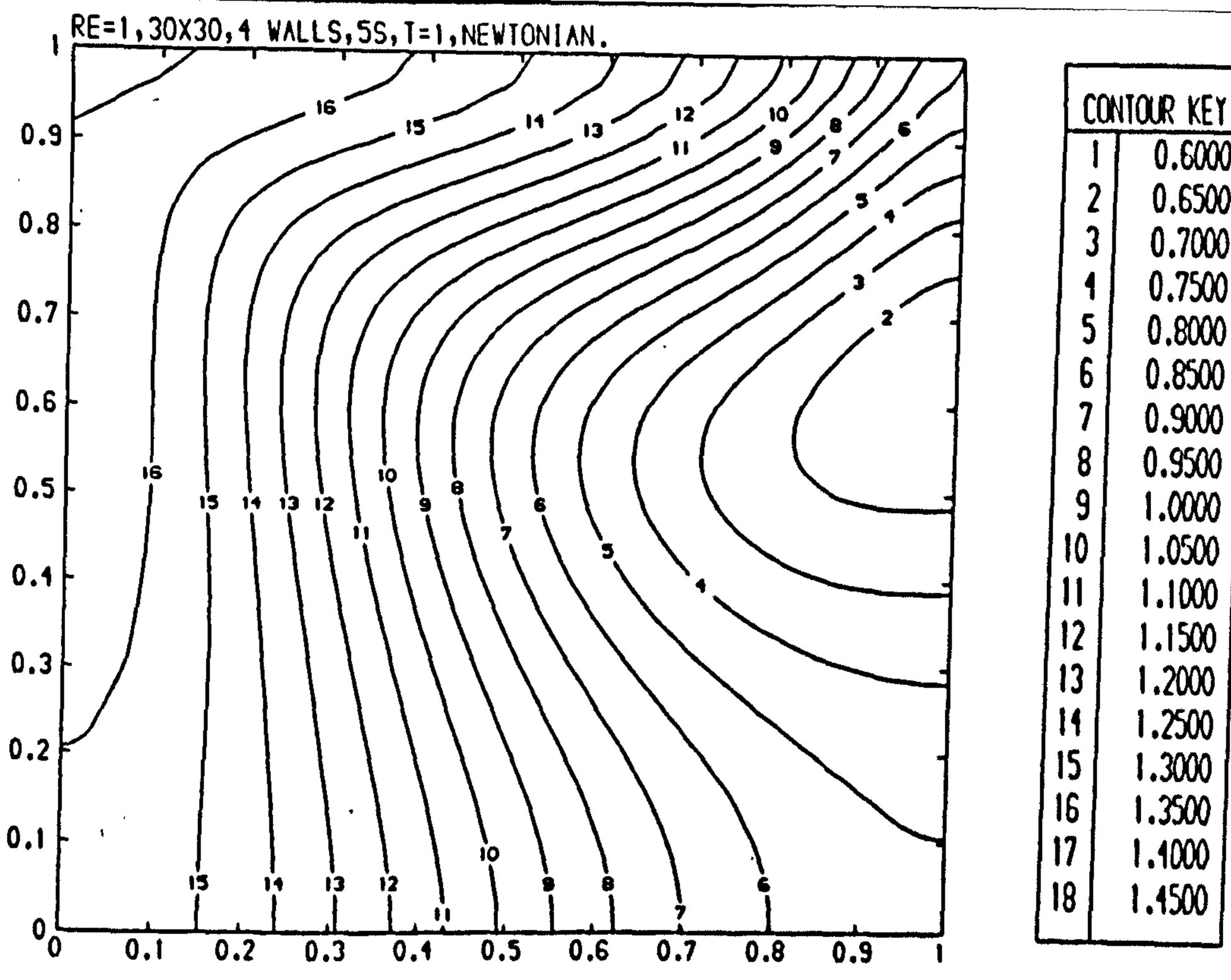

Figure (5.76) Concentration contours for a Newtonian fluid at Re=1,T=1s, time 5s, 4 walls in discontinuous co-rotational periodic motion.

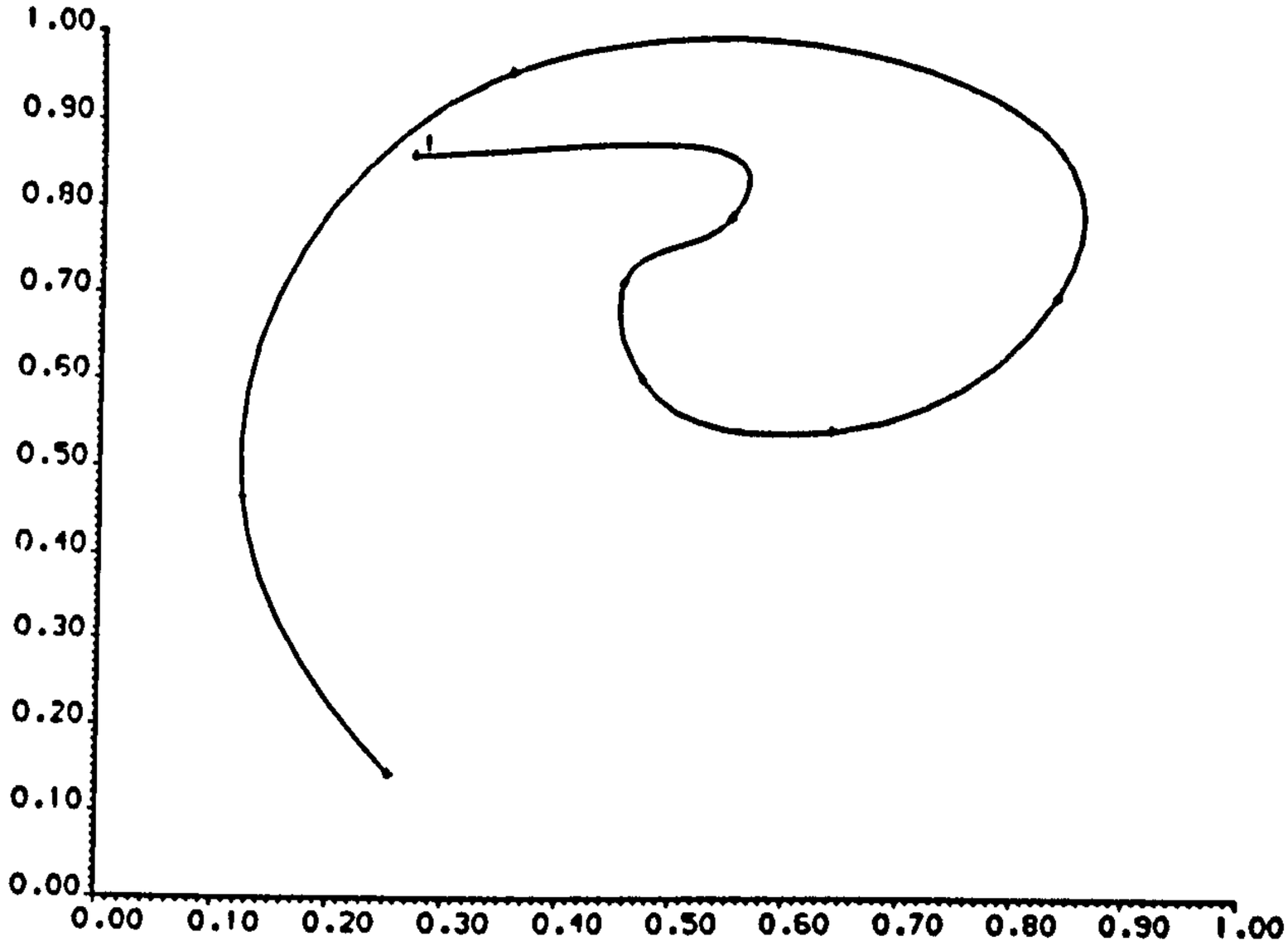

Figure (5.77) The deformation of a low diffusivity fluid line element, for a Newtonian fluid at Re=1, in standard cavity flow.

Figure (5.78) Experimental results of line deformation in the standard cavity flow experiment at low Re provided by Ottino[80].

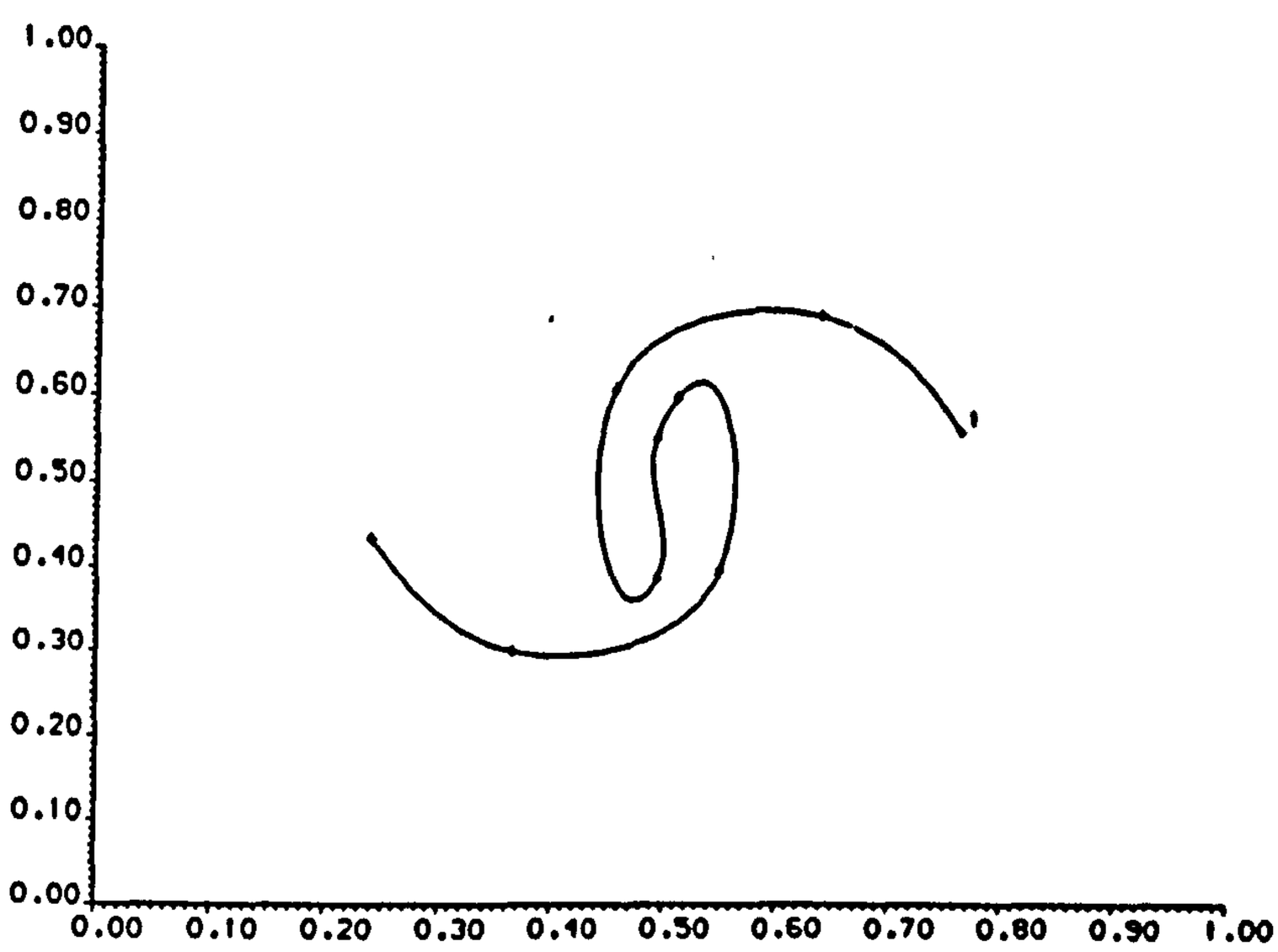

Figure (5.79) The deformation of a low diffusivity fluid line element, for a Newtonian fluid at Re=1, With two plates in simultaneous motion in opposite directions (vb=-vt=-1).

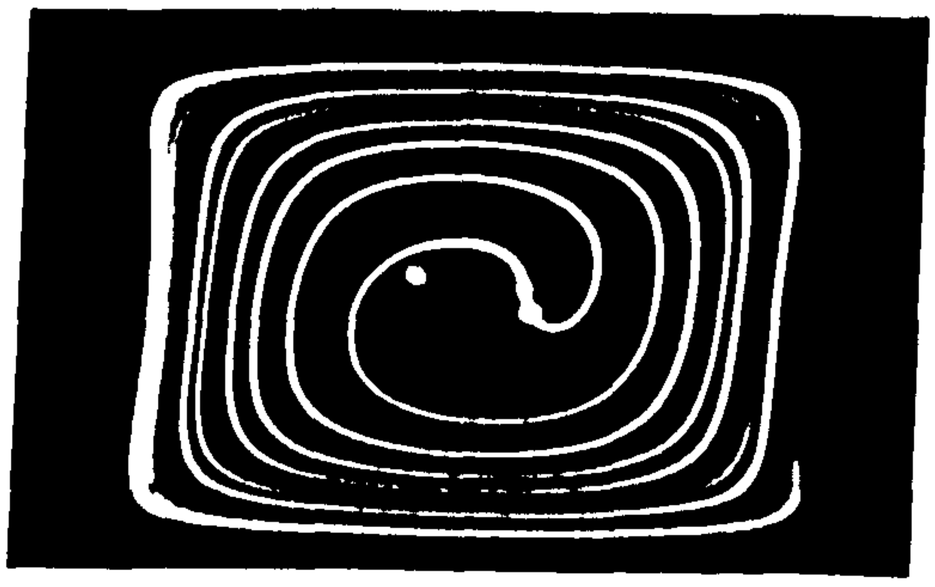

Figure (5.80) Experimental results of line deformation in the at low Re with two plates in simultaneous motion in opposite directions provided by Ottino[80].

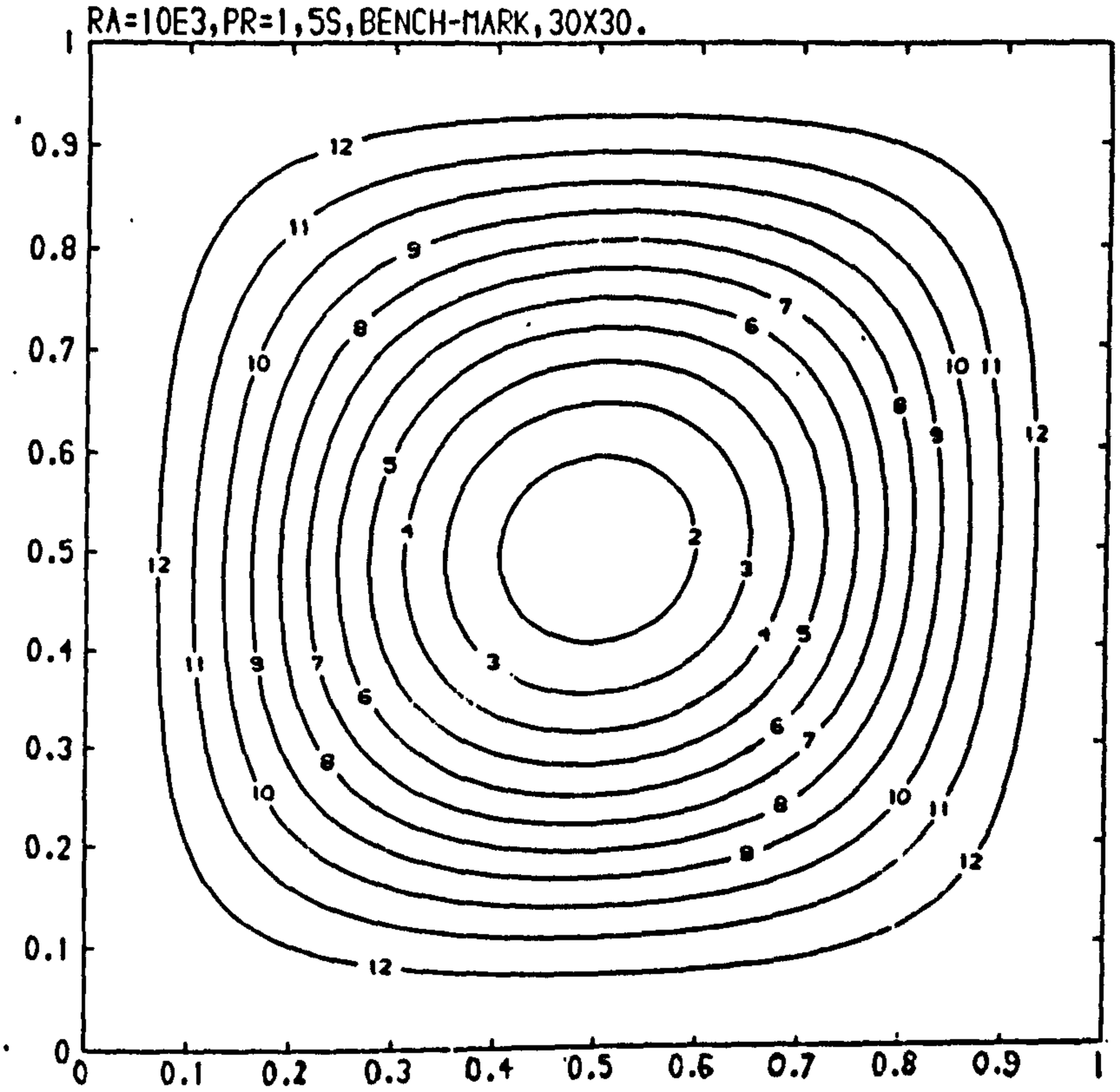

CONTOUR KEY	
1	-1.2000
2	-1.1000
3	-1.0000
4	-0.9000
5	-0.8000
6	-0.7000
7	-0.6000
8	-0.5000
9	-0.4000
10	-0.3000
11	-0.2000
12	-0.1000

Figure (7.2)

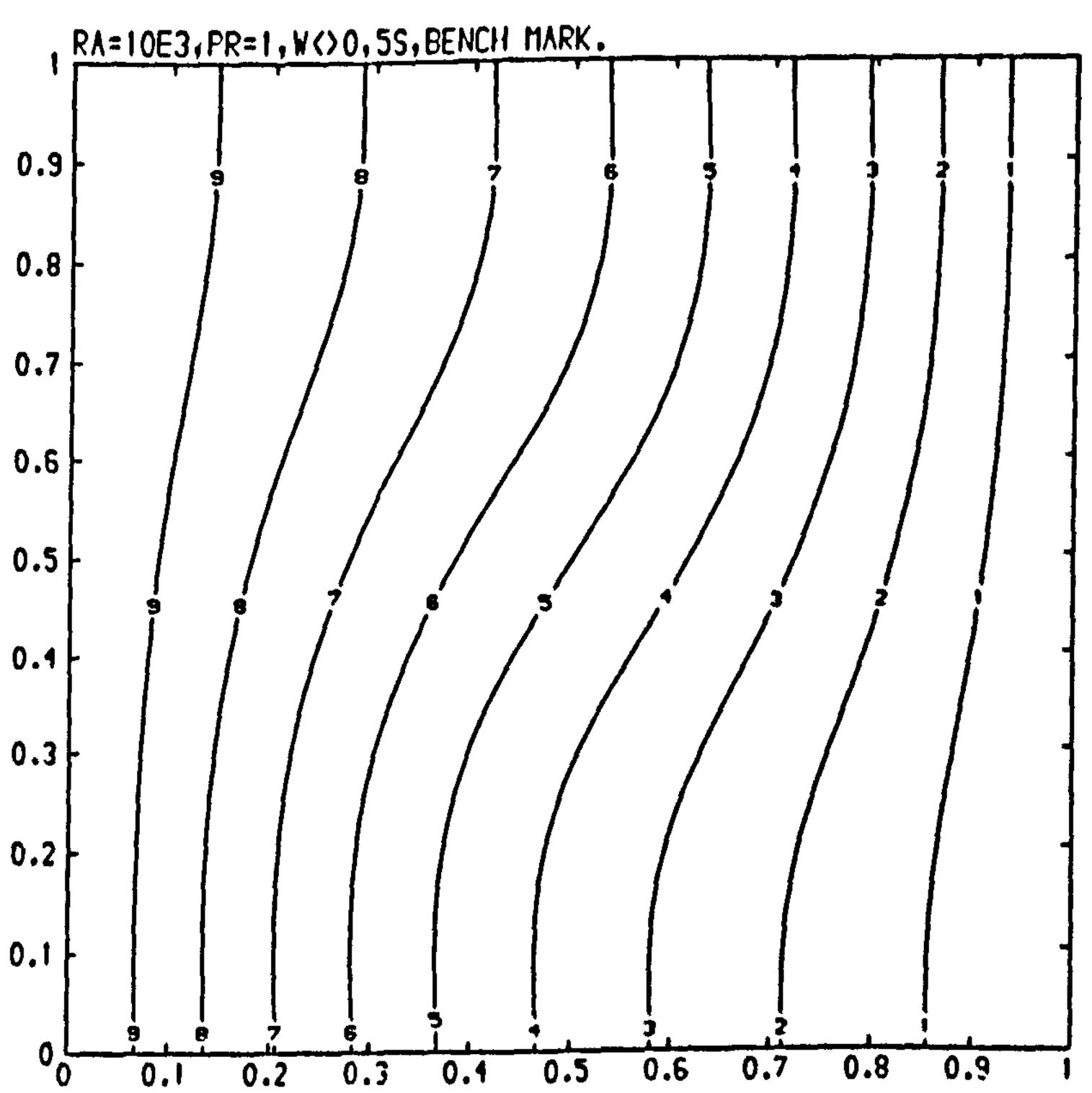

CONTOUR KEY	
1	0.1000
2	0.2000
3	0.3000
4	0.4000
5	0.5000
6	0.6000
7	0.7000
8	0.8000
9	0.9000
10	1.0000

Figure (7.3)

Streamline & temperature plots for a Newtonian fluid at $Ra=10^3$, $Pr=1$, $\omega<>0$.

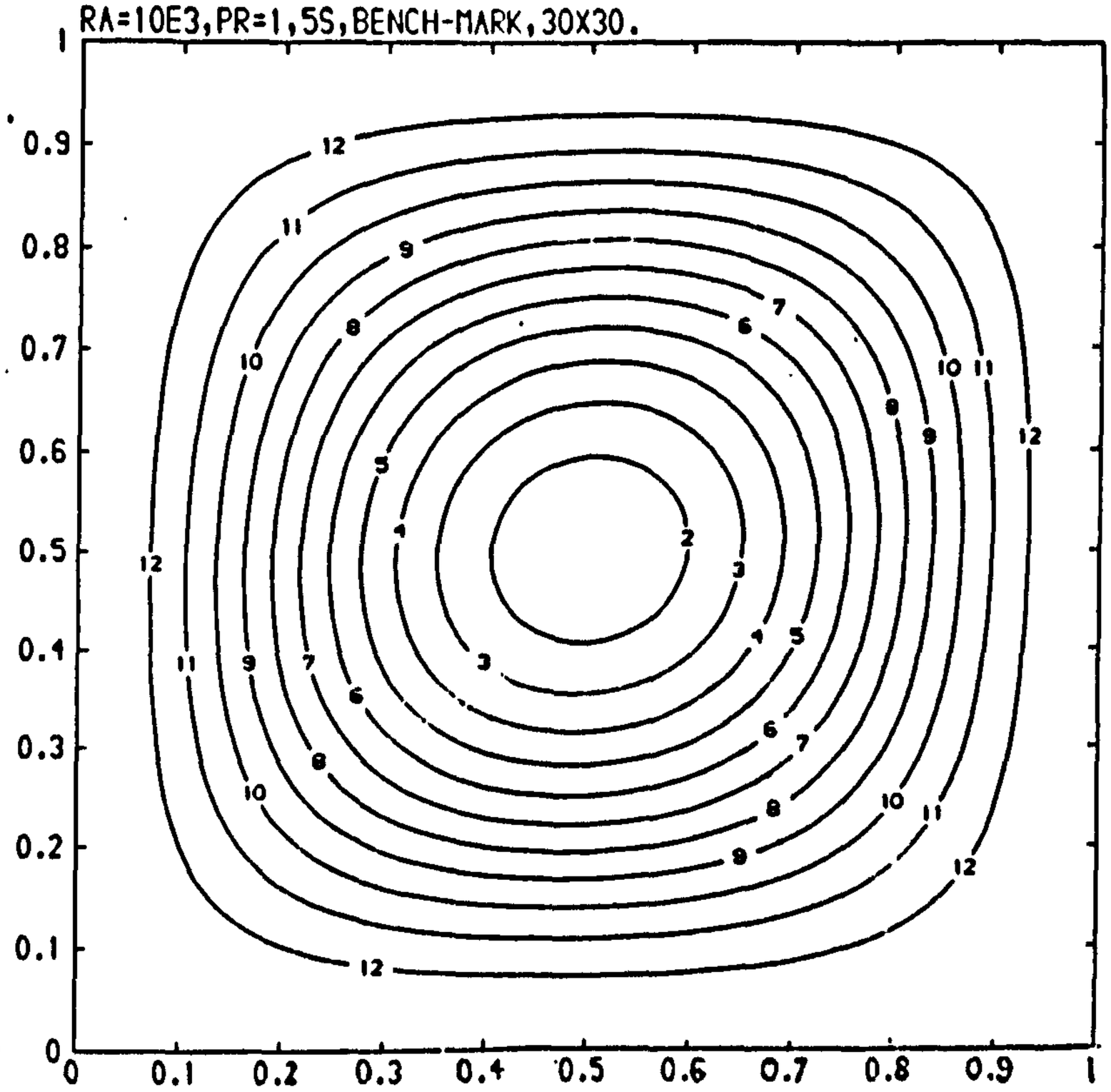

CONTOUR KEY	
1	-1.2000
2	-1.1000
3	-1.0000
4	-0.9000
5	-0.8000
6	-0.7000
7	-0.6000
8	-0.5000
9	-0.4000
10	-0.3000
11	-0.2000
12	-0.1000

Figure (7.2)

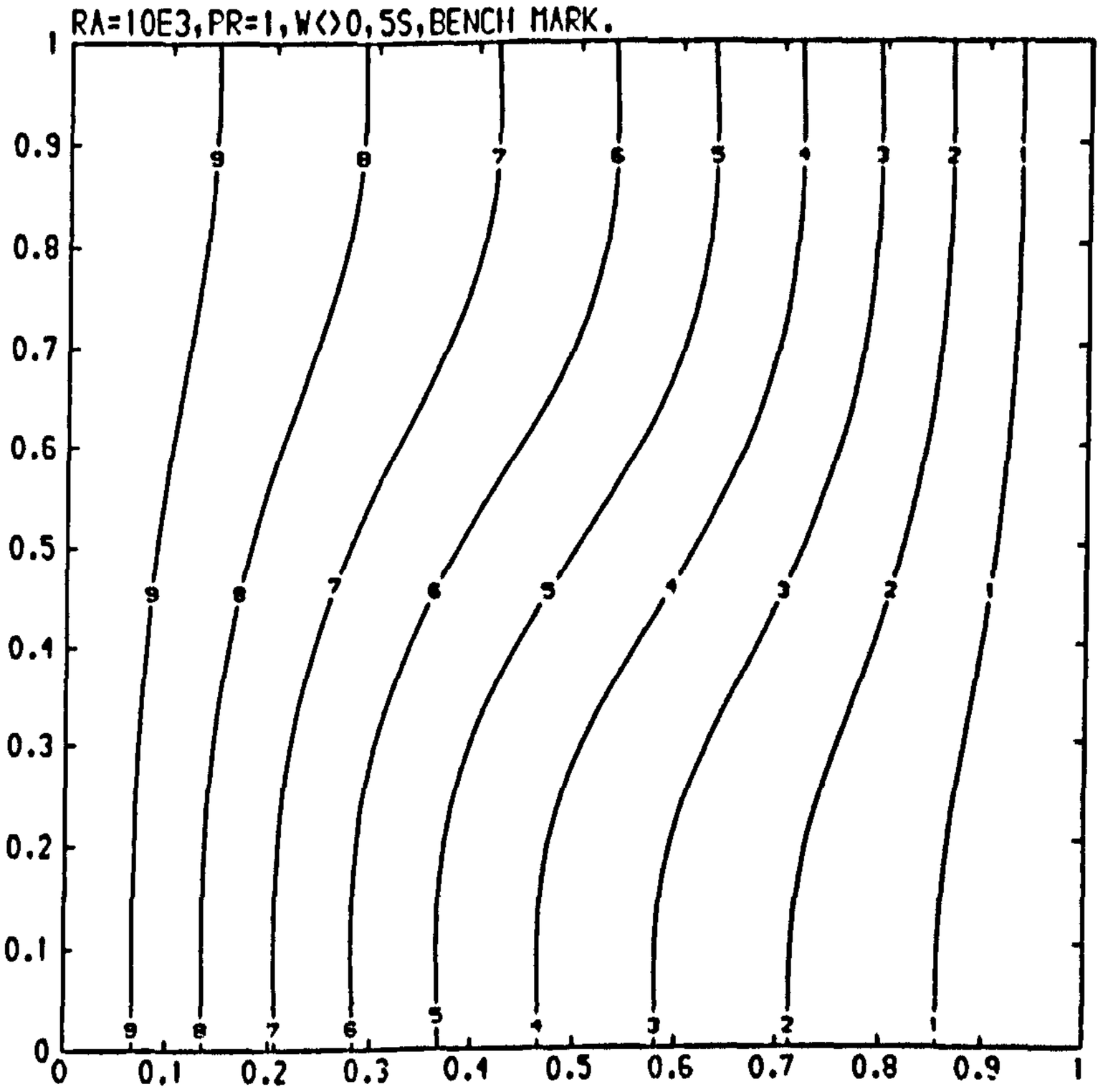

CONTOUR KEY	
1	0.1000
2	0.2000
3	0.3000
4	0.4000
5	0.5000
6	0.6000
7	0.7000
8	0.8000
9	0.9000
10	1.0000

Figure (7.3)

Streamline & temperature plots for a Newtonian fluid at $Ra=10^3$, $Pr=1$, $\omega<>0$.

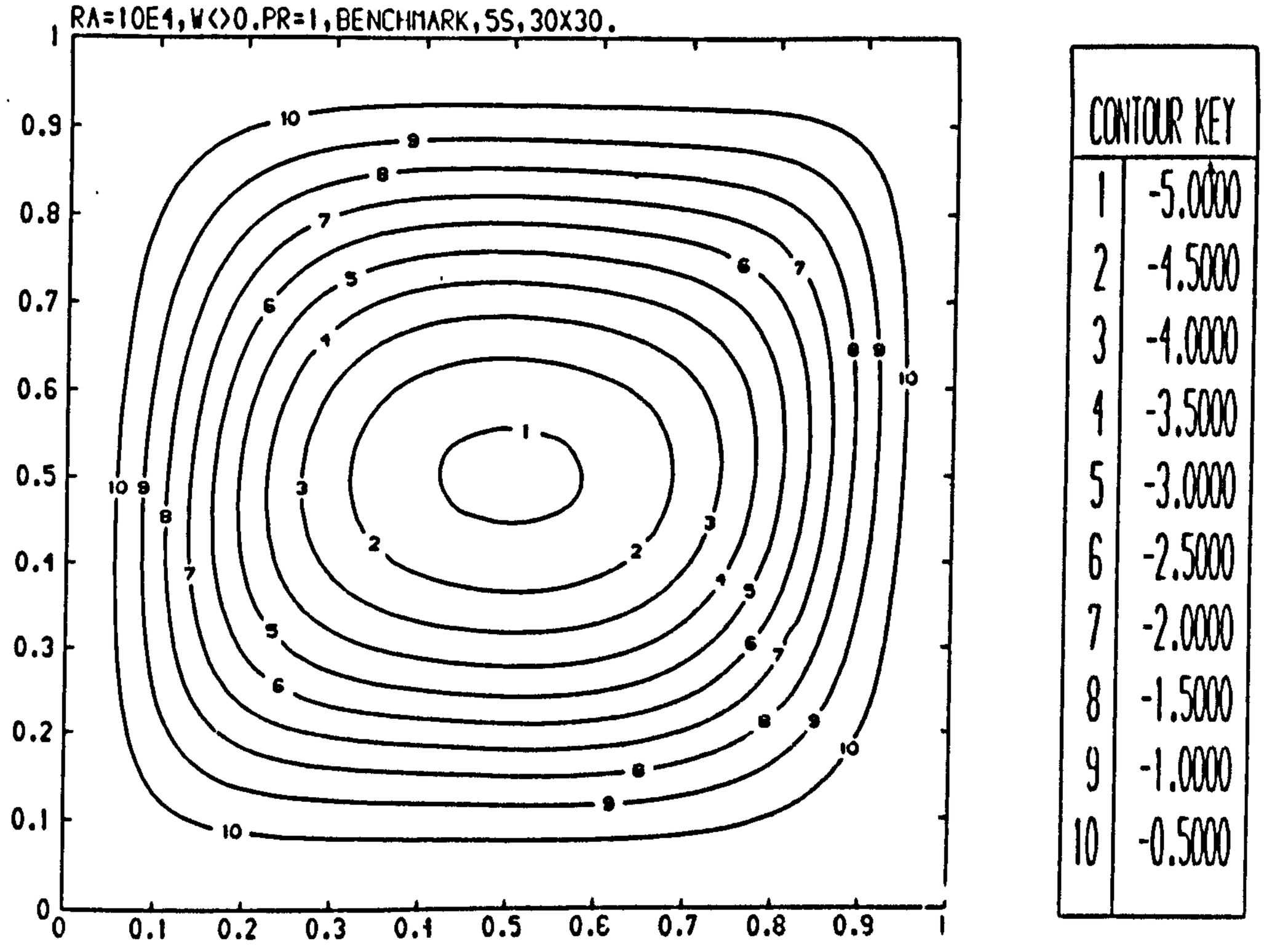

Figure (7.4)

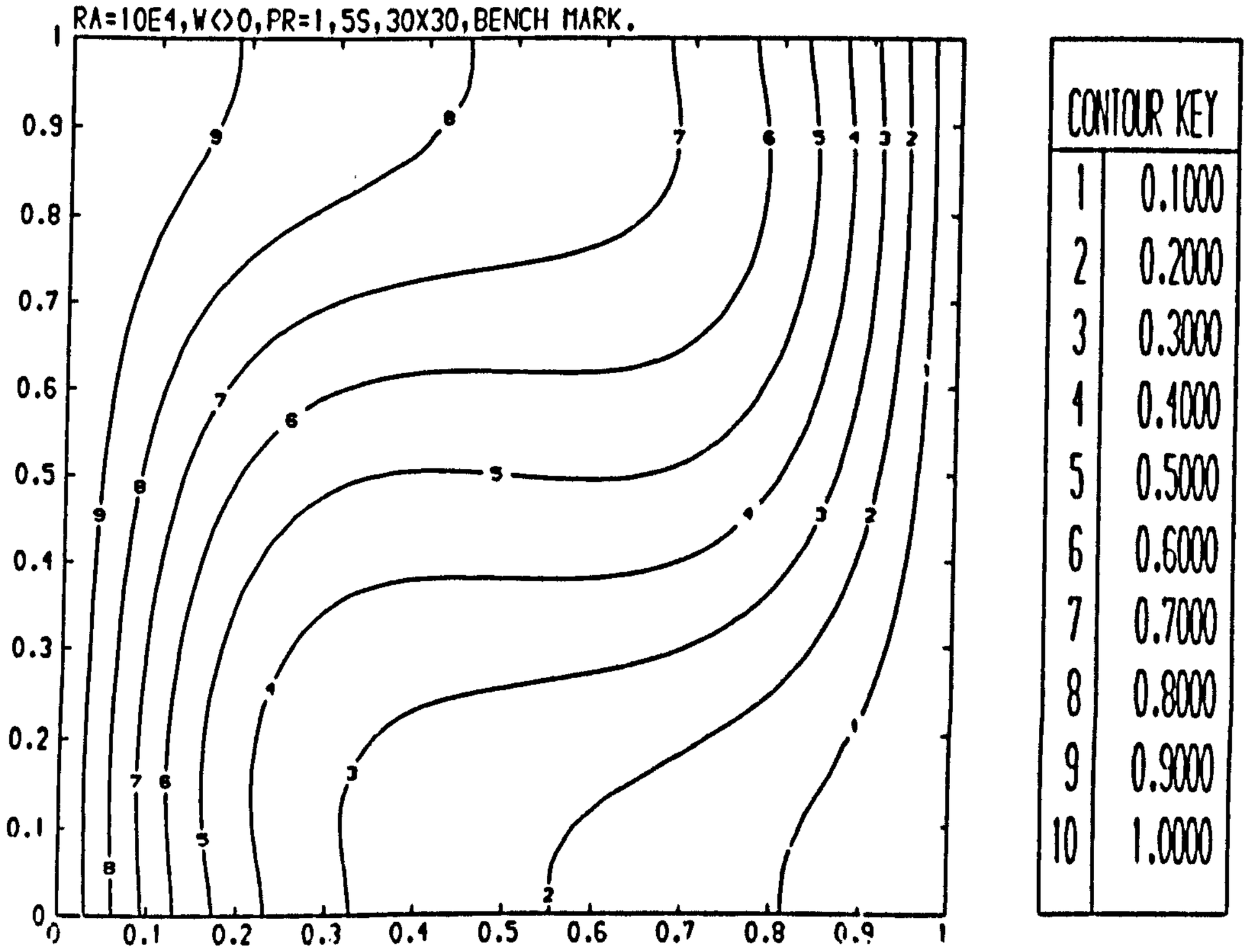

Figure (7.5)

Streamline & temperature plots for a Newtonian fluid at $Re=10^4$, $Pr=1$, $\omega<>0$.

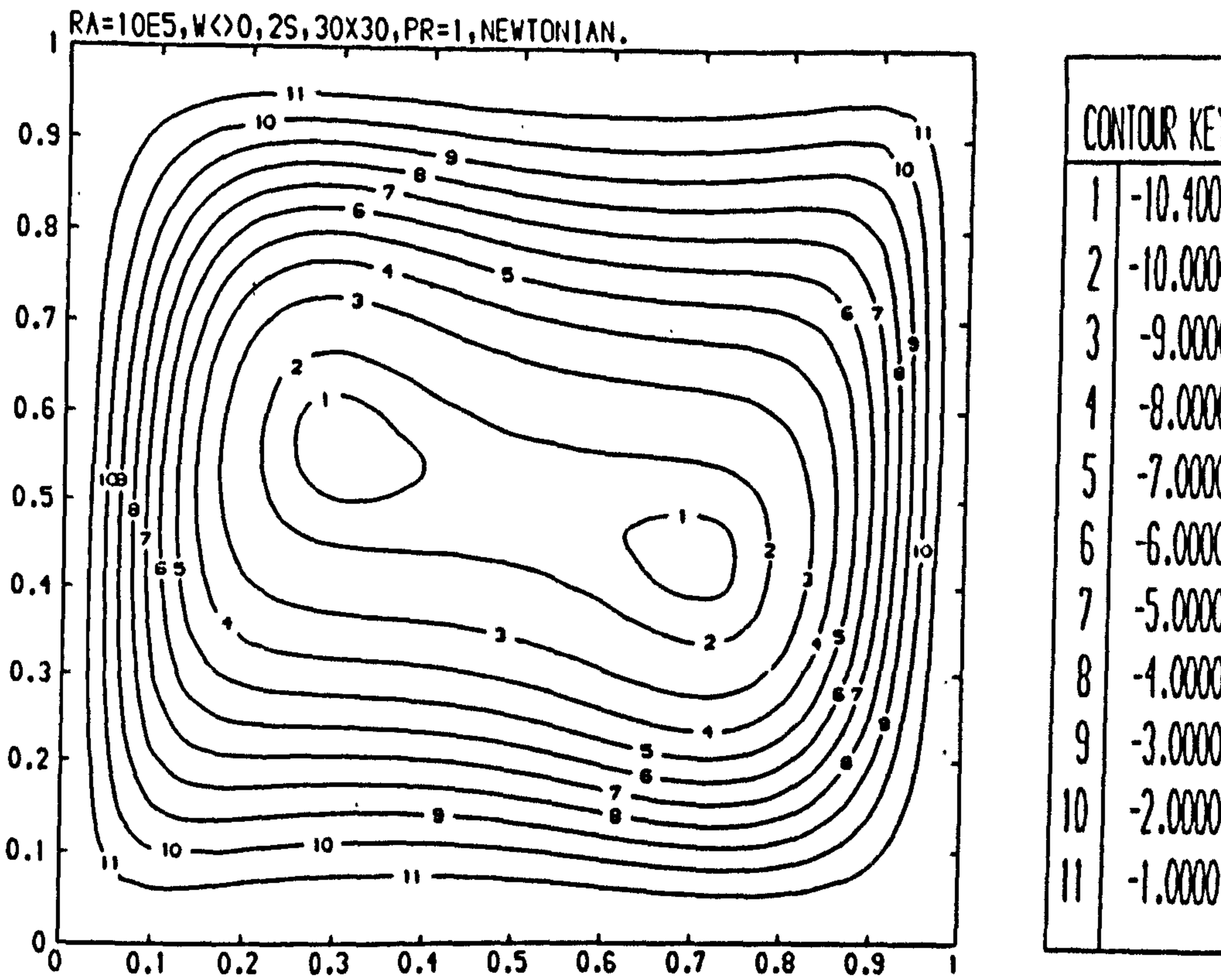

Figure (7.6)

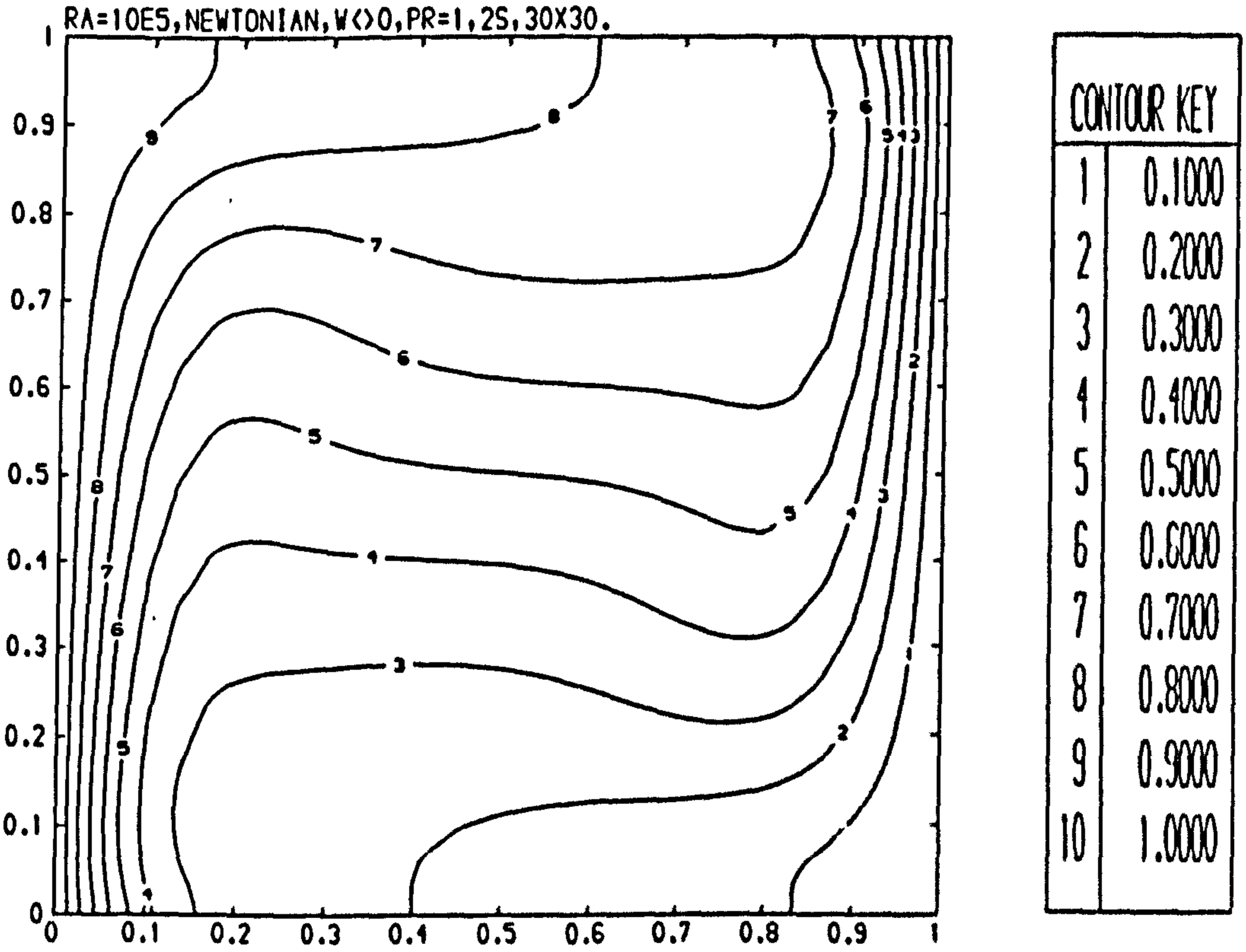

Figure (7.7)

Streamline & temperature plots for a Newtonian fluid at $Ra=10^5$, $Pr=1$, $\omega<>0$.

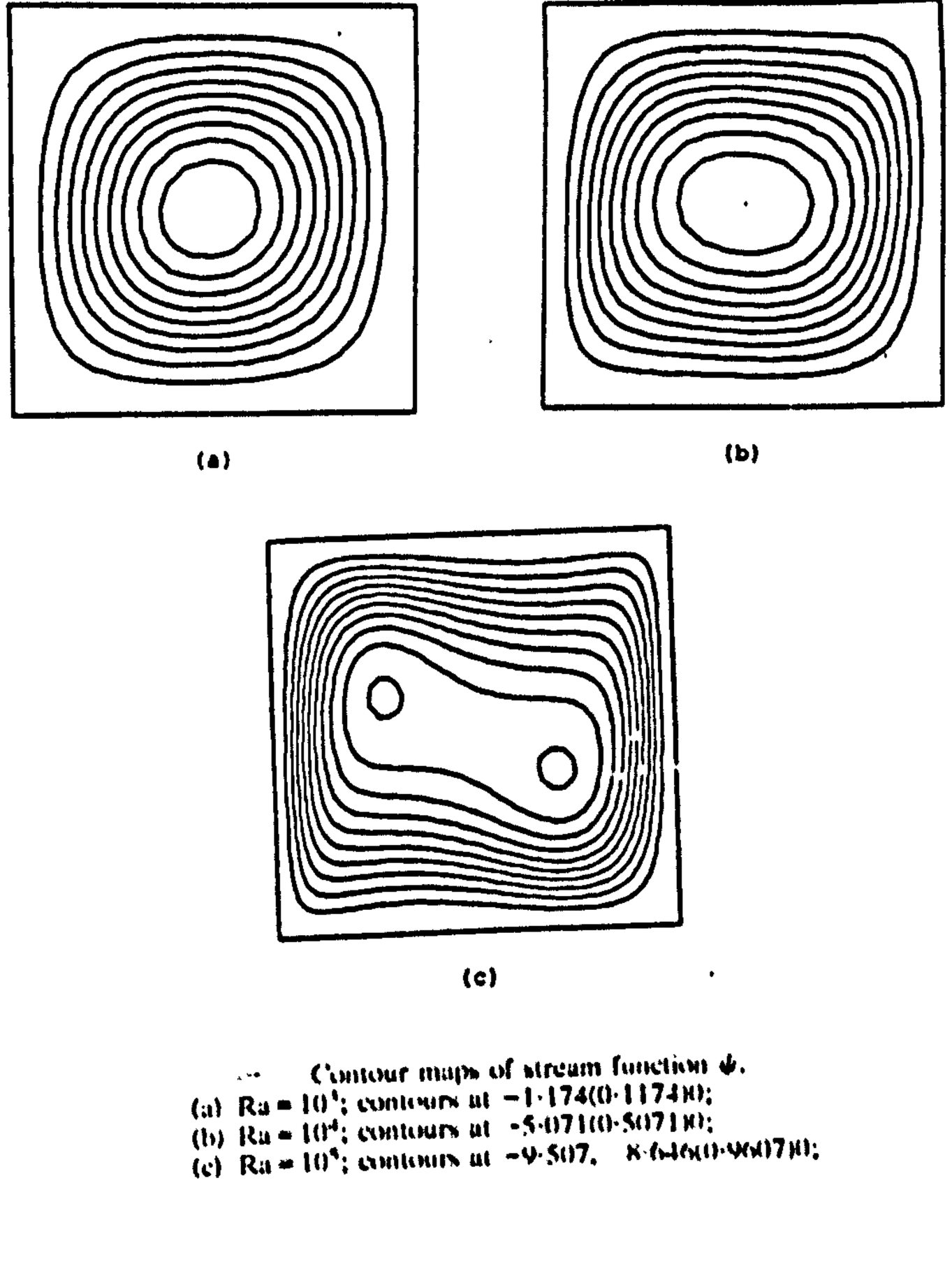

(a) (b)

(c)

Contour maps of stream function ψ.
(a) $Ra = 10^3$; contours at $-1{\cdot}174(0{\cdot}1174)0$;
(b) $Ra = 10^4$; contours at $-5{\cdot}071(0{\cdot}5071)0$;
(c) $Ra = 10^5$; contours at $-9{\cdot}507$, $8{\cdot}646(0{\cdot}9607)0$;

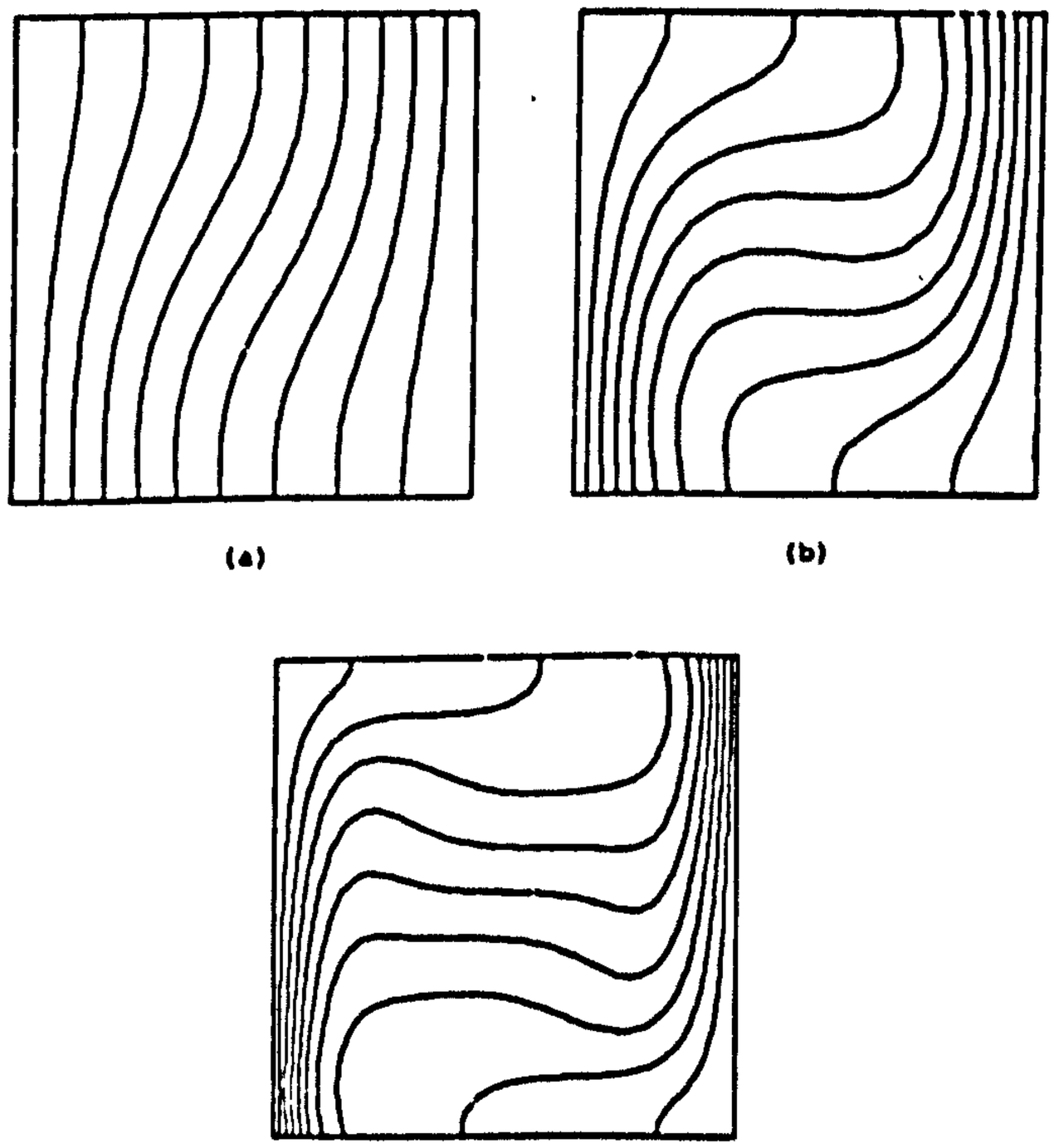

(a) (b)

(c)

Contour maps of temperature T:
(a) $Ra = 10^3$, (b) $Ra = 10^4$,
(c) $Ra = 10^5$,
Contours at (0·1) in each case

Figure (7.8) The bench mark solutions of De Vahl Davis[33].

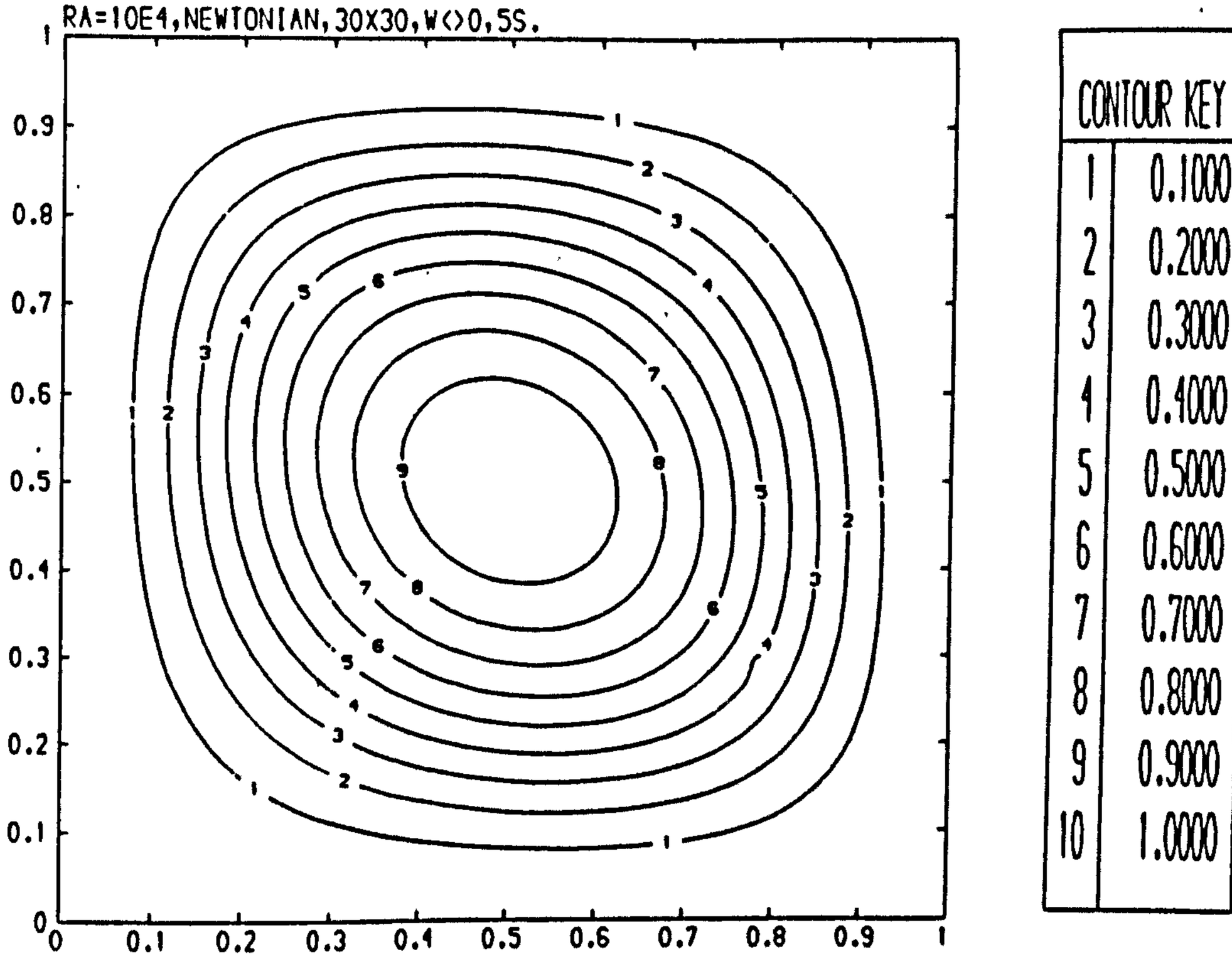

Figure (7.9)

Figure (7.10)

Streamline & temperature plots for a Newtonian fluid at $Ra=10^4$, $Pr=7$, $\omega<>0$.

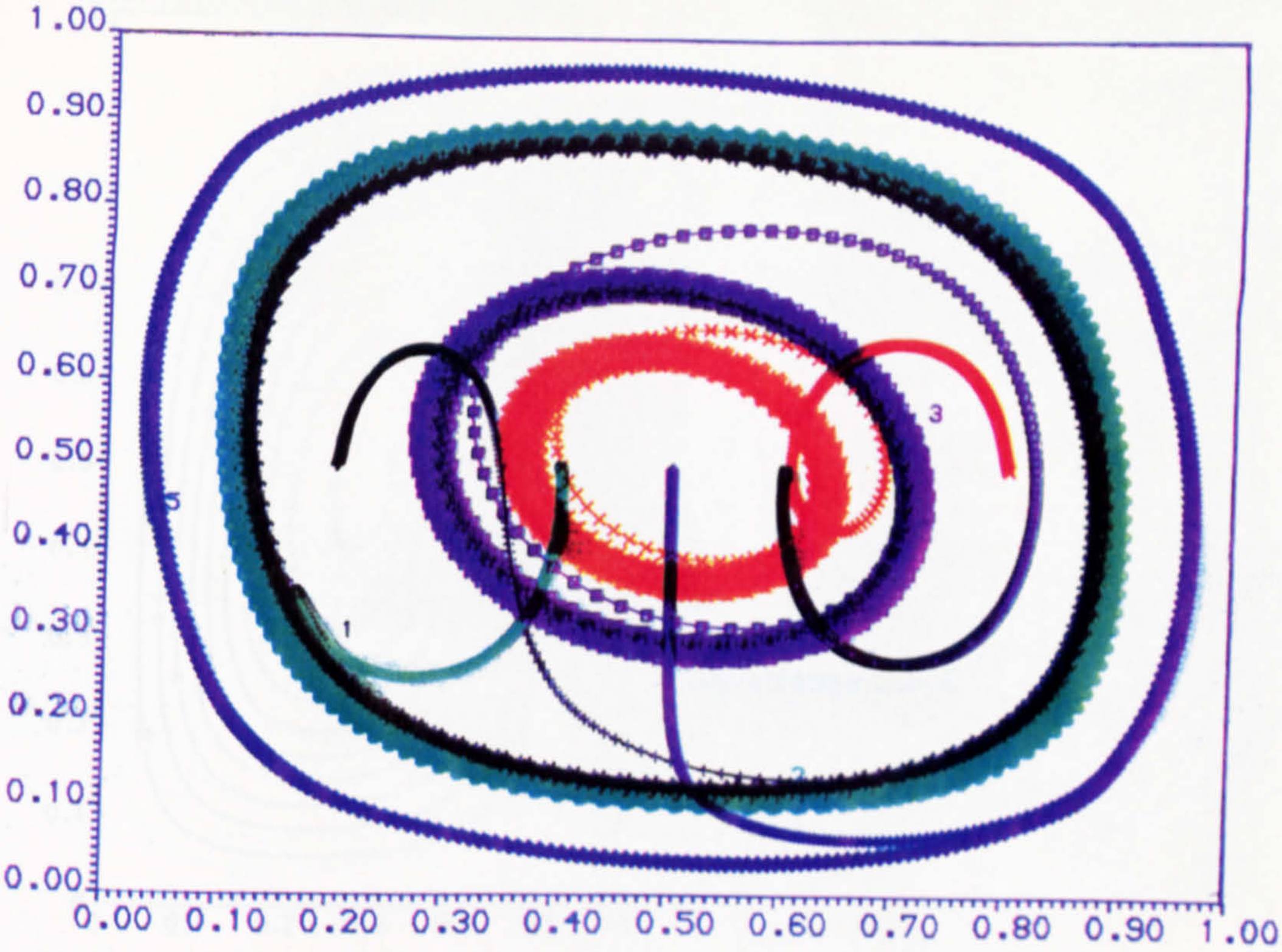

Figure (7.11) The evolutionary trajectories of an initially placed horizontal line of particles at $Ra=10^4$, $Pr=7$, $\omega<>0$.

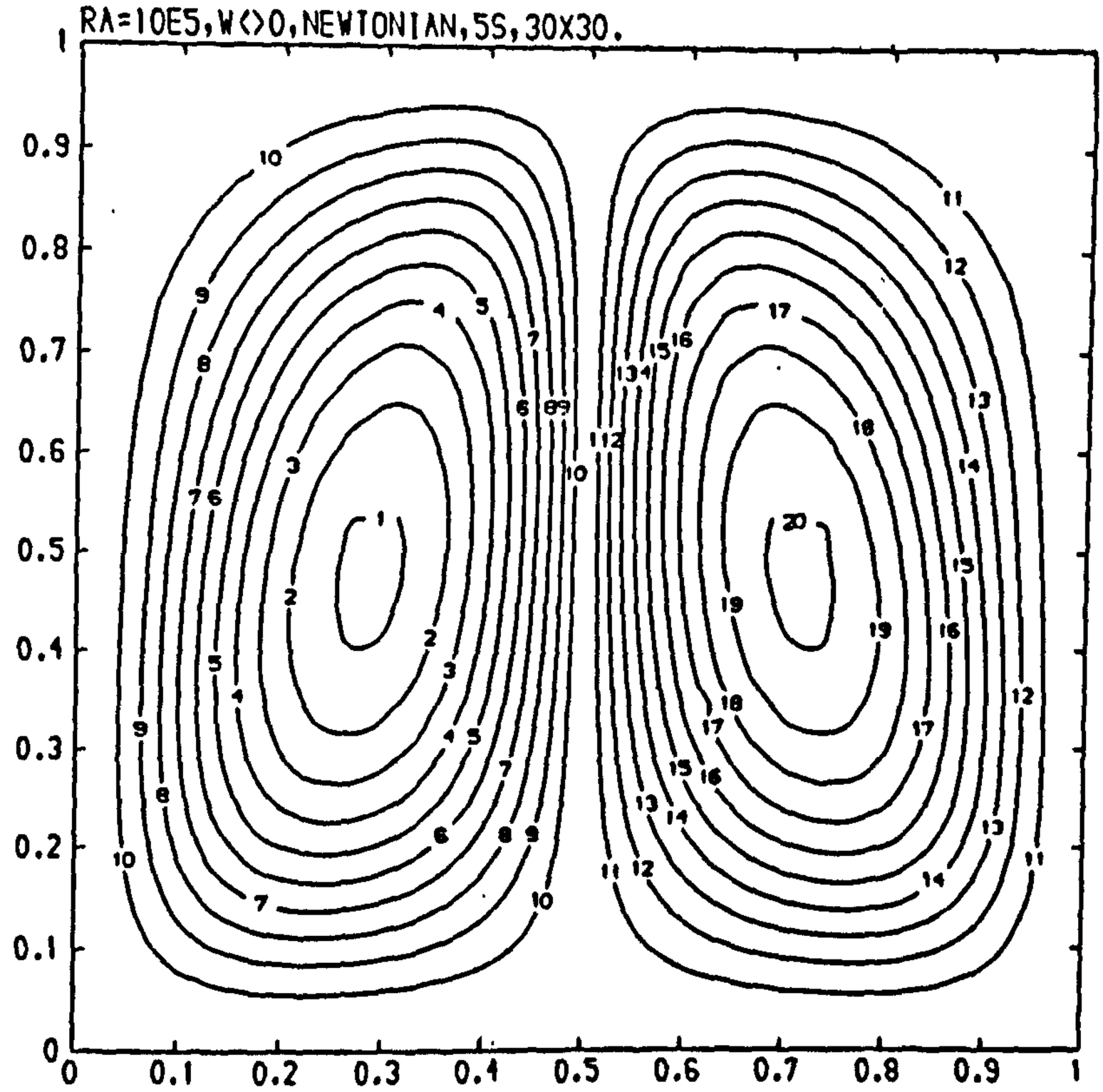

CONTOUR KEY	
1	-2.0000
2	-1.8000
3	-1.6000
4	-1.4000
5	-1.2000
6	-1.0000
7	-0.8000
8	-0.6000
9	-0.4000
10	-0.2000
11	0.2000
12	0.4000
13	0.6000
14	0.8000
15	1.0000
16	1.2000
17	1.4000
18	1.6000
19	1.8000
20	2.0000

Figure (7.12)

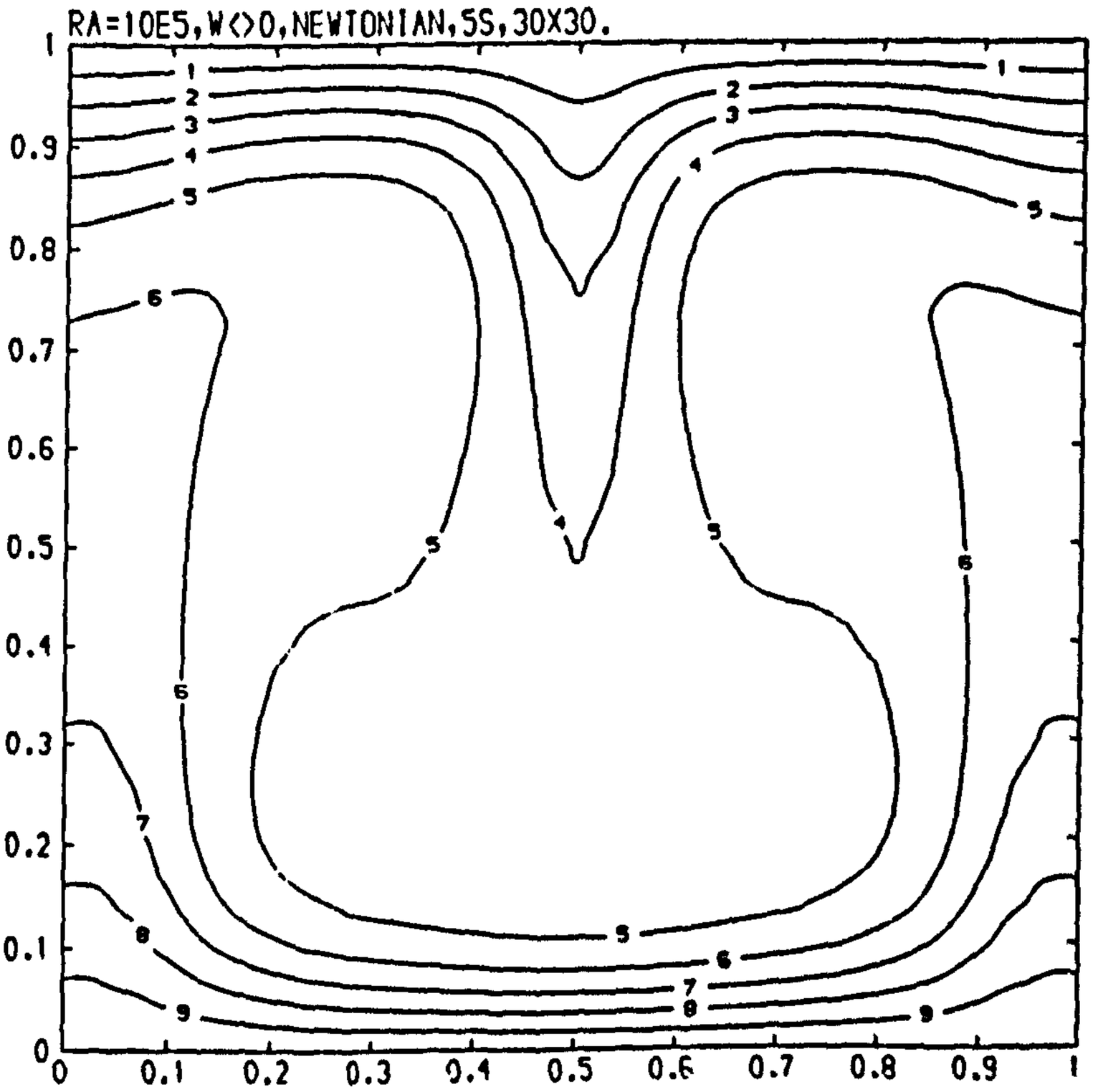

CONTOUR KEY	
1	0.1000
2	0.2000
3	0.3000
4	0.4000
5	0.5000
6	0.6000
7	0.7000
8	0.8000
9	0.9000
10	1.0000

Figure (7.13)

Streamline & temperature plots for a Newtonian fluid at $Ra=10^5$, $Pr=7$, $\omega<>0$.

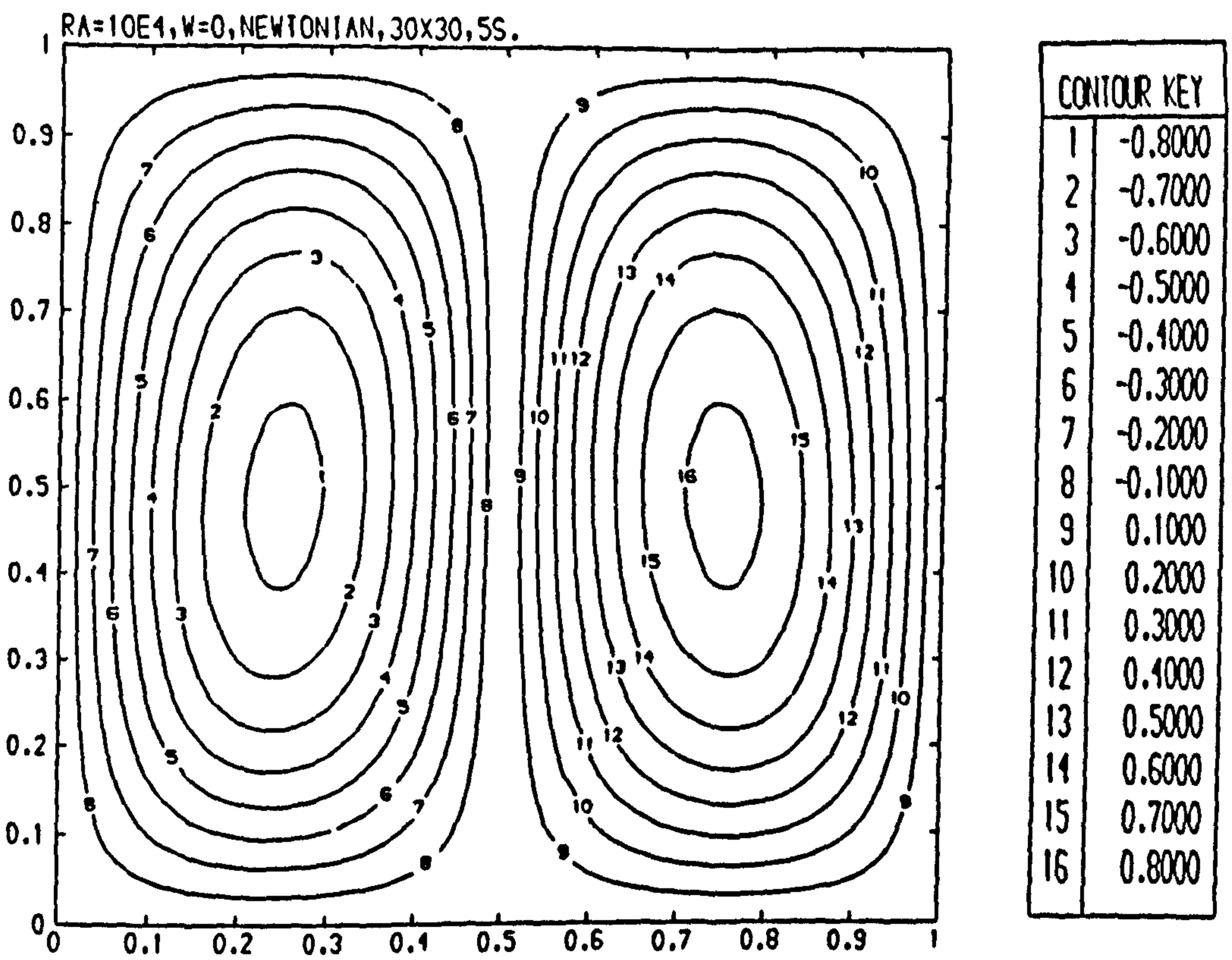

Figure (7.14)

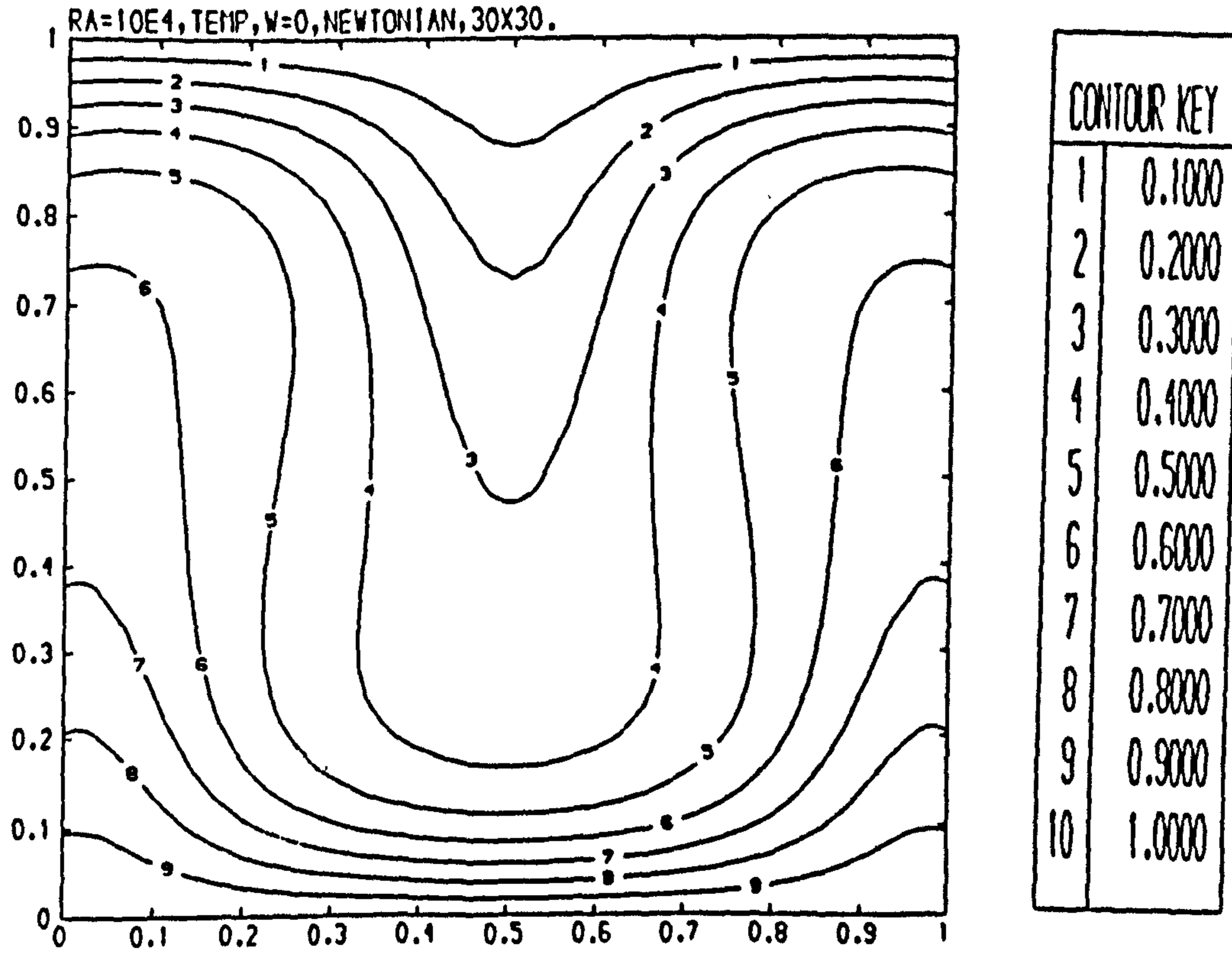

Figure (7.15)

Streamline & temperature plots for a Newtonian fluid at $Re=10^4$, $Pr=7$, $\omega=0$.

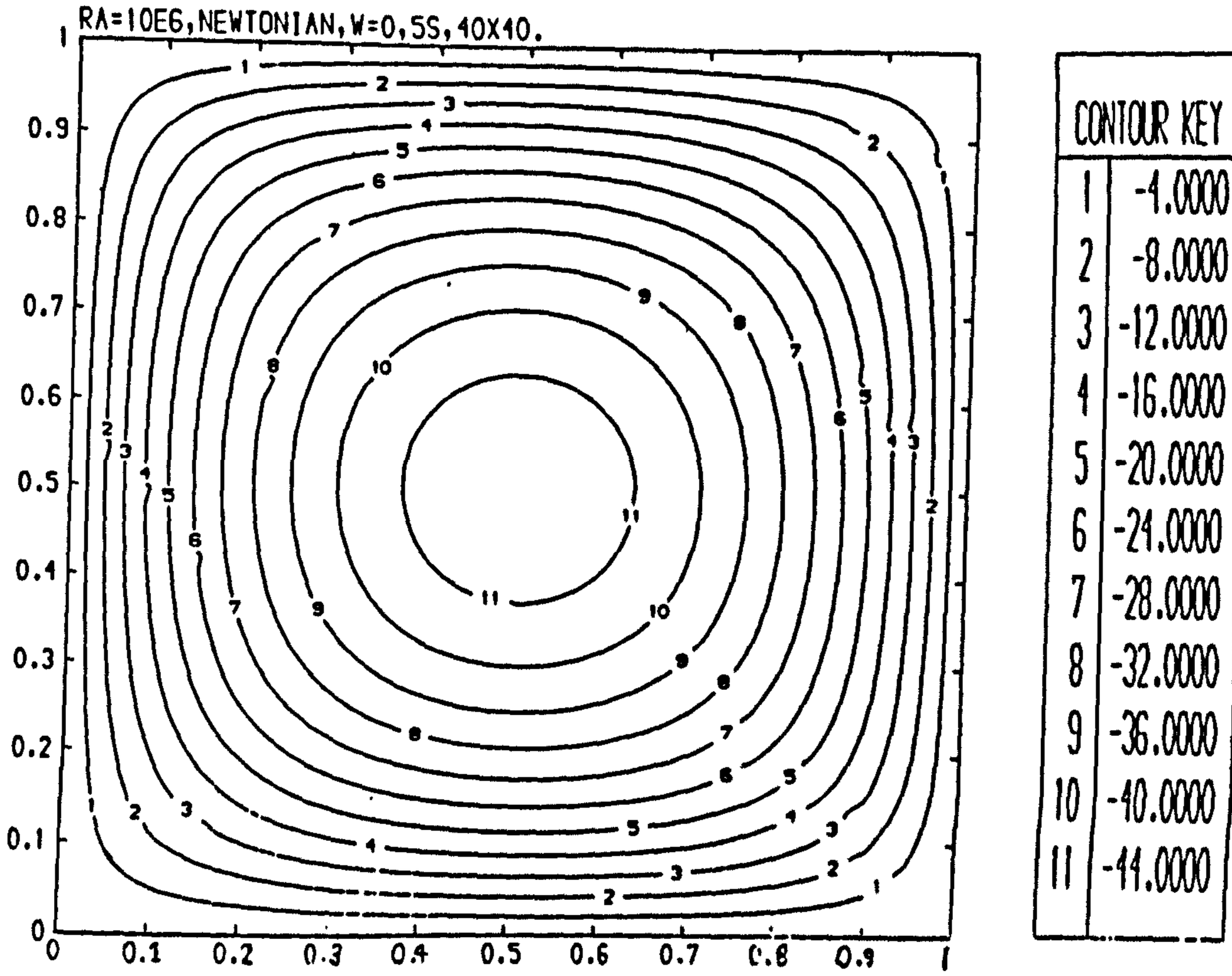

Figure (7.16)

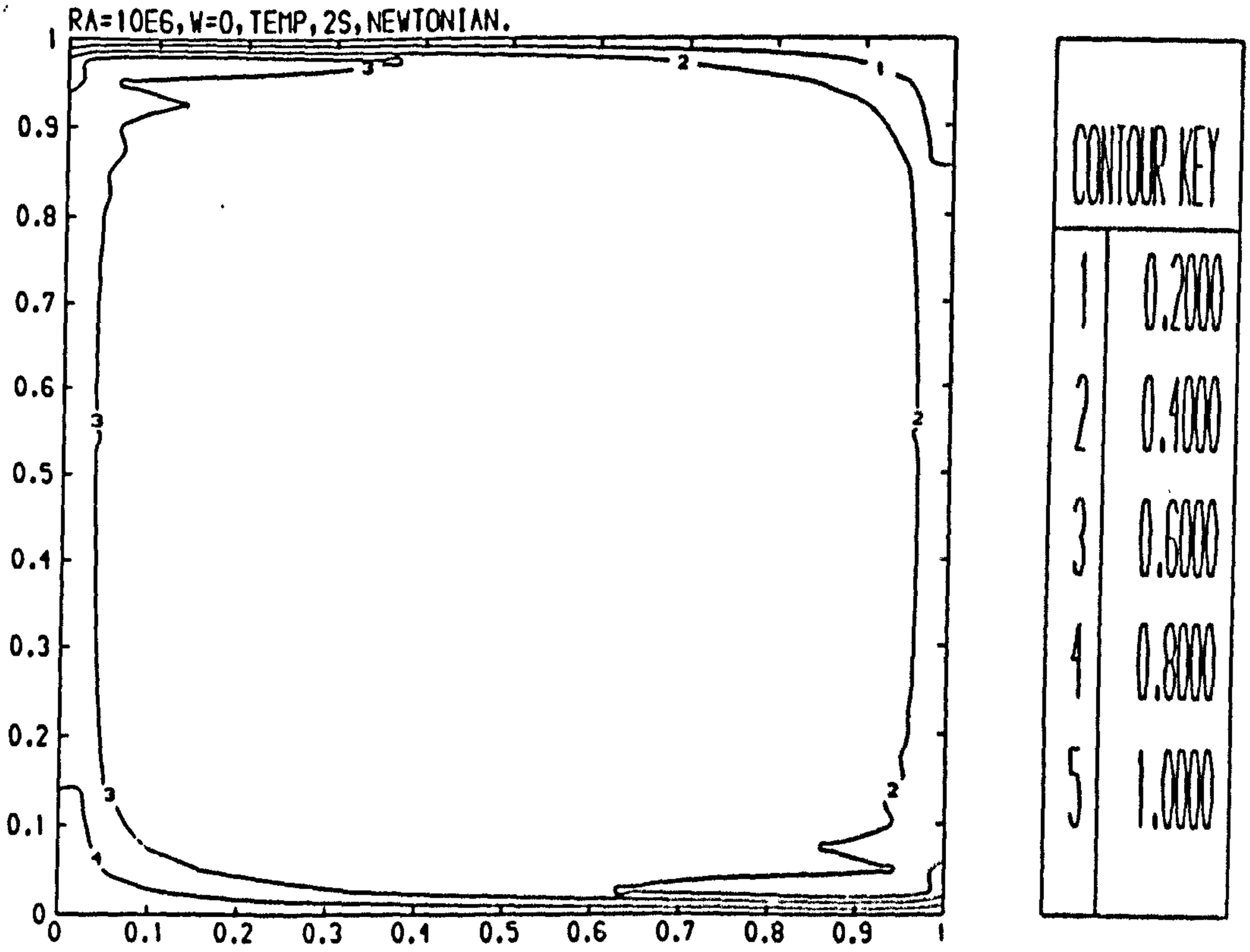

Figure (7.17)

Streamline & temperature plots for a Newtonian fluid at $Ra=10^6$, $Pr=7$, $\omega=0$.

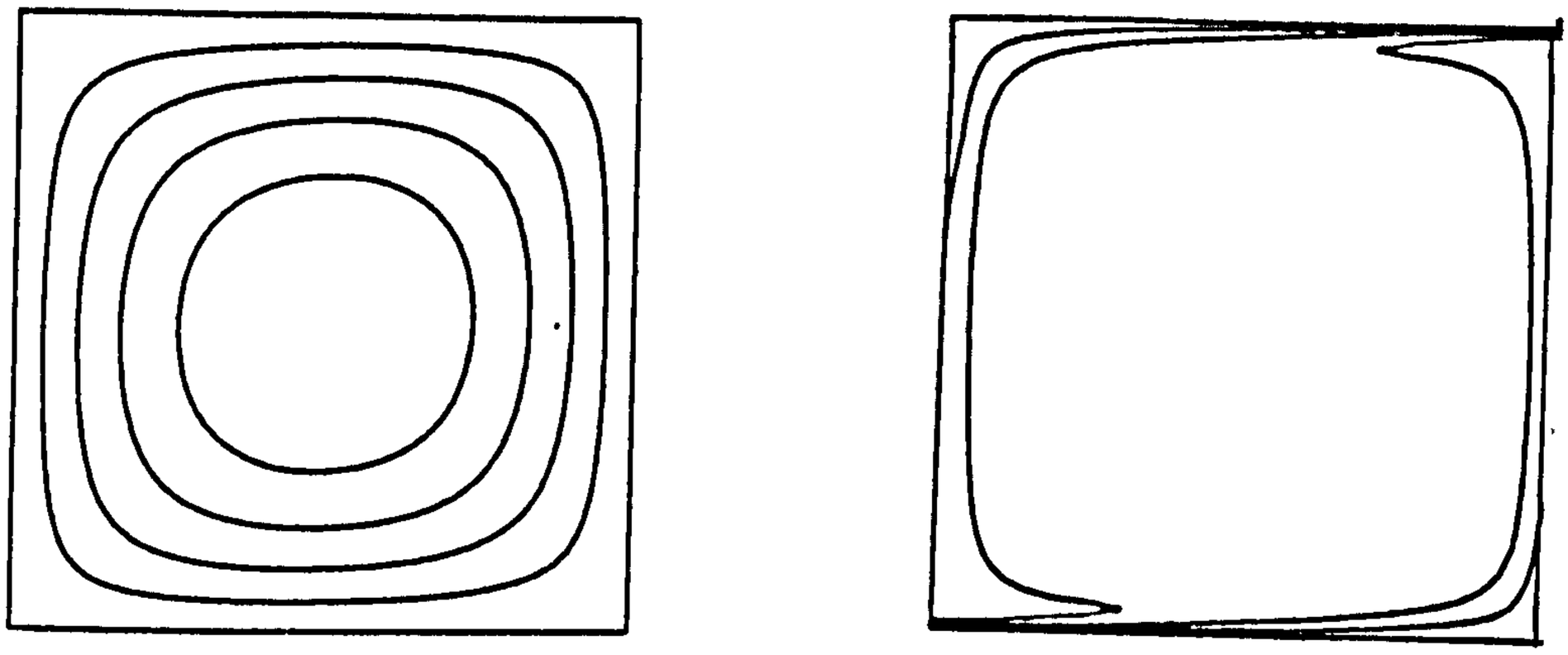

Figure (7.18) Streamline & temperature plots of Moore and weiss[69] at Ra=0.66×10^6, using an initially uniform temperature distribution throughout the cavity.

Figure (7.19) Streamline & temperature plots of Mckenzie et al[62] at Ra=10^6.

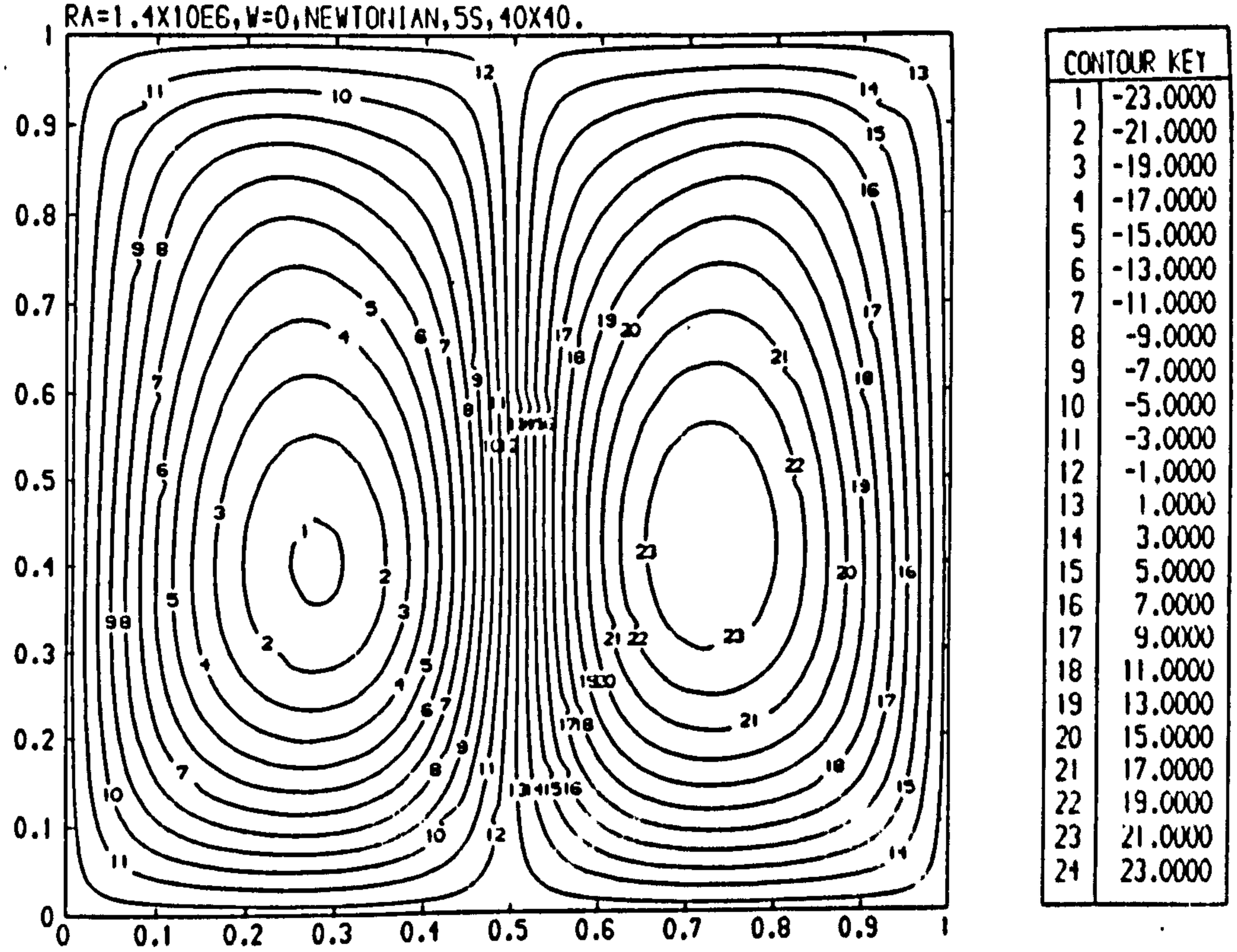

CONTOUR KEY	
1	-23.0000
2	-21.0000
3	-19.0000
4	-17.0000
5	-15.0000
6	-13.0000
7	-11.0000
8	-9.0000
9	-7.0000
10	-5.0000
11	-3.0000
12	-1.0000
13	1.0000
14	3.0000
15	5.0000
16	7.0000
17	9.0000
18	11.0000
19	13.0000
20	15.0000
21	17.0000
22	19.0000
23	21.0000
24	23.0000

Figure (7.20)

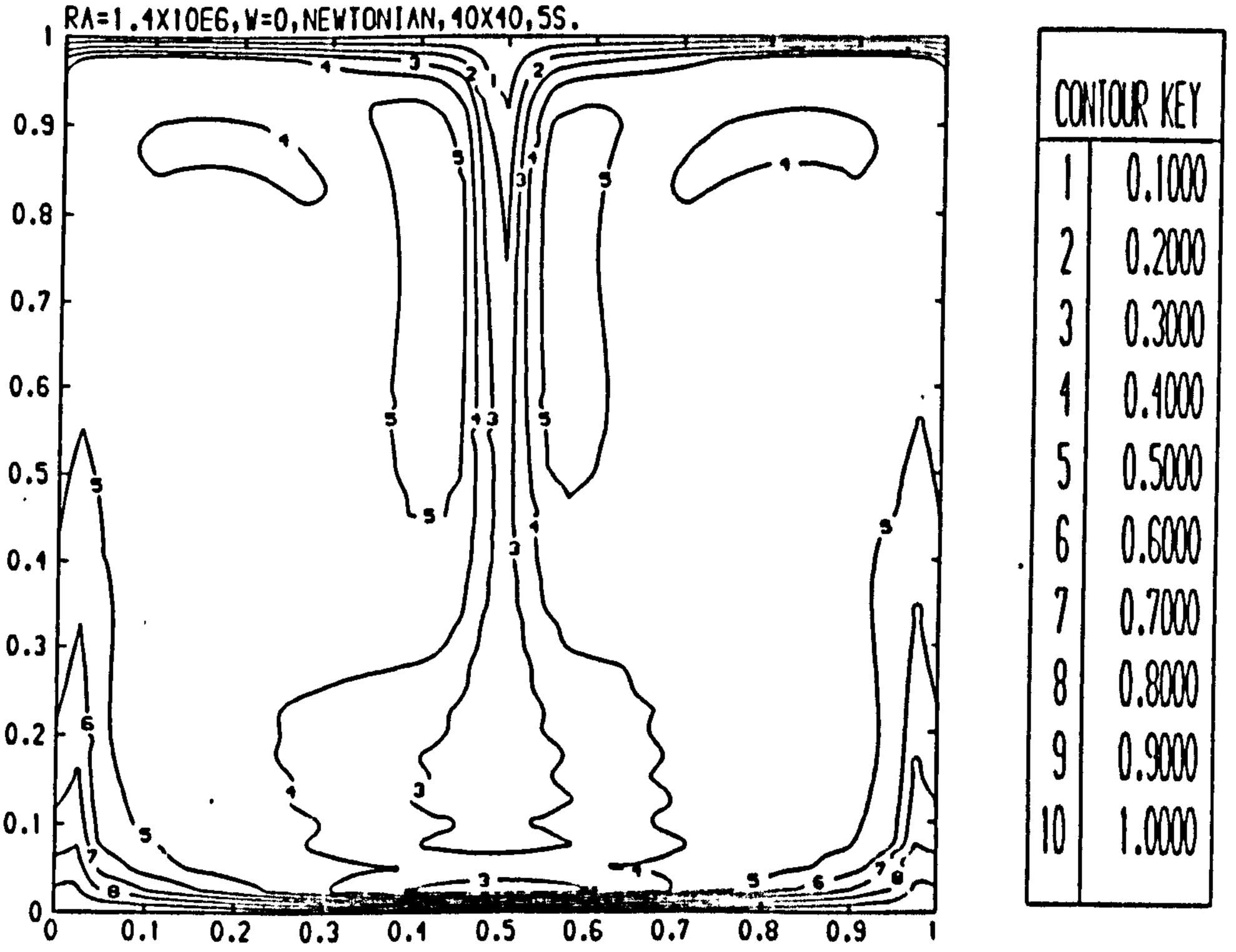

CONTOUR KEY	
1	0.1000
2	0.2000
3	0.3000
4	0.4000
5	0.5000
6	0.6000
7	0.7000
8	0.8000
9	0.9000
10	1.0000

Figure (7.21)

Streamline & temperature plots for a Newtonian fluid at $Ra = 1.4 \times 10^6$, $Pr = 7$, $\omega = 0$.

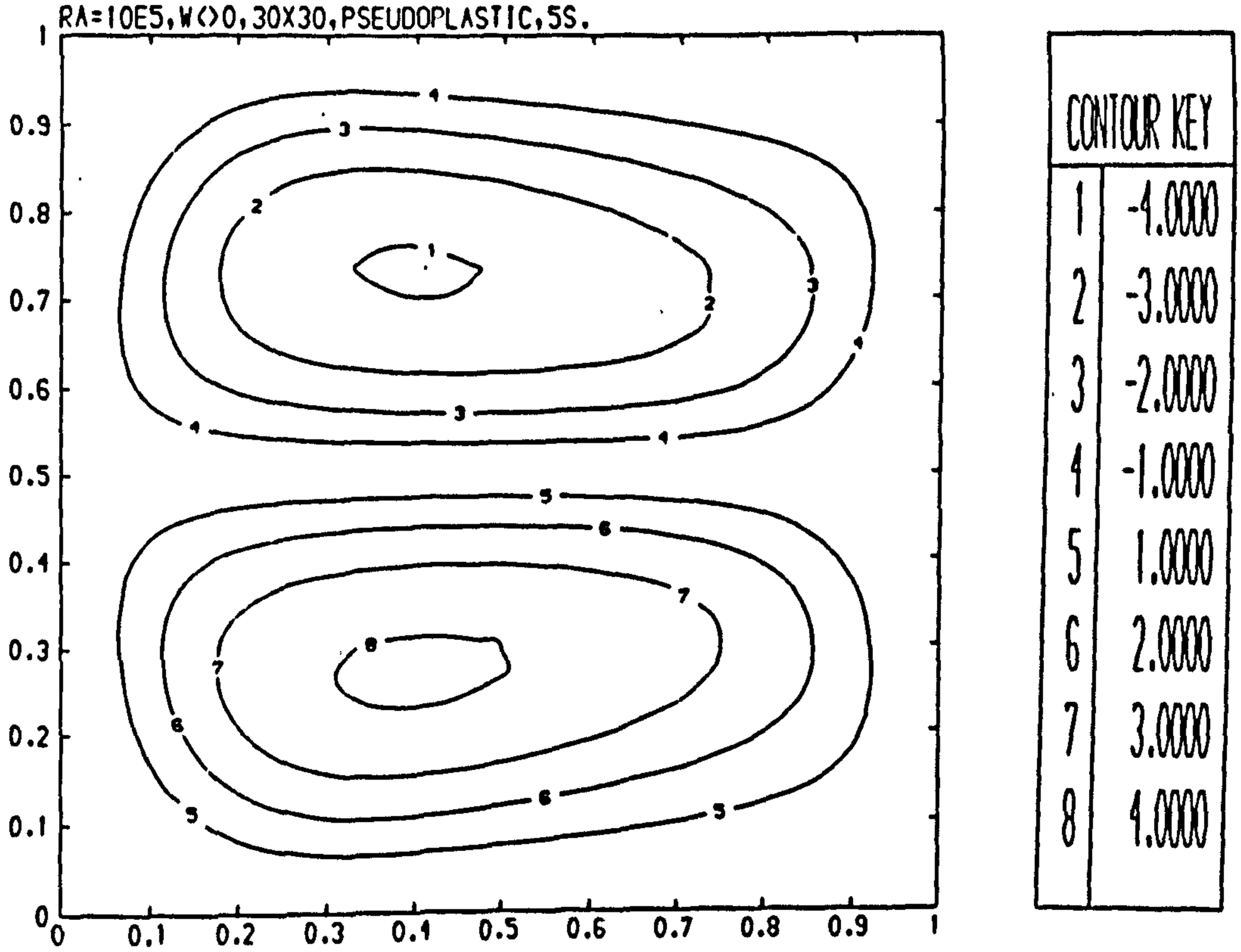

Figure (7.22)

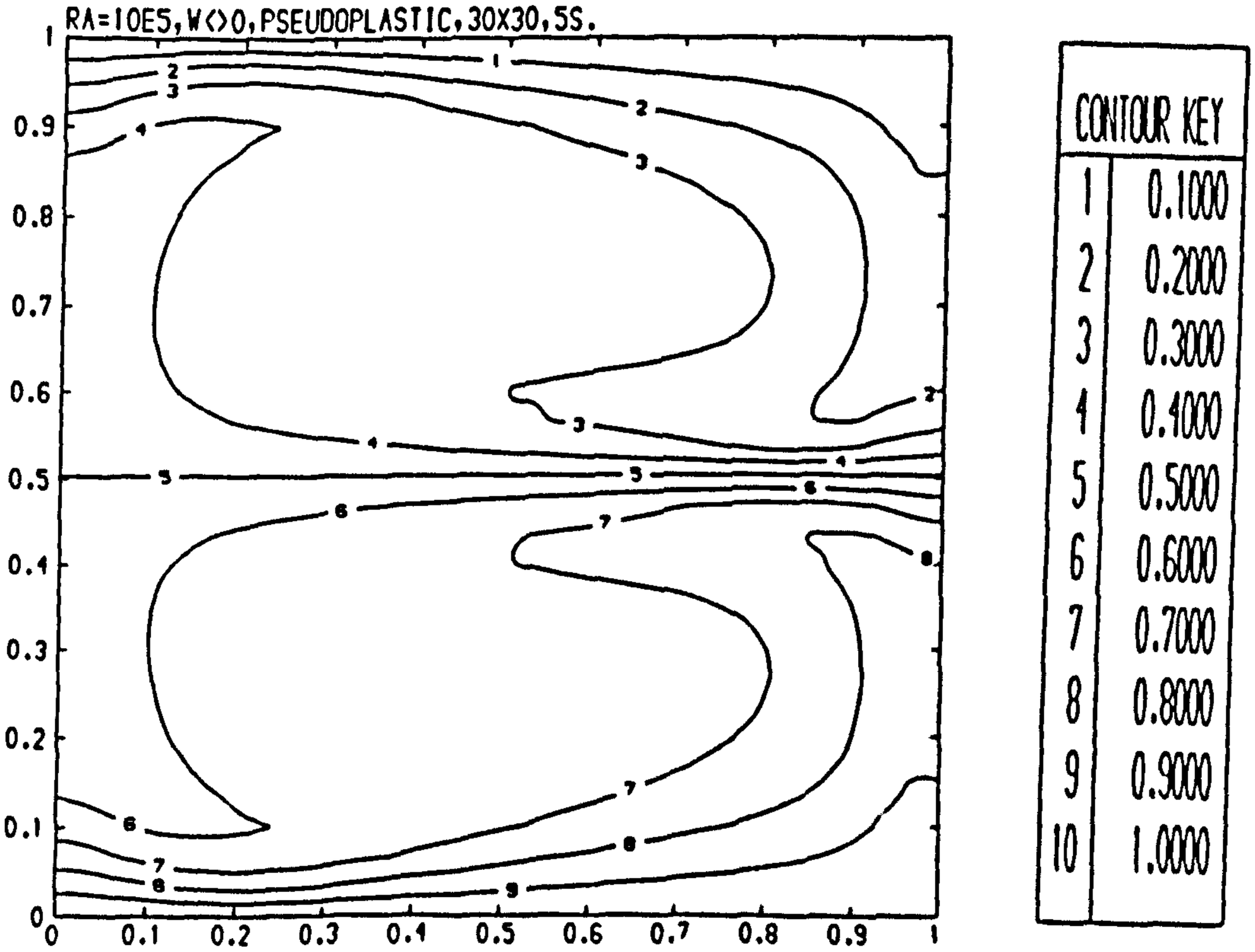

Figure (7.23)

Streamline & temperature plots for a pseudoplastic fluid at $Ra=10^5$, $Pr=7$, $\omega<>0$.

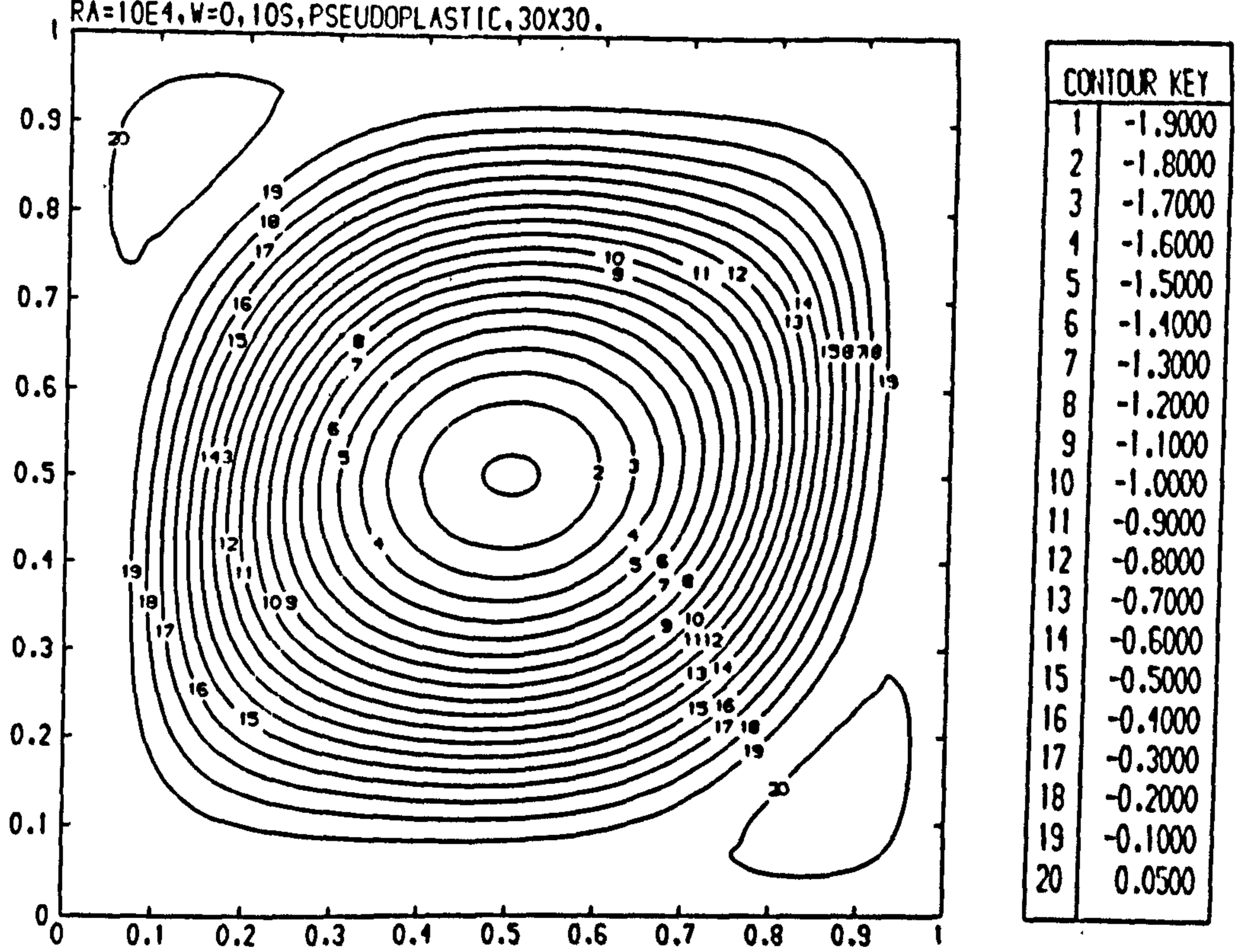

Figure (7.24)

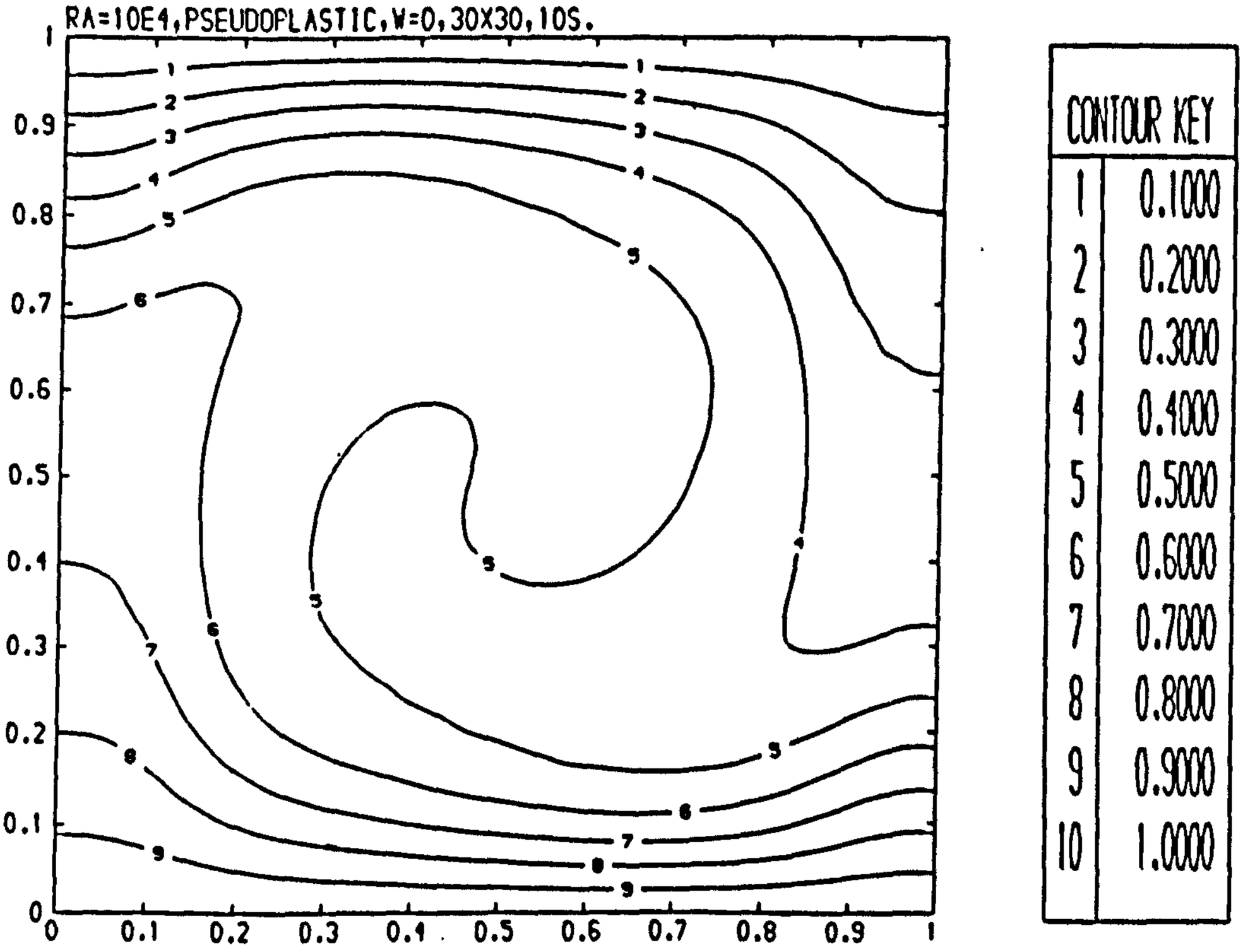

Figure (7.25)

Streamline & temperature plots for a pseudoplastic fluid at $Re=10^4$, $Pr=7$, $\omega=0$.

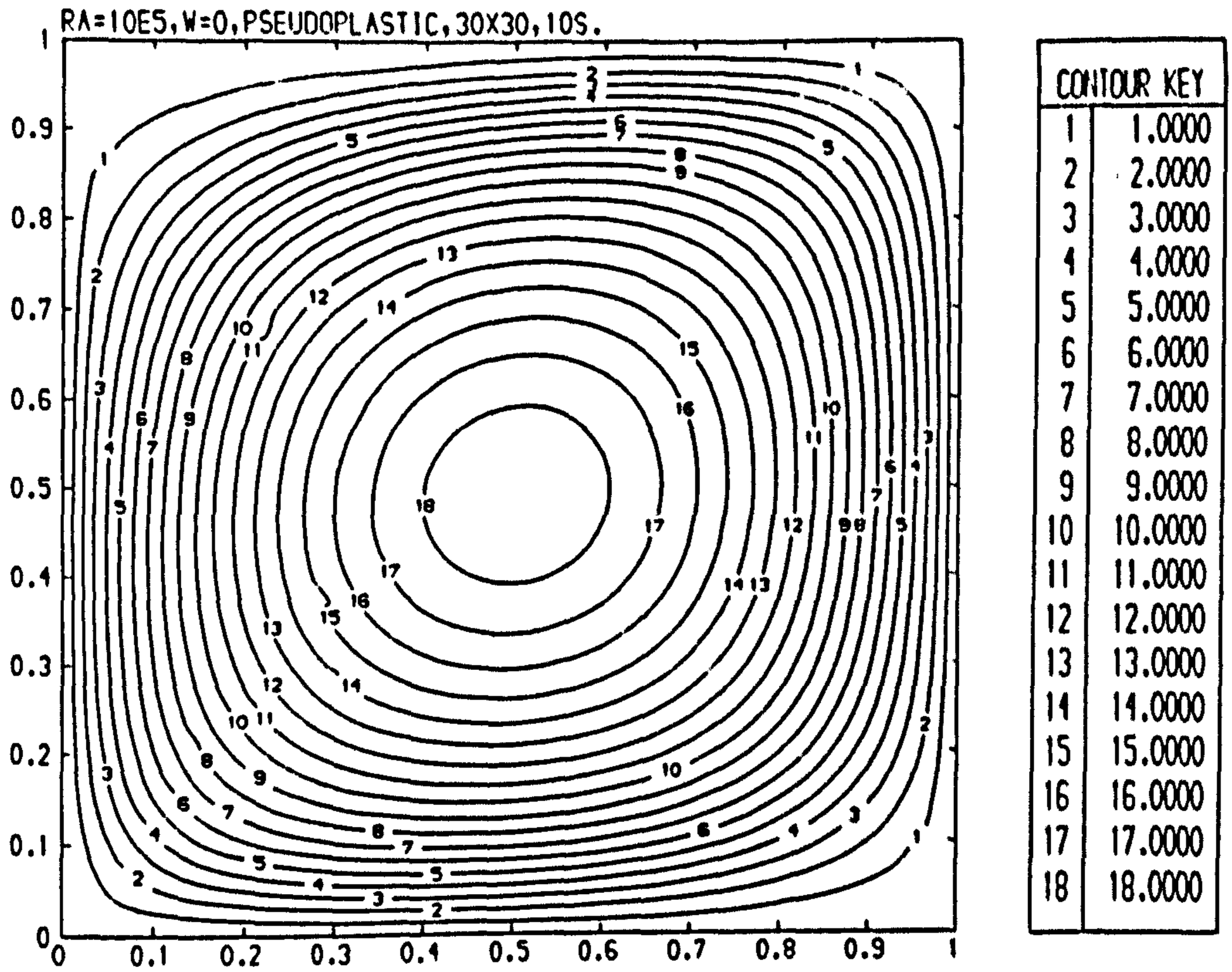

Figure (7.26)

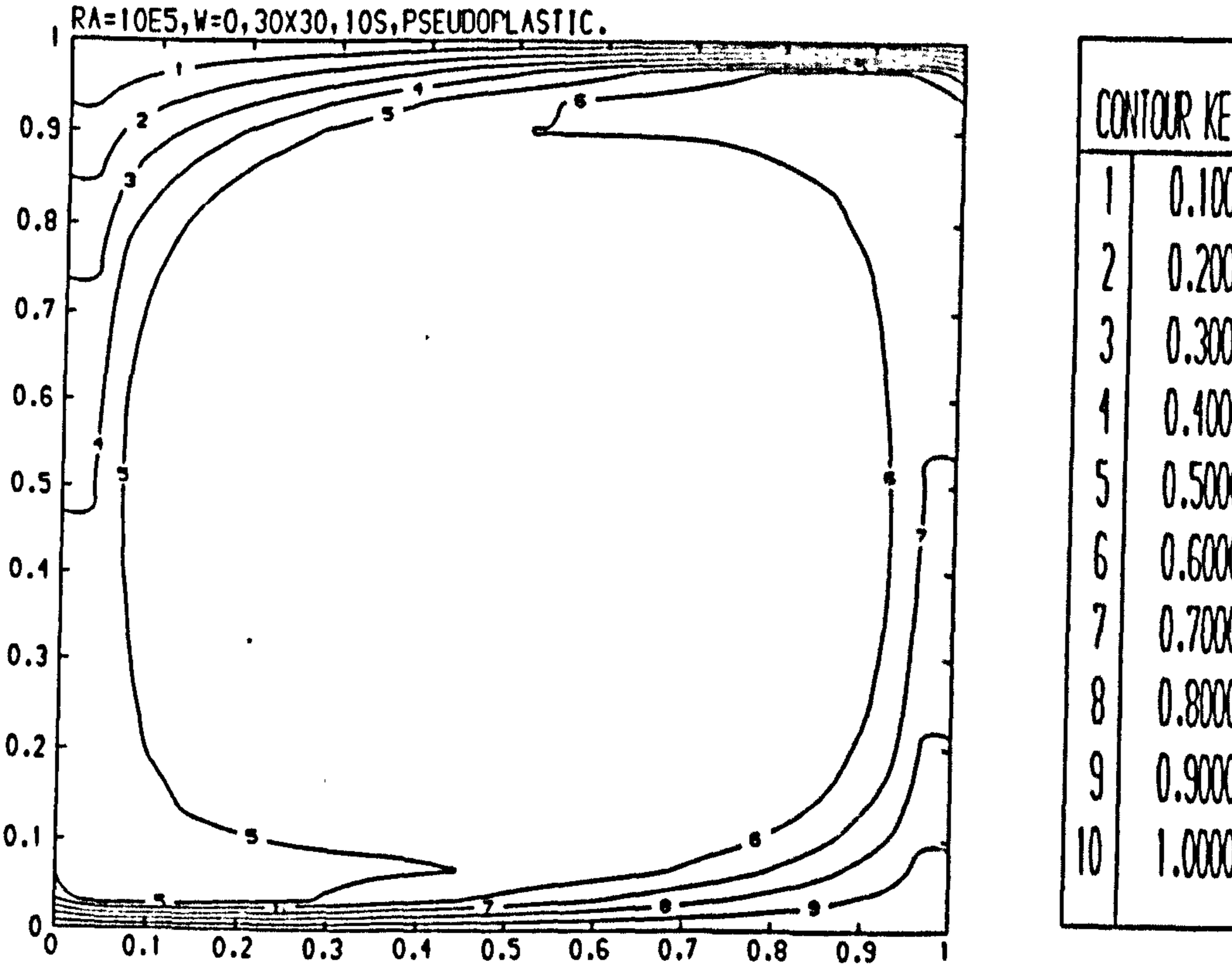

Figure (7.27)

Streamline & temperature plots for a pseudoplastic fluid at $Re=10^5$, $Pr=7$, $\omega=0$.

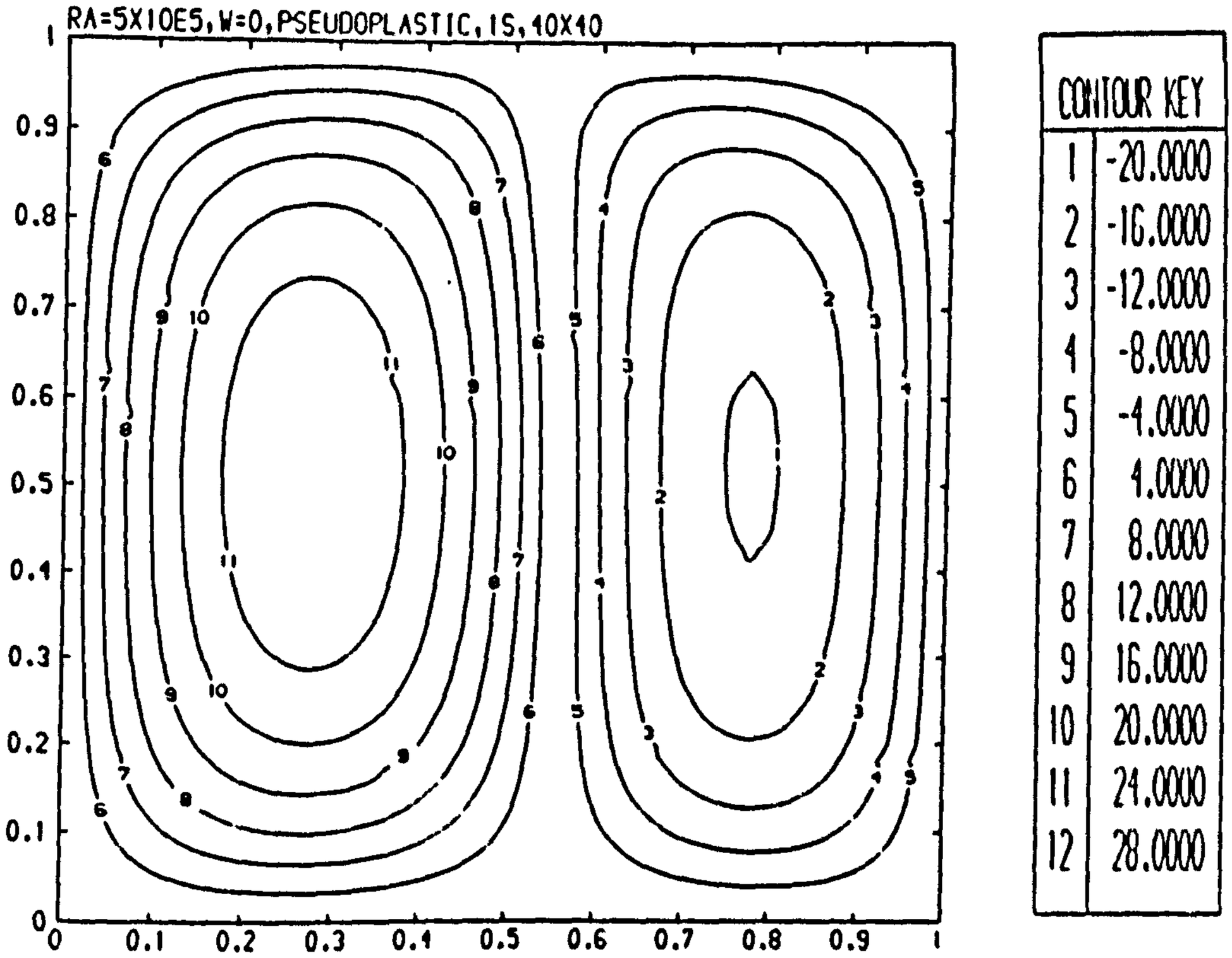

Figure (7.28)

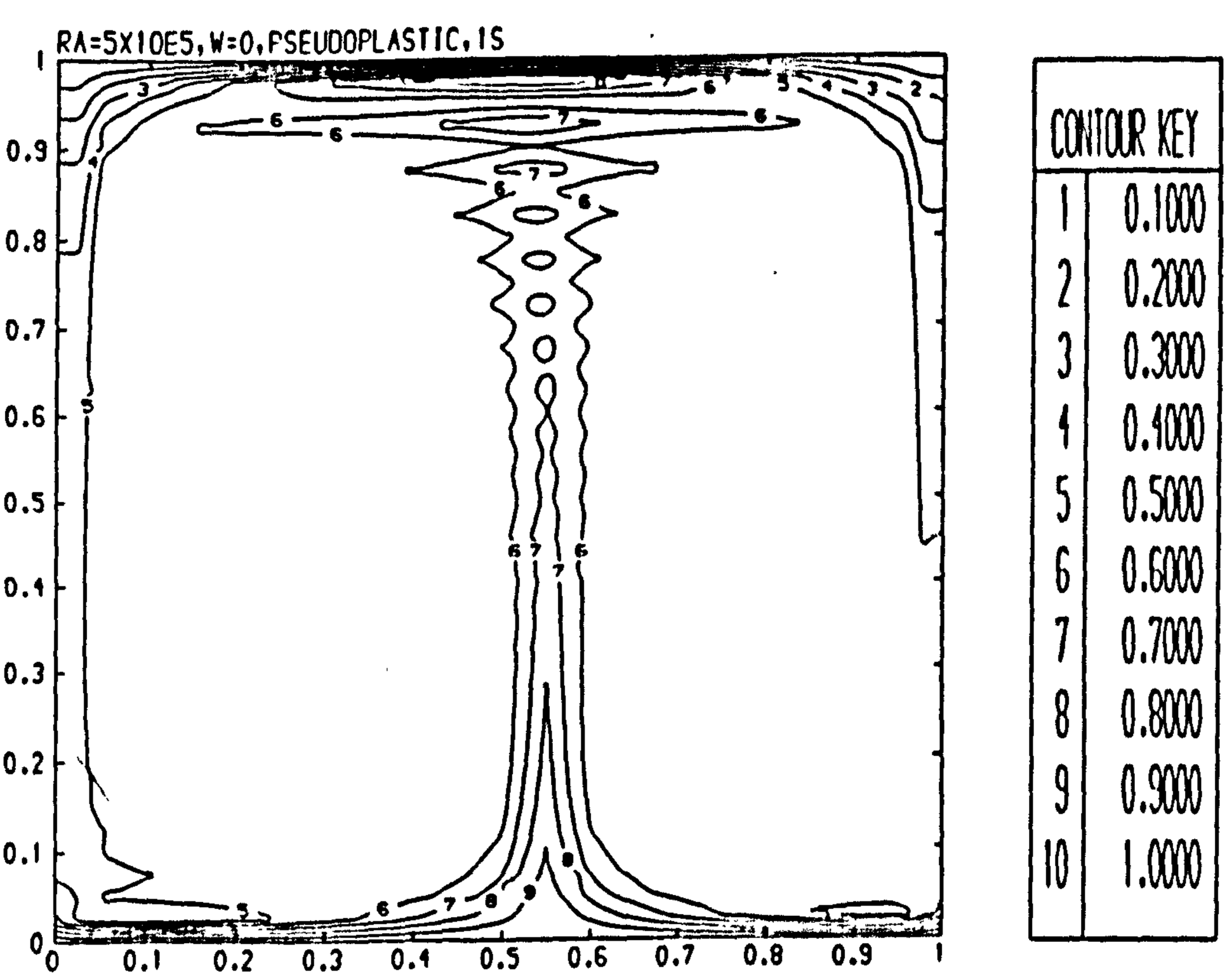

Figure (7.29)

Streamline & temperature plots for a pseudoplastic fluid at Re= 5 X10^5, Pr=7, ω=0.

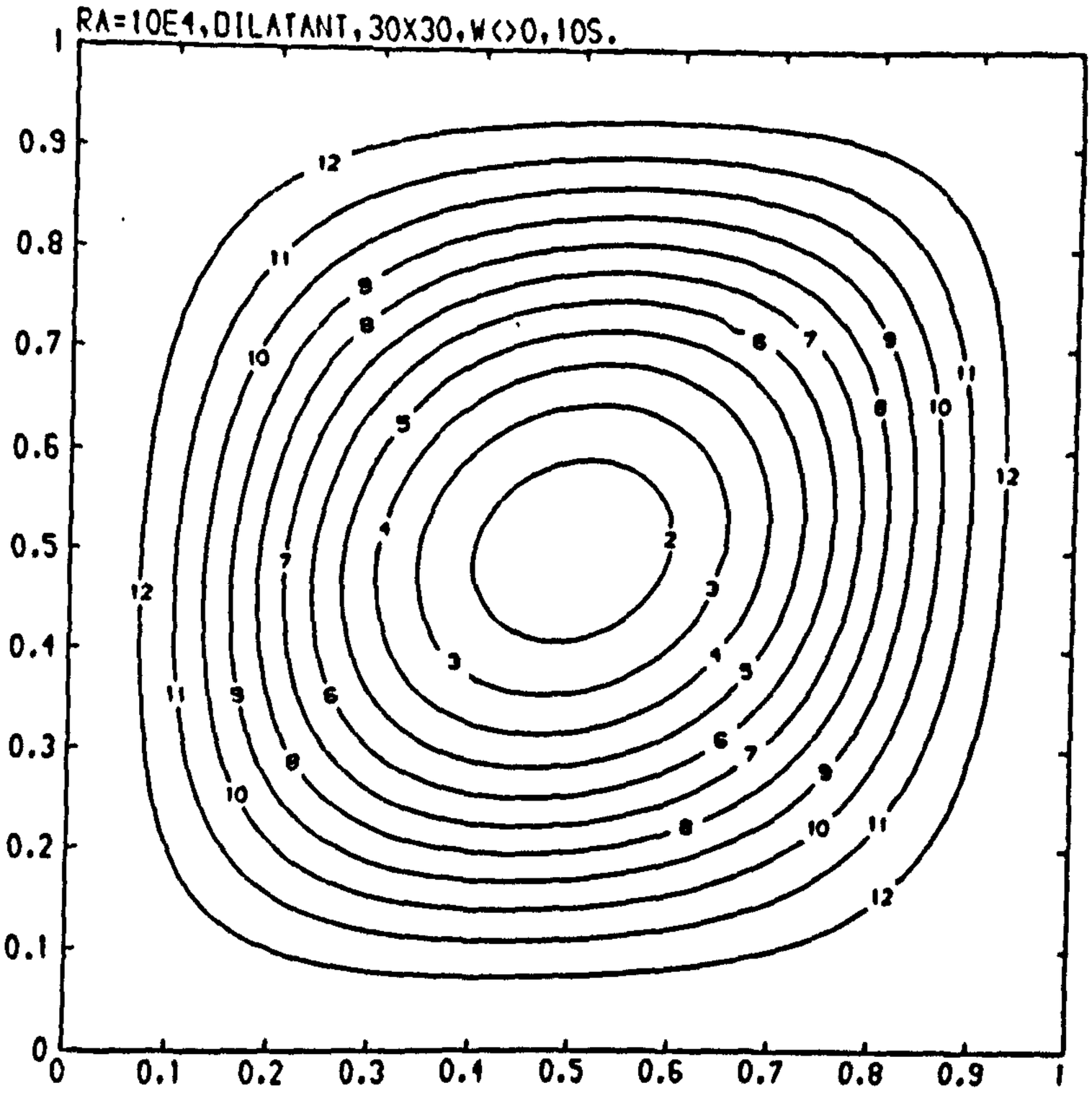

CONTOUR KEY	
1	-1.2000
2	-1.1000
3	-1.0000
4	-0.9000
5	-0.8000
6	-0.7000
7	-0.6000
8	-0.5000
9	-0.4000
10	-0.3000
11	-0.2000
12	-0.1000

Figure (7.30)

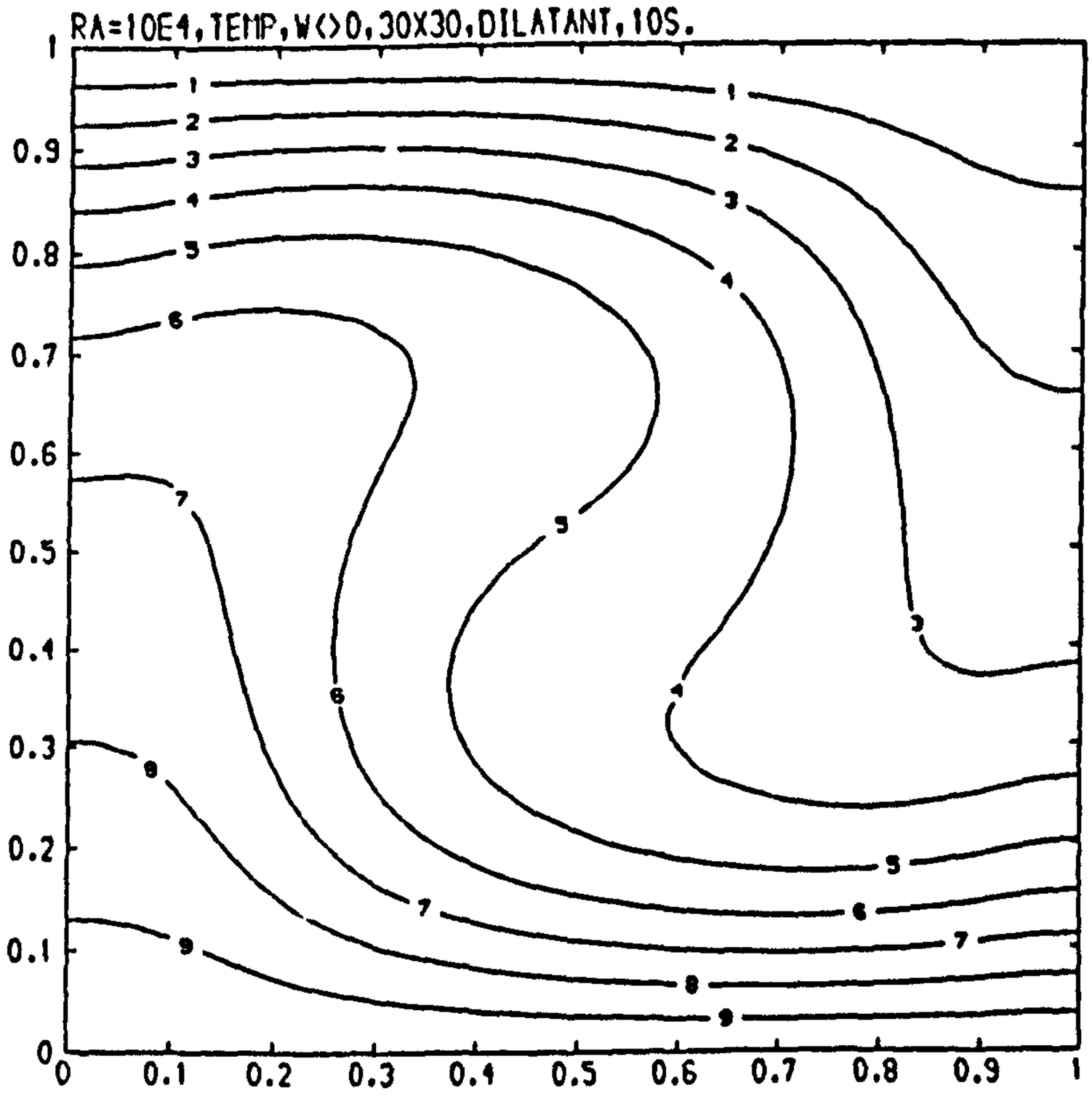

CONTOUR KEY	
1	0.1000
2	0.2000
3	0.3000
4	0.4000
5	0.5000
6	0.6000
7	0.7000
8	0.8000
9	0.9000
10	1.0000

Figure (7.31)

Streamline & temperature plots for a dilatant fluid at $Re=10^4$, $Pr=7$, $\omega<>0$.

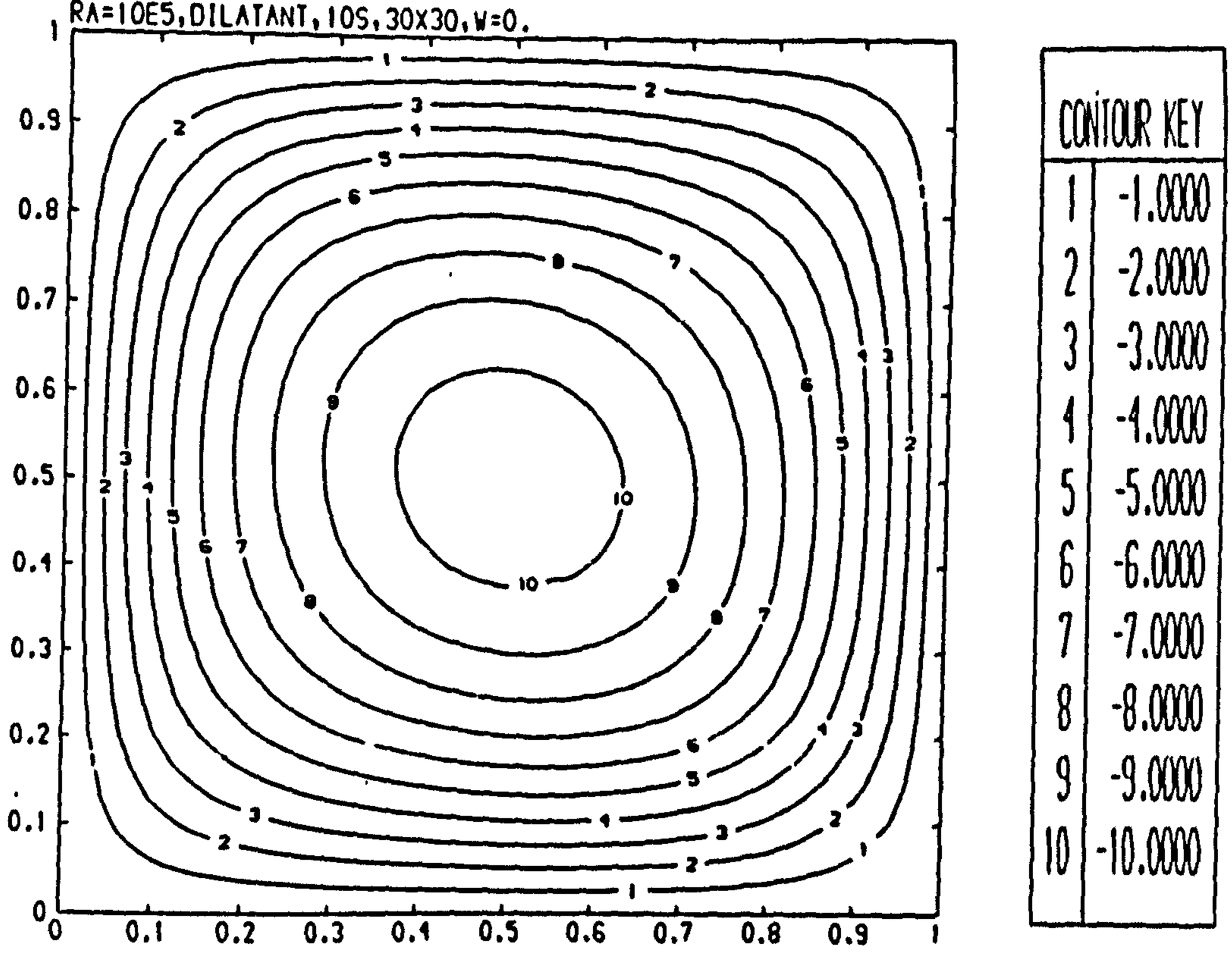

Figure (7.32)

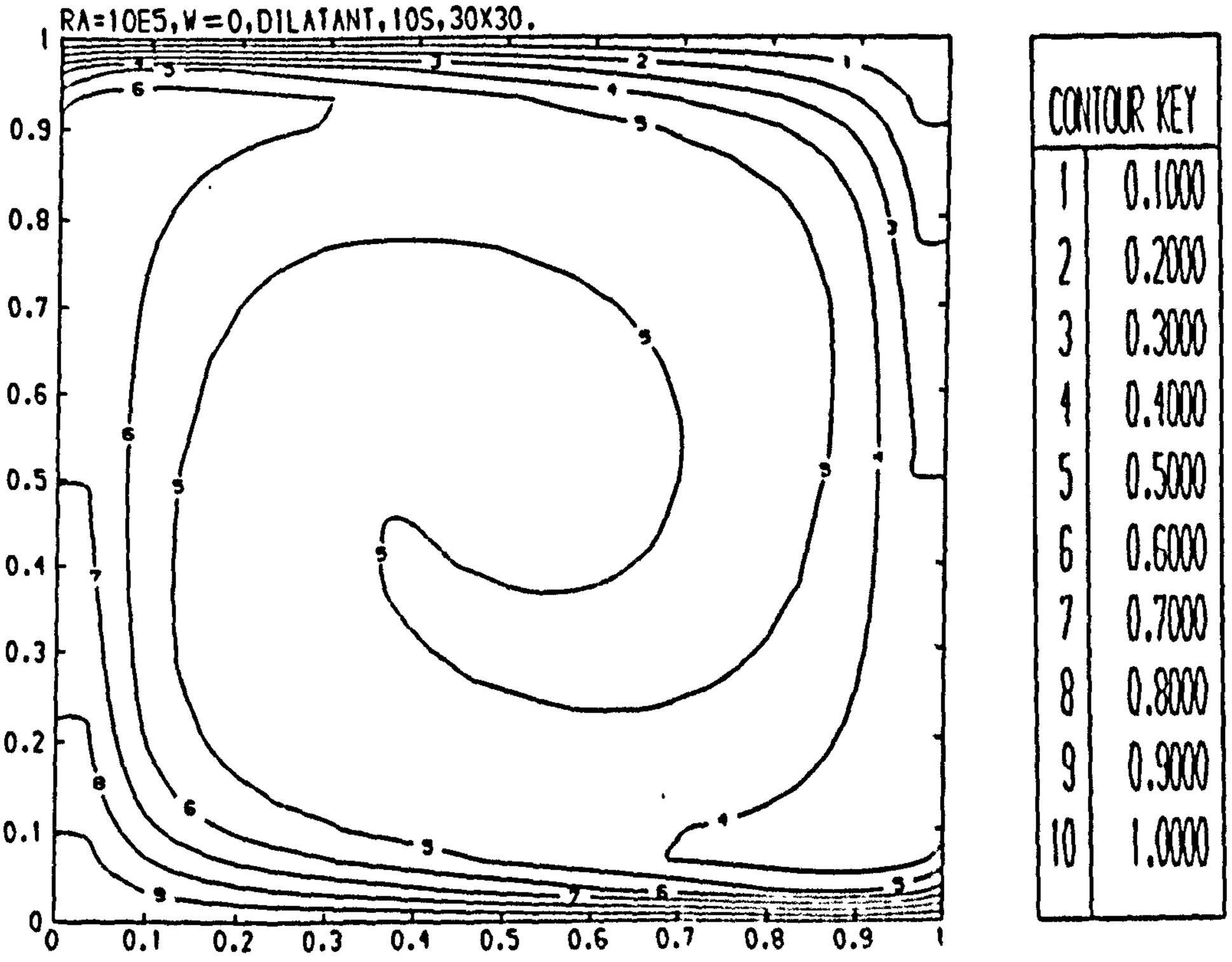

Figure (7.33)

Streamline & temperature plots for a dilatant fluid at $Re=10^5$, $Pr=7$, $\omega=0$.

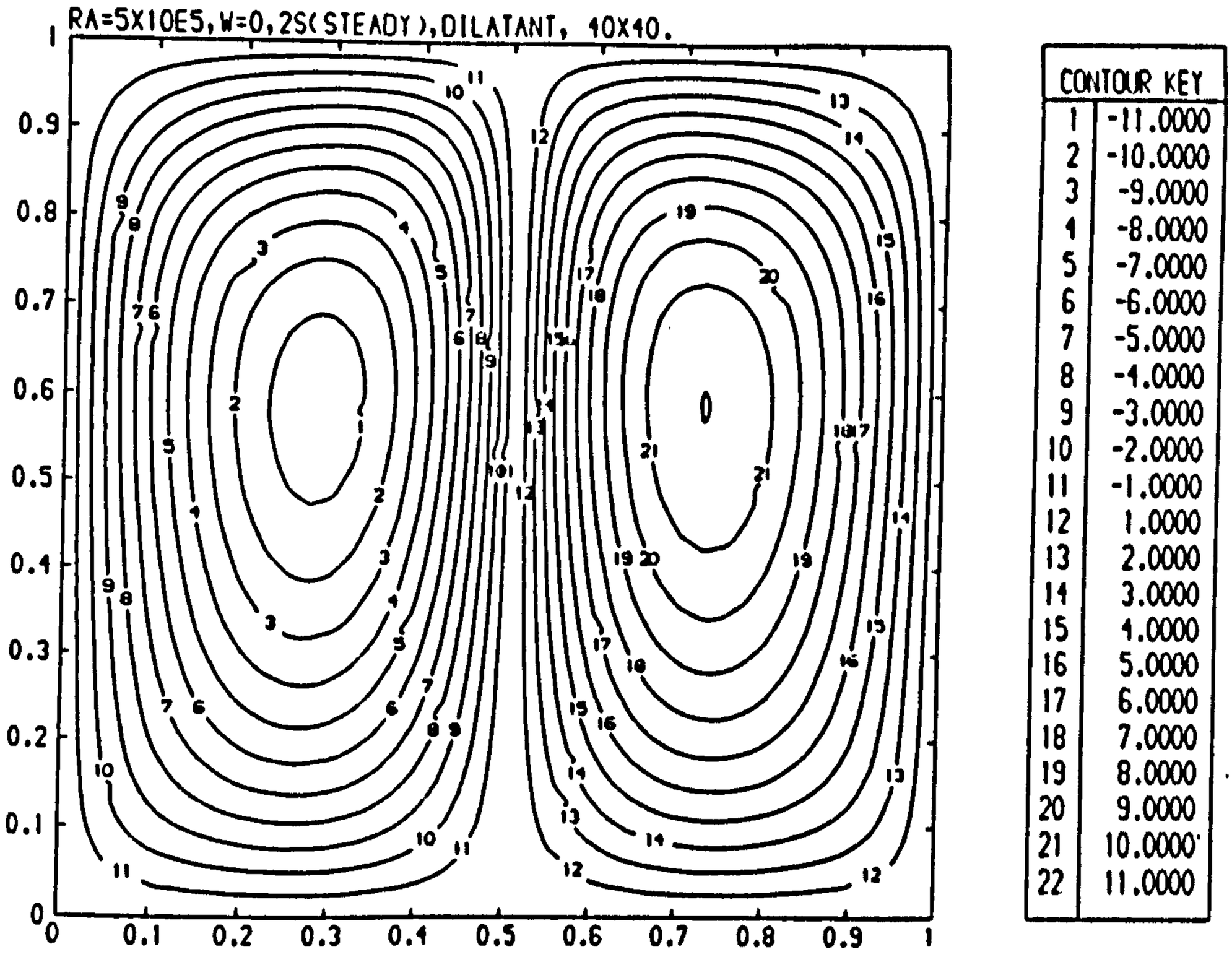

Figure (7.34)

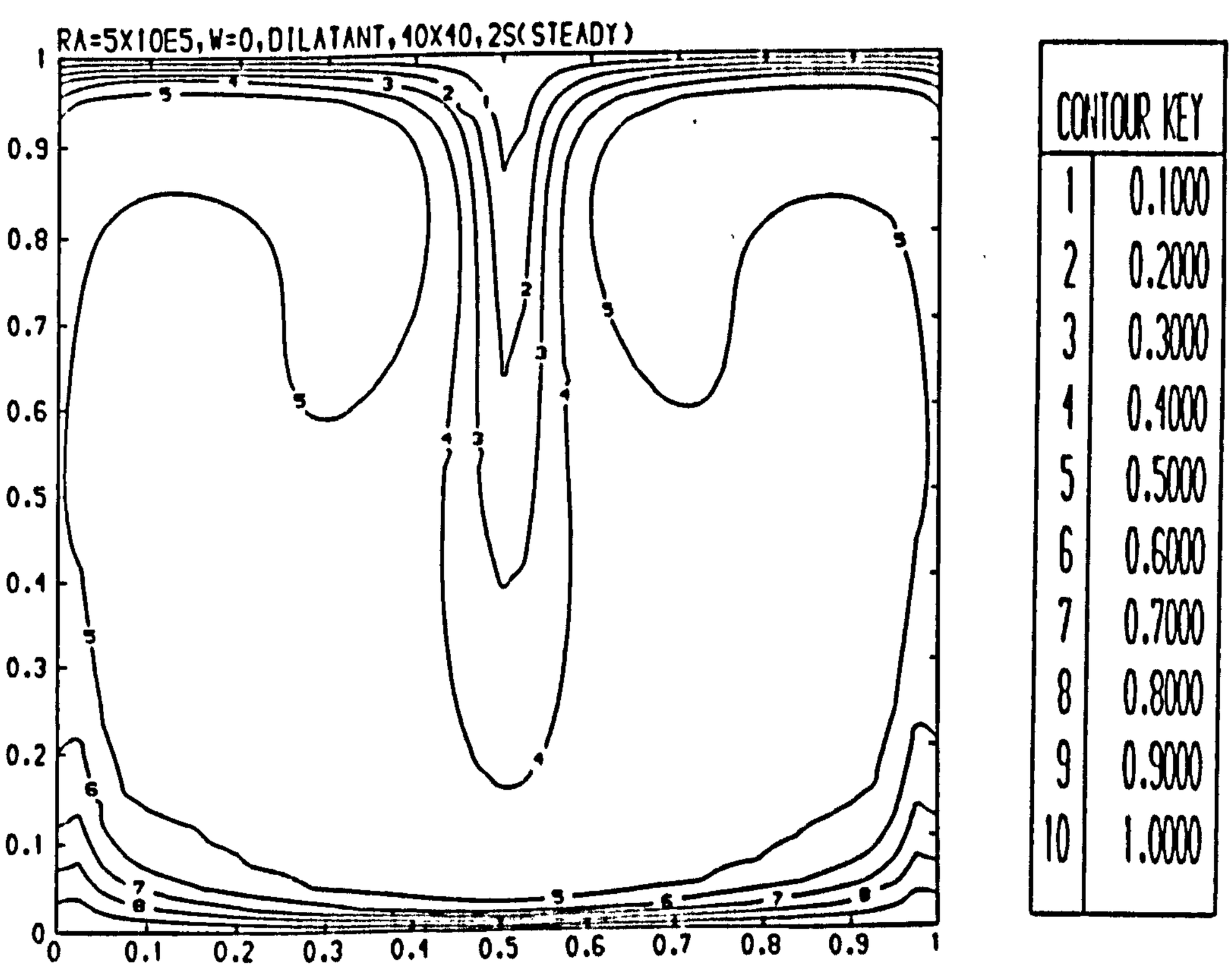

Figure (7.35)

Streamline & temperature plots for a dilatant fluid at $Re=5 \times 10^5$, $Pr=7$, $\omega=0$.

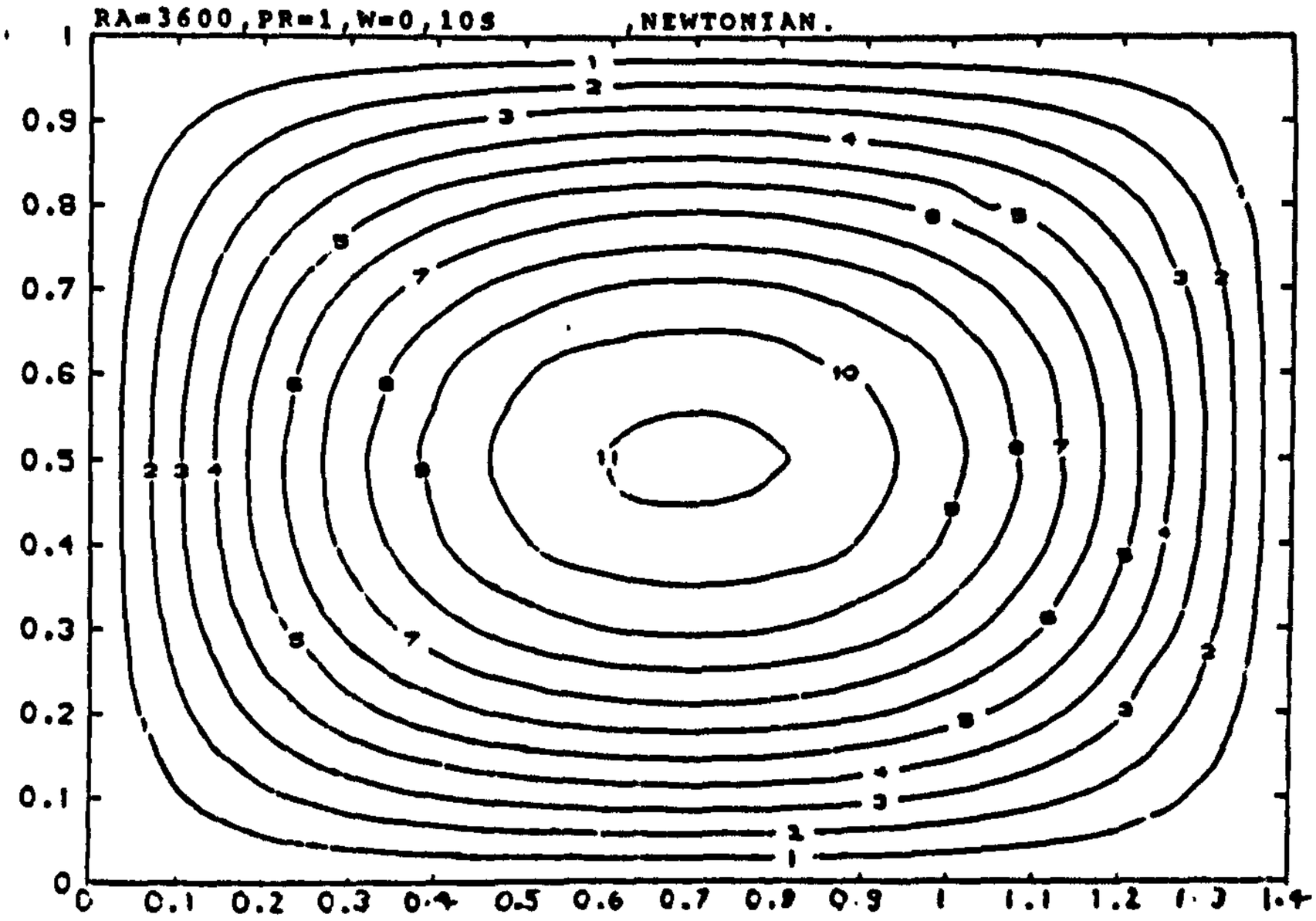

CONTOUR KEY	
1	-1.0000
2	-2.0000
3	-3.0000
4	-4.0000
5	-5.0000
6	-6.0000
7	-7.0000
8	-8.0000
9	-9.0000
10	-10.0000
11	-11.0000

Figure (7.36)

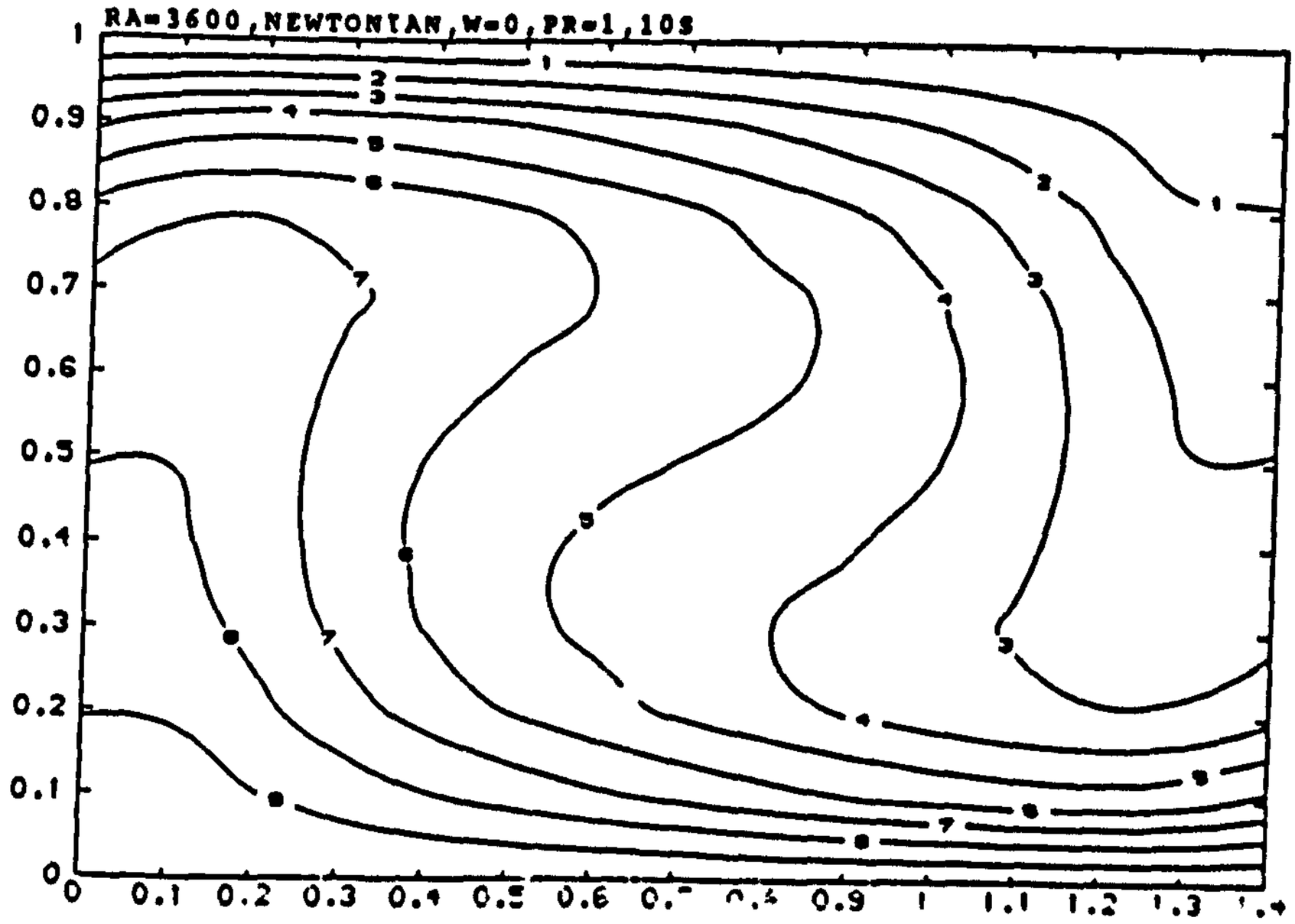

CONTOUR KEY	
1	0.1000
2	0.2000
3	0.3000
4	0.4000
5	0.5000
6	0.6000
7	0.7000
8	0.8000
9	0.9000
10	1.0000

Figure (7.37)

Streamlines & temperature plots for a Newtonian fluid at Ra=3600, Pr=1, ω=0.

Figure (7.38) Streamlines & temperature plots of Torrance & Turcotte[106] at Ra=3600, Pr=1, ω=0.

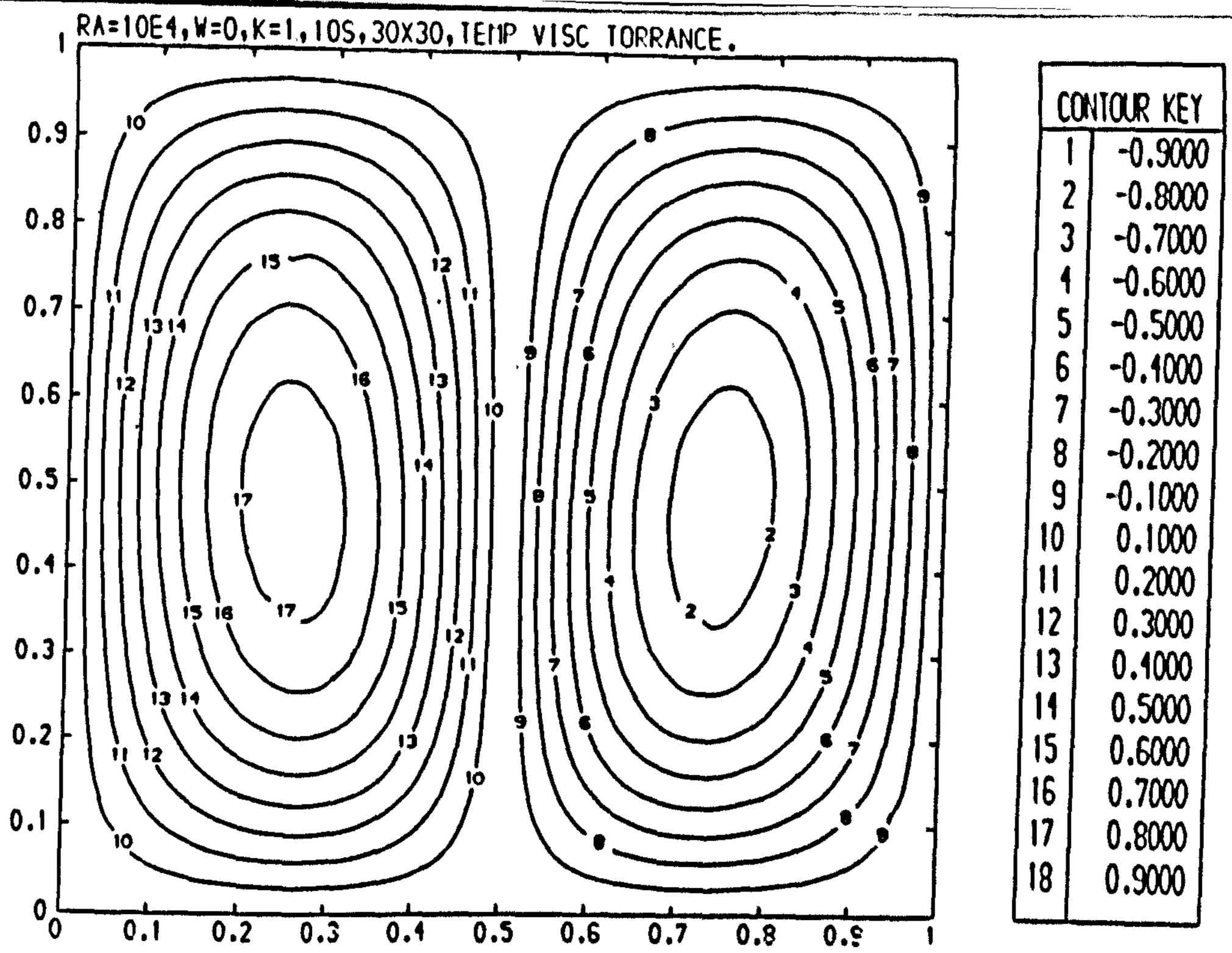

Figure (7.39)

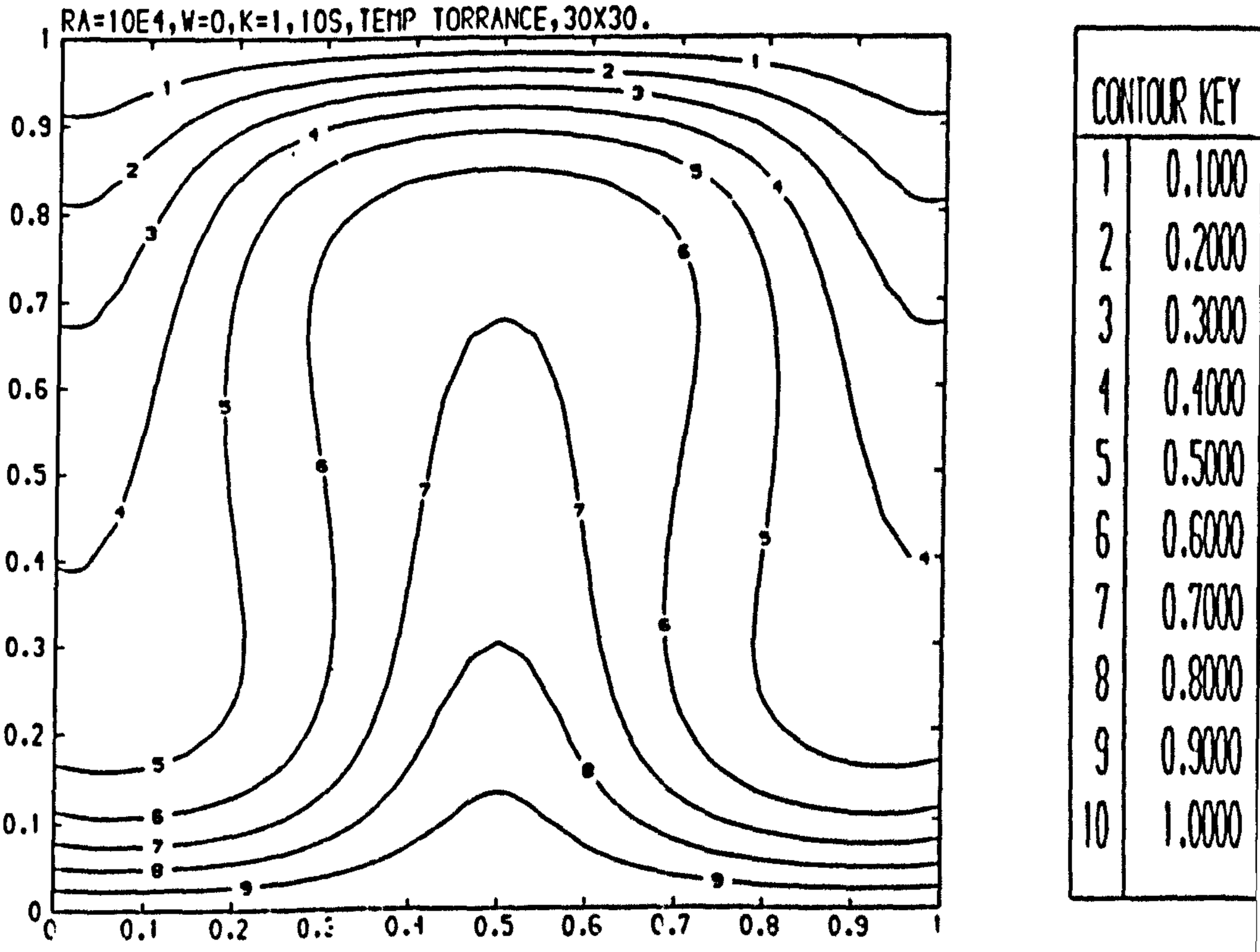

Figure (7.40)

Streamline & temperature plots for a temperature dependent viscous fluid at $Re=10^4$, $Pr=7$, $k=1$, $\omega=0$.

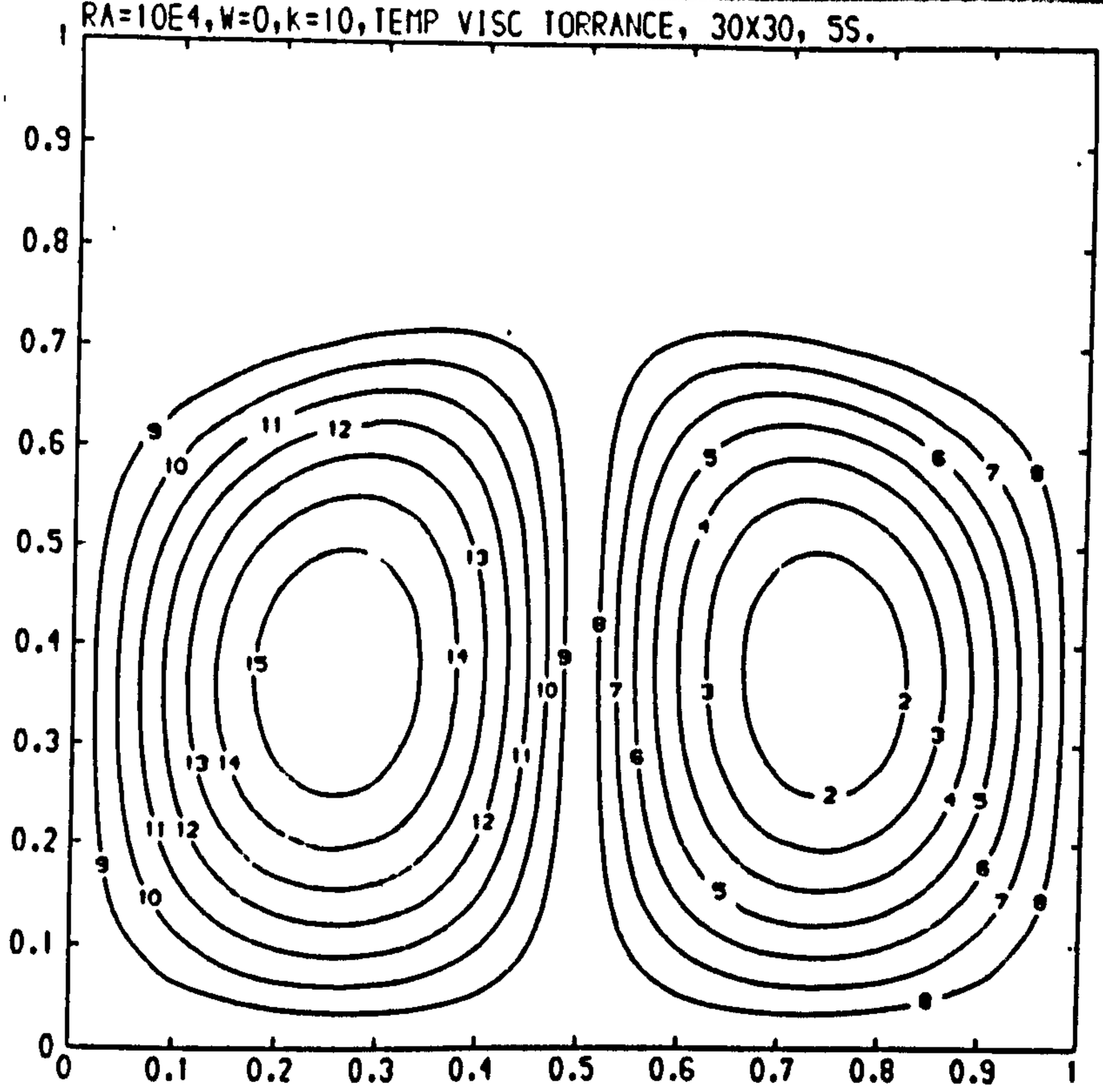

CONTOUR KEY	
1	-2.4000
2	-2.1000
3	-1.8000
4	-1.5000
5	-1.2000
6	-0.9000
7	-0.6000
8	-0.3000
9	0.3000
10	0.6000
11	0.9000
12	1.2000
13	1.5000
14	1.8000
15	2.1000
16	2.4000

Figure (7.41)

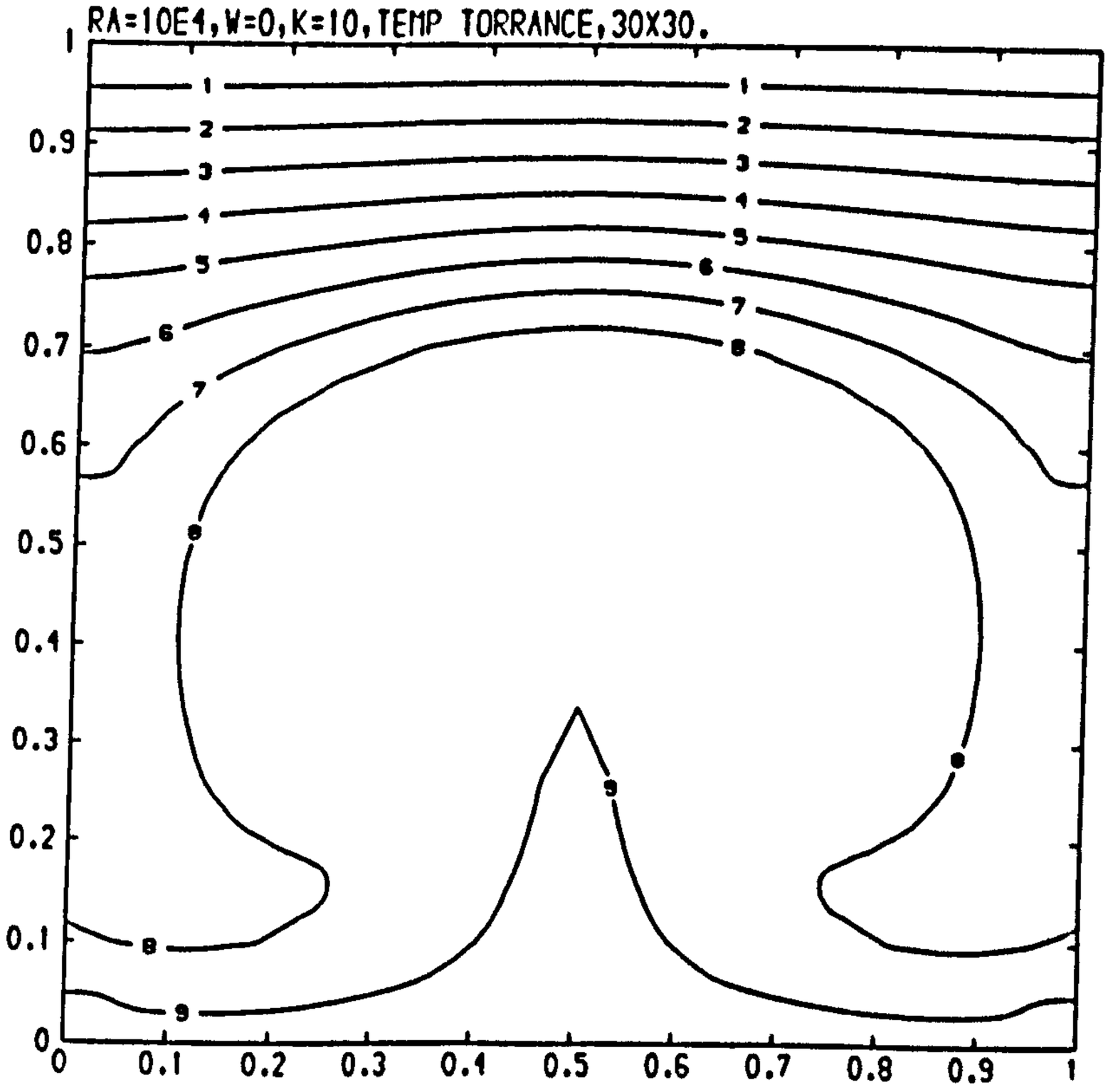

CONTOUR KEY	
1	0.1000
2	0.2000
3	0.3000
4	0.4000
5	0.5000
6	0.6000
7	0.7000
8	0.8000
9	0.9000
10	1.0000

Figure (7.42)

Streamline & temperature plots for a temperature dependent viscous fluid at $Ra=10^4$, $Pr=7$, $k=10$, $\omega=0$.

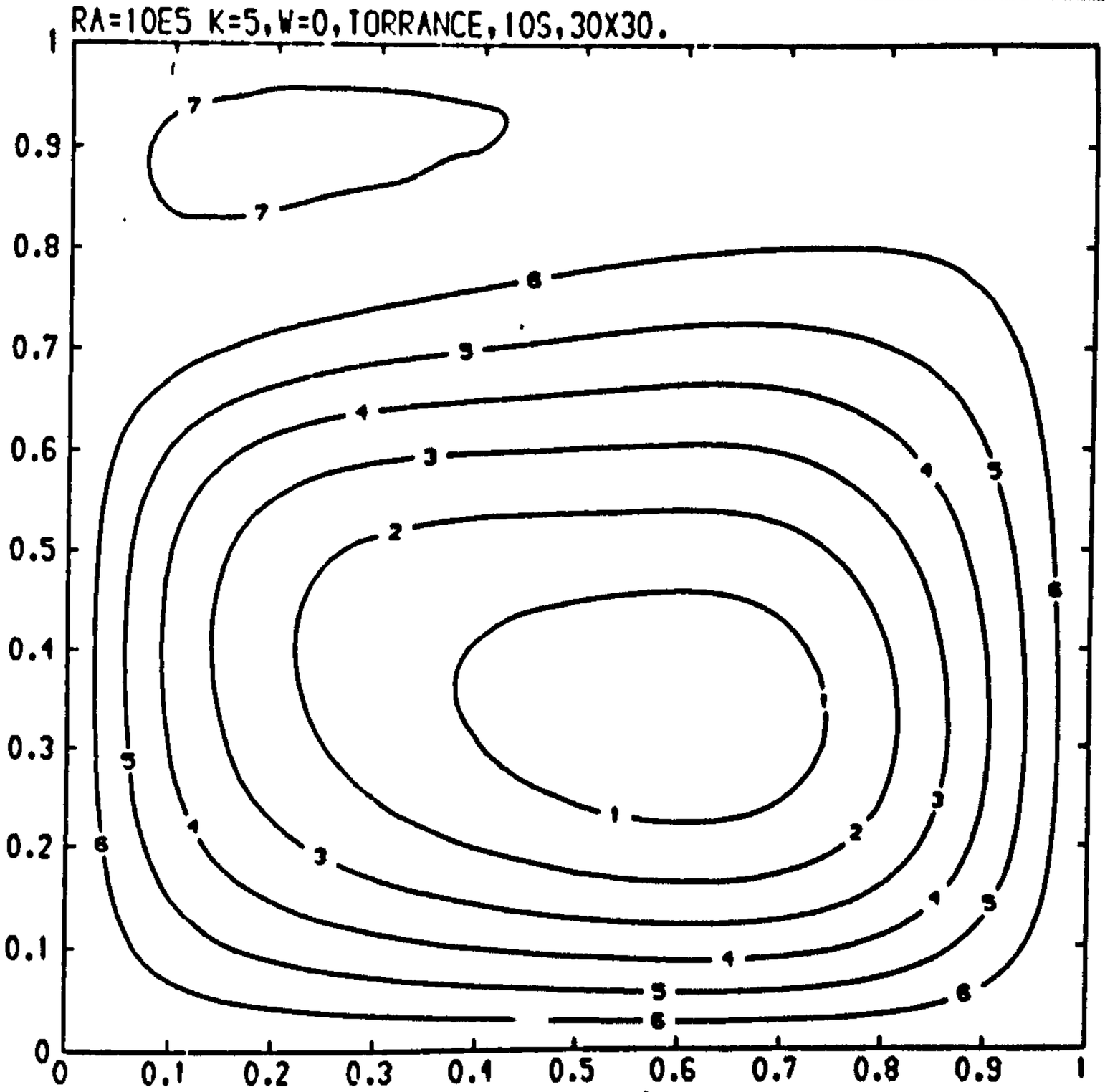

CONTOUR KEY	
1	-6.0000
2	-5.0000
3	-4.0000
4	-3.0000
5	-2.0000
6	-1.0000
7	0.1000
8	0.2000

Figure (7.43)

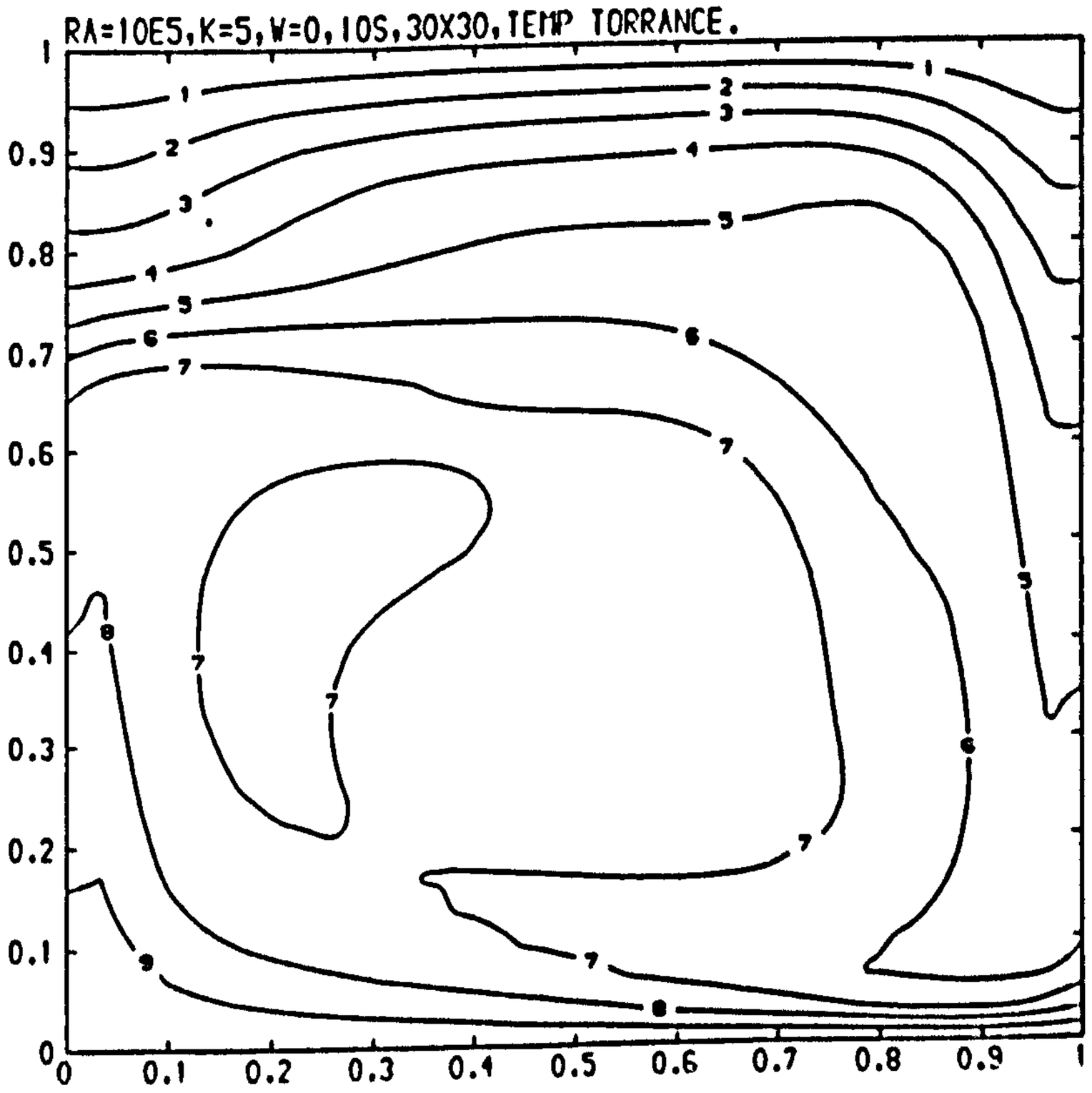

CONTOUR KEY	
1	0.1000
2	0.2000
3	0.3000
4	0.4000
5	0.5000
6	0.6000
7	0.7000
8	0.8000
9	0.9000
10	1.0000

Figure (7.44)

Streamline & temperature plots for a temperature dependent viscous fluid at $Ra=10^5$, $Pr=7$, $k=5$, $\omega=0$.

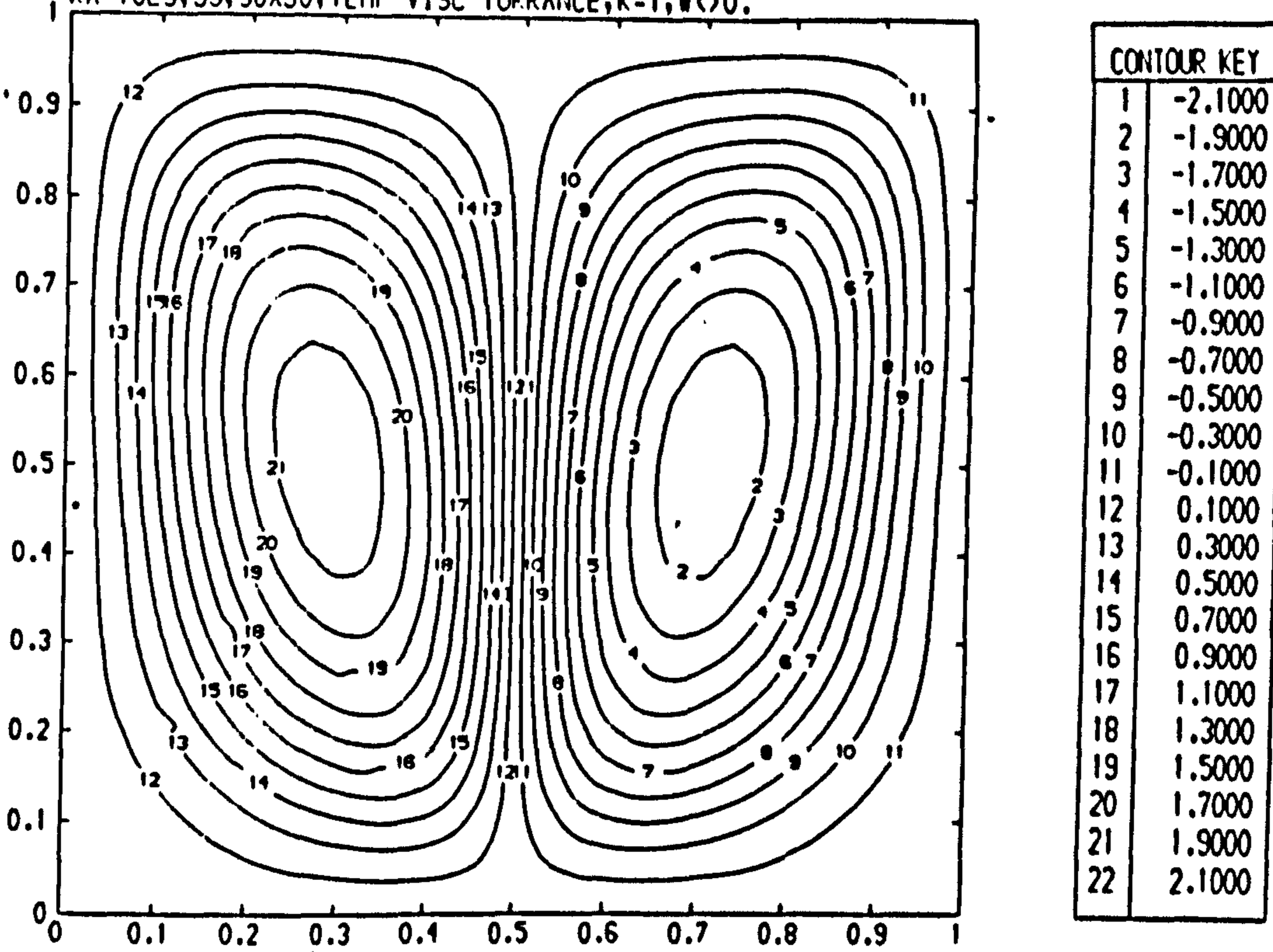

Figure (7.45)

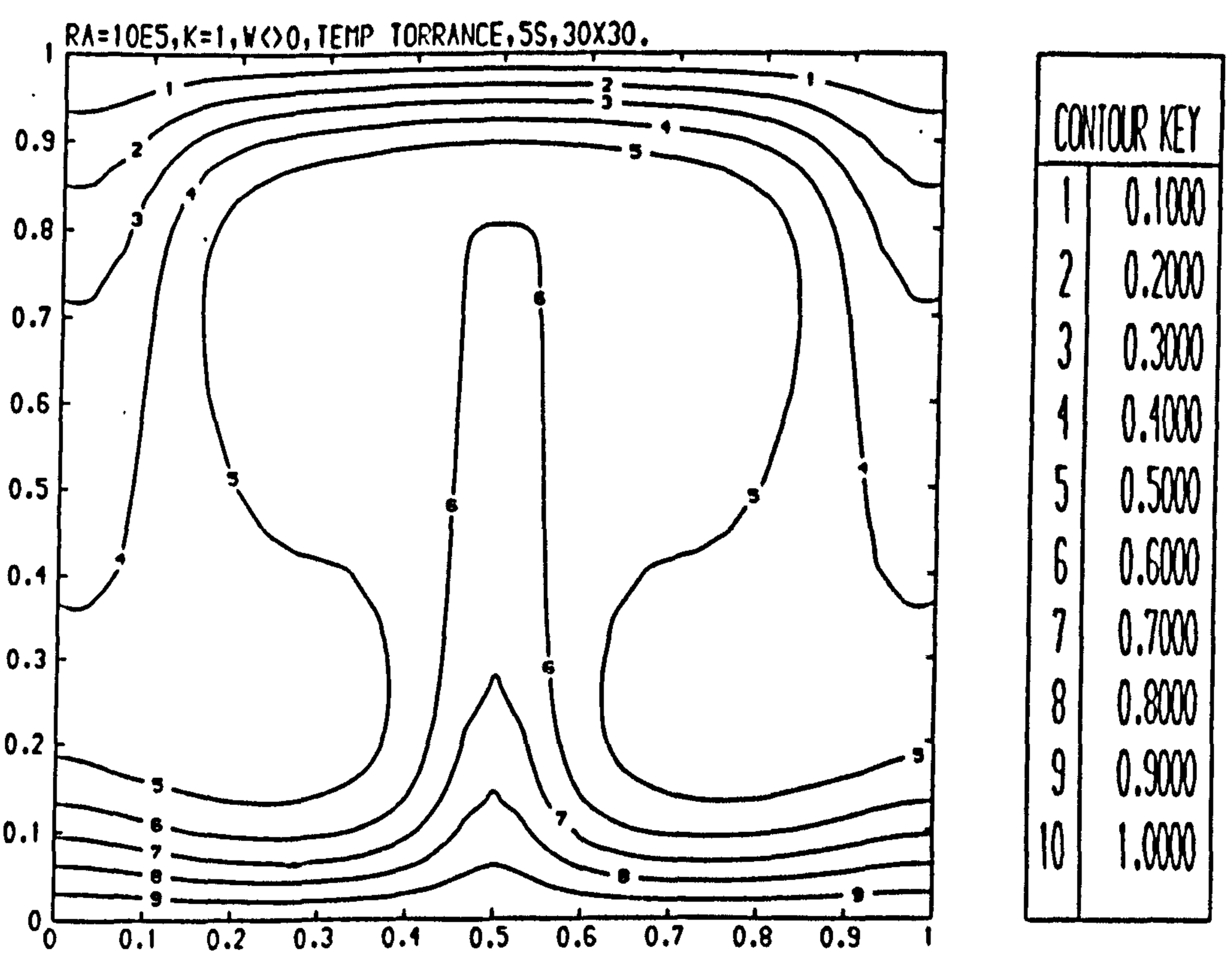

Figure (7.46)

Streamline & temperature plots for a temperature dependent viscous fluid at $Ra=10^5$, $Pr=7$, $k=1$, $\omega<>0$.

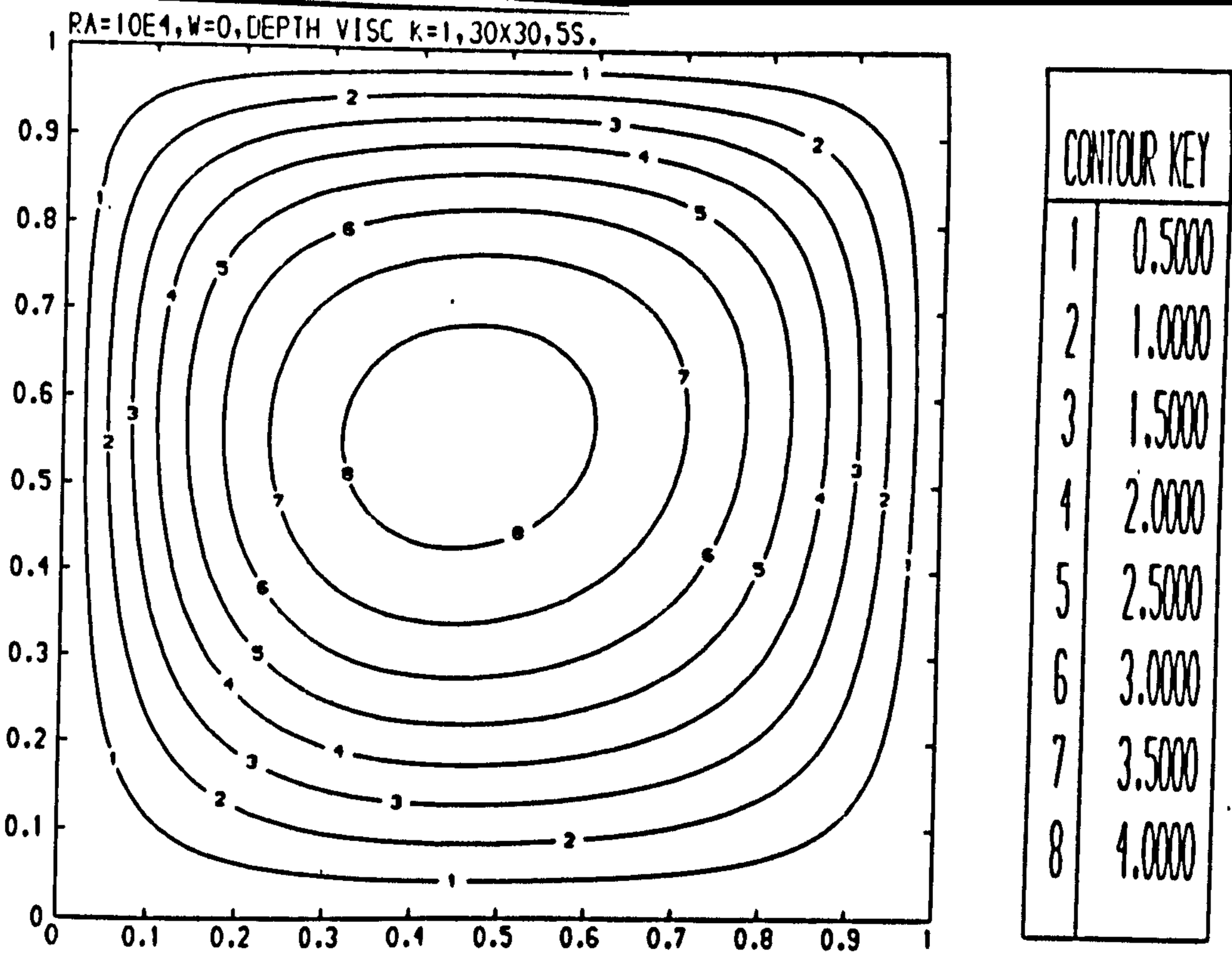

Figure (7.47)

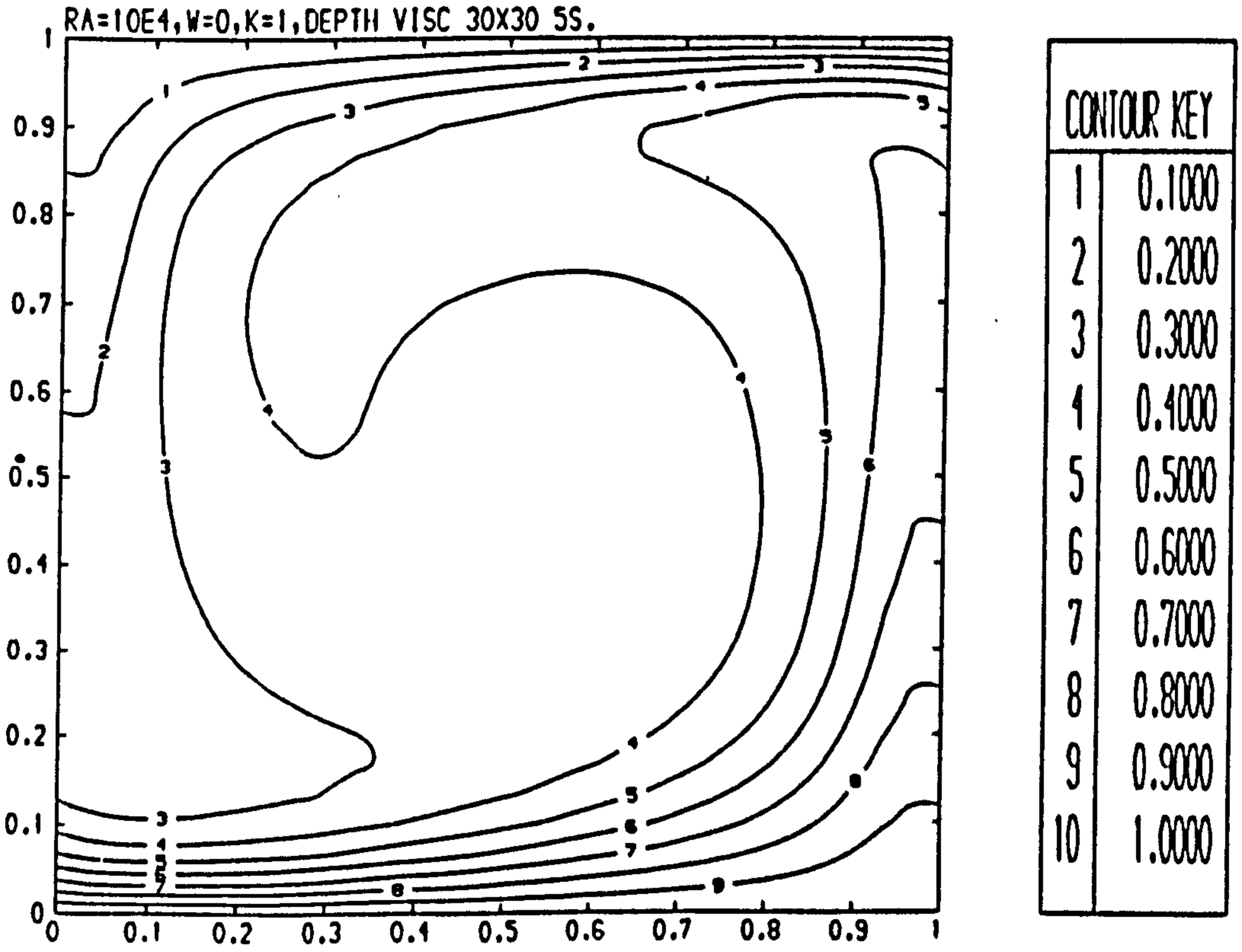

Figure (7.48)

Streamline & temperature plots for a depth dependent viscous fluid at $Ra=10^4$, $Pr=7$, $k=1$, $\omega=0$.

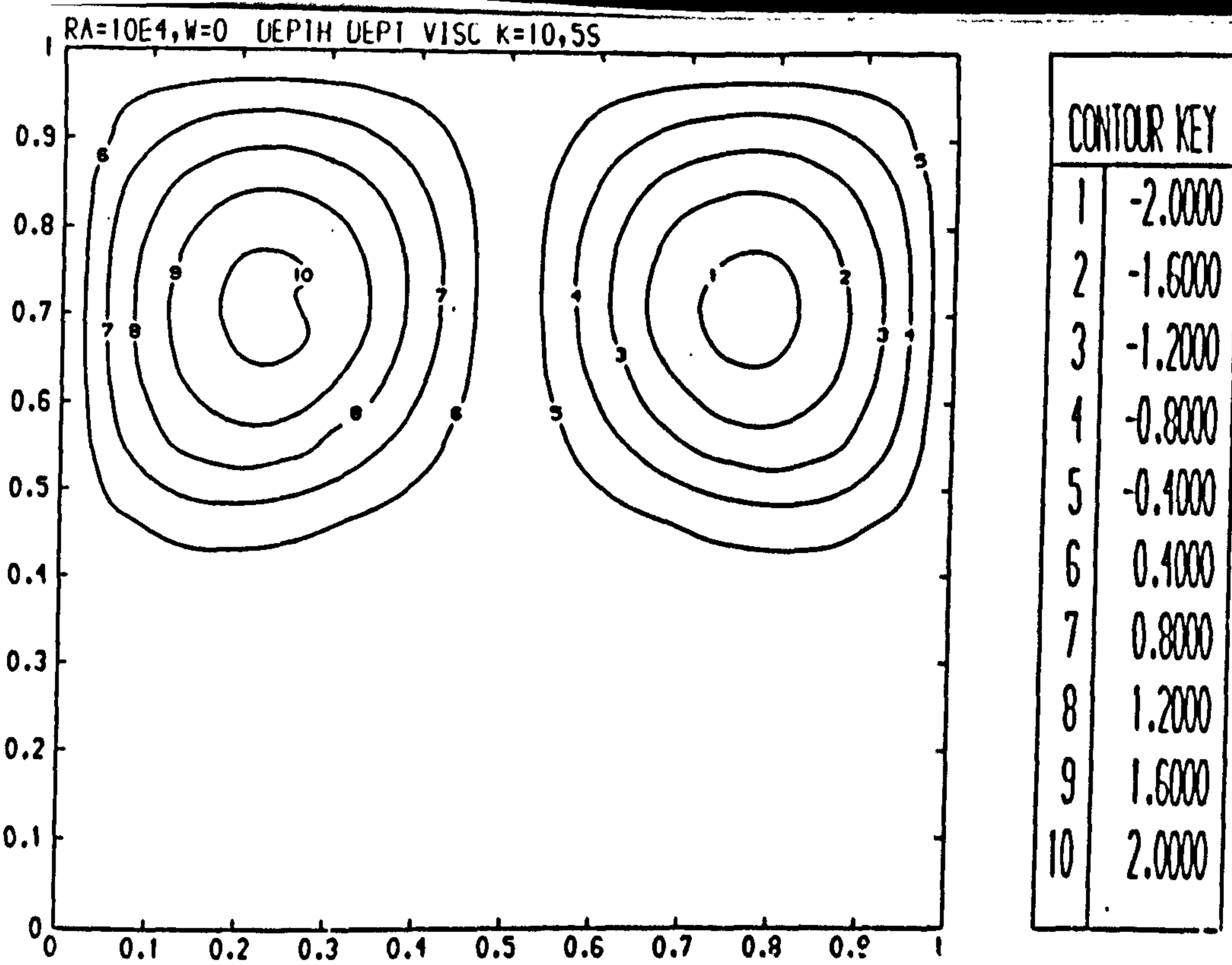

Figure (7.49)

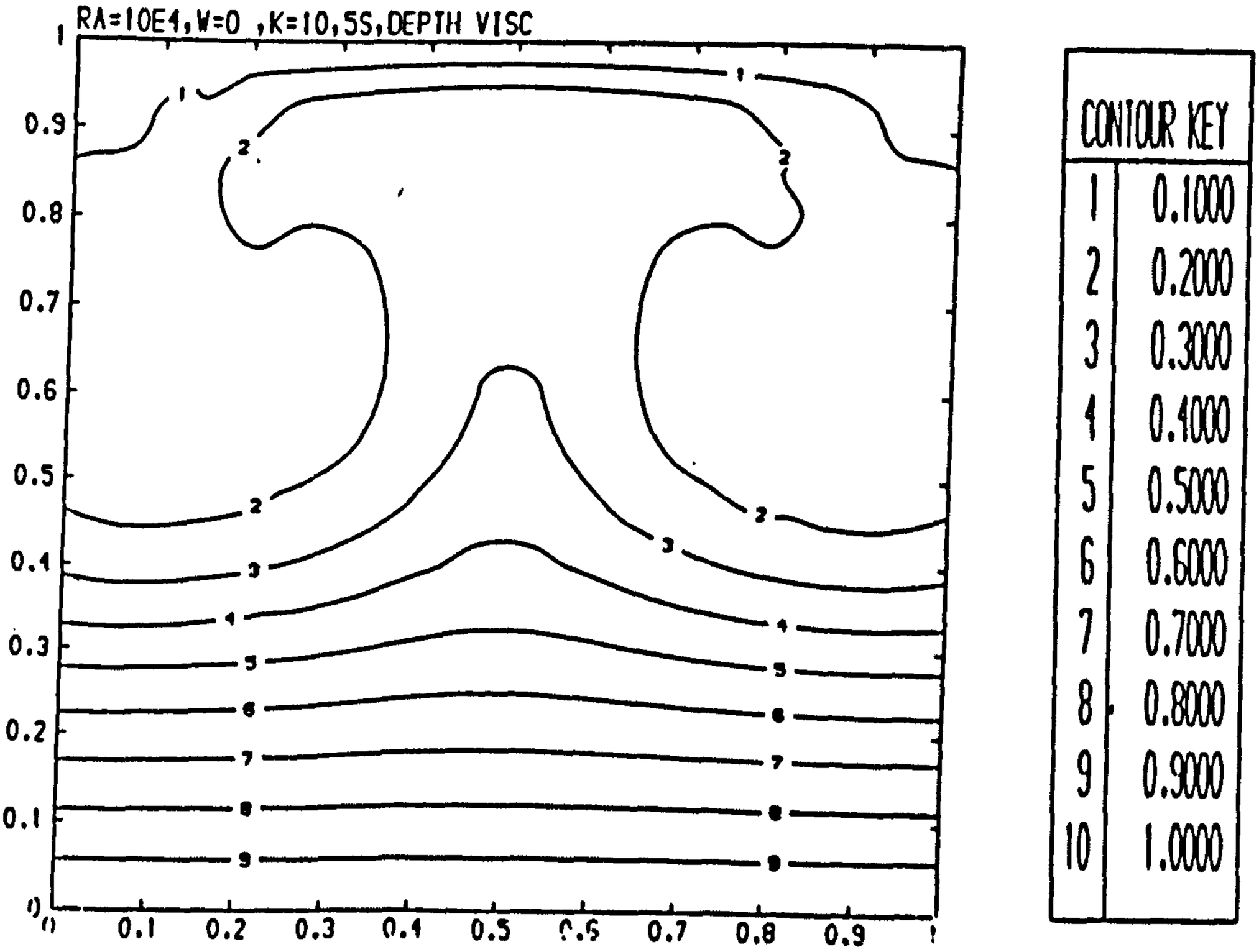

Figure (7.50)

Streamline & temperature plots for a depth dependent viscous fluid at $Ra=10^4$, $Pr=7$, $k=10$, $\omega=0$.

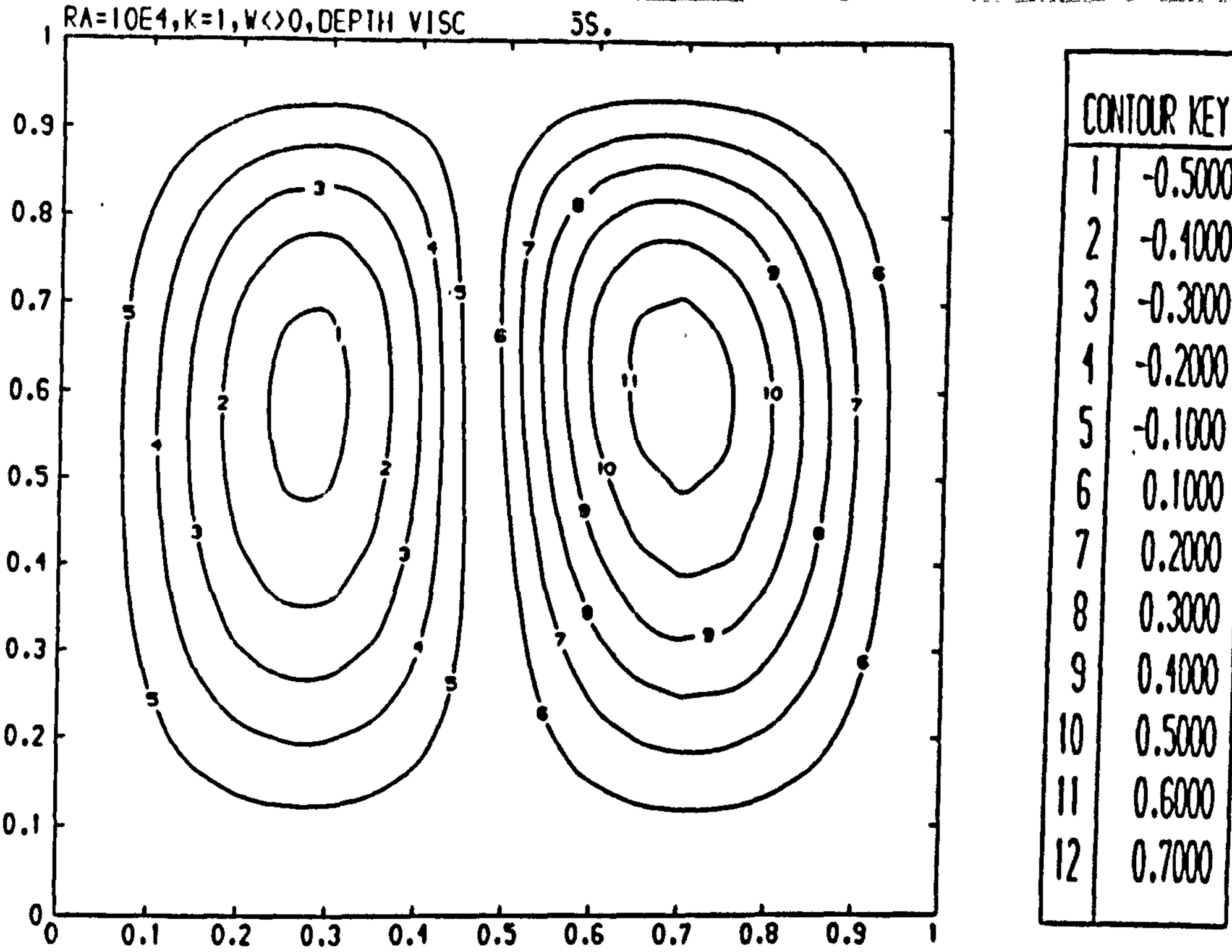

Figure (7.51)

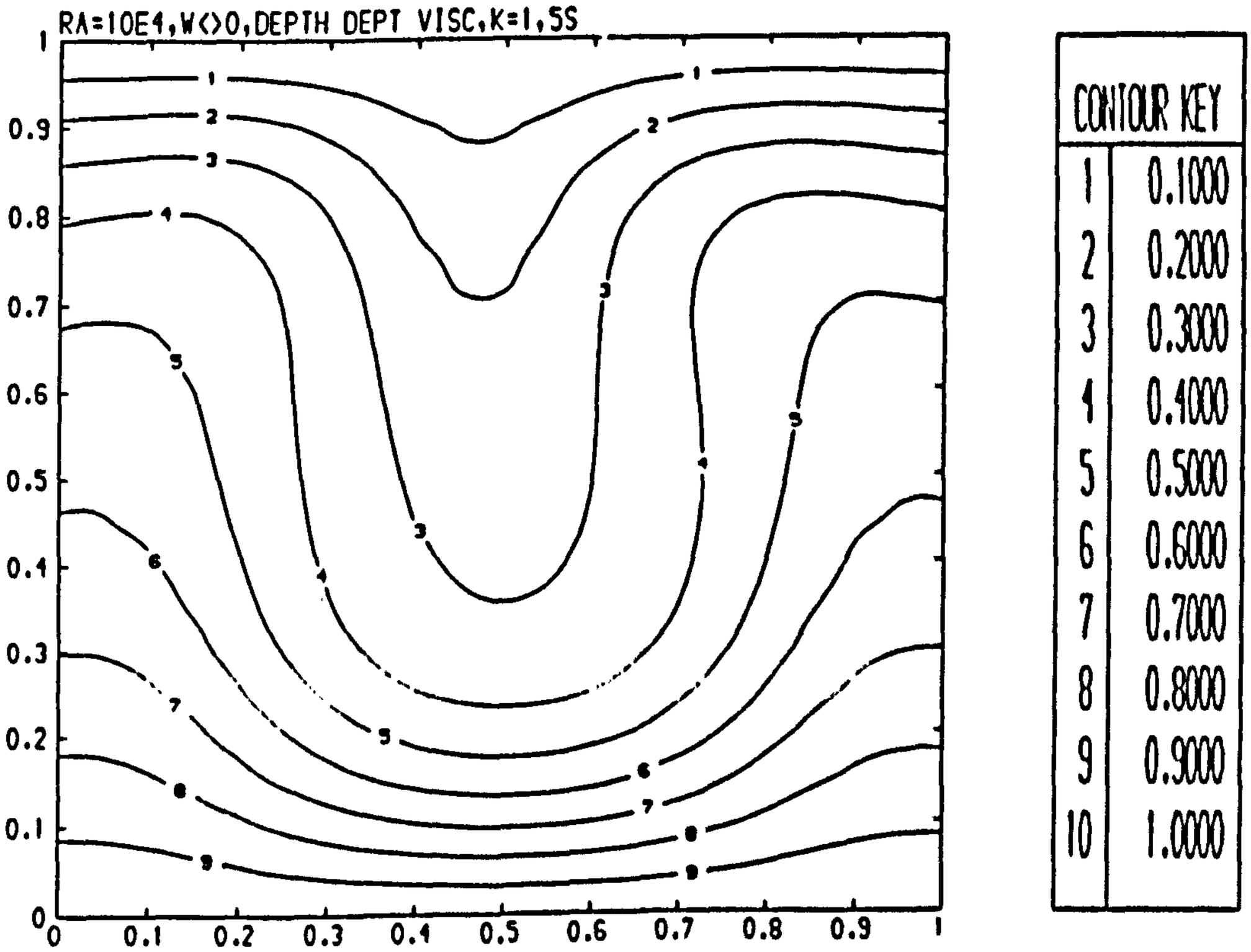

Figure (7.52)

Streamline & temperature plots for a depth dependent viscous fluid at $Ra=10^4$, $Pr=7$, $k=1$, $\omega<>0$.

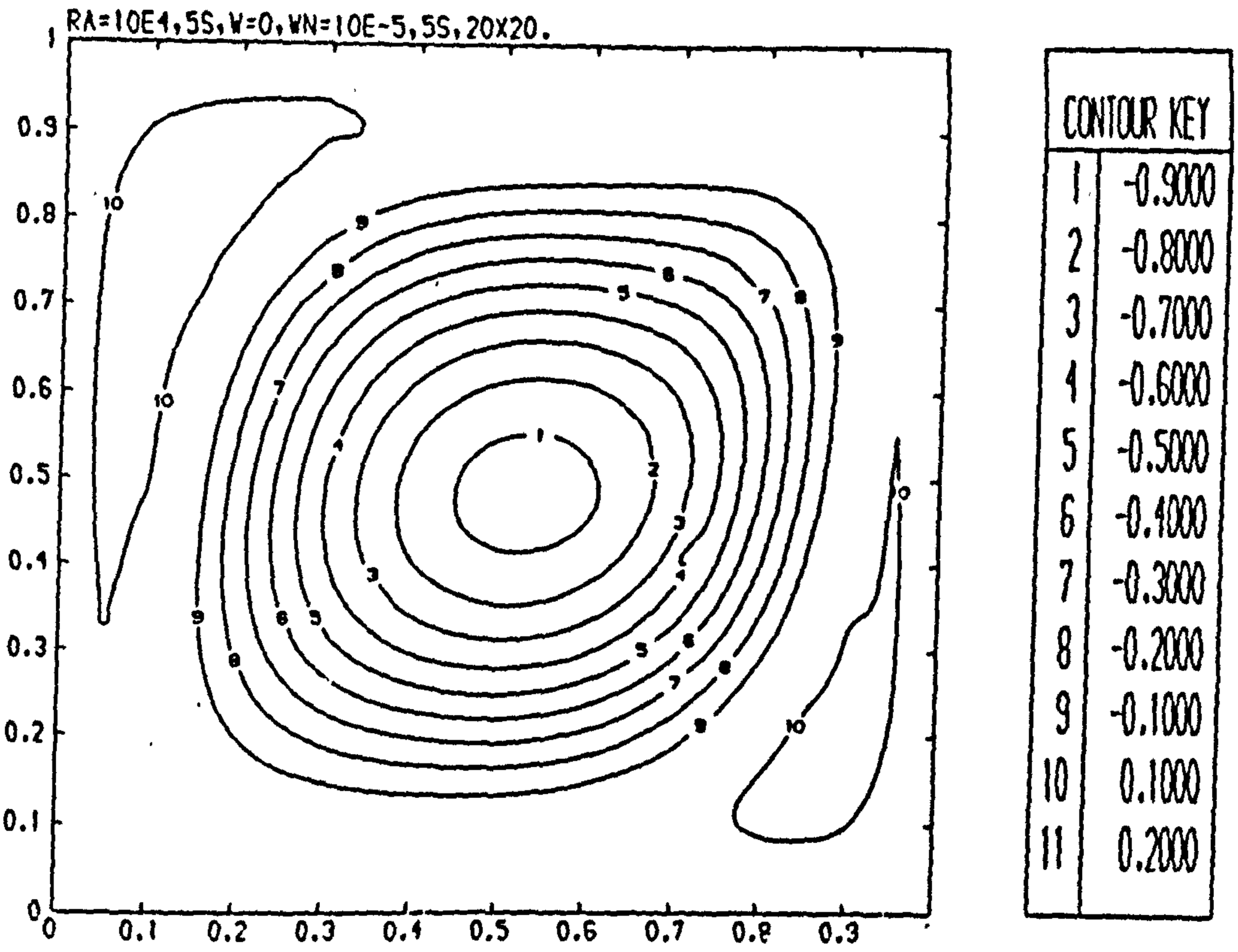

Figure (7.53)

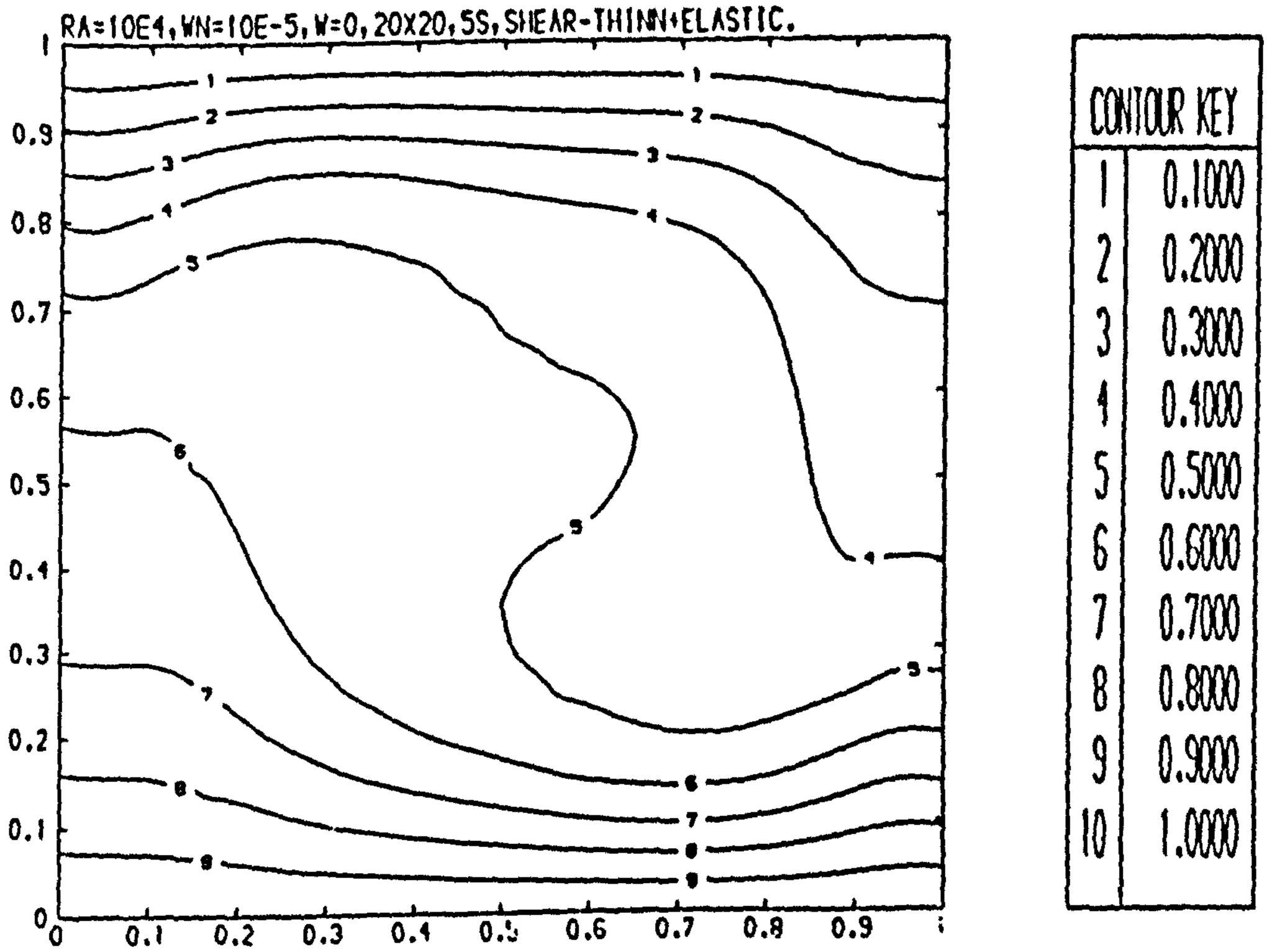

Figure (7.54)

Streamline & temperature plots for a viscoelastic-pseudoplastic fluid at $Ra=10^4$, $Pr=7$, $Wn=10^{-5}$, $\omega=0$, 5s.

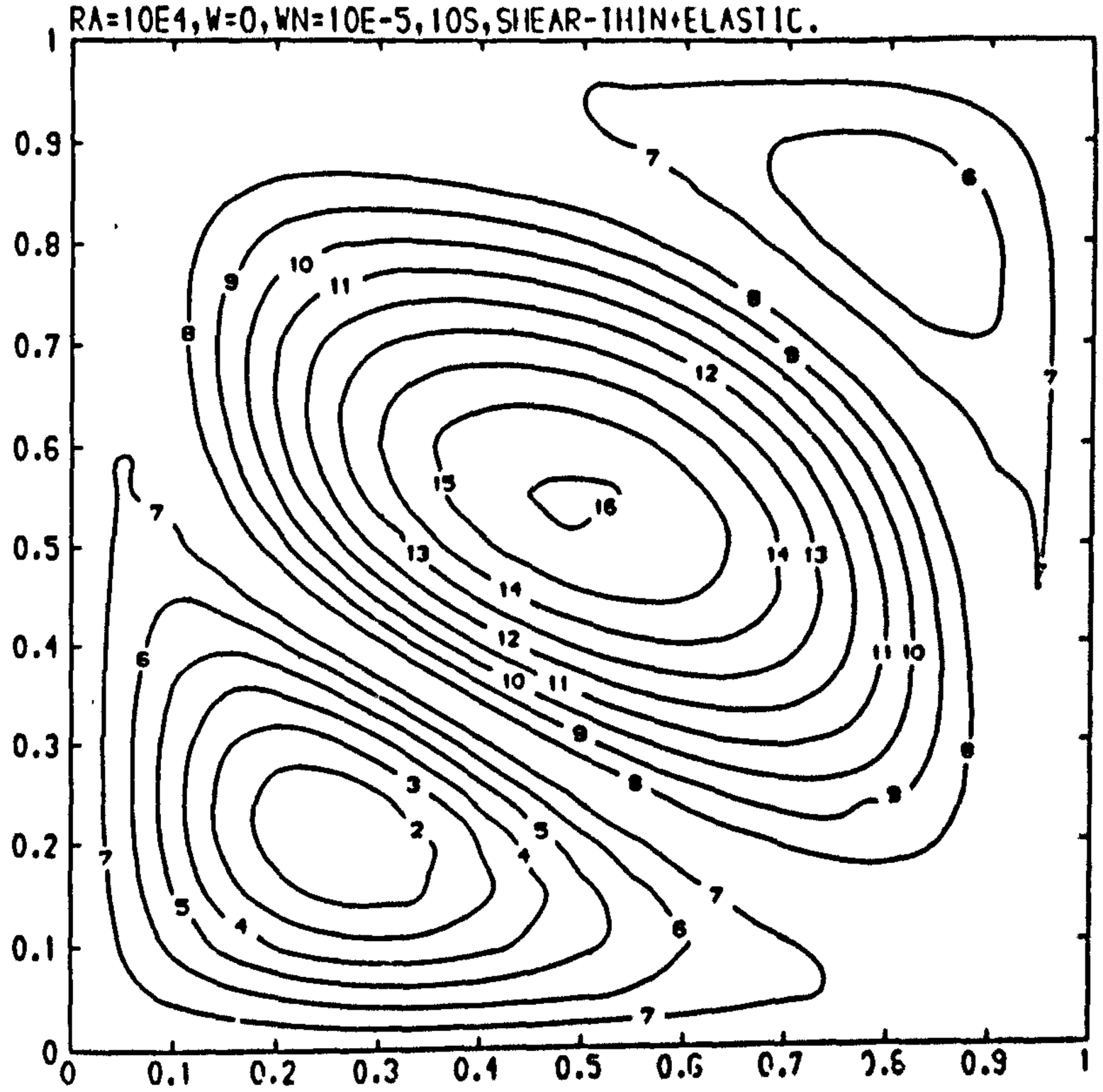

CONTOUR KEY	
1	-0.7000
2	-0.6000
3	-0.5000
4	-0.4000
5	-0.3000
6	-0.2000
7	-0.1000
8	0.1000
9	0.2000
10	0.3000
11	0.4000
12	0.5000
13	0.6000
14	0.7000
15	0.8000
16	0.9000

Figure (7.55)

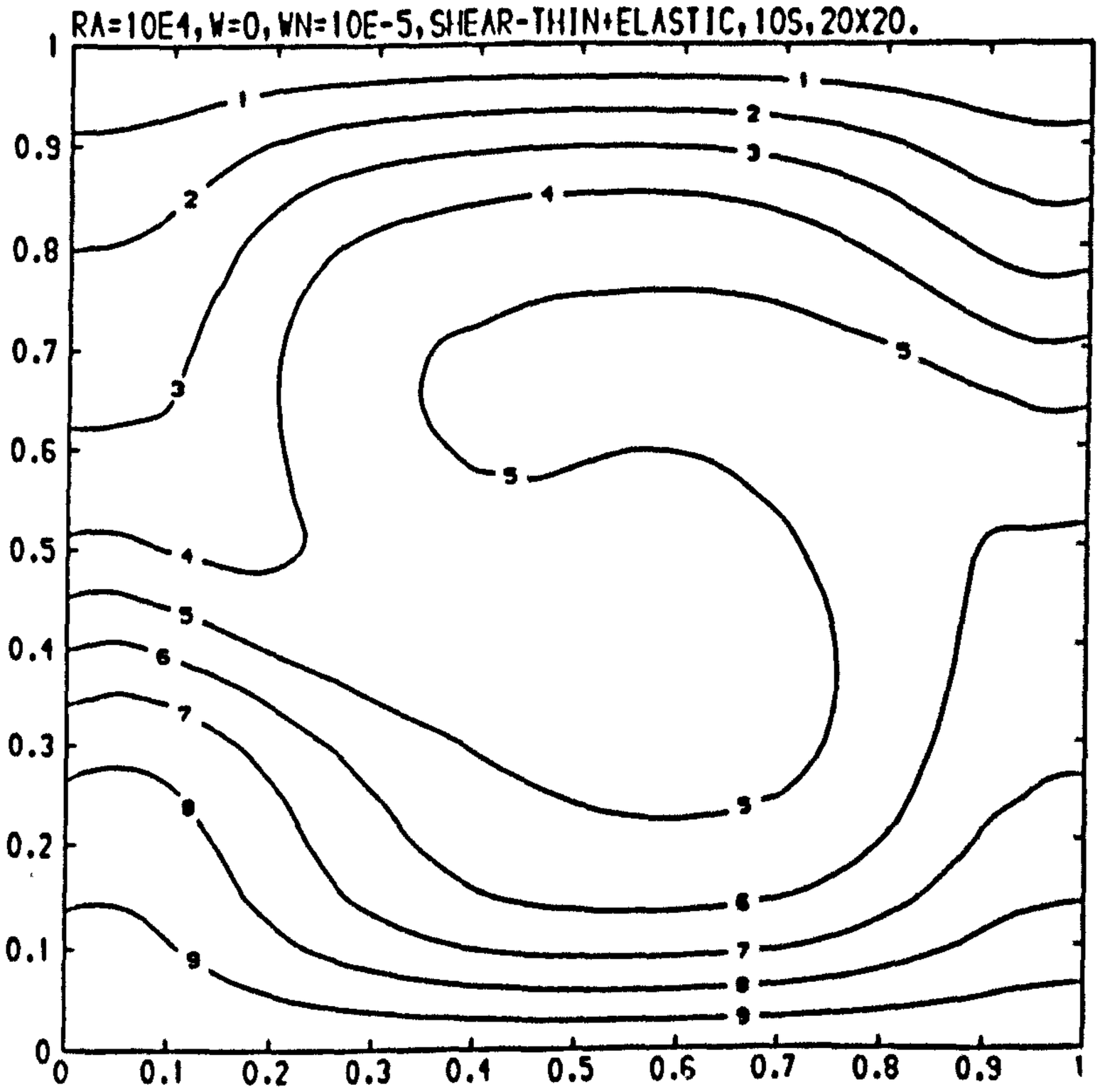

CONTOUR KEY	
1	0.1000
2	0.2000
3	0.3000
4	0.4000
5	0.5000
6	0.6000
7	0.7000
8	0.8000
9	0.9000
10	1.0000

Figure (7.56)

Streamline & temperature plots for a viscoelastic-pseudoplastic fluid at $Ra=10^4$, $Pr=7$, $Wn=10^{-5}$, $\omega=0,10s$.

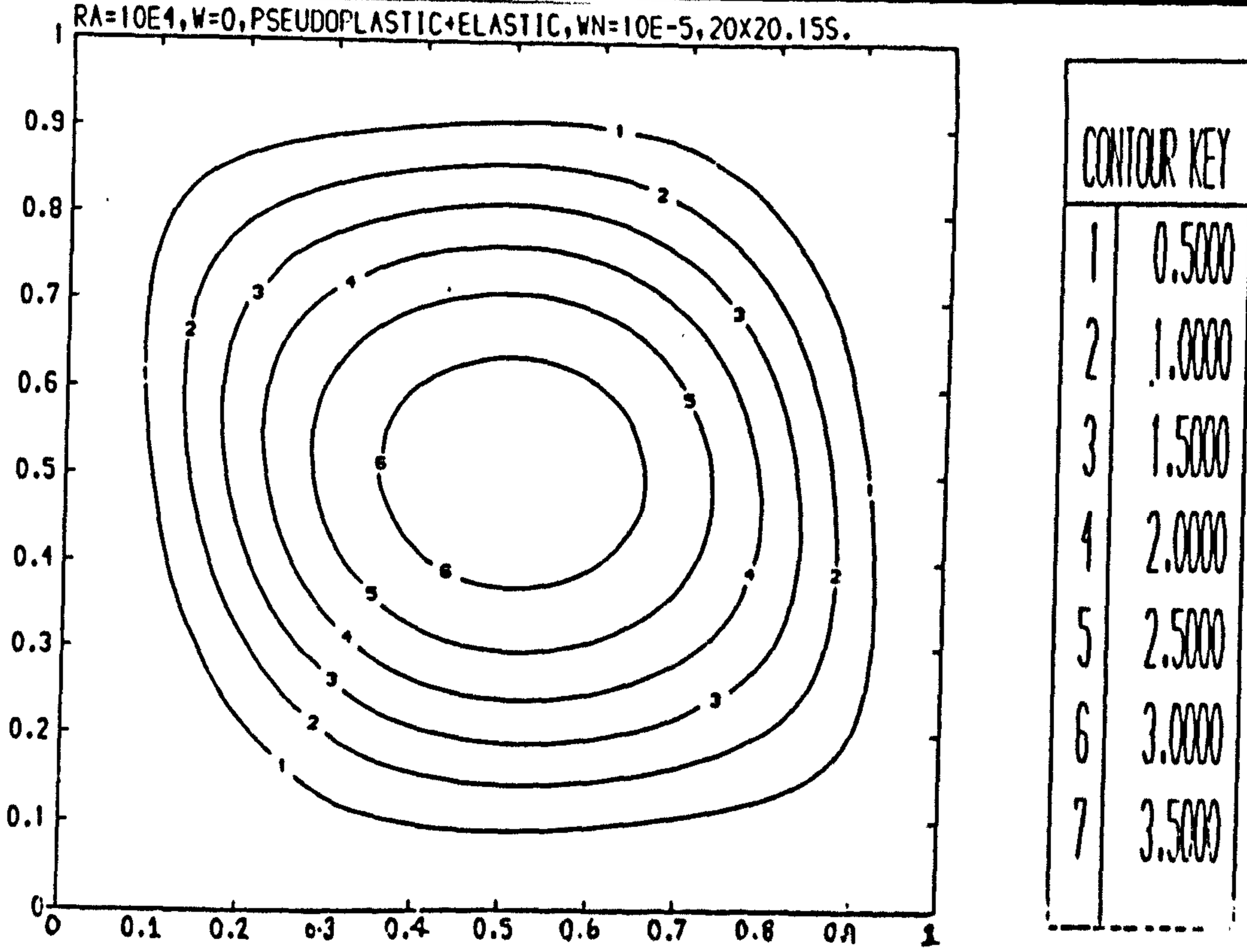

Figure (7.57)

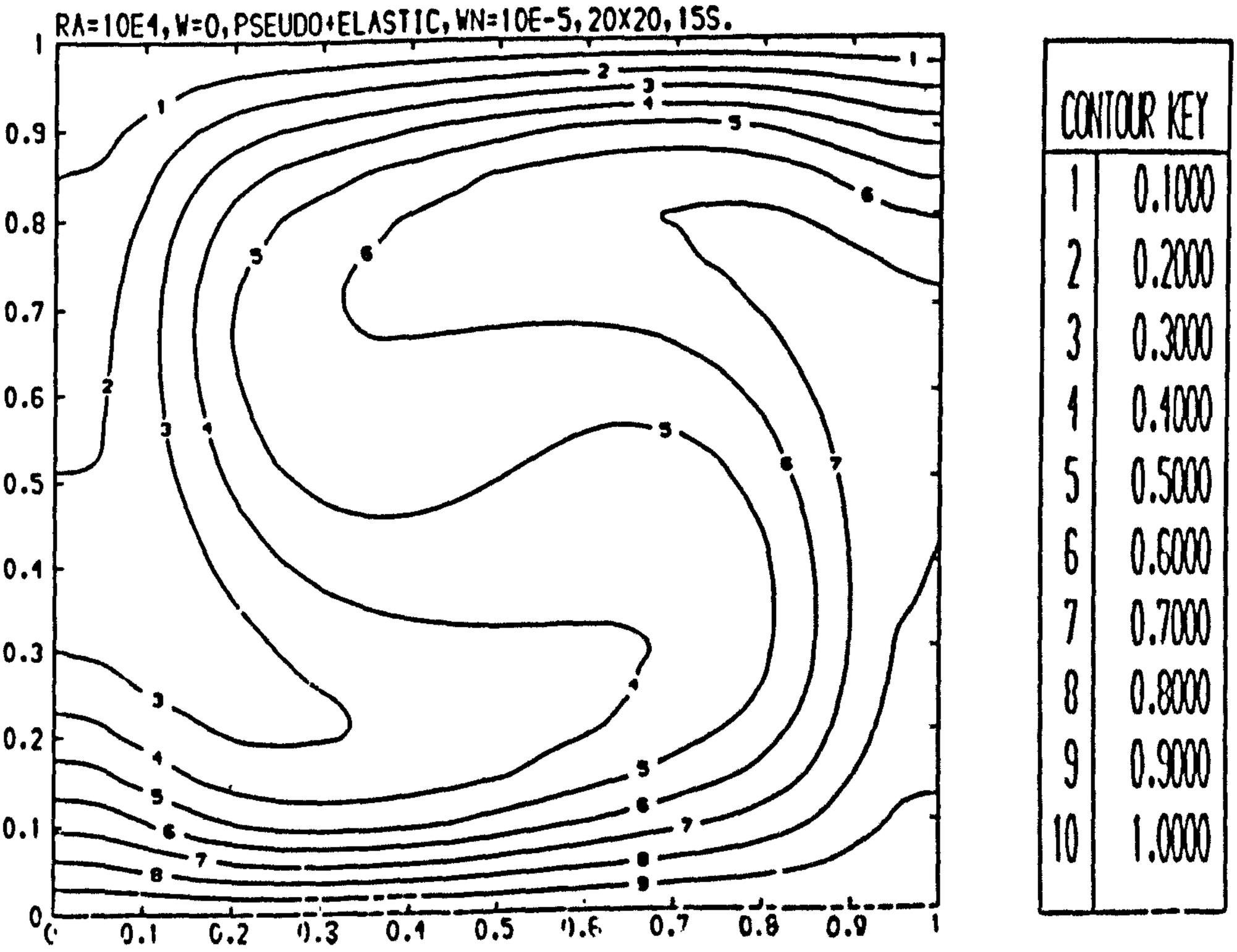

Figure (7.58)

Streamline & temperature plots for a viscoelastic-pseudoplastic fluid at $Ra=10^4$, Pr=7, $Wn=10^{-5}$, ω=0,15s.

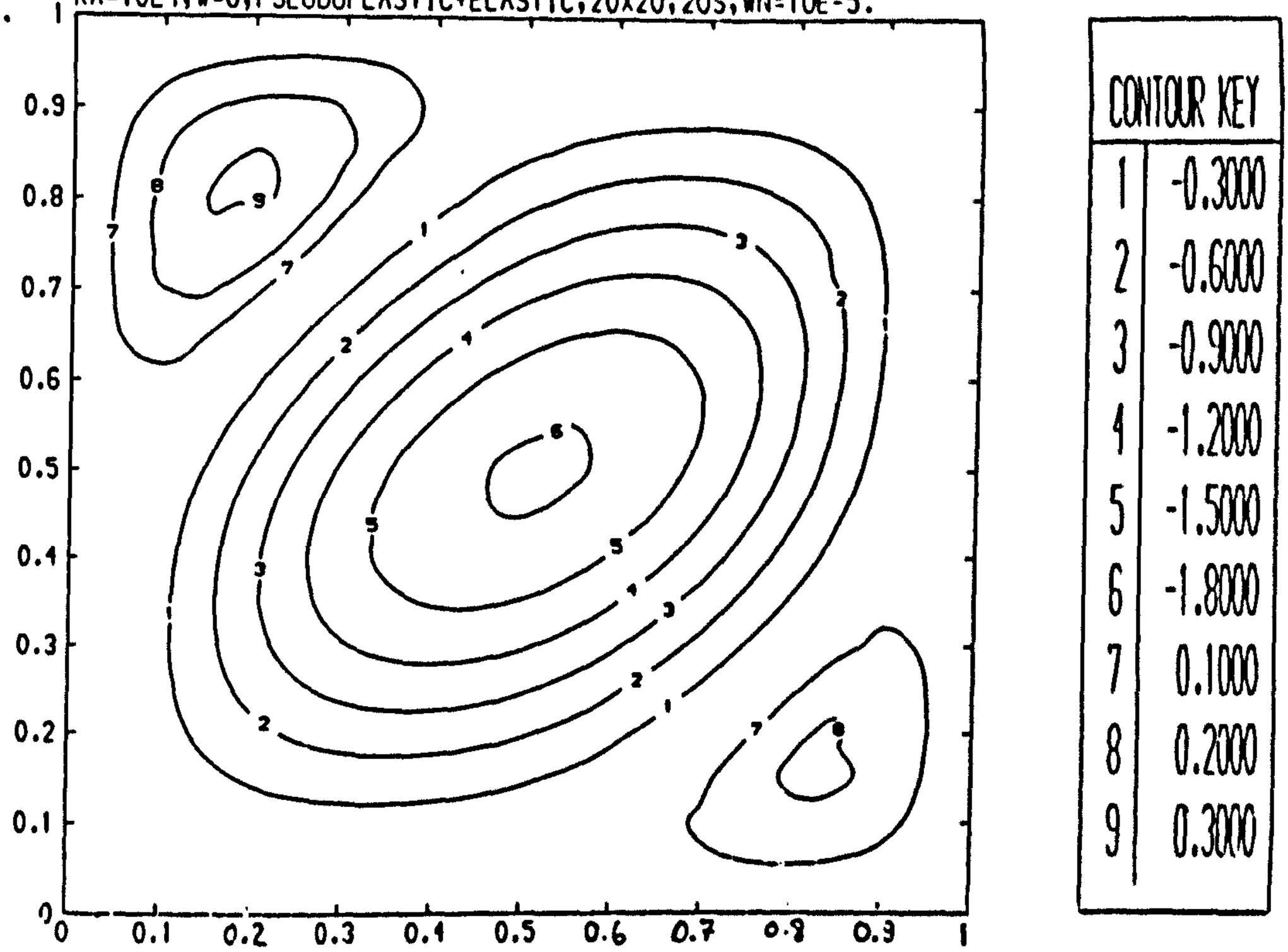

Figure (7.59)

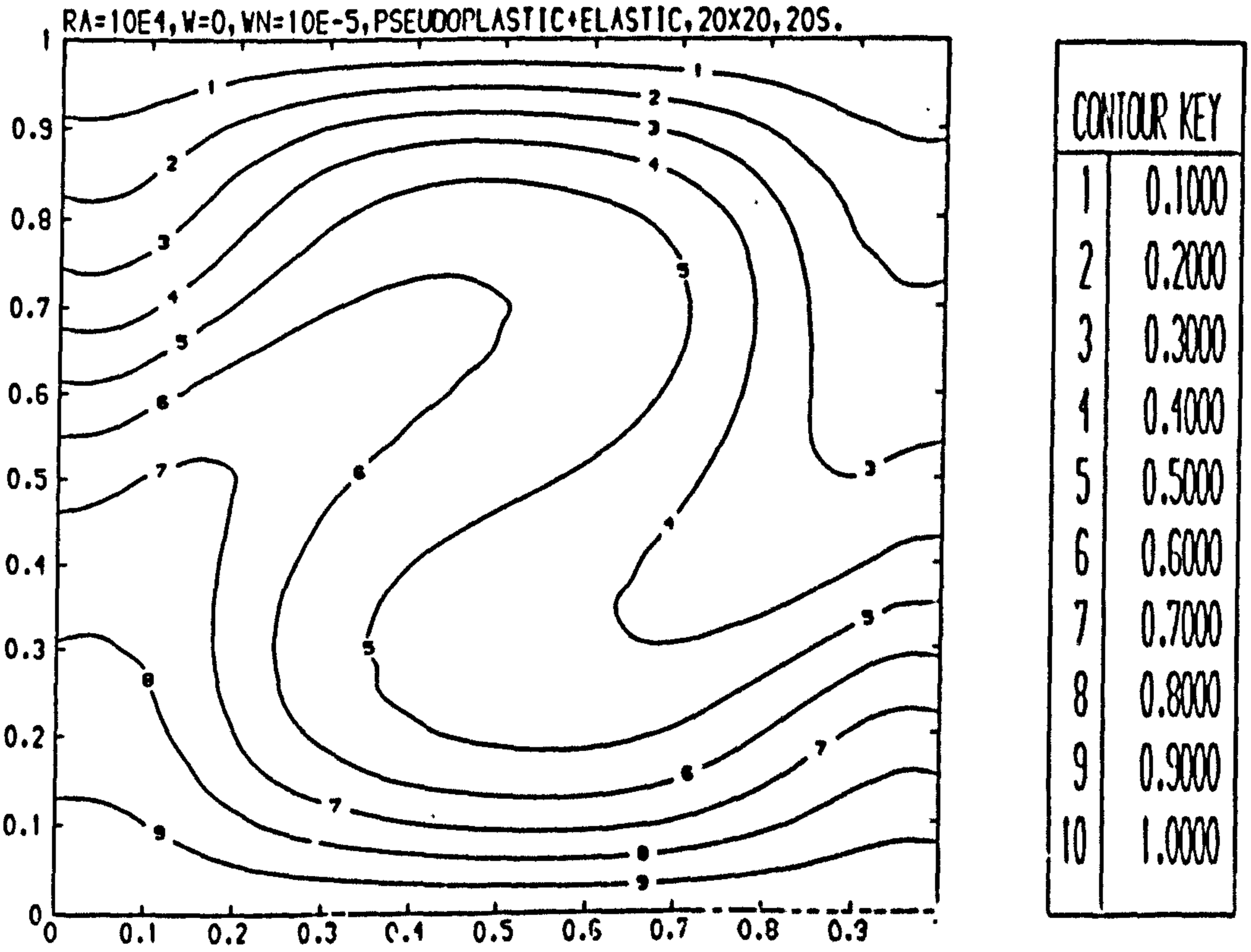

Figure (7.60)

Streamline & temperature plots for a viscoelastic-pseudoplastic fluid at $Ra=10^4$, $Pr=7$, $Wn=10^{-5}$, $\omega=0$, 20s.

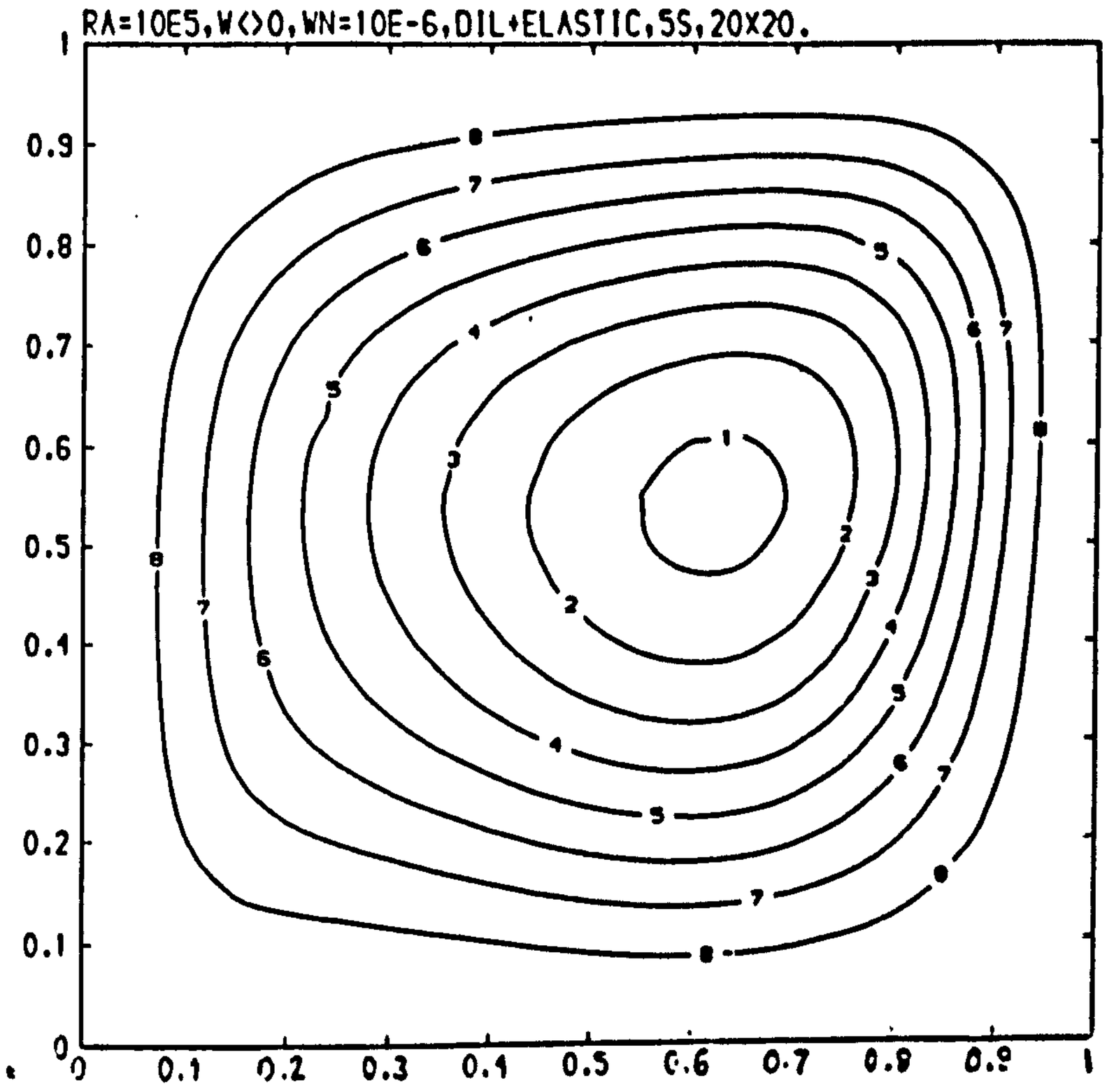

CONTOUR KEY-	
1	-4.0000
2	-3.5000
3	-3.0000
4	-2.5000
5	-2.0000
6	-1.5000
7	-1.0000
8	-0.5000

Figure (7.61)

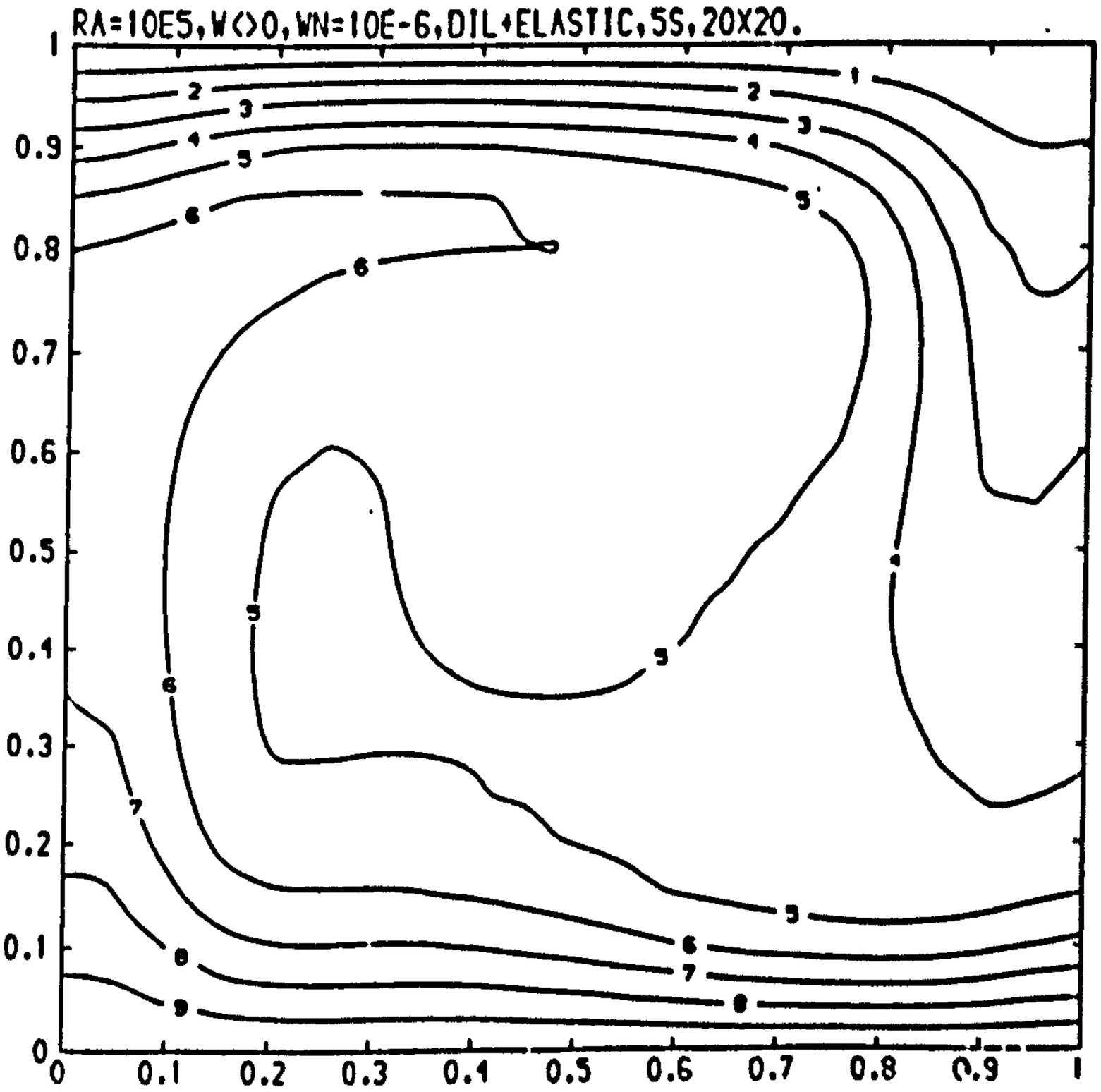

CONTOUR KEY	
1	0.1000
2	0.2000
3	0.3000
4	0.4000
5	0.5000
6	0.6000
7	0.7000
8	0.8000
9	0.9000
10	1.0000

Figure (7.62)

Streamline & temperature plots for a viscoelastic-dilatant fluid at $Re=10^5$, $Pr=7$, $Wn=10^{-6}$, $\omega=0$, 5s.

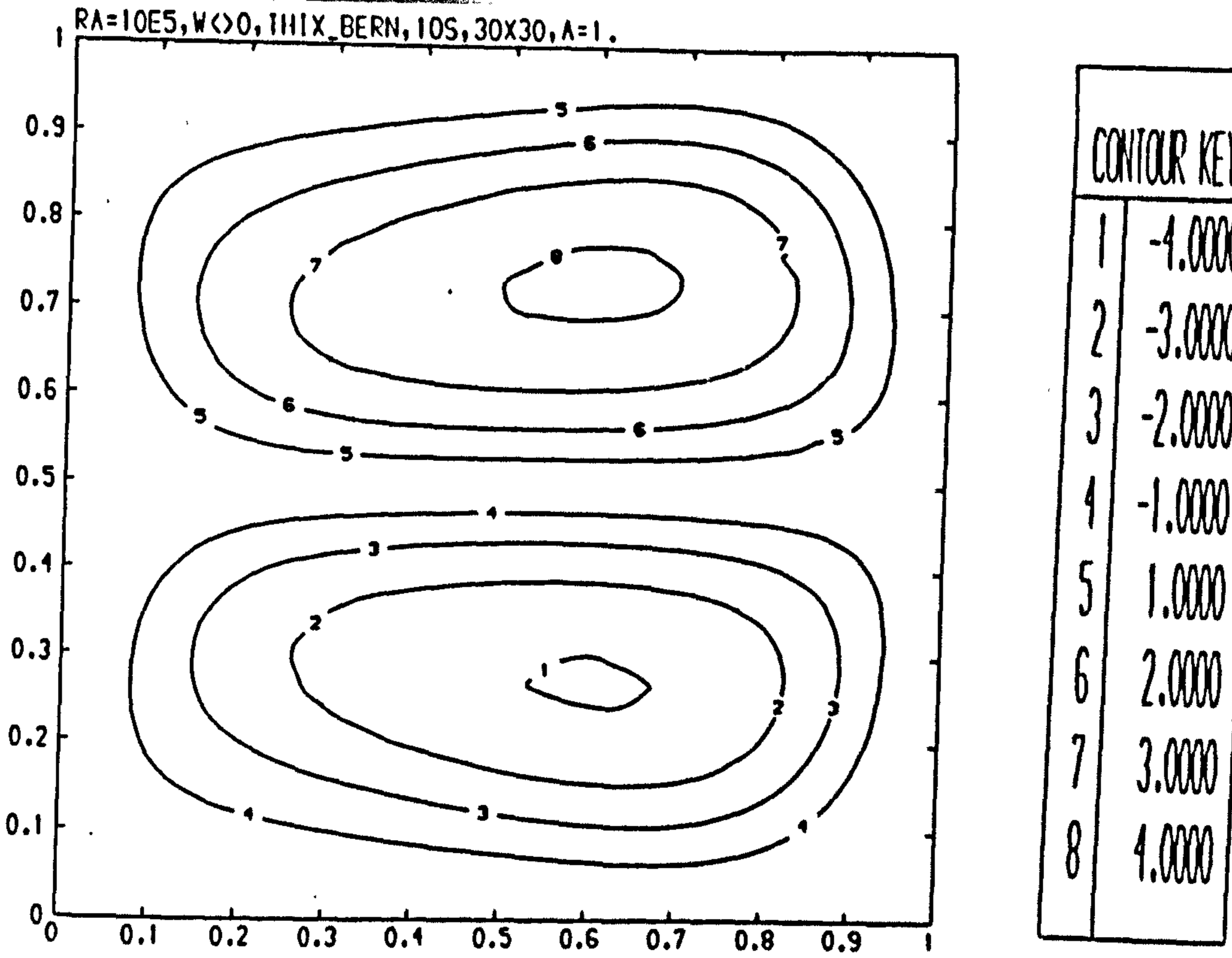

Figure (7.63)

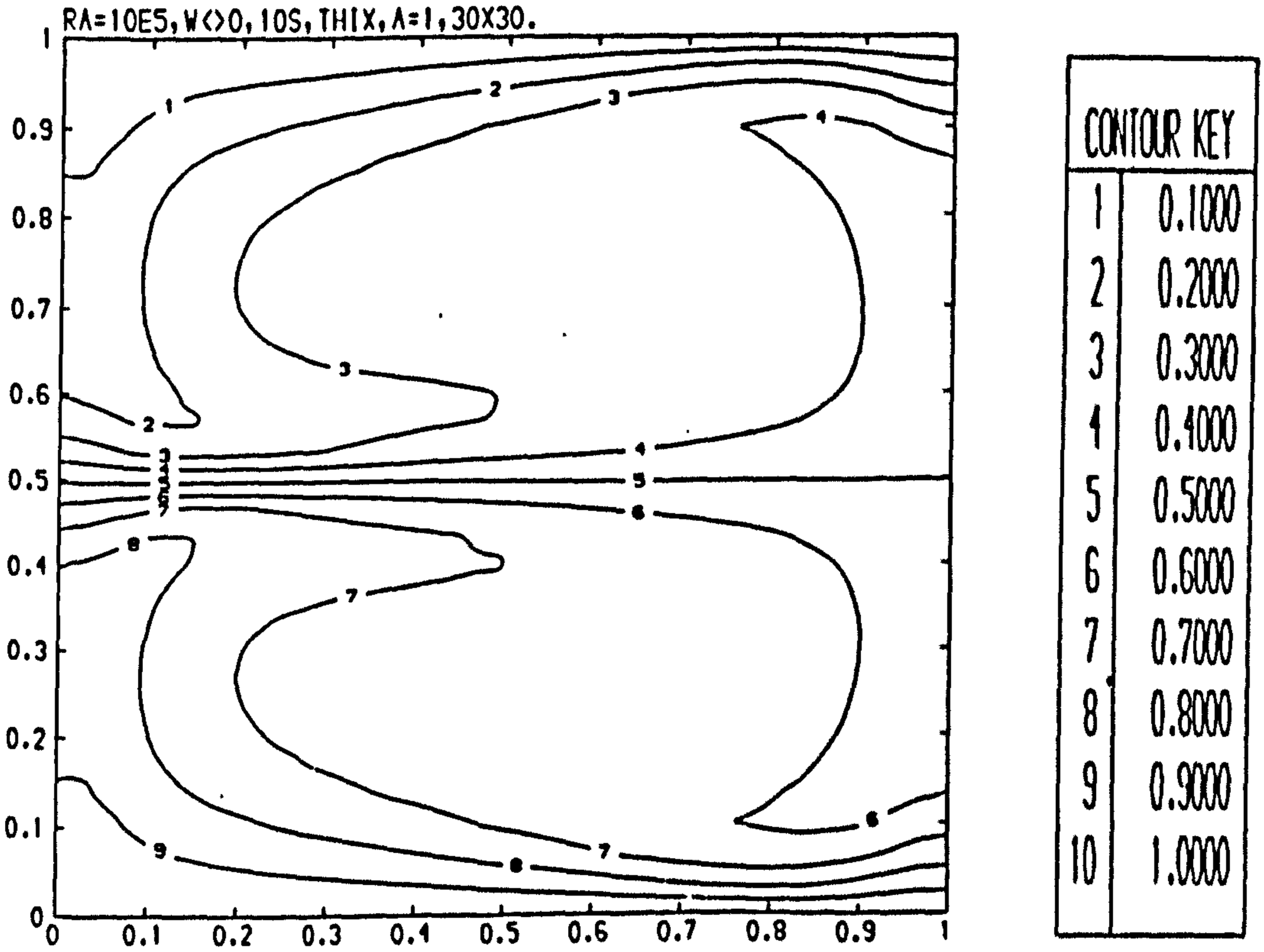

Figure (7.64)

Streamlines & temperature plots for a thixotropic fluid at $Ra=10^5$, $a=1$, $\omega<>0$, 10s.

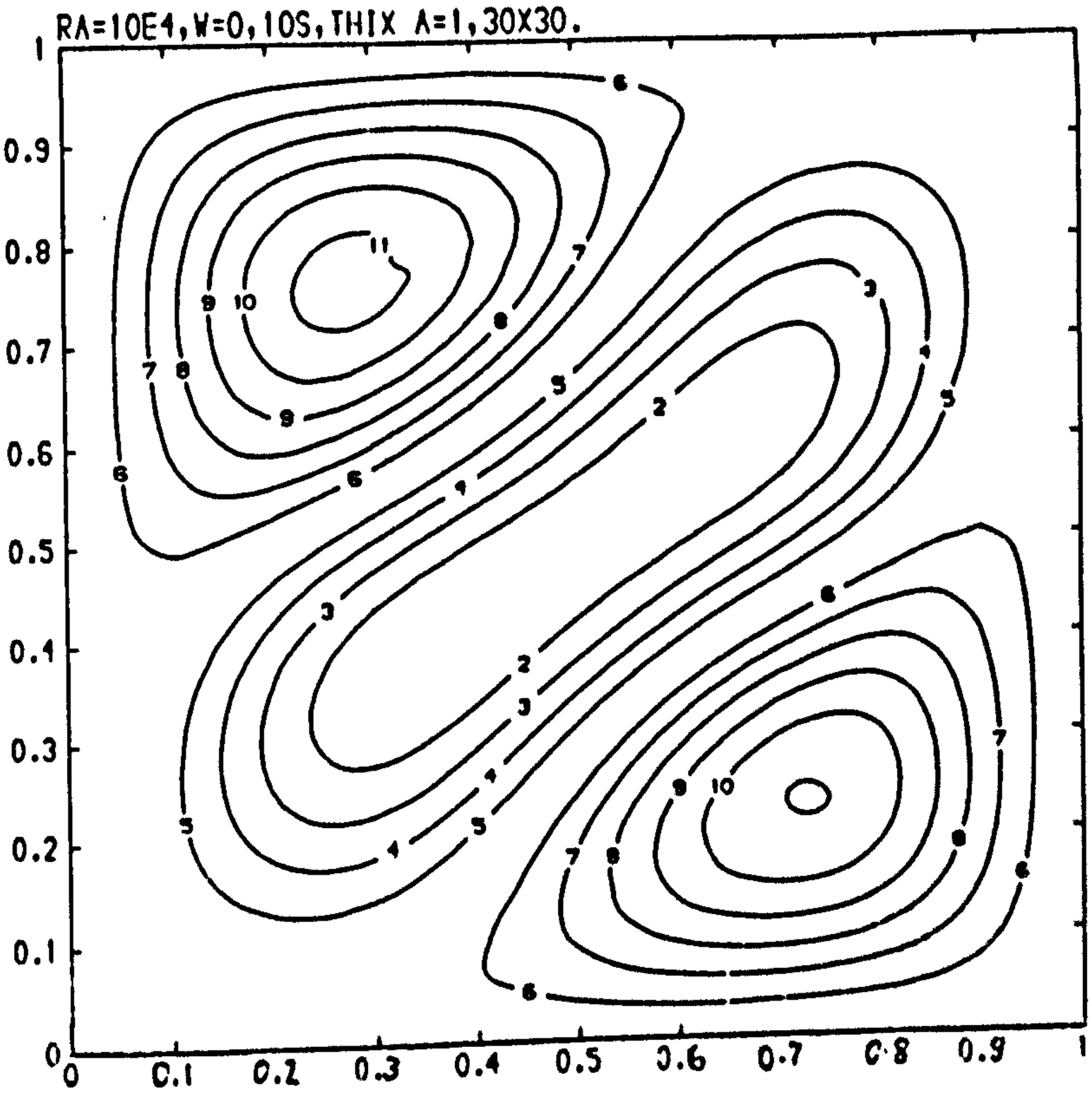

CONTOUR KEY	
1	-0.5000
2	-0.4000
3	-0.3000
4	-0.2000
5	-0.1000
6	0.1000
7	0.2000
8	0.3000
9	0.4000
10	0.5000
11	0.6000

Figure (7.65)

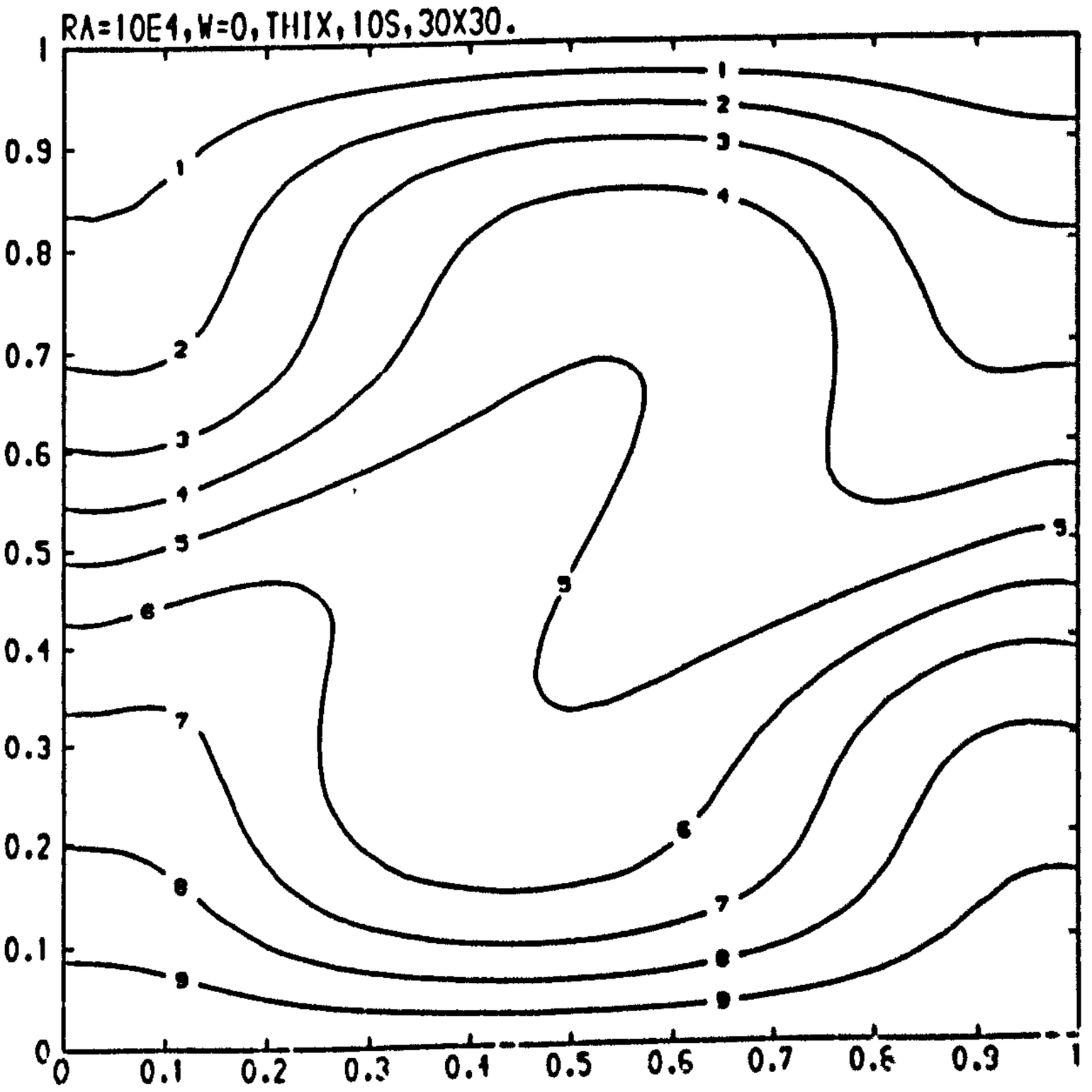

CONTOUR KEY	
1	0.1000
2	0.2000
3	0.3000
4	0.4000
5	0.5000
6	0.6000
7	0.7000
8	0.8000
9	0.9000
10	1.0000

Figure (7.66)

Streamlines & temperature plots for a thixotropic fluid at $Re=10^4$, $a=1$, $\omega=0,10s$.

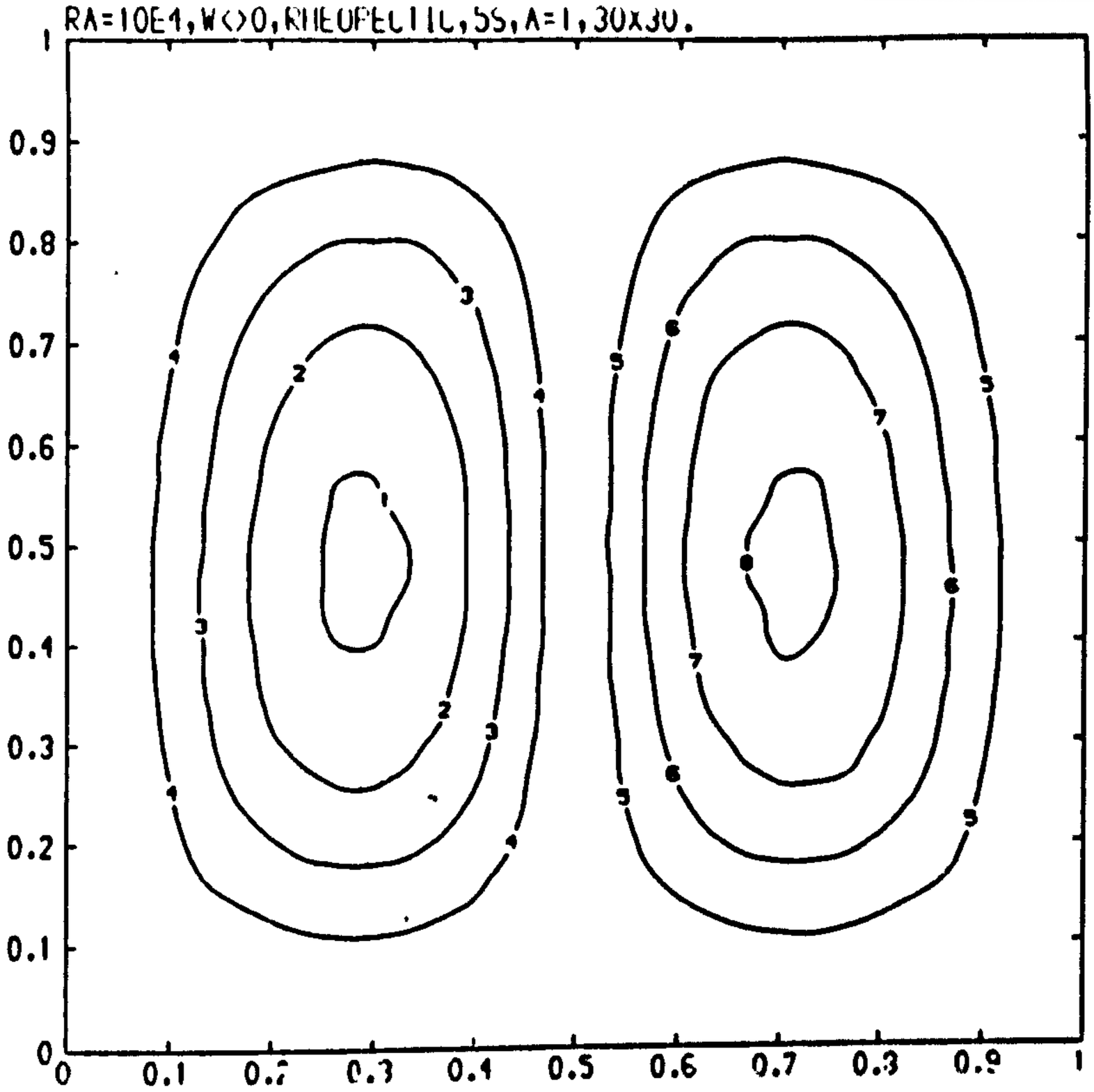

CONTOUR KEY	
1	-0.1000
2	-0.3000
3	-0.2000
4	-0.1000
5	0.1000
6	0.2000
7	0.3000
8	0.1000

Figure (7.67)

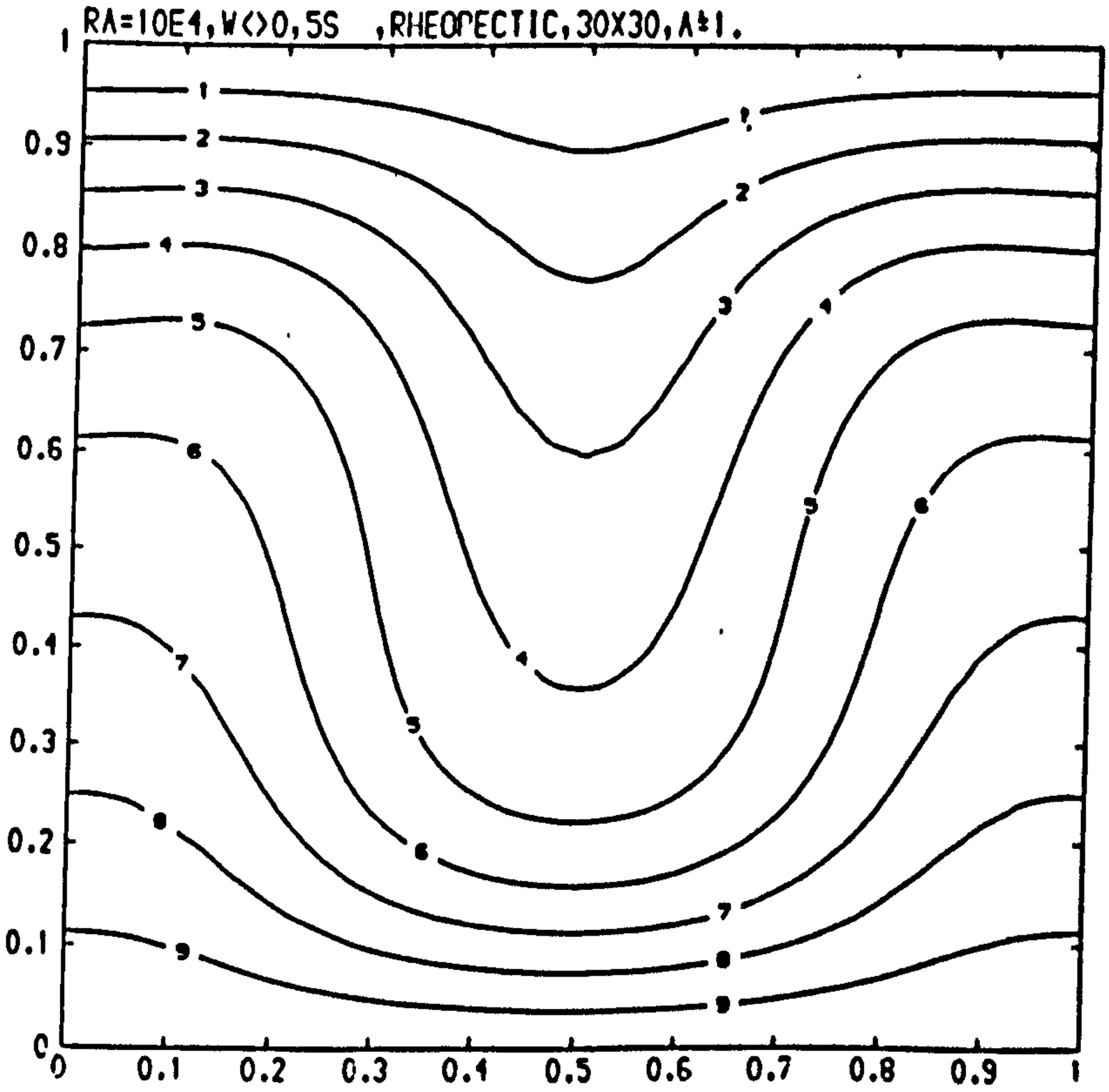

CONTOUR KEY	
1	0.1000
2	0.2000
3	0.3000
4	0.1000
5	0.5000
6	0.6000
7	0.7000
8	0.8000
9	0.9000
10	1.0000

Figure (7.68)

Streamlines & temperature plots for a rheopectic fluid at $Re=10^4$, $a=1$, $\omega<>0$, 5s.

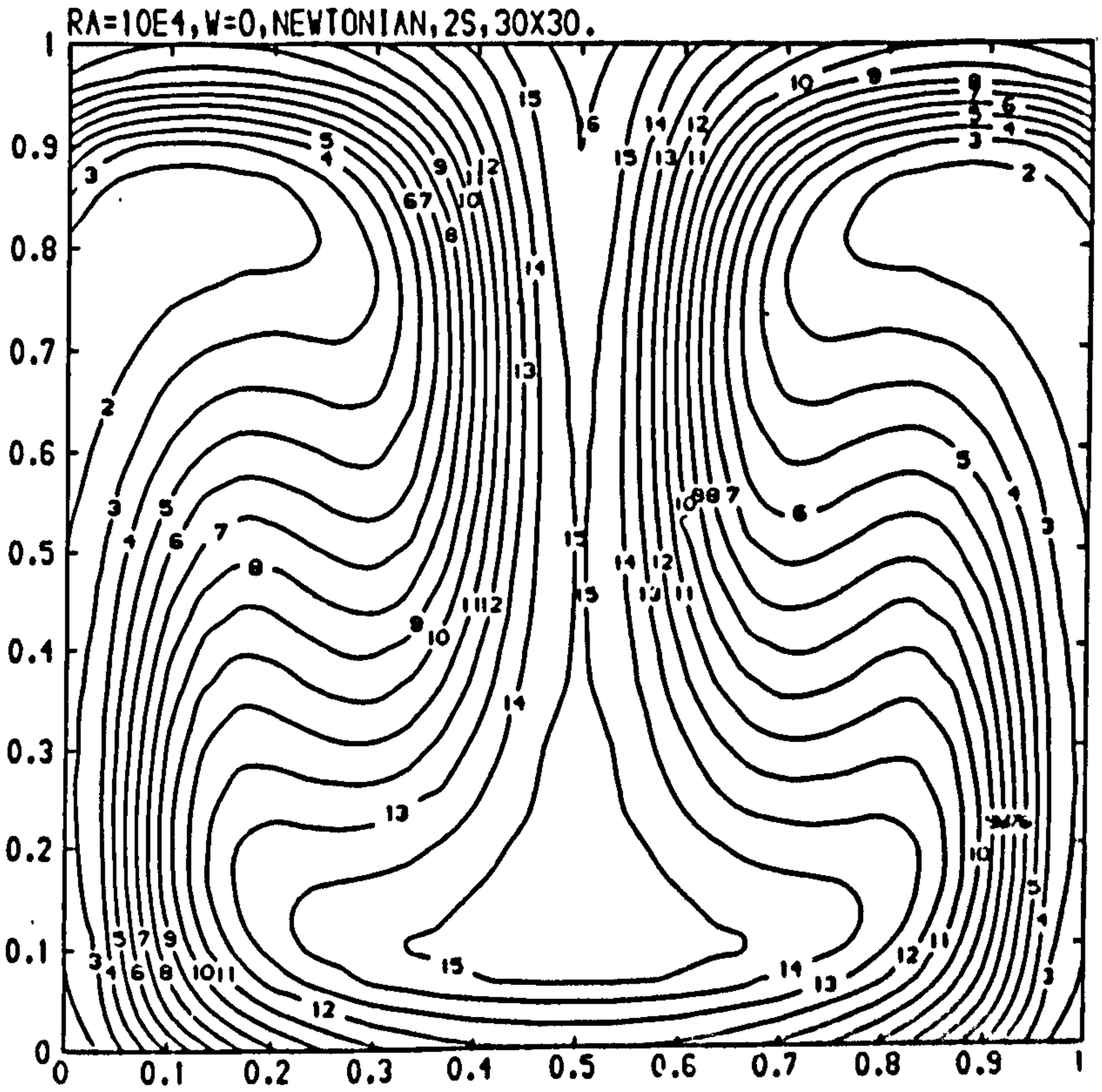

CONTOUR KEY	
1	0.3000
2	0.1000
3	0.5000
4	0.6000
5	0.7000
6	0.8000
7	0.9000
8	1.0000
9	1.1000
10	1.2000
11	1.3000
12	1.4000
13	1.5000
14	1.6000
15	1.7000
16	1.8000

Figure (7.69)

Concentration plot for a Newtonian fluid at $Ra=10^4$, $Pr=7$, $\omega=0$, 2s.

Figure (8.6) The chaotic attractor of a pseudoplastic fluid at r=18.12, time =30 seconds.
Scale: -30 < X < 30, 0 < Z < 60

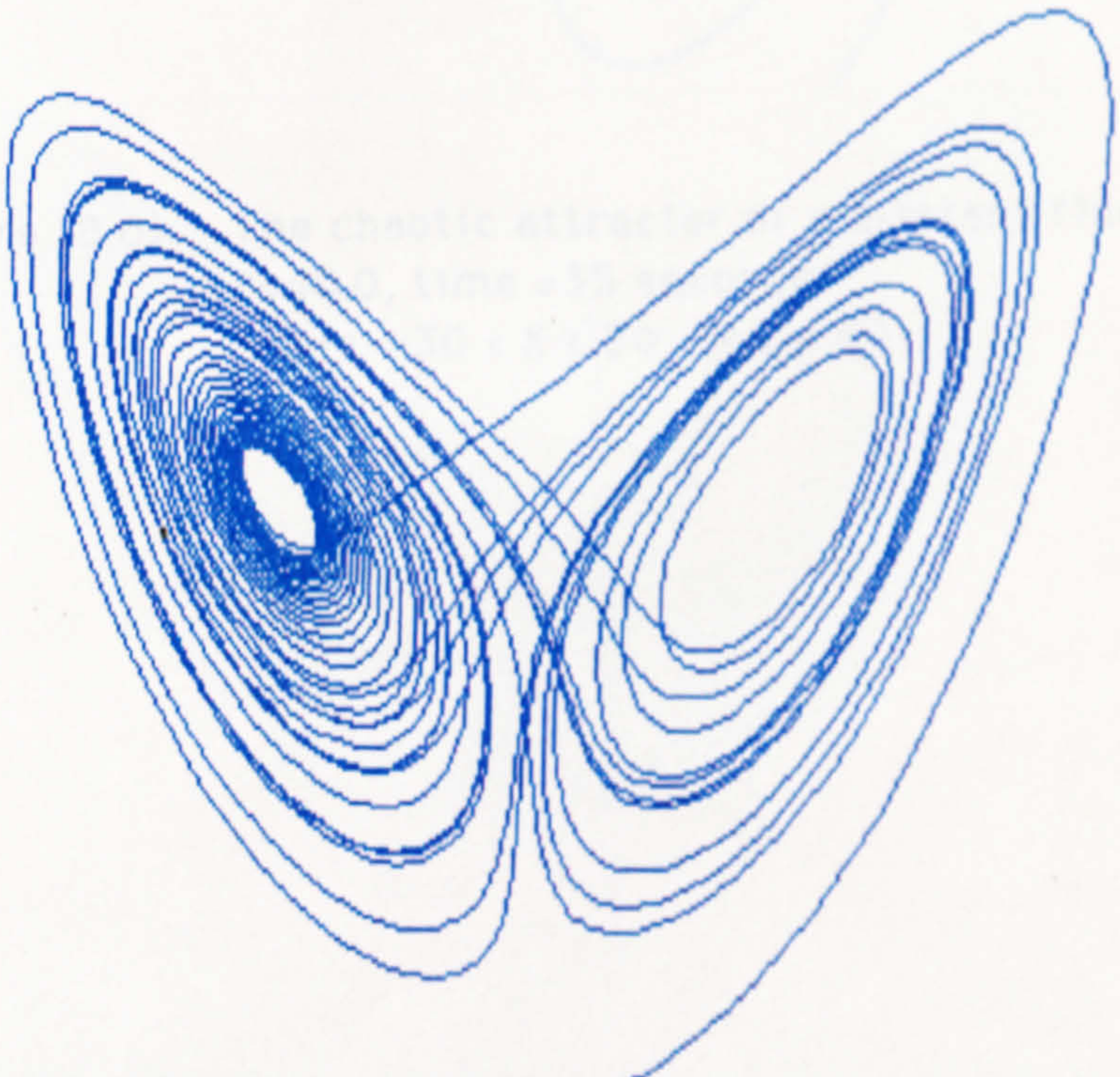

Figure (8.7) The chaotic attractor of a Newtonian fluid at r=28.0, time =30 seconds.
Scale: -30 < X <30, 0 < Z < 60

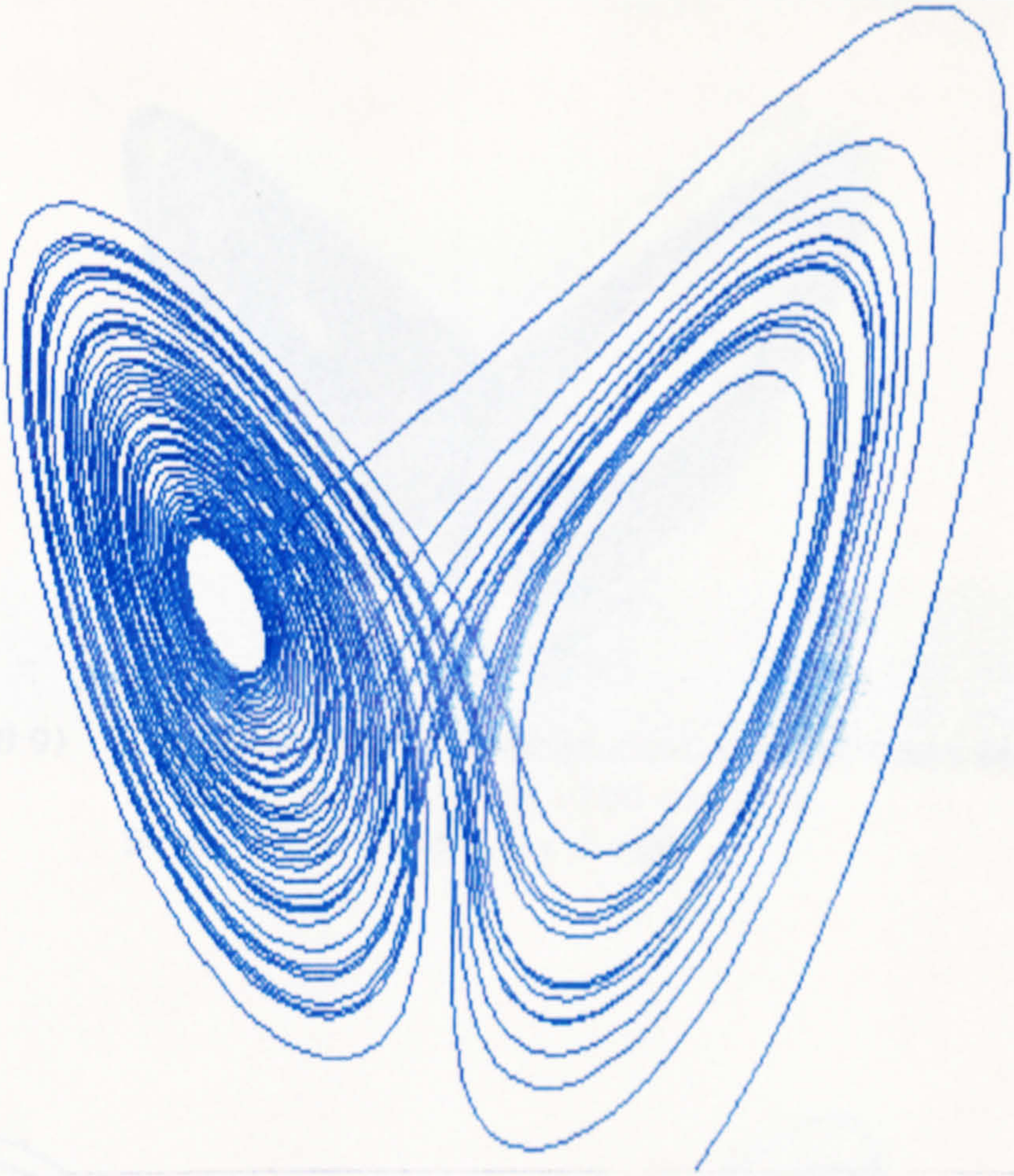

Figure (8.8) The chaotic attractor of a dilatant fluid at r=40.0, time =35 seconds.
Scale: -30 < X < 30, 0< Z < 90

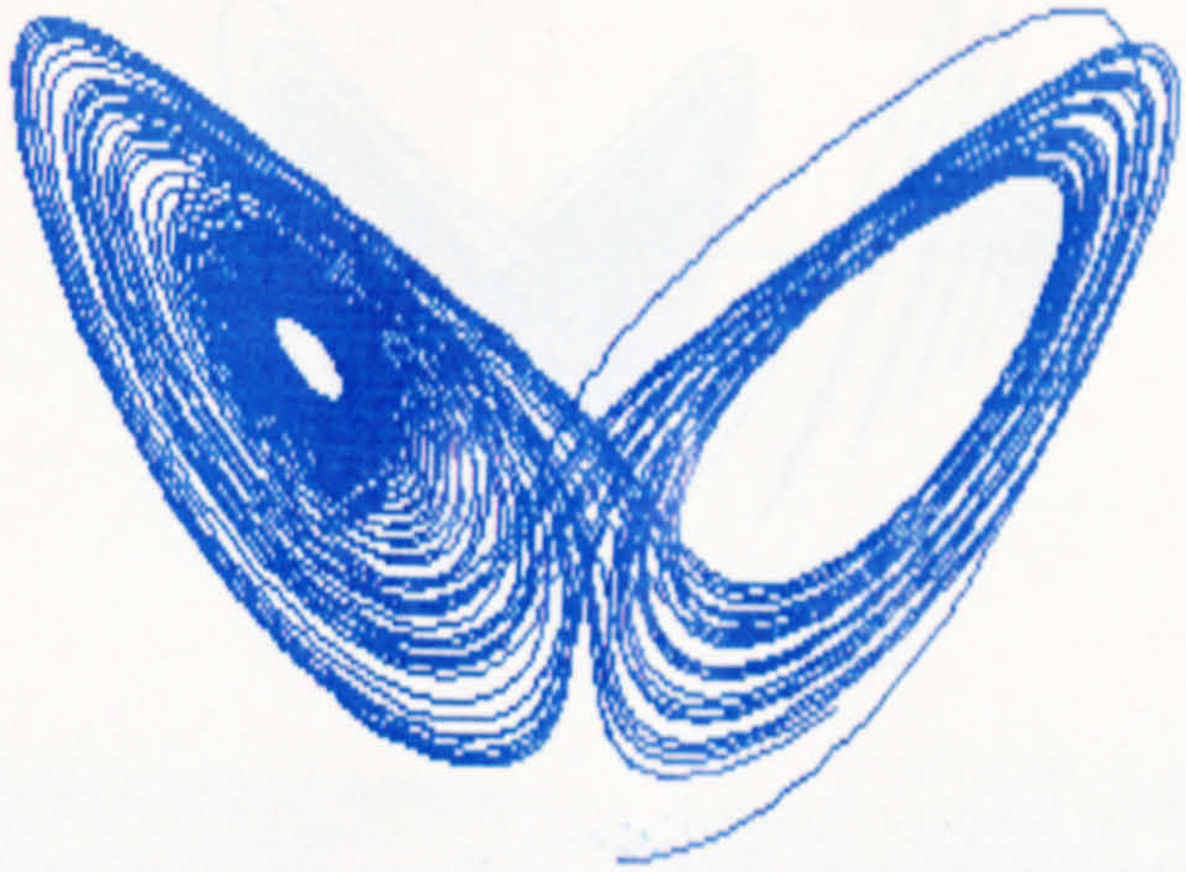

Figure (8.9) The chaotic attractor of a thixotropic fluid at r=18.12, a=0.05, time =100 seconds.
Scale: -30 < X < 30, 0 < Z < 60

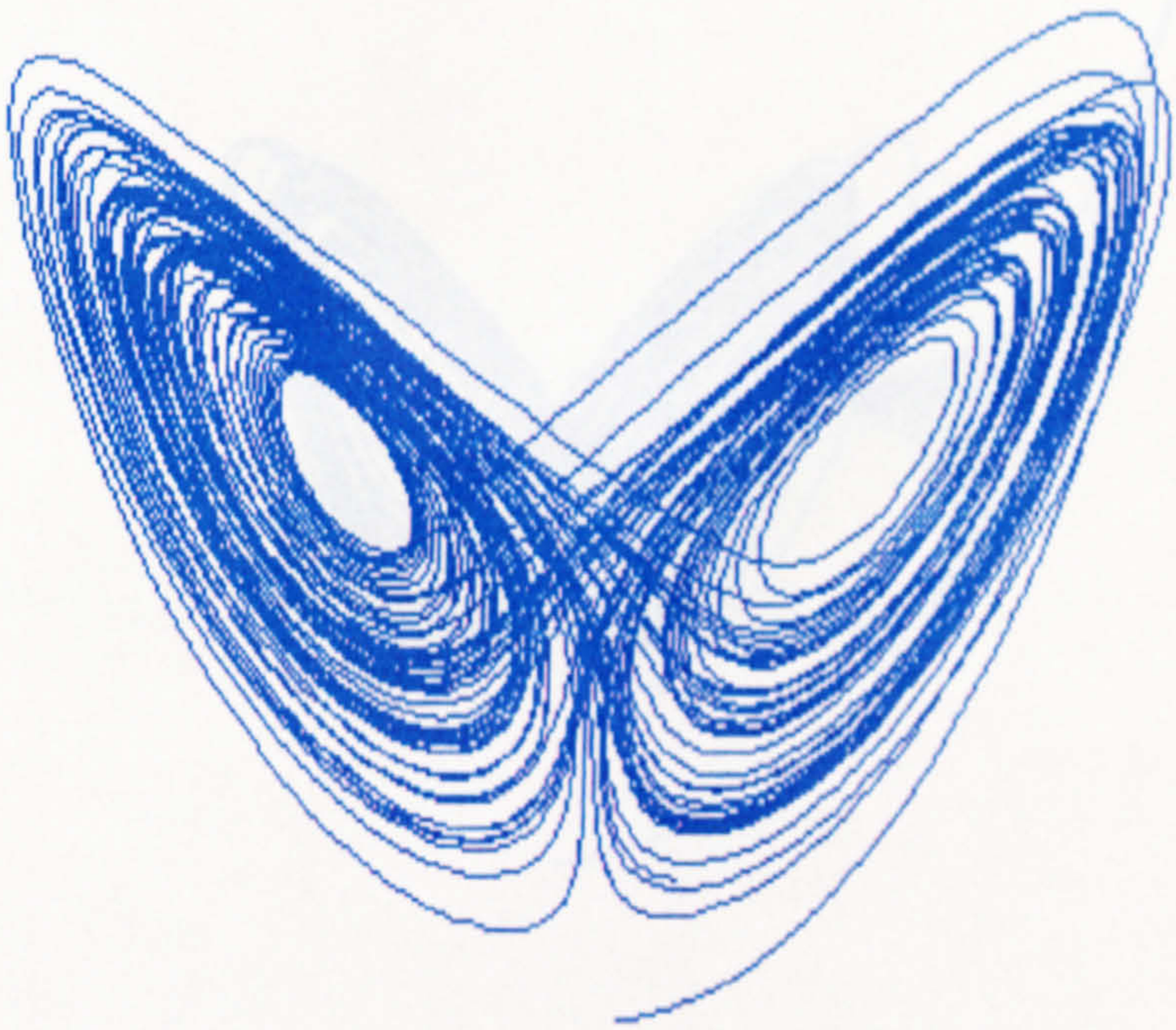

Figure (8.10) The chaotic attractor of a thixotropic fluid at r=25.0, a=0.05, time =60 seconds.
Scale: -30 < X < 30, 0 < Z < 60

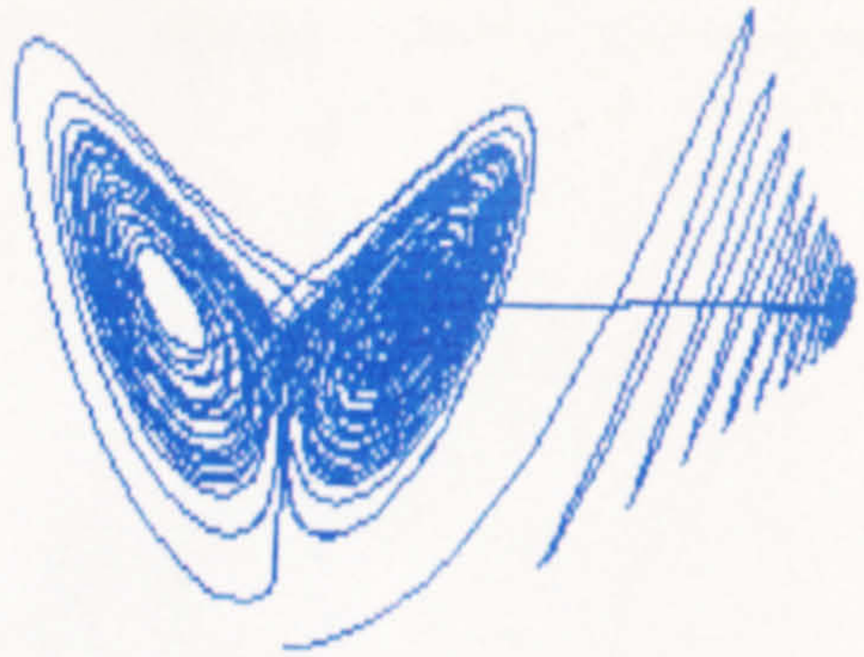

Figure (8.11) The chaotic attractor of a rheopectic fluid at r=40.0, a=0.01, time =100 seconds.
Scale: -100 < X < 100, 0 < Z < 100

Figure (8.12) The chaotic attractor of a rheopectic fluid at r=40.0, a=0.05, time =60 seconds.
Scale: -100 < X < 100, 0 < Z < 90